László Guczi · András Erdőhelyi *Editors*

Catalysis for Alternative Energy Generation

Catalysis for Alternative Energy Generation

László Guczi • András Erdőhelyi
Editors

Catalysis for Alternative Energy Generation

Editors
László Guczi
Department of Surface and Chemistry
and Catalysis
Institute of Isotopes
Hungarian Academy of Sciences
Budapest, Hungary

András Erdőhelyi
Department of Solid State
and Radiochemistry
University of Szeged
Szeged, Hungary

ISBN 978-1-4614-0343-2 ISBN 978-1-4614-0344-9 (eBook)
DOI 10.1007/978-1-4614-0344-9
Springer New York Heidelberg Dordrecht London

Library of Congress Control Number: 2012935430

Printed on acid-free paper

Springer is part of Springer Science+Business Media (www.springer.com)

Preface

Chemistry without catalysis is like a bell without sound, or a warrior without blade.

Alwin Mittasch

In the twenty-first century, human beings face the exhaustion of fossil energy feedstock. The amount of high quality and easily accessible feedstocks is decreasing, hence the use of heavy and dirty feedstocks must perforce be explored. Poisoned crudes need to be treated in order to remove contaminants such as Nitrogen- and Sulfur-containing molecules and metals. Thus it is imperative to consider alternative sources of energy – such as biomass – for chemicals and for transportation fuels. To underline its importance let me refer to President Bush: *President Bush launches the Hydrogen Fuel Initiative. "Tonight I am proposing $1.2 billion in research funding so that America can lead the world in developing clean, hydrogen-powered automobiles. With a new national commitment, our scientists and engineers will overcome obstacles to taking these cars from laboratory to showroom so that the first car driven by a child born today could be powered by hydrogen, and pollution-free."*

Alternative feedstocks, such as biomass and renewables, are being investigated in biorefineries for the production of biofuels and (bio)chemicals. These feedstocks contain many oxygen-containing molecules, hence they are more or less polar. This poses special problems for the development of catalytic technology to treat such new feedstocks.

Very pure and simple natural feedstocks, such as methane and light alkanes, can also be used as the basis for production of fuels and chemicals. The fundamental problems here are the selective activation of the C–H bond without the formation of excessive amounts of CO_2, hydrogenation of CO_2, or its conversion into other useful materials.

Looking through the possible technologies, it becomes clear that catalysis is the key technology to help solve the problems associated with the use of alternative feedstocks. Traditional catalysts are extremely efficient for pure, apolar oil

feedstocks. Heavy and dirty feedstocks require catalysts for removal and decomposition of poisonous molecules and for removal of heavy metals. Can these processes be combined in one catalyst? This "ideal" catalyst fixes the heavy metals in such a way that they serve as catalytic sites for decomposition and removal of the poisonous molecules. In addition, the catalyst contains the acid sites necessary for cracking and isomerization of long-chain hydrocarbons.

In the case of biomass and renewables, poisoning of the catalyst surface by polar molecules must be avoided. The "ideal" catalyst takes oxygen atoms out of the polar molecules and stores them in its structure in such a way that the catalyst becomes ready to do its job, the conversion of biomass into fuels and basic chemicals.

For methane conversion, catalytic research boils down to "selectivity": selective activation of the C–H bond while avoiding complete burning of methane into carbon dioxide and water.

The ideal catalysts, as described above, do not exist, except for the enzymes that activate methane by insertion of an oxygen atom in the C–H bond. We must rely on

1. The design and construction of improved catalyst materials, which are designed by either combinatorial methods or rational catalyst design, based on theory and advanced characterization methods
2. The intelligent combination of different types of catalysts, making use of the respective strengths of these catalytic materials; all combinations should be allowed: enzyme plus heterogeneous catalyst, homogeneous plus heterogeneous catalyst; and so on;. In this respect, photocatalysis also comes into the picture; and
3. Alternative reaction media in which catalytic and separation technologies are combined. Examples include catalysis in ionic liquids, supercritical conditions. In this way, nonreactive aggregates of molecules can be disentangled into monomolecular entities, which are more susceptible to catalytic attack.

Finally, irrespective of the catalytic process developed, questions will be raised about the sustainability of the catalyst, its impact on the environment, and its impact on climate. The economic, environmental, and social impacts of a process must be evaluated before production can start. Scientists must take these considerations into account in multidisciplinary studies.

Readers of this book will learn about the importance of catalysis in these processes. Introductory chapters discuss catalysis and catalytic processes to handle the broad variety of alternative feedstocks (biomass, methane, very heavy crude, and bitumen) that one can use for the production of transportation fuels and chemicals. The start of the discussion is knowledge of the performance of the catalysts currently on the market and the performance of catalysts in development. Further chapters explore the effect of impurities and poisons in these alternative feedstocks on the performance of existing catalyst materials and propose new challenges for improving these materials. In addition, several routes are designed to approach the "ideal" multifunctional catalyst or the "most appropriate" combination of "ideal" catalytic materials to handle these new feedstocks.

The role of new tools of investigation, in situ spectroscopic observation of catalysts in action, and theory in this process of catalyst development is highlighted. Finally, the socioeconomic implications in using these alternative feedstocks are briefly covered.

Budapest, Hungary — László Guczi
Szeged, Hungary — András Erdőhelyi

Contents

Contributors

Marc Armbrüster Max-Planck-Institut für Chemische Physik fester Stoffe, Dresden, Germany

Chinmoy Baroi Catalysis and Chemical Reaction Engineering Laboratories, Department of Chemical Engineering, University of Saskatchewan, Saskatoon, SK, Canada

Malte Behrens Department of Inorganic Chemistry, Fritz-Haber-Institut der Max-Planck-Gesellschaft, Berlin, Germany

Christina Bock Institute for Chemical Processes and Environmental Technologies, National Research Council of Canada, Ottawa, ON, Canada

Gabriele Centi Department of Industrial Chemistry and Engineering of Materials and CASPE (INSTM Laboratory of Catalysis for Sustainable Production and Energy), University of Messina, Messina, Italy

Jean-Philippe Dacquin Cardiff Catalysis Institute, School of Chemistry, Cardiff University, Cardiff, UK

Ajay K. Dalai Catalysis and Chemical Reaction Engineering Laboratories, Department of Chemical Engineering, University of Saskatchewan, Saskatoon, SK, Canada

Imre Dékány Supramolecular and Nanostructured Materials Research Group of the Hungarian Academy of Sciences, University of Szeged, Szeged, Hungary

Department of Physical Chemistry and Materials Science, University of Szeged, Szeged, Hungary

James A. Dumesic Department of Chemical and Biological Engineering, University of Wisconsin—Madison, Madison, WI, USA

András Erdőhelyi Department of Solid State and Radiochemistry, University of Szeged, Szeged, Hungary

Koichi Eguchi Department of Energy and Hydrocarbon Chemistry, Graduate School of Engineering, Kyoto University, Nishikyo-ku, Kyoto, Japan

Titipong Issariyakul Catalysis and Chemical Reaction Engineering Laboratories, Department of Chemical Engineering, University of Saskatchewan, Saskatoon, SK, Canada

Naoto Kamiuchi Department of Energy and Hydrocarbon Chemistry, Graduate School of Engineering, Kyoto University, Nishikyo-ku, Kyoto, Japan

László Kőrösi Supramolecular and Nanostructured Materials Research Group of the Hungarian Academy of Sciences, University of Szeged, Szeged, Hungary

Paola Lanzafame Department of Industrial Chemistry and Engineering of Materials and CASPE (INSTM Laboratory of Catalysis for Sustainable Production and Energy), University of Messina, Messina, Italy

Adam F. Lee Cardiff Catalysis Institute, School of Chemistry, Cardiff University, Cardiff, UK

Haris Matralis Department of Chemistry, University of Patras, Patras, Greece

Barry MacDougall Institute for Chemical Processes and Environmental Technologies, National Research Council of Canada, Ottawa, ON, Canada

Guido Mul Photocatalytic Synthesis Group, Faculty of Science and Technology, University of Twente, Enschede, The Netherlands

Christina Papadopoulou Department of Chemistry, University of Patras, Patras, Greece

Rita Patakfalvi Supramolecular and Nanostructured Materials Research Group of the Hungarian Academy of Sciences, University of Szeged, Szeged, Hungary

Szilvia Papp Supramolecular and Nanostructured Materials Research Group of the Hungarian Academy of Sciences, University of Szeged, Szeged, Hungary

Siglinda Perathoner Department of Industrial Chemistry and Engineering of Materials and CASPE (INSTM Laboratory of Catalysis for Sustainable Production and Energy), University of Messina, Messina, Italy

Juan Carlos Serrano-Ruiz Department of Chemical and Biological Engineering, University of Wisconsin—Madison, Madison, WI, USA

M. Aulice Scibioh NASA-URC Centre for Advanced Nanoscale Materials, University of Puerto Rico-Rio Piedras, San Juan, PR, USA

National Centre for Catalysis Research (NCCR), Indian Institute of Technology Madras (IITM), Chennai, India

C.-L. Sun Department of Chemical and Materials Engineering, Chang Gung University, TaoYuan, Taiwan

András Tompos Research Center for Natural Sciences, Hungarian Academy of Sciences, Budapest, Hungary

Xenophon Verykios Department of Chemical Engineering, University of Patras, Patras, Greece

B. Viswanathan National Centre for Catalysis Research (NCCR), Indian Institute of Technology Madras (IITM), Chennai, India

Karen Wilson Cardiff Catalysis Institute, School of Chemistry, Cardiff University, Cardiff, UK

Chapter 1
Introduction and General Overview

Gabriele Centi, Paola Lanzafame, and Siglinda Perathoner

Abstract Catalysis plays a key role to address the challenge of sustainable energy and alternative methods to produce energy with respect to using fossil fuels. This field of research and development has given a new impetus to research on catalysis in areas such as producing biofuels, development of advanced electrodes for a number of applications (from new-generation photovoltaic cells to fuel cells), production of renewable H_2 and in a longer-term perspective solar fuels. However, the discussion on the technical aspects on the development of catalysts in these areas should be complemented with considerations on the general economic and social context and related constrains which determine the choice of the research priorities. This introductory chapter was mainly focused on these aspects.

1.1 Introduction and Role of Catalysis

Energy lies at the heart of societal development and, not surprising, a correlation between energy consumption and gross domestic product (GDP) per capita exists [1]. However, market deviations are present from this relationship, due to different climate situations, type of production activities, and especially different styles of life and attitudes/politics in energy saving, as can be noted in Fig. 1.1 (filled symbols) which reports the relationship observed in different countries between GDP and energy use (in kilogram of oil equivalent) per capita. The reported data

G. Centi (✉) • P. Lanzafame • S. Perathoner
Department of Industrial Chemistry and Engineering of Materials and CASPE
(INSTM Laboratory of Catalysis for Sustainable Production and Energy),
University of Messina, Messina, Italy
e-mail: centi@unime.it

L. Guczi and A. Erdőhelyi (eds.), *Catalysis for Alternative Energy Generation*,
DOI 10.1007/978-1-4614-0344-9_1,

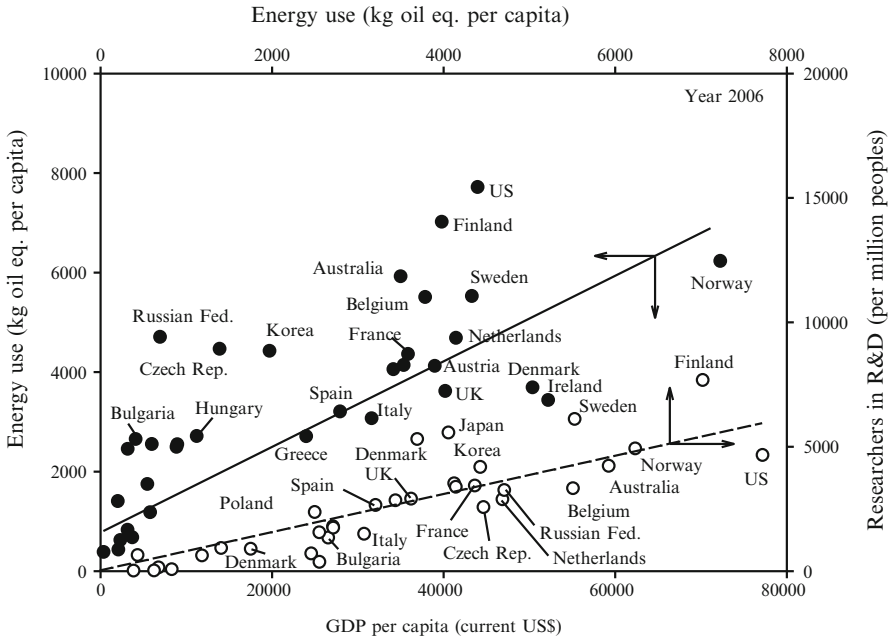

Fig. 1.1 Relationship (year 2006) between GDP and energy use per capita in different countries and energy use per capita and research activities (researchers involved in R&D activities per million persons). *Source*: World Bank and OECD (Organization for Economic Cooperation and Development) National Accounts data files (http://data.worldbank.org)

refer to the year 2006, being the last year for which systematic data are available from the World Bank and OECD (Organization for Economic Cooperation and Development) National Accounts data files. However, no major changes in the trend have been observed in last years.

A better relationship could be observed between energy use per capita and research activities, using as parameter for the latter the number of researchers involved in R&D (research and development) activities per million of persons (Fig. 1.1, open symbols). However, the relationship is inverse of that expected, i.e., that of an increased research effort should correspond to a lowering in the intensity of energy use per capita, because the development in science and technology should allow to introduce new energy-saving processes, devices, and solutions. Therefore, there is a stimulus to invest in R&D in energy-intensive countries due to the increasing cost of energy, but translating the innovation to a decreased intensity of energy use per capita is a slower process. It is thus necessary to accelerate and make more effective the mechanisms by which research innovation becomes a driver for energy-saving politics. In a future sustainable energy scenario, energy use and its impact on the sustainable development of society should thus become the indicators of the sociopolitical context and of the degree in S&T development.

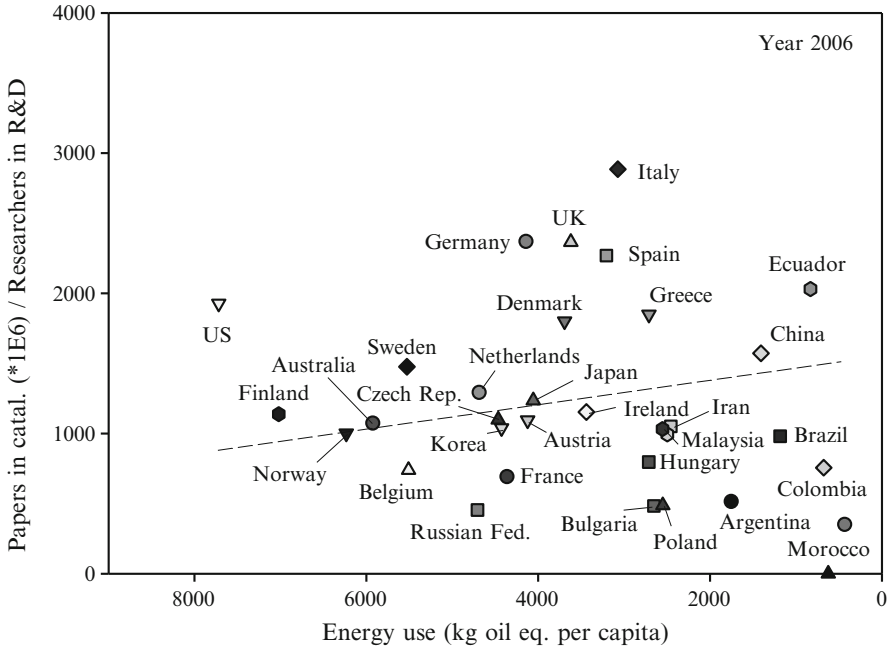

Fig. 1.2 Relationship (year 2006) between energy use per capita in different countries and number of papers ($\times 10^6$) containing the term catalysis as entered (*SciFinder*) normalized by the number of researchers in R&D in that country

In the last few years, the societal pressure has accelerated this transition, and the energy issue is becoming a major pushing element for R&D activities. In fact, the fifth oil price shock created intensive responses throughout the society on the shortage in availability and supply of fossil fuels on which the actual society is based. By coping with the increasing sensitivity on global issues (climate changes and environment protection), it was becoming evident in most of the countries that the present energy supply system needs some fundamental changes [2]. The finite resources of fossil fuels and the high awareness for the climate changes have sensitized the society and hence also the scientific community on the need to push more effort on the development of alternative energy sources.

Catalysis, particularly heterogeneous catalysis, has been over the last century at the center of S&T development to reply to the energy challenges created from the evolving society [3, 4]. Without catalytic processes, it is not possible to produce liquid fuels such as gasoline, diesel, and jet kerosene in the amount and quality necessary for societal mobility, neither to eliminate the pollutants associated to the production and use of these energy vectors, i.e., to allow a sustainable development. Nevertheless, the analysis of the relationship in different countries between numbers of publications containing the term catalysis (normalized to the number of R&D researchers) and energy use per capita (Fig. 1.2) indicates that there is no apparent clear relationship between research efforts in catalysis and intensity of

energy use per capita in that country. The interpretation of this observation is that still limited effort, and only in the few last years, has been dedicated to push research in catalysis toward the development of alternative (non-fossil fuel based) energy sources and vectors.

1.2 Future Sustainable Energy Scenario

The energy fluxes from primary energy sources to utilizations are summarized in Fig. 1.3, which refers to the specific situation for USA in 2009, but can be considered a typical situation in developed countries.

Fossil fuels are currently the primary energy source, with non-fossil fuel sources (including nuclear energy) accounting only 17% of the total energy use. Transport, industrial uses, and residential + commercial utilizations account about one-third each of the energy use. Electricity generation uses about 40% of the primary energy sources. Of the primary energy, only about 42% is used for energy services, while the remaining is waste (rejected) energy typically in the form of low temperature streams. In electricity generation, only about 32% of the input energy is effectively transformed to electrical energy. Similarly, in transport only, about 25% of the input energy is used for services. In industrial, commercial, and residential uses, the fraction of energy services is instead better, about 80%.

Figure 1.3 thus clearly evidences that a primary effort necessary toward a sustainable energy and a reduction of greenhouse gases (GHGs) emissions is to

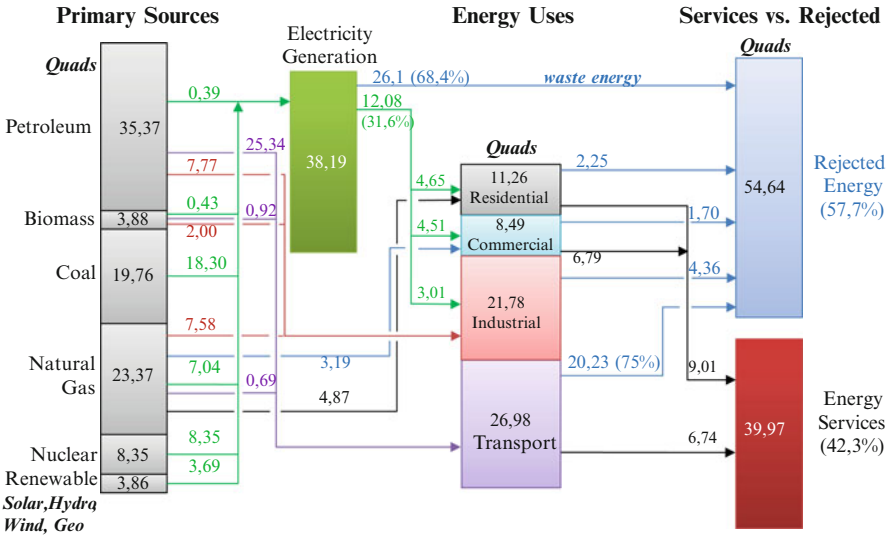

Fig. 1.3 Estimated main energy fluxes (in quads, equal to 1.055×10^{18} J–1.055 EJ) for year 2009 in USA. *Source*: adapted from Lawrence Livermore National Laboratory, USA

reduce the amount of waste energy. Catalysis plays multiple roles toward this objective:

- Allows improving the efficiency of chemical and energy processes, thus reducing their energy intensity.
- It is an enabling factor for many industrial productions of new materials which allow energy saving in their application, for example, foams for improved thermal isolation, new materials to reduce car consumption—lighter materials substituting steel, nanostructured paints to increase the vehicle aerodynamic, tires with reduced friction, etc.
- Many of the advances in the control of the nanostructure and reactivity of catalysts are often at the basis of the latest developments in closely related materials for energy applications, for example, electrodes for fuel cells, new-generation photovoltaic cells, Li-ion batteries and supercapacitors, new materials to recover electrical energy from waste low-temperature streams, etc. [5–9].

Improved materials are critical for energy saving, to enable more energy-efficient processes and more efficient transportation. Next-generation clean and energy-efficient technologies will emerge from new materials made available by emerging nanoscience and nanotechnologies. The development in nanotechnology over the last years allowed passing from the lab scale to the commercial application, and it is thus expect a boost in new materials with properties optimized to sustainable energy technology requirements [10, 11]. Nevertheless, a limit in actual R&D is that a greater emphasis is still given to the synthesis of novel (nano) materials with respect to the understanding of the relationship between their (nano) characteristics and functional behavior [9]. In this sense, catalysis, which core activity is the understanding of the catalyst surface reactivity, should have a leading role in R&D on nanomaterials. However, it is necessary to give more emphasis on the investigation and understanding of fundamental aspects regarding the nanoarchitecture of catalysts and their catalytic performances [12].

In general terms, catalysis and chemical science and technology play multiple key roles in sustainable energy scenarios [2] and particularly in the development of processes and materials for the following areas: (1) energy conversion reactions, (2) energy storage and transport, and (3) energy use efficiency. According to aims of this book, we focus discussion here on an alternative energy generation, i.e., only on the first of the above three areas. However, the other two mentioned areas are equally relevant and components to enable a sustainable energy future.

Another useful graph regarding energy future is reported in Fig. 1.4 which shows the estimations made from the International Energy Agency (IEA, http://www.iea.org) for the world CO_2 emissions up to year 2030 in the case of a reference scenario (business as usual) or in the case of limiting CO_2 stratospheric concentration to 450 ppm [13]. The latter value corresponds to the estimated CO_2 stratospheric concentration necessary to limit the mean world temperature increase to 2°C, as agreed in the last United Nations Climate Change Conference in Copenhagen (December 2009). Figure 1.4 reports also the estimation of the different

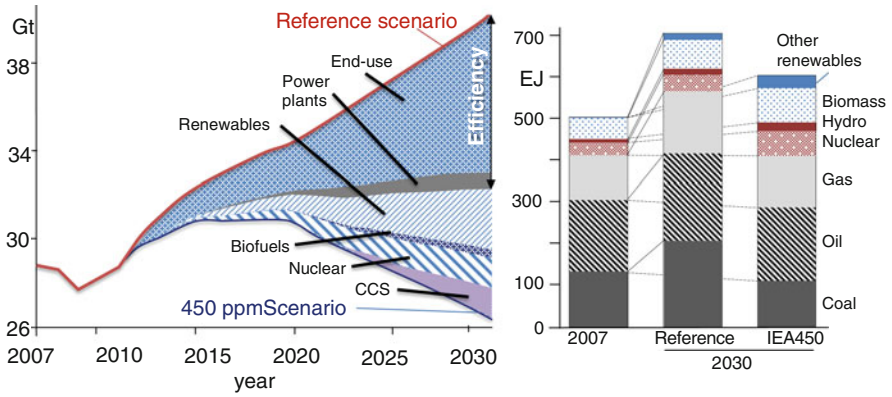

Fig. 1.4 (*Left graph*) World CO_2 emissions up to year 2030 in the case of a reference scenario (business as usual) or in the case of limiting CO_2 stratospheric concentration to 450 ppm. (*Right graph*) Estimated contributions of the different primary energy sources in year 2030 (with respect to year 2007) according to reference and 450 ppm scenarios. *Source*: adapted from International Energy Agency [13]

contributions necessary to meet this 450 ppm target. On the right of Fig. 1.4, the estimated contributions of the different primary energy sources in year 2030 (with respect to year 2007) according to reference and 450 ppm scenarios are also reported.

As previously commented, the major contribution in reducing CO_2 emissions should derive from energy saving (energy efficiency) both in end use and in power plants. However, the 450 ppm target cannot be reached in this IEA scenario without the substantial contribution of renewables (including biofuels), nuclear energy, and carbon capture and sequestration (CCS). We may note that probably, the expansion of the use of nuclear energy is overestimated, but this indicates that the effort in using renewable energy sources should be increased. The contribution of CCS is expected to be relevant after year 2020–2025, but there is an intensified effort to introduce earlier this technology, even if concerns regarding both the safe storage and the transport of CO_2 to long distance (most of the CO_2 emitting sites are far from the storage sites) exist [14, 15]. Assuming valid IEA outlooks, the amount of CO_2 captured by CCS will increase from 102 to 1,410 Mt from year 2020 to 2030. This means that very large amounts of CO_2 will become soon available at zero or even negative value. The possibility of recycling CO_2 to chemicals or fuels, particularly the latter, is thus of increasing interest [16, 17].

However, even in the 450 ppm scenario, the contribution of fossil fuels will remain dominant (about 70% of energy) and nearly unchanged with respect to the actual situation in terms of total energy consumption, with the use of oil and gas slightly increasing in percentage. Therefore, the use of renewable energies should compensate the increase in the energy consumption due to an increased fraction of world population accessing to a higher energy consumption per capita as a consequence of the increased GDP per capita in various countries (particularly in Asia).

The forecasts in a critical area such as that of energy have some obvious limits, but the point indicated from Fig. 1.4 is that still for long time fossil fuels and related energy infrastructure will be the dominating factor in energy scenario. Therefore, in discussing alternative energy generation and the role of catalysis, it is necessary to consider in depth these aspects, because they determine the choice between some alternatives, as discussed later in a more detail.

1.3 Energy Vectors

Another general concept to remark regarding energy is presented in Table 1.1 which overviews the possible energy carriers for different renewable energy resources. While all of them can produce electricity and nearly all of them heat, liquid fuels can be produced essentially only from biomass. A question mark was put on the possibility to produce liquid fuels from solar energy. As discussed later, the use of solar energy to convert CO_2 to liquid fuel is a growing area of research but still at the initial stage of development [18–20].

In order to understand the meaning of this table for a future energy scenario, it is necessary to briefly introduce the concept of energy vector. Actual society is largely based on the use of liquid hydrocarbons derived mainly from the refining of oil as indicated in Fig. 1.3, because energy needs to be distributed and stored. About 43% of the world energy final consumption is associated to oil and derived liquid fuels (gasoline, diesel, jet fuels, gasoil, etc.) [21], while only about 17% is accounted by electrical energy. The latter to be used requires to be connected to the grid, because the actual density of energy storage in batteries is still too low for many energy-intensive applications (see later). In transport, the clear tendency is toward hybrid vehicles more than full electrical ones, except for niche applications. In the future, it will be still necessary to carry onboard energy in a form with sufficiently high energy density and which can be easy refilled. In heavy vehicles (trucks, buses, etc.) or in airplanes, the problem is even more severe. The alternative possibility is to change the engine system by using fuel cells combined with H_2 as energy carrier. This option attracted large interest few years ago but appears less likely today due to many problems: storage of H_2 onboard, large cost of investment in changing to

Table 1.1 Possible energy carrier for different renewable energy resources

	Energy carrier			
Resource	Electricity	Heat	Mechanical energy	Liquid fuel
Biomass	•	•		•
Geothermal	•	•		
Hydro	•	•	•	
Ocean (tidal, wave, thermal)	•	•	•	
Solar	•	•		?
Wind	•		•	

new engines and new energy distribution models, cost of fuel cell production and limited lifetime, etc. [22]. For the transport sector, it is thus not forecasted a fast transition to energy vectors alternative to the liquid fuels actually used.

In the industrial and residential sectors, which account approximately one-third of each of the world energy demand, fossil fuels will also continue to play a dominant role in the future. Storage of energy will be also in these cases a critical aspect, as well as the need of power generation plants able to have a fast response to change in energy demand (sometimes by a factor up to ten). Nuclear energy does not allow a fast change in power output besides other issues, differently from power plants based on fossil fuels. Storage of electrical energy is based currently mainly on the conversion to and back to mechanical energy (water pumped to a higher storage reservoir using the excess base-load capacity; during peak hours, this water can be used for hydro-electric generation), but the efficiency of the storage is limited (<40%).

In conclusion, liquid fuels derived from fossil resources show a competitive advantage in terms of an easier storage and transport. Of the various possible sources of renewable energy (solar, wind, tides, hydro, etc.), only biomass can be converted to liquid fuels, while almost all the others produce electrical energy (Table 1.1). Heat and mechanical energy are instead energy vectors for only local uses. Biomass, however, is quite complex, and producing liquid fuels in a sustainable and economic way is still a challenge, even considering the fast developments in this area [23–26]. As indicated in Fig. 1.4, the forecast contribution of biofuels to future sustainable energy scenarios will be limited, due to the high costs.

Therefore, the further development of a sustainable energy scenario requires finding efficient solutions to store and transporting renewable energy. Being the conversion of electrical to chemical energy still the preferable option, the issue is thus the development of the optimal energy vectors to store and transport renewable energy. This is the base concept of developing solar fuels [18–20, 27, 28]. Solar energy will be the future dominating renewable energy. If the irradiance on only 1% of the Earth's surface could be converted into electric energy with 10% efficiency, it would provide a resource base of 105 TW, for example, ten times the estimated world energy increase by year 2050. By contrast, the estimated amount of energy extractable by wind is about 2–4 TW, by tides about 2–3 TW, by biomass 5–7 TW, and by geothermal energy 3–6 TW [29]. Suitable energy vectors must fulfill a number of requirements:

1. Have both a high energy density by volume and by weight
2. Be easy to store without need of high pressure at room temperature
3. Be of low toxicity and safe in handling, and show limited risks in their distributed (non-technical) use
4. Show a good integration in the actual energy infrastructure without need of new dedicated equipments
5. Have a low impact on the environment in both their production and use

H_2 could be an ideal energy vector [22, 30, 31] by limiting the analysis to the last aspect. Many authors have proposed H_2 as the future energy vector, because it is the ideal clean fuel and may be potentially produced from renewable sources [18, 28–30].

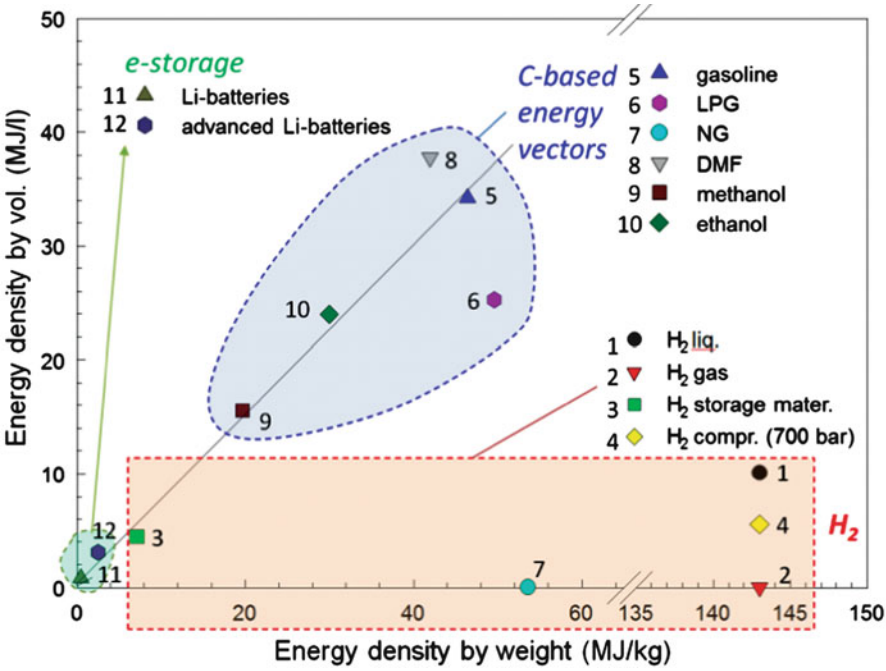

Fig. 1.5 Energy density per weight versus per volume in a series of liquid and gaseous fuels (from fossil sources, or renewables such as ethanol and DMF), H_2 (liquid, gas, compressed at 700 bar, and stored in advanced nanomaterial) and electrical energy (Li batteries, conventional and advanced). *NG* natural gas, *DMF* dimethylfuran, *LPG* liquefied petroleum gas. *Source*: adapted from [35]

"Hydrogen economy" is a popular term to indicate the future for a low- or no-carbon energy future [32, 33], notwithstanding some objections [34]. In fact, the energy density of H_2, even considering future possible developments in storage materials, will be still a main issue for practical large-scale use. Figure 1.5 further strengths this concept by reporting the energy density in a series of liquid fuels (from fossil or renewable sources), H_2 (gas, liquid, compressed or in storage materials), and electrical energy (in conventional or new-generation Li batteries) [35].

Current energy vectors based on liquid fuels are fulfilling all the requirements for suitable energy vectors, except the point (v), particularly regarding the emissions of GHGs, because the available catalytic technologies can effectively minimize the emissions of pollutants produced during the combustion. For a future sustainable energy scenario, it may be thus preferable to find an efficient solution to recycle the CO_2 produced during the combustion to form back fuels using renewable energy instead to develop new energy vectors and a new energy infrastructure. Producing solar fuels via recycling CO_2 is thus a carbon-neutral approach to store and transport solar energy (and of other renewable or non-carbon-based energy sources) which can be well integrated into the current energy infrastructure. We will further discuss this aspect later.

1.4 Biomass Conversion

Previous discussion has pointed out that biofuels are the preferable option on a short–medium term to produce liquid fuels which will still remain a dominating energy carrier for the next two decades, particularly in the transport sector. Various chapters in this book discuss the catalysts and catalytic technologies for biofuel conversion. In addition, several recent reviews have discussed in detail the topic [23–26, 36–38]. The attention is thus focused here on the discussion of the general context and constrains to be considered in evaluating the different possible options and alternatives, aspect not usually discussed but relevant for a correct definition of the research priorities in this area [39].

The transport sector accounts for about one-third of the world energy consumption, which is actually about 500 EJ (around 12,000 MToe) (Fig. 1.4). Although there is the need to decrease the specific energy consumption of the transport sector and thus the CO_2 emissions per kilometer as previously commented, the forecasts (Fig. 1.4) indicate that the introduction of more energy-efficient devices in the transport sector will not compensate the faster expansion in the use of liquid fuels due to the increased number of circulating vehicles in emerging countries (Asia and Latin America). Therefore, the reduction of the carbon footprint of transport for the next two decades will depend mainly on the introduction of fuels deriving from renewable resources such as biomass.

Notwithstanding the fast growing research in this area (it is currently a major research area for catalysis), most of the estimations indicate that the cost of biofuels in the next two decades will be still higher with respect to the cost of fossil fuels, apart from few special cases (mainly bioethanol from sugarcane in Brazil). Therefore, biofuel market will heavily depend in developed countries on the presence of economic subsidies (direct or indirect), putting a number of constrains in evaluating the different possible options and routes in biomass transformation [39].

However, there are several sociopolitical reasons which motivate the production of biofuels and the continuation of subsidies for their production:

– *Moving to a low-carbon footprint society*: Biofuels reduce the carbon footprint of mobility which requires liquid fuels to be integrated into the actual infrastructure (distribution, compatibility with actual fuels and engines, etc.) The alternative is to produce fuels from natural gas or coal (GTL and CTL processes) but which are also more expensive than fuels from oil. The life-cycle assessment (LCA) indicates that the effective contribution of biofuels to the reduction of CO_2 emissions is close to neutral and sometimes negative (depending on the boundary limits of LCA method, if aspects such as land use change effects and soil N_2O emissions are accounted, etc.) [40], and besides, it considerably depends on the type of raw materials and biofuel [38]. On the average, however, the use of biofuels leads to a reduction of carbon footprint of mobility with respect to fossil fuels.
– *Increasing energy security*: Reduction of dependence on fossil fuels is a main general value for the energy economy and geopolitical strategies. The possibility

of using biomass wastes is a further relevant incentive for the double benefit of reducing their environmental impact and an efficient valorization of unused resources.

– *Social and employment impact and promotion of rural areas*: The benefits for local agriculture and land preservation, with the creation of energy districts where biomass is used more efficiently through integration between the production of food, energy, and raw materials for chemical industry, are significant opportunities for creating and maintaining employment and improving rural quality of life.

Various aspects derive from above comments, but remarking that the following considerations are valid in general terms and can be different by case-to-case. The market for biofuels will depend on the future on subsidies, and thus, the growth will depend on the direct or indirect public financial support (subsidies). Often, it is considered that biofuel market will grow constantly, being an economic option, but if instead it will be true that the biofuel sector will be not economic in the absence of external financial support, it should be considered a short–medium-term solution (for about the next 20 years) and with limited market expansion, not going beyond about 10–15% of the market share of fuels for the transport sector (this accounts for about one-third of the global energy consumption). This is well consistent with the forecasts reported in Fig. 1.4. Many researchers and policymakers now agree that the contribution of biofuels in future energy scenarios will be limited and that the strategies and technologies to produce biofuels should be reconsidered from this perspective. Some of the possible options, such as thermochemical routes, require very large investments and long-term amortization costs. In an uncertain biofuel scenario as that outlined above, which will still depend on subsidies, large investment costs are a negative factor, also in terms of sustainability, because they will considerably limit the rate of introduction of new technologies [41].

In addition, the growing idea of agro-energy districts, as a pushing factor for rural development, also goes in the direction of competitive technologies on small–medium size, which are flexible in handling a variety of local raw materials (e.g., biomass waste, energy crops, and wood residues), but can be distributed over the territory and limit the (energy) cost of transporting biomass. For a modern society, it is very important to create the conditions for a true competition to avoid monopolization of the market, which will increase the costs. It is thus important for biofuels to incentivize the conditions and solutions favoring a large number of investors. In order words, solutions should be promoted (between the many possible) which can be efficient on a small–medium scale and which do not require very large investments.

The field of biofuels, due to the many relevant socioeconomic implications, cannot be thus evaluated with the conventional techno-economic parameters, and the societal implications and return in terms of sustainability and competitiveness have to be included. This is the perspective to use in discussing the second-generation biofuels and the role of catalysis/catalytic technologies.

We have not discussed here the ecoimpact of biofuels in order to focus the discussion. However, it is necessary to briefly mention that various environmental impact categories, such as abiotic depletion, ozone layer depletion, human toxicity and aquatic ecotoxicity, acidification, and eutrophication, have to be considered (e.g., through LCA analysis) in the comparison of the different paths to biofuels. The use of biofuels has a negative impact on acidification and eutrophication with respect to fossil fuels. Acidification is due to biomass production (related to fertilizers) and biomass combustion for heat and power production to sustain the higher energy demand. Eutrophication is mostly given by fertilization. Emissions induced by fertilizer application also influence other environmental categories, like terrestrial and freshwater ecotoxicity, human toxicity, and others. Therefore, the ecosocial dimension (in terms of sustainability and impact on the ecosystem) is also an important component for the selection of the optimal strategies for bioenergy and bioeconomy development and next-generation biofuels. However, very few studies have tried to combine the technical aspects to these other aspects [38]. Due to the very specific characteristics of biofuel area, these components cannot be considered separately and both concur in determining the sustainable paths for a future energy scenario.

There are other relevant aspects to consider in evaluating how to utilize the biomass in a sustainable perspective. Integration into the existing energy infrastructure is an important aspect, not only economic. In fact, the introduction of biofuels requiring major changes in the distribution system or engines implies large investments which prevent or considerably limit the possibility to be successful, given the actual economic situation and large uncertainty in the future market for biofuels. Being the introduction of biofuels, a critical element toward a sustainable mobility, to invest in R&D in areas having limited possibilities of success (from a more global view and not limiting to technical considerations), implies a negative impact on sustainability.

There are many other aspects necessary to take into account to evaluate the preferable paths in biomass conversion and type of biofuel components:

- *Commercial characteristics and compatibility with actual fuels*: There are many important parameters to consider for commercial use, from specific properties (viscosity, flash and pour point, water and sediment content, carbon residue and ash, distillation temperature range, specific gravity, heating value, carbon–hydrogen, and carbon–oxygen content) to fuel properties (octane or cetane number, boiling and solidification point, lubrication properties, smoke properties, etc.). Several of the proposed biofuels do not meet all these requirements.
- *Energy density and CO_2 emissions per kilometer*: Hydrocarbons have a higher energy density than oxygenated compounds, and thus using flex fuel, the kilometer per liter of fuel decreases of about 30% (for E85), thus going in the opposite direction of reducing CO_2 emissions per kilometer. From this perspective, diesel engines allow a reduction up to 30% in CO_2 emissions per kilometer with respect to gasoline, and this is one of the motivations why in Europe >60%

Table 1.2 Life-cycle GHG emission reduction for different time horizons. Adapted from [42]

Fuel pathway	30 years (%)	100 years (%)
Corn ethanol		
– Natural gas dry mill	+5	−16
– Optimized natural gas dry mill[a]	−18	−39
– Coal dry mill	+34	+13
– Biomass dry mill	−18	−39
– Biomass dry mill with combined heat and power	−26	−47
Sugarcane ethanol	−26	−44
Switchgrass ethanol	−124	−128
Corn stover ethanol	−116	−115
Soy-based biodiesel	+4	−22
Waste grease biodiesel	−80	−80

[a]Plants produce wet distillers grain coproduct and include the following technologies: combined heat and power (CHP), fractionation, membrane separation, and raw starch hydrolysis

of new light vehicles is based on diesel engines. However, still limited research is present on second-generation biodiesel.

- *Integration with chemical production*: Producing biofuels from platform molecules which may be converted to either chemicals (e.g., monomers for polymer) or biofuels gives to biorefinery the flexibility to fast adapt to a changing market. One of the elements of success of bioethanol in Brazil was the possibility to switch the production from bioethanol to sugar, following better the market and minimizing the risks.
- *C-efficiency*: A higher C-efficiency indicates lower CO_2 emissions in the process of production of biofuels, and thus includes direct CO_2 emissions in the process (e.g., during fermentation two ethanol molecules and two CO_2 molecules are formed from a glucose unit) and indirect CO_2 emissions, due to the need of H_2 in some production steps (H_2 could be produced either from biomass or from fossil fuels) and energy input in the biofuel production process.

An interesting result regarding the last aspect is presented in Table 1.2 [42], based on a very recent study made by US Environmental Protection Agency (EPA) of the life-cycle GHG emissions from increased renewable fuels use. Life-cycle GHG emissions are the aggregate quantity of GHGs related to the full fuel cycle, including all stages of fuel and feedstock production and distribution, from feedstock generation and extraction through distribution and delivery and use of the finished fuel. The life-cycle GHG emissions of the renewable fuel are compared to the life-cycle GHG emissions for gasoline or diesel.

Biofuel-induced land use change can produce significant near-term GHG emissions, which can be paid back over subsequent years. Therefore, the time horizons over which emissions are analyzed (near-term vs. longer-term emissions) are critical factors. EPA study analyzed two options: a 30- and a 100-year time period for assessing future GHG emissions impacts.

Table 1.2 evidences some interesting aspects. The first point is that on a short–medium time horizon (30 years), the use of first-generation biofuels (corn ethanol and soy-based biodiesel) leads to an increase (plus value) or very moderate decrease (depending on technology) in GHG emissions. Only on a longer time horizon all fuel pathways (except coal dry mill) lead to decreased GHG emissions. The use of second-generation bioethanol processes (switchgrass or corn stover ethanol) or the use of waste raw materials (waste grease biodiesel) leads instead to a more relevant effect on GHG emissions, which do not depend on the time horizon.

In a similar study promoted from the European Commission [43], but using a different assessment methodology and evaluating the global impact of the use of biofuels, it was also found that on the average, about 30 years are necessary after land use change before that biofuels can lead to a saving in CO_2 emissions. These results are based on the model developed by EU Joint Research Centre, but different results were found using different literature models, although these models have a more limited approach. The understanding of the real impact on GHG emissions of the use of biofuels is thus still a matter of question, but several concerns are raised on the effective benefits. It is thus necessary to consider biofuels as a transitional solution and select the preferable pathways accordingly.

Optimal integration with the fuels currently produced from fossil resources is thus a critical factor. From this perspective, biomass-based hydrocarbon fuels are essentially the same (also energetically, differently from the case of bioethanol) as those currently derived from petroleum, and thus, it will be not necessary to modify existing infrastructure (e.g., pipelines, engines), and hydrocarbon biorefining processes can be tied into the fuel production systems of existing petroleum refineries [37]. Hydrocarbons produced from biomass are immiscible in water. They could be easier recovered from aqueous biomass processes and with less energy-intensive separation processes with respect to more polar molecules such as oxygenated products. On the other hand, the production of hydrocarbons requires an extensive use of H_2 [externally produced or produced in situ through aqueous phase reforming (APR) processes]. Therefore, C-efficiency is low. The possibility of integration with chemical production is not efficient, because after defunctionalization by oxygen removal a functionalization by oxygen insertion could be then necessary. From this perspective, it would be thus better to select a pathway of transformation (e.g., producing platform molecules such as furfurals from selective deconstruction of the cellulosic components of lignocellulose raw materials) which can be easily tuned toward the production of fuels and chemicals [39]. It is thus evident that the preferable route has been not yet identified and that it is necessary to consider all the aspects of this complex problematic.

Catalysis has a pivotal role in this complex chemistry. We could note, however, that several of the catalytic reactions involved in producing biofuels involve in one or more steps hydrogenation or related reactions (hydrogenolysis, H-transfer, etc.). Not surprising, most of the catalysts used in biomass conversion are based on noble metals, but this could be a limit for the expansion of the sector, due to the shortage of noble metals. It is thus an R&D priority to develop novel active and stable catalysts for these reactions not containing noble metals.

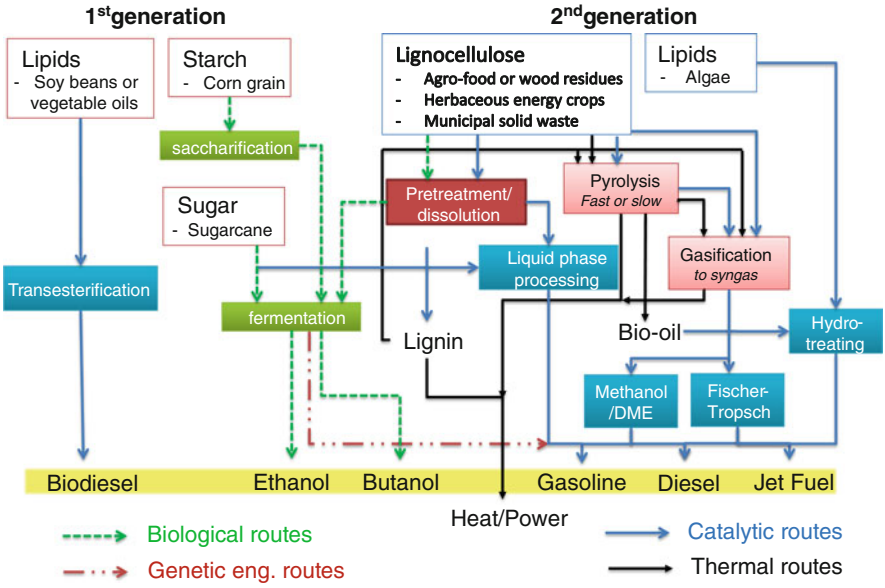

Fig. 1.6 Main routes to biofuels. *Source*: adapted from [44]

Figure 1.6 reports a schematic overview of the different pathways to produce liquid fuels from biomass [44]. Sugar and starch are used to produce bioethanol by fermentation and saccharification (in the case of starch). Various vegetable oils could be used to prepare biodiesel by catalytic transesterification or "green diesel" by hydrotreating (UOP/Eni Ecofining™ process, Neste Oil NExBTL Renewable Diesel and Petrobras H-Bio process). The same processes can be adapted to upgrade algal bio-oils.

Lignocellulosic feedstocks can be converted by three main routes: (1) thermochemical, (2) biochemical, and (3) chemo-catalytic. The thermochemical approach consists in the pyrolytic treatment processes of biomass to produce solid, liquid, or gaseous products that can be subsequently upgraded to fuels (synthetic biofuels). Depending on the reaction conditions, different types of pyrolysis and/or gasification are used. These primary treatment methods produce intermediates that should be first purified, often in multiple steps, and then further upgraded to fuels through catalytic treatments, for example, hydroprocessing, cracking, steam reforming, methanation, Fischer–Tropsch (FT), etc.

Biochemical routes are the most used currently, but reaction rates are lower with respect to catalytic routes, thus with the need to operate with larger volumes and more diluted solutions. Using novel catalytic processes would thus reduce fixed costs, produce lower volumes of wastes, reduce energy intensity of the process, and simplify separation. The amount of water needed for processing hydrocarbon fuels from biomass can be greatly reduced, compared with the dilute sugar solutions to which enzymes are constrained. This is because heterogeneous

Table 1.3 Summary of biofuel generations

First generation	Second generation	Third generation	Fourth generation
Biofuels produced from food crop	Biofuels produced from non-food crop	Genetically modified carbon-neutral crop	Genetically modified carbon-negative crops

catalysts work well in concentrated water solutions or alternative solvents (e.g., ionic liquids) Furthermore, heterogeneous catalysts allow continuous operations reducing costs of separation with respect to biocatalysts. The elimination of energy-intensive distillation, the higher reaction rates, and the much smaller process footprints can also lead to lower biofuel costs than those of currently available biological pathways for producing cellulosic ethanol. In other words, the increase of sustainability of biofuel productions means to develop improved processes using solid catalysts.

In the chemical or chemo-catalytic approach, the cellulosic biomass undergoes catalytic hydrolysis, using acids either in aqueous solution (commercial method, e.g., using diluted sulfuric acid) or heterogeneous phase using solid catalysts or ionic liquids. Chemo-catalytic routes are then necessary for the conversion of the intermediate platform molecules to synthetic fuels, bio-H_2, or chemicals. Various chapters in this book will discuss in detail these aspects and the role of catalysis in these reactions.

Being sometimes a disagreement about the classification of the various generations of biofuels, it is useful to make some final comments regarding these aspects. According to IEA Bioenergy Task 39 (2009):

- ****First-generation biofuels* are those which are on the market in considerable amounts today. Typical first-generation biofuels are sugarcane ethanol, starch-based or "corn" ethanol, biodiesel, and pure plant oil (PPO). The feedstock for producing first-generation biofuels either consists of sugar, starch, and oil-bearing crops or animal fats that in most cases can also be used as food and feed or consists of food residues.
- *Second-generation biofuels* are those produced from cellulose, hemicellulose, or lignin. The technologies are mainly in a pilot or demonstration stage and in few cases at a semicommercial scale (bioethanol from some lignocellulosic sources) and will be commercial within the next 10 years. Second-generation biofuel can either be blended with petroleum-based fuels combusted in existing internal combustion engines and distributed through existing infrastructure or is dedicated for the use in slightly adapted vehicles with internal combustion engines (e.g., vehicles for DME). Examples of second-generation biofuels are cellulosic ethanol and Fischer–Tropsch fuels.
- *Third- or fourth-generation biofuels* refer to the approaches under investigation with a time horizon above 10 years for the application. A distinction sometimes used (but not always accepted) refers to the use of carbon neutral or negative crops (or other biomass) (Table 1.3). Algal oil is often considered third-generation biofuels.

The *first-generation biofuels* include:

- *Bioalcohols*: These are alcohols produced by the use of enzymes and microorganisms through the process of fermentation of starches and sugar. Ethanol is the most common type of bioalcohol, whereas butanol and propanol are some of the lesser known ones. Already on a large scale are bioethanol from sugarcane (Brazil) and from corn (USA).
- *Biodiesel by transesterification of vegetable oils*: With methanol using homogeneous catalysts such as sodium hydroxide, mainly used in Europe and in countries such as Argentina or Malaysia exporting diesel to Europe. The use of heterogeneous catalysts instead of homogeneous is still quite limited and can be considered as *advanced first-generation biofuels*.
- *Vegetable oil*: Vegetable oil can even be used in most of the old diesel engines but only in warm atmosphere. In most of the countries, vegetable oil is mainly used for the production of biodiesel (see above).

Biodiesel can be produced by a different process from vegetable oils (and animal fats as well) by hydroprocessing (UOP/Eni Ecofining™ process, Neste Oil NExBTL Renewable Diesel and Petrobras H-Bio process). These are often considered second generation, but they are already a semicommercial stage (particularly the Neste Oil) and use sources such as vegetable oil in competition with food. The limit in using more extensively these processes is mainly related to the cost of vegetable oil and H_2 (usually not deriving from biosources). They should be thus more properly considered as *advanced first-generation biofuels*.

Another question regards *biogas*, produced after the anaerobic digestion of the organic materials. Biogas can also be produced with the biodegradation of waste materials which are fed into anaerobic digesters yielding the biogas. This is also a conventional technique largely used worldwide, and can be considered as *advanced first-generation biofuels*, even though several consider bio-SNG (substitute natural gas) as second-generation biofuels, because it uses waste biomass.

Finally, the processes of combined process of gasification, combustion, and pyrolysis of biomass to produce syngas (CO/H_2 mixtures) and the conversion of the syngas to oxygenated (biomethanol or bio-DME [CH_3OCH_3]) or hydrocarbons via Fischer–Tropsch are usually considered second-generation biofuels (see below) but are essentially based on known and available technologies. Also these processes could be considered probably as *advanced first-generation biofuels*, even though they are based on raw materials typical for second-generation biofuels.

According to a UN report on biofuels, "*second-generation fuels* are made from ligno-cellulosic biomass feedstock using advanced technical processes." Lignocellulosic sources include "woody" and "carbonous" materials that do not compete with food production, such as leaves, tree bark, straw, or woodchips. Waste biomass, deriving from agro-food production and part of the solid municipal waste, is also a valuable source. Second-generation biofuels are considered:

- *Cellulosic bioethanol*, by advanced pretreatment, enzymatic hydrolysis and fermentation technologies.

- *Hydrocarbons or additives for diesel, gasoline and jet fuel* by catalytic transformation of lignocellulosic sources. Heterogeneous or a combination of heterogeneous and biocatalytic transformation are used in these processes.
- *Synthetic biofuels via thermochemical routes*, in the various possible alternative: (1) biomass to liquids (BTL) via gasification and synthesis, (2) Fischer–Tropsch (FT) diesel synthetic diesel, (3) biomethanol, (4) heavier alcohols (butanol and mixed), and (5) dimethyl ether (DME). Note the comment above.
- *Substitute natural gas* (*SNG*) via gasification and synthesis, i.e., an alternative process to bio-SNG via anaerobic fermentation.
- *Biohydrogen*, via gasification (through syngas and consecutive WGS) or by catalytic synthesis (catalytic transformation in liquid phase—APR—or gas phase conversion of byproducts of biomass conversion, such as glycerol). Several concerns regard the economicity and GHG impact of producing H_2 with this approach. More advanced routes for bio-H_2, such as biological processes, using concentrated solar energy, and through semiconductors (water splitting or photoelectrolysis), should be instead considered third or fourth generation because they have an estimated time of application higher than 10–15 years.

In the longer term, many envisage biofuels being made from materials that are not even dependent on arable land, such as algal materials growing in water. Biofuels from algae or microalgae, however, are typically considered to be commercial after more than 10 years and are considered for this reason third generation. The use of solar energy (concentrated solar panels) to convert biomass to fuels is also considered third-generation processes. The method for the catalytic deconstruction and defunctionalization of lignin to selectively produce chemicals and fuels also belong to this category.

Fourth-generation biofuels are those at a very early stage of development and thus with a long-term (>15–20 years) perspective of application. Some fourth-generation technology pathways include solar to fuel and genetic manipulation of organisms to produce directly hydrocarbons or alcohols. Examples are the production of isobutanol and other long-chain alcohols using non-natural metabolic engineering approach (e.g., UCLA/Mitsubishi Chem.) or the direct production of isobutene (Global Bioenergies) also creating an artificial metabolic pathway.

1.5 Nanostructured Electrodes

The need to improve the sustainability and efficiency of the production, storage, and use of energy has greatly pushed the research interest on the development of new improved electrode with advanced nanoarchitecture [3–9]. There are several key technological areas of the energy sector, which require a better design of the electrode nanostructure to overcome current limits and/or move to new levels of their performances:

- *Reversible chemical to electrical energy conversion*: Low- and high-temperature fuel cells and advanced electrolysis

- *Solar to electrical or chemical energy conversion*: Third-generation photovoltaic cells (thin films and Grätzel type), water photoelectrolysis, photoelectrochemical solar cells, and PEC devices for the conversion of CO_2 to fuels
- *Thermal to electrical energy conversion*: Thermoelectric devices
- *Electrical energy storage*: Advanced Li batteries and supercapacitors

In all these electrodes, the common problem is how to control/optimize the mass and charge transport (i.e., electronic and ionic mobility), the electron-transfer kinetics in multiphase boundaries, and the modifications on these processes that occur upon application of a potential between the electrodes. Many aspects have to be simultaneously optimized in these devices. The electrodes of polymer electrolyte membrane (PEM) fuel cells may be cited as an example. The following aspects have to be optimized at the same time:

- The three-phase contact between the proton-conducting medium, the electron-transporting carbon substrate, and the gas phase
- The rate of transport of protons, electrons and reactants (H_2 at the anode and O_2 at the cathode), and products (H_2O at the cathode)
- The surface processes at the electrocatalytic sites (i.e., Pt-based nanoparticles) as well as their changes which occur upon charging the nanoparticles during electrochemical operations (application of a voltage or current between the electrodes)

In batteries, it is also necessary to coordinate mass transport, charge transport (electronic and ionic mobility), and electron-transfer kinetics in order to store or release energy. A poor charge-carrier mobility and electron-transfer to adsorbates limit the efficiency of energy conversion in TiO_2-based materials for water photoelectrolysis, because not only the rate of charge recombination increases but also that of surface quenching effects. Therefore, optimization of the performances requires the ability to control a complex reaction environment, where many kinetic aspects simultaneously concur in determining the performances. The parallel with catalytic reactions is well evident, and not surprising, there are very common aspects in the design of advanced electrodes and catalysts [9].

All these aspects are thus closely related to those encountered in the design of nanostructured catalysts, and the boundary between electrocatalysis and electrochemical effects in these materials is often ill-defined. For these reasons, there is an increasing R&D interest of catalysis on these devices and materials. Various chapters in this book will discuss in details these aspects.

Many of the controlling aspects are size dependent, and thus, the area of devices for energy conversion and storage has naturally dedicated large attention to prepare nanostructured electrodes. These materials for energy harvesting, conversion, and storage show an improvement of the performances with respect to micrometric-sized materials not only due to the increased surface-to-volume ratio but also due to "true size effects" related to a change in material properties when going to nanometric size.

Not only the nanodimension would be relevant, but critical is also the nanoarchitecture of these materials. There is a design problem related to the optimal compromise between nanosize, nanoarchitecture, robustness and stability, and performances per unit weight or volume, as well as to produce the electrode with cost-effective and scalable methods. The concept of hierarchical organized materials is a useful approach to reach the above objectives with the development of a multilevel 3D organization based on a host macrostructure, which allows the right tridimensional organization necessary for a fast mass transport, for example. On this host macrostructure, a secondary guest micro- and/or nanoscale substructure is built in order to take advantage of the properties of nanometer-sized building blocks and micron-sized assemblies. However, often, the studies on hierarchical-organized catalysts and electrodes are focusing attention on the micro- and mesoscale only, while many properties depend on the nanoscale organization and structure. This is the area on which it is necessary to focus future research attention.

Many advanced methods could be used to prepare tailored hierarchical organized structures for electrodes. Ordered metal nanostructures with hierarchical porosity can be prepared using colloidal crystals (or artificial opals), i.e., an ordered array of silica or polymer microspheres, as template on which the metal particles are deposited. The removal of the template leads to an ordered metal nanostructure. The synthesis of replica mesostructures by nanocasting could be considered an extension of the concept of template synthesis. Nanocasting [45] by using highly ordered mesoporous silica as a template has brought forward incredible possibilities in preparation of novel mesostructured materials with controlled nanostructures, which use is fast extending in the field of catalysis and advanced electrodes. The nanocasting method can be used for preparation of a variety of mesostructured and mesoporous materials, including mesostructured metal and semiconductor nanowires.

The use of self-assembling methods is also of growing interest. The approach is based on the synthesis of small-size particle units using the various available physicochemical methods, such as colloidal, solgel, and micelle methods as well as other wet or gas phase procedures. These nanounits may be then organized in 2D and 3D superstructures by self- or directed-assembling, seeded or field-induced growth, epitaxial growth, or other nanostructuring procedures. An interesting area in fast development is also that of assisting the self-assembling (in particular, to avoid a fractal-type growth) by an electrical field. An example of these electrochemical methods is the anodic oxidation. The electrical field created at the interface between the electrode and electrolyte is a powerful factor for orientation of nanostructure growth, as shown for titania (TiO_2) electrodes [46–48].

There are several other methods to prepare nanotailored materials for energy applications. The above discussion has given a glimpse of the possibilities. This is a very fast emerging R&D area with high relevance to produce new sustainable solutions for energy. Further aspects will be presented in the following chapters.

1.6 Going to Solar Fuels

Previous sections have already clarified that in a long-term perspective, solar energy should become a major source of renewable energy but also that the problem exists to convert solar to chemical energy in order to facilitate storage and transport of energy. Producing renewable electrical energy using photovoltaic (PV) cells is attractive, and valuable options are in fast expansion, but this is only part of the energy problem. Current methods to store electrical energy are not very efficient, and in general, a critical issue is still the storage of electrical energy, notwithstanding the R&D progresses in nanomaterials for these applications. Therefore, the conversion of solar to chemical energy is a necessary integration to current solar options for storing and transporting solar energy.

PV cells (or other renewable electrical energy sources or even nuclear energy) may be integrated with water electrolyzers to produce H_2 to be used then in PEM fuel cells to produce back electrical energy [49]. By matching the voltage and maximum power output of the PV device to the operating voltage of PEM electrolyzers, it is possible to reach efficiencies to 10–12%, with respect to 2–6% obtained by simple coupling of the two devices [50]. H_2 produced in this way has still a cost higher than H_2 from fossil fuels, for example, by methane steam reforming.

The DoE Hydrogen Program objective for distributed production of hydrogen from water electrolysis is \$3.70/gge (gallons of gasoline equivalent) by 2012. Current best processes for water electrolysis have an efficiency of 50–80%, so that 1 kg of hydrogen requires 50–80 kWh of electricity. Recent cost estimates [51] reported that on-site natural gas reformation could lead to a range of \$8–\$10/kg and on-site electrolysis could lead to \$10–\$13/kg hydrogen cost, i.e., not achieving the \$4/gge cost target (for H_2 one gge is 0.997 kg). The cost is highly depending on the cost of electrical energy. Considering that actual cost of production of electrical energy by PV cells (or other renewable energy sources) is about 2–4 times higher than the average electrical energy production cost (the cost varies considerably during peak hours), it is possible to derive that H_2 production cost by PV-PEM combination is about 6–8 times higher than that from fossil fuels, but this value would considerably depend on a number of factors, such as production capacity, efficiency of PV cell and solar irradiation, and fossil fuel cost.

There are other ways to produce renewable H_2 by (1) biological methods (using cyanobacteria or green algae), (2) photothermal water dissociation (assisted by redox metal oxides), and (3) photocatalysis/photoelectrolysis and/or photoelectrocatalytic approaches [18, 19]. It could be also produced by photoreforming of waste organic aqueous streams or by APR, as discussed in a more detail in the following chapters. Although it is difficult to make precise cost estimations in these cases, being data still too limited, in general, all these methods are more expensive in producing H_2 than the PV-PEM combination. In addition, in modern electrolyzers, H_2 is produced under pressure, while essentially at atmospheric pressure in the other cases. There is thus an additional cost of compressing H_2.

A limit in the approach of using H_2 to store renewable energy, and thus generally of the "hydrogen economy" approach, is the issue of efficient H_2 storage. Being hydrogen a gas, the density per volume is low. It is thus necessary either to liquefy H_2 (however, this requires very low temperatures, about −250°C at one atmosphere) or to use extremely high pressures. An intense research has been made on H_2-storage materials (metal hydrides, amine borane complexes, MOF, and other nanostructured materials) [22, 52, 53], but the prospects to reach the necessary densities appear now remote. Therefore, the use of alternative energy vectors to H_2 is now of increasing interest. However, if the renewable hydrogen is used directly for further chemical syntheses (e.g., converting CO_2 to methanol as discussed later), the issue of storage of H_2 is not critical.

Therefore, exists the interesting opportunity of addressing the issue of GHG by converting back CO_2 to liquid fuels which can be easy stored/transported and well integrate into the existing energy infrastructure, and use these C-based energy vectors as a convenient and sustainable way to store and distribute solar energy, i.e., develop new solar fuel solutions [35].

Different routes in converting CO_2 back to fuels are possible [16]. The most investigated area is the hydrogenation of CO_2 to form oxygenates and/or hydrocarbons. Methanol synthesis from CO_2 and H_2 has been investigated up to pilot-plant stage with promising results. The alternative possibility is the production of DME, a clean-burning fuel that is a potential diesel substitute. Ethanol formation, either directly or via methanol homologation, or the conversion of CO_2 to formic acid is also a potentially interesting route. Methanol, ethanol, and formic acid may be used as feedstock in fuel cells, providing a route to store energy from CO_2 and then produce electricity. Alcohols are in principle preferable over hydrocarbons because their synthesis requires less hydrogen per unit of product, but their energy density is lower with respect to (liquid) hydrocarbons.

While the stage of development of solar fuels is definitively less advanced with respect to solar to electrical energy conversion, the latter is only part of the future sustainable energy scenario. There is thus the urgent need to invest in R&D on solar fuels.

1.7 Perspectives

This introductory chapter has discusses some of the technical, economic, and social aspects of alternative energy generation and the related problems of energy and climate. The conclusions can be summarized as follows:

1. Still for a long time, fossil fuels and related energy infrastructure will be the dominating factor of energy scenario. The amount of effective resources of fossil fuels is still uncertain, depending on many factors, but many experts indicate that the reserves are enough to guarantee a smooth transition, i.e., fossil fuels will be still the dominating energy for the next 30–50 years. This does not imply that it is

not necessary to accelerate the transition to renewable energy, due to GHG emissions, geopolitical motivations, energy security, etc.

The key concept relevant for catalysis is that it is necessary to develop technical solutions which smoothly integrate into this scenario and thus minimize the investment necessary for energy infrastructure. This has many consequences in terms of choice of the catalytic technologies.

2. To decrease the CO_2 stratospheric concentration to acceptable level (450 ppm), the increasing energy efficiency has the dominant role. The use of nuclear and renewable energy, CCS technology, has also significance. Limiting CO_2 emissions in a world where there is a very fast growing fraction of the population accessing to a massive use of energy (the standard in "developed" countries, Fig. 1.1) requires an effort which we are still underestimating.

   It is thus necessary to have a double strategy, on a short- and medium-long term. On short terms, the key words are energy saving (thus improving energy efficiency) and store or reuse CO_2, together with increasing the share of non-fossil fuel-based energy (nuclear and biomass). The investments required and many other constrains (including social acceptance) suggest that these energy sources will have a share not higher than 20–25% in the next two decades (Fig. 1.4). Also, this aspect has consequences on catalysis because on a short term the effort should be in applying knowledge on (catalytic) nanomaterials to develop:

   - *Energy-efficient processes* (large-scale processes such as steam reforming and olefin production) have a poor energy efficiency—only about 60% of the energy is incorporated in the final product, and in general, attention is given to aspects such as atom economy instead that to *energy economy*.
   - *Energy-saving materials* (putting at the core of research aspects such as intrinsic energy content of the materials, i.e., including the energy for its production, disposal, reuse, etc.) or the capacity of the materials to save energy (lighter materials for mobility, e.g., producing better carbon nanotubes for nanocomposite, and high-performance nanofoams for thermal insulation).

     At the same time, there is the need to integrate "conventional" fossil fuel reserves with less conventional or unused reserves (strained natural gas, coal, oil shale, sand, etc.). It is necessary also to create a novel chemistry to transform and upgrade these resources.

3. The biofuels are not expected to have a market share of fuels for the transport sector more than 10–15%, but nevertheless, they have a relevant environmental, energy security, and rural employment impact. Transforming biomass is complex and costly, and without subsidies in a world which will still have enough fossil fuel resources for the next 20–30 years (forecasts indicate a stabilization of oil barrel to less than 120$), they will be not competitive. It is thus predicted that they will not grow more than about 10–15%, although different opinions exist on this question. However, after the much more optimistic forecasts of some year ago, there is a general revision of the estimations. In order to favor the market penetration of biofuels, which present advantages in terms of GHG impact with

respect to fossil fuels even if less relevant as often considered, it is necessary to realize pathways of transformation which:

- Minimize as much as possible the number of steps and the environmental impact (here the role of catalysis as enabler to reduce the steps of the transformation but the necessity to realize also solutions which make possible the simultaneous reaction-separation, e.g., by joining catalysis and membrane technologies)
- Make possible flexible operations on a variety of biomass sources available on a regional basis
- Enable the integration of the production of fuels and chemicals through common platform molecules and flexible technologies
- Develop the concept of small-scale specialized (few products) biorefineries which require low investment and well integrate on regional agro-districts

4. On the longer-term perspective (>15–20 years), the solar energy will become the major source of renewable energy. There is a need to invest in R&D on solar fuels, for example, to convert CO_2 back to liquid fuel using solar H_2. Solar is definitively the end target to enable a renewable energy but requires developing effective methodologies to "store and transport" solar energy, by converting solar to chemical energy. Solar fuels (based on CO_2 and water) are indicated as the target for long-term research in catalysis. However, to reach these goals, it is necessary to intensify from now R&D activities in this field, particularly fostering the basic research in this field. Catalysis is a key element to reach this objective.
5. Catalysis and nanotechnology should be a priority area of research on the field of alternative energy generation. Catalysis is the first and more effective (also in economic terms) example of nanotechnologies, and there is the need to extend the wide range of available knowledge on contiguous areas such as that of electrodes to develop improved technologies for energy storage and conversion.

Energy is a complex and pervasive problem that no one has the crystal ball to make exact predictions, and thus, the points summarized above remain in part personal opinions about the possible near and far future of the different technical approaches and their economic and social impacts. The reader can also draw their own conclusions, based on data and ideas presented.

It is also evident that on some critical aspect, such as the role of biofuels on the future of energy, there are some different ideas. The life-cycle GHG emission reduction of biofuels is good relative to that of gasoline and diesel (Table 1.2) but much less than that supposed by many "policymakers" when some of the directives and subsidies were decided. However, these will be revised due to this progress in understanding and also external pushing factors such as the economic crisis. For this reason, looking on Fig. 1.4, the total positive impact of the biofuel use seems to be very small on the CO_2 balance of the stratosphere. This conclusion is in apparent conflict with EU directives, but the estimation from the IEA (from which Fig. 1.4 derives) considers the evolving panorama on a global scale. It should be

remarked that these data do not indicate that it is not worth to convert biomass to biofuel. They indicate the need to consider the problem from a different perspective (as discussed above) and in particular the need to consider the integrated conversion of biomass to chemicals and biofuels. It should be also mentioned that novel high-efficient combustors for biomass offer a better energy efficiency to produce heat + electrical energy than converting biomass to biofuels and use these to produce heat and electrical energy. The biofuels are necessary for mobile applications but which account only about one-third of the total energy.

Another remark may be that the employment and security impacts of producing biofuel from biomass seem to disappear if solar fuel gains a higher share in the future as forecasted here. There are different time scales for development, and also, solar fuel offer equal, if not greater, opportunities for employment and energy security. It is not surprising that large investment in research on solar is made by countries, which have the higher fossil fuel resources such as the Kingdom of Saudi Arabia, or from oil companies. They have identified the need to prepare the transition already from now and not in a remote future.

Finally, a last comment deserves the question about the future direct use of hydrogen as engine fuel. We are skeptical about this possibility, but also, a number of car companies and many energy independent evaluators are moving to similar opinion. The problem is the need to avoid large-scale investments to change the energy infrastructure and the many issues in H_2 storage and transport. There is an increasing perception that it will be not possible to reach the necessary targets, and for this reason, US DoE have drastically reduced the research fund on this activity in 2010. The technologies which better integrate with the actual infrastructure are thus with the higher probability of success. This is the reason why we believe in the use of (renewable) hydrogen to convert back CO_2 to liquid fuel, i.e., renewable H_2 as intermediate to produce liquid fuels but which integrate into actual infrastructure. Therefore, the target is not to produce chemicals such as formic acid but alcohols such as methanol or longer carbon-chain hydrocarbons or oxygenated. The energy for this operation has to be clearly deriving from non-fossil fuel resources, solar energy first, but in part and on a short-term perspective also nuclear energy.

Are we proposing a "green" nuclear energy? No, but on a practical basis it should be considered that nuclear energy exists and that for a number of motivations the share of nuclear energy (in the energy pool) is expected to increase in the future, as indicated in Fig. 1.4. There is the opportunity to improve the energy efficiency of the nuclear reactors by producing fuels from CO_2 and water, using some of the waste heat. This is another opportunity and challenge for catalysis.

1.8 Conclusions

Catalysis research areas and priorities have changed significantly over the last decade, due to the evolved macroeconomic and societal scenario. At the beginning of the twentieth century, catalysis was a core technology in refinery and chemical

industrial production with over 90% of the processes using catalysts. Nevertheless, several company managers considered catalysis a mature area of development. The fifth energy crisis has accelerated to sociopolitical evolution putting the energy issue, and the question of renewable energy and alternative energy generation, at the heart of social and business strategies. This has given new impetus to the research on catalysis, being it one of the pillars to implement these strategies, from producing biofuels to the development of advanced electrodes for a number of applications (from new-generation photovoltaic cells to fuel cells), production of renewable H_2, and in a longer-term perspective solar fuels. As a consequence, research in catalysis worldwide has significantly changed in the last decades, and this book provides a comprehensive panorama of the new trends, opportunities, and research needs.

However, due to this evolving context, it is not possible to limit discussion to the technical aspects, but it is necessary to consider the general economic and social context and related constrains which also determine the choice of the research priorities, as evidenced in particular for the base of biomass conversion. For this reason, this introductory chapter was focused mainly on these aspects, leaving more specific aspects regarding the catalysts to the following chapters.

A general comment is necessary, however. The last decade was characterized from the exponential research activity on nanotechnologies and the development of novel materials/catalysts with advanced nanoarchitecture. The effort was mainly on the synthesis of these materials, with more limited attempts to correlate the properties of the nanostructure with the functional behavior (particularly, the catalytic activity). The challenge of sustainable energy requires to put more effort on these aspects. This should be a priority area for research on catalysis in the field of alternative energy generation.

Acknowledgments This contribution summarizes the discussions made in the frames of various projects which are gratefully acknowledged: PRIN08 project "Catalytic upgrading of the fraction C5 in ligno-cellulosic biorefineries," PRIN07 project "Sustainable processes of second generation for the production of H_2 from renewable resources," and the EU Network of Excellence IDECAT and of the Cost Action CM0903 (UBIOCHEM).

References

1. Spivey JJ (2005) Catalysis in the development of clean energy technologies. Catal Today 100:171–180
2. Schlögl R (2010) The role of chemistry in the energy challenge. ChemSusChem 3(2):209–222
3. Centi G, Perathoner S (2009) Catalysis: role and challenges for a sustainable energy. Top Catal 52(8):948–961
4. Centi G, Perathoner S (2008) Catalysis, a driver for sustainability and societal challenges. Catal Today 138(1–2):69–76
5. Liu J, Cao G, Yang Z, Wang D, Dubois D, Zhou X, Graff GL, Pederson LR, Zhang JG (2008) Oriented nanostructures for energy conversion and storage. ChemSusChem 1(8–9):676–697

6. Su DS, Schlögl R (2010) Nanostructured carbon and carbon nanocomposites for electrochemical energy storage applications. ChemSusChem 3(2):136–168
7. Rolison DR, Long JW, Lytle JC, Fischer AE, Rhodes CP, McEvoy TM, Bourg ME, Lubers AM (2009) Multifunctional 3D nanoarchitectures for energy storage and conversion. Chem Soc Rev 38:226–252
8. Garcia-Martinez J (ed) (2010) Nanotechnology for the energy challenge. Wiley-VCH, Weinheim
9. Centi G, Perathoner S (2009) The role of nanostructure in improving the performance of electrodes for energy storage and conversion. Eur J Inorg Chem 26:3851–3878
10. Li Y, Somorjai GA (2010) Nanoscale advances in catalysis and energy applications. Nano Lett 10:2289–2295
11. Gates BC, Huber GW, Marshall CL, Ross PN, Siirola J, Wang Y (2008) Catalysts for emerging energy applications. MRS Bull 33:429–435
12. Centi G, Perathoner S (2011) Creating and mastering nano-objects to design advanced catalytic materials for societal challenges. Coord Chem Rev 255:1480–1498
13. IEA (2009) World energy outlooks 2009. International Energy Agency, Paris
14. Maroto-Valer MM (ed) (2010) Developments and innovation in carbon dioxide (CO_2) capture and storage technology, volume 2: carbon dioxide (CO_2) storage and utilization. CRC Press, London
15. Jones W, Maginn EJ (guest eds) (2010) Carbon capture and sequestration (special issue). ChemSusChem 3(8):861–991
16. Centi G, Perathoner S (2009) Opportunities and prospects in the chemical recycling of carbon dioxide to fuels. Catal Today 148(3–4):191–205
17. Aresta M (ed) (2010) Carbon dioxide as chemical feedstock. Wiley-VCH, Weinheim
18. Centi G, Perathoner S (2010) Towards solar fuels from water and CO_2. ChemSusChem 3:195–208
19. Centi G, Perathoner S, Passalacqua R, Ampelli C (2012) Solar production of fuels from water and CO_2. In: Veziroglu N, Muradov N (eds) Carbon neutral fuels and energy carriers: science and technology. Taylor & Francis, London, Ch. 4, pp 291–323
20. Roy SC, Varghese OK, Paulose M, Grimes CA (2010) Toward solar fuels: photocatalytic conversion of carbon dioxide to hydrocarbons. ACS Nano 4(3):1259–1278
21. International Energy Agency (IEA) (2010) Key world energy statistics 2009. IEA, Paris
22. Züttel A, Borgschulte A, Schlapbach L (2008) Hydrogen as a future energy carrier. Wiley-VCH, Weinheim
23. Centi G, van Santen RA (2007) Catalysis for renewables. Wiley-VCH, Weinheim
24. Stöcker M (2008) Biofuels and biomass-to-liquid fuels in the biorefinery: catalytic conversion of lignocellulosic biomass using porous materials. Angew Chem Int Ed 47(48):9200–9211
25. Gallezot P (2008) Catalytic conversion of biomass: challenges and issues. ChemSusChem 1 (8–9):734–737
26. Huber GW, Iborra S, Corma A (2006) Synthesis of transportation fuels from biomass: chemistry, catalysts, and engineering. Chem Rev 106(9):4044–4098
27. Nozik AJ (2010) Nanoscience and nanostructures for photovoltaics and solar fuels. Nano Lett 10(8):2735–2741
28. Morris AJ, Meyer GJ, Fujita E (2009) Molecular approaches to the photocatalytic reduction of carbon dioxide for solar fuels. Acc Chem Res 42(12):1983–1994
29. Lewis NS, Crabtree G, Nozik A, Wasielewski M, Alivisatos P (2005) Basic research needs for solar energy utilization. US Department of Energy, Washington, DC
30. Mandal TK, Gregory DH (2010) Hydrogen: a future energy vector for sustainable development. Proc Inst Mech Eng C J Mech Eng Sci 224(3):539–558
31. Sartbaeva A, Kuznetsov VL, Wells SA, Edwards PP (2008) Hydrogen nexus in a sustainable energy future. Energy Environ Sci 1(1):79–86
32. Farrauto RJ (2009) Building the hydrogen economy. Hydrocarbon Eng 14(2):25–30

33. Muradov NZ, Veziroglu TN (2008) "Green" path from fossil-based to hydrogen economy: an overview of carbon-neutral technologies. Int J Hydrogen Energy 33(23):6804–6839
34. Strahan D (2008) Hydrogen's long road to nowhere. New Sci 200(2684):40–43
35. Centi G, Perathoner S (2010) CO_2-based energy vectors for the storage of solar energy. Greenhouse Gases Sci Technol 1:21–35
36. Vlachos DG, Caratzoulas S (2010) The roles of catalysis and reaction engineering in overcoming the energy and the environment crisis. Chem Eng Sci 65(1):18–29
37. Huber GW (ed) (2008) Breaking the chemical and engineering barriers to lignocellulosic biofuels: next generation hydrocarbon biorefineries. National Science Foundation, Washington, DC
38. Zinoviev S, Müller-Langer F, Das P, Bertero N, Fornasiero P, Kaltschmitt M, Centi G, Miertus S (2010) Next-generation biofuels: survey of emerging technologies and sustainability issues. ChemSusChem 3(10):1106–1133
39. Centi G, Lanzafame P, Perathoner S (2011) Analysis of the alternative routes in the catalytic transformation of lignocellulosic materials. Catal Today 167:14–30
40. Cherubini F, Jungmeier G (2010) LCA of a biorefinery concept producing bioethanol, bioenergy, and chemicals from switchgrass. Int J Life Cycle Assess 15(1):53–66
41. Cavani F, Centi G, Perathoner S, Trifiró F (2009) Sustainable industrial chemistry. Wiley-VCH, Weinheim
42. US Environmental Protection Agency (EPA) (2009) EPA lifecycle analysis of greenhouse gas emissions from renewable fuels. Report EPA-420-F-09-024
43. Hiederer R, Ramos F, Capitani C, Koeble R, Blujdea V, Gomez O, Mulligan D, Marelli L (2010) Biofuels: a new methodology to estimate GHG emissions from global land use change. European Commission, Joint Research Centre, report EUR 24483 EN—2010
44. Regalbuto JR (2010) An NSF perspective on next generation hydrocarbon biorefineries. Comput Chem Eng 34(9):1393–1396
45. Lu A-H, Schüth F (2006) Nanocasting: a versatile strategy for creating nanostructured porous materials. Adv Mater 18(14):1793–1805
46. Grimes CA, Mor GK (2009) TiO_2 nanotube arrays: synthesis, properties, and applications. Springer, Heidelberg
47. Shankar K, Basham I, Allam NK, Varghese OK, Mor GK, Feng X, Paulose M, Seabold A, Ky-S C, Grimes CA (2009) Recent advances in the use of TiO_2 nanotube and nanowire arrays for oxidative photoelectrochemistry. J Phys Chem C 113(16):6327–6359
48. Centi G, Perathoner S (2009) Nano-architecture and reactivity of titania catalytic materials. Part 2. Bidimensional nanostructured films. Catalysis 21:82–130, Royal Society of Chemistry Pub: Cambridge, UK
49. Tributsch H (2008) Photovoltaic hydrogen generation. Int J Hydrogen Energy 33(21):5911–5930
50. Gibson TL, Kelly NA (2008) Optimization of solar powered hydrogen production using photovoltaic electrolysis devices. Int J Hydrogen Energy 33(21):5931–5940
51. Wipke K, Sprik S, Kurtz J, Ramsden T (2010) Learning demonstration interim progress report—July 2010. Technical report NREL/TP-560-49129 (Sept 2010). National Renewable Energy Laboratory (NREL), Golden, CO
52. Liu C, Li F, Lai-Peng M, Cheng H-M (2010) Advanced materials for energy storage. Adv Mater 22(8):E28–E62
53. Serrano E, Rus G, García-Martínez J (2009) Nanotechnology for sustainable energy. Renew Sustain Energy Rev 13(9):2373–2384

Chapter 2
Catalytic Production of Liquid Hydrocarbon Transportation Fuels

Juan Carlos Serrano-Ruiz and James A. Dumesic

Abstract Lignocellulosic biomass resources are abundant worldwide and have the potential to displace petroleum in the production of liquid fuels for the transportation sector of our society. Bioethanol, the dominant biofuel used today, suffers from low energy density and high solubility in water, properties that are undesirable for transportation fuels. The production, from lignocellulosic sources, of liquid hydrocarbon fuels that are chemically similar to those currently used in the transportation sector is a promising alternative to overcome the limitations of bioethanol. The transformation of highly functionalized biomass into oxygen-free liquid fuels can be carried out by gasification, pyrolysis, and aqueous-phase processing, as outlined in this chapter, with particular emphasis on the catalytic aspects of these processes.

Abbreviations

APD/H	Aqueous-phase dehydration/hydrogenation
APR	Aqueous-phase reforming
BTL	Biomass to liquids
CTL	Coal to liquids
DALA	δ-aminolevulinic acid
FTS	Fischer–Tropsch synthesis
GTL	Gas to liquids
GVL	γ-Valerolactone
HMF	Hydroxymethylfurfural
lge	Liter of gasoline equivalent
MTHF	Methyltetrahydrofuran

J.C. Serrano-Ruiz • J.A. Dumesic (✉)
Department of Chemical and Biological Engineering, University of Wisconsin—Madison, Madison, WI 53706, USA
e-mail: jcserrano@ua.es; dumesic@engr.wisc.edu

L. Guczi and A. Erdőhelyi (eds.), *Catalysis for Alternative Energy Generation*,
DOI 10.1007/978-1-4614-0344-9_2,

Ppm	Parts per million
Syngas	Synthesis gas
WGS	Water–gas shift

2.1 Introduction

Fossil fuels (i.e., coal, natural gas, and petroleum) currently represent the primary source of energy for our modern society. According to the most recent statistics available, in 2008 these nonrenewable resources supplied about 85% of the total energy consumed in the USA [1] and almost 80% of the energy produced in the European Union [2]. This lower use of fossil fuels in the European Union is compensated by more extensive use of nuclear energy, since renewable energy accounted for the same fraction (8%) in both industrialized regions. The energy produced by fossil fuels is unevenly distributed among the different sectors (i.e., residential, commercial, industrial, transportation, and electrical power) of society. Thus, while coal supplies more than 50% of the energy for electricity production and natural gas prevails in the residential and commercial sectors, petroleum accounts for essentially all (96%) of the transportation energy [3]. On the other hand, renewable sources supply less than 10% of the energy to any single sector, with the transportation being the sector with the lowest contribution in this respect (2%). This contribution is expected to increase rapidly within the next few years. Thus, according to projections by the International Energy Agency, the world biofuel production will increase from 1.9 million of barrels per day (mbd) in 2010 to 5.9 mbd by 2030, which represents 6.3% of the world conventional fuel production [4].

The energy consumption data outlined above indicate that fossil fuels dominate the current global energy system. However, there are several important issues inherently associated with the usage of these nonrenewable resources. The first concern is related with availability. Fossil fuel reserves are finite and the current consumption rate increases yearly to meet the growing demand of industrialized countries and rapid development of emerging economies. In this respect, the US Energy Information Administration projects a 35% increase in the world energy consumption over the next 20 years [4], and recent analyses of proven reserves versus consumption rates indicate that oil, natural gas, and coal will be depleted within the next 40, 60, and 120 years, respectively [5]. The second important issue is environmental. The consumption of fossil fuels leads to net emissions of CO_2 into the atmosphere, contributing to global warming and the climatic issues [6]. Recent studies show that the burning of fossil fuels for energy production is responsible for 70% of the global warming problem [7]. The third important issue is derived from the geographical distribution of fossil fuel reserves. It is estimated that 60% of world proven oil reserves and 41% of natural gas supplies are situated in Middle-East countries, whereas USA, Russia, and China monopolize the 60% of the world recoverable coal reserves [4]. This uneven distribution of reserves can lead to political, economic, and security issues worldwide.

To address the above important concerns, governments, through aggressive directives [8, 9], are stimulating society to use renewable sources of energy (e.g., solar, wind, hydroelectric, geothermal, and biomass) to progressively displace oil, coal, and natural gas from the energy production system. Unlike fossil fuels, renewable resources are abundant and well distributed around the world. Additionally, they allow the development of zero-carbon or carbon-neutral technologies, thus contributing to mitigation of global warming effects.

In the same way that fossil fuels have different contributions to the various energy sectors of society, renewable technologies will also be implemented selectively in society. Recent studies indicate that solar, wind, geothermal, and hydroelectric power will be used to generate heat and electricity in stationary power applications, allowing the eventual substitution of coal and natural gas [10, 11]. On the other hand, biomass has been proposed as the only sustainable source of organic carbon currently available on earth [12] and thus, this resource is best suited as a potential substitute for petroleum for the production of fuels and chemicals [13, 14]. The petrochemical industry currently consumes a large fraction of the crude oil to generate liquid hydrocarbon fuels, whereas a minor fraction is used for chemicals production. Consequently, for biomass to effectively replace petroleum, new technologies for the production of liquid fuels from this resource, the so-called biofuels, are necessary. Unlike petroleum-based fuels, biofuels are conceptually carbon neutral, since CO_2 produced during fuel combustion is consumed by subsequent biomass regrowth [15]. However, CO_2 evolved during production and transportation of the biofuel must also be taken into consideration. Additionally, the large-scale production of biofuels can strengthen economies by reducing the dependence on the strong fluctuations in the price of the oil [16] and by creating new well-paid jobs in different sectors such as agricultural, forest management, and oil industries [7].

The liquid biofuels used most widely today for transport are ethanol and biodiesel. Ethanol is the predominant biomass-derived fuel at the present time, accounting for 90% of the total biofuel usage [17]. It is produced by anaerobic fermentation of corn and sugar cane-derived sugars, and only two countries (USA and Brazil) are responsible for 90% of the world production. The fermentation process produces a dilute aqueous solution of ethanol and thus, an expensive energy-consuming distillation step is necessary to completely remove water from the mixture. For ethanol to be used as a fuel in current spark ignition engines, only low-concentration (5–15%) blends with gasoline (i.e., E5–E15) are tolerated, and additional engine upgrades are required for ethanol-rich mixtures (E85). Utilization of edible biomass for its production, high miscibility with water, and the lower energy density compared to gasoline are also important limitations for the implementation of ethanol as a transportation fuel.

Biodiesel is a mixture of long-chain alkyl esters, typically derived from vegetable oils. It is produced by chemically combining the oil with an alcohol (such as methanol) in the presence of a basic catalyst, in a process known as transesterification. Glycerol, in the form of concentrated aqueous solutions, is the primary coproduct of biodiesel production and, as described below (Sect. 2.2.3), important

catalytic routes for the upgrading of this waste stream have already been developed. Similar to ethanol, biodiesel usage is currently limited to low-concentration blends with conventional diesel fuel (B5, B20), since pure biodiesel (B100) can cause rubber and other components in the engine or fuel lines to fail [17]. Additionally, the need for fossil fuel-derived methanol has led to research for utilization of renewable bioethanol as an esterification agent.

The transportation sector of society requires fuels that burn cleanly and have high energy densities for efficient storage at ambient conditions. These criteria are best fulfilled by petroleum-derived liquid hydrocarbon fuels, and infrastructure for the use of these fuels (e.g., engines, fueling stations, distribution networks, petrochemical processes) is already developed for these molecules. The effective and rapid implementation of ethanol and biodiesel has benefitted from this infrastructure, because these biofuels fit, although with several limitations, into the current hydrocarbon-based transportation system. The main limitations of ethanol and biodiesel alkyl esters as transportation fuels (e.g., need for low-concentration blends, lower energy density, miscibility with water in the case of ethanol) are, ultimately, derived from the different chemical composition of these molecules compared to hydrocarbon fuels. Thus, instead of using biomass to produce oxygenated fuels with new compositions, an attractive alternative to overcome these limitations would be to utilize biomass to generate liquid fuels chemically similar to those being used today, which are derived from oil [18]. When compared with ethanol, the production of hydrocarbon fuels from biomass has many important advantages, as outlined below:

(a) *Compatibility with existing energy infrastructure*. Renewable hydrocarbon fuels would be essentially the same as those currently obtained from petroleum, except that they are made from biomass. Therefore, it would not be necessary to modify existing infrastructure for their implementation in the transportation sector. Additionally, the processes for the production of hydrocarbon biofuels could be coupled with the fuel production systems of existing and well-developed petroleum refineries.
(b) *High-heating value*. The heating value (i.e., the heat released when a known quantity of fuel is burned under specific conditions) is an important quality of a fuel that finally determines the gas mileage of the vehicle. The oxygen content of the fuel negatively affects this parameter. For example, ethanol has only 66% of the heating value of gasoline and thus, cars running on ethanol-rich mixtures like E85 get a 30% lower gas mileage [19]. Biomass-based hydrocarbon fuels, in contrast, offer equivalent energy content and gas mileage performance to fuels derived from petroleum.
(c) *Hydrophobicity*. Fuels that do not absorb water are highly desirable. The addition of oxygenates to regular gasoline, however, increases the water solubility of the mixture. In the case of ethanol/gasoline blends, water contamination can trigger a phase separation of both components which is an important concern especially in cooler climates. The hydrophobic character of biomass-derived hydrocarbons eliminates this problem since these molecules are

immiscible in water. Additionally, the ability of hydrocarbons to spontaneously separate from water is also beneficial in that it eliminates the need for an expensive energy-consuming distillation step required in the ethanol purification process.

(d) *Smaller reactors*. The low energy density of biomass compared to fossil fuels is an intrinsic constraint of this resource. Thus, to process it into energy and fuels, a large amount of biomass will be required, leading to high cost (and probably use of fossil fuels) for transporting it from the biomass source to the processing location [20, 21]. Unlike ethanol, biomass-based hydrocarbon fuels can be produced at high temperatures and using concentrated water solutions [13], which allows for faster conversion reactions and smaller reactors. Thus, instead of having large central processing locations such as those required for ethanol production, these small units could be placed close to the biomass source, thereby avoiding transport of biomass over long distances. It has been suggested that this small-scale, geographically localized distribution of the biofuels industry would additionally benefit rural economies and reduce the vulnerability of infrastructure [15].

One of the main concerns when producing biofuels at large scale is the utilization of edible biomass as feedstocks (e.g., sugars, starches, and vegetable oils). Important moral and ethical questions arise because this practice creates a competition with food for land use. These issues have driven researchers around the world to develop technologies to process nonedible biomass (lignocellulosic biomass), thereby permitting sustainable production of a new generation of fuels (so-called second generation of fuels) without affecting food supplies. In this respect, lignocellulosic biomass is abundant [22] and can be grown faster and at lower price than food crops [23]. Lignocellulosic biomass consists of three major components (Fig. 2.1): cellulose, hemicellulose, and lignin [24, 25]. Cellulose is a linear polymer of glucose, connected linearly by β-1,4-glycoside linkages, that typically comprises about 40–50% of a given lignocellulosic source. As shown in Fig. 2.1, this arrangement allows a high degree of hydrogen bonding between different cellulose chains that confers this material with high stability and resistance to chemical attack [26], high crystallinity, and low surface area. Unlike cellulose, hemicellulose is amorphous and possesses a heterogeneous composition, since it is formed by polymers of five different C_5 and C_6 sugars. It surrounds the cellulose fibers and typically accounts for 20–30% of the total mass of a lignocellulose source. Lignin is a complex three-dimensional polymer of propyl–phenol groups bound together by ether and carbon–carbon bonds. It provides structural rigidity by holding the fibers of polysaccharides together. It is typically found in woody biomass and usually comprises 15–25% of lignocellulose depending on the source.

Two aspects currently limit the implementation of lignocellulose as a feedstock for transportation fuels: recalcitrance and complexity. The structure of lignocellulose, with lignin offering an extra protection to cellulose and hemicellulose, is naturally designed to provide stability and resistance to external attack. In contrast, edible biomass such as starch consists of glucose polymers with α linkages that

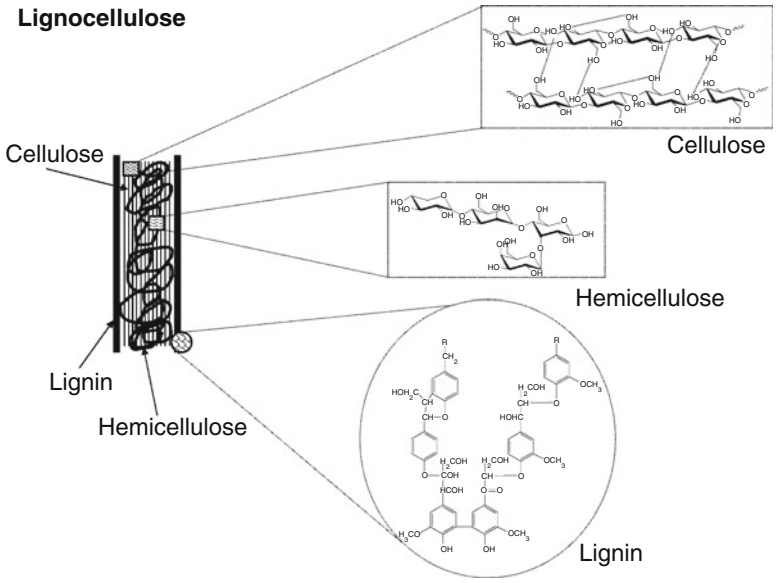

Fig. 2.1 Structure of lignocellulosic biomass and their components. Adapted from [47]

make the polymer highly amorphous and, consequently, more readily deconstructed into monomers [27]. This chemical structure of edible biomass allows simple and economic processing to take place. For example, while corn-derived ethanol can be generated at 0.6–0.8 $/liter of gasoline equivalent (lge), recent economic studies indicate that the use of lignocellulose for ethanol production would increase the cost to the level of 1.0$/lge [28]. Accordingly, research is being conducted worldwide on how to decrease recalcitrance of lignocellulosic biomass [29–31] in order to develop cost-competitive technologies for the generation of liquid fuels from nonedible sources. This latter aspect has been identified by experts as the key bottleneck for the large-scale implementation of lignocellulose-derived biofuel industry [32].

The structural and chemical complexity of lignocellulosic biomass suggests that a combination of different processes may be utilized to maximize yields. The most promising methodology used today for biomass processing resembles that used for oil in petroleum refineries, and involves the conversion of lignocellulosic feedstocks into simpler fractions that are subsequently converted into a variety of useful products. These transformations would be carried out in a facility, denoted as a biorefinery, that integrates biomass conversion processes and equipment to produce fuels, power, and chemicals from this resource [33–35]. Current technologies for conversion of lignocellulosic biomass into liquid hydrocarbon fuels involve three major primary routes: gasification, pyrolysis, and hydrolysis (Fig. 2.2), and they are described in separate sections of this chapter. The first technology (Sect. 2.2.1) allows biomass transformation into synthesis gas (syngas),

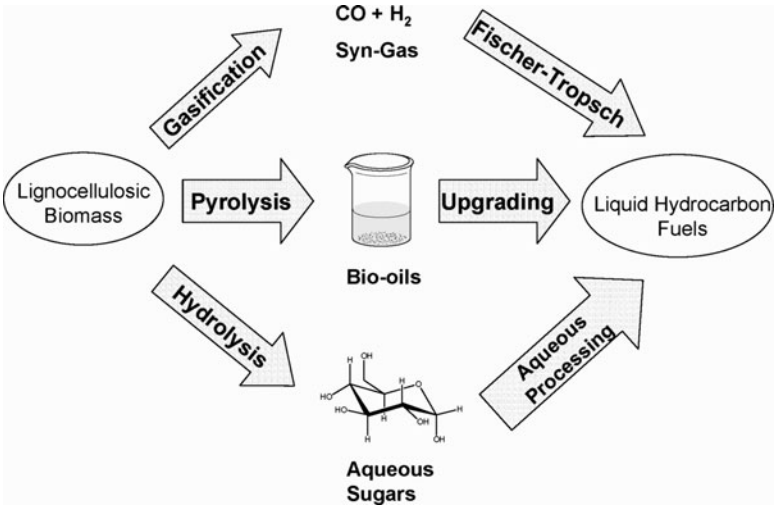

Fig. 2.2 Schematic representation of the different routes for the conversion of lignocellulosic biomass into liquid hydrocarbon transportation fuels

a valuable mixture of CO and H_2 which serves as a precursor of liquid hydrocarbon fuels. The second path (Sect. 2.2.2) converts solid biomass into a liquid fraction known as bio-oil, which can be further upgraded to gasoline and diesel components. Finally, the third route involves the hydrolysis of biomass to produce sugars and valuable intermediates that, as described in Sect. 2.2.3, can be catalytically processed in the aqueous phase to the full range of liquid hydrocarbon fuels including gasoline, diesel, and jet fuels.

2.2 Catalytic Routes for the Production of Liquid Hydrocarbon Transportation Fuels from Lignocellulosic Biomass

Solid biomass is converted by gasification and pyrolysis approaches to gas and liquid fractions, respectively, which are subsequently upgraded to the final fuel products. Gasification and pyrolysis are pure thermochemical routes, that is, biomass decomposition is carried out by increasing temperature and/or pressure under controlled atmosphere in the absence of catalysts, which are used downstream for syngas and bio-oil upgrading processes. Aqueous-phase processing of biomass derivatives, in contrast, involves a series of catalytic reactions to selectively convert water-soluble sugars (or molecules derived from these sugars) into liquid hydrocarbon fuels. A previous lignocellulose pretreatment (to break the lignin protection) and hydrolysis (to depolymerize cellulose and hemicellulose fractions) steps are necessary to generate the aqueous feeds used in this approach.

2.2.1 Biomass to Liquids

The biomass to liquids (BTL) route refers, similar to coal to liquids (CTL) or gas to liquids (GTL) technologies, to biomass conversion into liquid hydrocarbon fuels by the integration of two different processes: biomass gasification to syngas (H_2/CO) and subsequent Fischer–Tropsch synthesis (FTS) to hydrocarbon fuels. Individually, both technologies are relatively well developed. Biomass gasification resembles coal gasification, and FTS is an industrial process first developed in the early 1900s and is used extensively in countries like South Africa to produce liquid hydrocarbon fuels. The challenges of BTL arise when efficient integration of both technologies is required. Thus, the utilization of biomass for the production of syngas in substitution of classical feeds such as coal or natural gas introduces new difficulties that are outlined in this section.

Gasification is defined as a thermal degradation in the presence of an externally supplied oxygen-containing agent (e.g., air, steam, oxygen). By controlling the reaction atmosphere, biomass can be partially combusted to produce a high-heating value gaseous stream composed of CO, H_2, CO_2, CH_4, and N_2 (producer gas), or to generate mixtures enriched in CO and H_2 (syngas) [36]. While producer gas is generated with air as the oxidizing agent and is typically combusted to produce electricity and heat, syngas streams are produced when pure oxygen is used as the oxidizing agent and these streams are preferred as chemical feedstocks for fuels and chemicals. This latter route is the focus of this section.

Gasification of biomass to syngas is favored at high temperatures (e.g., 1,100–1,300 K) because the decomposition of carbohydrates to CO and H_2 is an endothermic reaction [37]. However, at such harsh conditions the control over the gas composition from the gasifier is difficult and depends on diverse factors such as biomass source and particle size, gasification conditions, and gasifier design. As indicated above, co-feeding oxygen below the stoichiometric regime allows mixtures enriched in CO and H_2 to be achieved by favoring partial oxidation reactions [24]. Biomass particle size is also an important factor affecting both gasification rate and gas stream composition. In order to maximize the amount of syngas in the outlet, the particle size of feedstocks should be small enough (lower than 1-mm diameter) for complete and efficient gasification to occur [38]. Regarding the gasifier type, the patent literature contains a large variety of designs depending on bed configurations (fixed or fluidized), feeding approaches (updraft, downdraft, or direct entrained), working pressure (atmospheric or pressurized), and heat supply (direct or indirect) [39]. Research indicates that direct air-blown gasifiers operated at atmospheric pressure are not suitable for BTL applications since the gas stream is obtained highly diluted in inert nitrogen. In contrast, direct entrained gasifiers allow processing at high pressures (10–60 bars), high temperatures (1,500–1,800 K), and short residence times, conditions that favor syngas production [40].

The main issue when biomass gasification is integrated with FTS is the gas cleaning between reactors. The gaseous stream obtained from the gasifier contains,

apart from CO and H_2, a number of contaminants that need to be removed before reaching the Fischer–Tropsch unit, which is highly sensitive to impurities. Tars (high molecular weight hydrocarbons produced by incomplete gasification of biomass) represent the main issue in any gasification technology [39]. They condense in the gasifier or in downstream processing equipment, causing blockages of pipelines and troublesome operations. The amount of tar can be reduced by proper choice of gasification conditions and reactor design [41], or by adding solid catalysts based on Pt, Ru, and Ni in the gasifier to assist in the gasification of heavy hydrocarbons [42–45]. Lignocellulosic biomass typically contains a variety of minor components such as proteins rich in sulfur and inorganic materials based on phosphorous, potassium, and halogens. Thus, the gas stream produced from biomass gasification carries alkali, HCl, NH_3, and volatile sulfur compounds that can corrode turbines used for electricity generation or, in the case of BTL technology, can poison the catalysts used in the Fischer–Tropsch downstream unit. Furthermore, the gasification stream, especially when small particle size is used as a feedstock, contains fine particles that can cause blockages and can clog filters.

For the reasons outlined above, BTL technologies must include a gas conditioning unit between the gasifier and the Fischer–Tropsch reactor. Sufficient gas cleaning has been noted as a key point for the development of effective BTL processes [46]. Because the cleaning includes a number of different contaminants (tars, particles, chemicals, etc.) which have to be removed to the ppm level [21], this unit typically comprises multiple steps and advanced technologies [47] that contribute significantly to the complexity and cost of the BTL plant. Another requirement in the gas composition for the Fischer–Tropsch units is related to the CO/H_2 molar ratio. Fischer–Tropsch processes to hydrocarbon fuels usually require syngas with a H_2/CO ratio close to 2 [48, 49], and, due to the high oxygen content of biomass, typical streams delivered from this resource contain a H_2/CO ratio of about 0.5 [50]. This ratio can be adjusted via water–gas shift (WGS) reactions, where CO reacts with steam to produce CO_2 and H_2:

$$CO + H_2O \rightarrow CO_2 + H_2 \tag{2.1}$$

This adjustment can be carried out in an additional WGS reactor between the gasifier and the Fischer–Tropsch unit or, alternatively, can be achieved without additional reactors by co-feeding extra water along with the biomass in the gasifier. This latter alternative, however, negatively affects the thermal efficiency of the gasification process.

After the syngas has been cleaned and "shifted," it is introduced into the FTS reactor, the last unit of the BTL process. FTS is a well-known industrial process to produce alkanes (C_nH_n) from syngas using Co-, Fe-, or Ru-based catalysts [49]:

$$CO + 2H_2 \rightarrow (1/n)C_nH_n + H_2O \tag{2.2}$$

The WGS reaction also takes place over Fischer–Tropsch catalysts (especially those based on Fe) allowing the eventual adjustment of the H_2/CO ratio in the same

synthesis bed. One of the main limitations of Fischer–Tropsch technologies is the lack of selectivity in the final alkane product, with broad distributions that can range from C_1 to C_{50}. The Anderson–Schulz–Flory (ASF) polymerization model, which governs the alkane chain growth probability, indicates that neither gasoline nor diesel fuels can be produced selectively without generating a large amount of undesired products [47]. In order to overcome this limitation, indirect routes involving the initial production on heavy hydrocarbons (waxes) and subsequent controlled hydrocracking of these heavy compounds to gasoline and diesel [51], and utilization of active materials for cracking and isomerization such as ZSM-5 as supports of Co and Fe catalysts to produce gasoline components [52] are currently used for selective FTS reactions.

Current BTL activities are at research, development, and demonstration stages. One small demonstration plant in the Netherlands to produce diesel fuel from woody biomass [53], and a more recent plant to produce 15,000 tons per year of liquid fuels from multiple lignocellulosic feedstocks in Germany [54] are the most promising BTL projects at the present time. A challenge for the commercialization of BTL technology is the cost of producing the fuel, negatively affected by the complexity of the process. Thus, this route is only economical on the large scale, requiring the use of large centralized facilities with the corresponding expense of transporting the low energy density biomass. The coproduction, along with hydrocarbon fuels, of higher value chemicals like methanol [55] and hydrogen [56, 57] from biomass-derived syngas is an alternative to improve the economics of the BTL process.

2.2.2 *Biomass Pyrolysis Integrated with Upgrading Processes*

When biomass is treated under inert atmosphere at temperatures ranging 648–800 K it forms gaseous products which condense, forming a dark viscous liquid commonly known as bio-oil. This liquid consists of a complex mixture of more than 400 highly oxygenated compounds, including acids, alcohols, aldehydes, esters, ketones, aromatic compounds, polymeric carbohydrates, and lignin fragments [58, 59]. The control over the final composition of the bio-oil is difficult, since it is affected by a large number of factors such as feedstock type (wood, agricultural wastes, forest wastes), reaction conditions (temperature, pressure, residence time of vapors), reactor design, alkali content of feedstock, particle size, and storage conditions [60]. In a typical pyrolysis process, bio-oil contains about 25 wt% water (contributed by the water in the initial biomass feedstock and from the conversion process) and 10 wt% of suspended char which is separated for subsequent utilization of the bio-liquid.

Similar to gasification, a key advantage of pyrolysis is that it allows conversion of all the organic matter in lignocellulosic biomass, including the highly resistant lignin portion. Furthermore, a large fraction of biomass energy (up to 70%) is retained in the bio-oil [47] allowing strategies to concentrate the energy of biomass

in a liquid that can be more easily handled and transported. Unlike BTL, pyrolysis is simple and only requires one single reactor, which favors cost-effective conversions on small scale, allowing the use of small portable pyrolysis units easily distributed close to the biomass source [15]. Thus, several small facilities (10–100 tons of biomass per day) are currently in commercial operation in the USA, Canada, and the Netherlands [61]. Bio-oils are currently used as boiler fuels for stationary power and heat production, as well as for chemical production.

There are important barriers for the utilization of bio-oils as transportation fuels. As indicated above, pyrolysis oils are complex mixtures of oxygenated compounds, which confer this liquid with low energy density (typically 50% of conventional hydrocarbon fuels), low volatility, and low stability, characteristics that are undesirable for transportation liquid fuels. Additionally, their high acidity (pH $\sim$ 2.5), viscosity, and water content could cause storage and engine issues. Therefore, bio-oils must be pretreated if they are to be used as transportation fuels. Thus, the main routes for upgrading bio-oils are described in the next sections.

2.2.2.1 Hydrodeoxygenation

The pyrolysis process does not involve deep chemical transformations in the feedstock and, consequently, the composition of the organic liquid resembles that of biomass rather than hydrocarbon fuels. Therefore, in the same way as petroleum feedstocks are refined to adjust their composition to that of conventional fuels, bio-oils must be chemically transformed to provide these liquids with characteristics of hydrocarbon fuels such as high energy density, volatility, and thermal stability. These changes can be accomplished through more extensive removal of oxygen, in contrast with removal of sulfur and nitrogen during refining of petroleum. One of the possibilities to reduce the oxygen content in bio-oils involves the utilization of hydrogen at elevated pressures and moderate temperatures in a process called hydrodeoxygenation [62, 63]. The hydrogenation of bio-oil components is typically carried out over sulfided CoMo- and NiMo-based catalysts, which are widely used for sulfur and nitrogen removal in the petrochemical industry. Precious metals like Pt and Ru have also been used for this purpose, although their high cost and low tolerance to sulfur impurities typically present in bio-oils are serious limitations for their commercial implementation. As a result of hydroprocessing, the oxygenated compounds in bio-oils are completely reduced and oxygen is removed in the form of water, which appears in the reactor as a separate phase. The resulting organic layer possesses hydrocarbon-like properties such as low viscosity, high stability, and high heating value required for fuel applications.

The hydrodeoxygenation of bio-oils has a number of drawbacks that must be addressed to make the process economically feasible. First, hydrodeoxygenation requires the consumption of high amounts of hydrogen, which is typically produced from fossil fuels. This limitation could be overcome by developing strategies to produce hydrogen from lignocellulosic biomass. In this approach, a fraction of the

biomass would be utilized to produce renewable hydrogen, which would be subsequently used for bio-oil deoxygenation. Several technologies for production of hydrogen are currently available and could be utilized for hydrodeoxygenation, including gasification-WGS routes (described in the previous section), steam reforming of water-soluble fractions of bio-oils [64], and aqueous-phase reforming (APR) of biomass-derived sugars [65, 66]. The second important issue of hydrodeoxygenation is derived from the complex composition of the bio-liquid, which includes a large number of compounds (e.g., acids, ketones, aldehydes, alcohols, aromatics) with very different reactivities toward hydrogenation. One of the challenges of this process is, thus, the control over the extent of hydrogenation. The objective is selectively remove oxygen versus hydrogenation of aromatic compounds (derived from lignin and useful as a gasoline components) to avoid unnecessary hydrogen consumption. Finally, the use of high hydrogen pressures (typically above 100 bars) for complete deoxygenation of bio-oils negatively affects the economics of the process by increasing the operational costs.

2.2.2.2 Zeolite Upgrading

An alternative route to achieve deoxygenation of bio-oils without using hydrogen is based on the catalytic cracking approach used in petroleum refining, and it involves the processing of the bio-liquid over acidic zeolites at atmospheric pressure and moderate temperatures [67–69]. As a result of this treatment, the oxygenates in bio-oil are converted, with modest yields, into a mixture of aromatic and aliphatic hydrocarbons, while oxygen is eliminated in the form of CO, CO_2, and water through a complicated set of reactions including dehydration, cracking, and aromatization. The distribution of aromatic and aliphatic hydrocarbons obtained is a function of the acidity and porous structure of the catalysts employed. Thus, while H-ZSM5 maximizes the aromatic to aliphatic ratio, amorphous silica–alumina achieves mostly aliphatic hydrocarbons. When compared with hydrodeoxygenation, zeolite upgrading offers significant processing and economic advantages, since no hydrogen is required and the reaction can be carried out at atmospheric pressure and moderate temperatures (623–773 K). Importantly, these temperatures are similar to those used in the production of bio-oil, which allows the integration of pyrolysis and zeolite upgrading in a single reactor [70]. The usefulness of zeolite upgrading is limited by two important aspects: the poor hydrocarbon yield and deactivation issues. The low hydrocarbon yield is caused by the large fraction of the organic carbon present in the bio-liquid (40–60 wt%) that is lost to the gas phase (in the form of light olefins, CO, and CO_2) and is deposited over the zeolite as coke. This coke deposition produces deactivation of the catalyst, although the initial activity can be recovered by burning off the carbonaceous material. Additionally, irreversible deactivation is observed, because zeolite structures undergo de-alumination at the water contents typically found in bio-oils and produced in situ through dehydration reactions.

2.2.2.3 Ketonization of Bio-oils

The main challenge associated with bio-oil upgrading is to achieve efficient deoxygenation while minimizing the consumption of hydrogen. In particular, the use of hydrogen during bio-oil upgrading allows clean processing without excessive coke formation, but, at the same time, its high cost increases the expense of the process. On the other hand, bio-oils typically contain a significant quantity (up to 30 wt%) of carboxylic acids [71], which provides these liquids with high acidity and corrosiveness. Furthermore, the high reactivity of acids leads to instability of the bio-oil. These undesired properties, along with the high amount of hydrogen consumed by carboxylic acids during hydrodeoxygenation to hydrocarbons, suggest that it would be desirable to develop techniques for effective removal of acidity from bio-oils. In this respect, an interesting route to process the acidic fraction of bio-oils without utilizing hydrogen involves catalytic ketonic decarboxylation or ketonization [72]. By means of this reaction, two molecules of carboxylic acids are condensed into a larger ketone ($2n-1$ carbon atoms) with the release of stoichiometric amounts of CO_2 and water:

$$2CH_3(CH_2)_nCOOH \rightarrow CH_3(CH_2)_nCO(CH_2)_nCH_3 + CO_2 + H_2O \qquad (2.3)$$

This reaction is typically catalyzed by inorganic oxides such as CeO_2, TiO_2, Al_2O_3, and ZrO_2 at moderate temperatures (573–773 K) and atmospheric pressure [73, 74]. Ketonization could find application for catalytic upgrading of bio-oils for several reasons. First, carboxylic acids present in the bio-oil can be selectively removed [75] (without affecting the rest of compounds) and transformed into a more hydrophobic, larger ketone at temperatures and pressures typically used in pyrolysis. Second, this transformation takes place with the simultaneous reduction of the oxygen content of the acid (in the form of water and CO_2) and without using hydrogen. Consequently, a pretreatment of the bio-oil over a ketonization bed could serve to reduce acidity and oxygen content, thereby reducing hydrogen consumption and leaving bio-oil more amenable for subsequent hydrodeoxygenation processing. Third, ketonization can be also applied to other compounds typically present in bio-oils like esters [76, 77], which are formed by reaction between acids and alcohols [78]. Finally, unlike zeolite upgrading, this reaction can be efficiently performed in the presence of moderate amounts of water [79], as typically found in bio-oils.

2.2.3 Aqueous-Phase Processing of Biomass Derivatives

As outlined earlier in this chapter, lignocellulosic biomass is composed of three units: cellulose, hemicellulose, and lignin. The first two units are polymers of C_5 and C_6 sugars which can be deconstructed by enzymatic or acid hydrolysis to yield

aqueous solutions of carbohydrates. However, to allow efficient depolymerization of cellulose and hemicellulose, the lignin protection must be previously broken or weakened. Several approaches, including chemical and physical treatments, have been developed for this purpose [29], and the effects of these pretreatments on the morphology and structure of biomass have been recently studied [31].

The aqueous solution of carbohydrates obtained after hydrolysis can then serve as a feedstock for the production of fuels like ethanol or, alternatively, can be used to produce a set of useful chemical derivatives through chemical and biological routes [80]. As outlined in this section, sugars, as well as some important chemicals derived from them, can also be catalytically processed in the aqueous phase to produce liquid alkanes chemically similar to those currently used in the transportation sector. Unlike the other two major routes for the conversion of lignocellulosic biomass to hydrocarbon fuels (i.e., gasification and pyrolysis), the aqueous-phase processing of biomass-derived compounds is carried out at mild temperatures, which potentially allows for better control of the catalytic chemistry and, with it, the possibility of achieving specific and well-defined liquid hydrocarbon fuels from biomass with high yields. However, the biomass must be previously treated to prepare the aqueous feeds for subsequent catalytic processing and, lignin fraction, once separated, cannot be utilized in this route. These factors represent disadvantages with respect to gasification and pyrolysis, which are designed to operate with raw biomass feedstocks including cellulose, hemicellulose, and lignin components.

Unlike petroleum feedstocks, biomass derivatives contain a high level of functionality (e.g., –OH, –C=O and –COOH groups). This chemical composition clearly determines the catalytic strategies used to upgrade these biomass-derived molecules into liquid hydrocarbon fuels. On one hand, the high oxygen content of these biomolecules has two important consequences: these molecules possess high chemical reactivity (with a natural tendency to decompose with temperature) and, in view of their high solubility in water, they will be typically be obtained from biomass in the form of aqueous solutions. These characteristics suggest that aqueous-phase processing at mild temperatures could be an effective approach for the catalytic treatment of these resources. Unfortunately, the chemical composition of the biomass derivatives, which is quite different from that of the targeted compounds (e.g., liquid alkanes), necessitates deep chemical transformations that typically require multiple processing steps. Consequently, various types of reactions are required, including dehydration, isomerization, C–C coupling, reforming, hydrogenation, and hydrogenolysis. Some of these reactions are especially useful to achieve the requisite deoxygenation of the biomass derivative (e.g., dehydration, hydrogenation, and hydrogenolysis) whereas other reactions (e.g., those of C–C coupling) allow adjustments in the molecular weight of the final hydrocarbon fuel.

Some of the most relevant biomass-derived molecules are discussed in the next subsections. They have been selected in view of their potential to produce liquid hydrocarbon fuels by means of aqueous-phase catalytic processing. Glycerol (Sect. 2.2.3.1) was selected because, as indicated in the Introduction, it is a waste stream of the important and growing biodiesel industry which, in addition, can be produced by bacterial fermentation of sugars [81]. Hydroxymethylfurfural (HMF)

is an important product of the dehydration of glucose and fructose, and it has been extensively studied as important intermediate for production of polymers [80], solvents [82], and fuel additives [83]. As outlined in Sect. 2.2.3.2, HMF can also serve as a platform molecule for the production of liquid hydrocarbon fuels suitable for diesel and jet fuel applications. Instead of using sugars to produce secondary products like glycerol and HMF, these molecules can be used directly as feeds for the production of liquid hydrocarbon fuels through a two-step cascade catalytic approach involving reforming and C–C coupling reactions. This important route, which allows flexible production of hydrocarbon fuels with different compositions for gasoline, diesel, and jet fuel, is the focus of Sect. 2.2.3.3. Deoxygenation of biomass to hydrocarbon fuels is a complicated process that should ideally be carried out with minimal utilization of external hydrogen to make the bio-process economically feasible and cost competitive with current petroleum-based technologies [84]. Thus, the development of catalytic routes for the production of hydrocarbon fuels from biomass without (or with minimal) hydrogen consumption is highly desirable, and recent advances in this respect are described in Sect. 2.2.3.4.

2.2.3.1 Glycerol Conversion Integrated with Fischer–Tropsch Synthesis

Glycerol (1,2,3-propanetriol) is a high boiling point (563 K), water-soluble hygroscopic compound. Glycerol contains three hydroxyl groups which are responsible for its physical properties and, additionally, provide this molecule with high versatility and high chemical reactivity. Thus, oxidation [85], dehydration [86, 87], reduction [88], hydrogenolysis [89, 90], acetalization [91], and etherification [92] reactions can be performed over this molecule to produce valuable chemicals.

Since the development of the biodiesel industry, the upgrading of glycerol into useful products has caught the attention of researchers around the world [88]. The reason for this interest is that significant amounts of glycerol (e.g., 100 kg of glycerol per ton of biodiesel [93]), in the form of concentrated aqueous solutions, are produced daily in biodiesel facilities and will be available in the market. Additionally, glycerol can also be obtained as a by-product of the conversion of lignocellulose into ethanol, which is expected to be an important industry in the near future [94]. Even though glycerol currently has a large number of applications in varied fields such as cosmetics, pharmaceuticals, foods, and drinks, the overproduction of biodiesel-derived glycerol exceeds the current demand of this compound for chemical production and, thus, new technologies for the large-scale usage of this feedstock will be required. The current production of glycerol has currently reached a plateau due to competition with food production, although the expected growth of biodiesel production levels both in Europe and in the US will stimulate researchers to find new applications for crude glycerol. One of the possibilities for large-scale consumption of glycerol would be to utilize glycerol as fuel for the transportation sector. Unfortunately, unlike ethanol, glycerol cannot be directly added to conventional fuels due to its low solubility in hydrocarbons. Additionally, the high viscosity and instability (at high temperatures) of this compound strongly discourage its use as an additive in

combustion engines. Therefore, glycerol must be chemically transformed (e.g., deoxygenated) to adjust its properties to those of liquid hydrocarbon fuels. In this respect, a promising route for glycerol conversion involves the production of syngas through APR processes [95]:

$$C_3O_3H_8 \rightarrow 3CO + 4H_2 \tag{2.4}$$

This reaction is typically carried out over platinum catalysts due to the ability of this metal to achieve C–C breaking reactions (leading to CO, H_2, and CO_2) versus C–O breaking reactions (leading to light hydrocarbons) [65, 96]. To selectively produce syngas, WGS processes [reaction (2.1)] must be avoided, for example, by using inert materials (e.g., carbon) as a catalyst support instead of using oxide supports that can activate water [95]. A combination of chemical inertness (which prevents acid-catalyzed polymerization reactions from occurring) and hydrophobicity (which provides stability under water environments) are probably responsible for the good stability of carbon catalysts in the aqueous-phase processing of glycerol to syngas.

The glycerol-derived syngas can subsequently be used for the production of liquid hydrocarbon fuels and/or chemicals by means of Fischer–Tropsch and methanol syntheses, respectively. This new route would represent an interesting alternative for BTL (Sect. 2.2.1) that would overcome many of the limitations of this complex technology in the production of liquid alkanes from renewable resources, as outlined below:

(a) In contrast to the high temperatures required for biomass gasification (1,100–1,300 K), glycerol reforming is typically carried out under relatively mild temperatures (498–620 K). These temperatures are within the range employed for FTS [reaction (2.2)] and, consequently, efficient combination of both processes is possible in a single reactor [97].
(b) Concentrated aqueous solutions of glycerol (as produced in biodiesel facilities) can be reformed in a single reactor and, thus, there is no need for large biomass gasifiers and oxygen-production plants required for BTL. Additionally, the syngas obtained is undiluted and free of impurities, which decreases the capital costs associated with the expensive gas-cleaning unit (Sect. 2.2.1). Consequently, this route allows cost-competitive operations at small scale which is, as outlined in Sect. 2.2.2, advantageous for the processing of distributed biomass resources.
(c) FTS processes suffer from low thermal efficiency [98]. The coupling of the endothermic glycerol processing to syngas with the exothermic FTS processing, as shown in reaction (2.5) for the case of octane, result in an energy-efficient route for the production of liquid hydrocarbon transportation fuels from a renewable resource.

$$C_3O_3H_8 \rightarrow \frac{7}{25}C_8H_{18} + \frac{19}{25}CO_2 + \frac{37}{25}H_2O \tag{2.5}$$

2.2.3.2 Dehydration of Sugars: HMF and Furfural Platforms to Hydrocarbon Fuels

Biomass-derived sugars, obtained from cellulose, hemicellulose, or starches, can be dehydrated to form furan compounds such as furfural and HMF. These molecules have a large number of applications as chemical intermediates in the production of industrial solvents, polymers, and fuel additives. While industrial production of furfural, based on acid-catalyzed dehydration of C_5 sugars, is well developed [99], HMF generation on large scales is currently limited by the lack of cost-effective technologies, and two main challenges remain in this respect. The first challenge deals with the development of processes for effective production of HMF directly from glucose. In particular, current technologies require a glucose isomerization step to fructose, because dehydration of fructose to HMF takes place with better selectivity and higher rates [100, 101]. The second important issue is related to the control over unwanted side reactions involving the reactant, intermediates, and the final HMF product. In this latter case, the use of biphasic reactors has shown promising results, where fructose is dehydrated to HMF in the aqueous phase and the HMF is subsequently extracted by an organic solvent to avoid further degradation reactions [102].

Apart from the applications noted above, furfural and HMF form the building blocks for the production of liquid hydrocarbon transportation fuels from biomass-derived carbohydrates by means of a cascade process involving dehydration, hydrogenation, and aldol-condensation reactions [103, 104] (Fig. 2.3). The multi-step process starts with acid hydrolysis of polysaccharides such as cellulose, hemicellulose, and starch to produce monosaccharides such as glucose, fructose, and xylose. These sugars can be further dehydrated in the same acid environment to form carbonyl-containing furan compounds such as furfural and HMF. In a subsequent step, these furfural compounds can be converted into larger molecules through aldol-condensation reactions with carbonyl-containing molecules such as acetone. Condensation reactions are typically carried out at low temperatures in polar solvents like water, and are catalyzed by basic solids such as Mg–Al oxides or homogenous base catalysts such as NaOH. The aldol adducts formed contain a higher number of carbon atoms and unsaturated C=C bonds and, consequently, these compounds display low solubility in water and precipitate out of the aqueous phase. Alternatively, the aldol condensation can be carried out in a biphasic reactor where furfural compounds (previously extracted in an organic solvent such as THF) are contacted with an aqueous phase containing NaOH [104]. This process represents an improvement, since the aldol adducts are extracted in situ into the organic phase. Interestingly, the aldol adducts can undergo a second condensation with initial furfural compounds thereby allowing the production of larger molecules (Fig. 2.3). The third step of the process involves the hydrogenation of the C=C and C=O bonds of the aldol adducts in the presence of a metal (typically Pd), thereby increasing the solubility and making large water-soluble organic compounds. Interestingly, aldol condensation and subsequent hydrogenation steps can be carried out in a single reactor by using a bifunctional (metal and basic sites) and

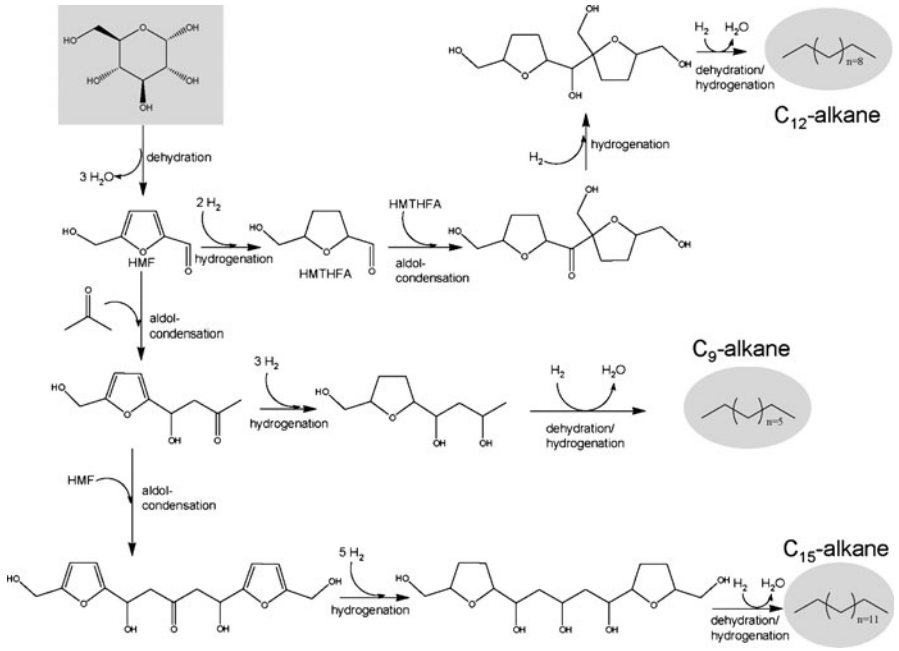

Fig. 2.3 Reaction pathways for the conversion of biomass-derived glucose into liquid alkanes via HMF. Adapted from [103]

water-stable Pd/MgO–ZrO_2 catalyst [105]. In the last step, hydrogenated aldol adducts are converted into liquid alkanes through aqueous-phase dehydration/hydrogenation (APD/H) reactions [106]. This process achieves oxygen removal from the water-soluble adduct by means of continuous cycles of dehydration and hydrogenation reactions over a bifunctional catalyst (Pt–SiO_2–Al_2O_3) containing metal and acid sites. This last step is carried out in a four-phase reactor containing an aqueous solution of adducts, a hydrogen gas inlet stream, a hexadecane sweep stream, and the solid catalyst [103]. As oxygen is removed from the hydrogenated adducts in the form of water, they become more hydrophobic and the hexadecane sweep stream assists the removal of these species from the catalysts surface avoiding overreaction to coke. A recent improvement in the ADP/H step allowed elimination of the hexadecane sweep stream by using water-stable bifunctional Pt/$NbPO_4$ catalysts [104], in which the niobium-based support presents superior dehydration activity and stability properties under water environments [107]. As a result of this improvement, the final products, liquid hydrocarbon fuels with targeted molecular weights (C_9–C_{15} for HMF and C_8–C_{13} for furfural), are obtained in the form of a pure organic stream that spontaneously separates from water and retains about 60% of the carbon of the initial sugar feed.

2.2.3.3 Reforming/Reduction of Sugars Over Pt–Re Catalysts

Biomass-derived carbohydrates (obtained from cellulose and hemicellulose) are typically C_5 or C_6 molecules with a high oxygen content (C:O stoichiometry of 1:1). This chemical composition contrasts with that of transportation fuels, which are larger (e.g., C_5–C_{12} for gasoline, C_9–C_{16} for jet fuel, and C_{10}–C_{20} for diesel applications) and do not contain oxygen. Consequently, the production of liquid hydrocarbon fuels from biomass-derived carbohydrates must involve reactions for oxygen removal (e.g., C–O hydrogenolysis, dehydration, hydrogenation) combined with C–C bond formation steps (e.g., aldol condensation, ketonization, oligomerization) to increase molecular weight. To ensure economic feasibility of the process, this deep chemical transformation should ideally be carried out (a) with minimum use of hydrogen from an external source and (b) with a limited number of reactors and purification/separation steps. Several approaches have been proposed to address these points. First, hydrogen necessary for deoxygenation processes can be provided by a fraction of the same sugar feedstock, utilizing APR reactions to produce hydrogen in situ [65], as indicated in the following equation for the case of glucose:

$$C_6O_6H_{12} + 6H_2O \rightarrow 6CO_2 + 12H_2 \tag{2.6}$$

Second, multifunctional catalysts, able to carry out different reactions in the same reactor, can be used to reduce the complexity of biomass upgrading processes [108].

Recently, a new technology that combines both approaches (e.g., in situ generation of hydrogen and use of multifunctional catalysts) has been used to transform aqueous solutions of sugars and sugar alcohols into liquid hydrocarbon fuels by means of a simple two-step process [75] (Fig. 2.4). In the first step, sugars and polyols are partially deoxygenated over a Pt–Re/C catalyst at temperatures near 500 K to yield a mixture of monofunctional hydrocarbons in the C_4–C_6 range (including acids, alcohols, ketones, and heterocycles) which are stored in an organic phase that spontaneously separates from water. The Pt–Re/C catalyst achieves partial deoxygenation of the sugar feedstock (up to 80% of the oxygen in the initial sugar is removed) by the proper control of the rates for C–C cleavage (leading to CO_2 and H_2) and C–O cleavage (leading to alkanes). The cleavage of C–O is accomplished by reaction with hydrogen (e.g., hydrogenolysis) and is promoted by Re [109, 110]. As oxygen is progressively removed from the intermediates in the form of water, their interaction with the surface of the catalyst becomes weaker, facilitating desorption and resulting in the formation of acids, alcohols, ketones, and heterocycles (Fig. 2.4). Interestingly, this process represents an improvement over pyrolysis (Sect. 2.2.2) since, unlike bio-oils, the monofunctional stream contains a well-defined mixture of hydrophobic compounds in an organic phase completely free of water.

The monofunctional compounds are not completely deoxygenated and they thus contain functionalities that can be used for subsequent upgrading processes.

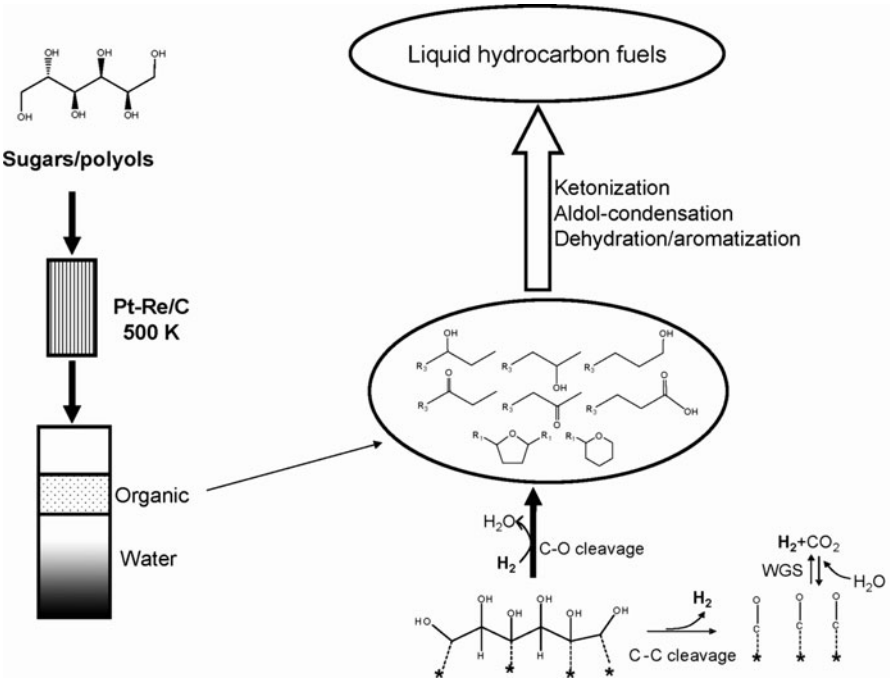

Fig. 2.4 Schematic representation of the reforming/reduction of sugars and polyols over Pt–Re/C to generate intermediate hydrophobic monofunctionals. The intermediates can be upgraded to liquid hydrocarbon fuels by means of C–C coupling reactions. Adapted from [75]

This strategy of partial removal of oxygen from the feed and subsequent upgrading of intermediates leads to better control of reactivity, and important biomass derivatives such as lactic acid and levulinic acid have been upgraded to fuels and chemicals by using this approach [84]. The organic stream of monofunctional compounds can be converted, through C–C coupling reactions, into targeted liquid hydrocarbon fuels of different classes (Fig. 2.4). Each type of monofunctional compound in the organic stream (e.g., alcohols, ketones, acids) can be upgraded to different hydrocarbons through different C–C coupling reactions (e.g., oligomerization, aldol condensation, and ketonization). For example, the hydrophobic stream derived from the sugar, previously enriched in alcohol by hydrogenation of the ketones, can be converted to aromatic compounds (gasoline components) at atmospheric pressure over an acidic H-ZSM5. Ketones can undergo aldol condensation over a bifunctional $Cu/Mg_{10}Al_7O_x$ (where the mixed oxide achieves aldol condensation and Cu hydrogenates the unsaturated aldol adduct) to yield larger compounds with low level of branching, as those required for diesel applications [111]. Finally, as noted in Sect. 2.2.2.3, ketonization can be used to upgrade the acidic fraction of the hydrophobic stream to larger ketones. This reaction acquires special importance when the organic stream is rich in carboxylic acids, as is the case when the feed is glucose [75].

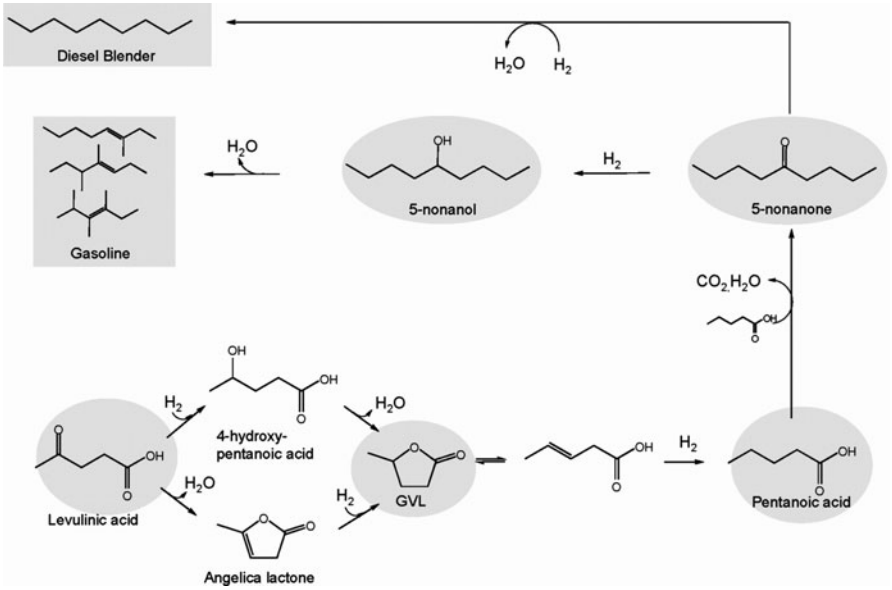

Fig. 2.5 Catalytic routes for the production of liquid hydrocarbon fuels from biomass-derived levulinic acid. Adapted from [84]

2.2.3.4 Levulinic Acid and γ-Valerolactone Platforms to Hydrocarbon Fuels

Levulinic acid (4-oxopentanoic acid) is an important biomass-derived acid that can be obtained in high yields via acid hydrolysis of cellulosic wastes, such as paper mill sludge, urban waste paper, and agricultural residues [112]. Additionally, levulinic acid is considered to be one of the 12 most promising biomass derivatives in view of its potential to serve as a building block for the development of biorefinery processes [80]. Levulinic acid contains two functional groups (C=O and COOH) which gives this molecule a variety of synthetic transformations [113] to generate value-added chemicals such as methyltetrahydrofuran (MTHF) (a gasoline additive) and δ-aminolevulinic acid (DALA) (a biodegradable pesticide) [114].

Recently, our group has developed a catalytic route to upgrade concentrated aqueous solutions of levulinic acid into liquid hydrocarbon fuels (gasoline and diesel) [115]. The catalytic approach involves dehydration/hydrogenation (to reduce the oxygen content of the molecule) and ketonization (to increase the molecular weight) reactions (Fig. 2.5). Interestingly, the use of a bifunctional (metal and acid sites) Pd/Nb_2O_5 catalyst allows these reactions to be carried out with a minimum number of reactors and separation steps. Levulinic acid is first hydrogenated at low temperatures (e.g., 423 K) to form γ-valerolactone (GVL) over a Ru/C catalyst. This hydrogenation step is requisite to prevent the catalytic route from passing through high concentrations of angelica lactone, a known coke

precursor [116] which is produced by dehydration at higher temperatures (e.g., 573–623 K). Aqueous GVL is subsequently transformed into hydrophobic pentanoic acid with high yields over Pd/Nb_2O_5 by means of ring opening (on acid sites) and hydrogenation reactions at moderate temperatures and pressures. Remarkably, when the space velocity is sufficiently low, pentanoic acid is upgraded to 5-nonanone over the same Pd/Nb_2O_5 bed with a 70% carbon yield, allowing the direct production of 5-nonanone from GVL in a single reactor [115]. 5-nonanone, which is obtained in an organic layer that spontaneously separates from water, serves as a platform molecule for the production of liquid hydrocarbon fuels for the transportation sector (Fig. 2.5). For example, the organic C_9-ketone stream can be processed (through hydrogenation/dehydration cycles) over a bifunctional metal–acid catalyst such as Pt/Nb_2O_5 [104] into linear *n*-nonane, with excellent cetane number and lubricity to be used as a diesel blender agent. Alternatively, 5-nonanol, obtained by the hydrogenation of the C_9-ketone, can be dehydrated and isomerized in a single step over an USY zeolite catalyst to produce a mixture of branched C_9 alkenes with the appropriate molecular weight and structure for use in gasoline after hydrogenation to the corresponding alkanes.

GVL is an interesting biomass derivative that has been proposed to be a potential gasoline additive [117] as well as a precursor of polymers [118] and fine chemicals [119]. It is typically produced by catalytic hydrogenation of levulinic acid. This reduction is normally carried out at low temperatures to avoid GVL over reduction to MTHF. However, what makes GVL a very interesting biomass feedstock is the potential to produce it without using any external source of hydrogen. In particular, as a result of the dehydration of C_6 sugars, levulinic acid is produced along with stoichiometric amounts of formic acid, which can be converted to CO_2 and H_2 at the same temperatures used for levulinic acid reduction to GVL. Consequently, formic acid can be utilized as a renewable source of hydrogen for levulinic acid reduction to GVL [120].

Recently, a new catalytic route has taken advantage of this important characteristic of GVL to develop a process that converts aqueous solutions of GVL into liquid hydrocarbon fuels without the need of an external source of hydrogen [121]. In this process, the GVL feed undergoes decarboxylation at elevated pressures (e.g., 36 bar) over a silica/alumina catalysts, producing a gas stream composed of butene isomers and CO_2. This gaseous stream is then passed over an acidic catalyst (H-ZSM5, Amberlyst) that achieves oligomerization of butenes yielding alkenes with molecular weights suitable for gasoline and jet fuel applications. Prior to oligomerization, liquid water must be removed from the gas stream in a separator to achieve effective oligomerization of butene in the second reactor. This technology presents important economic and environmental advantages: (a) no external hydrogen is required in the process, (b) precious metal catalysts are not required, and (c) a gas stream of pure CO_2 is produced at the elevated pressures, thereby permitting effective utilization of sequestration or capture technologies to mitigate greenhouse gas emissions.

2.3 Conclusions

Our society is highly dependent on fossil fuels, which are nonrenewable and contribute to global warming. The production of liquid hydrocarbon transportation fuels from nonedible lignocellulosic biomass is an interesting alternative that can mitigate these issues and overcome many of the limitations of ethanol and biodiesel as biofuels. Recalcitrance and complexity are the two main barriers for the large-scale utilization of lignocellulose as a source of liquid hydrocarbon fuels. Several routes exist for achieving the deep chemical transformations required to convert biomass into liquid hydrocarbon fuels (e.g., BTL, pyrolysis integrated with upgrading processing, and aqueous-phase processing of biomass derivatives), and all of these routes involve the judicious use of heterogeneous catalysts to control the specifications of the final fuel.

References

1. EIA Annual Energy Review (2008) http://www.eia.doe.gov/aer/pdf/aer.pdf. Accessed 7 Jul 2010
2. Eurostat (2009) Statistical aspects of the energy economy in 2008, issue number 55/2009. http://epp.eurostat.ec.europa.eu/cache/ITY_OFFPUB/KS-SF-09-055/EN/KS-SF-09-055-EN.PDF. Accessed 7 Jul 2010
3. Simonetti D, Dumesic JA (2008) Catalytic strategies for changing the energy content and achieving C–C coupling in biomass-derived oxygenated hydrocarbons. ChemSusChem 1:725–733
4. Energy Information Administration, International Energy Outlook (2009) http://www.eia.doe.gov/oiaf/ieo/pdf/0484%282009%29.pdf. Accessed 7 Jul 2010
5. BP (2009) Statistical review of world energy. http://bp.com/statisticalreview. Accessed 7 Jul 2010
6. Intergovernmental Panel on Climate Change (2007) Climate change 2007: synthesis report. http://www.ipcc.ch/publications_and_data/ar4/syr/en/contents.html. Accessed 7 Jul 2010
7. Worldwatch Institute Center for American Progress (2006) American energy: the renewable path to energy security. http://www.worldwatch.org/files/pdf/AmericanEnergy.pdf. Accessed 7 Jul 2010
8. White House (2007) President Bush state on the union address. http://usgovinfo.about.com/b/2007/01/23/bush-delivers-his-seventh-state-of-the-union-address.htm. Accessed 7 Jul 2010
9. Official Journal of the European Union (2003) Directive 2003/30/EC of the European Union Parliament. http://ec.europa.eu/energy/res/legislation/doc/biofuels/en_final.pdf. Accessed 7 Jul 2010
10. Kreith F, Goswami DY (2007) Handbook of energy efficiency and renewable energy. CRC Press, Boca Raton
11. Graziani M, Fornasiero P (2007) Renewable resources and renewable energy: a global challenge. CRC Press, Boca Raton
12. Klass DL (1998) Biomass for the renewable energy, fuels and chemicals. Academic, London
13. Chheda J, Huber GW, Dumesic JA (2007) Liquid-phase catalytic processing of biomass-derived oxygenated hydrocarbon to fuels and chemicals. Angew Chem Int Ed 46:7164–7183
14. Ragauskas AJ et al (2006) The path forward for biofuels and biomaterials. Science 311:484–489

15. NSF (2008) Breaking the chemical and engineering barriers to lignocellulosic biofuels: next generation hydrocarbon biorefineries. http://www.ecs.umass.edu/biofuels/Images/Roadmap2-08.pdf. Accessed 7 Jul 2010
16. US Energy Information Administration (2009) Petroleum navigator. http://tonto.eia.doe.gov/dnav/pet/hist/wtotworldw.htm. Accessed 7 Jul 2010
17. Worldwatch Institute (2007) Biofuels for transport. Earthscan, London
18. Regalbuto JR (2009) Cellulosic biofuels—got gasoline? Science 325:822–824
19. EPA/DOE sponsored web site. http://www.fueleconomy.gov/feg/flextech.shtml. Accessed 7 Jul 2010
20. Hamelinck CN, Suurs RAA, Faaij APC (2005) International bioenergy transport costs and energy balance. Biomass Bioenergy 29:114–134
21. Spath PL, Dayton DC (2003) Preliminary screening-technical and economic assessment of synthesis gas to fuels and chemicals with emphasis on the potential for biomass-derived syngas. United States Department of Energy, National Renewable Energy Laboratory. http://www.nrel.gov/docs/fy04osti/34929.pdf. Accessed 7 Jul 2010
22. Perlack RD, Wright LL, Turhollow AF, Graham RL, Stokes BJ, Erbach DC (2005) Biomass as feedstock for a bioenergy and bioproducts industry: the technical feasibility of a billion-ton annual supply. DOE/GO-102005-2135, Oak Ridge National Laboratory. http://feedstockreview.ornl.gov/pdf/billion_ton_vision.pdf. Accessed 7 Jul 2010
23. Klass DL (2004) Biomass for the renewable energy and fuels. In: Cleveland CJ (ed) Encyclopedia of energy. Elsevier, London
24. Lange JP (2007) Lignocellulose conversion: an introduction to chemistry, process and economics. Biofuels, Bioprod Biorefin 1:39–48
25. Stocker M (2008) Biofuels and biomass-to-liquid fuels in the biorefinery: catalytic conversion of lignocellulosic biomass using porous materials. Angew Chem Int Ed 47:9200–9211
26. US Department of Energy (2005) Feedstock composition glossary. http://www1.eere.energy.gov/biomass/feedstock_glossary.html#C. Accessed 7 Jul 2010
27. US Department of Energy (2005) Feedstock composition glossary. http://www1.eere.energy.gov/biomass/feedstock_glossary.html#S. Accessed 7 Jul 2010
28. International Energy Report (2007) Energy technology essentials, biofuel production. http://www.iea.org/techno/essentials2.pdf. Accessed 7 Jul 2010
29. Kumar P, Barrett DM, Delwiche MJ, Stroeve P (2009) Methods for pretreatment of lignocellulosic biomass for efficient hydrolysis and biofuel production. Ind Eng Chem Res 48:3713–3729
30. Carrol A, Somerville C (2009) Cellulosic biofuels. Annu Rev Plant Biol 60:165–182
31. Kumar R, Mago G, Balan V, Wyman CE (2009) Physical and chemical characterizations of corn stover and poplar solids resulting from leading pretreatment technologies. Bioresour Technol 100:3948–3962
32. Bozell JJ (2008) Feedstocks for the future: biorefinery production of chemicals from renewable carbon. Clean Soil Air Water 36:641–647
33. Lynd LR, Wyman C, Laser M, Johnson D, Landucci R (2002) Strategic biorefinery analysis: analysis of biorefineries, technical report. US National Renewable Energy Laboratory. http://www.nrel.gov/docs/fy06osti/35578.pdf. Accessed 7 Jul 2010
34. Kamm B, Gruber PR, Kamm M (2006) Biorefineries-industrial processes and products: status quo and future directions. Wiley-VCH, Weinheim
35. Kamm B (2007) Production of platform chemicals and synthesis gas from biomass. Angew Chem Int Ed 46:5056–5058
36. Bridgwater AV (2001) Progress in thermochemical biomass conversion. Blackwell Science Ltd, Oxford
37. Lange JP (2007) Lignocellulose conversion: an introduction to chemistry, process and economics. In: Centi G, van Santen RA (eds) Catalysis from renewables: from feedstock to energy production. Wiley, Weinheim

38. Kavalov B, Peteves SD (2005) European commission joint research centre. Status and perspectives of biomass-to-liquid fuels in the European Union. http://www.mangus.ro/pdf/Stadiul%20actual%20si%20perspectivele%20bio-combustibililor%20in%20Europa.pdf. Accessed 7 Jul 2010
39. Milne TA, Evans RJ, Abatzoglou N (1998) Biomass gasifier tars: their nature, formation and conversion; Report No. NREL/TP-570-25357. National Renewable Energy Laboratory. http://www.nrel.gov/docs/fy99osti/25357.pdf. Accessed 7 Jul 2010
40. Boerrigter H, Van Der Drift A (2004) Biosyngas: description of R&D trajectory necessary to reach large-scale implementation of renewable syngas from biomass. Energy Research Centre of the Netherlands. http://www.ecn.nl/docs/library/report/2004/c04112.pdf. Accessed 7 Jul 2010
41. Devi L, Ptasinski KJ, Janssen FJJG (2003) A review of the primary measures for tar elimination in biomass gasification processes. Biomass Bioenergy 24:125–140
42. Rapagna S, Jand N, Kiennemann A, Foscolo PU (2000) Steam-gasification of biomass in a fluidised-bed of olivine particles. Biomass Bioenergy 19:187–197
43. Tomishige K, Asadullah M, Kunimori K (2004) Syngas production by biomass gasification using $Rh/CeO_2/SiO_2$ catalysts and fluidized bed reactor. Catal Today 89:389–403
44. Sutton D, Kelleher B, Ross JRH (2001) Review of literature on catalysts for biomass gasification. Fuel Process Technol 73:155–173
45. Mudge LK, Baker EG, Mitchell DH, Brown MD (1985) Catalytic steam gasification of biomass for methanol and methane production. J Solar Energy Eng 107:88–92
46. Stahl K, Waldheim L, Morrim M, Johnsson U, Gardmark L (2004) Biomass IGCC at Värnamo, Sweden: past and future, GCEP Energy Workshop. http://gcep.stanford.edu/pdfs/energy_workshops_04_04/biomass_stahl.pdf. Accessed 7 Jul 2010
47. Huber GW, Iborra S, Corma A (2006) Synthesis of transportation fuels from biomass: chemistry, catalysts, and engineering. Chem Rev 106:4044–4048
48. Caldwell L (1980) Selectivity in Fischer-Tropsch synthesis: review and recommendations for further work. http://www.fischer-tropsch.org/DOE/DOE_reports/81223596/pb81223596.pdf. Accessed 7 Jul 2010
49. Dry ME (2002) The Fischer–Tropsch process: 1950–2000. Catal Today 71:227–241
50. Boerrigter H, Zwart R (2004) High efficiency co-production of Fischer-Tropsch (FT) transportation fuels and substitute natural gas (SNG) from biomass. Energy Research Centre of the Netherlands. http://www.biosng.com/fileadmin/biosng/user/documents/reports/rx04042.pdf. Accessed 7 Jul 2010
51. Steynberg A, Dry M (2004) Fischer-Tropsch technology. In: Steynberg A, Dry M (eds) Studies on surface science and catalysis, vol 152. Elsevier, New York
52. Martinez A, Lopez C (2005) The influence of ZSM-5 zeolite composition and crystal size on the in situ conversion of Fischer–Tropsch products over hybrid catalysts. Appl Catal A Gen 294:251–259
53. Boerrigter H, Calis H, Slort D, Bodenstaff H, Kaandorp A, Den Uil D, Rabou L (2004) Gas cleaning for integrated biomass gasification (BG) and Fischer-Tropsch (FT) synthesis. Energy Research Centre of the Netherlands and Shell Global Solutions International. http://www.ecn.nl/docs/library/report/2004/c04056.pdf. Accessed 7 Jul 2010
54. Choren Industries Press Release. http://www.choren.com/en/choren_industries/information_press/press_releases/?nid=195. Accessed 7 Jul 2010
55. Lange JP (2001) Methanol synthesis: a short review of technology improvements. Catal Today 64:3–8
56. Zhang R, Cummer K, Suby A, Brown RC (2005) Biomass-derived hydrogen from an air-blown gasifier. Fuel Process Technol 86:861–874
57. Koppatz S, Pfeifer C, Rauch R, Hofbauer H, Marquard-Moellensted T, Specht M (2009) H_2 rich product gas by steam gasification of biomass with in situ CO_2 absorption in a dual fluidized bed system of 8 MW fuel input. Fuel Process Technol 90:914–921

58. Elliott DC, Beckman D, Bridgwater AV, Diebold JP, Gevert SB, Solantausta Y (1991) Developments in direct thermochemical liquefaction of biomass: 1983–1990. Energy Fuel 5:399–410
59. Mohan D, Pittman CU, Steele PH (2006) Pyrolysis of wood/biomass for bio-oil: a critical review. Energy Fuel 20:848–889
60. Diebold JP (2000) A review of the chemical and physical mechanisms of the storage stability of fast pyrolysis bio-oils, Report No. NREL/SR-570-27613. National Renewable Energy Laboratory: Golden, CO. http://www.p2pays.org/ref/19/18946.pdf. Accessed 7 Jul 2010
61. Czernik S, Bridgwater AV (2004) Overview of applications of biomass fast pyrolysis oil. Energy Fuel 18:590–598
62. Elliott DC (2007) Historical developments in hydroprocessing bio-oils. Energy Fuel 21:1792–1815
63. Furimsky E (2000) Catalytic hydrodeoxygenation. Appl Catal A Gen 199:147–190
64. Czernik S, French R, Feik C, Chornet E (2002) Hydrogen by catalytic steam reforming of liquid byproducts from biomass thermoconversion processes. Ind Eng Chem Res 41:4209–4215
65. Cortright RD, Davda RR, Dumesic JA (2002) Hydrogen from catalytic reforming of biomass-derived hydrocarbons in liquid water. Nature 418:964–967
66. Davda RR, Dumesic JA (2004) Renewable hydrogen by aqueous-phase reforming of glucose. Chem Commun 36–37
67. Ramesh K, Sharma N, Bakhshi N (1993) Catalytic upgrading of pyrolysis oil. Energy Fuel 7:306–314
68. Adjaye JD, Katikameni SPR, Bakhshi NN (1996) Catalytic conversion of a biofuel to hydrocarbons: effect of mixtures of HZSM-5 and silica-alumina catalysts on product distribution. Fuel Process Technol 48:115–143
69. Gayubo AG, Aguayo AT, Atutxa A, Aguado R, Bilbao J (2004) Transformation of oxygenate components of biomass pyrolysis oil on a HZSM-5 zeolite. Ind Eng Chem Res 43:2610–2618
70. Carlson TR, Vispute TP, Huber GW (2008) Green gasoline by catalytic fast pyrolysis of solid biomass derived compounds. ChemSusChem 1:397–400
71. Milne TA, Aglevor F, Davis MS, Deutch D, Johnson D (1997) Development in thermal biomass conversion. Blackie Academic and Professional, London
72. Renz M (2005) Ketonization of carboxylic acids by decarboxylation: mechanism and scope. Eur J Org Chem 6:979–988
73. Dooley KM, Bhat AK, Plaisance CP, Roy AD (2007) Ketones from acid condensation using supported CeO_2 catalysts: effect of additives. Appl Catal A Gen 320:122–133
74. Hendren TS, Dooley KM (2003) Kinetics of catalyzed acid/acid and acid/aldehyde condensation reactions to non-symmetric ketones. Catal Today 85:333–351
75. Kunkes EL, Simonetti DA, West RM, Serrano-Ruiz JC, Gartner CA, Dumesic JA (2008) Catalytic conversion of biomass to monofunctional hydrocarbons and targeted liquid-fuel classes. Science 322:417–421
76. Klimkiewicz R, Fabisz E, Morawski I, Grabowska H, Syper L (2001) Ketonization of long chain esters from transesterification of technical waste fats. J Chem Technol Biotechnol 76:35–38
77. Glinski M, Szymanski W, Lomot D (2005) Catalytic ketonization over oxide catalysts: transformations of various alkyl heptanoates. Appl Catal A Gen 281:107–113
78. Gaertner CA, Serrano-Ruiz JC, Braden DJ, Dumesic JA (2009) Catalytic upgrading of bio-oils by ketonization. ChemSusChem 2:1121–1124
79. Serrano-Ruiz JC, Dumesic JA (2009) Catalytic upgrading of lactic acid to fuels and chemicals by dehydration/hydrogenation and C–C coupling reactions. Green Chem 11:1101–1104
80. Werpy T, Petersen G (2004) Top value added chemicals from biomass. US Department of Energy, Office of Scientific and Technical Information. http://www.nrel.gov/docs/fy04osti/35523.pdf. Accessed 7 Jul 2010

81. Gong CS, Du JX, Gao NJ, Tsao GT (2000) Coproduction of ethanol and glycerol. Appl Biochem Biotechnol 84:543–559
82. Lichtenthaler FW, Peters S (2004) Carbohydrates as green raw materials for the chemical industry. C R Chimie 7:65–90
83. Paul SF (2001) US patent 6309430
84. Serrano-Ruiz JC, West RM, Dumesic JA (2010) Catalytic conversion of renewable biomass resources to fuels and chemicals. Annu Rev Chem Biomol Eng 1:79–101
85. Gulen D, Lucas M, Claus P (2005) Liquid phase oxidation of glycerol over carbon supported gold catalysts. Catal Today 102–103:166–172
86. Chiu CW, Dasari MA, Suppes GJ, Sutterlin WR (2006) Dehydration of glycerol to acetol via catalytic reactive distillation. AICHE J 52:3543–3548
87. Katryniok B, Paul S, Capron M, Dumeignil F (2009) Towards the sustainable production of acrolein by glycerol dehydration. ChemSusChem 2:719–730
88. Pagliaro M, Rossi M (2008) Future of glycerol, new usages for a versatile raw material. RSC publishing, London
89. Wang H, Liu H (2007) Selective hydrogenolysis of glycerol to propylene glycol on Cu–ZnO catalysts. Catal Lett 117:62–67
90. Maris EP, Davis RJ (2007) Hydrogenolysis of glycerol over carbon-supported Ru and Pt catalysts. J Catal 249:328–337
91. Ruiz VR, Velty A, Santos LL, Leyva-Perez A, Sabater MJ, Iborra S, Corma A (2010) Gold catalysts and solid catalysts for biomass transformations: valorization of glycerol and glycerol–water mixtures through formation of cyclic acetals. J Catal 271:351–357
92. Karinen RS, Krause AOI (2006) New biocomponents from glycerol. Appl Catal A Gen 306:128–133
93. Wiinikainen TS, Karinen RS, Krause AOI (2007) Conversion of glycerol into traffic fuels. In: Centi G, Van Santen RA (eds) Catalysis for renewables: from feedstocks to energy production. Wiley-VCH, Weinheim
94. Carbohydrate Economy Bulletin (2000) http://www.carbohydrateeconomy.org/library/admin/uploadedfiles/Carbohydrate_Economy_Bulletin_Volume_1_Numb_3.htm. Accessed 7 Jul 2010
95. Soares RR, Simonetti DA, Dumesic JA (2006) Glycerol as a source for fuels and chemicals by low-temperature catalytic processing. Angew Chem Int Ed 45:3982–3985
96. Alcala R, Mavrikakis M, Dumesic JA (2003) DFT studies for cleavage of C–C and C–O bonds in surface species derived from ethanol on Pt(111). J Catal 218:178–190
97. Simonetti DA, Rass-Hansen J, Kunkes EL, Soares RR, Dumesic JA (2007) Coupling of glycerol processing with Fischer–Tropsch synthesis for production of liquid fuels. Green Chem 9:1073–1083
98. Bartholomew CH, Farrauto RJ (2006) Fundamental of industrial catalytic processes. Wiley, Hoboken
99. Zeitsch KJ (2000) The chemistry and technology of furfural and its many by-products. Elsevier, Amsterdam, pp 34–69
100. Chheda J, Roman-Leshkov Y, Dumesic JA (2007) Production of 5-hydroxymethylfurfural and furfural by dehydration of biomass-derived mono- and poly-saccharides. Green Chem 9:342–350
101. Moreau C, Belgacem M, Gandini A (2004) Recent catalytic advances in the chemistry of substituted furans from carbohydrates and in the ensuing polymers. Top Catal 27:11–30
102. Roman-Leshkov Y, Chheda J, Dumesic JA (2006) Phase modifiers promote efficient production of hydroxymethylfurfural from fructose. Science 312:1933–1937
103. Huber GW, Chheda JN, Barrett CJ, Dumesic JA (2005) Production of liquid alkanes by aqueous-phase processing of biomass-derived carbohydrates. Science 308:1446–1450
104. West RM, Liu ZL, Peter M, Dumesic JA (2008) Liquid alkanes with targeted molecular weights from biomass-derived carbohydrates. ChemSusChem 1:417–424

105. Barret C, Chheda J, Huber GW, Dumesic JA (2006) Single-reactor process for sequential aldol-condensation and hydrogenation of biomass-derived compounds in water. Appl Catal B Environ 66:111–118
106. Huber GW, Cortright RD, Dumesic JA (2004) Renewable alkanes by aqueous-phase reforming of biomass-derived oxygenates. Angew Chem Int Ed 43:1549–1551
107. West RM, Braden DJ, Dumesic JA (2009) Dehydration of butanol to butene over solid acid catalysts in high water environments. J Catal 262:134–143
108. Simonetti DA, Dumesic JA (2009) Catalytic production of liquid fuels from biomass-derived oxygenated hydrocarbons: catalytic coupling at multiple length scales. Catal Rev 51:441–484
109. Pallassana V, Neurock M (2002) Reaction paths in the hydrogenolysis of acetic acid to ethanol over Pd(111), Re(0001), and PdRe alloys. J Catal 209:289–305
110. Kunkes EL, Simonetti DA, Dumesic JA, Pyrz WD, Murillo LE, Chen JG, Buttrey DJ (2008) The role of rhenium in the conversion of glycerol to synthesis gas over carbon supported platinum–rhenium catalysts. J Catal 260:164–177
111. Kunkes EL, Gurbuz E, Dumesic JA (2009) Vapour-phase C–C coupling reactions of biomass-derived oxygenates over Pd/$CeZrO_x$ catalysts. J Catal 266:236–249
112. Fritzpatrick SW (1997) World patent 9640609
113. Leonard R (1956) Levulinic acid as a basic chemical raw material. Ind Eng Chem 48:1330–1341
114. Bozell JJ, Moens L, Elliott DC, Wang Y, Neuenscwander GG et al (2000) Production of levulinic acid and use as a platform chemical for derived products. Resour Conserv Recycl 28:227–239
115. Serrano-Ruiz JC, Wang D, Dumesic JA (2010) Catalytic upgrading of levulinic acid to 5-nonanone. Green Chem 12:574–577
116. Ayoub P, Lange JP (2008) World Patent WO/2008/142127
117. Horvath IT, Mehdi H, Fabos V, Boda L, Mika LT (2008) γ-valerolactone-a sustainable liquid for energy and carbon-based chemicals. Green Chem 10:238–242
118. Lange JP, Vestering JZ, Haan RJ (2007) Towards bio-based Nylon: conversion of γ-valerolactone to methyl pentenoate under catalytic distillation conditions. Chem Commun 3488–3490
119. Manzer LE (2004) Catalytic synthesis of α-methylene-γ-valerolactone: a biomass-derived acrylic monomer. Appl Catal A Gen 272:249–256
120. Heeres H, Handana R, Chunai D, Rasrendra CB, Girisuta B, Heeres HJ (2009) Combined dehydration/(transfer)-hydrogenation of C_6-sugars (D-glucose and D-fructose) to γ-valerolactone using ruthenium catalysts. Green Chem 11:1247–1255
121. Bond JQ, Martin-Alonso D, Wang D, West RM, Dumesic JA (2010) Integrated catalytic conversion of γ-valerolactone to liquid alkenes for transportation fuels. Science 327:1110–1114

Chapter 3
Utilization of Biogas as a Renewable Carbon Source: Dry Reforming of Methane

Christina Papadopoulou, Haris Matralis, and Xenophon Verykios

Abstract Environmental concerns and sustainability issues demand the production of energy carriers from renewable resources using, if possible, technologies and infrastructure developed for fossil fuels. Biogas, a product of waste biomass anaerobic digestion, is a promising raw material for this purpose. As it consists mainly of CH_4 and CO_2, the most suitable process for its utilization is the dry reforming of methane (DRM) to synthesis gas and then to liquid energy carriers via the Fischer–Tropsch technology. This chapter reviews the chemistry of DRM and the catalytic systems developed for this process, with emphasis on the most important issue, namely, catalyst deactivation due to accumulation of carbonaceous deposits.

3.1 Introduction

Considerable alterations regarding global energy and material resources are occurring over recent decades. Energy demand is rapidly increasing worldwide, especially due to growing economies, primarily in Asia. The volatility of oil and natural gas prices illustrates the necessity of diversity, sustainability, and security in energy supply. On the other hand, global environmental protection has become a significant vector. Energy production is still based mainly on combustion processes using fossil fuels, a fact which is unlikely to change in the near future (see Fig. 3.1) [1, 2].

C. Papadopoulou (✉) • H. Matralis
Department of Chemistry, University of Patras, GR 26504 Patras, Greece
e-mail: cpapado@chemistry.upatras.gr; matralis@chemistry.upatras.gr

X. Verykios
Department of Chemical Engineering, University of Patras, GR 26504 Patras, Greece
e-mail: verykios@chemeng.upatras.gr

L. Guczi and A. Erdőhelyi (eds.), *Catalysis for Alternative Energy Generation*,
DOI 10.1007/978-1-4614-0344-9_3,

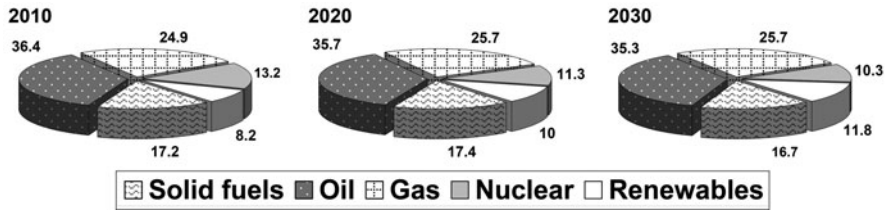

Fig. 3.1 Estimated contribution of various energy resources in total primary energy, expressed as % (based on data obtained from [1])

For this reason, CO_2 emissions are expected to increase. Furthermore, deforestation and changes in land usage aggravate the problem of the greenhouse phenomenon, causing global warming and unpredictability of weather patterns. Restrictions concerning gas emissions urgently demand the development of clean technologies with minimum environmental impact.

Electricity production from renewable sources (wind, solar, geothermal, hydro) is gaining ground in many EU countries. However, the overall progress is hindered mainly due to impediments in the transport sector and, as it can be observed in Fig. 3.1, it is uncertain whether the goal of 20% share of energy from renewable sources could be achieved by 2030 [1, 3, 4]. The problem in security of supply and cost efficiency of easily transportable energy carriers coming from renewables is most acute, influencing the market for transport fuel. Furthermore, the conversion of land use for the production of biofuels is discouraged. Thus, it is necessary to provide criteria ensuring that biofuels and bioliquids can qualify as alternatives only when it can be guaranteed that they do not originate in biodiverse or protected areas [3].

Biomass can be converted to energy or energy carriers following different routes, depending on the source and the type of biomass feedstock, the conversion process, the infrastructure, the form in which the energy is required, the economic aspects, and the environmental requirements. The main processes can be categorized as thermochemical conversion (combustion, gasification, pyrolysis, liquefaction), biochemical conversion (anaerobic digestion, fermentation), and extraction methods [5–8]. Biomass combustion technologies from classic firewood to modern systems are widely deployed, especially in Northern Europe, but produce energy in the form of electricity or heat to be used at the point of production, while waste incineration presents much higher capital costs and lower efficiency [5, 6]. Thus, combustion processes cannot contribute to the production of liquid energy carriers. Pyrolysis, fermentation, and extraction (transesterification) produce liquid fuels suitable for use in internal combustion engines, whereas biomass gasification processes produce a combustible gas mixture (consisting of H_2, CO, CO_2, CH_4, and traces of other hydrocarbons) that can be either burnt directly or used as fuel for gas engines and turbines or as feedstock (syngas) in the production of liquid fuels and methanol [5–8]. However, the above processes are faced with various limitations such as high costs

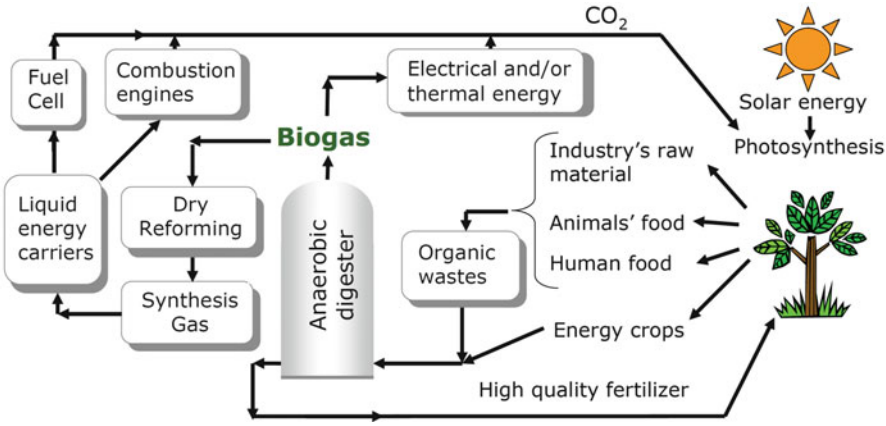

Fig. 3.2 The biogas cycle

and critical operational demands (gasification), thermal stability of the product (pyrolysis), and, most importantly, the feedstock quality required (pyrolysis, fermentation, extraction) [5, 6]. Anaerobic digestion is a commercially proven technology and is widely used for treating high-moisture-content organic wastes, i.e., 80–90% moisture [6]. The digester's feedstock can be any biodegradable raw material, originating from sewage sludge, municipal solid wastes, animal manures, agro-industrial wastes, energy crops, and by-products from biofuels' production [9–16]. The main product of digestion is biogas. The flexibility regarding the raw material used is the major advantage of the process. In principle, biomass derivatives can be considered as quasi-carbon neutral as carbon dioxide added in the atmosphere by the utilization of its products has previously been consumed by plants through photosynthesis. However, there are some reservations lately whether biomass fuels are always carbon neutral as in some cases biofuels can be far more carbon positive than fossil fuels mainly due to extensive land use change and deforestation [17]. This does not apply for anaerobic digestion as digester's feedstock is often sewage and wastes and the exploitation of biogas is truly carbon neutral (Fig. 3.2) [10, 12, 18]. In addition, residues can be used as fertilizers [10, 12]. Therefore, in most cases, the use of this technology is not only of negative cost regarding the feedstock, but it results also in a considerable reduction of disposable wastes, having thus both financial and environmental benefits. Therefore, it is an important process for waste exploitation and valorization.

Summarizing, it can be concluded that among the biomass conversion processes, thermal gasification and anaerobic digestion produce gas mixtures that can be used as carbon source for the synthesis of liquid energy carriers. However, the latter has substantial advantages regarding the feedstock, final products, and total costs. Thus, biogas is being acknowledged to be a very promising renewable carbon resource.

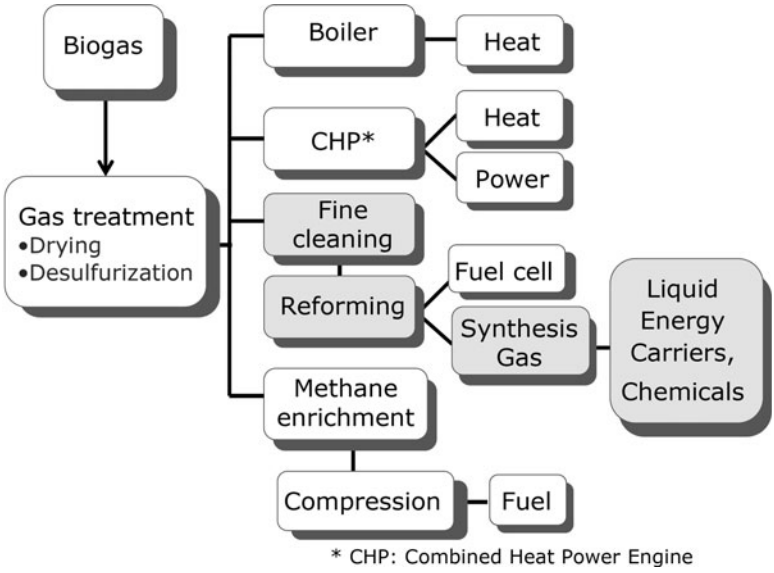

Fig. 3.3 Biogas for energy production

3.2 Biogas, a Renewable Carbon Source

3.2.1 Production and Current Use

Biogas refers to a mixture primarily comprised of methane and carbon dioxide, produced from the anaerobic decomposition of organic materials [19]. Technologies related to its exploitation are considered among the most efficient for waste upgrading to valuable fertilizer and renewable energy, meeting many EU criteria [9–13].

Biogas is produced via the anaerobic fermentation or digestion of organic matter due to microbiological action of bacteria. As already mentioned, the digester's feedstock can be any biodegradable raw material, originating from sewage sludge, municipal solid wastes, animal manures, agro-industrial wastes, energy crops, and by-products from biofuels' production [9–16]. Regarding energy crops, competition with food production can be limited, choosing plants with maximum gas yields that can grow in poor soils inappropriate for other crops [3].

Currently, biogas originating from manure and agricultural waste processing has found use in farms for heating and electricity production in block-type thermal power plants (Figs. 3.2 and 3.3). However, recovery of biogas energy content is not always satisfactory through these methods ([19] and references therein). The utilization of biogas mixtures as feed for high-temperature fuel cells with

internal or external reforming has also been proposed [11, 20, 21]. Alternatively, a more attractive way of biogas valorization could be its utilization as a renewable carbon source for the production of liquid energy carriers (Fig. 3.3). The development of viable processes for this purpose will contribute to the implementation of the EU environmental and energy-related policies in the transport sector.

Another aspect regarding biogas utilization is its high content in carbon dioxide. CO_2 removal and disposal is a major issue in industry ([22] and references therein). A process that could not only successfully operate in the presence of CO_2 but convert it to a desired product would present important economic and environmental advantages. The catalytic conversion of carbon dioxide into liquid fuels has also been designated by the US Department of Energy as one of the priority research directions [23]. From this point of view, the CO_2 reforming of methane, known as dry reforming of methane (DRM), seems to be the most suitable process for biogas full exploitation. Furthermore, this process may be the only way for the cost-effective use of landfill gas, which, having low methane content, is often not collected but is being emitted into the atmosphere, creating environmental and health hazards [14]. Nevertheless, in order for a process to be marketable, every parameter must be considered regarding feedstock availability, supply efficiency, and diversity in biogas composition.

3.2.2 Biogas Composition and Impurities

The chemical composition and physical properties of "raw" biogas are strongly related to the type of feedstock, the technical design of the digester–fermenter, and operating conditions [11, 16, 19, 24]. More specifically, important parameters are the composition of the organic material, water content, density of feedstock, temperature of the anaerobic digestion, and feeding rate of the digester [25]. Composition can differ from site to site as well as over time at a single site as variation between different batches or lots of the same substrate result in products with different characteristics [11, 12, 14, 15, 24, 26]. Biogas compositions reported in the literature are listed in Table 3.1. As it can be seen, the nature of the substrate is affecting methane content and impurities to a considerable extent. The two major components are always methane and carbon dioxide, but their ratio varies significantly. Thus, the CH_4 content in biogas derived from sewage is approximately 70%, that originating from waste of food industry can be as high as 85%, while CH_4 content of landfill gas can be as low as 30% [26]. The higher methane content the better for biogas use as fuel. On the other hand, a methane/carbon dioxide ratio near to unity is required for biogas to be used in dry reforming reaction. This can be regulated by partial combustion of biogas that could also offer heat for the endothermic DRM.

Hydrogen sulfide is the impurity that can cause the most important nuisance in biogas applications as it is a malodorous, corrosive, and toxic gas. Landfill gas and biogas produced from treatment of manure have considerably higher levels of

Table 3.1 Dependence of biogas composition on its origin

Components	Wastewater treatment sludge[a]	Sewage[b] Gothenburg Sweden	Sewage[b] Stockholm Sweden	Sewage[b] Lille France	Sewage digester[d]	Sewage digester[d]	Farm plant biogas[d]	Biogas[c]
CH_4% vol.	60–75	~65	~65	63.5 l	61–65	58	55–58 l	60–70
CO_2% vol.	19–33	~34.4	~35	35.5	36–38	33.9	37–38	30–40
N_2% vol.	0–1	<0.5	1	<0.7	<2	8.1	<1–2	~0.2 l
O_2% vol.	<0.5	<0.1	–	<0.2	<1	0	<1	0
H_2O% vol.	≤6 (40°C)	–	–	–	–	–	–	–
H_2S	1,000–4,000 mg/m^3	15 mg/m^3 (10 ppm)	–	4,550 mg/m^3 (3,000 ppm)	Beyond detection	37 mg/m^3 (24.1 ppm)	49–257 mg/m^3 (32–169 ppm)	0–6,000 mg/m^3 (0–4,000 ppm)
H_2% vol.	–	–	–	–	–	–	–	0–3
NH_3	–				–	–	–	~76 mg/m^3 (100 ppm)
Aromatics	–	–	–	–	2.9–12.1 mg/m^3	–	0.9–2.0 mg/m^3	–
Other	–	–	–	–	–			–

Components	Agricultural waste[a]	Waste of agrifood industry[a]	Household waste[a]	Landfill gas Rome Italy[b]	Landfill gas[c]	Landfill gas[d]	Natural gas (Danish)[c]	Natural gas (Dutch)[c]
CH_4% vol.	60–75	68	50–60	50–60	35–65	47–57	89	81
CO_2% vol.	19–33	26	34–38	37–47	15–50	37–41	0.67	1
N_2% vol.	0–1	–	0–5	Rest	5–40	<1–17	0.28	14
O_2% vol.	<0.5	–	0–1	Rest	0–5	<	0	0
H_2O% vol.	≤6 (40°C)	≤6 (40°C)	≤6 (40°C)	–	–	–	–	–
H_2S	3,000–10,000 mg/m^3	400 mg/m^3	100–900 mg/m^3	1,500–7,589 mg/m^3 (1,000–5,000 ppm)	0–150 mg/m^3 (0–100 ppm)	55–228 mg/m^3 (36–115 ppm)	2.9% vol.	–
H_2	–	–	–	–	0–3% vol.	–	0% vol.	–
NH_3	50–100 mg/m^3	–	–	–	~4 mg/m^3 (5 ppm)	–	0% vol.	–
Aromatics	–	–	0–200 mg/m^3	–	–	2.3–7.4 mg/m^3	–	–
Chlorinated or fluorinated organic	–	–	100–800 mg/m^3	5–10 ppm	–	–	–	–
Other	–	–			–	–	Other H/Cs 9.4% vol.	Other H/Cs 3.5% vol.

[a][16]
[b][26]
[c][27]
[d][14]

sulfur [19, 24]. Higher hydrocarbons, aromatics (benzene, toluene, xylenes), chloro/fluorocarbons, organic sulfur components such as mercaptans, oxygenated compounds, chlorine, fluorine, and sulfur dioxide can also be present, especially in landfill-derived biogas [14, 19, 24]. Ammonia is formed during the degradation of proteins, and its content in raw biogas depends upon the substrate composition and the pH in the digester. Organic silicon compounds (siloxanes) which are used in deodorants and shampoos are present in landfill and sewage digester gases at ppm levels [15, 27].

3.2.3 Biogas Pretreatment

Various processing techniques can be used to remove impurities and to upgrade biogas to suitable quality, depending on its initial properties and the intended application (Fig. 3.3) [15, 27]. For example, for biogas to be used directly as a fuel (biomethane), moisture and CO_2 removal is necessary in order to be enriched in methane and upgraded to natural gas-like quality, having comparable energy content [24, 26]. Moreover, landfill gas may be more treatment demanding because of the low methane content and the presence of trace compounds and nitrogen [14].

The presence of CO_2, water, and oxygen in the biogas to be used as feed for dry reforming processes is not a problem as the CO_2 is one of the reactants and the other two are benign for the reaction. Furthermore, high carbon dioxide content is beneficial for the reaction, as it will be discussed later. Thus, raw biogas pretreatment is simpler, and this is one of the major advantages of the dry reforming process. The main problem originates in the presence of hydrogen sulfide, which has to be removed from the feed so as to prevent corrosion and mechanical wear of process equipment and catalyst deactivation. Most of other contaminants, such as siloxanes, are below the specifications of the natural gas grid, or not detectable, while they can be removed during removal of hydrogen sulfide [13, 19, 27]. Particulates which are present in the biogas are separated by mechanical filters [27].

H_2S is the impurity present in higher concentrations and, besides being malodorous and toxic, it is particularly poisonous to metal catalysts used for CH_4 conversion. The exposure of a metallic nickel surface to gas streams containing 1 ppm H_2S results in the formation of surface Ni_xS_y phases, inhibiting the adsorption of reactant molecules [28]. Many approaches have been suggested for the removal of hydrogen sulfide, which include biological, absorptive, chemical, adsorptive, and catalytic treatments [19, 27–29]. Available processes can be classified in two categories: methods that can be applied in the digester for basic desulfurization and those which treat the raw biogas produced, aiming for fine desulfurization.

Biological processes, often used in the digester, are based on hydrogen sulfide-consuming microorganisms (species *Thiobacillus* and *Sulfolobus* occurring naturally in the fermentation mass) which oxidize H_2S to sulfur in the presence of oxygen. Sulfur can be further oxidized to sulfate [19, 27]. Oxygen is provided by injection of air (8–12 vol.% of the biogas flow volume). The method is technically

easy to perform particularly in small biogas plants. A critical aspect of this process is the precise control of air injection to a suitable dosage: Low oxygen concentration may lead to partial and incomplete desulfurization, while high air injection may impose safety issues (formation of explosive mixtures) and results to very high levels of oxygen and nitrogen in the biogas. The latter may be a problem for the other uses of biogas but not if it is meant to be used as a dry reforming feed. The effectiveness of the process also depends on the temperature, reaction time, the specific surface, and the available contact surface (as microorganisms are immobilized), as well as the place and quantity of the injected air. Desulfurization rates of up to 99% can be achieved with this process. In the digester, sulfur can also be removed by the precipitation of a sulfide salt with low solubility, such as FeS. Iron salts (chlorides or sulfates) are added to the substrate as a premixed salt solution.

Biological desulfurization can also be performed as an external process in especially dedicated reactors and bioscrubber and biofilter equipment in order to achieve higher desulfurization levels in larger biogas plants [28–30]. Bioscrubbers already used in wastewater treatment are suitable for the cleaning of biogas, involving a two-stage process, firstly absorption of H_2S by a liquid followed by biological oxidation of H_2S in the liquid [29]. Biofiltration is also effective for the removal of H_2S, volatile organic compounds, and NH_3 present in biogases [29, 31]. Anaerobic biofiltration of H_2S can provide the same advantages of aerobic biofiltration including the use of low-cost materials, the exclusion of aeration costs, as well as the elimination of safety risks associated with operation in an oxygen-rich environment [29].

The most convenient fine desulfurization can be performed using technologies applied in the natural gas industry for gas conditioning on a large scale and also proposed for the upgrading of biomass and coal-gasification gas [28, 30, 32–40]. The reactive adsorption technology can be applied for the removal of the H_2S from biogas produced in landfills or anaerobic digesters [41]. The main step is an irreversible chemical reaction between the solid (a metal oxide, MO_x) and gas phase:

$$MO_x + xH_2S \rightarrow MS_x + xH_2O.$$

The efficiency of the process is a function of a number of variables including the nature and properties of the adsorbent, the biogas flow rate and the contact time, the geometry of the adsorption columns and the linear velocity of the flow, the concentration of the contaminant (H_2S), and humidity in the biogas. Rates of the external diffusion and internal diffusion are often relatively low [41]. Iron oxide supported on materials with high specific surface areas is often used, forming iron sulfide. In the regeneration, iron sulfide is oxidized with air, and iron oxide or hydroxide is recovered. Activated carbon can be used to catalytically convert hydrogen sulfide to elementary sulfur and water [42, 43]. The carbon can be impregnated with potassium iodide (KI) or sulfuric acid to increase the reaction rate. Using a 2% potassium iodide-impregnated activated carbon, 100% H_2S removal efficiency could be achieved from a feed with an average inlet H_2S concentration of about 2,400 ppm [43]. The use of natural and synthetic zeolites has also been explored [44].

The average sulfur content in the biogas is of the order of 100 ppm, but concentrations as high as 2,000–3,000 ppm have also been measured (Table 3.1 and corresponding references). The requirement for engine and fuel cell applications is ca. 1 ppm, and this can be achieved by catalytic methods [28, 42]. On the other hand, for dry reforming applications, the selective poisoning of Ni-based catalysts by adding H_2S in the feed (a few ppm) can retard carbon accumulation, according to the "ensemble size control" strategy as in the SPARG process [28, 45].

3.3 Thermodynamic Considerations for the Dry Reforming of Methane

Among the various methane reforming reactions, steam reforming (SRM) is the principal industrial process for the production of synthesis gas or hydrogen from natural gas. Already developed in industrial scale just before World War II, SRM has many applications, especially in hydrogen-demanding processes such as hydrotreatment of petroleum fractions and ammonia synthesis. Recently, reforming reactions and synthesis gas technology attract attention as alternative pathways for production of clean synthetic fuels to replace petroleum for conventional engines [22, 46].

In reforming reactions, methane reacts with either steam [SRM (3.1)] or carbon dioxide [DRM (3.2)] or oxygen [partial oxidation of methane (POM) (3.3)] to form hydrogen and carbon monoxide as per the stoichiometries below:

$$CH_4 + H_2O \rightleftarrows CO + 3H_2 \quad \Delta H^0{}_{298} = +206\ \text{kJ/mol} \quad \text{SRM.} \tag{3.1}$$

$$CH_4 + CO_2 \rightleftarrows 2CO + 2H_2 \quad \Delta H^0{}_{298} = +247\ \text{kJ/mol} \quad \text{DRM.} \tag{3.2}$$

$$CH_4 + \frac{1}{2}O_2 \rightleftarrows CO + 2H_2 \quad \Delta H^0{}_{298} = -38\ \text{kJ/mol} \quad \text{POM.} \tag{3.3}$$

From these reactions, DRM seems more suitable for the exploitation of biogas since no CO_2 separation processes are needed and, at the same time, both carbon atoms are incorporated in the final product, increasing yield and decreasing waste. Biogas, generally, has a higher methane content compared to carbon dioxide (Table 3.1). On the other hand, a slightly higher CO_2 concentration would have a positive effect on the catalysts' stability (see next paragraphs and Sect. 3.6). The near unity CO_2/CH_4 ratio, necessary for DRM, can be regulated by combusting an adequate quantity of biogas and introducing flue gas into the feed. This would also offer heat, required by this highly endothermic reaction.

Since no steam is used, it can be applied in areas where water is not readily available, while simpler installation is required, reducing both equipment and operational costs, as compared to steam reforming [47]. The reaction is characterized

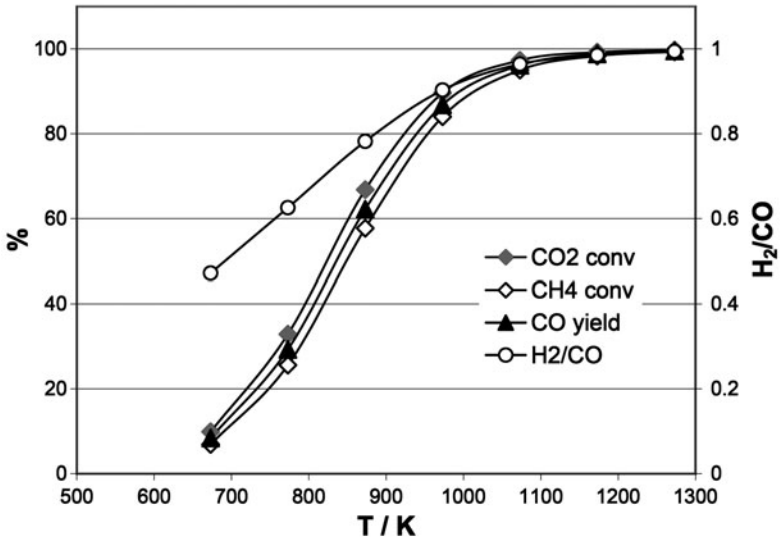

Fig. 3.4 Calculated equilibrium conversions, CO yield, and H_2/CO ratio for stoichiometric carbon dioxide reforming of methane (at 1 atm) as a function of temperature [46]

by the high thermodynamic conversion of CH_4 which can be achieved using appropriate reaction conditions (Fig. 3.4). Furthermore, as DRM has a large heat of reaction and is reversible, it has potential thermochemical heat-pipe applications for the recovery, storage, and transmission of energy from solar and other renewable sources in chemical energy storage and transmission systems (CETS) [48–50]. Compared to POM, it is easier to achieve higher selectivity to syngas, while it presents lower safety risks.

It is often said that another advantage of DRM is the H_2/CO ratios of the synthesis gas produced, considered more suitable for the Fischer–Tropsch (FT) synthesis than the hydrogen-rich gas obtained from SRM [22, 46, 51]. Stoichiometric DRM H_2/CO ratio is unity but, due to the reverse water–gas shift (RWGS) reaction, this ratio is often slightly lower. In FT synthesis, selectivity for the production of liquid fuels depends, among other factors, also on H_2/CO ratio [52]. H_2/CO ratio higher than 2, as that obtained by SRM, favors the formation of light hydrocarbons, e.g., methane and ethane. For the synthesis of alkenes and alcohols, a ratio equal to 2 is used irrespective of chain length, but for alkanes, lower ratios are required so as not to limit carbon chain growth. For cobalt-based FT catalysts, which have little or no WGS activity, and typical FT synthesis conditions, ratios between 2.05 and 2.15 are chosen. If an iron-based catalyst, presenting high WGS activity, is used, the H_2/CO ratio approximates 1.65 at low temperatures (500 K), while at high temperatures, high conversions can be achieved, provided that the Ribblett ratio $H_2/(2CO + 3CO_2)$ is about 1.05 [52]. Thus, the required properties of the syngas vary with the synthesis in question [51]. For large-scale FT units, autothermal reforming, a heat-balanced combination of exothermic POM and

endothermic SRM in a single reactor, is considered as the most cost-effective solution [53–55]. Adjustment of the amounts of air, methane, and steam provides the energy necessary to compensate the endothermic term of the SRM reaction while fulfilling the requirements for the H_2/CO ratio. Following the same concept, DRM could also be combined with SRM or even with both SRM and POM as in the tri-reforming process proposed by Song and his coworkers [56–59].

Negative aspects include the fact that the DRM reaction is highly endothermic and thus energy intensive, demanding enhanced installation and operational costs. At the high reaction temperatures required, catalysts suffer from sintering. However, the major problem encountered in this process is deactivation due to formation of carbonaceous deposits which lead to the decline of activity and reactor blockage [22, 46, 47, 49, 55, 60].

In parallel to the main DRM reaction (3.2), the following reactions also take place:

$$CH_4 \rightleftarrows C + 2H_2 \quad \Delta H^0{}_{298} = +75 \text{ kJ/mol} \quad \text{methane decomposition.} \tag{3.4}$$

$$CO_2 + H_2 \rightleftarrows CO + H_2O \quad \Delta H^0{}_{298} = +41 \text{ kJ/mol} \quad \text{reverse water} - \text{gas} - \text{shift.} \tag{3.5}$$

$$2CO \rightleftarrows C + CO_2 \quad \Delta H^0{}_{298} = -171 \text{ kJ/mol} \quad \text{Boudouard reaction.} \tag{3.6}$$

$$C + H_2O \rightleftarrows CO + H_2 \quad \Delta H^0{}_{298} = +131 \text{ kJ/mol} \quad \text{carbon gasification.} \tag{3.7}$$

The main reaction (3.2) is favored at high temperatures and low pressures, conditions which also favor methane decomposition [(3.4) and Fig. 3.5] [61]. Minimum operating temperatures for DRM and methane decomposition, calculated using the standard free energy, are 918 K and 830 K, respectively [62, 63]. The Boudouard reaction is exothermic and will not proceed at temperatures higher than 974 K, while the RWGS (3.5) is hindered above 1,090 K [61–63]. Methane decomposition (3.4) and CO disproportionation [Boudouard reaction (3.6)] are responsible for the formation of carbon. In the temperature range of 830–973 K, where DRM reaction is not favored (Fig. 3.5), both methane decomposition and Boudouard reaction contribute to carbon formation [63]. For a given CO_2/CH_4 ratio, the temperature limit, below which carbon is deposited, decreases as the pressure decreases, while at constant pressure, the temperature limit increases as the CO_2/CH_4 ratio decreases [62–64]. For a reforming feed ratio CO_2/CH_4 of 1:1, carbon deposition is thermodynamically possible at temperatures up to 1,143 K at 1 atm and up to 1,303 K at 10 atm [63]. Using excess CO_2 in the feed may avoid carbon formation at lower temperatures, while in the case of stoichiometric feeds, temperatures as high as 1,000 K can suppress carbon formation when there is a thermodynamic potential [47]. Besides the negative effect on carbon formation, as pressure increases, the conversion of CO_2 and the yield of CO and H_2O also increase while CH_4 conversion and H_2 yield decrease [62]. These results indicate that the RWGS reaction is favored at higher pressures. This reaction is normally

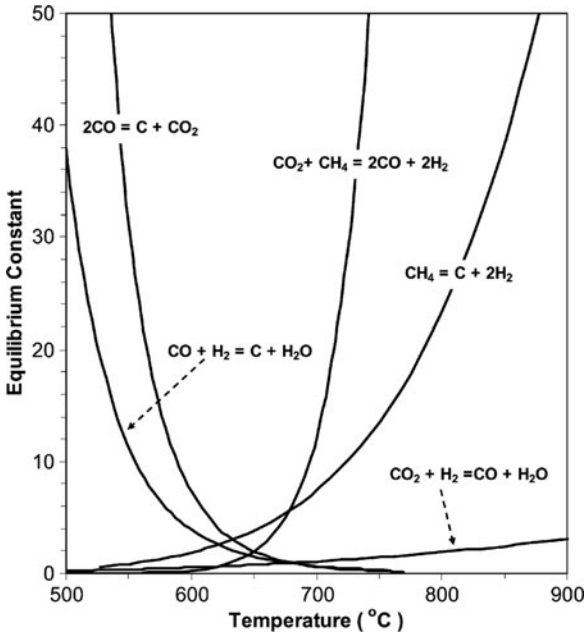

Fig. 3.5 Equilibrium constants of reactions occurring during the dry reforming of methane, as a function of temperature Reprinted with permission from reference [61]. Copyright (2007) by Elsevier

pressure independent. Gadalla and Bower [62] gave the following explanation: An increase in pressure results in a corresponding increase in the limiting equilibrium temperature and consequently to the corresponding equilibrium constant, K_{RWGS}. Thus, a dependency between the pressure and the RWGS results. Nevertheless, it is advantageous for industrial processes to operate at high pressures and lower temperatures with CO_2/CH_4 ratios near unity in order to minimize the reactor size and energy use [22, 47]. Therefore, the development of active reforming catalysts exhibiting improved resistance to the formation of carbon is a prerequisite for an effective process. Consequently, there is significant investment in research efforts regarding this issue.

3.4 Reaction Mechanism

As illustrated in Fig. 3.5, the DRM equilibrium constant increases dramatically at temperatures higher than 973 K, allowing almost complete conversions above this limit [61, 63]. Thus, above this temperature, there are no thermodynamic restrictions to achieve high CH_4 and CO_2 conversions, provided that a suitable catalyst is applied [49]. A suitable catalyst for the DRM reaction is one which presents both high activity and stability under reaction conditions. In addition to the target reaction, the other endothermic reaction, also enhanced at temperatures higher than 900 K, is the CH_4 decomposition (3.4) which results in the formation

Table 3.2 Elementary DRM reaction steps generally accepted to occur on the catalysts' surface

Methane adsorption and dissociation			
$CH_4 + S_1 \rightleftarrows S_1 - CH_4$	$K1$	Equilibrium	(3.8)
$S_1 - CH_4 + (4-x)S_1 \rightarrow S_1 - CH_x + (4-x)S_1 - H$	$k1$	RDS	(3.9)
$S_1 - CH_4 + S_1 \rightarrow S_1 - CH_3 + S_1 - H$	k_a1		(3.9a)
$S_1 - CH_3 + S_1 \rightarrow S_1 - CH_2 + S_1 - H$	k_b1		(3.9b)
$S_1 - CH_2 + S_1 \rightarrow S_1 - CH + S_1 - H$	k_c1		(3.9c)
$S_1 - CH + S_1 \rightarrow S_1 - C + S_1 - H$	k_d1		(3.9d)
$2S_1 - H \rightleftarrows H_2 + 2S_1$	$K2$		(3.10)
Carbon dioxide adsorption and dissociation			
$CO_2 + S_2 \rightleftarrows S_2 - CO_2$	$K3$		(3.11)
$S_2 - CO_2 + S_2 - -O^{2-} \rightleftarrows S_2 - CO_3{}^{2-}$	$K4$		(3.12a)
$S_2 - CO_2 + S_1 - H \rightleftarrows S_2 - CO + S_1 - OH$	$K5$		(3.12b)
$S_2 - CO_2 + S_2 \rightleftarrows S_2 - CO + S_2 - O$	$K'5$		(3.12c)
Formation of surface hydroxyls and water			
$S_2 - O + S_1 - H \rightleftarrows S_2 - OH + S_1$	$K6$		(3.13a)
$S_1 - OH + S_1 - H \rightleftarrows H_2O + 2S_1$	$K'7$		(3.13b)
CH_x oxidation, CO and H_2 formation and desorption			
$S_1 - CH_x + S_1 - OH \rightleftarrows S_1 - CH_xO + S_1 - H$	$K8$		(3.14a)
$S_1 - CH_x + S_1 - ODS_1 - CH_xO + S_1$	$K'8$		(3.14b)
$S_1 - CH_xO \rightarrow S_1 - CO + x/2H_2$	$k9$	RDS	(3.14c)
$S_1 - CH_x + CO_2 \rightleftarrows S_1 - CO + CO + x/2H_x$	$K10$		(3.14d)
$S_1 - CH_x + S_1 - OH + xS_1 \rightleftarrows S_1 - CO + (x+1)S_1 - H$	$k'9$	RDS	(3.14e)
$S_1 - C + S_1 - OH \rightleftarrows S_1 - CO + S_1 - H$	$K11$		(3.15)
$S_1 - CO \rightarrow S_1 + CO$	$K12$		(3.16)
$2S_1 - H \rightleftarrows H_2 + 2S_1$	$K13$		(3.17)

K and k stand for thermodynamic (equilibrium) and kinetic constants, respectively. S_1 and S_2 denote active sites on the metal and metal–support interface, respectively. Alternative or successive paths are indicated with the same number and a letter. In CH_x, x can take values between 1 and 3

of carbonaceous deposits. Therefore, a basic criterion for the choice of catalyst is its capacity to kinetically hinder carbon formation. For this purpose, it is essential to consider the mechanism of the target and the side reactions on various catalytic systems. The main reaction steps are presented in Table 3.2 and discussed in the following paragraphs. Although there are some slightly different suggestions, most researches agree with the main reaction steps in this scheme.

3.4.1 Methane Adsorption and Activation

The first step in the reaction sequence is the adsorption of methane. At low temperatures, the adsorption is precursor-mediated, while at higher temperatures, it is direct [47]. It has been suggested that CH_4 adsorbs reversibly on the surface of transition metals [Table 3.2 (3.8)], arriving at equilibrium. This conclusion is

derived from results of steady-state isotopic tracing kinetic analysis (SSITKA) which detected methane on the surface of Ni/La_2O_3, Pd/ZrO_2, $Pd/ZrO_2–La_2O_3$, and $Pd/\gamma\text{-}Al_2O_3$ catalysts under reaction conditions [65, 66]. However, Nandini et al. [67] considered that methane adsorbs and decomposes irreversibly on a $Ni–K/CeO_2–Al_2O_3$ catalyst [67]. This conclusion is based on the fact that hydrogen addition to the feed does not influence the rate of methane consumption, being both irreversible and not at thermodynamic equilibrium. Therefore, whether the adsorption of methane is irreversible or not may depend on the catalytic system.

There is general agreement that one of the slow reaction steps in the reaction sequence is the cracking of methane on the metal surface [Table 3.2 (3.9)], as the dissociation energy of the $CH_3–H(g)$ bond is high (439.3 kJ/mol) [68]. However, the total dissociation energy of the bond $CH_x–H$ depends on the hosting surface and the entire catalytic system which may be controlling the surface metal work function. Consequently, lower $CH_x–H$ bond dissociation energies are required in catalyzed decomposition. Nevertheless, for many catalytic systems, methane decomposition is considered as the rate-determining step (RDS) [22, 47, 49, 55].

The path which methane dissociation follows has been the subject of several studies. CH_4 possesses four filled bonding MOs and four empty antibonding MOs. It is suggested that in order to dissociate, CH_4 must be substantially distorted from its tetrahedral shape to form a trigonal pyramidal structure [22, 47]. This is the result of electron interactions between the adsorbed methane molecule and the metal which dominate the dissociative CH_4 adsorption ([47] and references therein). An early study on unsupported Pt clusters shed light on the nature of these interactions, explaining the distinct cluster size dependence of methane activation [69]. In order to understand the observed dependence of methane chemisorption on the size of platinum clusters, Trevor et al. [69] took into account two issues: (1) electronic effects relating reactivities with ionization potentials (IPs) or availability of an occupied or unoccupied molecular orbital with a particular symmetry and (2) the geometric structure of the metal, i.e., the availability of a type of active site or degree of coordination that acts as the kinetic driving force [69]. They suggested that the reactivity for the dissociative chemisorption does not depend only on the ability of the highest occupied orbital of the metal to contribute electron density to any of the lowest unoccupied antibonding molecular orbitals (LUMO) of the adsorbed molecule but also on the electron donation from HOMO (highest occupied molecular orbital) of the reactant to low-lying unoccupied or partially occupied orbitals of the metal cluster, within the constraints of symmetry restrictions. This weakens the C–H bond, thus stimulating its dissociation. As the size of the Pt cluster increases, the cluster ionization potential decreases and activity decreases. Trevor et al. [69] concluded that very small platinum clusters have high ionization potentials, which makes them good charge acceptors.

The effect of metal cluster size and the structure sensitivity of CH_4 dissociation were also observed on Ni surfaces [55, 70]. Kuijpers et al. [70] noticed that the decomposition of methane preferentially proceeds on small nickel crystallites [70]. Bradford and Vannice ([47] and references therein) have reviewed theoretical studies on the formation of CH_x species ($1 \leq x \leq 3$) on various metals, showing

that each CH_x species is preferentially located at a site which completed its tetravalency; thus, CH_3 can adsorb on top of a metal atom, CH_2 presents bridged adsorption, while CH and C require the concomitant occupation of higher coordination sites and are adsorbed on hollow sites with three of four nearest neighboring sites. This hypothesis, however, does not take into account neither the metal work function and its alteration brought about by adsorbed CH_x species nor the presence of other adsorbed species in the vicinity [68]. Bengaard et al. [71] performed density functional theory (DFT) calculations for the steam reforming of methane over a Ni(111) surface and over a stepped Ni(211) surface. They have concluded that for the activation of methane, step sites are more reactive than close-packed surfaces. According to Bengaard et al. [71], the reaction channel associated with steps has a lower activation barrier than that associated with terraces. Furthermore, atomic carbon presents much higher stability on steps than on terrace sites. Thus, the availability of step sites is essential both for a large turnover rate and for graphite formation. The latter explains the structure sensitivity in the formation of surface carbon because of the large ensemble of metal atoms needed. Norskov and coworkers [72] have continued the work of Bengaard et al. [71], and they have studied the dissociation of methane on Ni(111) theoretically and experimentally. Their results have verified that the activation of the first C–H bond in methane over the top of a surface Ni atom on Ni(111) has an energy barrier of 105 kJ/mol while on Ni(211); the activation follows a similar reaction path but with a barrier of only 88 kJ/mol. This result has been attributed to the stronger binding of CH_3 at the step edge, the latter exhibiting higher activity than terraces. Recently, Haroun et al. [73], employing periodic DFT calculations and studying the adsorption of CH_4 on a perfect and on a defective Ni(111) face, showed that the interaction of methane with a perfect surface is very weak and largely of physical origin, while chemical interactions become sizeable when CH_4 is adsorbed on top of a Ni adatom, considered as surface defect. The structure sensitivity of CH_4 activation was also reported for Ru-based catalysts [74]. On the contrary, Yamaguchi and Iglesia [66], performing isotopic tracing and kinetic isotope analysis, showed that the C–H bond activation rate constants did not vary with Pd dispersion in spite of a monotonic increase in the fraction of exposed surface Pd atoms at corners and edges with increasing Pd dispersion. They concluded that low-index surfaces prevail on large Pd clusters, exhibiting much higher reactivity than on other metals because of stronger binding of C(ads) on Pd, making contributions from edge and corner sites even less likely than on the other metals.

Attempts have also been made to define the number of hydrogen atoms in CH_x species adsorbed on transition metal surfaces. Such species have been detected using both steady-state and transient isotopic tracing experiments, the latter being more representative of phenomena on working metal surfaces ([47, 55] and references therein). Bradford and Vannice [47] consider that, under DRM conditions, the dissociation of CH_4 yields a distribution of CH_x species with x depending on the metal and the support. Osaki et al. [75, 76] reported x values as high as 2.7 for Ni/MgO, 2.5 for Ni/ZnO, 2.4 for Ni/Al_2O_3, 1.9 for Ni/TiO_2, and 1.0 for Ni/SiO_2, while for Co/Al_2O_3, x is only 0.75, as shown in Table 3.3. According to

Table 3.3 Degree of methane cracking on various catalytic systems; the acidity of the corresponding support, expressed as its isoelectric point; and the binding energies of $Ni_{2p1/2}$ measured for Ni supported on various oxides

Catalyst	x value for CH_x[a]	Supports' IEPS[b]	B.E. of $Ni_{2p1/2}$ (eV)[c]
Ni/MgO	2.7	12.1–12.7	856.7 ± 0.1
Ni/ZnO	2.5	8.7–9.7	
Ni/Al_2O_3	2.4	7.0–9.0	
Ni/TiO_2	1.9	~6	854.5 ± 0.1
Ni/SiO_2	1.0	1.0–2.0	856.3 ± 0.1
Co/Al_2O_3	0.75	7.0–9.0	

[a][75, 76]
[b][77]
[c][78]

their studies, the degree of methane decomposition depends on the transition metal and the nature of the support. As can be seen in Table 3.3, for the same transition metal, x values are higher for more basic supports. As a coarse measure of acidity–basicity of metal oxides, their isoelectric points are used (Table 3.3) as given by Pinna [77]. In other words, the extent of methane cracking is enhanced with the increase of acidity of the support. On the other hand, as the activation of the C–H bond cleavage requires electron donation from the metal surface, the electronic environment of Ni must be important. Different B.E. of Ni2$p_{½}$ (Table 3.3) and metal–support interactions (MSIs) have been reported for nickel supported on various oxides [78]. Then again, the ability of different Ni-based materials to activate the C–H bond cleavage correlates well with their catalytic activity in DRM, following the order $Ni/TiO_2 > Ni/SiO_2 > Ni/MgO$ [50].

Trevor et al. [69], studying unsupported Pt clusters, observed that the metal cluster single-carbon-containing species (PtC) are the primary products and that as the cluster size increases, the products go from PtC to $Pt_{11}CH_2$. They predicted that very large Pt particles or surfaces would probably produce $–CH_3$ adsorbed species as has been reported for Ni(111) surfaces [69]. Moreover, the electronic effects induced by the support are also influenced by the size of the metallic particles; being negligible for large particles (>10 nm), they may become significant when the nickel is highly dispersed, as is the case of Ni/TiO_2, or diffused in the support's lattice to form a solid solution, as it is the case for Ni/MgO [50]. Kuijpers et al. [70], using a low-field magnetic method, noticed that carbon–hydrogen complexes CH, CH_2, or CH_3 are covering the Ni surface, being chemisorbed without affecting ferromagnetism. Tsipouriari and Verykios [79], studying a Ni/La_2O_3 catalyst, report that the active carbon-containing species which exist on the catalyst surface under reaction conditions consist exclusively of carbon, and not of CH_x species with $x > 0$. Topalidis et al. [80] report that the value of x is in the range $0 \leq x \leq 4$ and depends on the metal substrate and the temperature, most often taking values around zero. Yamaguchi and Iglesia [66], based on isotopic tracing kinetic measurements, indicated that the chemisorbed carbon, C(ads), and unoccupied Pd atoms are the most abundant surface intermediates. In general, there are no conclusive results relating the degree of methane dissociation on a catalyst surface to its reactivity.

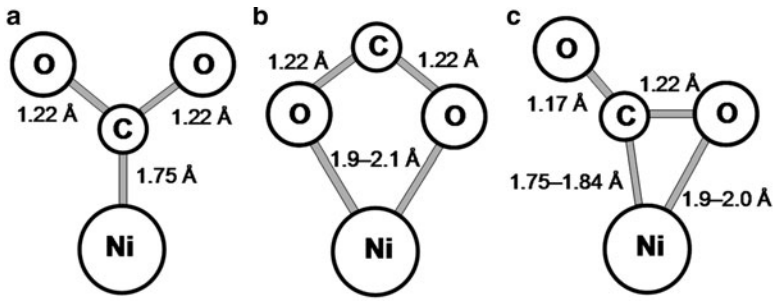

Fig. 3.6 Schematic representation of the three coordination geometries of adsorbed CO_2: (**a**) pure carbon coordination, (**b**) pure oxygen coordination, (**c**) mixed carbon–oxygen coordination. CO_2 coordination modes and indicated structural parameters from Reprinted with permission from reference [81]. Copyright (1986) by Elsevier

3.4.2 Carbon Dioxide Adsorption and Activation

Like methane, the dissociation and reduction of CO_2 are also reported to be structure sensitive, promoted at defect sites such as corner atoms [47]. Ab initio valence–bond calculations and spectroscopic data indicate that CO_2 can adsorb dissociatively on various metal surfaces (Pt, Pd, Rh, Re, Ni, Fe, Cu, Ag, Al, Mg) involving electron transfer [81, 82]. The adsorption can occur through three different coordination geometries: (1) pure carbon coordination, (2) pure oxygen coordination, and (3) mixed carbon–oxygen coordination, the last two being more favorable (Fig. 3.6) [81]. Electron transfer to the CO_2 moiety is accompanied by an elongation of the C–O bond with respect to the free molecule. Intermolecular interaction between the formed CO_2^- anion and surrounding neutral CO_2 molecules via "solvation" is also considered. According to Freund and Messmer [81], three reaction channels can be followed: (1) dissociation into CO and O^-, more likely to occur on transition metal surfaces; (2) oxidation to CO_3^- and CO_3^{2-}, more likely on noble metals; and (3) disproportionation reaction of CO_2^- with a gaseous CO_2 molecule to form CO_3^- and CO. Solymosi [82], reviewing the relative literature, reports that the characteristics of the adsorption, activation, dissociation, and reactions of CO_2 depend on the metal. A negatively charged anionic CO_2^- precursor is formed, which, depending on the nature of the metal, may dissociate into CO and O or transform into CO_3 and CO adsorbed species, very similar to the conclusions of Freund and Messmer [81]. The adsorption of CO_2 is dissociative on Fe, Ni, Re, Al, and Mg surfaces. The presence of surface adatoms dramatically influences the adsorption and reactivity of CO_2. The presence of preadsorbed oxygen (adatoms) promotes the bonding of CO_2 on metals in the form of different carbonates and leads to its stabilization [82]. Alkali adatoms increase the binding energy of adsorbed CO_2, promoting the formation of surface CO_2^- radical and the formation of CO_3 and O species [82]. The promoting effect of alkali metals has been also reported by Freund and Roberts [83]. Alkali metals (such as cesium and

potassium) and specific surface structure play an essential role on the efficiency of the electron transfer from the surface to CO_2 to form $CO_2^{\delta-}$. In the presence of alkali metal promoters, high chemical reactivity is observed for both transition and sp metals, the reaction pathway followed depending on the alkali metal coverage [83]. Oxidized multilayers of cesium provide specific oxygen states which are highly reactive to both CO and CO_2, forming $CO_2^{\delta-}$ and carbonate, respectively. Furthermore, Freund and Roberts [83] report that the coadsorption of CO_2 with other molecules, e.g., ammonia or methyl iodide, can provide low energy pathways to products where again the formation of $CO_2^{\delta-}$ anionic species is crucial to the mechanism. However, one must remember that spectroscopic studies were performed under conditions far from those applied in the DRM.

Erdőhelyi et al. [84], studying supported palladium catalysts, concluded that on Pd, the dissociative adsorption of carbon dioxide takes place in the temperature range of 473–673 K to give adsorbed carbon monoxide of different coordinations. In the presence of methane, the dissociation of CO_2 is promoted, although there are no indications for the formation of any surface complexes between the two reactants. The enhanced dissociation of CO_2 was attributed to the presence of surface hydrogen species originating from the decomposition of methane and the consecutive formation of carbonyl–hydride species [84]. The effect of the support for the dissociation of CO_2 to CO is crucial, the activity for the dissociation at 773 K decreasing in the order $Pd/TiO_2 > Pd/A1_2O_3 > Pd/SiO_2 > Pd/MgO$ [84]. As the DRM activity of the catalysts, based on turnover frequencies, follows the same order, Erdőhelyi et al. [84] suggested that it must be related to the efficiency of the catalyst to dissociate CO_2, considering the activation of carbon dioxide an important step in the DRM reaction. The high activity of Pd/TiO_2 was associated with the extended electronic interaction between Pd and n-type TiO_2, resulting in an increase of the back donation of electrons from the palladium to lower antibonding MO of the CO_2 and facilitating its dissociation. Enhanced carbon dioxide decomposition results in higher surface concentration of reactive oxygen species. As the latter are required for the oxidation of CH_x species [Table 3.2 (3.14)], their increase leads to the enhancement of the DRM rate. On the other hand, Erdőhelyi et al. [84] do not exclude the importance of the support: more oxygen vacancies are present on the titania surface, promoting the adsorption and the dissociation of carbon dioxide.

CO_2 is known to adsorb on the metal oxides usually serving as supports for DRM catalysts. CO_2 is probably the most popular molecule for probing surface basicity as it is a small molecule and has merits in probing both O^{2-} and OH^- basic sites [85]. Spectroscopic data show that a variety of surface species can be formed, involving both anions and cations, forming mixtures of bidentate, bridged, and multidentate carbonate structures [85]. Recently, there is a renewed interest in studying the chemical behavior of this refractory molecule. Burghaus [86] confirmed the correlation of CO_2 adsorption kinetics with the structural features of surfaces of various metals (Cu, Cr), metal oxides (ZnO, TiO_2, CaO), as well as on so-called model catalysts (Cu-on-ZnO, Zn-on-Cu) and nanocatalysts. CO_2 binding energies on metal oxides are typically larger than those on metal surfaces, further increasing on oxygen vacancies as compared to adsorption on pristine sites of the oxides [86].

Moreover, adsorbate-assisted adsorption is weakened by defects and strong surface corrugation, suggesting a dynamic effect rather than the influence of lateral interactions. According to Burghaus [86], CO_2 adsorption on CaO occurs via the C atom adsorbed on O sites of CaO involving lattice oxygen, in contrast to metal surfaces where carbonates form (in most cases thermally activated) in oxygen–CO or oxygen–CO_2 coadsorption phases. Surface carbonates (CO_{3ads}) formed on CaO powders are very stable, and desorption-carbonate decomposition temperatures as high as 1,100 K have been observed. An interesting outcome of this study is the prediction that CaO could be unexpectedly reactive to decompose alkanes as well as carbonates, having higher activity compared with MgO. This is related to more delocalized electron distribution of surface oxygen that leads to a more efficient overlap with the orbitals of adsorbing molecules [86].

Pan et al. [87] have performed DFT slab calculations to study CO_2 adsorption and activation over alumina-supported 3*d* transition metal dimers, M_2/γ-Al_2O_3 (M = Sc, Ti, V, Cr, Mn, Fe, Co, Ni, Cu). Their conclusions are in accordance with many experimental results reported in the literature. CO_2 is suggested to adsorb on M_2/γ-Al_2O_3, forming a negatively charged and, in a bent configuration species, indicating partial activation of CO_2. They suggested that both the metal dimer and the γ-Al_2O_3 support contribute to the activation of adsorbed CO_2 by electron donation to the adsorbed molecule, distorting CO_2 from its linear configuration in the gas phase. The most favorable adsorption sites, either on the dry or the partially hydroxylated support, are expected to be found at the interface between the metal dimer and the support [87]. As a consequence, highly dispersed metal phase (small metal particles) is expected to exhibit good activity as the metal–support interface is maximized. Another important result of this study, especially for DRM, is that hydroxylation of the support surface reduces the amount of charge transferred to CO_2 for the same metal dimer and weakens the CO_2 chemisorption bonds as compared to the corresponding dry M_2/γ-Al_2O_3 [87]. On the contrary, Cheng et al. [88] suggest that the formation of hydroxyl species, formed by hydrogen spillover onto the support, promotes the dissociative adsorption of CO_2 through the formation of surface formates (Al–COOH + O*).

Differences in carbon dioxide adsorption behavior related to the metal oxide used as support have been reported for various catalytic systems. Bradford and Vannice [50] have studied the chemisorption of carbon dioxide on the Ni/TiO_2 catalyst and estimated the heat of adsorption to be of the order of 1 kcal/mol, indicative of weak adsorption. On a Ru/SiO_2, both CH_4 and CO_2 are activated on the metallic phase, while a bifunctional mechanism is proposed for Ru/Al_2O_3 [74]. Although Ru is able to activate and dissociate CO_2, in the presence of a support such as alumina, a bifunctional mechanism takes place: while methane adsorbs on ruthenium, an alternative and more effective path for CO_2 activation is followed, comprising the formation of HCO_2^- on the alumina surface and its decomposition to CO and hydroxyl groups on the support. The latter diffuse toward the metal particles where oxidation of the carbonaceous adspecies located on the metallic surface takes place [74]. Topalidis et al. [80], based on their kinetic studies, concluded that CH_4 and CO_2 adsorption occur on distinct and discreet active sites

of a 0.5%Pt/$SrTiO_3$ catalyst; namely, methane is weakly bound on the metallic phase, while CO_2 is strongly adsorbed on the oxidic phase of the catalyst.

An important category of oxide materials which are used as catalyst components for the DRM are the oxides of rare earths, particularly ceria and lanthana. There are good reasons for that, one of them being the high activity of these materials for the adsorption and activation of CO_2 [55, 65, 89–91]. De Leitenburg et al. [89] aimed to elucidate the interaction of CO_2 with ceria-supported noble metals and its activation, using temperature-programmed techniques and transient kinetic studies. According to their results, the mechanism of interaction between M/CeO_2 (M = Rh, Ru, Pt, Pd, Ir) and CO_2 is strongly influenced by the reduction temperature, regardless of the metal employed. By increasing the reduction temperature from 473 to 773 K, a progressive reduction of bulk CeO_2 takes place, which is not promoted by the presence of the metal. CO_2 adsorption and activation takes place on a surface Ce^{3+} site with the formation of CO, while Ce^{3+} is oxidized to Ce^{4+}. Oxygen vacancies act as "additional driving force" for the reduction of CO_2 to CO [89]. Tsipouriari and Verykios [65], investigating the DRM reaction pathways over Ni/La_2O_3 and Ni/Al_2O_3 catalysts by isotopic tracing techniques, proposed that adsorption and dissociation of CO_2 molecule is faster over Ni/La_2O_3 than over Ni/Al_2O_3. Over Ni/La_2O_3, the CO_2 molecule interacts with the carrier to form $La_2O_2CO_3$ species which decompose to produce CO and oxygen species important for the DRM reaction mechanism [(3.14a) or (3.14b)]. The much higher affinity of Ni/La_2O_3 catalyst for CO_2 chemisorption could be attributed to the higher basicity of lanthana as compared to that of alumina [77]. Stagg-Williams et al. [90] consider that, on Pt/ZrO_2 catalysts promoted with La and Ce oxides, CO_2 adsorbs on the support and when the adsorption sites are near the metal particle, it dissociates to form CO and O. The dissociative adsorption of carbon dioxide on the support of Ce-promoted Pt/ZrO_2 catalysts is also considered significant by Ozkara-Aydinoglu et al. [91].

Concluding, it seems that the nature of active sites depends on the nature of the metal and metal oxide components of the catalytic system and the preparation and thermal treatment procedures followed. For many catalytic systems, the adsorption of CO_2 is a fast step and arrives at thermodynamic equilibrium (see Table 3.2), while there are studies which suggest a Rideal–Eley mechanism with carbon dioxide reacting from the gas phase [46, 92]. However, in most cases, kinetic studies of DRM consider a Langmuir–Hinshelwood reaction mechanism. The dissociative CO_2 adsorption is important for catalytic activity and stability, and many research efforts are focused on the development of catalytic materials for the enhancement of the adsorption and activation of carbon dioxide.

3.4.3 Surface Reactions

Limited work has been done on the mechanism of dry reforming in comparison to steam reforming, and most studies support mechanisms based on steam reforming [46]. Wei and Iglesia [93], conducting a kinetic study on supported Rh catalysts, concluded that the resulting first-order rate constants were identical for H_2O and

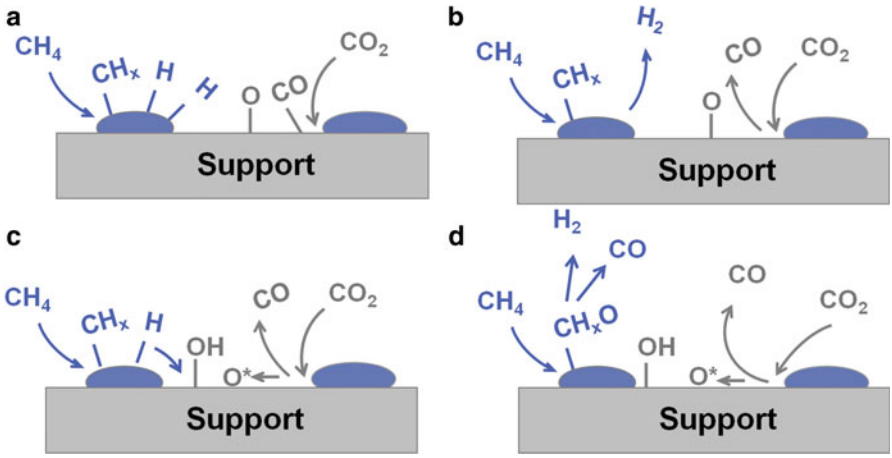

Fig. 3.7 Reaction steps for the dry reforming of methane. (**a**) Adsorption and dissociation of CH_4 and CO_2 on the metal and the metal–support interface, respectively. (**b**) CO and H_2 desorption are fast steps. (**c**) Surface hydroxyls are formed from hydrogen and oxygen spillover. (**d**) Surface oxygen species or hydroxyls oxidize the hydrogen-depleted surface methyl-like species (S_1–CH_x), forming S_1–CH_xO species and finally CO and H_2

CO_2 reforming and for CH_4 decomposition. Primary elementary steps of the DRM reaction are the adsorption and decomposition of CH_4 on active sites on the metallic surface, forming hydrogen and methyl-like adsorbed species, and the dissociative adsorption of CO_2 on the metal oxide surface, preferably on the metal-support interface, forming CO and adsorbed oxygen species (Table 3.2, Fig. 3.7a). Once methane and carbon dioxide are adsorbed, many surface reactions occur, leading to desired or undesired products (Table 3.2). Most of the reaction steps are fast and arrive at equilibrium, e.g., desorption of CO from the support and of hydrogen from the metallic surface (Fig. 3.7b). Kinetic investigations of DRM have shown that the WGS reaction is near equilibrium over a wide range of temperatures, a fact which leads to the H_2/CO ratios to be a function of feed conversion [47]. The quasiequilibrium of the WGS reaction implies that the surface reaction steps related to the reaction are fast [Table 3.2 (3.11–3.13)]. Most kinetic models predict hydrogen spillover from the metal surface to the support where hydrogen reacts with oxygen species forming hydroxyl groups [Table 3.2 (3.13a) and Fig. 3.7c], while oxygen spillover from the support to the metal also occurs (Fig. 3.7d). However, at temperatures higher than 1,073 K, the presence of hydroxyl groups on the support is not likely [90]. Oxygen migrating on the metal surface reacts with hydrogen-depleted S_1–CH_x species ($0 \leq x \leq 3$), forming either S_1–CH_xO species or S_1–CO species [(3.14) and Fig. 3.7d]. It has been suggested that H_2O, produced on the support and migrating to the metal–support interfacial region, participates in the formation of S_1–CH_xO [88]. Some researchers consider

the formation of S_1–CH_xO as an intermediate surface species (3.14a and 3.14b), while others propose the direct formation of S_1–CO (3.14e). Bradford and Vannice [94] suggested that CH_xO species are formed during CH_4 adsorption on reduced TiO_2-supported transition metals (Ni, Pd, Pt, Rh, Cu) at 423 K and considered that these species are intermediate products of the reaction [50, 95]. Osaki and Mori [96] performed a kinetic study on K-promoted Ni/Al_2O_3 catalysts. According to them, the RDS must be ascribed to the dissociation of CH_xO_{ads} to CO and $x/2H_2$. Cheng et al. [88] suggest the formation of surface formates (Al–COOH + O*). Portugal et al. [97] consider that formate-type intermediate CH_xO species may form on Rh/NaY zeolites during DRM reaction. Gheno et al. [98] interpret their results, suggesting that the improved performance of the Ti-containing catalysts is due to the acceleration of CH_xO decomposition, considered as precursor for CO formation, on metal-support interface. Nandini et al. [67], performing a kinetic study of DRM to synthesis gas over Ni–K/CeO_2–Al_2O_3 catalyst, consider CH_4 and CH_xO decomposition as the RDSs. Bitter et al. [99] suggested the generation of formates on the support, close to the metal–support boundary, following the mechanism: methane decomposes on the metal to CH_x (average value of $x = 2$) and H_2, while CO_2 forms carbonates; carbon on the metal reduces carbonate to formate which decomposes rapidly to CO and a surface hydroxyl group. Many other studies, although not supporting this intermediate step with their results, consider that the formation of CH_xO is probable, while others suggest the direct formation of S_1–CO [93, 100–102]. Depending on the reaction temperature and the catalytic system, CH_xO species may be short-lived intermediates. However, one cannot exclude their formation on the catalyst surface. In CH_x, x may take values between 0 and 3. It is difficult to accept that for $x \geq 2$ all hydrogen atoms are simultaneously eliminated to form S_1–CO. The fact that there is no general consensus regarding the dry reforming mechanism is reasonable as it is expected to depend on many factors such as the catalyst's composition (nature and acidity of the support and presence of promoters) and the reaction conditions (mainly the temperature). Furthermore, the DRIFTS method does not offer a clear picture as the maximum temperature of sample chambers usually cannot exceed 873 K and the reaction mechanism is probably different at higher temperatures.

The formation and/or the decomposition of S_1–CH_xO species to CO and H_2 are considered as RDSs [49, 65, 79]. What seems to be crucial is the relative rate of oxidation of S_1–CH_x species as compared to its dissociation: Higher rates of oxidation [Table 3.2 (3.14)] means $x > 0$ in S_1–CH_xO species, while higher S_1–CH_x decomposition rate (3.9) leads to the complete decomposition of the S_1–CH_x species, forming surface carbon (S_1–C). If the rate of oxidation of S_1–C is not fast enough, carbonaceous species start to form and accumulate, leading to catalyst deactivation. The deactivation of the catalyst due to coking is an important issue for the DRM.

3.4.4 Deactivation Due to Coking

Deactivation of catalysts operating under DRM conditions may occur via different mechanisms such as accumulation of carbonaceous deposits, sintering of the metallic phase, and poisoning caused by impurities contained in the feed (most commonly H_2S). As in many hydrocarbon reforming processes, the most important deactivation factor is the formation of carbon-rich deposits, known as carbon or coke. The latter term represents various carbonaceous species, differing in nature and structure and described as on-surface carbon, graphene islands, graphene, filamentary or whisker type, encapsulating, pyrolytic, amorphous, carbide-like bulk carbon, laminar or polymeric carbon, while the terms ordered and disordered carbon have also been used [46, 103–107]. It is obvious that there is no common agreement for the description of the carbonaceous formations, and more than one expression can often be applied as the classification depends on reactivity/stability, crystallography, and shape/form factors. In general, amorphous and graphitic carbon islands are initially formed, while carbon accumulation results either in the encapsulation of the metallic phase or in the growth of filamentous, whisker-type carbon. The formation of bulk metal carbides is unlikely, but surface carbides can be formed [46, 108]. The terms C_α or carbidic carbon which can be hydrogenated at temperatures below 323 K, C_β or amorphous carbon which is hydrogenated between 373 and 573 K, and C_γ or graphitic carbon hydrogenated at temperatures >673 K are also used to denote carbon types removed at different temperatures under TPH (or TPO) conditions [109, 110]. The nature, structure, and rate of formation depend on various parameters such as catalyst characteristics (nature of the metal and the support, composition, texture, and structure), feed composition, and reaction conditions [105].

In general, carbonaceous deposits form via complicated chemistry, following a sequence of elementary steps. The mechanism is believed to include coke formation and coke gasification reactions proceeding through several different routes. In the end, the net accumulation of coke depends on the differences of the rates of the deposition–removal reactions. In DRM, carbon originates from methane decomposition [Table 3.2 (3.9d)], carbon monoxide disproportionation (Boudouard reaction), and carbon condensation reactions, and there is no thermodynamic hindrance for any of these reactions. CH_4 decomposition is dominating at temperatures higher than 973 K and the Boudouard reaction at temperatures lower than 873 K [22, 46, 61, 111]. Both reactions proceed on the metal surface, and the extent of the contribution of each on carbon accumulation depends on operating conditions and catalyst composition. York et al. [46] assert that at temperatures higher than 1,050 K, the amount of carbon due to the Boudouard reaction is expected to be very low as compared to that originating from methane decomposition or the POM. Nevertheless, this is not a point of common agreement as there is evidence that the contribution of the Boudouard reaction (3.6) is not negligible [112].

Nickel catalysts are prone to carbon formation which results in fast deactivation. As already described, methane is known to adsorb dissociatively on the surface of nickel nanoclusters, releasing hydrogen and forming S_1–CH_x surface species. If reactive oxygen and/or hydroxyl surface species are available to react with the hydrogen-depleted species, then S_1–CH_xO or S_1–CO species are rapidly formed (3.14), eventually producing CO and H_2 [(3.16 and 3.17) and Fig. 3.7d]. In the opposite case, S_1–CH_x undergoes further decomposition to produce carbon atoms and/or groups of atoms (Fig. 3.8a). As carbon has a high solubility in the nickel lattice, carbon atoms can either remain on the surface or diffuse in the subsurface toward carbon growth centers, such as grain boundaries (Fig. 3.8b) [103, 106]. Figueiredo and Trimm [113], calculating the concentration of carbon in the nickel phase to be the carbon content of Ni_3C, assumed that coke accumulation probably proceeds through the formation of carbides as intermediates. These carbides decompose to give free carbon which can migrate through the nickel lattice. Following an induction period, these carbonaceous species are incorporated into the graphene layer which forms at the nickel–support boundaries. Depending on the carbon growth mechanism and the catalytic system, the graphene layer may encapsulate the particles or detach the nickel particles from the support and grow filamentous carbon (whiskers), nanofiber, and/or nanotubes of carbon with nickel particles at their top edge (Fig. 3.8c) [103]. In many Ni-based systems, the formation of filamentous carbon predominates [22, 114–117]. In that case, as the nickel surface is still accessible to the reactants, the catalyst remains operational for some time, but carbon continues to accumulate, finally leading to drop of the activity, increase of the pressure, and reactor's blockage [46, 106, 114, 118]. Helveg et al. [119] used in situ HRTEM to monitor the carbon nanofiber growth derived by catalytic decomposition of methane. The HRTEM images revealed that graphitic nanofibers grow with a Ni nanocluster at the front end and the graphene layers are aligned into multiwalled carbon nanofiber structures (Fig. 3.9). The nucleation and growth of the graphene layers forming nanofibers proceed by reshaping or restructuring the monoatomic step edges at the nickel nanocrystal surface, and carbon nanofibers have usually similar size to the nickel cluster: The smaller Ni particles tend to obtain an elongated shape, forming partial multiwalled carbon nanotubes, whereas larger Ni particles tend to obtain pear shape and whisker-type carbon nanofibers are formed with graphene layers inclined with respect to the fiber axis [119].

It has been proposed that the carbon formation mechanism is facilitated by the comparable activation energies of diffusion of carbon through the nickel lattice (33 kcal/mol) and of carbon filament growth (30 kcal/mol) [106, 120, 121]. Xu and Saeys [104, 122] report that the diffusion to the octahedral sites of the Ni bulk is thermodynamically preferred by 50–120 kJ/mol, while the corresponding activation energy is rather low (70 kJ/mol). Furthermore, carbon chemisorption at the octahedral sites of the first subsurface layer is suggested to be preferred over on-surface chemisorption [104]. A concentration gradient established between the gas–metal and metal–graphene interfaces was believed to act as the driving force for carbon transport in a direction perpendicular to the Ni surface through the bulk nanocluster

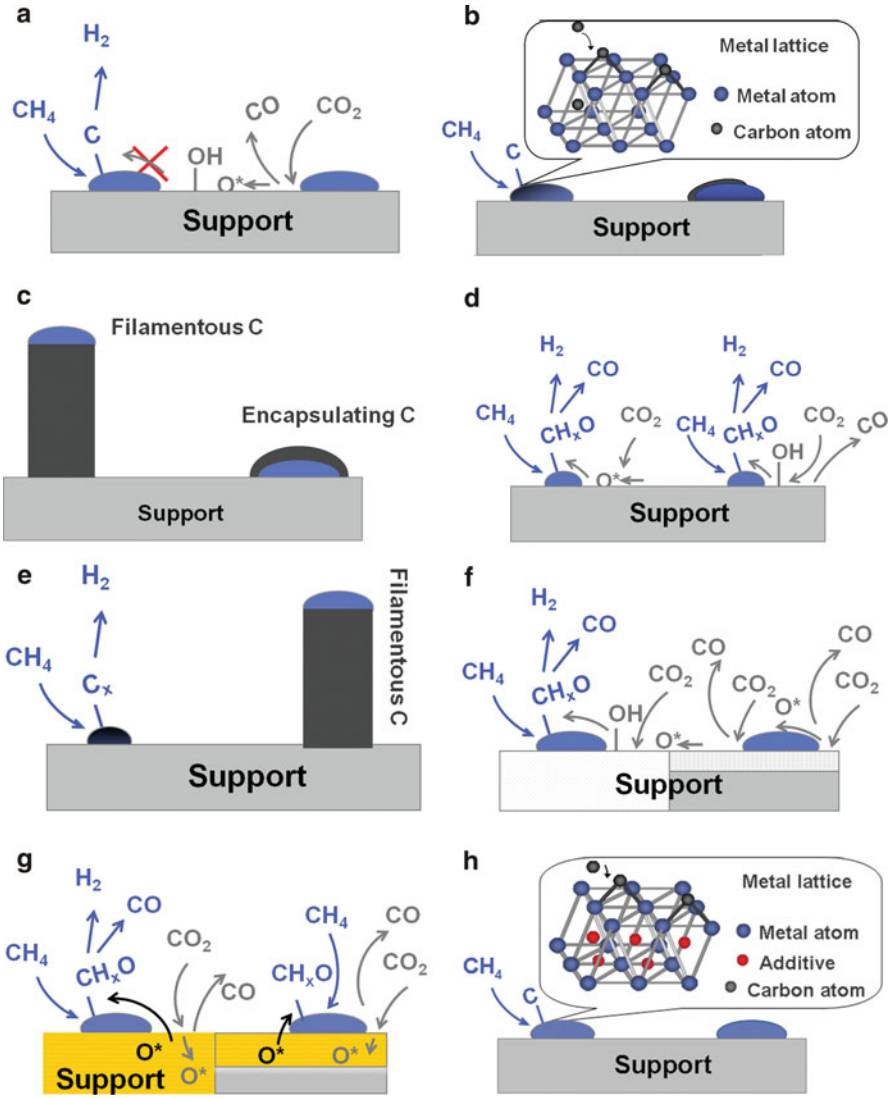

Fig. 3.8 Schematic representation of carbon diffusion in the nickel lattice, the formation of filamentous carbon, and the various approaches for the inhibition of carbon accumulation. (**a**) Active oxygen species or hydroxyls not available fast enough, S_1–CH_x surface species undergo further decomposition, forming carbon atoms and/or carbon group of atoms. (**b**) These carbon atoms and/or carbon group of atoms can either remain on the surface, covering active sites, or diffuse in the subsurface of the metal lattice to carbon growth centers at the grain boundaries or the surface steps. (**c**) At carbon nucleation centers, the carbon atoms and/or carbon group of atoms can be incorporated into the graphene layer progressively, forming encapsulating or filamentous graphitic carbon. (**d**) In catalysts with well-dispersed metallic phase, CH_4 adsorption-activation centers on the metallic particles are closer to CO_2 adsorption-activation centers on the support, and S_1–CH_x can be easily oxidized by oxygen/hydroxyl surface species. (**e**) In catalysts with well-dispersed metallic phase, small metal crystallites are fast saturated with carbon before graphitic carbon reaches the critical size to form graphene layer. (**f**) Supports (MgO) or support components–additives (CaO) enhancing the adsorption of CO_2, forming active oxygen species/hydroxyls in excess. (**g**) Supports (CeO_2–ZrO_2) or support's components, providing surface active oxygen species (S_2–O) through a Mars–van Krevelen-type mechanism. (**h**) Additives that can "block" carbon growth centers in the metal lattice or the surface steps, preventing carbon diffusion

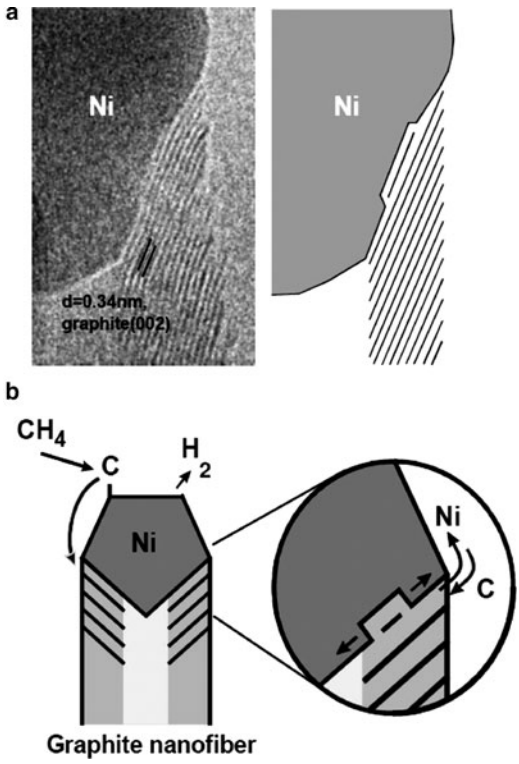

Fig. 3.9 (**a**) High-resolution transmission electron microscopy image of carbon nanofiber growth (*left*), obtained in situ during the catalytic decomposition of methane on Ni nanoclusters supported on $MgAl_2O_4$ and showing the interface between the nickel nanoparticle and the carbon whisker and (*right*) the schematic presentation of the graphene–nickel interface specifying the growth of a graphene layer between monoatomic Ni step sites at the nickel surface. (**b**) Illustration of the growth mechanism for carbon nanofibers suggested based on in situ HRTEM observations and DFT calculations . Reprinted with permission from reference [130]. Copyright (2006) by the American Physical Society

during steady-state growth of graphite whiskers [123]. Although the calculated lattice constant of graphene closely matched the lattice constant of the Ni(111) surface, the interaction between graphene and the Ni(111) surface is very weak and even slightly repulsive. Bartholomew [124] concluded that carbon formation from methane decomposition is more difficult on Ni(111) than on Ni(100) or Ni(110). Abild-Pedersen et al. [103] and Helveg et al. [119] studied the carbon formation mechanism for various methane reactions, combining ab initio DFT calculations and experimental results. DFT calculations of methane decomposition showed that diffusion inside the bulk Ni cluster is highly unlikely and that carbon diffusion could occur along the surface in the subsurface layer [103]. Abild et al. [103] demonstrated that nickel step-edge sites act as the preferential growth centers for graphene layers on the nickel surface (Fig. 3.9).

The carbon formation mechanism described above gives a plausible explanation for the higher carbon formation resistance of noble metal catalysts. As the calculated equilibrium constants for methane decomposition are smaller for noble metals than for nickel, the concentration of intermediate surface carbon species will be lower. In the presence of oxygen species, these intermediate carbon species will produce CO before carbonaceous deposits start to form. Furthermore, the dissolution of carbon into these noble metals lattices proceeds to a smaller extent [125].

There is a debate regarding the effect of metal particle size on the formation of filamentous carbon. Although small metallic particles comprise more steps and defects, it has been observed that filamentous carbon formation is less on smaller crystallites. There is a good explanation for this observation, taking into account the carbon formation mechanism. According to Trimm [106], carbon diffusion in the nickel lattice proceeds until the nickel particle is saturated with carbon and then it stops. It is expected that the saturation with carbon occurs much faster in small nickel particles. Bengaard et al. [71] have shown that the small carbon clusters must be unstable. There is a certain critical graphene cluster size of about 80 atoms of carbon above which graphene island is stabilized. Since the critical nucleus is quite large, the process is slow. If the facets or step edges of nickel particles are too small, carbon nucleation cannot proceed and graphite formation is suppressed [71]. This explains why graphitic carbon (encapsulating or filamentous) is not formed on small metal particles. The difficult point is to identify the critical size for nickel particles. According to Lercher et al. [126], the critical Ni particle diameter is 2 nm, below which the carbon formation rate is slowed dramatically. However, most experimental results conclude that the critical size must be higher, about 7–10 nm [127–134].

Many research efforts aim in decreasing carbon formation on Ni-based catalysts by:

1. Improving the dispersion of the nickel phase, employing suitable preparation methods, or using metal oxides, as supports or modifiers, which favor the formation of small Ni^0 particles (Fig. 3.8e)
2. Increasing the availability of surface oxygen species by using metal oxides, as supports or modifiers, which can enhance the adsorption and dissociation of CO_2 (Fig. 3.8f, g)
3. Blocking nickel step-edge sites that act as the preferential carbon growth centers using sulfur, as in the industrial SPARG process, or other poisons (Sn, B, Au) (Fig. 3.8h)

The results of many of these studies are discussed in the following paragraphs.

3.5 Catalyst Studies

The most important parameters which influence activity, selectivity, and stability seem to be (1) the nature and particles size of the supported metal; (2) the nature, texture, and structure of the support; and (3) reaction conditions. Thus, considerable research efforts focus on shedding light on the importance and the control of these parameters via proper selection of metallic component and support, catalyst preparation method, and addition of promoters–modifiers, so as to retain high activity while suppressing carbon formation.

3.5.1 Noble Metal Catalysts

As already mentioned above, catalysts based on noble metals (Rh, Ru, Pt, Pd, Ir) are generally very active for DRM, without significant coke formation, due to small equilibrium constants for methane decomposition and low dissolution of carbon into their lattices [55, 135–142]. Activity and resistance to carbon deposition largely depend on the metal but also on the nature of the support [55, 66, 95, 97, 100, 101, 135–140, 143–153]. Rostrup-Nielsen and Hansen [135], in a comparative study of various transition metals supported on MgO-stabilized Al_2O_3, found the following activity order: Ru > Rh, Ni > Ir > Pt > Pd under atmospheric pressure and at 773 and 923 K, while the order for carbon formation was Ni > Pd ≫Ir > Pt > Ru, Rh, being negligible for the last two. Ruthenium-based catalysts emerge as ideal candidates for DRM as their high activity is accompanied with low carbon formation rate. However, the availability of Ru is too low to permit a major impact on the total reforming catalyst market [135]. Rhodium catalysts, although exhibited activity comparable to that of nickel catalysts, showed carbon deposition rates similar to those of Ru [135].

In another study, aiming to elucidate the role of the transition metal and that of the support over a wide range of temperatures (673–1,023 K), Ferreira-Aparicio et al. [136] studied the transition metals Co, Ni, Ru, Rh, Ir, and Pt supported on either silica or γ-alumina. The activity at 723 K, expressed as turnover frequency, followed the order Rh > Ni > Ir > Pt, Ru > Co for the alumina-supported catalysts and Ni > Ru > Rh, Ir for the silica-supported series (Fig. 3.10) [136]. Higher performance is not directly related to the number of surface metallic sites; e.g., Ir/SiO_2 and Rh/SiO_2 catalysts possess higher metal dispersion than Al_2O_3-based catalysts, while their catalytic activities are significantly lower. It can be inferred that the support exerts a significant influence not only on the turnover frequency of a given metal (Fig. 3.10) but also on the reaction mechanism and on catalysts' stability under reaction conditions. The results of this study showed that selectivity toward syngas does not seem to be greatly affected by the nature of either metal or support. As a general rule, hydrogen selectivity increases with temperature while that of carbon monoxide remains practically constant. The rate of carbon generation and its migration toward the support are factors affecting activity and stability of a given catalyst [136]. Thus, catalytic stability seems to depend on the nature of the carrier on which the metal is dispersed and on the interaction between the metallic phase and the support. MSIs control the sintering process, and as they are weaker for silica-supported metals, sintering is affecting these catalysts more [136]. In accordance to the results of Rostrup-Nielsen and Hansen [135], the study of Ferreira-Aparicio et al. [136] also showed that Rh/Al_2O_3 catalyst exhibits high turnover frequency and excellent stability, while nickel- and cobalt-based catalysts are resistant to deactivation. An interesting finding of this study is the absence of whisker-type carbon (filamentous) on Pt/Al_2O_3, Ru/Al_2O_3, and Ru/SiO_2, as TEM micrographs revealed. Thus, the structure of carbon deposits, in particular for the Ru/SiO_2 sample, comes out to be amorphous together with some carbon layers encapsulating the metal particles [136].

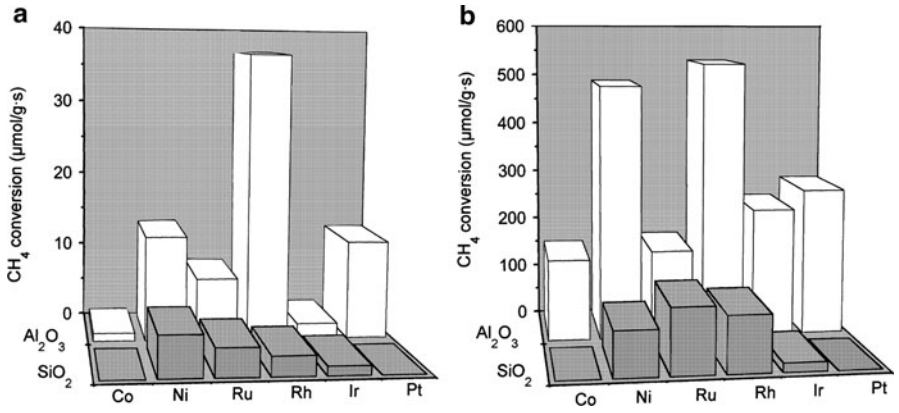

Fig. 3.10 Methane conversion for transition metal catalysts supported on either silica or alumina [reacting mixture: CH_4:CO_2:He (10:10:80); total flow rate: 100 ml/min]: (**a**) at 723 K, TOS 45 min; (**b**) at 1,023 K, TOS 5 min Reprinted with permission from reference [136]. Copyright (1998) by Elsevier

Since supported Rh catalysts appear to exhibit the best performance, considerable research efforts have been dedicated toward understanding the reaction mechanism as well as the factors which influence their activity and stability. Wang and Ruckenstein [138] investigated the physicochemical characteristics and catalytic behavior of reduced Rh catalysts supported on two kinds of oxides: reducible (CeO_2, Nb_2O_5, Ta_2O_5, TiO_2, ZrO_2) and irreducible (γ-Al_2O_3, La_2O_3, MgO, SiO_2, Y_2O_3). According to this study, the reducible oxides seemed unsuitable for the dry reforming reaction at atmospheric pressure and 1,073 K mainly due to low activity. However, recent studies have revealed improved catalytic performance of CeO_2- and ZrO_2-based Ni and Pt catalysts (see relevant paragraphs). Among the irreducible oxides, γ-Al_2O_3, La_2O_3, and MgO are active and stable, with the activity increasing in the sequence La_2O_3 < MgO < γ-Al_2O_3 [138]. Verykios and coworkers [139–142] have studied Rh catalysts supported on metal oxides and binary supports, performing also mechanistic studies [102, 151–153]. Their results show that the specific activity of Rh catalysts strongly depends on the carrier employed to disperse the metal, decreasing in the order YSZ (yttria-stabilized-zirconia) > Al_2O_3 > TiO_2 > SiO_2 > La_2O_3 > MgO, while deactivation is higher over Rh supported on TiO_2 and MgO. Metal particle size was proven to be important for the initial intrinsic activity as well as the rate of deactivation, both decreasing with increasing Rh particle size. However, the degree of these dependencies was found to be affected by the nature of the carrier, suggesting different MSIs. Factors contributing to catalyst deactivation have been shown to be carbon deposition, metal sintering, and poisoning of surface Rh sites by species originating from the carrier [139, 140]. Mechanistic studies performed by steady-state tracing and transient techniques at 923 K and 1 atm pressure indicate that the origin of carbon formed on Rh/Al_2O_3 catalyst is mainly the disproportionation of CO, while the contribution of CH_4 is small at this reaction temperature [141, 142]. The relative

quantities of the different carbon species and total amount of carbon formed on this catalyst under reaction conditions of 823–1,023 K and 1 atm depend on temperature and time on stream [141, 142].

The effect of the support and the activation procedure on Rh catalysts (1–3 wt% Rh), supported on various supports, such as NaY zeolite, γ-Al_2O_3, Nb_2O_5, and TiO_2, were studied by Portugal et al. [97]. TOF for CO formation and the dispersion of metal particles are strongly affected by the type of the support, in accordance with previous studies of Wang and Ruckenstein [138] and Verykios and coresearchers [139–142]. The order followed for the metal dispersion is Rh/NaY $\approx$ $Rh/Al_2O_3 \gg Rh/Nb_2O_5 > Rh/TiO_2$, while some zeolite-supported samples have better dispersions, depending on the activation procedure. The pre-treatment-activation procedure was investigated only for the Rh/NaY zeolites where the highest dispersion was observed for samples previously calcined and then activated in H_2. Catalysts activated directly in H_2 or steam or submitted directly to the reaction conditions showed large metal particles. A correlation between the specific activity in CO_2 reforming and the dispersion of metal particles of Rh/NaY zeolites was revealed. Portugal et al. [97] concluded that the activity of oxide-supported Rh catalysts is mainly determined by the participation of the RWGS reaction. Rh catalysts supported on oxides exhibited significantly higher turnover frequencies due to a higher degree of participation of the RWGS reaction. The thermal stability and the relative catalyst resistance to coking of oxide-supported catalysts followed the same order as that observed for the metal dispersion, $Rh/Al_2O_3 > Rh/Nb_2O_5 > Rh/TiO_2$. The coking resistance was attributed to the support ability to stabilize CH_x decomposition and carbon monoxide dissociation. On the other hand, catalysts supported on Na^+-neutralized zeolites exhibited remarkable thermal stability regarding metal dispersion and zeolite structure, suggesting that zeolite-supported Rh catalysts can be stable DRM catalysts.

The effects of Rh loading and reaction temperature were studied by Wang and Au [143] on silica-supported catalysts. The increase in rhodium loading up to 0.05% caused an increase in the CO yield, while further increase in Rh content had almost no effect. An important increase of CH_4 conversion is observed for temperatures higher than 973 K, exceeding than that of CO_2 at 1,073 K. Based on the results that rhodium oxide has higher ability for methane oxidation than metallic rhodium, Wang and Au [143] proposed the following mechanism: The dissociation of CO_2 could lead to CO or surface carbon, together with surface oxygen. At 1,073 K, a small amount of rhodium oxide could be temporally formed, and thus, besides the dominant methane reforming reaction over metallic rhodium sites, some methane would be oxidized to CO_x ($x = 1$ or 2) by the rhodium oxide, which is then simultaneously reduced to metallic rhodium. Thus, CO and H_2 formation can proceed through two possible pathways for methane dissociation: direct dissociation and oxygen-assisted dissociation, the contribution of the latter increasing with temperature. This mechanism explains the higher CH_4 conversion as compared to that of CO_2 at 1,073 K. Wang and Au [143] also suggested that surface hydroxyls might be the main pathway for surface carbon removal [Table 3.2 (3.15)].

Recently, two kinetic studies were performed over Rh/Al_2O_3 catalysts [100, 101]. Maestri et al. [100], using a thermodynamically consistent microkinetic model, showed that for both steam and dry reforming on Rh/Al_2O_3 catalysts, methane dissociation is the RDS, regardless of the coreactant (either CO_2 or H_2O). Methane conversion proceeds via pyrolysis and carbon oxidation by $OH_{(ads)}$ ($CH_4 \rightarrow S_1–C \rightarrow S_1–CO$), and the role of the coreactant is to provide the main oxidizer, $OH_{(ads)}$. In line with isotopic kinetic experiments reported by Wei and Iglesia [102] for nickel catalysts, methane activation is predicted to be the RDS, and all steps involving coreactant turn out to be quasiequilibrated [first-order dependence on CH_4 concentration and independent of the coreactant (H_2O or CO_2)]. An unexpected finding of this study is that for intermediate and high temperatures, the $S_1–CH_4$, $S_1–CH_2$, and $S_1–CH$ dissociation steps quickly reached quasiequilibrium, whereas $S_1–CH_3$ decomposition [Table 3.2 (3.9b)] was far from equilibrium, due to the high activation energy of the reverse reaction. Consequently, Maestri et al. [100] considered this step to be the RDS. As the RDS is independent of oxidizer, the coreactant is not expected to play any kinetically relevant role in the rate of the reaction [100]. It is worth noting that, based on the above model, $OH_{(ads)}$ is considered as the main oxidizer and not $O_{(ads)}$, which is different from most qualitative mechanisms reported in the literature [93, 141, 154]. Moreover, it was also confirmed that under typical experimental conditions, SRM and DRM always occur with the WGS reaction close to equilibrium. Donazzi et al. [101] agree with the importance of the presence of surface hydroxyls, suggesting that DRM is actually a combination of SRM and RWGS reactions, i.e., that surface hydroxyls are the effective coreactants of adsorbed CH_x species. However, Donazzi et al. [101] consider that the RWGS is dependent on CO_2 concentration, and, consequently, the kinetics of methane conversion is a function of the kinetics of both reactions. On the other hand, since under most conditions the RWGS is equilibrated, the CO_2 kinetic dependence becomes prominent only in specific cases, defined by the combination of high space velocity and low CO_2 concentrations. A kinetic study was also performed using a Rh/La_2O_3 catalyst [144]. The results are comparable to those obtained by Verykios and his coworkers on Ni/La_2O_3 catalysts [49, 65, 79]. In the reduced catalyst, a mixture of La_2O_3 and $La_2O_2CO_3$ (oxycarbonates) on which reduced rhodium particles are well dispersed was detected by XPS, while the only surface species detected on the used catalyst were lanthanum oxycarbonate and mainly Rh^0. Munera et al. [144] concluded that the slow steps are both the decomposition of methane [Table 3.2 (3.9)] and the reaction of the carbon species formed with the lanthanum oxycarbonates present in the working catalyst, exactly like the mechanism occurring on the Ni/La_2O_3 catalysts [49]. This slow reaction occurs most likely at the metal/support interface and provides a rationale for the stability of Rh/La_2O_3 catalyst [144].

Another recent study, which focused on the viability of a process based on Rh/γ-Al_2O_3 monolithic catalyst, revealed that equilibrium conversions of CH_4 and CO_2 can be achieved both under dry reforming and under autothermal conditions [145]. No deactivation was observed under DRM condition when using a stoichiometric feed, but some deactivation was seen after long-term exposure to 1.4:1 ratios of CH_4:CO_2 without O_2. After regeneration in air, catalytic activity was restored.

Other noble metal-based catalysts have also been studied, aiming to elucidate the importance of the support, the presence of additives on the activity, and the stability of catalysts as well as the reaction and carbon formation mechanism [95, 146–153]. The reader should turn to the specific literature for more details.

3.5.2 Ni-Based Catalysts

Ni-based catalysts are very active for reforming reactions. Furthermore, Ni is abundant in nature, has lower price compared to noble metals, and is more suitable for a cost-effective commercial DRM process. Unfortunately, nickel catalysts are more prone to carbon formation. During the last decade, these catalysts have been the subject of intensive investigations to obtain insight into the catalytic phenomena occurring on these materials in relation with their physicochemical properties. For the above reasons, catalytic systems on Ni-based materials are extensively discussed, focusing on the effect of catalyst composition (oxides used as supports or additives, second metal, metal loading), preparation method, and thermal treatment procedures.

3.5.2.1 The Nature, Texture, and Structure of the Support

Considering all the catalytic phenomena occurring during the DRM reaction, it is easy to understand the vital role of the supporting material, which, especially in the case of nickel catalysts, is far beyond the classical view of a carrier which provides high surface area and mechanical and thermal stability to the catalyst. As the adsorptive dissociation of methane, occurring on the metal surface, is one of the rate-limiting steps, the support must obviously offer maximum metal dispersion, ensuring, in addition, stability under reaction conditions and avoidance of sintering. Moreover, metal dispersion has a dramatic effect on carbon deposition as the ensembles necessary for carbon formation are larger than those needed for CH_4 reforming [55]. Furthermore, the support must provide the active sites for the adsorption and dissociation of CO_2 in the framework of the bifunctional mechanism described earlier. Surface acidity–basicity is also a major factor influencing activity and carbon formation. Increased Lewis basicity of the support leads to increased adsorption of CO_2 which produces surface species which react with carbon to form CO [55, 60].

The role of MSIs on the performance and the stability of a nickel catalyst is crucial [50]. MSI, in addition to stabilizing the metallic nickel phase against sintering, can also increase the electron density in the metal crystallites [78]. As a consequence, the electron donation ability of Ni^0 to antibonding LUMO of methane increases and so does the ability to activate C–H bond cleavage as in the case of TiO_2-supported catalysts [50]. The support-induced electronic effects are significant for the smaller nickel crystallites, becoming negligible for large (ca. 10–40 nm) metallic particles.

Bradford and Vannice [50], in a comparative study of Ni-based catalysts, supported on MgO, TiO_2, SiO_2, and activated carbon, tried to shed light on the role of the support on activity and carbon deposition. They concluded that the physicochemical and catalytic properties of the catalyst cannot be linearly related to the alteration of only one parameter, brought about by the metal oxide used. For example, the catalytic behavior of Ni/TiO_2 is a combination of various phenomena originating from strong metal–support interactions (SMSIs). Its high activity is attributed to the increased electron density in the Ni crystallites, while its improved coking resistance is believed to be due to the low carbon monoxide binding energy and the high barrier for carbon monoxide dissociation. Furthermore, TEM results implicate the miscibility of nickel and TiO_x phases during reduction and/or reaction, implying that large ensembles of nickel atoms are either removed by reacting with TiO_x species or are covered by mobile TiO_x species. Thus, the high carbon deposition resistance of Ni/TiO_2 can be explained in terms of electronic as well as geometric effects [50].

3.5.2.2 Alumina

Alumina is one of the most common supports as it is inexpensive and has great mechanical and thermal stability while high dispersion of the nickel phase can be achieved [88]. Ni/Al_2O_3 is considered as the state-of-the-art catalyst, and many articles have been devoted to the elucidation of the reaction mechanism and the effective suppression of carbon formation on this catalytic system. Its acidity–basicity depends on the preparation method and the impurities it contains. Its CO_2 adsorption capacity is moderate.

Crystallographic forms, preparation procedure, and nickel loading have a significant effect on catalytic performance. High-surface area aluminas with low Ni loadings (e.g., 5–10 wt% Ni) give satisfactory results, provided that good Ni dispersion is achieved by the preparation and the thermal treatment procedure [88, 118, 131]. The latter is an important procedure, determining the degree of reduction, the formation of $NiAl_2O_4$, and thus the catalytic behavior and stability of these catalysts [88, 131, 155]. Reduction of the Ni/Al_2O_3 catalyst is a prerequisite for an active catalyst. Unreduced catalysts are less active than reduced ones, the former improving under reaction conditions at 1,173 K [88]. Cheng et al. [88] observed that the degree of nickel reduction had almost no effect on the reforming activity (especially at high temperatures ~1,173 K) and concluded that the RDS must be the CO_2 dissociation occurring on the support and not the methane dissociation on Ni^0 or the reaction steps occurring at the metal–support interfacial region. On the other hand, Juan-Juan et al. [131] concluded that the pretreatment procedure is not essential for the activity of a Ni/Al_2O_3 catalyst, evaluated at 773 and 973 K, but affects noticeably the amount of deposited coke. They suggested that calcination pretreatment could be avoided since the lowest carbon deposition is observed for the Ni/Al_2O_3 catalyst which is not calcined but directly reduced at 973 K [131]. Regarding the formation of nickel aluminate, Sahli et al. [155] claimed that the

catalysts consisting of a solid solution of Al_2O_3 and $NiAl_2O_4$ without any detectable NiO exhibited high activity in the temperature range 773–1,073 K, forming significantly less carbon than the catalyst initially containing NiO.

Conventional preparation methods give Ni particles usually larger than 10 nm, having the tendency to sinter upon reduction and/or under reaction conditions and to form filamentous carbon. In addition, at high temperatures, nickel aluminate can be formed, a phase difficult to reduce and consequently inactive for the decomposition of methane. Thus, alternative preparation methods as well as catalysts' pretreatments have been proposed, e.g., the use of plasma techniques [156, 157]. The plasma treatment of the Ni/Al_2O_3 catalyst followed by calcination resulted in smaller Ni particles with a narrower size distribution, smoothened Ni particle surface (provoking moderate reduction of methane decomposition rate and thus a better balance of carbon formation–gasification rates), and enhanced Ni–alumina interactions, leading to high catalytic activity and excellent resistance to the formation of carbon [156, 157]. Nevertheless, the most common path followed for the improvement of Ni/Al_2O_3 catalysts is the introduction of one or more textural or chemical promoters, targeting the increase of Ni dispersion, the promotion of surface reactions which consume surface carbon clusters, and the blockage of carbon growth centers. Selected cases such as the use of alkaline or rare earths and/or bimetallic catalysts will be discussed in following paragraphs.

3.5.2.3 Silica

The lack of SMSI in the Ni/SiO_2 catalysts results in deactivation due to nickel sintering and extensive coking ([50, 55] and references therein). Energetically, silica-supported nickel catalysts are susceptible to carbon formation due to a combination of higher carbon monoxide binding energy and a lower barrier for carbon monoxide dissociation [50]. Pan et al. [158], aiming to enhance the interactions between Ni particles and silica and improve Ni dispersion, applied glow discharge plasma for the decomposition of nickel nitrate on the SiO_2 support. The plasma-treated catalyst exhibited comparable activity to that of the Ni/SiO_2 catalyst prepared by the conventional incipient wetness method. Yet the resistance to coke deposition of the Ni/SiO_2 catalyst is significantly improved by plasma treatment, and this was explained by the smaller size of Ni particles and the more homogeneous dispersion of Ni after the plasma treatment, as revealed by CO chemisorption and TEM studies [158]. Following another methodology, the influence of the addition of different amounts of Gd_2O_3 on a Ni/SiO_2 catalyst was studied [159]. Gd_2O_3 had a dual effect on the catalyst: (1) higher dispersion of Ni attributed to strong interaction among Ni, Gd_2O_3, and SiO_2 and (2) Gd_2O_3-modified Ni/SiO_2 catalysts possessed higher ability for CO_2 adsorption and activation, forming surface carbonate species. All modified catalysts exhibited higher activity and stability, the best being that having Gd/Ni atomic ratio of 0.45 [159].

3.5.2.4 MgO and Hydrotalcite-Type Materials

MgO possesses two important advantages for practical applications as it is inexpensive and has high thermal stability. Furthermore, it is a unique carrier for nickel catalysts, having multiple beneficial effects. Mg^{2+} and Ni^{2+} ions have similar crystal ionic radius, 0.65–0.72 Å, respectively, while MgO has the same crystal structure as NiO. Thus, nickel ions can diffuse in magnesia lattice, creating NiO–MgO solid solutions with strong interactions between the two phases [55, 60]. As a result, NiO is well dispersed and can only be partially reduced, forming very small nickel crystallites on the surface of the solid solution (Fig. 3.8d, e), which in some cases cannot be detected even by HRTEM [55, 60]. Therefore, metal sintering and carbon deposition are hindered. In addition, magnesia is an alkaline earth oxide of high surface basicity and thus high affinity to adsorb CO_2, contributing further to the suppression of carbon deposition (Fig. 3.8f). Tomishige et al. [160] suggested that there are two paths for the activation of CO_2 on $Ni_{1-x}Mg_xO$ solid solutions: (1) adsorption and activation of CO_2 on the support at the interface between metal and support and (2) activation of CO_2 on nickel metal surface. In the case of $Ni_{1-x}Mg_xO$ solid solutions, CO_2 dissociation at the metal–support interface is considered as more effective in providing oxygen species which can react with intermediates such as CH_x adsorbed on Ni, surface Ni carbide, and bulk Ni carbide, strengthening the resistance to carbon formation [160]. However, the first attempts to prepare NiO–MgO catalysts for DRM resulted in low activity and selectivity, low stability, and high coking rate ([50, 55] and references therein). Since then, NiO–MgO catalysts have been the subject of many studies, revealing that active and relatively stable catalysts can be based on this solid solution, provided that they are suitably prepared [161]. Apparently, there is a complex interconnection of various parameters (surface area, defect concentration, basicity, and nickel dispersion) that can have varying impacts on DRM performance of Ni/MgO catalysts. More specifically, depending on composition (Ni/Mg ratio), the properties of the MgO used, the preparation method, and thermal treatment, different $Ni_xMg_{1-x}O$ solid solutions and catalysts can be obtained that can have very diverse textural, structural, and catalytic properties.

Impregnation of MgO with an aqueous Ni^{2+} solution seems the most appropriate preparation method, while coprecipitation is unsuitable [50, 55, 60, 162–166]. The textural and crystallographic properties of MgO, i.e., surface area, pore size distribution, and lattice parameters, may affect notably the performance of the final Ni/MgO catalyst: Smaller nickel particles leading to higher catalytic activity and carbon formation resistance were formed on MgO supports with more porous structure into which metal ions could easily diffuse during impregnation [163, 167]. NiO loading in Ni/MgO also regulates metallic particle size [168]. Ni content in the range of 5–15 wt% has been found to be effective for DRM, whereas at higher loadings, Ni particles become large and behave like bulk materials. Thermal treatment procedures are decisive for the extent of nickel diffusion in the magnesia lattice and the formation of solid solution and, consequently, the effectiveness and the stability of the catalyst [60, 164, 166].

In summary, the most important factors affecting the properties of the catalyst is the formation of solid solution and the MSIs it induces which regulate the Ni^0 dispersion, the metal-support interface, and the reducibility of the nickel phase. However, it seems that too SMSI can result in inactive catalysts as in the case of those prepared by coprecipitation [163].

Another important category of nickel–magnesia catalysts are composites derived from hydrotalcite (HT)-type precursors, in which the active phase is homogeneously distributed in a matrix. HT compounds have the general formula $[M^{2+}_{1-x}M^{3+}_{x}(OH)_2]^{x+}(A^{n-}_{x/n})\cdot mH_2O$, where M^{2+} and M^{3+} are metal cations, e.g., Mg^{2+} and Al^{3+}, A is an anion, n = charge of the anion, $1-x > x$, and m is the number of interlayer water molecules. HTs present a unique layered structure very similar to that of brucite, $Mg(OH)_2$ [169–171]. In brucite structure, each magnesium cation is octahedrally surrounded by hydroxyls, the structure having no net charge. In HT compounds, some of the Mg^{2+} ions are replaced by Al^{3+} ions, resulting in partially substituted $Mg(OH)_6$ octahedra forming positively charged layers, where the excess charge is balanced by anions (e.g., carbonate ions) located in the interlamellar space together with water molecules [171]. The Mg/Al molar ratio and the interlayer anions can widely vary, while monovalent and tetravalent cations have also been used, in addition to divalent and trivalent cations indicated by the chemical formula. The size and orientation of the interlayer anions determine interlayer spacing [170]. The flexibility in the nature and in the relative proportions of cations and interlayer anions permits tailoring of the physicochemical characteristics of the HT compounds. The final catalysts can have the desired basic and/or redox properties, while the dispersion of the cations in the hydroxylated layers is retained after thermal treatment [171]. Having these advantages, HT-derived materials found many applications and appear ideal as stable catalysts for DRM, STR, POM, or ATM [153, 170, 172–179]. The method followed for the preparation of the layered hydroxides is usually the coprecipitation, although other techniques as the urea method, the reverse microemulsion, or the reconstruction of the HT structure have also been tested [169, 171, 173–175, 178–180]. These preparation methods which embed Ni particles into the support and the MSI exerted could hinder the formation of carbon nanotubes and/or encapsulating layers around the particles [176]. For Ni-based DRM catalysts derived from HT precursor, the main advantage is connected to nickel dispersion. The random distribution of Ni ions in the layered structure hinders the aggregation of nickel phase upon reduction, facilitates the formation of smaller nickel crystal size, and increases the resistance to coking as compared to the conventional catalysts [46].

3.5.2.5 Rare Earths

As the oxidation of S_1–CH_x species is one of the slow steps in the DRM reaction, considered as rate determining and controlling the formation of carbonaceous deposits, the availability of surface oxygen species or hydroxyl species is critical

for a satisfactory catalytic performance. Materials such as rare earth oxides, which can enhance the availability of $O_{(ads)}$ and $OH_{(ads)}$ species, are expected to contribute significantly to the efficiency of a DRM catalyst.

Ceria is known for its high oxygen storage/transport capacity (OSC), i.e., its ability to release oxygen under oxygen-poor environments and quickly reoxidize under oxygen-rich environments. In redox reactions which utilize oxygen, ceria is expected to play a key role as it can supply oxygen originating from its lattice and replace it through the dissociation of carbon dioxide on its surface, in other words a Mars–van Krevelen mechanism (Fig. 3.8g) [94, 181, 182]. Under dry reforming conditions, the catalytic behavior of ceria is the outcome of a complicated series of surface reactions. Ceria can be reduced by H_2 and CO, the latter being an even better reducing agent than H_2 [183]. CO_2 adsorption and activation takes place on Ce^{3+} surface sites with formation of CO and simultaneous oxidation of Ce^{3+} to Ce^{4+}, while bulk oxygen vacancies act as "additional driving force" for the reduction of CO_2 to CO [89]. In addition, ceria can chemisorb large amounts of H_2 and CO, the uptake being also dependent on its physicochemical properties as well as thermal treatment conditions ([183, 184] and references therein). In general, the redox properties of CeO_2 are very sensitive to the textural, structural, and morphological properties of the catalytic system, brought about by the preparation method, the presence of metals or metal oxide additives, the pretreatment, etc. [89, 94, 181–187]. The extent of ceria reduction is expected to affect its reactivity; CO_2 adsorption and activation depends on the electron donor ability of the surface; consequently, the more reduced is ceria, the higher its electron donor ability ([94] and references therein). Unfortunately, the OSC of pure ceria declines under high temperatures and reductive conditions.

In addition to its promotional effect on CO_2 dissociative adsorption, ceria can also improve the dispersion and stabilization of small metal particles. It is one of the oxides known to exert strong interactions on the supported metallic phase, resulting in significant alterations of the physicochemical, chemisorptive, and catalytic properties of both the oxide and the metal ([183] and references therein). Thus, the high thermal stability of dispersed metal as well as the formation of Ce–M alloys under reductive atmosphere are considered to be due to SMSI effects. These SMSIs are often expressed by remarkable changes in the reducibility of the oxide and its catalytic properties [185]. Gonzalez-DelaCruz et al. [185] observed that nickel particles in a Ni/CeO_2 catalyst undergo unexpected modifications in their size and morphology under DRM conditions. The catalyst, prepared by a combustion method and reduced in hydrogen at 1,023 K, was studied using X-ray absorption spectroscopy (XAS). Nickel particles were flattened and strongly stabilized on the partially reduced ceria surface. Gonzalez-DelaCruz et al. [185] suggested that these morphology changes reflect a kind of SMSI and could account for the higher stability observed for the dry reforming reaction. As Bernal et al. [186] have shown, the chemical and structural changes occurring on M/CeO_2 and related lanthanide systems upon reductive treatment at elevated temperatures ($T_{redn} \geq 973$ K) resemble those observed on M/TiO_2 catalysts at lower temperatures ($T_{redn} \geq 773$ K). The M–Ce alloying could be definitely established only if very high reduction

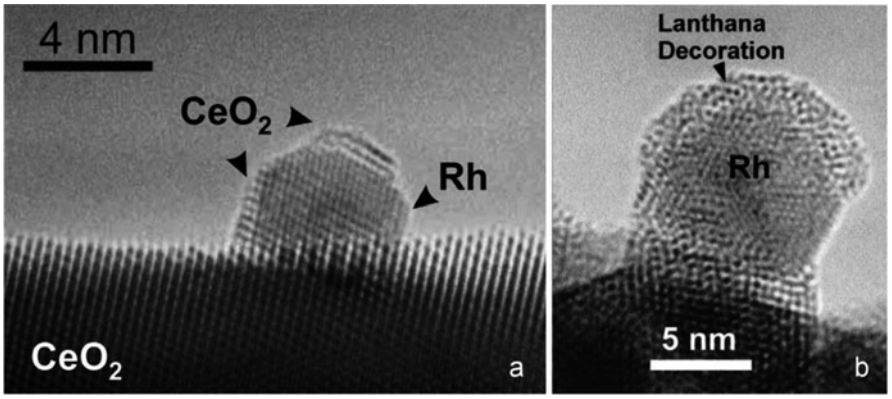

Fig. 3.11 HREM representative images of rare earth oxide overlayer decorating metal particles in reduced catalysts: (**a**) a 2.5% Rh/CeO_2 catalyst reduced at 1,173 K and (**b**) a 10% Rh/La_2O_3 catalyst reduced at 773 K Reprinted with permission from reference [186]. Copyright (2003) by Elsevier

temperatures are applied, while for the ceria-supported Rh catalysts, alloying effects have never been reported to occur. Metal deactivation occurring at moderate reduction temperatures ($T_{redn} \leq 773$ K) may be attributed to electronic perturbations, associated with the interaction between the metal microcrystals and the reduced ceria support. Moreover, HREM has also proved the occurrence of metal decoration effects in CeO_2-catalytic systems upon reduction at temperatures higher than 973 K (Fig. 3.11a).

Although bulk CeO_2 does not seem to be a suitable support for nickel as MSIs reduce catalytic activity, a major part of the recent literature on DRM is devoted to the development of improved ceria-containing binary and ternary supports [55, 181, 182, 188–195]. One of the most studied catalytic systems is ceria–zirconia. Zr^{4+} stabilizes ceria, forming solid solutions over all Ce/Zr atomic ratios having cubic face-centered fluorite structures in ceria-rich samples. $Ce_{1-x}Zr_xO_2$ phases exhibit improved textural features, thermal resistance, catalytic activity at lower temperatures, and, most importantly, oxygen storage/transport properties [182, 188, 191–195]. Recent studies of $Ce_{1-x}Zr_xO_2$ (111) surfaces, combining first principles DFT calculations and experimental data, confirmed that Zr^{4+} doping induces severe distortion of the atomic structures of reduced and unreduced ceria surface [196, 197]. As a result, formation of oxygen vacancy around the Zr^{4+} dopant is facilitated, while oxygen mobility and the OSC are improved. As the availability of surface oxygen species is vital for the DRM reaction, ceria–zirconia binary oxides have been applied as catalyst components [182, 191–195]. Several studies have shown that binary oxides have improved catalytic properties as compared to catalysts supported on either pure CeO_2 or pure ZrO_2, although results vary considerably with the preparation method, the Ce/Zr ratio, the nickel content and dispersion, the presence of other elements, and the reaction conditions. Nickel is well dispersed on these supports, metallic nickel crystallites being smaller than

10–15 nm, and for loadings ≤5%, their size could not be calculated [182, 192–195]. However, there is no general agreement whether nickel is incorporated into ceria–zirconia fluorite structure. Chen et al. [195], studying Ni–$Ce_{0.75}Zr_{0.25}O_2$ catalysts (2.1–4.8 wt% Ni) prepared by various methods, calculated smaller lattice parameters for the catalysts prepared by coprecipitation than for the corresponding supports. They attributed this decrease to the incorporation of the smaller nickel ions (0.72 Å) into the ceria–zirconia solid solution. Koubaissy et al. [198] suggested that some metal atoms could be incorporated in the fluorite lattice of the $Ni_yCe_{2-x-y}Zr_x$ (3–5 wt% Ni) catalysts, the degree of incorporation decreasing with the increase of ceria content. Kambolis et al. [182] observed a decrease of the fluorite lattice parameter only in the case of Ni/ceria catalyst that could be attributed to the presence of nickel ions in the lattice of ceria, while this is not obvious for their zirconia-containing Ni/Ce_xZr_{1-x} catalysts. On the other hand, Kuznetsova and Sadykov [197] state that the unit cell parameter of the fluorite structure increases with the increase of the cation radius introduced while upon the introduction of zirconium and the unit cell parameter decreases because the zirconium ion has a smaller radius than cerium. However, lower valence ions (such as copper, manganese, aluminum) in CeO_2 lattice, although generating pure anionic vacancies, do not change the unit cell parameter of CeO_2 fluorite structure even at very high concentrations, in contrast to what is observed for the Zr^{4+} ions [197]. The $Ni/Ce_{1-x}Zr_xO_2$ catalysts are more reducible than the corresponding supports, i.e., nickel species promote the reducibility of the solid solution, indicative of important MSIs [182, 193]. Although catalysts supported on $Ce_{1-x}Zr_xO_2$ binary oxides were more active for dry reforming than those supported on pure ceria or zirconia, there is no general agreement on the optimum Ce/Zr ratio regarding catalytic performance and carbon formation resistance, and this is an example of the importance of the preparation procedure and the reaction conditions [182, 192, 193, 195]. Furthermore, carbon formation may not be the only cause of the activity loss as phase transition and support sintering can also occur [192].

Proof of the participation of the ceria lattice oxygen in the DRM reaction sequence (Fig. 3.8g) has been provided by Otsuka et al. [199] and Wang et al. [200]. Otsuka et al. [199] explored the activity of a series of $Ce_{1-x}Zr_xO_2$ solid solutions for the gas–solid reaction with CH_4, in the absence of gaseous oxidant and supported metal. The materials were pretreated in O_2 at 1,073 K for 1 h, while the reaction took place at 973 K using a feed of CH_4 diluted with Ar. $Ce_{1-x}Zr_xO_2$ composite oxides as well as CeO_2 produced H_2 and CO as the main products for about 40 min. Higher H_2 and CO production was achieved by the incorporation of ZrO_2 into CeO_2, forming $Ce_{1-x}Zr_xO_2$ composite oxides up to a Zr content of 20% [199]. On the contrary, doping ceria with yttria decreases the activity in DRM of Ni-supported catalysts, while more carbon is deposited [200]. EPR and XPS results provide evidence that this negative effect on catalytic activity and carbon formation resistance is due to the inhibition of oxygen mobility in the yttria-doped ceria, the inhibition increasing with yttria loading [200]. These results are additional evidence of the important contribution of the ceria lattice oxygen in the reaction. On the other hand, Akpan et al. [92], performing kinetic, experimental, modeling, and simulation

studies over a new Ni/CeO_2–ZrO_2 catalyst, suggest an Eley–Rideal (ER) mechanism, assuming the dissociative adsorption of methane as the RDS. These results are rather surprising for a catalytic system containing $Ce_{1-x}Zr_xO_2$ solid solution, as the adsorption and activation of carbon dioxide should be enhanced.

Lanthana has also been used as main support for DRM catalysts [49, 65, 74, 79, 139, 140, 144]. The results of these studies have shown that no matter which is the active metal, Ni or Rh, lanthanum oxycarbonate ($La_2O_2CO_3$), formed by the interaction of La_2O_3 with CO_2, plays a vital role in the reaction mechanism. In both systems, there are two RDSs: the decomposition of methane and the reaction of the carbon species left on the surface with the oxycarbonates present on the working catalyst [49]:

$$S_1 - CH_4 \rightarrow S_1 - C + 2H_2 \quad \text{RDS.}$$

$$S_1 - C + La_2O_2CO_3 \rightarrow La_2O_3 + 2CO + S_1 \quad \text{RDS.}$$

Lanthana can also adsorb and react with CO when heated in CO at 670 K, resulting in carbonate formation, desorbing CO_2 under TPD conditions [201]. Still, the catalytic properties of lanthana are strongly dependent on the structure of the oxide and the thermal treatment, as lanthana annealed at 1,700 K is less active than that heated at 1,100 K. Changes of the redox properties of lanthana and deactivation are considered as the result of structural changes in the oxide upon heating, causing the crystallization of amorphous species, increasing the crystallite size of lanthana, or changing the types of the exposed crystal facets of the oxide [201]. Putna et al. [201] concluded that the reducibility of the cluster depends on its size, deactivation occurring by increasing crystallite size, or removing the active surface facets from lanthana. Verykios and coresearchers [49, 65, 79, 139, 140] suggest that the very good stability of the Ni/La_2O_3 catalyst is also due to the increased metal support interphase as the Ni particles are partially covered (decorated) by $La_2O_2CO_3$ species and catalytic activity occurs at the Ni–$La_2O_2CO_3$ interface. Tsipouriari and Verykios [65], investigating the DRM reaction pathways over Ni/La_2O_3 and Ni/Al_2O_3 catalysts by isotopic tracing techniques, consider the CO_2 adsorption as important. Adsorption and dissociation of CO_2 molecules is faster over the Ni/La_2O_3 catalyst than over Ni/Al_2O_3. During dry reforming of CH_4 over Ni/La_2O_3, the CO_2 molecule interacts with the carrier to form the $La_2O_2CO_3$ species which decompose to produce CO and oxygen species important for the DRM reaction mechanism [(3.14a) or (3.14b)]. The much higher affinity of Ni/La_2O_3 catalyst for CO_2 chemisorption could be attributed to the higher basicity of lanthana as compared to that of alumina. These observations are supported by the work of Bernal et al. [186] who have shown that the basicity of the metal catalysts supported on lanthanide sesquioxide (Ln_2O_3) is the key parameter which influences their properties rather than their reducibility. During the impregnation step, dissolution of the support can take place as the aqueous solution containing the metal precursor is usually acidic, especially in the case of noble metals [186]. For 4*f*-sesquioxide supports, textural changes associated with the dissolution occur, resulting in

profound chemical modifications of the support, which is converted into a complex mixture of hydrated and carbonated phases. After drying, simultaneous reprecipitation of both metal and La ions results in material in which metal atoms are so finely embedded into the support matrix that metal nanoparticles are not visible in the HREM images of catalysts reduced at low temperature [186]. At higher reduction temperatures (773–973 K), metal species segregate forming observable metal particles, while the thermal decomposition of the support phases (lanthanum hydroxide and hydroxycarbonate) results in the formation of La_2O_3. In the final catalyst, well-dispersed nanosized metal particles covered by patches of lanthana can be detected (Fig. 3.11b). The degree of the support decomposition and the growth of metallic particles increased with the increase of reduction temperature. Bernal et al. [186] believe that the chemisorption and catalytic properties of the catalysts supported on lanthanide sesquioxides must be primarily related to the nanostructure of the catalysts (controlled during the preparation procedure) and the intrinsic basic character of this family of oxides and not to their reduction under very mild conditions [186]. On the other hand, a comparative study of Ni and Rh metal catalysts supported on SiO_2 and La_2O_3 showed that lanthana-supported catalysts were less active at relatively low temperature (<873 K) and form more carbon than silica-supported ones [202]. This behavior was explained as follows: Lanthana activates the CO_2 dissociation, supplying CO to the metal. At low reaction temperatures, i.e., <873 K, the Boudouard reaction is the main cause of carbon formation and thus, it is enhanced in the presence of lanthana. Furthermore, lanthana has a positive effect when the metal has low methanation activity, but fast C deposition and deactivation occurs with metals like Ni with high activity for methanation [202].

3.5.2.6 Other Supports

Recently, certain other materials have been studied as supports for Ni catalysts, such as zeolites, mesoporous materials (MCM-41, SBA-15, SBA-16, etc.), and SiC. [203–208]. The suggestion of the use of zeolites as promising supports for DRM is based on their well-defined structure (allowing for a high dispersion of active metal), high surface area, high thermal stability, and high affinity for CO_2, properties expected to enhance both catalytic activity and stability [205]. The type of zeolite (ZSM5, HY, USY, A, X, etc.) and the use of modifiers (Mg, Mn, K, Ca, La) permit to regulate activity, carbon resistance, and stable catalytic performance [203–205, 208].

Luengnaruemitchai and Kaengsilalai [205] compared nickel catalysts supported on various zeolites. Conversions at 973 K, at atmospheric pressure, and at a CH_4/CO_2 ratio equal to 1 followed the order Ni/zeolite Y > Ni/zeolite X > Ni/ZSM-5 > Ni/zeolite A. Deactivation rates followed the order Ni/zeolite Y < Ni/zeolite X < Ni/ZSM-5 < Ni/zeolite A. However, the amount of carbon deposited on Ni/zeolite Y indicates that the cause of deactivation of the other catalysts must not be solely due to carbon formation. Best catalytic activity was obtained for 7 wt% Ni loading for every zeolite support, producing, however, larger amounts of coke [205].

The influence of various promoters on zeolite-supported catalysts was also explored [203, 204]. Doping of the ZSM-5 zeolite-supported Ni catalyst with La species had a positive effect with respect to activity and selectivity toward CO and H_2 formation and also demonstrated superior coke resistance [203]. The improvement in the catalytic properties of the composite material was attributed to the selective adsorption of CO_2 on sites adjacent to Ni, to form $La_2O_2CO_3$ species, which then react with the surface carbon species to form CO. The influence of various promoters (Mg, Mn, K, Ca) on zeolite-supported catalysts was also explored by Jeong et al. [204] on Ni/HY catalysts. Most promoters (except K) improved nickel dispersion as the calculated Ni particles size was much smaller on modified catalysts, the smallest being detected on Ni–Mg/HY. This catalyst gave the highest CH_4 conversion. The resistance to deactivation of Ni–Mg/HY catalyst is believed to be related not only to the highly dispersed nickel species, which did not sinter under DRM conditions, but also to carbonate species formed on magnesium oxide [204].

SiC seems a promising support for highly endothermic and exothermic reactions, due to its low specific weight, high mechanical strength, and, especially, its high thermal conductivity [206]. A Ni/SiC foam monolithic catalyst proved to be active and stable. However, the SSA (4.4 m^2g^{-1} for 7 wt% Ni/SiC) is very low and the metal loading relatively high, while no estimation of the quantity of carbon formed is reported. Thus, further investigations are required before concluding on the practical use of these materials.

3.5.2.7 Additives

An additive (metal oxide or element), in order to be used as a modifier, must fulfill at least one of the following requirements: (1) improve the dispersion of the metallic phase forming nanosized metal particles (Fig. 3.8e); (2) enhance the adsorption and activation of CO_2 (Fig. 3.8f); (3) readily provide active surface oxygen species, being reoxidized by the dissociative adsorption of CO_2 through a Mars–van Krevelen-type mechanism (Fig. 3.8g); and (4) "block" carbon growth centers in the metal lattice or the surface steps, preventing carbon diffusion (Fig. 3.8h). Metal oxides that showed enhanced activity but poor stability or have low surface area have been examined as promoters—constituents of a multicomponent catalytic system, usually meeting more than one of the above requirements. Again, the nature of the metal oxides used, the catalyst composition, and the preparation and pretreatment methods are very diverse, and results vary to a great extent while the literature is so vast that we will only attempt to present the outlines and some examples of materials not discussed previously. For more details, the interested reader is referred to the relevant literature.

As already mentioned, strong Lewis basicity of the DRM catalyst is expected to attenuate or even suppress carbon deposition, promoting CO_2 chemisorption. Besides MgO which is commonly used as a support or catalyst component (hydrotalcite precursors), other alkaline earth oxides have also been investigated,

most frequently CaO [134, 162, 204, 209–229]. CaO as a support gives a poor outcome. Zhang and Verykios [210] showed that a Ni(17 wt%)/CaO catalyst exhibited decreased Ni dispersion and lower DRM rate compared to an equally loaded Ni/γ-Al_2O_3 catalyst. The poor catalytic performance of NiO/CaO for DRM has also been reported by Ruckenstein and Hu [162] who studied nickel catalysts supported on alkaline earth metal oxides (MgO, CaO, SrO, and BaO). The NiO/MgO catalyst gave the best results. In contrast, the NiO/CaO and NiO/SrO samples exhibited lower reforming activity and selectivity and very low stability, while the NiO/BaO sample was practically inactive.

Aiming to take advantage of the basic character of CaO, this material has been extensively studied as additive. Zhang and Verykios [210] reported that modifying a Ni/γ-Al_2O_3 catalyst with CaO slightly increased reaction rate and improved stability. They suggested that the increased reaction rate may be related to the enhancement of the reducibility of the nickel phase due to the retardation of the formation of stable (and difficult to reduce) nickel aluminate. In situ FTIR and O_2-TPSR showed three types of carbonaceous species (designated as C_α, C_β, and C_γ) formed on both the unpromoted and the CaO-promoted catalysts [210]. Although the quantity of the active carbonaceous species responsible for the formation of synthesis gas (C_α) was approximately the same on both catalysts, the amounts of the inactive species (C_β and C_γ) were significantly larger on the Ca-promoted catalyst. However, they could be removed at lower temperatures. The authors [210] suggested that the increase of the carbon formation rate could be due to either the larger Ni crystallites on the promoted catalyst, which favorably accommodate more carbon in the form of Ni carbide and/or graphitic carbon, or to the increased amount of the formate species which are strongly bound on the promoted catalyst. An increase of carbon deposition on CaO-modified Ni/$A1_2O_3$ catalysts was also observed by Tang et al. [212] and Wang and Lu [219].

In a comparative study, Wang and Lu [219] investigated the effect of various promoters, namely, an alkali metal oxide (Na_2O), alkaline earth metal oxides (MgO, CaO), and rare earth metal oxides (La_2O_3, CeO_2), on the catalytic performance of 5 wt% Ni/γ-Al_2O_3. The behavior of the promoted Ni/γ-Al_2O_3 catalysts was found to depend on the nature of the promoter. The decrease of the activity of Na_2O- or MgO-promoted catalysts was attributed to the decrease of the specific surface area and the blockage of Ni active sites. In contrast, CaO, La_2O_3, and CeO_2 were well dispersed and exhibited practically the same initial activity as the unpromoted Ni/γ-Al_2O_3. Modification by CaO caused an important increase of carbon deposition, in accordance with the results of Zhang and Verykios [210] and Tang et al. [212], while modification by the other promoters suppressed carbon deposition. Wang and Lu [219] deduced that the process of carbon deposition on a Ca-promoted catalyst must be different than that occurring on the other promoted catalysts. As CaO was the only promoter to increase Ni dispersion (MgO, La_2O_3, or CeO_2 had no effect, while Na_2O deteriorated it), they attributed the increased coke deposition on the Ni–CaO/γ-Al_2O_3 catalyst to the enhancement of the CH_4 decomposition brought about by the smaller size of nickel particles. On the other hand, CaO (as well as La_2O_3 and CeO_2) enhances the reactivity of carbon species formed

on the surface toward CO production, Ca-promoted sample exhibiting better stability despite of the higher amount of coke formed compared to the undoped Ni/γ-Al_2O_3 catalyst, in accordance with the suggestions of Zhang and Verykios [210].

In contrast to these studies, which demonstrated that modification of nickel catalysts by CaO does not influence, in a significant way, dry reforming activity, others concluded that calcium may have an important effect (either positive or negative) on activity. Cheng et al. [215] reported that a Ni(10 wt%)/CaO (5 wt%)−γ-Al_2O_3 catalyst, prepared by impregnating the CaO-modified support with nickel, was markedly more active than the corresponding unpromoted catalyst in the temperature range of 923–1,123 K. The enhancement of catalytic activity was even more pronounced when the alumina support was modified by 5 wt% MgO instead of CaO. They suggested that the promoting action of alkaline earth oxides (CaO or MgO) could be associated to the weakening of the interactions between nickel and support, leading to the formation of more easily reducible supported NiO_x species. This weakening of interactions is caused by the competition of Ni(II) and Ca(II) (or Mg(II)) to interact with alumina when these ions coexist on its surface. On the other hand, Horiuchi et al. [216] investigated the effect of modifying Ni/γ-Al_2O_3 catalyst with basic metal oxides (Na_2O, K_2O, CaO, and MgO). They reported that, although CO_2 reforming was suppressed by all these oxides, carbon deposition was markedly decreased during both DRM and CH_4 decomposition. The hindrance of the CO_2 reforming rate was most pronounced in the case of K_2O, closely followed by CaO, while Na_2O had not a significant effect. According to the authors, this is probably due to the enrichment of the electron density of the Ni metal caused by the presence of these modifiers. The enrichment of the electron density inhibits the adsorption of methane on the Ni active sites, thus decreasing the activity of the catalyst for CH_4 decomposition [216]. The discrepancies, regarding the effect of CaO on reforming activity and carbon deposition, are most probably due mainly to the differences in composition and method of synthesis of the catalysts used in these studies.

There is a general agreement that the influence of Ca is strongly dependent on the Ca content of the catalyst, investigated in a number of studies [213, 220–222, 228]. When in low content, Ca may reduce carbon deposition and, in general, increases activity, whereas higher Ca loadings increase the amount of coke and may leave the activity unaffected or even deteriorate it. Goula et al. [213] reported that a $CaO/Al_2O_3 = 1/2$ molar ratio gave a slightly more active catalyst but accumulated significantly lower amounts of carbon than the one with $CaO/Al_2O_3 = 12/7$, the difference being attributed to the influence of the mixed support composition on the morphology and particle size distribution of the nickel metal. Quincoces et al. [220] investigated a series of Ni(15 wt%)/CaO–γ-Al_2O_3 catalysts, with CaO content ranging from 0 up to 5 wt%, and reported that, for this composition region, the addition of CaO had not any significant impact on the DRM activity. However, CaO content influences the stability of the catalysts: In low loading (up to 3 wt%), CaO reduces the amount of carbon formed on the surface of the used catalyst, while for higher loading of CaO, higher coke deposits were formed on the modified sample than on the unpromoted Ni/γ-Al_2O_3 catalyst. The authors suggested that the

decreased coke formation on the low-loaded CaO-promoted samples may be attributed to the increase of basicity which, by favoring the CO_2 adsorption, promotes the inverse Boudouard reaction. Dias and Assaf [222] observed an increased reforming activity of Ni(8 wt%)–CaO/γ-Al_2O_3 catalysts with low Ca loading (up to 3.6 wt% Ca) attributed to the favoring of CO_2 adsorption on the surface, while the decline of the activity of the higher Ca content (5.5 and 7.4 wt% Ca) may be due to the increase of the nickel electron density provoked by the presence of calcium in such high loadings, in accordance with the work of Horiuchi et al. [216]. Moreover, these authors reported that the order of deposition of Ni and Ca in their successively impregnated samples had only minor influence on catalytic activity.

Among the various parameters affecting the outcome of the presence of CaO in the DRM behavior of nickel catalysts is the nature of the support. Hou et al. [221] compared the performance of three Ca-modified nickel catalysts supported on SiO_2, γ-Al_2O_3, or α-Al_2O_3, prepared by coimpregnation and having a molar ratio of Ca/Ni = 0.04. Calcium provoked a decrease in the reforming activity of SiO_2 and γ-Al_2O_3 catalysts, while coke formation rate was decreased for SiO_2 but increased for γ-Al_2O_3. In contrast, small amounts of Ca increased the reforming activity of Ni/α-Al_2O_3 accompanied by a slight variation in the coke formation rate. The beneficial effect of CaO in Ni(8 wt%)–CaO/α-Al_2O_3 catalysts was presumed to be due to the improved dispersion of Ni, the strengthening of interaction between Ni and Al_2O_3, and the prevention of Ni^0 sintering. According to Hou et al. [221], Ca/Ni = 0.2 is a critical point, above which an excess amount of Ca would cover the surface of α-Al_2O_3 hindering the interaction of Ni with the support while increasing the decomposition of CH_4, this being the main reason for the deactivation of the samples modified with high Ca contents. In line with the above, Roh and Jun [228] also observed an improvement in catalytic behavior with low loading of CaO (molar ratio of Ca/Al = 0.04) in θ-Al_2O_3-supported nickel catalysts, while similarly small molar ratios (0.05–0.06) were also needed for the highest DRM activity when, instead of calcium, La or Mg was used as the promoter. The beneficial effect of these additives is attributed to the strong interaction between Ni and CaO, the stabilization of CaO on Al_2O_3, and the prevention of carbon formation by the strong basicity of CaO.

Quincoces et al. [218] reported that modification of Ni/SiO_2 catalysts with CaO deteriorated the textural properties and reduced the dispersion of the active phase. The increase of the Ca content increases both dry reforming activity and carbon formation. Ping et al. [225] investigated the effect of promoting Ni/SiO_2 by alkali metals (K or Cs) or alkaline earth metals (Mg, Ca, Sr, or Ba) on the DRM performance. According to these authors, Mg- and Ca-promoted Ni/SiO_2 catalysts exhibited excellent coke resistance with only minor loss of activity relative to the unmodified Ni/SiO_2 sample. Although K- and Cs-promoted catalysts could decrease carbon deposition, their reforming activity was also heavily decreased. Finally, modification by Ba or Sr led to poor coking resistance.

Yamazaki et al. [209] reported that smaller amounts of carbon were formed on Ni/MgO–CaO than on the unmodified Ni/MgO. This was attributed to the higher

basicity induced by CaO, which, by enhancing the adsorption of CO_2, promotes the reverse Boudouard reaction and, thus, lowers the amounts of accumulated carbon. Ni(13 wt%)/HY catalysts promoted by Mg, Mn, or Ca exhibited improved catalytic performance without experiencing severe deactivation [204]. The optimum performance was observed for the Mg-promoted sample, while promotion by K provoked a severe deactivation due to the formation of large amounts of coke. Mesoporous Ni–CaO–ZrO_2 nanocomposites exhibited excellent activity and coking resistance for the DRM reaction [134]. Liu et al. [134] reported that low Ni content resulted in high metal dispersion and good catalytic performance, while the basicity of the matrices provoked by CaO improved the chemisorption of CO_2 and promoted the gasification of deposited coke on the catalyst. Adding CaO to the ZrO_2 support of nickel catalysts increased the activity of Ni(5 wt%)/CaO–ZrO_2 catalysts with CaO content up to 8 mol% and sharply decreased it for higher CaO loading [229]. Bellido et al. [229] observed a similar trend for the variation of the oxygen ionic conductivity of the supports with the CaO content and suggested that DRM activity may be influenced by the electrical conductivity of the CaO–ZrO_2 supports, mainly through the step of CO_2 activation by oxygen vacancies.

In several cases, the enhancement of DRM catalytic performance has been attempted by simultaneously modifying nickel catalysts with more than one promoter. Chang et al. [214] showed that the modification by alkaline promoters (Ca and K) of a Ni(5.3 wt%)/ZSM-5 catalyst markedly inhibited coke deposition during DRM. This superior coke resistance was attributed to the favorable adsorption of CO_2 adjacent to Ni sites to form carbonate species (mainly on Ca) and to the dissociative adsorption of CO_2 on the Ni surface.

Hou et al. [223] and Yashima [224] reported that a copromoted KCaNi/α-Al_2O_3 catalyst exhibited high activity, stability, and excellent coke resistance. According to these authors, copromotion by K and Ca strengthened the interaction between Ni and α-Al_2O_3, promoting the formation of a unique $NiAl_2O_4$ phase; increased the dispersion of Ni; and retarded its sintering during DRM. According to Chang et al. [226], the simultaneous alteration of the support and Ni surface of Ni/ZrO_2 catalysts with a Ce modifier and a Ca promoter led to a high-performance catalyst. The observed high stability was mainly attributed to the synergistic effect of the Ca promoter and the Ce modifier for coke resistance and high-temperature catalyst aging.

Rare earths generally exhibit good dispersion of the active phase, but the catalytic performance and stability of catalysts supported on their oxides are usually not satisfactory. Thus, efforts have been exerted to develop stable catalysts using rare earth oxides as a promoter, usually on γ-Al_2O_3-supported catalysts [189, 230]. Wang and Lu [189] showed that CeO_2 has a different effect as a support or promoter. They compared the catalytic performance of Ni catalysts supported on γ-Al_2O_3, CeO_2, and CeO_2–Al_2O_3. Ni/CeO_2 had the lowest surface area and the lowest activity, consequently the lowest carbon deposition rate of all catalysts studied. SMSIs which induced coverage of active sites, combined with thermal sintering, were considered the reasons of the poor performance. However, even at low loadings of 1–5 wt% CeO_2, CeO_2 had a positive effect on catalytic activity, stability, and carbon suppression when used as a promoter in Ni/γ-Al_2O_3 catalysts.

Ceria in $Ni/CeO_2–Al_2O_3$ catalysts inhibited the formation of $NiAl_2O_4$, increased the dispersion of NiO, and prevented the formation of large metal ensembles, thus reducing carbon deposition. The oxidative properties of CeO_2 also contribute to higher resistance toward carbon accumulation [189].

Nandini et al. [230] studied the effect of K–, CeO_2–, and Mn– addition on Ni/Al_2O_3 catalysts. The stability and lower amount of coking on $Ni–K/CeO_2–Al_2O_3$ and $Ni–K/MnO–Al_2O_3$ catalysts were attributed to the improved Ni dispersion due to CeO_2 or MnO and to partial coverage of the surface of nickel by patches of promoters, increasing CO_2 adsorption and the formation of surface-reactive carbonate species [230]. Unfortunately, no characterization data were provided to support these assumptions.

As discussed earlier, the mechanism of carbon formation implies that coordinatively unsaturated sites, such as step-edge sites, are more active for the DRM reaction but also for carbon diffusion into nickel lattice toward carbon growth centers [71, 72, 103, 119]. Furthermore, carbon presents much higher stability on steps than on terrace sites. Consequently, another approach for the suppression of carbonaceous deposits is the selective blocking of these sites (Fig. 3.8h). Although this affects to some extent the activity of the catalysts, it may effectively retard carbon deposition. In the industrial SPARG process, the partial passivation of nickel catalysts with sulfur is aiming to the kinetic resistance to carbon formation [45, 46, 63]. Gold is also believed to block highly reactive Ni edge and kink sites, forming a surface alloy (Au is immiscible in bulk Ni) that is active for steam reforming but more resistant toward carbon formation than the pure Ni catalyst [231, 232]. A recent study on DRM over 8 wt% $NiMgAl_2O_4$ modified with 0.5 wt% Au showed that addition of gold improves the catalytic activity while carbon nanotubes, observed on the unpromoted used catalyst, are not detected on the bimetallic catalyst [233]. However, the XRD results revealed that Au also prevents agglomeration of Ni particles; the latter, after the first reaction-regeneration cycle, surprisingly become undetectable in the Au-promoted catalyst, while their average Ni^0 particle is about 35 nm on the unpromoted catalyst. Thus, carbon suppression may also be due to the smaller nickel particles. Another structural promoter, aiming to improve the performance of the catalysts in various reactions, is boron. It was suggested that boron can affect the activity through the increase of the Ni phase dispersion and electron interactions between Ni and B [110]. Xu and Sayes [104, 122], based on ab initio DFT calculations, suggested that boron atoms preferentially adsorb on the octahedral sites of the first subsurface layer of the nickel lattice, blocking effectively carbon diffusion into the bulk. Furthermore, boron is also expected to provoke a decrease of the on-surface carbon binding energy [104]. Xu and Sayes [104] suggested that carbon atoms/groups of atoms remain on the surface, available for reaction. Consequently, the nucleation rate of graphene islands decreases and the coking resistance of boron-promoted Ni catalysts is expected to improve. Fouskas et al. [132] studied the influence of boron addition on the dry reforming activity and the carbon formation resistance of $Ni/\gamma\text{-}Al_2O_3$ catalysts, prepared by coimpregnation, in order to maximize the mutual contact of the two phases. Catalytic activity slightly decreased, as predicted by Xu and Sayes

[104], while the amount of carbon formed was remarkably suppressed. As in the case of gold catalysts studied by Guczi et al. [233], XRD and TEM results showed that nickel particles in the B-modified catalyst are smaller than those on unpromoted Ni/γ-Al_2O_3 or on the catalyst with high boron content [132]. Best results are obtained for B/(B + Ni) ratio equal to 0.5.

3.5.3 Bimetallic Catalysts

The addition of a second metal aims to improve the stability by affecting various properties of the catalysts. Inui et al. [234] were among the first to report on the beneficial effects of small amounts of precious metals such as Ru, Pt, Pd, Ir, and Rh on Ni catalysts. A marked enhancement in the rate of CO_2 reforming of methane was observed by the addition of a small amount of Rh to Ni–Ce_2O_3–Pt supported on alumina wash-coated ceramic fiber. Inui et al. [234] suggested that these metals function as "a porthole for hydrogen spillover" toward the main components of the catalyst and keep the catalyst surface a reductive one.

Chen et al. [235] observed that $Ni_{0.03}Mg_{0.97}O$ solid solution, prepared by coprecipitation method and reduced at high temperatures, although having an excellent anticoking performance at 1,123 K, exhibited poor activity and stability at low reaction temperatures such as at 773 K. This was thought to be due to the oxidation of Ni species by CO_2 and/or H_2O, which could be prevented by hydrogen spillover. The addition of small amounts of noble metals [atomic ratio of M/(Ni + Mg) between 0.007 and 0.032%, M = Pt, Pd, or Rh] improved significantly both catalytic activity (two times higher) and stability at 773 K. Chen et al. [235] concluded that the synergistic effect is due to the formation of Pt–Ni alloy particles which favor catalyst reducibility and accelerate the dissociation of CH_4. As a result, the RDS is changed from dissociation of CH_4 to dissociation of CO_2 or to the oxidation of surface hydrocarbon species with adsorbed oxygen.

The presence of small amount of noble metal was proven to be beneficial also for a Ni catalyst prepared from a hydrotalcite doped with Rh [236]. The reversible loss of activity of Ni/MgAl at 773 K was accredited to the oxidation of metallic Ni, while the enhanced stability of NiRh/MgAl was accredited to H_2 spillover from Rh in the NiRh alloy, hindering the oxidation of Ni. The results of Nagaoka et al. [236] also show that addition of Rh results in the formation of relatively small NiRh particles and higher fraction of metals exposed, in accordance with the results of Inui et al. [234] and Chen et al. [235]. The nickel and rhodium bimetallic system was also studied in catalysts supported on MCM-41 like mesoporous materials [237]. It was observed that the influence of Rh depends on the catalyst's preparation method: Rh incorporation into the Ni–MCM-41 in one step (together with nickel nitrate, sodium silicate, and a surfactant) improved both activity and stability of the catalyst, whereas Rh incorporation by impregnation of the Ni–MCM-41 caused instabilities due to coke formation at long reaction times. Another interesting finding of the work of Arbag et al. [237] is that Rh addition caused a decrease of the contribution of the RWGS reaction in CO_2 consumption, resulting in higher hydrogen yield.

Pt was also tested as a second metallic component of Ni-based catalysts [238]. Monometallic (Ni and Pt) and bimetallic (PtNi) nanostructured catalysts were prepared by the reverse microemulsion (ME) method and were supported on a nanofibrous alumina either in one step or by wetness impregnation of the support. The addition of Pt and the preparation of the catalysts by the ME method promoted the formation of NiO instead of $NiAl_2O_4$ and facilitated its reduction to Ni^0 during catalyst pretreatment [238]. As in the case of Rh, introduction of small amount of Pt results in a decrease of the Ni^0 particle size, as compared to the corresponding monometallic catalyst. The decrease of Ni particle size in the presence of Pt was attributed to a dilution effect causing Ni redispersion and decreasing the mobility of the Ni metal particles. The enhanced catalyst stability and selectivity toward H_2 and CO of the bimetallic catalysts are suggested to be the results of Pt–Ni interaction between metallic centers [238].

Cobalt seems also to be a good promoter [61, 116, 133]. Zhang et al. [61] explored the effectiveness of other bimetallic catalysts, preparing Ni–Me–Al–Mg–O (Me = Co, Fe, Cu, Mn) composite materials by coprecipitation. The initial activity followed the order Ni–Co > Ni–Mn > Ni–Fe > Ni–Cu, whereas the activity decay followed the same order as the carbon formation rate: Ni–Fe > Ni–Mn > Ni–Cu > Ni–Co. In a 2,000-h stability test, the Ni–Co catalyst was found to be very stable with very low carbon formation [61]. The reduction of Ni and Co content from 6.1 and 9.3 to 3.6 and 4.9 mol% (metal base), respectively, gave an impressive result: No decrease in activity was observed, whereas TG and DTG profiles showed almost complete elimination of carbon deposition. Zhang et al. [61, 133] performed comparative studies with Ni and Co monometallic catalysts and Ni–Co bimetallic catalyst and concluded that the superior performance of Ni–Co catalysts comes from the synergetic effect, high metal dispersion, SMSI, and formation of different types of stable solid solutions. San-Jose-Alonso et al. [116] tried to define the synergistic effects of Ni and Co in alumina-supported monometallic and bimetallic Ni–Co catalysts. They observed that monometallic Co and Co-rich catalysts are the most active, the activity decreasing with the decrease of cobalt and the increase of nickel content. The amount of carbon formed follows almost the same order, but deactivation follows the inverse order, i.e., catalysts accumulating large quantities of carbon are the most stable (monometallic Co and Co-rich catalyst), whereas monometallic Ni is the least stable of all, although the amount of carbon formed on its surface is very low. It is obvious that carbon accumulation is not the main reason for the deactivation of Ni. In contrast to other studies on bimetallic catalysts, San-Jose-Alonso et al. [116] observed no beneficial effect of the second metal on the Ni phase dispersion, while no synergy was observed on either catalytic activity or suppression of carbon formation.

The effect of copper on the stability of a $Cu/Ni/SiO_2$ catalyst was investigated by Chen et al. [239]. Although the effect of copper is not fully explained by the ensemble effect of the Cu on Ni metal, it has been concluded that copper may stabilize the structure of the active sites for methane dissociation on the Ni surface, preventing the deactivation of the Ni catalyst caused by sintering or by loss of nickel crystallites. Furthermore, the catalytic activity is “finely tuned” so that the

CH_4 dissociation and coke removal by CO_2 are balanced and carbon formation is inhibited. The stability of the Cu/Ni catalysts depends on the reaction temperature and Cu/Ni ratio. Additives such as Sn, Ca, and Ge may have different effects [240]. Sn alloyed with transition metals decreased the activity but was very effective for the inhibition of carbon deposition from methane decomposition. Ge, although did not affect the activity, promoted drastically carbon formation. Catalytic activity was slightly increased by the addition of Ca, while the influence on carbon deposition was found to depend on Ca loading [240].

3.5.4 Perovskites

Since methane dissociation and carbon formation steps are structure sensitive, materials originating from hydrotalcites, fluorite, olivine, dolomite, or perovskite precursors, which present well-defined structures via "solid phase crystallization," could offer advantages for DRM catalysts [56, 80, 241–255]. Perovskites have the general formula ABO_3 and perovskite-type structure formula A_2BO_4, in which cation A (larger size, a rare earth and/or alkaline earth) provides thermal stability and cation B (smaller size, a transition metal) is related with the catalytic redox properties of the material. Partial substitution of either A and/or B cations by other cations permits the preparation of a vast family of materials (general formula $A_{1-x}A'_xB_{1-x}B'_xO_3$) with varying characteristics. Several perovskite-type oxides containing lanthanides in the A sites exhibit high oxygen mobility, whereas transition metals in the B site show mixed electronic/ionic conductivity [244, 247, 256]. It is worth noting that the perovskite structure can stabilize transition metals in oxidation states which are usually very reactive and unstable [244]. These properties as well as the flexibility in the choice and the stoichiometry of A- and B-site cations offer the potential to obtain materials with tailor-made properties regarding catalytic performance and structural stability. However, there is an important drawback in that the final catalysts are characterized by very low surface areas.

La in A site and Ni in B site are the main and the most common elements in these type of materials [251, 252, 256]. Various preparation and treatment methods have been performed as well as partial or total replacement of La (by Ce, Ca, Sr, Sm, Nd) and/or Ni (by Ru, Co, Mg) in order to ensure narrow distribution of small metal crystallites, higher oxygen mobility in the metal oxide, and strong Lewis basicity [56, 241, 244, 247, 248, 250–255]. The reductive pretreatment is an important step for the activation of the catalyst and the formation of well-dispersed small nickel particles and La_2O_3 [243, 251, 252]. The presence of the latter is vital for the activity and the coking resistance of the final catalyst as the reaction mechanism proposed assumes a step of carbon dioxide adsorption on La_2O_3 to form $La_2O_2CO_3$, in line with the results of Verykios and coresearchers [49, 65, 79, 243, 251, 257, 258].

Substitution of the A site metal ion (La) with a larger lanthanide cation (Ce, Pr), even to a small degree, leads to increased catalytic activity and stability as carbon formation is suppressed, due to the enhancement of the RWGS reaction, which is

favored on a Ce-enriched surface [248, 253]. Partial substitution of La with Sr increases catalytic activity as well as carbon formation [243, 255, 259, 260]. Small amounts of Sr increase carbon deposition in the form of filaments on the catalyst surface, but higher amounts of Sr suppress coking and increase the CO_2 conversion and the CO production [255]. The advantageous influence of strontium is attributed to the increased basicity of the catalyst surface. Pichas et al. [255], performing a kinetic study, assumed a Langmuir–Hinshelwood reaction mechanism with the reactants adsorbed on distinct active sites of the solids and concluded that the activation energy of CO_2 is much lower in comparison to that of CH_4. Lanthanum substitution by calcium increases the basicity of the catalysts and further inhibits coke formation [259].

The partial replacement of Ni by Co does not seem to be beneficial, probably because Co-substituted perovskites are more difficult to reduce while the Co–Ni alloy decreases the ability of C–H bond cleavage, as computational studies predict [252, 254, 257]. In another study of catalysts derived from La–Sr–Ni–Co–O perovskite-type solid solutions, the degree of Ni substitution by Co was found to affect carbon formation, exhibiting a minimum for the $La_{0.8}Sr_{0.2}Ni_{0.7}Co_{0.3}O_3$ material, while CO/H_2 ratio decreases with increasing cobalt content due to secondary reactions of carbon formation and water–gas shift [260]. Partial substitution of nickel with iron in $LaNi_xFe_{(1-x)}O_3$ perovskites ($0 \leq x \leq 1$) gave interesting results [261]. The catalysts are active for the DRM, but the starting mixed structures are destroyed under reaction conditions. However, for $x \leq 0.5$, the catalysts can be regenerated by recalcination, presenting a structure close to the initial. For nickel-rich mixed catalysts, it was not possible to get the mixed perovskite structure back after recalcination. Instead, the formation of two separate perovskite phases $LaNiO_3$ and $LaFeO_3$ was observed [261, 262]. For $0.3 \leq x \leq 0.8$, Ni–Fe alloys are formed, with Ni/Fe ratios depending on x. Provendier et al. [261] suggested that the addition of iron into the perovskite structure and the alloy formed permits limiting the mobility of the active nickel and preventing surface poisoning by carbon through a dilution effect on Ni particles. Small amounts of Mg improve the activity and decrease the amount of coke produced during the reaction [254]. The catalysts derived from $LaNi_{1-x}Ru_xO_3$ perovskites had initially very low activity, but after 2 h under reaction conditions, their activity became comparable to that of the catalyst coming from $LaNiO_3$, indicating that active sites were developed during reaction but not during the reductive pretreatment [244]. It seems that the partial replacement of Ni by Ru in the perovskite structure renders metal reduction more difficult due to higher strength of Ru–O–La bond as compared to the Ni–O–La one. Nickel substitution by ruthenium results in carbon suppression [244]. Low carbon formation was also observed by Goldwasser et al. [258] in Ru-substituted Ni catalyst, but the effect of Ru on DRM activity is more important.

Incorporation of Ni-based perovskite-type oxides $LaNiO_3$, $La_{0.8}Ca_{0.2}NiO_3$, and $La_{0.8}Ca_{0.2}Ni_{0.6}Co_{0.4}O_3$ in the SBA-15 mesoporous silica-host gives rise to well-dispersed nanometallic (Ni–Co) particles inside the mesoporous SBA-15 silica-host by decomposition and further reduction of the built-in perovskite [263]. The resulting catalytic materials exhibited an increase in the conversion of CH_4 and CO_2 and in the

H_2/CO ratio compared to the corresponding unsupported perovskite, whereas there is a dilution effect exerted by the mesoporous material minimizing the heat diffusion problems related to this highly endothermic reaction. Unfortunately, the study does not provide any data regarding the amount of carbon formed [263].

3.6 Reaction Conditions

Studies comparing catalytic performance at various temperatures have shown that the increase of the reaction temperature retards the formation/accumulation of carbon. This observation has been attributed to the enhancement of carbon gasification reactions (3.7) as a result of the presence of more water on the catalyst surface. The increase of the amount of water or hydroxyls at higher temperatures is due to the RWGS (3.5), promoted at high temperatures (Fig. 3.7). On the other hand, high temperatures restrain the Boudouard reaction as it is exothermic and will not proceed at temperatures higher than 974 K [63].

As DRM reaction is thermodynamically favored at low pressures, almost all of the above-mentioned studies are performed at 1 atm. There are not many studies of the reaction at higher pressures or studying the effect of pressure [240]. Tomishige et al. [240] investigated the activity and carbon deposition behavior of $Ni_xMg_{1-x}O$ catalysts at 1.0 and 2.0 MPa. At total pressure 1.0 MPa (~10 atm) and reaction temperature 1,123 K, methane conversion and H_2/CO obtained were near the thermodynamically predicted. At 2.0 MPa, methane conversions are lower, as expected. What is very interesting is the observation of Tomishige et al. [240] that the aggregation of Ni metal particles proceeding during the catalytic reaction was not caused by the heat treatment and hydrogen reduction, but it was caused by the atmosphere of pressurized reforming of methane with carbon dioxide. As carbon formation is related to nickel particles, the suppression of Ni aggregation is important for catalysts' stability. Low-surface area $Ni_xMg_{1-x}O$ catalysts exhibited a lower carbon formation rate than other NiO–MgO solid solution and MgO-supported Pt catalysts [240]. Nagaoka et al. [264] studied Ru catalysts supported on various supports (SiO_2, Al_2O_3, MgO, and TiO_2) under 2.0 and 0.1 MPa and 1,023 K. Coking is higher in high pressure as thermodynamically predicted. The key step of the reaction changes with reaction pressure, pointing out that catalytic activity under atmospheric pressure does not always predict the catalytic behavior under high pressure [264]. Shamsi and Johnson [265] arrived at similar conclusions studying CO_2 reforming of $^{13}CH_4$ over Ni-, Pt-, and Rh-supported catalysts at 1,073 K and at pressures of 1 and 14 bar. The carbon formation reaction path is different for the reactions conducted at low pressure compared to those performed at higher pressure over noble metal catalysts. At low pressure, the amounts of carbon formed on these catalysts were insignificant and came predominantly from $^{12}CO_2$. At high pressure, both methane and carbon dioxide equally contributed to carbon deposition, the total amount of which was higher regardless of catalyst type or composition. However, at 14 bar and on the

Ni-supported catalysts, the deposited carbon comes from both methane and CO_2, depending on reactant partial pressure. Corthals et al. [266], conducting a high-throughput screening of various catalytic systems at 1,023 K and 7 bar, showed that promoter effects, reported at atmospheric pressure, not always hold at elevated pressure. Ni and $MgAl_2O_4$ seem the active element and support, respectively, with the highest potential for the dry reforming reaction at elevated pressure, whereas La_2O_3, Y_2O_3, ZrO_2, MnO, and BaO were defined as promising promoters.

Regarding methane/carbon dioxide ratio, DRM requires a ratio near unity. In general, methane concentration in biogas is higher than that of carbon dioxide (Table 3.1). If used as produced, there will not be enough oxygen to generate synthesis gas. In that case, either methane conversions will be low and recycling will be needed and/or methane will decompose on the metallic surface, forming a lot of carbon. However, there are studies focused on developing catalysts able to perform under methane-rich feed [233, 267]. Guczi et al. [233] studied the reaction in the temperature range 773–1,073 K, over 8.8 wt% $Ni/MgAl_2O_4$ catalyst pretreated in helium using a reaction mixture of 29.6 vol.% CO_2 and 70.4 vol.% CH_4. Carbon dioxide conversion being less than 20% at 773 K is complete at 1,073 K. After TPO up to 823 K and calcination in 10 vol.% O_2/He up to 973 K, the initial activity could be achieved at 1,073 K, indicating the complete carbon removal. At CO_2/CH_4 feed ratio equal to 1, an almost equimolar amount of H_2 and CO is generally produced. As the CO_2 content increases, the yield of H_2 decreases because of the RWGS reaction ([63] and references therein). On the other hand, using excess CO_2 has a beneficial effect on the resistance of the catalysts toward carbon accumulation, as more oxygen/hydroxyl surface species are generated, the CH_x species are more readily oxidized and the carbon formation rate is delayed. Taking the above under consideration, it is reasonable that in most studies a stoichiometric CO_2/CH_4 ratio is used.

From the practical point of view, low temperatures, pressures higher that 1 atm, and CO_2/CH_4 feed ratios near unity are required [22, 47]. As these conditions are also favorable for carbon accumulation, the solution may be found in the development of advanced catalytic material.

3.7 Concluding Remarks

Biogas, a biomass derivative consisting primarily of methane and carbon dioxide, is a potential carbon source for gas-to-liquid processes aiming to replace fossil fuels. Produced from the anaerobic digestion of any biodegradable raw material, biogas is renewable, easily available, carbon neutral, and of negative cost. The most appropriate process for its conversion to transportable energy carriers comprises two steps: Biogas is converted to synthesis gas which in turn is used for alcohol or hydrocarbon production.

DRM appears to be the most suitable process for the first step, as it presents several advantages: (1) No CO_2 separation process is needed but, instead, CO_2 is incorporated in the final product, increasing yield and decreasing waste; (2) steam is

not required and, thus, DRM can be applied in areas where water is not available, reducing both equipment and operational costs; (3) high thermodynamic conversion of CH_4 is achievable by a suitable catalyst; (4) being highly endothermic and reversible, DRM can be applied in CETS; (5) it is selective and more safe compared to POM; and (6) the H_2/CO ratio of the produced synthesis gas is more suitable for the Fischer–Tropsch synthesis. However, the process is energy demanding, favored at high temperatures (>973 K), while catalysts may suffer from sintering and the formation of carbonaceous deposits. The latter constitutes the most important challenge of the process.

In the DRM reaction sequence, the dissociative adsorption of methane on the metal surface, forming hydrogen and methyl-like adsorbed species (S_1–CH_x), is one (if not the only) of the RDSs. Involving electron transfer, it proceeds preferentially on small metal crystallites and on step sites. Although CO_2 can occur on metals, CO_2 binding energies on metal oxides are larger, further increasing on oxygen vacancies. The most favorable CO_2 adsorption sites seem to be located at the interface between the metal and the support. Whether a bifunctional mechanism will take place, i.e., adsorption of methane on the metal and of carbon dioxide on the support, depends on the metal–metal oxide catalytic system. The reaction mechanism involves the oxidation of CH_x formed by the decomposition of methane with oxygen and/or hydroxyl groups formed by the carbon dioxide dissociation. What seems to be crucial for carbon formation is the relative rate of the oxidation of the S_1–CH_x surface species (depending on the availability of surface oxygen/hydroxyls) compared to the complete dissociation of these species to surface carbon. If S_1–CH_x surface species oxidation is not fast enough, surface carbon will form. As carbon has a high solubility in the metal lattice, particularly in nickel, and carbon atoms can diffuse into the subsurface toward carbon growth centers where graphene layers are formed. Depending on the carbon growth mechanism and the catalytic system, the graphene layer may encapsulate the metal particles or detach them from the support and grow filamentous carbon with nickel particles at their top edge. Nickel step-edge sites act as preferential carbon formation centers. Nevertheless, the formation of filamentous carbon is limited on small metallic particles, although they comprise more steps and defects. This has been attributed to the saturation of the small nickel particle with carbon before the graphene cluster is stabilized by obtaining a critical size. Other possible explanations are that the step edges of small nickel particles are too small for carbon nucleation to proceed or that metal–support interface is large and oxidizing agents from the support surface can easily reach S_1–CH_x.

Since methane and carbon dioxide dissociative adsorption as well as carbon formation steps have been proven to be structure sensitive, geometric and electronic characteristics of the catalytic materials exert a decisive influence on their activity and stability. The composition, texture, and structure of the support; the nature, dispersion, and loading of the supported metal; the MSIs; the presence of a second metal or an additive (modifier–promoter); the preparation method; and thermal pretreatment procedures, as well as the reaction conditions, are important factors affecting physicochemical and catalytic properties.

Catalysts based on noble metals are more resistant to coking due to small equilibrium constants for methane decomposition and low dissolution of carbon into their lattices. Activity and reaction mechanism depend on the metal but also on the nature of the support, while catalytic stability regarding metal sintering and carbon formation is determined by MSIs.

Ni-based catalysts, although more prone to carbon formation, are more suitable for a cost-effective commercial DRM process. Consequently, they have been the subject of intensive investigations. The nature of the support, its acid–base properties, and MSIs are crucial parameters in the case of nickel catalysts, maximizing metal dispersion, ensuring stability and avoidance of sintering under reaction conditions, as well as providing active sites for the dissociative adsorption of CO_2 in the metal–support interphase. Moreover, SMSIs can also increase the electron density in the metal crystallites and, thus, the ability to activate C–H bond cleavage. Ni/Al_2O_3 is considered as the state of the art. Besides Al_2O_3, a number of other supports for Ni-based catalysts gave most promising results regarding the suppression of carbonaceous deposits and catalytic stability. Among these, the most extensively studied and promising include MgO, $Ce_{1-x}Zr_xO_2$ solid solutions, and La_2O_3, as well as relevant structured materials such as hydrotalcites, fluorites, and perovskites. Crystallographic forms, preparation and activation procedures, and nickel loading have a significant effect on catalytic performance. Improvement of Ni-based catalysts is attempted by the introduction of one or more textural or chemical promoters, targeting the increase of Ni dispersion; the promotion of surface reactions, which consume surface carbon clusters; and the blockage of carbon growth centers. Examples of promoters include CaO or MgO (to increase basicity and Ni dispersion) and CeO_2 (to increase activity, Ni dispersion, and stability and suppress carbon formation). The addition of a second metal (Ru, Pt, Pd, Rh, Co) improves the stability of Ni catalysts, increasing hydrogen spillover and catalysts' reducibility, hindering Ni^0 oxidation and sintering, and, most importantly, forming smaller metal particles. Other elements (S, Sn, Au, or B) have been used for the selective blocking of carbon growth centers.

During the last 15 years, many systematic studies based on thorough catalytic testing and physicochemical characterization using classical and more sophisticated in situ experimental techniques, often in combination with DFT calculations or kinetic studies, have attempted to shed light on parameters which control DRM reaction and the carbon formation mechanisms. Nevertheless, challenges for the complete elucidation of fundamental catalytic phenomena and the development of viable commercial processes still remain.

References

1. Capros P, Mantzos L, Papandreou V, Tasios N (2008) European energy and transport trends to 2030—update 2007. European Commission, Directorate-General for Energy and Transport. http://ec.europa.eu/dgs/energy_transport/figures/trends_2030_update_2007/energy_transport_trends_2030_update_2007_en.pdf. Accessed 9 Sept 2010

2. European Commission, Eurostat (2010) Energy, yearly statistics 2008. http://epp.eurostat.ec.europa.eu/cache/ITY_OFFPUB/KS-PC-10-001/EN/KS-PC-10-001-EN.PDF. Accessed 9 Sept 2010
3. European Parliament and Council (2009) Directive 2009/28/EC of the European Parliament and of the Council of 23 April 2009 on the promotion of the use of energy from renewable sources and amending and subsequently repealing Directives 2001/77/EC and 2003/30/EC. Official Journal of the European Union L 140/16. http://eur-lex.europa.eu/LexUriServ/LexUriServ.do?uri=OJ:L:2009:140:0016:0062:en:PDF. Accessed 9 Sept 2010
4. European Commission, Eurostat (2010) Energy, energy statistics and quantities, primary production of renewable energy. http://epp.eurostat.ec.europa.eu/tgm/table.do?tab=table&plugin=1&language=en&pcode=ten00081. Accessed 9 Jan 2011
5. Faaij A (2006) Modern biomass conversion technologies. Mitig Adapt Strateg Glob Change 11:343–375. doi:10.1007/s11027-005-9004-7
6. McKendry P (2002) Energy production from biomass (part 2): conversion technologies. Bioresour Technol 83:47–54. doi:10.1016/S0960-8524(01)00119-5
7. Yoshida Y, Dowaki K, Matsumura Y, Matsuhashid R, Li D, Ishitani H, Komiyama H (2003) Comprehensive comparison of efficiency and CO_2 emissions between biomass energy conversion technologies—position of supercritical water gasification in biomass technologies. Biomass Bioenergy 25:257–272. doi:10.1016/S0961-9534(03)00016-3
8. Anex RP, Aden A, Kazi FK, Fortman J, Swanson RM, Wright MM, Satrio JA, Brown RC, Daugaard DE, Platon A, Kothandaraman G, Hsu DD, Dutta A (2010) Techno-economic comparison of biomass-to-transportation fuels via pyrolysis, gasification, and biochemical pathways. Fuel 89:S29–S35. doi:doi.org/10.1016/j.fuel.2010.07.015
9. Converti A, Oliveira RPS, Torres BR, Lodi A, Zilli M (2009) Biogas production and valorization by means of a two-step biological process. Bioresour Technol 100:5771–5776. doi:10.1016/j.biortech.2009.05.072
10. Seppala M, Paavola T, Lehtomaki A, Rintala J (2009) Biogas production from boreal herbaceous grasses—specific methane yield and methane yield per hectare. Bioresour Technol 100:2952–2958. doi:10.1016/j.biortech.2009.01.044
11. Ferreira-Aparicio P, Benito MJ, Sanz JL (2005) New trends in reforming technologies: from hydrogen industrial plants to multifuel microreformers. Catal Rev 47:491–588. doi:10.1080/01614940500364958
12. Martins das Neves LC, Converti A, Penna TCV (2009) Biogas production: new trends for alternative energy sources in rural and urban zones. Chem Eng Technol 32:1147–1153. doi:10.1002/ceat.200900051
13. Holm-Nielsen JB, Al Seadi D, Oleskowicz-Popiel P (2009) The future of anaerobic digestion and biogas utilization. Bioresour Technol 100:5478–5484. doi:10.1016/j.biortech.2008.12.046
14. Rasi S, Veijanen A, Rintala J (2007) Trace compounds of biogas from different biogas production plants. Energy 32:1375–1380. doi:10.1016/j.energy.2006.10.018
15. Rasi S, Lehtinen J, Rintala J (2010) Determination of organic silicon compounds in biogas from wastewater treatments plants, landfills, and co-digestion plants. Renew Energy 35:2666–2673. doi:10.1016/j.renene.2010.04.012
16. Biogas Renewable Energy (2009) www.biogas-renewable-energy.info. Accessed 3 Aug 2010
17. Johnson E (2009) Goodbye to carbon neutral: getting biomass footprints right. Environ Impact Assess Rev 29:165–168. doi:10.1016/j.eiar.2008.11.002
18. Poschl M, Ward S, Owende P (2010) Evaluation of energy efficiency of various biogas production and utilization pathways. Appl Energy 87:3305–3321. doi:10.1016/j.apenergy.2010.05.011
19. Prassl H (2008) Biogas purification and assessment of the natural gas grid in Southern and Eastern Europe. Ing. Gerhard Agrinz GmbH, Leibnitz. http://www.big-east.eu/bigeast_reports/WP%202_Task%202.5-Report.pdf. Accessed 12 Sept 2010

20. Li ZL, Devianto H, Kwon HH, Yoon SP, Lim TH, Lee HI (2010) The catalytic performance of Ni/$MgSiO_3$ catalyst for methane steam reforming in operation of direct internal reforming MCFC. J Ind Eng Chem 16:485–489. doi:10.1016/j.jiec.2010.01.058
21. Shiratori Y, Sasakia K (2008) NiO–ScSZ and $Ni_{0.9}Mg_{0.1}O$–ScSZ-based anodes under internal dry reforming of simulated biogas mixtures. J Power Sources 180:738–741. doi:10.1016/j.jpowsour.2008.03.001
22. Fan MS, Abdullah AZ, Bhatia S (2009) Catalytic technology for carbon dioxide reforming of methane to synthesis gas. ChemCatChem 1:192–208. doi:10.1002/cctc.200900025
23. Bell AT, Gates BC, Ray D (2007) Basic research needs: catalysis for energy. Report from the US Department of Energy, Office of Basic Energy Sciences Workshop August 6–8, 2007, Bethesda, MD. http://www.sc.doe.gov/bes/reports/files/CAT_rpt.pdf. Accessed 5 Aug 2010
24. Roloson BD, Scott NR, Bothi K, Saikkonen K, Zicari S (2006) Biogas processing—the New York State Energy Research and Development Authority, Agreement No: NYSERDA 7250, Albany, NY
25. Manna L, Zanetti MC, Genon G (1999) Modeling biogas production at landfill site. Resour Conserv Recycl 26:1–14. doi:10.1016/S0921-3449(98)00049-4
26. Bruijstens AJ, Beuman WPH, Molen Mvd, Rijke Jd, Cloudt RPM, Kadijk G, Camp Ood, Bleuanus S et al. (2008) Biogas composistion and engine performance, including database and biogas property model. Project supported by the European Commission under RTD contract: 019795. http://www.biogasmax.eu/media/r3_report_on_biogas_composition_and_engine_performance__092122100_1411_21072009.pdf. Accessed 6 Jan 2011
27. Petersson A, Wellinger A (2009) Biogas upgrading technologies–developments and innovations. Task 37 IEA Bioenergy. http://www.iea-biogas.net/Dokumente/upgrading_rz_low_final.pdf. Accessed 6 Sept 2010
28. Torres W, Pansare SS, Goodwin JG Jr (2007) Hot gas removal of tars, ammonia, and hydrogen sulfide from biomass gasification gas. Catal Rev 49:407–456. doi:10.1080/01614940701375134
29. Syed M, Soreanu G, Falletta P, Béland M (2006) Removal of hydrogen sulfide from gas streams using biological processes—a review. Can Biosyst Eng 48:2.1–2.14
30. Wakker JP, Gerritsen AW, Moulijn JA (1993) High temperature hydrogen sulfide and carbonyl sulfide removal with manganese oxide (MnO) and iron oxide (FeO) on gamma-alumina acceptors. Ind Eng Chem Res 32(1):139–149. doi:10.1021/ie00013a019
31. Ramírez-Saenz D, Zarate-Segura PB, Guerrero-Barajas C, García-Pena EI (2009) H_2S and volatile fatty acids elimination by biofiltration: clean-up process for biogas potential use. J Hazard Mater 163:1272–1281. doi:10.1016/j.jhazmat.2008.07.129
32. Sanchez JM, Ruiz E, Otero J (2005) Selective removal of hydrogen sulphide from gaseous streams using a zinc-based sorbent. Ind Eng Chem Res 44:241–249. doi:10.1021/ie0497902
33. Jung SY, Lee SJ, Lee TJ, Ryu CK, Kim JC (2006) H_2S removal and regeneration properties of Zn-Al-based sorbents promoted with various promoters. Catal Today 111:217–222. doi:10.1016/j.cattod.2005.10.029
34. Park DW, Kim BG, Kim MI, Kim I, Woo HC (2004) Production of ammonium thiosulfate by the oxidation of hydrogen sulfide over Nb-Fe mixed oxide catalysts. Catal Today 93–95:235–240. doi:10.1016/j.cattod.2004.06.047
35. Shin MY, Park DW, Chung JS (2001) Development of vanadium-based mixed oxide catalysts for selective oxidation of H_2S to sulphur. Appl Catal B Environ 30:409–419. doi:10.1016/S0926-3373(00)00262-9
36. Kim BG, Ju WD, Kim I, Woo HC, Park DW (2004) Performance of vanadium-molybdenum mixed oxide catalysts in selective oxidation of hydrogen sulfide containing excess water and ammonia. Solid State Ion 172:135–138. doi:10.1016/j.ssi.2004.02.043
37. Slimane RB, Abbasian J (2000) Copper-based sorbents for coal gas desulfurization at moderate temperatures. Ind Eng Chem Res 39:1338–1344. doi:10.1021/ie990877a
38. Chung JB, Chung JS (2005) Desulfurization of H_2S using cobalt-containing sorbents at low temperatures. Chem Eng Sci 60:1515–1523. doi:10.1016/j.ces.2004.11.002

39. Vamvuka D, Arvanitidis C, Zachariadis D (2004) Flue gas desulfurization at high temperatures. A review. Environ Eng Sci 21:525–548. doi:10.1089/1092875041358557
40. Bu X, Ying Y, Ji X, Zhang C, Peng W (2007) New development of zinc based sorbents for hot gas desulfurization. Fuel Process Technol 88:143–147. doi:10.1016/j.fuproc.2005.01.025
41. Truong LVA, Abatzoglou N (2005) A H_2S reactive adsorption process for the purification of biogas prior to its use as a bioenergy vector. Biomass Bioenergy 29:142–151. doi:10.1016/j.biombioe.2005.03.001
42. Osorio F, Torres JC (2009) Biogas purification from anaerobic digestion in a wastewater treatment plant for biofuel production. Renew Energy 34:2164–2171. doi:10.1016/j.renene.2009.02.023
43. Pipatmanomai S, Kaewluan S, Vitidsant T (2009) Economic assessment of biogas-to-electricity generation system with H_2S removal by activated carbon in small pig farm. Appl Energy 86:669–674. doi:10.1016/j.apenergy.2008.07.007
44. Alonso-Vicario A, Ochoa-Gomez JR, Gil-Río S, Gomez-Jiménez-Aberasturi O, Ramírez-Lopez CA, Torrecilla-Soria J, Domínguez A (2010) Purification and upgrading of biogas by pressure swing adsorption on synthetic and natural zeolites. Microporous Mesoporous Mater 134:100–107. doi:10.1016/j.micromeso.2010.05.014
45. Rostrup-Nielsen JR (1984) Sulfur-passivated nickel catalysts for carbon-free steam reforming of methane. J Catal 85:31–43. doi:10.1016/0021-9517(84)90107-6
46. York APE, Xiao T, Creen MLH, Claridge JB (2007) Methane oxyforming for synthesis gas production. Catal Rev 49:511–560. doi:10.1080/0161494070158
47. Bradford MCJ, Vannice MA (1999) CO_2 reforming of CH_4. Catal Rev Sci Eng 41:1–42. doi:10.1081/CR-100101948
48. McCrary JH, McCrary GE, Chubb TA, Nemecek JJ, Simmons DE (1982) An experimental study of the CO_2–CH_4 reforming-methanation cycle as a mechanism for converting and transporting solar energy. Sol Energy 29:141–151. doi:10.1016/0038-092X(82)90176-1
49. Verykios XE (2003) Catalytic dry reforming of natural gas for the production of chemicals and hydrogen. Int J Hydrogen Energy 28:1045–1063. doi:10.1016/S0360-3199(02)00215-X
50. Bradford MCJ, Vannice MA (1996) Catalytic reforming of methane with carbon dioxide over nickel catalysts. I. Catalyst characterization and activity. Appl Catal A Gen 142:73–96. doi:10.1016/0926-860X(96)00065-8
51. Rostrup-Nielsen JR (2000) New aspects of syngas production and use. Catal Today 63:159–164. doi:10.1016/S0920-5861(00)00455-7
52. Dry ME (2004) Fischer-Tropsch technology. Stud Surf Sci Catal 152:196–257. doi:10.1016/S0167-2991(04)80460-9
53. Rostrup-Nielsen JR (1994) Catalysis and large-scale conversion of natural gas. Catal Today 21:257–267. doi:10.1016/0920-5861(94)80147-9
54. Rostrup-Nielsen JR (2002) Syngas in perspective. Catal Today 71:243–247. doi:10.1016/S0920-5861(01)00454-0
55. Hu YH, Ruckenstein E (2004) Catalytic conversion of methane to synthesis gas by partial oxidation and CO_2 reforming. Adv Catal 48:297–345. doi:10.1016/S0360-0564(04)48004-3
56. Pereniguez R, Gonzalez-DelaCruz VM, Holgado HP, Caballero A (2010) Synthesis and characterization of a $LaNiO_3$ perovskite as precursor for methane reforming reactions catalysts. Appl Catal B Environ 93:346–353. doi:10.1016/j.apcatb.2009.09.040
57. Song C (2001) Tri-reforming: a new process for reducing CO_2 emissions. Chem Innovat 31:21–26
58. Song C, Pan W (2004) Tri-reforming of methane: a novel concept for catalytic production of industrially useful synthesis gas with desired H_2/CO ratios. Catal Today 98:463–484. doi:10.1016/j.cattod.2004.09.054
59. Halmann M, Steinfeld A (2009) Hydrogen production and CO_2 fixation by flue-gas treatment using methane tri-reforming or coke/coal gasification combined with lime carbonation. Int J Hydrogen Energy 34:8061–8066. doi:10.1016/j.ijhydene.2009.08.031

60. Hu YH, Ruckenstein E (2002) Binary MgO based solid solution catalysts for methane conversion to syngas. Catal Rev Sci Eng 44:423–453. doi:10.1081/CR-120005742
61. Zhang J, Wang H, Dalai AK (2007) Development of stable bimetallic catalysts for carbon dioxide reforming of methane. J Catal 249:300–310. doi:10.1016/j.jcat.2007.05.004
62. Gadalla AM, Bower B (1988) The role of catalyst support on the activity of nickel reforming methane with CO_2. Chem Eng Sci 43:3049–3062. doi:10.1016/0009-2509(88)80058-7
63. Wang S, Lu G, Millar GJ (1996) Carbon dioxide reforming of methane to produce synthesis gas over metal-supported catalysts: state of the art. Energy Fuel 10:896–904. doi:10.1021/ef950227t
64. Li Y, Wang Y, Zhang X, Mi Z (2008) Thermodynamic analysis of autothermal steam and CO_2 reforming of methane. Int J Hydrogen Energy 33:2507–2514. doi:10.1016/j.ijhydene.2008.02.051
65. Tsipouriari VA, Verykios XE (1999) Carbon and oxygen reaction pathways of CO_2 reforming of methane over Ni/La_2O_3 and Ni/Al_2O_3 catalysts studied by isotopic tracing techniques. J Catal 187:85–94. doi:10.1006/jcat.1999.2565
66. Yamaguchi A, Iglesia E (2010) Catalytic activation and reforming of methane on supported palladium clusters. J Catal 274:52–63. doi:10.1016/j.jcat.2010.06.001
67. Nandini A, Pant KK, Dhingra SC (2006) Kinetic study of the catalytic carbon dioxide reforming of methane to synthesis gas over $Ni\text{-}K/CeO_2\text{-}Al_2O_3$ catalyst. Appl Catal A Gen 308:119–127. doi:10.1016/j.apcata.2006.04.014
68. Enger BC, Lodeng R, Holmen A (2008) A review of catalytic partial oxidation of methane to synthesis gas with emphasis on reaction mechanisms over transition metal catalysts. Appl Catal A Gen 346:1–27. doi:10.1016/j.apcata.2008.05.018
69. Trevor DJ, Cox DM, Kaldor A (1990) Methane activation on unsupported platinum clusters. J Am Chem Soc 112:3742–3749. doi:10.1021/ja00166a005
70. Kuijpers EDM, Breedijk AK, Van der Wal WJJ, Geus JW (1983) Chemisorption of methane on Ni/Sio_2. Catalysts and reactivity of the chemisorption products toward hydrogen. J Catal 81:429–439. doi:10.1016/0021-9517(83)90181-1
71. Bengaard HS, Nørskov JK, Sehested J, Clausen BS, Nielsen LP, Molenbroek AM, Rostrup-Nielsen JR (2002) Steam reforming and graphite formation on Ni catalysts. J Catal 209:365–384. doi:10.1006/jcat.2002.3579
72. Abild-Pedersen F, Lytken O, Engbaek J, Nielsen G, Chorkendorff I, Norskov JK (2005) Methane activation on Ni(111): effects of poisons and step defects. Surf Sci 590:127–137. doi:10.1016/j.susc.2005.05.057
73. Haroun MF, Moussound PS, Legare P (2008) Theoretical study of methane adsorption on perfect and defective Ni(1 1 1) surfaces. Catal Today 138:77–83. doi:10.1016/j.cattod.2008.04.040
74. Ferreira-Aparicio P, Rodrıguez-Ramos I, Anderson JA, Guerrero-Ruiz A (2000) Mechanistic aspects of the dry reforming of methane over ruthenium catalysts. Appl Catal A Gen 202:183–196. doi:10.1016/S0926-860X(00)00525-1
75. Osaki T, Masuda H, Mori T (1994) Intermediate hydrocarbon species for the CO_2–CH_4 reaction on supported Ni catalysts. Catal Lett 29:33–37. doi:10.1007/BF00814249
76. Osaki T, Masuda H, Horiuchi T, Mori T (1995) Highly hydrogen-deficient hydrocarbon species for the CO_2-reforming of CH_4 on $Co/A1_2O_3$ catalyst. Catal Lett 34:59–63. doi:10.1007/BF00808322
77. Pinna F (1998) Supported metal catalysts preparation. Catal Today 41:129–137. doi:10.1016/S0920-5861(98)00043-1
78. Imelik B, Vedrine JC (eds) (1994) Catalyst characterization, physical techniques for solid materials. Springer, New York
79. Tsipouriari VA, Verykios XE (2001) Kinetic study of the catalytic reforming of methane with carbon dioxide to synthesis gas over Ni/La_2O_3 catalyst. Catal Today 64:83–90. doi:10.1016/S0920-5861(00)00511-3

80. Topalidis A, Petrakis DE, Ladavos A, Loukatzikou L, Pomonis PJ (2007) A kinetic study of methane and carbon dioxide interconversion over 0.5%Pt/$SrTiO_3$ catalysts. Catal Today 127:238–245. doi:10.1016/j.cattod.2007.04.01
81. Freund HJ, Messmer RP (1986) On the bonding and reactivity of CO_2 on metal surfaces. Surf Sci 172:1–30. doi:10.1016/0039-6028(86)90580-7
82. Solymosi F (1991) The bonding, structure and reactions of CO_2 adsorbed on clean and promoted metal surfaces. J Mol Catal 65:337–358. doi:10.1016/0304-5102(91)85070-I
83. Freund HJ, Roberts MW (1996) Surface chemistry of carbon dioxide. Surf Sci Rep 25:225–273. doi:10.1016/S0167-5729(96)00007-6
84. Erdőhelyi A, Cserenyi J, Papp E, Solymosi F (1994) Catalytic reaction of methane with carbon dioxide over supported palladium. Appl Catal A Gen 108:205–219. doi:10.1016/0926-860X(94)85071-2
85. Cimino A, Stone FS (2002) Oxide solid solutions as catalysts. Adv Catal 47:141–306. doi:10.1016/S0360-0564(02)47007-1
86. Burghaus U (2009) Surface science perspective of carbon dioxide chemistry—adsorption kinetics and dynamics of CO_2 on selected model surfaces. Catal Today 148:212–220. doi:10.1016/j.cattod.2009.07.082
87. Pan YX, Liu CJ, Wiltowski TS, Ge Q (2009) CO_2 adsorption and activation over γ-Al_2O_3-supported transition metal dimers: a density functional study. Catal Today 147:68–76. doi:10.1016/j.cattod.2009.05.005
88. Cheng ZX, Zhao XG, Li JL, Zhu QM (2001) Role of support in CO_2 reforming of CH_4 over a Ni/γ-Al2O3 catalyst. Appl Catal A Gen 205:31–36. doi:10.1016/S0926-860X(00)00560-3
89. De Leitenburg C, Trovarelli A, Kaspar J (1997) A temperature-programmed and transient kinetic study of CO_2 activation and methanation over CeO_2 supported noble metals. J Catal 166:98–107. doi:10.1006/jcat.1997.1498
90. Stagg-Williams SM, Noronha FB, Fendley G, Resasco DE (2000) CO_2 reforming of CH_4 over Pt/ZrO_2 catalysts promoted with La and Ce oxides. J Catal 194:240–249. doi:10.1006/jcat.2000.2939
91. Ozkara-Aydinoglu S, Ozensoy E, Aksoylu AE (2009) The effect of impregnation strategy on methane dry reforming activity of Ce promoted Pt/ZrO_2. Int J Hydrogen Energy 34:9711–9722. doi:10.1016/j.ijhydene.2009.09.005
92. Akpan E, Yanping Suna Y, Kumar P, Ibrahim H, Aboudheir A, Idem R (2007) Kinetics, experimental and reactor modelling studies of the carbon dioxide reforming of methane (CDRM) over a new Ni/CeO_2–ZrO_2 catalyst in a packed bed tubular reactor. Chem Eng Sci 62:4012–4024. doi:10.1016/j.ces.2007.04.044
93. Wei J, Iglesia E (2004) Structural requirements and reaction pathways in methane activation and chemical conversion catalyzed by rhodium. J Catal 225:116–127. doi:10.1016/j.jcat.2003.09.030
94. Bradford MCJ, Vannice MA (1999) The role of metal-support interactions in CO_2 reforming of CH_4. Catal Today 50:87–96. doi:10.1016/S0920-5861(98)00465-9
95. Bradford MCJ, Vannice MA (1999) CO_2 reforming of CH_4 over supported Ru catalysts. J Catal 183:69–75. doi:10.1006/jcat.1999.2385
96. Osaki T., Mori T (2001) Role of potassium in carbon-free CO_2 reforming of methane on K-promoted Ni/Al_2O_3 catalysts. J Catal 204:89–97. doi:10.1006/jcat.2001.3382
97. Portugal UL, Santos ACSF, Damyanova S, Marques CMP, Bueno JMC (2002) CO_2 reforming of CH_4 over Rh-containing catalysts. J Mol Catal A Chem 184:311–322. doi:10.1016/S1381-1169(02)00018-3
98. Gheno SM, Damyanova S, Riguetto BA, Marques CMP, Leite CAP, Bueno JMC (2003) CO_2 reforming of CH_4 over Ru/zeolite catalysts modified with Ti. J Mol Catal A Chem 198:263–275. doi:10.1016/S1381-1169(02)00695-7
99. Bitter JH, Seshan K, Lercher JA (1998) Mono and bifunctional pathways of CO_2/CH_4 reforming over Pt and Rh based catalysts. J Catal 176:93–101. doi:10.1006/jcat.1998.2022

100. Maestri M, Vlachos DG, Beretta A, Groppi G, Tronconi E (2008) Steam and dry reforming of methane on Rh: microkinetic analysis and hierarchy of kinetic models. J Catal 259:211–222. doi:10.1016/j.jcat.2008.08.008
101. Donazzi A, Beretta A, Groppi G, Forzatti P (2008) Catalytic partial oxidation of methane over a 4% Rh/α-Al_2O_3 catalyst part II: role of CO_2 reforming. J Catal 255:259–268. doi:10.1016/j.jcat.2008.02.010
102. Wei J, Iglesia E (2004) Isotopic and kinetic assessment of the mechanism of reactions of CH_4 with CO_2 or H_2O to form synthesis gas and carbon on nickel catalysts. J Catal 224:370–383. doi:10.1016/j.jcat.2004.02.032
103. Abild-Pedersen F, Norskov JK, RostrupNielsen JR, Sehested J, Helveg S (2006) Mechanisms for catalytic carbon nanofiber growth studied by ab initio density functional theory calculations. Phys Rev B 73:115419-1–115419-13. doi:10.1103/PhysRevB.73.115419
104. Xu J, Saeys M (2006) Improving the coking resistance of Ni-based catalysts by promotion with subsurface boron. J Catal 242:217–226. doi:10.1016/j.jcat.2006.05.029
105. Wolf EE, Alfani F (1982) Catalysts deactivation by coking. Catal Rev Sci Eng 24:329–371. doi:10.1080/03602458208079657
106. Trimm DL (1977) The formation and removal of coke from nickel catalyst. Catal Rev Sci Eng 16:155–189. doi:10.1080/03602457708079636
107. Armor JN, Martenak DJ (2001) Studying carbon formation at elevated pressure. Appl Catal A Gen 206:231–236. doi:10.1016/S0926-860X(00)00608-6
108. Coad JP, Riviere JC (1971) Auger spectroscopy of carbon on nickel. Surf Sci 25:609–624. doi:10.1016/0039-6028(71)90148-8
109. Koerts T, Van Santen RA (1991) A low temperature reaction sequence for methane conversion. J Chem Soc Chem Commun 1281–1283. doi:10.1039/C39910001281
110. Chen L, Lu Y, Hong Q, Lin J, Dautzenberg FM (2005) Catalytic partial oxidation of methane to syngas over Ca-decorated-Al_2O_3-supported Ni and NiB catalysts. Appl Catal A Gen 292:295–304. doi:10.1016/j.apcata.2005.06.010
111. Claridge JB, Green MLH, Tsang SC, York APE, Ashcroft AT, Battle PD (1993) A study of carbon deposition on catalysts during the partial oxidation of methane to synthesis gas. Catal Lett 22:299–305. doi:10.1007/BF00807237
112. Shamsi A (2004) Carbon formation on Ni–MgO catalyst during reaction of methane in the presence of CO_2 and CO. Appl Catal A Gen 277:23–30. doi:10.1016/j.apcata.2004.08.015
113. Figueiredo JL, Trimm DL (1975) Gasification of carbon deposits on nickel catalysts. J Catal 40:154–159. doi:10.1016/0021-9517(75)90241-9
114. Hao Z, Zhu Q, Lei Z, Li H (2008) CH_4–CO_2 reforming over Ni/Al_2O_3 aerogel catalysts in a fluidized bed reactor. Powder Technol 182:474–479. doi:10.1016/j.powtec.2007.05.024
115. Corthals S, Van Nederkassel J, Geboers J, De Winne H, Van Noyen J, Moens B, Sels B, Jacobs P (2008) Influence of composition of $MgAl_2O_4$ supported $NiCeO_2ZrO_2$ catalysts on coke formation and catalyst stability for dry reforming of methane. Catal Today 138:28–32. doi:10.1016/j.cattod.2008.04.038
116. San-Jose-Alonso D, Juan-Juan J, Illan-Gomez MJ, Roman-Martȥnez MC (2009) Ni, Co and bimetallic Ni–Co catalysts for the dry reforming of methane. Appl Catal A Gen 371:54–59. doi:10.1016/j.apcata.2009.09.026
117. Rivas ME, Fierro JLG, Goldwasser MR, Pietri E, Perez-Zurita MJ, Griboval-Constant A, Leclercq G (2008) Structural features and performance of $LaNi_{1-x}Rh_xO_3$ system for the dry reforming of methane. Appl Catal A Gen 344:10–19. doi:10.1016/j.apcata.2008.03.023
118. Al-Fatish ASA, Ibrahim AA, Fakeeha AH, Soliman MA, Siddiqui MRH, Abasaeed AE (2009) Coke formation during CO_2 reforming of CH_4 over alumina-supported nickel catalysts. Appl Catal A Gen 364:150–155. doi:10.1016/j.apcata.2009.05.043
119. Helveg S, Lopez-Cartes C, Sehested J, Hansen PL, Clausen BS, Rostrup-Nielsen JR, Abild-Pedersen F, Nørskov JK (2004) Atomic-scale imaging of carbon nanofibre growth. Nature 427:426–429. doi:10.1038/nature02278

120. Baker RTK, Harris PS, Feates FS, Waite RJ (1972) Nucleation and growth of carbon deposits from the nickel catalyzed decomposition of acetylene. J Catal 26:51–62. doi:10.1016/0021-9517(72)90032-2
121. Baker RTK, Harris PS, Thomas RB, Waite RJ (1973) Formation of filamentous carbon from iron, cobalt and chromium catalyzed decomposition of acetylene. J Catal 30:86–95. doi:10.1016/0021-9517(73)90055-9
122. Xu J, Saeys M (2007) First principles study of the coking resistance and the activity of a boron promoted Ni catalyst. Chem Eng Sci 62:5039–5041. doi:10.1016/j.ces.2006.11.050
123. Rostrup-Nielsen JR, Trimm DL (1977) Mechanisms of carbon formation on nickel-containing catalysts. J Catal 48:155–165. doi:10.1016/0021-9517(77)90087-2
124. Bartholomew CH (1982) Carbon deposition in steam reforming and methanation. Catal Rev Sci Eng 24:67–112. doi:10.1080/03602458208079650
125. Rostrup-Nielsen JR (1993) Production of synthesis gas. Catal Today 18:305–324. doi:10.1016/0920-5861(93)80059-A
126. Lercher JA, Bitter JH, Hally W, Niessen W, Seshan K (1996) Design of stable catalysts for methane-carbon dioxide reforming. Stud Surf Sci Catal 101:463–472. doi:10.1016/S0167-2991(96)80257-6
127. Tang S, Ji L, Lin J, Zeng HC, Tan KL, Li K (2000) CO_2 reforming of methane to synthesis gas over sol-gel-made Ni/γ-Al_2O_3 catalysts from organometallic precursors. J Catal 194:424–430. doi:10.1006/jcat.2000.2957
128. Kim JH, Suh DJ, Park TJ, Kim KL (2000) Effect of metal particle size on coking during CO_2 reforming of CH_4 over Ni-alumina aerogel catalysts. Appl Catal A Gen 197:191–200. doi:10.1016/S0926-860X(99)00487-1
129. Frusteri F, Spadaro L, Arena F, Chuvilin A (2002) TEM evidence for factors affecting the genesis of carbon species on bare and K-promoted Ni/MgO catalysts during the dry reforming of methane. Carbon 40:1063–1070. doi:10.1016/S0008-6223(01)00243-3
130. Liu H, Li S, Zhang Z, Chen L, Zhou G, Wang J, Wang X (2008) Catalytic performance of monolithic foam Ni/SiC catalyst in carbon dioxide reforming of methane to synthesis gas. Catal Lett 120:111–115. doi:10.1007/s10562-007-9260-0
131. Juan-Juan J, Roman-Martinez MC, Illan-Gomez MJ (2009) Nickel catalyst activation in the carbon dioxide reforming of methane. Effect of pre-treatments. Appl Catal A Gen 355:27–32. doi:10.1016/j.apcata.2008.10.058
132. Fouskas A, Kollia M, Kambolis A, Papadopoulou C, Matralis H (2010) Effect of Boron on the coking resistance of Ni/Al_2O_3 catalysts for the dry reforming of methane. 9th Novel gas conversion symposium: C1–C4 chemistry: from fossil to bio resources, Lyon, France 30th May–3rd June
133. Zhang J, Wang H, Dalai AK (2008) Effects of metal content on activity and stability of Ni–Co bimetallic catalysts for CO_2 reforming of CH_4. Appl Catal A Gen 339:121–129. doi:10.1016/j.apcata.2008.01.027
134. Liu S, Guan L, Li J, Zhao N, Wei W, Sun Y (2008) CO_2 reforming of CH_4 over stabilized mesoporous Ni–CaO–ZrO_2 composites. Fuel 87:2477–2481. doi:10.1016/j.fuel.2008.02.009
135. Rostrup-Nielsen JR, Hansen JHB (1993) CO_2 reforming of CH_4 over transition metals. J Catal 144:38–49. doi:10.1006/jcat.1993.1312
136. Ferreira-Aparicio P, Guerrero-Ruiz A, Rodriguez-Ramos I (1998) Comparative study at low and medium reaction temperatures of syngas production by methane reforming with carbon dioxide over silica and alumina supported catalysts. Appl Catal A Gen 170:177–187. doi:10.1016/S0926-860X(98)00048-9
137. Pena MA, Gomez JP, Fierro JLG (1996) New catalytic routes for syngas and hydrogen production. Appl Catal A Gen 144:7–57. doi:10.1016/0926-860X(96)00108-1
138. Wang HY, Ruckenstein E (2000) Carbon dioxide reforming of methane to synthesis gas over supported rhodium catalysts: the effect of support. Appl Catal A Gen 204:143–152. doi:10.1016/S0926-860X(00)00547-0

139. Tsipouriari VA, Efstathiou AM, Zhang ZL, Verykios XE (1994) Reforming of methane with carbon dioxide to synthesis gas over supported Rh catalysts. Catal Today 21:579–587. doi:10.1016/0920-5861(94)80182-7
140. Zhang ZL, Tsipouriari VA, Efstathiou AM, Verykios XE (1996) Reforming of methane with carbon dioxide to synthesis gas over supported rhodium catalysts. I. Effects of support and metal crystallite size on reaction activity and deactivation characteristics. J Catal 158:51–63. doi:10.1006/jcat.1996.0005
141. Efstathiou AM, Kladi A, Tsipouriari VA, Verykios XE (1996) Reforming of methane with carbon dioxide to synthesis gas over supported rhodium catalysts. II. A steady-state tracing analysis: mechanistic aspects of the carbon and oxygen reaction pathways to form CO. J Catal 158:64–75. doi:10.1006/jcat.1996.0006
142. Verykios XE (2003) Mechanistic aspects of the reaction of CO_2 reforming of methane over Rh/Al_2O_3 catalyst. Appl Catal A Gen 255:101–111. doi:10.1016/S0926-860X(03)00648-3
143. Wang HY, Au CT (1997) Carbon dioxide reforming of methane to syngas over SiO_2-supported rhodium catalysts. Appl Catal A Gen 155:239–252. doi:10.1016/S0926-860X(96)00398-5
144. Munera JF, Irusta S, Cornaglia LM, Lombardo EA, Cesar DC, Schmal M (2007) Kinetics and reaction pathway of the CO_2 reforming of methane on Rh supported on lanthanum-based solid. J Catal 245:25–34. doi:10.1016/j.jcat.2006.09.008
145. Kohn MP, Castaldi MJ, Farrauto RJ (2010) Auto-thermal and dry reforming of landfill gas over a Rh/gAl_2O_3 monolith catalyst. Appl Catal B Environ 94:125–133. doi:10.1016/j.apcatb.2009.10.029
146. Souza MMVM, Aranda DAG, Schmal M (2001) Reforming of methane with carbon dioxide over $Pt/ZrO_2/Al_2O_3$ catalysts. J Catal 204:498–511. doi:10.1006/jcat.2001.3398
147. Damyanova S, Bueno JMC (2003) Effect of CeO_2 loading on the surface and catalytic behaviors of CeO_2–Al_2O_3-supported Pt catalysts. Appl Catal A Gen 253:135–150. doi:10.1016/S0926-860X(03)00500-3
148. Souza MMVM, Schmal M (2003) Combination of carbon dioxide reforming and partial oxidation of methane over supported platinum catalysts. Appl Catal A Gen 255:83–92. doi:10.1016/S0926-860X(03)00646-X
149. O'Connor AM, Schuurman Y, Ross JRH, Mirodatos C (2006) Transient studies of carbon dioxide reforming of methane over Pt/ZrO_2 and Pt/Al_2O_3. Catal Today 115:191–198. doi:10.1016/j.cattod.2006.02.051
150. Gigola CE, Moreno MS, Costilla I, Sanchez MD (2007) Characterization of Pd-CeO_x interaction on α-Al_2O_3 support. Appl Surf Sci 254:325–329. doi:10.1016/j.apsusc.2007.07.062
151. Zhao Y, Pan Y, Xie Y, Liu C (2008) Carbon dioxide reforming of methane over glow discharge plasma-reduced Ir/Al_2O_3 catalyst. Catal Commun 9:1558–1562. doi:10.1016/j.catcom.2007.12.024
152. Bitter JH, Hally W, Sechan K, van Ommen JG, Lercher JA (1996) The role of the oxidic support on the deactivation of Pt catalysts during the CO_2 reforming of methane. Catal Today 29:349–353. doi:10.1016/0920-5861(95)00303-7
153. Tsyganok AI, Inaba M, Tsunoda T, Uchida K, Suzuki K, Takehira K, Hayakawa T (2005) Rational design of Mg–Al mixed oxide-supported bimetallic catalysts for dry reforming of methane. Appl Catal A Gen 292:328–343. doi:10.1016/j.apcata.2005.06.007
154. Erdőhelyi A, Cserenyi J, Solymosi F (1993) Activation of CH_4 and its reaction with CO_2 over supported Rh catalysts. J Catal 141:287–299. doi:10.1006/jcat.1993.1136
155. Sahli N, Petit C, Roger CA, Kiennemann A, Libs S, Bettahar MM (2006) Ni catalysts from $NiAl_2O_4$ spinel for CO_2 reforming of methane. Catal Today 113:187–193. doi:10.1016/j.cattod.2005.11.065
156. Cheng D, Zhu X, Ben Y, He F, Cui L, Liu C (2006) Carbon dioxide reforming of methane over Ni/Al_2O_3 treated with glow discharge plasma. Catal Today 115:205–210. doi:10.1016/j.cattod.2006.02.063

157. Zhu X, Huo P, Zhang Y, Cheng D, Liu C (2008) Structure and reactivity of plasma treated Ni/Al_2O_3 catalyst for CO_2 reforming of methane. Appl Catal B Environ 81:132–140. doi:10.1016/j.apcatb.2007.11.042
158. Pan YX, Liu CJ, Shi P (2008) Preparation and characterization of coke resistant Ni/SiO_2 catalyst for carbon dioxide reforming of methane. J Power Sources 176:46–53. doi:10.1016/j.jpowsour.2007.10.039
159. Guo J, Hou Z, Gao J, Zheng X (2008) Syngas production via combined oxy-CO_2 reforming of methane over Gd_2O_3-modified Ni/SiO_2 catalysts in a fluidized-bed reactor. Fuel 87:1348–1354. doi:10.1016/j.fuel.2007.06.018
160. Tomishige K, Yamazaki O, Chen Y, Yokoyama K, Li X, Fujimoto K (1998) Development of ultra-stable Ni catalysts for CO_2 reforming of methane. Catal Today 45:35–39. doi:10.1016/S0920-5861(98)00238-7
161. Rostrup-Nielsen JR, Sehested J, Norskov JK (2002) Hydrogen and synthesis gas by steam- and CO_2 reforming. Adv Catal 47:65–139. doi:10.1016/S0360-0564(02)47006-X
162. Ruckenstein E, Hu YH (1995) Carbon dioxide reforming of methane over nickel/alkaline earth metal oxide catalysts. Appl Catal A Gen 133:149–161. doi:10.1016/0926-860X(95)00201-4
163. Wang S, Lu GQM (1998) CO_2 reforming of methane on Ni catalysts: effects of the support phase and preparation technique. Appl Catal B Environ 16:269–277. doi:10.1016/S0926-3373(97)00083-0
164. Chen YG, Tomishige K, Yokohama K, Fujimoto K (1999) Catalytic performance and catalyst structure of nickel-magnesia catalysts for CO_2 reforming of methane. J Catal 184:479–490. doi:10.1006/jcat.1999.2469
165. Xu BQ, Wei JM, Wang HY, Sun KQ, Zhu QM (2001) Nano-MgO: novel preparation and application as support of Ni catalyst for CO_2 reforming of methane. Catal Today 68:217–225. doi:10.1016/S0920-5861(01)00303-0
166. Djaidja A, Libs S, Kiennemann A, Barama A (2006) Characterization and activity in dry reforming of methane on NiMg/Al and Ni/MgO catalysts. Catal Today 113:194–200. doi:10.1016/j.cattod.2005.11.066
167. Ruckenstein E, Hu YH (1997) The effect of precursor and preparation conditions of MgO on the CO_2 reforming of CH_4 over NiO/MgO catalysts. Appl Catal A Gen 154:185–205. doi:10.1016/S0926-860X(96)00372-9
168. Hu YH, Ruckenstein E (1996) An optimum NiO content in the CO_2 reforming of CH_4 with NiO/MgO solid solution catalysts. Catal Lett 36:145–149. doi:10.1007/BF00807611
169. Cavani F, Trifiro F, Vaccari A (1991) Hydrotalcite-type anionic clays: preparation, properties and applications. Catal Today 11:173–301. doi:10.1016/0920-5861(91)80068-K
170. Bhattacharyya A, Chang VW, Schumacher DJ (1998) CO_2 reforming of methane to syngas I: evaluation of hydrotalcite clay-derived catalysts. Appl Clay Sci 13:317–328. doi:10.1016/S0169-1317(98)00030-1
171. Basile F, Benito P, Fornasari G, Vaccari A (2010) Hydrotalcite-type precursors of active catalysts for hydrogen production. Appl Clay Sci 48:250–259. doi:10.1016/j.clay.2009.11.027
172. Basile F, Fornasari G, Poluzzi E, Vaccari A (1998) Catalytic partial oxidation and CO_2-reforming on Rh- and Ni-based catalysts obtained from hydrotalcite-type precursors. Appl Clay Sci 13:329–345. doi:10.1016/S0169-1317(98)00031-3
173. Tsyganok AI, Tsunoda T, Hamakawa S, Suzuki K, Takehira K, Hayakawa T (2003) Dry reforming of methane over catalysts derived from nickel-containing Mg–Al layered double hydroxides. J Catal 213:191–203. doi:10.1016/S0021-9517(02)00047-7
174. Tsyganok AI, Inaba M, Tsunoda T, Suzuki K, Takehira K, Hayakawa T (2004) Combined partial oxidation and dry reforming of methane to synthesis gas over noble metals supported on Mg–Al mixed oxide. Appl Catal A Gen 275:149–155. doi:10.1016/j.apcata.2004.07.030

175. Takehira K, Kawabata T, Shishido T, Murakami K, Ohi T, Shoro D, Honda M, Takaki K (2005) Mechanism of reconstitution of hydrotalcite leading to eggshelltype Ni loading on Mg–Al mixed oxide. J Catal 231:92–104. doi:10.1016/j.jcat.2005.01.025
176. Olafsen A, Daniel C, SchuurmanY RLB, Olsbye U, Mirodatos C (2006) Light alkanes CO_2 reforming to synthesis gas over Ni based catalysts. Catal Today 115:179–185. doi:10.1016/j.cattod.2006.02.053
177. Ohi T, Miyata T, Li D, Shishido T, Kawabata T, Sano T, Takehira K (2006) Sustainability of Ni loaded Mg–Al mixed oxide catalyst in daily startup and shutdown operations of CH_4 steam reforming. Appl Catal A Gen 308:194–203. doi:10.1016/j.apcata.2006.04.025
178. Lucredio AF, Assaf EM (2006) Cobalt catalysts prepared from hydrotalcite precursors and tested in methane steam reforming. J Power Sources 159:667–672. doi:10.1016/j.jpowsour.2005.10.108
179. Lucredio AF, Jerkiewicz G, Assaf EM (2008) Cobalt catalysts promoted with cerium and lanthanum applied to partial oxidation of methane reactions. Appl Catal B Environ 84:106–111. doi:10.1016/j.apcatb.2008.03.008
180. Vaccari A (1998) Preparation and catalytic properties of cationic and anionic clays. Catal Today 41:53–71. doi:10.1016/S0920-5861(98)00038-8
181. Aneggi E, De Leitenburg C, Dolcetti G, Trovarelli A (2006) Promotional effect of rare earths and transition metals in the combustion of diesel soot over CeO_2 and CeO_2–ZrO_2. Catal Today 114:40–47. doi:10.1016/j.cattod.2006.02.008
182. Kambolis A, Matralis H, Trovarelli A, Papadopoulou C (2010) Ni/CeO_2–ZrO_2 catalysts for the dry reforming of methane. Appl Catal A Gen 377:16–26. doi:10.1016/j.apcata.2010.01.013
183. Trovarelli A (1996) Catalytic properties of ceria and CeO_2-containing materials. Catal Rev 38(4):439–520. doi:10.1080/01614949608006464
184. Fierro JLG, Soria J, Sanz J, Rojo JM (1987) Induced changes in ceria by thermal treatments under vacuum or hydrogen. J Solid State Chem 66:154–162. doi:10.1016/0022-4596(87)90230-1
185. Gonzalez-DelaCruz VM, Holgado JP, Pereniguez R, Caballero A (2008) Morphology changes induced by strong metal–support interaction on a Ni–ceria catalytic system. J Catal 257:307–314. doi:10.1016/j.jcat.2008.05.009
186. Bernal S, Calvino JJ, Cauqui MA, Gatica JM, Lopez Cartes C, Pérez Omil JA, Pintado JM (2003) Some contributions of electron microscopy to the characterisation of the strong metal-support interaction effect. Catal Today 77:385–406. doi:10.1016/S0920-5861(02)00382-6
187. Valentini A, Carreno NLV, Probst LFD, Barison A, Ferreira AG, Leite ER, Longo E (2006) Ni:CeO_2 nanocomposite catalysts prepared by polymeric precursor method. Appl Catal A Gen 310:174–182. doi:10.1016/j.apcata.2006.05.037
188. Terribile D, Trovarelli A, De Leitenburg C, Primavera A, Dolcetti G (1999) Catalytic combustion of hydrocarbons with Mn and Cu-doped ceria–zirconia solid solutions. Catal Today 47:133–140. doi:10.1016/S0920-5861(98)00292-2
189. Wang S, (Max) Lu GQ (1998) Role of CeO_2 in Ni/CeO_2-Al_2O_3 catalysts for carbon dioxide reforming of methane. Appl Catal B Environ 19:267–277. doi:10.1016/S0926-3373(98)00081-2
190. Kaspar J, Di Monte R, Fornasiero P, Graziani M, Bradshaw H, Norman C (2001) Dependency of the oxygen storage capacity in zirconia–ceria solid solutions upon textural properties. Top Catal 16–17:83–87. doi:10.1023/A:1016682831177
191. Damyanova S, Pawelec B, Arishtirova K, Martinez Huerta MV, Fierro JLG (2009) The effect of CeO_2 on the surface and catalytic properties of Pt/CeO_2–ZrO_2 catalysts for methane dry reforming. Appl Catal B Environ 89:149–159. doi:10.1016/j.apcatb.2008.11.035
192. Montoya JA, Romero-Pascual E, Gimon C, Del Angel P, Monzon A (2000) Methane reforming with CO_2 over Ni/ZrO_2–CeO_2 catalysts prepared by sol-gel. Catal Today 63:71–85. doi:10.1016/S0920-5861(00)00447-8

193. Roh HS, Potdar HS, Jun KW, Kim JW, Oh YS (2004) Carbon dioxide reforming of methane over Ni incorporated into Ce–ZrO_2 catalysts. Appl Catal A Gen 276:231–239. doi:10.1016/j.apcata.2004.08.009
194. Kumar P, Sun Y, Idem RO (2007) Nickel-based ceria, zirconia, and ceria–zirconia catalytic systems for low-temperature carbon dioxide reforming of methane. Energy Fuel 21:3113–3123. doi:10.1021/ef7002409
195. Chen J, Wu Q, Zhang J, Zhang J (2008) Effect of preparation methods on structure and performance of Ni/$Ce_{0.75}Zr_{0.25}O_2$ catalysts for CH_4–CO_2 reforming. Fuel 87:2901–2907. doi:10.1016/j.fuel.2008.04.015
196. Yang Z, Wei Y, Fu Z, Lu Z, Hermansson K (2008) Facilitated vacancy formation at Zr-doped ceria(111) surfaces. Surf Sci 602:1199–1206. doi:10.1016/j.susc.2008.01.013
197. Kuznetsova TG, Sadykov VA (2008) Specific features of the defect structure of metastable nanodisperse ceria, zirconia, and related materials. Kinet Catal 49:840–858. doi:10.1134/S0023158408060098
198. Koubaissy B, Pietraszek A, Roger AC, Kiennemann A (2010) CO_2 reforming of methane over Ce-Zr-Ni-Me mixed catalysts. Catal Today 157:436–439. doi:10.1016/j.cattod.2010.01.050
199. Otsuka K, Wang Y, Nakamura M (1999) Direct conversion of methane to synthesis gas through gas-solid reaction using CeO_2–ZrO_2 solid solution at moderate temperature. Appl Catal A Gen 183:317–324. doi:10.1016/S0926-860X(99)00070-8
200. Wang JB, Tai YL, Dow WP, Huang TJ (2001) Study of ceria-supported nickel catalyst and effect of yttria doping on carbon dioxide reforming of methane. Appl Catal A Gen 218:69–79. doi:10.1016/S0926-860X(01)00620-2
201. Putna ES, Shereck B, Gorte RJ (1998) Adsorption and reactivity of lanthana with CO. Appl Catal B Environ 17:101–106. doi:10.1016/S0926-3373(98)00006-X
202. Gronchi P, Centola E, Del Rosso R (1997) Dry reforming of CH_4 with Ni and Rh metal catalysts supported on SiO_2 and La_2O_3. Appl Catal A Gen 152:83–92. doi:10.1016/S0926-860X(96)00358-4
203. Zhang WD, Liu BS, Zhu C, Tian YL (2005) Preparation of La_2NiO_4/ZSM-5 catalyst and catalytic performance in CO_2/CH_4 reforming to syngas. Appl Catal A Gen 292:138–143. doi:10.1016/j.apcata.2005.05.018
204. Jeong H, Kim KL, Kim D, Song IK (2006) Effect of promoters in the methane reforming with carbon dioxide to synthesis gas over Ni/HY catalysts. J Mol Catal A Chem 246:43–48. doi:10.1016/j.molcata.2005.10.013
205. Luengnaruemitchai A, Kaengsilalai A (2008) Activity of different zeolite-supported Ni catalysts for methane reforming with carbon dioxide. Chem Eng J 144:96–102. doi:10.1016/j.cej.2008.05.023
206. Liu H, Li S, Zhang S, Wang J, Zhou G, Chen L, Wang X (2008) Catalytic performance of novel Ni catalysts supported on SiC monolithic foam in carbon dioxide reforming of methane to synthesis gas. Catal Commun 9:51–54. doi:10.1016/j.catcom.2007.05.002
207. Boukha Z, Kacimi M, Pereira MFR, Faria JL, Figueiredo JL, Ziyad M (2007) Methane dry reforming on Ni loaded hydroxyapatite and fluoroapatite. Appl Catal A Gen 317:299–309. doi:10.1016/j.apcata.2006.10.029
208. Kaengsilalai A, Luengnaruemitchai A, Jitkarnka S, Wongkasemjit S (2007) Potential of Ni supported on KH zeolite catalysts for carbon dioxide reforming of methane. J Power Sources 165:347–352. doi:10.1016/j.jpowsour.2006.12.005
209. Yamazaki O, Nozaki T, Omata K, Fujimoto K (1992) Reduction of carbon dioxide by methane with Ni-on-MgO-CaO containing catalysts. Chem Lett 1953–1954. doi:10.1246/cl.1992.1953
210. Zhang ZL, Verykios XE (1994) Carbon dioxide reforming of methane to synthesis gas over supported Ni catalysts. Catal Today 21:589–595. doi:10.1016/0920-5861(94)80183-5

211. Choudhary VR, Rajput AM, Prabhakar B (1994) NiO/CaO-catalyzed formation of syngas by coupled exothermic oxidative conversion and endothermic CO_2 and steam reforming of methane. Angew Chem Int Ed Engl 33:2104–2106. doi:10.1002/anie.199421041
212. Tang SB, Qiu FL, Lu SJ (1995) Effect of supports on the carbon deposition of nickel catalysts for methane reforming with CO_2. Catal Today 24:253–255. doi:10.1016/0920-5861(95)00036-F
213. Goula MA, Lemonidou AA, Efstathiou AM (1996) Characterization of carbonaceous species formed during reforming of CH_4 with CO_2 over Ni/CaO-Al_2O_3 catalysts studied by various transient techniques. J Catal 161:626–640. doi:10.1006/jcat.1996.0225
214. Chang JS, Park SE, Chon H (1996) Catalytic activity and coke resistance in the carbon dioxide reforming of methane to synthesis gas over zeolite-supported Ni catalysts. Appl Catal A Gen 145:111–124. doi:10.1016/0926-860X(96)00150-0
215. Cheng Z, Wu Q, Li J, Zhu Q (1996) Effects of promoters and preparation procedures on reforming of methane with carbon dioxide over Ni/Al_2O_3 catalyst. Catal Today 30:147–155. doi:10.1016/0920-5861(95)00005-4
216. Horiuchi T, Sakuma K, Fukui T, Kubo Y, Osaki T, Mori T (1996) Suppression of carbon deposition in the CO_2-reforming of CH_4 by adding basic metal oxides to a Ni/Al_2O_3 catalyst. Appl Catal A Gen 144:111–120. doi:10.1016/0926-860X(96)00100-7
217. Zhang Z, Verykios XE, MacDonald SM, Affrossman S (1996) Comparative study of carbon dioxide reforming of methane to synthesis gas over Ni/La_2O_3 and conventional nickel-based catalysts. J Phys Chem 100:744–754. doi:10.1021/jp951809e
218. Quincoces CE, Perez de Vargas S, Diaz A, Montes M, Gonzalez MG (1998) Morphological changes of Ca promoted Ni/SiO_2 catalysts and carbon deposition during CO_2 reforming of methane. Stud Surf Sci Catal 119:837–842. doi:10.1016/S0167-2991(98)80536-3
219. Wang S, Lu GQ (2000) Effects of promoters on catalytic activity and carbon deposition of Ni/γ-Al_2O_3 catalysts in CO_2 reforming of CH_4. J Chem Technol Biotechnol 75:589–595. doi:10.1002/1097-4660(200007)
220. Quincoces CE, Dicundo S, Alvarez AM, González MG (2001) Effect of addition of CaO on Ni/Al_2O_3 catalysts over CO_2 reforming of methane. Mater Lett 50:21–27. doi:10.1016/S0167-577X(00)00406-7
221. Hou Z, Yokota O, Tanaka T, Yashima T (2003) Characterization of Ca-promoted Ni/α-Al_2O_3 catalyst for CH_4 reforming with CO_2. Appl Catal A Gen 253:381–387. doi:10.1016/S0926-860X(03)00543-X
222. Dias JAC, Assaf JM (2003) Influence of calcium content in Ni/CaO/γ-Al_2O_3 catalysts for CO_2-reforming of methane. Catal Today 85:59–68. doi:10.1016/S0920-5861(03)00194-9
223. Hou Z, Yokota O, Tanaka T, Yashima T (2003) A novel KCaNi/α-Al_2O_3 catalyst for CH_4 reforming with CO_2. Catal Lett 87:37–42. doi:10.1023/A:1022849009431
224. Yashima T (2005) High coke-resistance of K-Ca-promoted Ni/α-Al_2O_3catalyst for CH_4 reforming with CO_2. React Kinet Catal Lett 84:229–235. doi:10.1007/s11144-005-0214-5
225. Ping C, Yin HZ, Ming ZX (2005) Production of synthesis gas via methane reforming with CO_2 on Ni/SiO_2 catalysts promoted by alkali and alkaline earth metals. Chin J Chem 23:847–851. doi:10.1002/cjoc.200590847
226. Chang JS, Hong DY, Li X, Park SE (2006) Thermogravimetric analyses and catalytic behaviors of zirconia-supported nickel catalysts for carbon dioxide reforming of methane. Catal Today 115:186–190. doi:10.1016/j.cattod.2006.02.052
227. Zhang WD, Liu BS, Tian YL (2007) CO_2 reforming of methane over Ni/Sm_2O_3–CaO catalyst prepared by a sol-gel technique. Catal Commun 8:661–667. doi:10.1016/j.catcom.2006.08.020
228. Roh H, Jun K (2008) Carbon dioxide reforming of methane over Ni catalysts supported on Al_2O_3 modified with La_2O_3, MgO, and CaO. Catal Surv Asia 12:239–252. doi:10.1007/s10563-008-9058-0

229. Bellido JDA, De Souza JE, M'Peko J, Assaf EM (2009) Effect of adding CaO to ZrO_2 support on nickel catalyst activity in dry reforming of methane. Appl Catal A Gen 358:215–223. doi:10.1016/j.apcata.2009.02.014
230. Nandini A, Pant KK, Dhingra SC (2005) K–, CeO_2–, and Mn-promoted Ni/Al_2O_3 catalysts for stable CO_2 reforming of methane. Appl Catal A Gen 290:166–174. doi:10.1016/j.apcata.2005.05.016
231. Molenbroek AM, Nørskov JK, Clausen BS (2001) Structure and reactivity of Ni–Au nanoparticle catalysts. J Phys Chem B 105:5450–5458. doi:10.1021/jp0043975
232. Besenbacher F, Chorkendorff I, Clausen BS, Hammer B, Molenbroek AM, Nørskov JK, Stensgaard I (1998) Design of a surface alloy catalyst for steam reforming. Science 279:1913–1915. doi:10.1126/science.279.5358.1913
233. Guczi L, Stefler G, Geszti O, Sajo I, Paszti Z, Tompos A, Schay Z (2010) Methane dry reforming with CO_2: a study on surface carbon species. Appl Catal A Gen 375:236–246. doi:10.1016/j.apcata.2009.12.040
234. Inui T, Saigo K, Fujii Y, Fujioka K (1995) Catalytic combustion of natural gas as the role of on-site heat supply in rapid catalytic CO_2–H_2O reforming of methane. Catal Today 26:295–302. doi:10.1016/0920-5861(95)00151-9
235. Chen Y, Tomishige K, Yokohama K, Fujimoto K (1997) Promoting effect of Pt, Pd and Rh noble metals to the $Ni_{0.03}Mg_{0.97}O$ solid solution catalysts for the reforming of CH_4 with CO_2. Appl Catal A Gen 165:335–347. doi:10.1016/S0926-860X(97)00216-0
236. Nagaoka K, Jentys A, Lercher A (2005) Methane autothermal reforming with and without ethane over mono- and bimetal catalysts prepared from hydrotalcite precursors. J Catal 229:185–196. doi:10.1016/j.jcat.2004.10.006
237. Arbag H, Yasyerli S, Yasyerli N, Dogu G (2010) Activity and stability enhancement of Ni-MCM-41 catalysts by Rh incorporation for hydrogen from dry reforming of methane. Int J Hydrogen Energy 35:2296–2304. doi:10.1016/j.ijhydene.2009.12.109
238. Garcia-Dieguez M, Pieta IS, Herrera MC, Larrubia MA, Alemany LJ (2010) Improved Pt-Ni nanocatalysts for dry reforming of methane. Appl Catal A Gen 377:191–199. doi:10.1016/j.apcata.2010.01.038
239. Chen HW, Wang CY, Yu CH, Tseng LT, Liao PH (2004) Carbon dioxide reforming of methane reaction catalyzed by stable nickel copper catalysts. Catal Today 97:173–180. doi:10.1016/j.cattod.2004.03.067
240. Tomishige K, Himeno Y, Matsuo Y, Yoshinaga Y, Fujimoto K (2000) Catalytic performance and carbon deposition behavior of a NiO–MgO solid solution in methane reforming with carbon dioxide under pressurized conditions. Ind Eng Chem Res 39:1891–1897. doi:10.1021/ie990884z
241. Goldwasser MR, Rivas ME, Pietri E, Pérez-Zurita MJ, Cubeiro ML, Gingembre L, Leclercq L, Leclercq G (2003) Perovskites as catalysts precursors: CO_2 reforming of CH_4 on $Ln_{1-x}Ca_xRu_{0.8}Ni_{0.2}O_3$ (Ln=La, Sm, Nd). Appl Catal A Gen 255:45–57. doi:10.1016/S0926-860X(03)00643-4
242. Goldwasser MR, Rivas ME, Lugo ML, Pietri E, Pérez-Zurita MJ, Cubeiro ML, Griboval-ConstantA LG (2005) Combined methane reforming in presence of CO_2 and O_2 over $LaFe_{1-x}Co_xO_3$ mixed-oxide perovskites as catalysts precursors. Catal Today 107–108:106–113. doi:10.1016/j.cattod.2005.07.073
243. Valderrama G, Goldwasser MR, de Navarro CU, Tatibouet JM, Barrault J, Batiot-Dupeyrat C, Martinez F (2005) Dry reforming of methane over Ni perovskite type oxides. Catal Today 107–108:785–791. doi:10.1016/j.cattod.2005.07.010
244. De Araujo GC, De Lima SM, Assaf JM, Pena MA, Fierro JLG, Rangel MC (2008) Catalytic evaluation of perovskite-type oxide $LaNi_{1-x}Ru_xO_3$ in methane dry reforming. Catal Today 133–135:129–135. doi:10.1016/j.cattod.2007.12.049
245. Gallego GS, Mondragon F, Tatibouet JM, Barrault J, Batiot-Dupeyrat C (2008) Carbon dioxide reforming of methane over La_2NiO_4 as catalyst precursor—characterization of carbon deposition. Catal Today 133–135:200–209. doi:10.1016/j.cattod.2007.12.075

246. Kharton VV, Viskup AP, Naumovich EN, Tikhonovich VN (1999) Oxygen permeability of $LaFe_{1-x}Ni_xO_{3-\delta}$ solid solutions. Mater Res Bull 34:1311–1317. doi:10.1016/S0025-5408(99)00117-8
247. Mawdsley JR, Krause TR (2008) Rare earth-first-row transition metal perovskites as catalysts for the autothermal reforming of hydrocarbon fuels to generate hydrogen. Appl Catal A Gen 334:311–320. doi:10.1016/j.apcata.2007.10.018
248. Gallego GS, Marın JG, Batiot-Dupeyrat C, Barrault J, Mondragon F (2008) Influence of Pr and Ce in dry methane reforming catalysts produced from $La_{1-x}A_xNiO_{3-\delta}$ perovskites. Appl Catal A Gen 369:97–103. doi:10.1016/j.apcata.2009.09.004
249. Choudhary VR, Mondal KC (2006) CO_2 reforming of methane combined with steam reforming or partial oxidation of methane to syngas over $NdCoO_3$ perovskite-type mixed metal-oxide catalyst. Appl Energy 83:1024–1032. doi:10.1016/j.apenergy.2005.09.008
250. Rivas ME, Fierro JLG, Guil-Lopez R, Pena MA, La Parola V, Goldwasser MR (2008) Preparation and characterization of nickel-based mixed-oxides and their performance for catalytic methane decomposition. Catal Today 133–135:367–373. doi:10.1016/j.cattod.2007.12.045
251. Gallego GS, Mondragon F, Barrault J, Tatibouet JM, Batiot-Dupeyrat C (2006) CO_2 reforming of CH_4 over La–Ni based perovskite precursors. Appl Catal A Gen 311:164–171. doi:10.1016/j.apcata.2006.06.024
252. Guo J, Lou H, Zhu Y, Zheng X (2003) La-based perovskite precursors preparation and its catalytic activity for CO_2 reforming of CH_4. Mater Lett 57:4450–4455. doi:10.1016/S0167-577X(03)00341-0
253. Lima SM, Assaf JM, Pena MA, Fierro JLG (2006) Structural features of $La_{1-x}Ce_xNiO_3$ mixed oxides and performance for the dry reforming of methane. Appl Catal A Gen 311:94–104. doi:10.1016/j.apcata.2006.06.010
254. Gallego GS, Batiot-Dupeyrat C, Barrault J, Florez E, Mondragon F (2008) Dry reforming of methane over $LaNi_{1-y}B_yO_{3-d}$ (B = Mg, Co) perovskites used as catalyst precursor. Appl Catal A Gen 334:251–258. doi:10.1016/j.apcata.2007.10.010
255. Pichas C, Pomonis P, Petrakis D, Ladavos A (2010) Kinetic study of the catalytic dry reforming of CH_4 with CO_2 over $La_{2-x}Sr_xNiO_4$ perovskite-type oxides. Appl Catal A Gen 386:116–123. doi:10.1016/j.apcata.2010.07.043
256. Balachandran U, Dusek JT, Mieville RL, Poeppel RB, Kleefisch MS, Pei S, Kobylinski TP, Udovich CA, Bose AC (1995) Dense ceramic membranes for partial oxidation of methane to syngas. Appl Catal A Gen 133:19–29. doi:10.1016/0926-860X(95)00159-X
257. Valderrama G, Kiennemann A, Goldwasser MR (2008) Dry reforming of CH_4 over solid solutions of $LaNi_{1-x}Co_xO_3$. Catal Today 133–135:142–148. doi:10.1016/j.cattod.2007.12.069
258. Goldwasser MR, Rivas ME, Pietri E, Pérez-Zurita MJ, Cubeiro ML, Griboval-Constant A, Leclercq G (2005) Perovskites as catalysts precursors: synthesis and characterization. J Mol Catal A Gen 228:325–331. doi:10.1016/j.molcata.2004.09.030
259. Khalesi A, Arandiyan HR, Parvari M (2008) Effects of lanthanum substitution by strontium and calcium in La-Ni-Al perovskite oxides in dry reforming of methane. Chin J Catal 29:960–968. doi:10.1016/S1872-2067(08)60079-0
260. Valderrama G, Kiennemann A, Goldwasser MR (2010) La-Sr-Ni-Co-O based perovskite-type solid solutions as catalyst precursors in the CO_2 reforming of methane. J Power Sources 195:1765–1771. doi:10.1016/j.jpowsour.2009.10.004
261. Provendier H, Petit C, Estournes C, Kiennemann A (1998) Dry reforming of methane. Interest of La-Ni-Fe solid solutions compared to $LaNiO_3$ and $LaFeO_3$. Stud Surf Sci Catal 119:741–746. doi:10.1016/S0167-2991(98)80520-X
262. Provendier H, Petit C, Estournes C, Libs S, Kiennemann A (1999) Stabilisation of active nickel catalysts in partial oxidation of methane to synthesis gas by iron addition. Appl Catal A Gen 180:163–173. doi:10.1016/S0926-860X(98)00343-3

263. Rivas I, Alvarez J, Pietri E, Pérez-Zurita MJ, Goldwasser MR (2010) Perovskite-type oxides in methane dry reforming: effect of their incorporation into a mesoporous SBA-15 silica-host. Catal Today 149:388–393. doi:10.1016/j.cattod.2009.05.028
264. Nagaoka K, Okamura M, Aika K (2001) Titania supported ruthenium as coking-resistant catalyst for high pressure dry reforming of methane. Catal Commun 2:255–260. doi:10.1016/S1566-7367(01)00043-7
265. Shamsi A, Johnson CD (2003) Effect of pressure on the carbon deposition route in CO_2 reforming of $^{13}CH_4$. Catal Today 84:17–25. doi:10.1016/S0920-5861(03)00296-7
266. Corthals S, Witvrouwen T, Jacobs P, Sels B (2011) Development of dry reforming catalysts at elevated pressure: D-optimal vs. full factorial design. Catal Today 159:12–24. doi:10.1016/j.cattod.2010.06.021
267. Horvath A, Stefler G, Geszti O, Kienneman A, Pietraszek A, Guczi L (2010) Methane dry reforming with CO_2 on CeZr-oxide supported Ni, NiRh and NiCo catalysts prepared by sol-gel technique: relationship between activity and coke formation. Catal Today 169 (1):102–111. doi:10.1016/j.cattod.2010.08.004

Chapter 4
Reforming of Ethanol

András Erdőhelyi

4.1 Introduction

The use of hydrogen for fuel cell application represents one of the most environmental friendly processes for the production of electric energy for automotives in the near future.

Currently, the steam reforming of methane is the most frequently used and nowadays the most economical way to obtain hydrogen. However, the use of fossil fuels as primary hydrogen sources enhances the CO_2 emission.

The increasing cost of natural gas, its environmental impact, and greenhouse gas effect as well as the need for securing energy supplies are accelerating the transition to bio-based energy carriers.

The production of hydrogen efficiently and economically from renewable source, however, remains a challenge for the academic research and for the industrial development. Finding alternatives to natural gas or other fossil fuels has been the subject of many.

Seven common fuels are compared [1] for their utilities as hydrogen sources. The study concluded that the combination of steam reforming and partial oxidation of methanol is theoretically the most qualified in terms of energy input and possible by-products. However, the toxicity and the current infrastructure for the production of methanol make it an unlikely candidate for commercial use, because the raw materials of methanol synthesis are mainly fossil fuels nowadays.

Ethanol is much less hazardous and can be produced renewably from biomass, thus making it an attractive source for hydrogen formation. Ethanol production can

A. Erdőhelyi
Department of Solid State and Radiochemistry, University of Szeged, Szeged, Hungary
e-mail: erdohelyi@chem.u-szeged.hu

L. Guczi and A. Erdőhelyi (eds.), *Catalysis for Alternative Energy Generation*,
DOI 10.1007/978-1-4614-0344-9_4,

be considered environmentally sustainable, because the CO_2 formed during the ethanol reforming is the same depleted by the plants and drawn from the environment via photosynthesis.

The first argument against bioethanol is that the use of it has a negative energy balance. Recently, it was shown [2] that 1 L of bioethanol obtained from a conventional large-scale corn plant requires for its production 19.16 MJ L^{-1} amount of energy. The energy content of ethanol is 21.2 MJ L^{-1}, and taking into account that of the distillation residue, which could be used in animal nutrition (4.16 MJ L^{-1}) the net energy excess of the whole process is 6.2 MJ L^{-1} ethanol.

Although the use of biomass-derived materials, especially ethanol, as fuel is disputed now, because ethanol is made mainly from sugarcane or different starch-containing material such as potato, corn, cereal, which are also used in food production. In the public perception this has led to an emotional resistance against biofuel.

It is well understood by the members of the society that ethanol can be also made from cellulosic materials such as wood, grass, and wastes [3]. The technology for ethanol production from cellulosic materials is different from that for production from food crops.

Intensive research on the utilization of lignocellulosic biomass as feedstock has been conducted in the recent years. Any further increase in ethanol production will necessarily involve the use of feedstock rather than corn grain due to limited supplies. Feedstocks are typically grouped under the heading "biomass" and include agricultural residues, wood, municipal solid waste, and dedicated energy crops [4, 5]. Biomass is seen as an interesting energy source for several reasons, the main one being the contribution provided by bioenergy to sustainable development [6]. Resources are often available locally, and conversion into secondary energy carriers is feasible without high capital investments [7].

Hydrogen production from ethanol steam reforming would not only be environmentally friendly but would also open a new opportunity for the utilization of renewable resources. In our days ethanol is used as fuel additive but the efficiency of fuel cells operating with hydrogen is much higher than that of heat engines.

So it would be most impressive that we could generate energy by H_2/O_2 fuel cell and the hydrogen would be produced from a renewable source such as ethanol.

In the last 10 years the steam reforming of ethanol was investigated in detail, and the results are summarized in different reviews [8–11]. The numbers of papers dealing with this field does not allow summarizing all results obtained, so we review only the most important observations.

4.2 The Thermodynamics of Ethanol Reforming

H_2 can be produced from ethanol in three main ways. The steam-reforming reaction is strongly endothermic and produces theoretically only H_2 and CO_2.

$$C_2H_5OH + 3H_2O \rightarrow 2CO_2 + 6H_2 \quad \Delta H = 174\,\mathrm{kJ\,mol^{-1}}, \tag{4.1}$$

(all data refer to 298 K)

Partial oxidation

$$C_2H_5OH + 1.5O_2 \rightarrow 2CO_2 + 3H_2 \quad \Delta H = 510\,\mathrm{kJ\,mol^{-1}}. \tag{4.2}$$

Oxidative steam reforming

$$C_2H_5OH + 2H_2O + 0.5O_2 \rightarrow 2CO_2 + 5H_2 \quad \Delta H = 61.6\,\mathrm{kJ\,mol^{-1}} \tag{4.3}$$

In the oxidative steam reforming of ethanol the ratio of the endothermic and exothermic reactions could result in an energetically neutral system when the oxygen-to-ethanol ratio is 0.61.

During the ethanol reforming other undesirable reactions could also occur, which have to be taken into account either in the thermodynamic or in the kinetic considerations.

The dehydrogenation of ethanol could produce acetaldehyde (4.4), the dehydration of it to ethylene (4.5) or diethyl ether (4.6), and the ethanol decomposition is also possible.

$$C_2H_5OH \rightarrow CH_3CHO + H_2 \quad (\Delta H = 68\,\mathrm{kJ\,mol^{-1}}), \tag{4.4}$$

$$C_2H_5OH \rightarrow C_2H_4 + H_2O \quad (\Delta H = 45\,\mathrm{kJ\,mol^{-1}}), \tag{4.5}$$

$$2C_2H_5OH \rightarrow C_2H_5 - O - C_2H_5 + H_2O, \tag{4.6}$$

$$2C_2H_5OH \rightarrow CO_2 + 3CH_4 \quad (\Delta H = -74\,\mathrm{kJ\,mol^{-1}}), \tag{4.7}$$

$$C_2H_5OH \rightarrow CO + CH_4 + H_2 \quad (\Delta H = 49\,\mathrm{kJ\,mol^{-1}}). \tag{4.8}$$

In the ethanol + water reaction not only CO_2 but also CO can form [12].

$$C_2H_5OH + H_2O \rightarrow 2CO + 4H_2 \quad (\Delta H = 256\,\mathrm{kJ\,mol^{-1}}), \tag{4.9}$$

and the products could react with ethanol or with each other

$$C_2H_5OH + H_2 \rightarrow 2CH_4 + H_2O \quad (\Delta H = 157\,\mathrm{kJ\,mol^{-1}}), \tag{4.10}$$

$$2CO \rightleftharpoons CO_2 + C \quad (\Delta H = -171\,\mathrm{kJ\,mol^{-1}}), \tag{4.11}$$

$$CO_2 + 4H_2 \rightleftharpoons CH_4 + 2H_2O \quad (\Delta H = -165\,\mathrm{kJ\,mol^{-1}}), \tag{4.12}$$

$$CO + 3H_2 \rightleftharpoons CH_4 + H_2O \quad (\Delta H = 206\,\mathrm{kJ\,mol^{-1}}), \tag{4.13}$$

$$CO_2 + CH_4 \rightleftharpoons 2CO + 2H_2 \quad (\Delta H = 247\,\mathrm{kJ\,mol^{-1}}), \tag{4.14}$$

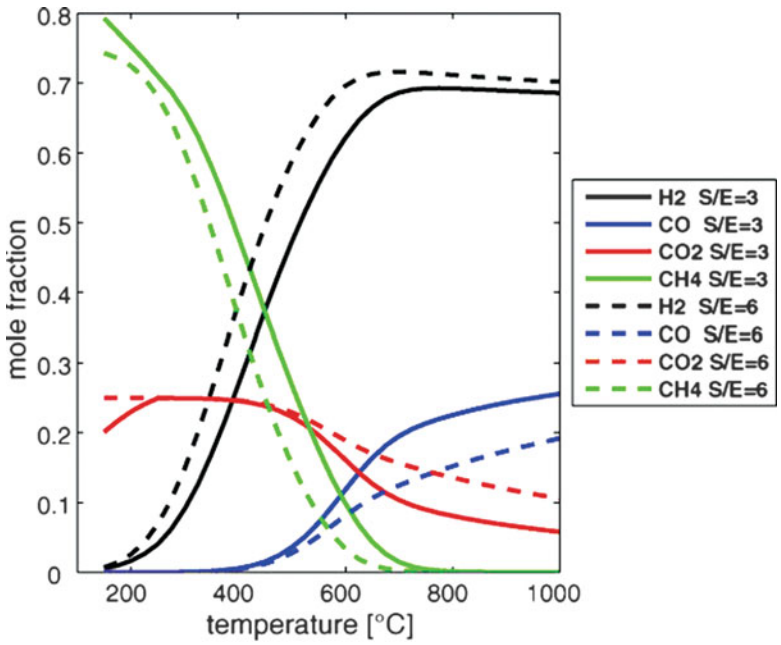

Fig. 4.1 Reformate product composition in mole fraction on dry basis for steam reforming of ethanol at steam-to-ethanol ratio 3 and 6 at atmospheric pressure [13]

$$CO + H_2O \rightleftharpoons CO_2 + H_2 \quad (\Delta H = 41\,\mathrm{kJ\,mol^{-1}}). \tag{4.15}$$

The ethanol reforming (4.1) is endothermic and results in the increase of the number of moles. Increasing the temperature (Fig. 4.1) [13] and decreasing the pressure (Fig. 4.2) [14] is in favor of this reaction.

The thermodynamically predicted equilibrium conversion of ethanol in steam-reforming reaction is always 100%. Figure 4.1 shows the changes of the equilibrium product distribution with changing steam-reforming temperature. At low temperatures mostly methane and carbon dioxide occur, besides that a small amount of hydrogen and almost no carbon monoxide. When the steam-reforming temperature is raised the methane content decreases whereas the hydrogen content increases concurrently. Reasonable hydrogen concentrations can be achieved using steam-reforming temperatures of 823 K. At higher temperatures $T > 773$ K the carbon monoxide content is strongly increasing, which can be attributed to the thermodynamics of the reverse water–gas shift reaction (4.15). Increasing the steam-to-ethanol ratio moves the aforementioned temperature points to slightly moderate temperatures [13].

Fishtik et al. [15], Vasudeva et al. [16], and Rossi et al. [17] thermodynamically analyzed the ethanol steam reforming with the following products taken into consideration: CO_2, H_2, CO, CH_4, and CH_3CHO. The Gibbs free energy minimization method was employed. The equilibrium product distribution shows that the hydrogen

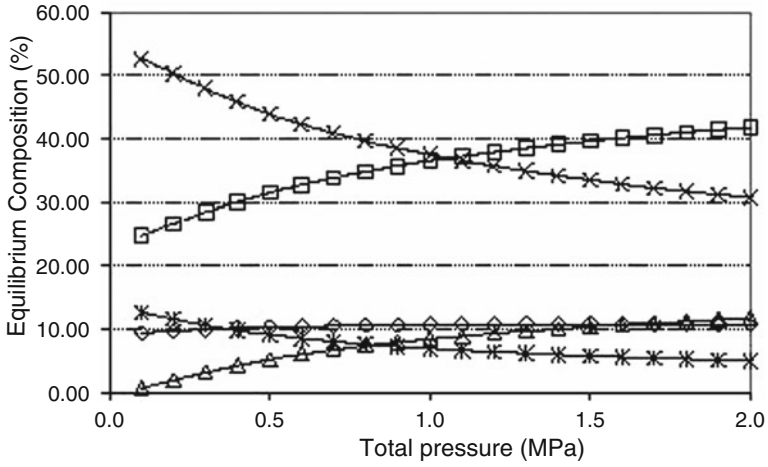

Fig. 4.2 Evolution of the equilibrium composition in H_2 (*crosses*), CO_2 (*diamond*), CO (*asterisk*), CH_4 (*triangle*), and H_2O (*square*) as a function of the total pressure in the ethanol steam reforming reaction at 973 K, the water/ethanol ratio was 4 [14]

yield increased and that of CO_2 and CH_4 decreased as a function of temperature. Unfortunately, at higher temperature the CO production also increased.

The impact of the total pressure on the thermodynamic equilibrium was also investigated [14]. It appears, as shown in Fig. 4.2, that an increase in the total pressure leads to the decrease in the hydrogen and carbon monoxide yields while the equilibrium composition in methane increases widely. Below 500 K the steam reforming of ethanol does not occur by reason of $\Delta G^{o} > 0$ [18]. On the other hand it is easy to carry out the decomposition of ethanol at the same temperature because the value of ΔG^{o} is sufficiently negative.

Vasudeva et al. [16] calculated the effect of water content on the equilibrium composition of the products of ethanol reforming at different temperatures. It was found that the conversion of ethanol was nearly complete (between 800 and 1,200 K with water/ethanol ratio 0:1–20:1) and only traces of acetaldehyde and ethylene were in the equilibrium mixture, mainly hydrogen, CO, and CO_2 were formed.

Garcia and Laborde found [19] that in the ethanol reforming, higher temperature and higher water–ethanol ratio are needed to obtain the best hydrogen production than in the methanol–water reaction. According to the calculation of the thermodynamic equilibrium they suggested to work at a temperature higher than 650 K, and to use in the feed a high water–ethanol ratio (10) to maximize the H_2 production, minimize the formation of CO and CH_4, and avoid the carbon deposition.

Ioannides reported [20] that the most important parameter that affects the efficiency in hydrogen production is the water/ethanol ratio of the feed. Using higher ratio than the stoichiometry results in reduced efficiency in hydrogen production because of increased enthalpy needed for water evaporation.

However, he found that the H_2 yield is nearly 100% at 1,000 K when the water to ethanol ratio is 5. The same results were obtained on the basis of their theoretical calculation by Freni et al. [21], they also suggested that a high water-to-ethanol ratio in the feed reduced the yield of CO and CH_4.

Mas et al. [22] concluded that ethanol is completely converted to ethylene and/or acetaldehyde. Taking into account the equilibrium constant values of formation and transformation reactions of ethylene and acetaldehyde, where both compounds are intermediates in this system. They concluded that while high temperature and high water–ethanol ratio favor H_2 production, low temperature and high water–ethanol ratio are suitable to minimize CO formation.

The carbon formation on different supported metal catalysts often results in activity decay. For example, the coke deposition on Ni/Al_2O_3 catalyst is the main cause of deactivation during ethanol steam reforming. The routes for carbon formation include Boudouard reaction (4.11), methane decomposition (4.16), polymerization of ethylene which could be produced on the acidic sites of the support [23, 24]. Thermodynamic analysis of it was done by minimization of Gibbs free energy as a function of temperature at various H_2O/C_2H_5OH ratios [25]. It was found that the graphitic carbon formation is unfavorable at higher H_2O/C_2H_5OH ratios and is maximized around 773–873 K. This behavior suggests that the endothermic reaction of CH_4 decomposition prevails at that temperature:

$$CH_4 \rightleftharpoons C + 2H_2 \quad \Delta H = 74\,\mathrm{kJ\,mol^{-1}}. \tag{4.16}$$

The carbon gasification and Boudouard reaction (4.11) maybe also important routes for carbon deposition or removal depending on the conditions applied

$$C + H_2O \rightleftharpoons CO + H_2 \quad \Delta H = 131\,\mathrm{kJ\,mol^{-1}}. \tag{4.17}$$

It can be observed that for H_2O/C_2H_5OH ratios above 3, the graphitic carbon deposition is practically zero above 600 K.

In a recent paper [26], not only graphitic but amorphous carbon and multiwall carbon nanotube formation was also taken into account in the considerations. In equilibrium, carbon deposits are formed when the steam/ethanol ratio is below 4. In this zone, temperature defines which carbon type is formed; below 673 K the presence of graphite dominates, while above 673 K multiwall carbon nanotube formation prevails. No amorphous carbon was obtained in equilibrium.

4.3 Comparison of the Activity of Different Catalysts in the Steam Reforming of Ethanol

The most important reaction pathways of ethanol steam reforming are summarized above, but the secondary reactions of the products are mentioned only briefly. It can be seen that the products and the hydrogen formation varies significantly with different pathways. However, each catalyst could induce different reactions and

therefore the selection of the suitable catalyst plays a vital role in ethanol steam reforming for hydrogen formation. An active and selective catalyst should maximize hydrogen or other product formation and inhibit the coke formation as well as the production of other undesirable compounds such as CO.

Supported metals are well known for their high catalytic activity and have been studied extensively in terms of ethanol steam reforming reactions.

Alumina-supported catalysts are very active at low temperatures in the dehydration of ethanol to ethylene but the formation of it decreased as the temperature increased, for example, on Rh/Al_2O_3 it disappeared above 923 K. Above this temperature ethanol is converted into H_2, CO, CO_2, and CH_4. The activity order of metals for hydrogen formation is Rh > Pd > Ni = Pt [27]. When ceria/zirconia was the support, ethylene formation was not observed and the order of activity at higher temperature was Pt ≥ Rh > Pd. Acetaldehyde formation was not detected either on alumina- or on ceria/zirconia-supported samples.

Auprêtre et al. [28] studied the effect of both the metal and the support in the steam reforming of bioethanol. They found that the hydrogen yield on alumina-supported metal catalysts decreased in the following order at 973 K: 9.7% Ni > 1% Rh > 0.5% Pd > 1% Pt > 9.1% Cu = 9.8% Zn > 0.67% Ru = 8.7% Fe. They concluded that the high activity of metals in the ethanol steam reforming and their poor efficiency in the water–gas shift reaction would give active and selective catalysts for ethanol reforming. In these works only the conversion or the hydrogen yield was compared, but both results depend on the number of surface metal atoms of the catalysts.

Liguras et al. [29] also found that among the low-loaded catalysts, Rh was significantly more active and selective toward hydrogen formation than Ru, Pt, and Pd, which show a similar behavior. The catalytic performance of Rh and, particularly, Ru was greatly improved by the increase of metal loading. It was shown that the catalytic activity and selectivity of highly loaded Ru catalysts were comparable to those of Rh. It was found that under certain reaction conditions the 5% Ru/Al_2O_3 catalyst is able to convert ethanol with selectivities toward hydrogen above 95%, the only by-product being methane [29]. Rh/MgO showed the best performance in the steam reforming of ethanol at 923 K in terms of activity and stability among the MgO-supported Pd, Rh, Ni, and Co catalysts, but it was not so selective toward hydrogen production [30]. Ni, Co, and Pd catalysts are affected by deactivation mainly due to metal sintering. Ni/MgO catalyst displays the best performance in hydrogen selectivity. Kinetic measurements revealed large differences in metal specific activities: Rh sites were 2.3, 3.7, and 5.8 times more active than Pd, Co, and Ni sites, respectively [30].

On alumina-supported noble metals mainly ethylene was formed under steady-state conditions, while on CeO_2-supported samples a significant amount of acetaldehyde was also detected at 723 K [31]. It was found that the selectivity of hydrogen formation decreased but that of ethylene increased in time while the conversion was stable on alumina-supported noble metals. The hydrogen selectivity was the highest on Ru/Al_2O_3, about 70%, and decreased in the order of Rh > Ir > Pd > Pt while the ethanol conversion was higher than 90% in all cases.

The activity order of alumina-supported noble metals was different than mentioned above in the temperature range of 573–723 K [32]. It has been found that the catalytic performance decreased in the Pt > Pd > Rh > Ru order, with Pt habiting high activity and selectivity toward hydrogen production as well as long-term stability. It was shown that the reaction occurs in a bifunctional manner with the participation of both the dispersed metallic phase and the support. The catalytic performance depends strongly on the nature of the dispersed metallic phase.

On CeO_2-supported noble metals the conversion considerably decreased in time at 723 K. The highest hydrogen selectivity was found on Rh/CeO_2, but it was not stable, it also decreased in time and that of acetaldehyde and ethylene increased [31].

The efficiency of the ceria-supported Co, Ir, and Ni was also studied in the ethanol steam reforming in the temperature range of 573–973 K. At low temperature, ethanol dehydrogenation to acetaldehyde and the decomposition to methane and carbon monoxide were the primary reactions [33]. At higher temperature where all the ethanol and other intermediate compounds like acetaldehyde were completely converted into hydrogen, carbon oxides and methane were the main products. The H_2 selectivity above 723 K was higher than 65% in all cases. It was found that above 723 K the ethanol converted completely. It seems that it contradicts to the above-mentioned results [31], but in these cases the space velocity was lower (6,000 mL $g^{-1}h^{-1}$) than in the previous ones. The long stability test revealed that Ir/CeO_2 showed rather stable catalytic performance for 300 h time-on-stream without any deactivation [33].

The ethanol reforming was studied on zirconia-supported Ni, Co, and Cu catalysts by Benito et al. [34]. The results show that Ni- and Co-supported zirconia exhibits high catalytic activity and stability. At 973 K, 100% ethanol conversion was achieved on these samples and the selectivity to hydrogen was close to 70%. On the other hand, on Cu/ZrO_2 ethanol dehydrogenation, i.e., acetaldehyde formation, occurred [34].

Similar behavior was observed on ZnO-supported Ni and Cu catalysts, but in the authors' interpretation these samples did not exhibit good catalytic performance in the ethanol steam reforming for hydrogen production [35]. On Ni/ZnO sample the total conversion was achieved at 623 K, probably ethanol decomposition occurred, while on Cu/ZnO the conversion was only about 82% at 723 K. The yield of hydrogen production improved over ZnO-supported, Na-promoted Ni–Co sample with respect to Co catalyst at low temperatures due to an increase of catalytic activity. No similar improvement was observed over a similar Co–Cu sample [35].

Rh- and Co-based catalyst performance was compared for steam reforming of ethanol under conditions suitable for industrial hydrogen production [36]. It was shown that Co/ZnO was much more selective to CO_2 and H_2 than Rh at 15 bar pressure. On Rh the CH_4 selectivity approaches the thermodynamic equilibrium. This observation was explained with different pathways that occurred on Co and Rh. In the previous case, the CH_4 is a secondary product formed through the methanation of CO and CO_2. In contrast, CH_4 was produced by direct decomposition on Rh [36].

Recently, papers appeared in which a combinatorial approach was used in the preparation of catalysts for ethanol steam reforming [37]. A number of catalysts based on Al_2O_3-loaded Ce–Zr mixed oxides doped with La, Pr, Sm, and different metal components Cu, Cu–Ni, Cu–Ni–Cr, Ru, Pt were used in the reaction. The results of the screening test show that the activity of the catalysts in terms of syngas yields decrease in the order: $RuCVS_{0.2}$ > $Cu–NiCZS_{0.2}$ > Cu–NiCZ > $Cu–Ni–CrCZP_{0.1}$ (where the abbreviations are the following: C means CeO_2; Z, ZrO_2; S, Sm; and P, Pr). Some correlations of the catalytic performance with the surface/lattice oxygen mobility and reactivity change due to the dopant nature and content were observed [37].

4.4 Reforming of Ethanol on Supported Noble Metal Catalysts

4.4.1 Supported Rh Catalysts

Noble metals such as Ru, Rh, Pd, Pt, Ir are well known for their high catalytic activity and have been studied extensively in terms of ethanol steam-reforming reactions. Earlier, it was shown that supported Ru and Rh exhibited the best performance in this reaction [27–31].

The ethanol steam reforming on Rh/Al_2O_3 was carried out at a programmed temperature from 323 to 923 K [38]. The reaction starts with the initial dehydrogenation and/or dehydration of ethanol followed by the rapid conversion of products into methane, carbon monoxide, and carbon dioxide. The acidic support assists the dehydration of alcohol while the other reactions are catalyzed by the metal, although to different extent. For this reason with the increase of Rh content, there is a progressive increase in the amount of C_1 products (CH_4, CO, CO_2) while the C_2 products (C_2H_4, CH_3CHO) disappear gradually from the outlet gas stream. The acetaldehyde is formed during an intermediate stage, but rapidly decomposes to CH_4 and CO at higher temperatures [38]. Cavallaro et al. found [39] that high temperature and relatively low space velocity are required to optimize the hydrogen production by steam reforming of bioethanol (water/ethanol ratio = 8.4) on 5% Rh/Al_2O_3. However, deactivation of the catalyst could be caused by the sintering of the metal and coke formation. It was found that the addition of a small amount of oxygen (0.4 vol%) in the fed gas resulted in a drastic decrease of the catalyst deactivation, but promoted the metal sintering [39].

Diagne et al. observed [40] that at 673–773 K, Rh supported on ZrO_2, CeO_2, and on CeO_2–ZrO_2 mixed oxide show high activity and selectivity toward hydrogen production (between 5 and 5.7 mol of H_2 per mol of ethanol inlet). The best catalysts were not necessarily the most basic samples but that which can bind CO_2 mildly. The results clearly show that the ethanol reforming on these catalysts does not appear to be sensitive to Rh dispersion.

On Rh/ZrO_2, the product distribution of the ethanol reforming depends on the acidic character of the support [41]. When the ethanol adsorption was strong—the relative strong Lewis acidic sites are responsible for it—the number of C_2 oxygenates were accumulated on the catalyst surface. When the ethanol adsorption was weak and the C–C bond breakage was the dominating reaction, CO, carbonates, and CH_x species accumulation was observed. Therefore, it was believed that in order to promote the adsorption of ethanol molecules and reduce the formation of C_2 oxygenates during the reaction, the catalyst should be enhanced both with Lewis acidity and with C–C bond breakage function. It was also found that in these cases, the Rh particle size and distribution as well as the surface area of the catalysts were not important factors in determining the catalytic performance [41]. This finding is in harmony with the earlier results [40].

The hydrogen formation was found to decrease in time on 1% Rh/Al_2O_3 at 723 K while the ethylene production increased [31]. At the beginning of the reaction the hydrogen selectivity was about 75% but after 2 h it was only 58%. The hydrogen selectivity increased and that of ethylene decreased as a function of temperature on 1% Rh/Al_2O_3 [27], and at 923 K it was higher than 70% [27, 29].

It was found [42] that at low temperature the support plays an important role in the ethanol steam reforming. Ethanol dehydration, the ethylene formation is favorable over either acidic or basic oxide such as γ-Al_2O_3- and $MgAl_2O_4$-supported Rh while ethanol dehydrogenation is occurred mainly over neutral supports. On zirconia-promoted ceria supports the reaction pathway favors an acetaldehyde intermediate. On 2% $Rh/Ce_{0.8}Zr_{0.2}O_2$ catalyst the hydrogen yield exceeding thermodynamic equilibrium can be achieved. The authors did not exclude a strong interaction between Rh and support, and the enhanced oxygen transfer efficiency plays an important role during ethanol steam reforming. Similar results were obtained when a series of Rh catalysts on various supports (Al_2O_3, $MgAl_2O_4$, ZrO_2, and ZrO_2–CeO_2) have been applied to H_2 production from the ethanol steam-reforming reaction [43]. In terms of ethanol conversion at low temperatures (below 723 K) with 1 wt% Rh catalysts, the activity decreases in the order: Rh/ZrO_2–CeO_2 > Rh/Al_2O_3 > $Rh/MgAl_2O_4$ > Rh/ZrO_2. The Rh/ZrO_2–CeO_2 catalyst exhibits the highest CO_2 selectivity up to 823 K, which is due to the highest water–gas shift activity at low temperatures. Among the catalysts evaluated in this study, the 2 wt% Rh/ZrO_2–CeO_2 catalyst exhibited the highest H_2 yield at 723 K, which is possibly due to the high oxygen storage capacity of ZrO_2–CeO_2 resulting in efficient transfer of mobile oxygen species from the H_2O molecule to the reaction intermediate.

Aupretre and his coworker [12] studied the reaction on $Mg_xNi_{1-x}Al_2O_4$-supported Rh at 973 K (H_2O/ethanol ratio = 4). It was stated that acidic and basic properties of the catalysts are crucial parameters inasmuch as they control the primary selectivity for ethylene or acetaldehyde. To avoid the ethylene formation which leads to a significant carbon deposit all acidic sites should be neutralized.

CeO_2 and ceria containing mixed oxides have also been widely used as support for Rh in the ethanol steam reforming. At 723 K a significant activity loss was measured on 1% Rh/CeO_2, the hydrogen formation was found to decrease with time, while that of acetaldehyde changed oppositely [31]. The effect of CeO_2

morphology on hydrogen selectivity was also studied in the ethanol steam reforming [44]. Three catalysts using CeO_2 nanorods, nanocubes, and irregular particles were prepared on alumina surface. The results indicated that all catalysts suffered a small deactivation during 24 h on stream at 1,073 K. The hydrogen selectivity when the support was the nanorods varied insignificantly, but in the presence of nanocubes the efficiency of the catalyst altered significantly. These results indicate clearly that CeO_2 nanoparticles with a specifically exposed surface affect the overall catalytic activity under working conditions. Why the catalyst with cubic CeO_2 showed the least activity after 24 h of reaction is unclear.

To improve the performances of the catalyst in the steam reforming of ethanol, ceria-containing supports with enhanced OH surface mobility were used as support [28]. Although at 873 K 1% Rh/Al_2O_3 showed the highest hydrogen selectivity while 1% Rh/CeO_2–ZrO_2 exhibited the highest yield in hydrogen. In descending order the following sequences was established for the yield: 1% $Rh/Ce_{0.63}Zr_{0.37}O_2$ > 1% Rh/12% CeO_2–Al_2O_3 > 1% Rh/CeO_2. These results were explained with a bifunctional mechanism; the activity of the catalyst in the steam reforming of ethanol increases as the OH groups mobility at the catalyst surface increases.

The CeO_2–ZrO_2 ratio was systematically varied to evaluate the effect of CeO_2/ZrO_2 ratio on ethanol steam reforming [45]. From the results it is clear that the $Rh/CeO_{0.8}ZrO_{0.2}O_2$ catalyst exhibits the highest hydrogen yield at 723 K. The ratio of H_2 formed/ethanol converted was 4.3 and the space velocity was 133,000 $cm^3/g_{catalyst}h$. At a lower temperature of 623 K this catalyst lost its activity; on the surface carbonaceous deposit was formed. To suppress the ethylene formation potassium (0.5%) was added to the $Rh/CeO_{0.8}ZrO_{0.2}O_2$ catalyst which has a beneficial effect on the catalyst stability, while 5% K reduce the activity.

Diagne et al. [46] also studied the ethanol reforming on a series of Rh/CeO_2–ZrO_2 catalysts. His XPS results indicate that the presence of Rh has resulted in partial reduction not only of CeO_2 but also ZrO_2. It was found that at the temperature range of 673–773 K all catalysts showed complete conversion of ethanol (H_2O/ethanol = 8) with high selectivity toward hydrogen formation, approaching the theoretical value (6 mol H_2 per mol of ethanol inlet). The effect of the support was mainly noticed on the CO_2/CO ratio.

Idriss and his coworkers studied the reaction over bimetallic CeO_2 catalysts (Rh and Pd or Pt) for the production of hydrogen [47–49]. They concluded that the reaction occurs at interface between Ce and metal ions. The presence of Rh atom is crucial for the reforming of ethanol since they initiate the terminal carbon–hydrogen bond dissociation, and thus favoring the formation of the possible oxametallacycle intermediate needed for further interaction with the surface and dissociation of the carbon–carbon bond. The high activity of the bimetallic catalysts is linked to the presence of the two metals with two different properties. Rh for breaking the carbon–carbon bond and Pd for the water–gas shift reaction and hydrogen recombination reaction.

4.4.2 Supported Pt Catalysts

The supported Pt catalysts belong to the most active and selective catalysts in the ethanol steam reforming according to different comparative studies, so the efficiency of it and the effect of the support on the Pt were investigated in detail. The reaction was studied on 1% Pt/Al_2O_3 at 723 K (H_2O/ethanol ratio was 3) and it was found that while the selectivity of hydrogen decreased in time, the formation of ethylene increased parallel to it but the ethanol conversion was higher than 95% [50]. This trend was attenuated by increasing water concentration, metal loading, and reaction temperature. At 923 K the hydrogen selectivity was about 80%. It was assumed that this behavior of Pt/Al_2O_3 in the ethanol + water reaction can be attributed to the formation of surface acetate groups which was detected during the reaction by means of DRIFT [51] and these species hindered the reaction on the metal, although these species were located rather on the support. When the catalyst was doped with potassium the decrease in the hydrogen selectivity was lower, the ethylene formation was strongly diminished but in these cases significant amount of methane was formed. It was proved that the K had a destabilizing effect onto the surface acetate groups and thus improved the steam-reforming activity of 1% Pt/Al_2O_3 [51]. The drastic changes of the hydrogen and ethylene selectivities on Pt/Al_2O_3 were also found by Sanchez-Sanchez et al. [52]. When bimetallic $PtNi/Al_2O_3$ was used, higher activity toward hydrogen and C_1 products formation was obtained than on the monometallic counterparts. The improvement in the catalytic performance was associated with higher activity in the gasification of methyl groups formed in the decomposition of acetate species [52].

Using Al_2O_3–ZrO_2 mixed oxide as support the decay in the selectivity of H_2 and CO_2 caused by the surface acetate species on Pt/Al_2O_3 decreased, while the zirconia destabilized the surface acetate groups. The highest turnover rate and yield was found on Pt/Al_2O_3–ZrO_2 (1:3) [53]. Breen et al. found that Pt/Al_2O_3 showed very poor activity in hydrogen formation; in these cases mainly ethylene was formed [27]. When CeO_2–ZrO_2 was the support a small amount of methane and no ethylene were detected above 823 K. These results also show that the alumina support can play an important role by the dehydration of ethanol to ethylene even at low temperature. Contrary with it, much higher hydrogen selectivity was found on Pt/Al_2O_3 above 700 K and the C_2H_4 selectivity was below 5%. It has to be noted that the γ-Al_2O_3 used in these experiments as support has only negligible catalytic effect under the same experimental conditions [29].

Navarro et al. [54] studied the oxidative steam reforming of ethanol on Pt/Al_2O_3 modified by Ce and La. The presence of Ce was beneficial for hydrogen production. The presence of La, however, did not promote conversion.

4.4.3 Supported Pd, Ru, and Ir Catalysts

Goula et al. [55] studied the steam reforming of ethanol over commercial Pd/Al_2O_3 and reported 95% selectivity to hydrogen at 923 K. Ethanol conversion was 100%

even at lower temperatures (573–623 K), and the H_2/CO molar ratio was maximal at about 723 K. The amount of coke formed was negligible even at stoichiometric water to ethanol ratios [56]. Frusteri et al. [30], however, observed that the Pd/MgO catalyst drastically deactivated during the reaction at 923 K due to the metal sintering. Coke formation on Pd/MgO occurred at a higher rate than on MgO-supported Rh, Ni, or Co catalysts.

Liguras et al. [29] studied Ru-catalyzed steam reforming of ethanol in the temperature range of 873–1,123 K. The catalytic performance significantly improved with increasing metal loading; the 5% Ru/Al_2O_3 sample showed almost 100% selectivity toward hydrogen around 1,070 K. Vaidya and Rodrigues [57] performed detailed kinetic investigation in the steam reforming of ethanol on Ru/Al_2O_3 catalyst in the temperature range of 873–973 K (see later). They found that the higher the extent of ethanol conversion, the higher is the relative yield of hydrogen. The investigation of the effect of space time on the hydrogen yield at 973 K shows that when the space time increased from 0.68 to 2.04 g h mol^{-1}, the hydrogen yield increased from 0.27 to 0.41 mol/mol.

Alumina-supported monometallic Ru and bimetallic Ru–Pt nanoparticles derived from different organometallic cluster precursors (such as $[HRu_3(CO)_{11}]^-$, $Ru_3(CO)_{12}$, and $[Ru_5PtC(CO)_{15}]^{2-}$) were found to be highly efficient ethanol steam-reforming catalysts [58, 59]. The high catalytic efficiency of the cluster-derived catalysts is attributed to the very small size of the metallic nanoparticles. Although all three types of catalysts exhibit similar activity and selectivity, it appears that the presence of Pt might help promote water–gas shift reaction at low temperatures, while ethanol C–C bond cleavage also appears to be facilitated over the bimetallic cluster-derived catalysts.

Ir supported on Al_2O_3 or on CeO_2 was not the best catalyst among the noble metals [31], but Ir/CeO_2 showed rather stable catalytic performance for 300 h time-on-stream without any deactivation [33]. The strong interaction between Ir and CeO_2 effectively prevented the sintering of highly dispersed Ir particles and facilitated coke gasification through the high oxygen storage capacity of ceria [33]. Similar results were found by Cai et al. [60]; the Ir/CeO_2 has a stable activity at 823–923 K with no apparent deactivation. Structural analysis of the used catalysts indicates that the 2–6 nm Ir particles remained highly dispersed on the enlarged ceria particles.

4.5 Reforming of Ethanol on Supported Transition Metal Catalysts

Besides noble metal-based systems the reforming of ethanol occurs with high hydrogen selectivity over supported Ni and Co catalysts, and the reaction has also been studied extensively on these samples.

4.5.1 Supported Ni Catalysts

The steam reforming of ethanol was investigated over La_2O_3, Al_2O_3, YSZ, and MgO-supported Ni catalysts [61]. The hydrogen selectivity at 1,023 K was higher than 80% in all cases. The Ni/La_2O_3 was the most selective toward H_2 and this sample was very stable for almost 100 h on stream. The enhanced stability of this catalyst may be due to scavenging of coke deposition on the Ni surface by lanthanum oxycarbonate species which exist on top of Ni particles under reaction conditions [61].

The conversion and H_2 yield increased on Ni/Al_2O_3 catalysts produced from Ni (II)–Al(III) lamellar double hydroxide (LDH) precursor, when temperature or contact time increased [62, 63]. When the ethanol conversion approached 100% the hydrogen yield approximates. It means that the products were only H_2, CO, CO_2, and traces of CH_4. It was found that the ethanol conversion has maxima as a function of water concentration either at 989 or 923 K. This means that both water and ethanol are competitively adsorbed on the same type of active site.

Contrary with it significant deactivation was observed on Ni/α–Al_2O_3 at 1,173 K, since huge amount of carbon deposit was observed [64]. Similar results were found on Ni/γ-Al_2O_3 [65], this catalyst presents high activity and selectivity toward hydrogen production at elevated temperature, but as temperature is reduced a significant amount of ethylene appeared in the gas phase. This results in rapid carbon accumulation on the catalyst and in loss of its reforming activity. Impregnation of Al_2O_3 with La_2O_3 significantly reduced the rate of carbon formation [65].

The modification of alumina-supported Ni catalyst with Ce, Mg, Zr, and La affect the acidity of the catalyst, structure, and morphology of Ni particles and influenced their reforming activity [66]. The higher efficiency of Mg-modified catalyst was explained in terms of the lower acidity and better dispersion, while for Ce- and Zr-promoted catalysts the improvement in intrinsic activity was ascribed to the enhancement of water adsorption/dissociation on the Ni–Ce and Ni–Zr interfaces. On the other hand, the lower activity of La-added catalyst was explained in terms of the dilution effect caused by the presence of lanthanum on Ni surface [66]. It was found that the Ce and La additives prevent formation of carbon filaments on Ni surfaces, which is responsible for the changes in product selectivities observed in other cases.

In spite of this observation, Ni supported on La_2O_3 exhibited the highest activity and selectivity toward hydrogen and, most important, long-term stability for steam reforming of ethanol comparing the efficiency of La_2O_3, Al_2O_3, YSZ, and MgO-supported Ni catalysts [61, 65, 67]. The enhanced stability of these catalysts as mentioned above may be due to scavenging of coke deposition on the Ni surface by lanthanum oxycarbonate species, which exist on top of the Ni particles under reaction condition.

Comparing the activity of Ni/La_2O_3, Ni/Y_2O_3, and Ni/Al_2O_3 [68], it was found that the catalytic activity and selectivity of hydrogen formation decreased in the above-mentioned order which is consistent with the order of the activation energy and crystal grain size of the catalysts. The ethanol conversion at 523 K was 80.7%

and the hydrogen selectivity was 49.5% but at 593 K these values were 99.5 and 48.5%, respectively, on Ni/La_2O_3 catalyst. Other authors found that on Ni/La_2O_3 catalyst formed from $LaNiO_3$ perovskite-type oxide, the initial ethanol conversion at 700 K with H_2O/ethanol ratio of 2 was around 100% but significantly decreased after 6 h. When the H_2O/ethanol ratio was higher the ethanol conversion remained stable, but the deactivation begins later. Catalyst deactivation occurs from the deposition of carbon on the surface. Lower reaction temperature and lower H_2O/ethanol ratios favor the deposition of filamentous carbon. Addition of O_2 to the feed significantly improved catalyst stability, less carbon formation occurred. Similar observation was found in the case of $Ni–Cu/SiO_2$ catalyst, the introduction of higher amount of O_2 during the oxidative steam reforming of ethanol increased the stability of the catalyst [69].

Hydrogen production in the steam reforming of ethanol over $MgAl_2O_4$-supported catalysts has been investigated applying combinatorial and high-throughput approaches [70]. It has been revealed that practically no noble metal is required to achieve high hydrogen yield. At 773 K, a four component catalyst containing Ni, Co, Ce, and Mo has resulted in 4.4 mol hydrogen per mol of ethanol. Its advantage is the strong suppression of the formation of carbonaceous deposit. In this system Ni is considered as the active metal, while Co, Ce, and Mo are promoters.

4.5.2 Supported Co Catalysts

Cobalt is another non-noble metal catalyst which is active and selective for hydrogen formation in the ethanol reforming while Co could break the C–C bond [71]. Earlier, Co-based catalysts were deemed as appropriate systems for steam reforming of ethanol. The reaction occurred to a large degree over ZnO-, La_2O_3-, Sm_2O_3-, and CeO_2-supported Co catalysts; CO-free hydrogen was produced [72]. Depending on the support different cobalt-based phases were identified: metallic Co particles, Co_2C, CoO, and when La_2O_3 was the support, La_2CoO_4. The extent and the nature of carbon deposition depended on the catalyst and on the temperature. The ZnO-supported sample showed the best catalytic performance. Only a bit less than 100% ethanol conversion at 723 K and selectivity up to 73.8% for H_2 and 24.2% for CO_2 was obtained [72]. Llorca et al. [73] proposed ZnO-supported Co catalysts for steam reforming of ethanol. The use of $Co(CO)_8$ as precursor produced a highly stable catalyst that enabled the production of CO-free H_2 at low temperatures (623 K). They concluded that the method of catalyst preparation affected its performance and structural characteristics. It was stated that acetaldehyde is the primary product of the reaction and the cobalt catalyzes the reforming of acetaldehyde via the C–C bond scission of bidentate acetate species. Acetone is also produced on Co/ZnO probably on the surface of the support [71]. The sodium addition to the Co–ZnO-based catalyst has a positive effect on the steam reforming of ethanol [74]. Under total conversion in the 623–723 K temperature range the hydrogen production increased by about 5–8%.

Haga et al. found that the supports vastly influenced the properties of Co catalysts [18]. The formation of H_2 decreased in the order: $Co/Al_2O_3 > Co/ZrO_2 > Co/MgO > Co/SiO_2 > Co/C$. The Co/Al_2O_3 catalyst exhibited the highest selectivity to H_2 (67% at 673 K) by suppressing methanation of CO and decomposition of ethanol. Cavallaro et al. [75] found that Co/MgO is more resistant to coke formation than Co/Al_2O_3 at 923 K. Batista et al. [76] studied the reaction on the same catalysts and found that after reduction of the samples at 673 K CoO_x species remained on the surface. The average conversion was higher than 70% at 673 K. The metal loading influenced ethanol conversion and product distribution. CO produced in the ethanol reformation can react with water or H_2 on Co sites. Both reactions show high conversion on Co/Al_2O_3 and on Co/SiO_2, but Co/Al_2O_3 has higher efficiency in CO removal [76].

The auto-thermal reforming of ethanol was studied on iron-promoted Co/Al_2O_3 [77]. In this process, oxygen was also introduced in the feed and thus included in the endothermic steam-reforming process as well as the exothermic oxidation process can be a self-sustaining heat process controlled through the oxygen ratio in the feed. The iron-promoted Co-based catalysts show higher activity and better stability than the unpromoted samples [77]. The better performance was attributed to the effect of iron which results in more Co metal on the surface and which remains stable during the oxidative atmosphere of auto-thermal reforming. The authors suppose that iron promotes the ethanol dehydrogenation too. The hydrogen yield remains around 3.13 mol H_2/mol ethanol at 873 K and stays stable in a 30 h test.

Various supported Co catalysts were characterized by in situ magnetic measurements under ethanol steam-reforming reaction [78]. The catalyst that performed well in the reaction presented metallic cobalt particles and oxidized cobalt species. An easy exchange between small metallic cobalt particles and oxidized Co species was found in the reaction. In contrast to this study Batista et al. [76] suggested that only Co^0 sites are active for the steam reforming of ethanol. The metallic cobalt sites were also found to correlate with the catalytic activity. The reaction and H_2 chemisorption showed that ZrO_2-supported catalyst has the best dispersion and best catalytic activity. Over the 10%-Co/ZrO_2 catalyst, using a H_2O:ethanol:inert molar ratio of 10:1:75 and a GHSV = 5,000 h^{-1}, 100% ethanol conversion and a yield of 5.5 mol H_2/mol ethanol were obtained at 823 K and atmospheric pressure [79].

The hydrogen selectivity and product distribution were found to be dependent on the preparation method and the nature of the support used [80]. On Co/SiO_2 prepared by sol–gel method and Co/Al_2O_3 made by impregnation the maximum hydrogen selectivity at 753 K was ca. 62 and 67%, respectively. With sol–gel silica-based catalysts methane formation was drastically decreased while acetaldehyde production was increased.

Sahoo et al. found that 15%-Co/Al_2O_3 prepared by wet impregnation has the best efficiency for ethanol steam reforming, the 10- and 20%-Co/Al_2O_3 samples deactivated rapidly [81]. The H_2 concentration was maximum at 773 K when the water/ethanol ratio was 3 and the contact time was 17 kg cat/(mol/s). Above 773 K, the ethanol decomposition reaction is favored, which decreases the hydrogen selectivity and increases the CO and CH_4 evolution [81].

Profeti et al. on noble metal-promoted Co/Al_2O_3 studied the ethanol reforming [82]. The results showed that the promoting effect of noble metals included a marked decrease of reduction temperature of both Co_3O_4 and cobalt surface species interacting with support due to the hydrogen spillover. Better catalytic performance for ethanol steam reforming at 673 K was obtained for $CoRu/Al_2O_3$ catalyst, which presented the highest H_2 selectivity (69% instead of 56%) and the reasonably low CO formation (5% instead of 8%) [82].

The effect of the nature of the cobalt precursor used in the catalysts synthesis was also investigated [73, 83, 84]. It was concluded that any parameter that would give a higher Co dispersion is likely to improve the catalytic performance [74, 84]. Although it was stated that the product composition depends on the starting material of the Co the differences in the results are not higher than 10%, though in the crystal size there are triple differences. The highest CO_2 selectivity (94.6%) was obtained at 723 K on Co/CeO_2 when the catalyst was prepared from cobalt acetyl acetonate [83]. The authors supposed that the organic ligand bound to the cobalt species might facilitate its dispersion on the surface of the CeO_2 support, resulting in the improved activity.

The effect of the preparation method on the catalytic effect of the CeO_2-supported Co catalysts was recently reported [85, 86]. The Co/CeO_2 prepared in ethanol medium showed significant improvement in catalytic performance (higher H_2 yield, higher stability, and fewer side reactions) compared to the ones prepared in aqueous media. Characterization results showed the presence of oxygenated carbon species possibly metal-coordinated acetate on the surface. These species are likely to play a role in the improved performance. Although the nature of this role is not clear, possibilities include a segregation effect that prevents sintering, a site-blocking effect that suppresses the side reactions or an "imprinting effect" that makes it easier for the acetate intermediates to form on the surface.

In the physical properties of $Co/ZrO_2–CeO_2$ samples there were no significant differences when the samples were prepared either by impregnation or by co-precipitation. The impregnated samples show the highest catalytic activity for hydrogen production [86]. The authors supposed that the different preparation conditions resulted in differences in the metal-support interaction which influenced the reduction behavior of $Co/ZrO_2–CeO_2$ catalysts; a stronger interaction suppresses the reduction of cobalt species. They supposed that under the ethanol steam-reforming conditions at 723 K, the interaction between this partially reduced cobalt and $ZrO_2–CeO_2$ species over the impregnated sample leads to the formation of unidentified active sites [86].

The effect of the oxygen mobility of the support on the steam reforming of ethanol was investigated on ZrO_2- and CeO_2-supported cobalt catalysts [87]. On 10%-Co/ZrO_2 sample at 723 K significant deactivation was observed through the deposition of carbon on the surface mostly in the form of carbon fibers. The addition of ceria appears to improve the catalyst stability due to its high oxygen storage capacity and high oxygen mobility allowing gasification and/or oxidation of deposited carbon as soon as it forms [87]. The insertion of ZrO_2 into CeO_2 structure has been found to enhance the redox properties and the thermal stability of CeO_2.

Vargas et al. [88] examined fluorite type Ce–Zr–Co as a catalyst for ethanol steam reforming. They found that after in situ controlled partial reduction of the catalysts at 713 K a part of the Co was reduced into nanoparticles of Co^0, which were active and selective for reactions at 713 K while with the further increase in reaction temperature (813 K) catalysts underwent a deeper reduction, leading to deactivation.

The insertion of a small amount of noble metal Rh in this ceria–zirconia fluorite structure doped with cobalt does not improve the hydrogen production but increases 30 times the lifetime of the catalyst [89]. It was found that the deactivation process of the catalyst is related not only to the carbon deposit but also to carbonate species which can form in acetaldehyde reaction sequence. The beneficial effect of Rh could be ascribed to its ability to avoid carbonate formation by preventing the blocking of active oxygen vacancies of the mixed oxide support.

4.6 Reforming of Ethanol on Supported Cu-Containing Catalysts

The first papers which reported on the decomposition and reforming of ethanol over different supported copper catalysts were published 20 years ago. In the ethanol decomposition at 493 K at 50% conversion mainly dehydration occurred and acetaldehyde was formed. The selectivity of it was between 77.9% on Cu/SiO_2 and 54.1% on Cu/Al_2O_3. Beyond that Cu/ZrO_2 and Cu/ZnO were highly selective for ethyl acetate formation; C_4 species and diethyl ether were produced over Cu/Al_2O_3 [90].

In the steam reforming of ethanol over copper-based catalysts at 523 K and at 80% conversion, acetic acid formed (S% of CH_3COOH on Cu/ZnO was 38%) together with the products of dehydrogenation and ethyl acetate [90].

Cavallaro and Freni [91] studied the ethanol reforming on $CuO/ZnO/Al_2O_3$ mixed oxide catalyst, showing that the main products, CO, CO_2, and H_2 formed above 623 K. Furthermore, $CuO/ZnO/Al_2O_3$ and $NiO/CuO/SiO_2$ catalysts did not produce appreciable quantities of coke and/or unexpected oxygenated by-products even with H_2O/ethanol ratios lower than 3 [91].

The Cu/Nb_2O_5 catalyst presents as high conversion as Ni/Al_2O_3 catalyst for the steam reforming of ethanol [92]; however, the formation of hydrogen at the same level occurs at much lower temperature, 473 K. It is important that there is little formation of CO on the Cu/Nb_2O_5 compared to the Ni/Al_2O_3, which can be attributed to the strong interaction between the metal and the support. Similar behavior was observed by Alonso et al. [93] on this catalyst. Promotion with Pd or Ru improved the catalytic performance for hydrogen formation and the resistance to deactivation.

Cu/ZnO was a relatively poor catalyst in the ethanol reforming [35]. Below 723 K ethanol conversion was less than 20% and mainly the dehydrogenation of

ethanol occurred, and acetaldehyde was formed. No significant improvement was observed over bimetallic Cu–Co or Cu–Ni catalysts.

Ethyl acetate and acetic acid formation was observed on different supported Cu catalysts. The selectivities to ethyl acetate and acetic acid markedly depended upon the support used [90]. The highest selectivities for which acetaldehyde formation (77.9%) was found on Cu/SiO_2 and that of ethyl acetate (28.1%) was on Cu/ZnO at 493 K. Acetaldehyde was formed by the dehydrogenation of ethanol which transformed to either ethyl acetate or acetic acid through steps in which a nucleophilic addition of ethanol (or ethoxy species) or water (or hydroxide group) to acetaldehyde occurred.

The steam reforming of ethanol on Cu/CeO_2 produces at 533 K mainly acetaldehyde and hydrogen but at higher temperature, 653 K, acetone was the main product [94]. The formation of hydrogen accompanied by the production of acetone was considered to proceed through the following consecutive reactions: dehydrogenation of ethanol to acetaldehyde, aldol condensation of acetaldehyde and the reaction of the aldol with the lattice oxygen of the support to form a surface intermediate followed by its dehydrogenation and decarboxylation. Ceria played an important role in this reaction as an oxygen supplier. Since the aldol condensation is promoted by bases the Cu/CeO_2 catalyst was promoted with MgO. Larger amounts of acetone and hydrogen were produced at lower temperature compared with the un-promoted sample [94].

Copper is frequently used as catalyst in the steam reforming of ethanol in bimetallic systems while this metal is active in the reforming of methane and CO which could be produced in one of the first steps of ethanol conversion.

The Ni–Cu system was studied in detail in this reaction. Unsupported Ni–Cu [95] was used as catalyst in the ethanol steam reforming while the acidic and/or basic character of the support could influence the reaction. It was found that this sample was active and stable for the steam reforming of ethanol even at a stoichiometric feed composition. Ethanol and the reaction intermediates were entirely reformed into hydrogen and C_1 products at 673 K; CH_4 steam reforming and reverse water–gas shift became the major reactions at higher temperature. The Ni–Cu catalyst exhibited stable performance at 923 K without apparent deactivation. Condensed carbon was deposited on the Ni–Cu surface probably through the decomposition of methane formed during ethanol steam reforming.

Ni–Cu catalysts were prepared as supported on single oxide [35, 96], on oxide mixtures [97, 98], or on samples which are promoted with different other materials [99, 100].

Neither copper nor nickel alone supported on ZnO appears as appropriate catalysts for the steam reforming of ethanol under the desired low temperature (below 723 K) for hydrogen production. Over the copper sample dehydrogenation of ethanol into acetaldehyde occurs, but the reforming reaction does not further progress significantly into H_2 and CO. On the other hand, over the nickel sample the decomposition reaction of ethanol to CH_4 and CO_x is favored [35]. The yield of H_2 production is improved over ZnO-supported, Na-promoted Co–Ni sample with respect to Co catalyst at low temperature due to an increase of catalytic activity. No significant improvement was observed over a similar Co–Cu sample [35]. The reforming and the oxidative

reforming of ethanol were studied on silica-supported Ni–Cu catalysts [69, 96, 101]. This sample shows high activity and selectivity toward H_2 production in contrast to Ni/SiO_2 catalyst that deactivates rapidly due to coke deposition [69]. It was stated that generally the hydrogen selectivity increases with increasing reaction temperature, and decreases with decreasing the ratio of H_2O/ethanol in the feed. Introduction of oxygen favors the production of hydrogen, while limits the formation of methane and carbon deposition [96].

The effect of Mg and Ca incorporation into CuNi/SBA-15 for hydrogen production by ethanol steam reforming was also studied [102]. The Ca or Mg additives strengthened the interaction between the support and the Cu–Ni phase and reduced the metallic particle size. Both promoting effects of Mg and Ca lead to a better catalytic behavior of CuNi/SBA-15 catalyst. In the ethanol steam reforming at 873 K all the catalysts reached the complete ethanol conversion, but on the promoted sample the hydrogen selectivity was higher, about 80%, and lower CH_4, and acetaldehyde selectivity and lower coke deposition were observed [102].

The effect of additives on the $Cu–Ni/Al_2O_3$ catalyst was also studied [99, 100, 103, 104]. The gasification of ethanol was investigated on K-promoted $Cu–Ni/Al_2O_3$. The catalytic behavior of the samples strongly depends on the conditions of the thermal treatments. Thus, the increase of the calcination temperatures of the precursors produces a strong interaction between nickel and aluminum, decreasing the nickel reducibility and selectivity to C_1 compounds [104]. $Cu–Ni–K/\gamma\text{-}Al_2O_3$ catalysts are suitable for the ethanol reforming since these samples are able to produce acceptable amounts of hydrogen working at atmospheric pressure and at 573 K [103]. Increasing the nickel content enhances ethanol gasification increasing the gas yield and reducing acetaldehyde and acetic acid production [103].

Ni–Cu-based bimetallic catalyst supported on $Al_2O_3–M_yO_z$ (M = Si, La, Mg, or Zn) were prepared to study the effect of the composite support on the catalytic performance in the steam reforming of ethanol [100]. The catalysts supported on Al_2O_3–MgO and Al_2O_3–ZnO have much higher H_2 selectivity than on $Al_2O_3–SiO_2$. For 30% Ni–5% Cu/Al_2O_3–MgO catalyst the H_2 selectivity was 73.3% at 723 K and increased to 94% at 973 K. On 30% Ni–5% Cu/Al_2O_3–ZnO catalyst the H_2 selectivity was 63.6% at 723 K and increased to 95.2% at 873 K [100].

A series of CuNiZnAl multicomponent mixed oxide catalysts with various Cu/Ni ratio were used in the oxidative steam reforming of ethanol [98]. Dehydrogenation of ethanol to acetaldehyde is favored by Cu-rich catalyst. Introduction of Ni leads to C–C bond rupture and production of CO, CO_2, and CH_4. H_2 yield varied between 2.6 and 3 mol/mol of ethanol converted (50–55%) for all catalysts at 573 K.

Ethanol steam reforming was studied over a mixed oxide CuCoZnAl with potassium additives [105]. The preparation method led to the formation of spinel matrix mainly $ZnAl_2O_4$ with high dispersion of oxidized species of Cu and Co. At 873 K the H_2 yield was 5.2 mol H_2 per mol ethanol fed and the activity was stable. Although the extent of sintering of metal particles of Cu and Co was high at this temperature, the sintering does not contribute in an important way to the deactivation phenomenon.

4.7 The Effect of Oxides and Carbides on the Conversion of Ethanol

The nature of the support strongly influenced the activity, the product distribution, and the stability of the catalysts during the ethanol reforming.

In spite of their lower activity related to supported metal catalysts, metal oxides are also able to catalyze the ethanol decomposition and the ethanol reforming depending on the reaction conditions used. We think it is important to discuss the effect of the support separately, because it is very difficult to distinguish the efficiency of it from the effect of the metal in the case of supported metal catalysts.

It is well known for a long time that ethanol is dehydrogenated on alumina surface producing ethylene and diethyl ether [23]. Llorca et al. report [106] the behavior of several oxides with wide range of redox and acid–base properties in the steam reforming of ethanol in the temperature range of 573–723 K and 5,000 h^{-1} space velocity. The temperature required for total conversion was lower for V_2O_5 and Al_2O_3 (623 K) than for the other oxides, and even at 723 K a conversion of $<10\%$ were obtained on MgO and SiO_2 and it was about 20% over La_2O_3 and CeO_2. In the case of TiO_2 and Sm_2O_3 significant deactivation was observed. Negligible steam reforming of ethanol occurred over MgO and Al_2O_3. In the previous case, ethanol dehydrogenation and acetaldehyde formation and in the latter case dehydration and ethylene formation occurred. The product distribution for the other oxides indicates that the steam reforming of ethanol took place but in some cases dehydration and dehydrogenation also occurred. On ZnO [106] and on CeO_2 [94] in the decomposition of ethanol after different successive reactions such as dehydrogenation, aldol condensation, decarboxylation, significant amount of acetone was also formed. In contrast to it, over CeO_2 at 1,173 K the main products in the steam reforming of ethanol were H_2 (with the selectivity of 67.5%), CH_4, CO, and CO_2 [64]. Pure ZrO_2 [41] resulted in higher hydrogen production yield compared to the ZrO_2 decorated with CeO_2, Al_2O_3, La_2O_3, or Li_2O at 573 K, but above 723 K all samples exhibited similar activity.

Nb_2O_5 presented good initial activity for hydrogen production at 573 K but fast deactivation was observed; mainly the dehydrogenation of ethanol occurred [93].

Tungsten oxides–carbides supported on alumina was also studied in ethanol steam reforming. The aim of this work was preparing new and inexpensive supported catalysts [91], but unfortunately the reaction rate was one order of magnitude less at 903–973 K than on $CuO/ZnO/Al_2O_3$.

In spite of this, Mo_2C [107] and supported Mo_2C [108, 109] are effective catalysts for hydrogen production in the decomposition of ethanol; the extent of the reaction approached 100% even at 623–673 K on Mo_2C deposited on silica. Besides H_2 several C-containing compounds were produced, which caused the low yield of hydrogen. Mo_2C prepared on carbon nanotube or on carbon (Norit), however, dramatically altered the product distribution. The formation of H_2 came into prominence; about 40% of H_2 content of ethanol decomposed at 523–723 K has been converted into gaseous H_2. Adding water to ethanol further enhanced the hydrogen production [108, 109].

4.8 Kinetic Study of Ethanol Reforming

Kinetic studies of ethanol reforming demonstrated that not only Langmuir–Hinshelwood model but also the Eley–Rideal-like model distributed to the reaction rate depends on the catalysts, the temperature, and the ethanol water ratio.

Works related to ethanol steam reforming kinetics are scarce. Some kinetic studies have been published in which power law, the Eley–Rideal-like model, and the Langmuir–Hinshelwood model kinetic expressions are reported [57, 68, 81, 110]. Vaidya and Rodrigues [57] studied the ethanol steam reforming over a Ru/γ-Al_2O_3 catalyst in the temperature range of 873–973 K. Their results showed that the reaction order with respect to ethanol was one. The rate expression was based on the assumption that the decomposition of an activated complex formed during the reaction into intermediate products was the rate-determining step.

Morgenstern and Fornango [111] also studied the reaction at low temperatures (523–573 K) using a copper–nickel catalyst with a Raney-type structure. They suggested that the kinetics fitted to a two-step model in which ethanol was dehydrogenated to acetaldehyde in a first-order reaction followed by the decarbonylation of acetaldehyde, which was also first order.

Sun et al. [68] studied the ethanol steam reforming in 523–623 K temperature range using three nano-sized nickel catalysts: Ni/Y_2O_3, Ni/La_2O_3, and Ni/Al_2O_3. The authors found that the Ni/La_2O_3 catalysts exhibited relatively high activity. They proposed a first-order reaction with respect to ethanol and estimated activation energy values for the three catalysts used.

Akande et al. studied the reforming of crude ethanol on 15% Ni/Al_2O_3 [110, 112] in the temperature range of 569–793 K. A kinetic model was set up [110] for hydrogen production. This was an Eley–Rideal-type rate model based on the assumption of dissociative adsorption of ethanol on active sites as the rate-determining step. The model was of the form

$$r_A = \frac{\left(2.08 \times 10^3 \, e^{4{,}430/RT} N_A\right)}{\left(1 + 3.83 \times 10^7 N_A\right)^2},$$

where r_A is the rate of ethanol conversion and N_A is the molar flow rate of ethanol. The kinetics model agreed well with the empirical power low rate model [110].

Mas et al. [62] proposed two kinetic models using Langmuir–Hinshelwood approach for ethanol reforming on Ni-based catalysts. The first was a general model including four reactions, two of them corresponding to ethanol steam reforming and the other two to methane steam reforming. When high temperatures and/or high water ethanol ratio were used the system could be reduced to two ethanol steam reforming reactions.

On Ni–Al LDH catalyst the ethanol order was found to be lower than one (0.75–0.8). His results revealed the existence of competition between ethanol, water, and methane to be adsorbed on the same type of active sites [63].

Table 4.1 Activation energies of the ethanol reforming on different catalysts

Catalyst	Temperature range (K)	E_a (kJ/mol)	References
$Ru/\gamma\text{-}Al_2O_3$	873–973	96	[57]
Cu–Ni Raney type	523–573	149	[111]
Ni-based commercial catalyst	673–863	59.7	[114]
Ni–Al LDH	823–923	144	[63]
Ni/Al_2O_3	823–923	112.9	[62]
Rh/Pt on ceramic		85	[115]
Co/Al_2O_3	673–973	82.7	[81]
Pt/CeO_2	573–723	18	[113]
Ni/Al_2O_3		16.88	[68]
Ni/Y_2O_3		7.04	[68]
Ni/La_2O_3		1.87	[68]

Ciambelli et al. studied the reaction on Pt/CeO_2 catalyst [113]. It was found that the ethanol conversion is almost constant for a particle size ranging from 50 to about 400 μm, indicating that the reaction rate is not limited by internal diffusion resistance in this range. An empirical power function rate equation has been proposed and apparent reaction orders of 0.5 and 0 have been calculated for ethanol steam reforming.

Sahoo et al. [81] carried out a kinetic study of ethanol steam reforming using Co/Al_2O_3 catalysts. A mechanistic kinetic model using the Langmuir–Hinshelwood approach was developed considering surface reaction mechanisms for ethanol steam reforming, water–gas shift, and ethanol decomposition reactions. These authors claim that the formation of acetaldehyde from ethoxy is the rate-determining step for reforming reaction. Their kinetic model is able to describe the steam reforming of ethanol process adequately for a wide range of experimental data. Akpan et al. [114] proposed mechanistic kinetic models based on the Langmuir–Hinshelwood and Eley–Rideal approaches using a Ni-based commercial catalyst. Working with crude ethanol and at temperatures between 673 and 863 K, they used the overall reaction (4.1) for the development of kinetic models. It must be noted that these authors, using a Ni-based catalyst and reaction temperatures up to 863 K, do not report the presence of methane and carbon monoxide in the effluent stream.

Ciambelli et al. [113] proposed an empirical power function rate equation and the apparent reaction orders of 0.5 and 0 have been calculated for ethanol and water, respectively. On RhPt wash coated monolith catalyst the order of water was found to be also 0 but that of ethanol was 1.2 [115].

In the mathematical model of Görke et al. [116] for ethanol steam reforming on Rh/CeO_2, the rate-determining steps were CO_2 desorption, dissociative ethanol adsorption, and reaction of adsorbed methane with steam from the gas phase. Benito et al. [117] proposed similar important reaction steps for ethanol steam reforming as mentioned above—the ethanol dehydrogenation, acetaldehyde decomposition, the reforming of methane, and the water–gas shift reaction—without judging about the rate-determining step.

The activation energy of the steam reforming of ethanol was found in a wide range on different catalysts. Some data are collected in Table 4.1. The high discrepancy and some low values of activation energy could be explained by surface diffusion of reactants and/or products. Mariño et al. [99] observed the presence of diffusion resistances even at the temperature as low as 573 K and using catalyst particles in the size range 125–177 μm.

4.9 Interaction of Ethanol with the Catalysts and with the Support

4.9.1 Infrared Spectra of Adsorbed Ethanol

It is generally accepted that ethanol adsorbs molecularly at 100 K on Pt surface; however, there are discrepancies between the published studies regarding the extent of ethanol decomposition. Panja et al. [118] found that the entire ethanol monolayer desorbs reversibly. In contrast to this observation, Sexton and coworkers estimated that about 10% of the monolayer decomposed to H_2 and CO [119] and Rajumon et al. [120] stated that a significant amount of surface carbon was detected following ethanol adsorption on Pt(111) at room temperature. Lee et al. [121] reported that ethanol multilayer desorbs above 150 K, while ~60% of the monolayer desorbs intact above 200 K in competition with decomposition pathways. Reaction initially proceeds via progressive dehydrogenation to form a metastable acetyl intermediate, which in turn undergoes decarbonylation above 250 K to give chemisorbed CO and methyl groups. A significant fraction of the latter is hydrogenated above 270 K, desorbing as CH_4, with the remainder further decomposing to liberate H_2 and surface CH_x moieties.

The initial step in alcohol activation on Pd(111) [122], Ni(111) [123], is alkoxide formation via O–H bond cleavage. In the chemisorbed ethoxy species methylene (CH_2) C–H bond scission occurs as the second step in ethanol decomposition, which is followed by the C–C bond breaking and the CO formation. On Rh(111) [124] surfaces, predominantly the carbon–carbon bond dissociates during ethanol adsorption at room temperature and the carbon–oxygen bond is preserved leading to adsorbed CO but not to adsorbed atomic O. In addition to CO, also significant amounts of methylidyne and ethylidyne species are formed on Rh(111), the latter presumably via a reforming reaction. No significant amounts of atomic C formed on Rh(111) indicating incomplete dehydrogenation. The ethoxy species formed on Cu (100) was stable to approximately 370 K but decomposed at higher temperature to yield gaseous products and a clean surface [125].

Ethanol has been found to adsorb on various metal oxide surfaces by the dissociation of the OH bond, with the proton going to surface lattice oxygen and the ethoxide species bonded to the surface cation. The formation of adsorbed surface ethoxy species was first reported by Greenler [126] who adsorbed ethanol on aluminum oxide at 308 K. For example, adsorbed ethoxy species have been

detected upon the adsorption of ethanol on various oxide surfaces including MgO [127], TiO_2 [128], CeO_2 [129, 130], Al_2O_3 [131], ZnO [71], ZrO_2 [53, 87], Nb_2O_5 [92], and La_2O_3 [65, 132]. On Mo_2C it was also found that the primary step of ethanol activation is the ethoxy formation [133].

After the adsorption of ethanol at room temperature the bands of molecularly adsorbed ethanol and ethoxy were detected on alumina and alumina-supported noble metals [31, 50]. The bands observed during ethanol adsorption on different supports and on different catalysts and their possible assignments have been collected in Table 4.2. Other bands not involved in Table 4.2 originate from the products of surface reaction(s) and they will be discussed later. The negative spectral features at 3,718 and 3,677 cm^{-1} and the broad absorptions centered at 3,405 cm^{-1} (not shown) are from the adsorption of molecular ethanol through the formation of hydrogen bridge bonding with the OH groups of the support. In the spectral range of 2,200–1,800 cm^{-1}, bands of adsorbed CO were detected even at 300 K on alumina-supported noble metals (Fig. 4.3) [31].

The bands observed at 300 K in the C–H stretching region (3,100–2,600 cm^{-1}) monotonously lost their intensities with the increase of the temperature up to 573 K. Above this temperature the intensities of these bands dramatically decreased. On the spectra of Al_2O_3 and other alumina-supported noble metal samples similar characteristics could be observed in the 1,800–900 cm^{-1} range. On supported metals, however, at and above 373 K new bands appeared at 1,575 and 1,474–1,468 cm^{-1} attributed to surface acetate species [134], which were the only stable bands at 673 K (Fig. 4.3). A band due to δ(OH) in molecularly adsorbed ethanol (1,277 cm^{-1}) could be observed up to 473 K on the surfaces. Spectral features due to H-bridge bonding of molecular ethanol (not shown) were detected up to 573 K on Al_2O_3 [135] and up to 623 K on 1% Ir/Al_2O_3.

From the comparison of the corresponding spectra in Fig. 4.3a, b it turned out that the presence of water led to the appearance of the bands at 1,574 and 1,458 cm^{-1} even at 300 K. In the presence of water, on the other hand, the band at 1,074 cm^{-1} could be observed even after the treatment at 673 K.

In order to distinguish the bands of adsorbed ethanol molecules and ethoxide(s) formed in the dissociation of ethanol, the method proposed by Hussein et al. [136] was followed: they attributed the band at 1,380 cm^{-1} (δ[CH_3] in ethanol) and 1,270 cm^{-1} (δ[OH] in ethanol) to ethanol molecularly adsorbed on TiO_2 surface. They suggested that the 1,270 cm^{-1} band is from strongly held C_2H_5OH probably coordinatively bonded to Lewis acid sites [128, 135].

The negative features and the broad absorptions above 3,400 cm^{-1} on the spectra of alumina-supported noble metal catalysts show that a part of the ethanol molecules was absorbed by hydrogen bridge bonding to the surface OH groups of the catalyst.

It has also been proposed [135] that bands below 1,200 cm^{-1} could be assigned to ethoxides ($C_2H_5O(a)^-$). The band around 1,120 cm^{-1} was attributed to ethoxide coordinated to a single surface cation of the support (monodentate ethoxide) and the band around 1,070 cm^{-1} to an ethoxide bridge bonded (bidentate) to adjacent surface cations of the supporting oxide [35, 135, 137].

Table 4.2 Observed wave numbers (cm^{-1}) of absorption bands due to the surface species produced by the adsorption of ethanol on different catalysts

	MgO [127]	TiO_2 [136]	TiO_2 [128]	CeO_2 [129]	Al_2O_3 [12]	Al_2O_3 [50]	1% Pt/Al_2O_3 [50]	Cu/Nb_2O_5 [92]	Co/ZrO_2 [87]	Co/ZnO [71]
ν_a (CH_3)	2,967	2,975	2,969	2,960	2,970	2,969	2,974	2,969	2,970	2,973
ν_s(CH_3) or ν_a (CH_2)	–	2,930	2,921–2,925	–	2,930	2,925	2,930	2,914	2,928	2,928
ν_s (CH_2)	–	–	2,898	2,866	2,900	–	2,902	2,901	2,867	2,900
ν_s (CH_3)	2,834	2,875	2,873	–	2,870	2,874	2,877	2,867	2,710	2,874
δ_a (CH_3) or γ (CH_2)	–	1,470–1,450	–	1,473	–	–	–			
δ_a (CH_3)	1,437	1,440	1,446	–	1,450	1,446	1,450	1,400	1,443	
δ_s (CH_3)	1,383	1,380	1,398	1,383	1,390	1,387	1,392	1,313	1,381	1,381
Δ (OH) in ethanol	–	1,270	1,263	–	–	1,272	1,276		1,280	
ρ (CH_3)	–	1,160	–	–	1,170	1,164	1,161			
ν_a (CCO) (monodentate)	1,115	1,105	1,113	1,107	1,115	1,111	1,106		1,110	1,100
ν_a (CCO) (bidentate) or ν (C–C)	1,063	1,070	1,065	–	1,070	1,071	1,073	1,080	1,066	
ν_a (CCO) (bidentate)	–	–	–	1,057	–	1,052	1,052	1,047		1,057

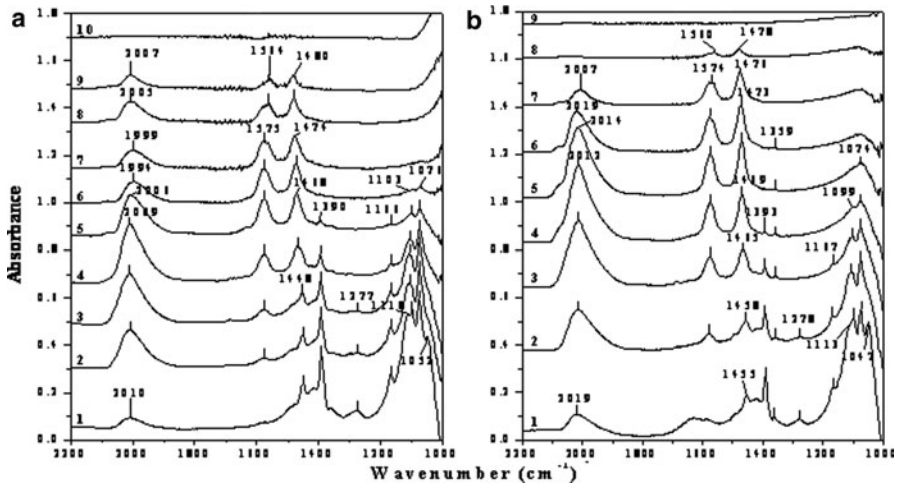

Fig. 4.3 IR spectra registered at 300 K on 1% Ir/Al_2O_3 after heating the adsorbed C_2H_5OH layer to different temperatures under constant evacuation (**a**) and in 1.33 h Pa water (**b**): 1—300, 2—373, 3—423, 4—473, 5—523, 6—573, 7—623, 8—673, 9—723, and 10—773 K [31]

At 373 K (in ethanol decomposition) and already at 300 K in the presence of water other surface reactions occurred, the result of which is the appearance of stable bands at 1,575 and 1,474–1,458 cm^{-1}. These bands are tentatively assigned to surface acetate species. After ethanol adsorption on Pt/TiO_2 Rachmadi and Vannice [134] found bands at 1,550 and 1,442 cm^{-1} assigned to $\nu_a(COO)$ and $\nu_s(COO)$ vibrations in the surface acetate species.

Similar results were obtained on different supported metals. The main differences were the appearance temperature and the structure of the acetate species. On CeO_2 and on Pd/CeO_2 [129], the bands at 1,572 and 1,424 cm^{-1} characteristic of the $\nu_{as}(OCO)$ and $\nu_s(OCO)$ vibration of acetate were detected. Ethoxy species adsorbed on Co/ZrO_2 [87] disappeared with increasing temperature due to oxidation with the lattice oxygen from the support. Surface acetate formed subsequently at 1,552 cm^{-1} ($\nu_{as}[OCO]$), 1,441 cm^{-1} ($\nu_s[OCO]$), and 1,346 cm^{-1} as an intermediate then dissociated into CO_2, but these peaks were observed even at 773 K. It has to be noted that in the CO region there were no peaks during the entire run on Co/ZrO_2.

DRIFTS results obtained on Cu/Nb_2O_5 are in accordance with TPD analysis and the formation of acetate at room temperature suggests the reactivity of the surface and its oxidative dehydrogenation capacity [92]. The peaks detected at 1,080 and 1,047 cm^{-1} are from ethoxy species adsorbed on the surface in bidentate form [138]. Bands at 1,140, 1,378, and 1,260 cm^{-1} indicate the presence of acetate species (COC) adsorbed on the oxygen of the niobia lattice, which remain very stable with the temperature. A small band at 1,762 cm^{-1} indicates acetaldehyde in the gas phase (δ C=O), but disappears after flushing with He. The results show that

ethanol adsorbs as ethoxide and is oxidized to acetate species at room temperature, probably due to the redox property of niobia. The band intensities decrease with increasing temperature. The ethoxide species are decomposed at about 473 K. It is in accordance with the formation of CO, CO_2, and H_2 during TPD of ethanol, also attributed to these ethoxide species. The TPD results confirm the decomposition of ethanol at 443 K and above 618 K, which is attributed to the oxidative dehydrogenation of adsorbed ethanol, and is in accordance with DRIFTS results, showing the formation of acetaldehyde at 1,700 cm^{-1}. Yee et al. [130] suggested that these acetaldehyde species may decompose into CH_4 and CO or into carbonates, which are then oxidized with the formation of CO_2.

The effect of water on the formation and stability of surface species in ethanol adsorption was studied on TiO_2 and on Rh/TiO_2. It was found that water enhanced the stability of strongly held C_2H_5OH while the stability of monodentate ethoxy was less due to water. Acetaldehyde formation both on the surface and in the gas phase was experienced on Rh/TiO_2 (both in the presence and absence of water) and on TiO_2 in the presence of water [128].

On CeO_2-supported catalysts after the adsorption of ethanol [31, 129, 135, 139, 140] at room temperature, absorption bands were found which can be attributed to ethoxy species and molecularly adsorbed ethanol. However, bands characteristic of acetate species were also found at different temperatures. Silva et al. [139] reported that the acetate bands were detectable already at 373 K, but Yee et al. [129] observed these species only at higher temperature (523 K). Song et al. [83] found that the Co/CeO_2 catalyst oxidized the surface ethoxy group into acetate even at room temperature with residue η^2-type adsorbed acetaldehyde species present (1,713, 1,261, and 1,024 cm^{-1}) [71]. The appearance of carbonates is due to the further oxidation of acetate and the formation of carbon dioxide as a decomposition product of acetate is observed during temperature increase [83]. On $CeZrO_2$ mixed oxide the ethoxy and acetate species formed at room temperature. The ethoxy adsorb over Ce cations in bidentate and monodentate mode. It was stated [141] that these species are associated not only to the Ce^{3+} as was suggested earlier [142], because the reduction degree of ceria was low at temperatures below 700 K. On increasing the temperature the intensity of the ethoxy groups decreased and that of acetate increased. At temperatures higher than 573 K the intensities of acetate bands significantly decreased and carbonate bands are formed. Over $Pt/CeZrO_2$ catalyst at room temperature the same infrared bands were observed as mentioned before. In this case, the formation of acetate was described not by the oxidation of acetyl species but by surface O as in the case of the clean oxide; another route was suggested from ethoxy to acetate involving OH groups, while in the $Pt/CeZrO_2$ the ceria on the surface of the catalyst reduced to Ce^{3+} [141].

The band intensities of acetate species as a function of temperature exhibited a maximum of around 573 K on alumina-supported noble metals; this value proved to be independent on the metals [31] but the bands were detectable up to 700–800 K. The disappearance temperature of surface acetate bands depended on the metal; it was 50 K lower value on Ru/Al_2O_3 than on Pt/Al_2O_3 [31]. The stability of surface acetate is influenced by the additives of the support, too. On potassium-doped

Pt/Al_2O_3 it was found that the acetate species disappeared from the surface above 673 K while the same occurred only at higher temperatures (above 723 K) on the potassium-free sample [51].

Ethanol adsorbed on $LaNiO_3$ catalyst at room temperature produced absorption bands characteristic of molecularly bonded ethanol (1,245 cm^{-1}) and acetyl species (1,636 cm^{-1}) [132]. Ethoxy and acetate species were not detected, although the BET surface of the sample was only 3.8 m^2/g. On increasing the temperature the acetate bands appeared on the spectra above 373 K.

In addition to the bands assigned to ethanol, ethoxy, and acetate species the spectra of supported metal catalysts also exhibited bands attributed to adsorbed CO in different forms. The formation of this species could be explained by the decomposition of ethanol, acetaldehyde, or the ethoxy species. The CO remained adsorbed on the metal, while hydrogen and methane were detected in the gas phase [50].

4.9.2 Temperature-Programmed Desorption of Ethanol

The surface interaction of ethanol or ethanol + water mixture was often studied by temperature-programmed desorption. Ethanol TPD is conducted under conditions not necessarily close to those of reforming reactions, but it brings essential information needed for the study of ethanol reaction. After adsorption of ethanol on Al_2O_3 mainly C_2H_4 desorbed in TPD experiments, but small amounts of CH_3CHO, CO_2, and CH_4 were also detected. C_2H_4 appeared in a narrow peak ($T_{max} = 565$ K). CO_2 and acetaldehyde desorbed in a lower and broader temperature range, at 420–570 K, where the ethanol desorption was also detected [135].

In the case of alumina-supported noble metals two desorption steps were observed. In the first stage (350–550 K), CO_2, H_2, traces of ethylene, acetaldehyde, methane, and ethanol were found. Small amounts of diethyl ether, benzene, crotonaldehyde, and ethyl acetate were also detected on Ru/Al_2O_3 and Ir/Al_2O_3 samples. At higher temperatures, above 650 K, only methane and CO_2 ($T_{max} = 750$ K) were found. These results were attributed to the formation and decomposition of surface acetate species [135], which was clearly demonstrated by IR spectroscopy [31, 135]. The high temperature desorption peak maxima for CO_2 and CH_4 formation, both in the absence and in the presence of water, shifted to higher temperature on all catalysts in the order of $Rh/Al_2O_3 < Pd/Al_2O_3 < Ru/Al_2O_3 < Ir/Al_2O_3 < Pt/Al_2O_3$ [26]. Interestingly, the addition of water to the carrier gas did not influence the feature of TPD experiments on noble metal/Al_2O_3 catalysts. Similar results were obtained by Basagiannis et al. [32] on Al_2O_3 and on Pt/Al_2O_3, but in the latter case the TPD curves were more complex. They suggested that three processes seem to compete in the temperature range of 470–570 K, namely the decomposition of adsorbed ethanol toward CO, H_2, and CH_4, and ethanol dehydrogenation and dehydration to ethylene and acetaldehyde. The appearance of the high temperature CO_2, CO, and H_2 desorption was attributed to the water–gas shift reaction and to the dry reforming of methane.

The TPD spectrum of ethanol adsorbed on Co/Al_2O_3 catalyst also shows two desorption stage and the high temperature peak shifted to higher temperature as the crystal size decreased [84].

On the TPD spectrum obtained after ethanol adsorption on La_2O_3 very weak signals were observed. Ethanol, acetaldehyde, ethylene, CO, and H_2 evolved in the low temperature range. Above 770 K CO_2 seems to be the main desorbing species. CO_2 originates probably from the decomposition of carbonates formed during the adsorption, decomposition of ethanol, or from other products bonded to the surface. Addition of Ni to La_2O_3 results in an entirely different TPD spectrum [65]. Nickel leads to the fast decomposition of adsorbed ethanol as witnessed by the appearance of H_2, CH_4, and CO peaks below 373 K. At higher temperature, up to 573 K, mainly H_2 was formed probably from the dehydrogenation of adsorbed ethanol, and above this temperature the decomposition product of acetaldehyde was detected. Contrary to it on the TPD spectra of ethanol adsorbed on $NiLaO_3$, the high temperature desorption stage was attributed to the decomposition of surface acetate and carbonate species [132].

From the surface of 1% Pt/ZrO_2 only molecular ethanol desorbed in traces at low temperatures and after that CO_2 and CH_4 were detected above 600 K. The maximum temperature of the desorption peaks for both CO_2 and CH_4 was the same, 675 K. de Lima et al. [143] found CO_2 and CH_4 desorption in the same temperature range after ethanol adsorption, but at high temperatures they observed CO and H_2 evolution too.

Significant differences between TPD profiles taken on Co/ZnO and ZnO are evidenced at higher temperatures [71]. Co/ZnO exhibited a second maximum at ca. 563 K for the evolution of CO_2, methane, acetaldehyde, and dimethyl ketone. The comparison of IR spectra after TPD experiments at 473 and 673 K for this catalyst showed the almost total disappearance of bands due to acetate species. Thus, it can be proposed that the products evolved come from surface bidentate acetate species, which easily decompose over Co/ZnO by C–C scission. The presence of surface –OH may favor this pathway, giving the final products CO_2, CH_4, and H_2. H_2 did not show a maximum at this temperature, probably due to its consumption in the hydrogenation of acetate species to give acetaldehyde under the TPD experimental conditions. On the other hand, dimethyl ketone and CO_2 may be formed from the coupling of two acetate species.

In contrast with the behavior of Co/ZnO, the TPD experiment corresponding to ZnO did not show a second maximum for the evolution of different products at ca. 573 K, and the IR spectrum indicated a less diminution of the intensity of bands due to surface acetate species over ZnO when the sample was heated from 473 to 673 K. Over ZnO the decomposition of surface acetate species via C–C scission was not favored, and probably only some of these species evolved to dimethyl ketone and CO_2 via an aldolization reaction.

de Lima et al. [140] found that the TPD profile of adsorbed ethanol on Co/CeO_2 shows that at low temperatures (392 K) H_2 and CH_4 formation took place but CO and ethanol formation was not detected. On the contrary, Song et al. [83] detected only ethanol and water up to 400 K. At higher temperature, about 560–580 K,

de Lima et al. [140] found significant amounts of H_2, ethylene, and acetaldehyde formation, but Song et al. [83] detected CH_4, CO, and CO_2 nearly in the same temperature range. These results clearly show that the surface character basically influenced the product distribution of desorption. Both papers explain the high temperature peak with the decomposition of surface species formed in the ethanol adsorption.

The TPD of ethanol adsorbed on ceria-supported different noble metals (Pt/CeO_2 [113, 130, 143–145], Ir/CeO_2 [60], Pd/CeO_2 [129], Rh/CeO_2 [146], $Rh–Pt/CeO_2$ [48, 49], $Rh–Pd/CeO_2$ [47]) was studied in detail.

On the TPD curves of Pt/CeO_2 at low temperature de Lima et al. [143–145] detected mainly H_2, CH_4, and ethanol desorption, which were attributed to the decomposition of ethoxy groups. At higher temperatures, above 550 K, CO and CH_4 were produced indicating the decomposition of acetaldehyde and/or acetate.

Yee et al. [130] first detected ethanol and acetaldehyde desorption, but above 600 K CO_2, CH_4, CO, CH_3CHO, and benzene formation was observed. It was supposed that benzene formed from the reaction of crotonaldehyde and acetaldehyde giving 2,4 hexadienol, and after the C–H bond scission of methyl groups, and after intramolecular cyclization followed by H_2 elimination benzene may form. Crotonaldehyde could be produced by the β-aldolization of acetaldehyde on the surface of CeO_2 [95].

Two different temperature domains of desorption were observed on Rh/CeO_2 [146]. Unreacted ethanol and acetaldehyde were desorbed at a peak temperature of about 460 K. Similar to the TPD of ethanol from Pd/CeO_2 [129] and Pt/CeO_2 [130], the higher temperature domain was dominated by desorptions of CO_2, CO, and CH_4. Two main differences were noticed, however, over Rh/CeO_2: (1) no evidence of benzene formation was observed and (2) significant amount of CH_4 desorption at 450 K was clearly seen. The latter point indicates that Rh/CeO_2 is more active toward carbon–carbon bond dissociation than Pd/CeO_2 or Pt/CeO_2.

Using bimetallic catalyst for ethanol adsorption [47–49] the product distribution of TPD was very simple in contrast to that observed on monometallic catalysts [129, 130, 146]. This is indicative of the high activity of the bimetallic catalysts for ethanol decomposition. This high activity is due to a combined (synergetic) effect of Rh with Pd or Pt. The main observation was that when the catalyst contains Rh mainly CH_4, CO_2, CO, and a small amount of acetaldehyde were formed, but on $Pt–Pd/CeO_2$ acetaldehyde was the main product. This difference was explained by the assumption that the Pt and Pd catalyze the oxidative dehydrogenation of ethanol or ethoxy, while Rh favors the removal of the terminal hydrogen of the CH_3 group of ethoxy and this results in an oxametallacycle intermediate [49]. This assumption is supported by a DFT calculation which indicated that the decomposition of ethanol has a low energy path via oxametallacycle intermediate at the interface between Rh and Ce ions: $Rh–CH_2–CH_2–O–Ce$ [147].

On CeO_2 and on CeO_2-supported metal catalysts ethylene formation was not detected [129], while the addition of ZrO_2 to ceria increased the C_2H_4 formation; the CeO_2 favors the dehydrogenation of ethanol to acetaldehyde instead of the dehydration route to ethylene [44, 141, 148].

4.10 Mechanism of Ethanol Reforming

4.10.1 The Process of Ethanol Reforming

The possible reactions which could occur in the ethanol steam reforming are summarized in Chap. 2. Not only the reactions of ethanol but most of the side reactions are also enumerated. The mechanism of the reaction means more than the totality of the possible processes it also helps understand, for example, the differences in the product distribution, the reasons of the change in the activity and selectivity on different catalysts. In view of the reaction mechanism the catalyst composition could be changed leading to better catalytic performance.

The mechanism of ethanol reforming has been systematically studied by both energy calculations to examine ethanol decomposition and by electronic structure analysis to investigate the redox capability of Co, Ni, Cu, Rh, Pd, Ag, Ir, Pt, and Au with the same crystal structure and surface orientation [149]. The computed results show that the dissociation barriers for the (111) surface of Co, Ni, Rh, and Ir are lower than those on the same surface of Cu, Ag, and Au. The initial C–H bond dissociation, forming the doubly adsorbed *$C(H_2)C(H_2)O(H)$* and *$C(H_2)C(H_2)O$*, with a lower barrier than those in the initial C–C and C–O bond dissociations is considered as the most feasible decomposition route. Electronic structure analysis showed that Rh(111) and Ir(111) surfaces with higher density of state (DOS) distributions around the Fermi level can efficiently accept/donate electrons from/to the reacting ethanol and its fragments, showing better redox capability. Therefore, the excellent efficiency of Rh- and Ir-based catalysts, as observed in the reforming experiment, can be attributed to both the lower decomposition barrier and the higher DOS distribution around the Fermi level based on the first-principles calculation [149].

On supported metal catalysts, it is generally accepted that the first step of the ethanol conversion is the ethoxy formation and the dehydrogenation of these species

$$CH_3CH_2OH \rightarrow CH_3CH_2O_{(a)} + H_{(a)}, \tag{4.18}$$

$$CH_3CH_2O_{(a)} \rightarrow CH_3CHO_{(a)} + H_{(a)}. \tag{4.19}$$

Rh has a unique effect on the decomposition pathway of ethoxy species. It abstracts H from the CH_3 group making a stable oxametallacycle intermediate [40, 138, 147].

$$CH_3CH_2O_{(a)} \rightarrow {}_{(a)}CH_2CH_2O_{(a)} + H_{(a)}. \tag{4.20}$$

The following step may be the decomposition of this species

$$_{(a)}CH_2CH_2O_{(a)} \rightarrow CH_{4(g)} + CO_{(g)}. \tag{4.21}$$

CH_4 and CO could react further with water [69].

Contrary to the general assumption that the first step of the reaction is the ethoxy formation, Zhong et al. [41] suggested that while ethanol adsorbed molecularly on the Lewis acidic sites [127, 135] the further reaction of it depends on the type and the strength of the acidic sites

$$CH_3CH_2OH \rightarrow CH_3CH_2OH_{(a)} \rightarrow C_2H_4, \tag{4.22}$$

$$CH_3CH_2OH \rightarrow CH_3CH_2OH_{(a)} \rightarrow C_2H_4O, CH_3CO, CH_3COO^-. \tag{4.23}$$

These processes take place on the proper Lewis acidic sites but ethylene (4.22) formed on the Bronsted acidic sites. Ethanol adsorbed on very weak Lewis acidic sites decomposed to CO, CO_2, and to carbonates [41].

There is a different suggestion as regards to the further reaction of $CH_3CHO_{(a)}$ species. Several research groups stated that this surface compound decomposes to methane and CO, others supposed that this species oxidized further to surface acetate and there is an idea that both reaction could occur on the surface.

For example, Guarido et al. [92] proposed the following reaction pattern for the ethanol reforming on Cu/Nb_2O_5 in which both reaction routes are supposed:

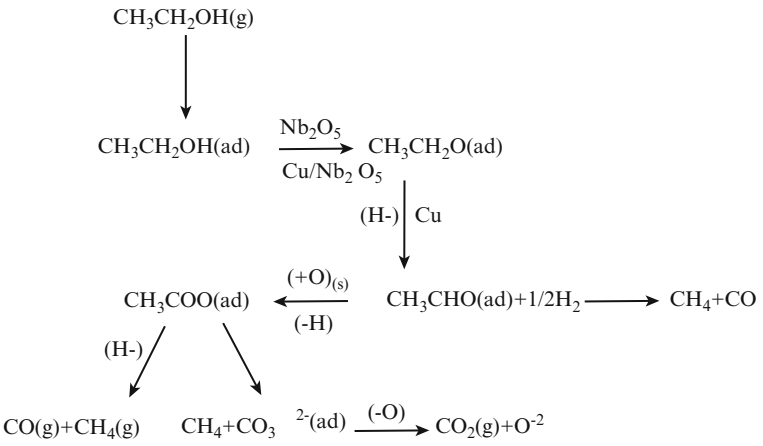

In the mechanism proposed by Frusteri et al. [30] investigating the performance of MgO-supported metal catalysts the decomposition of the acetaldehyde is the key step of the reaction. It was suggested that the ethanol is first dehydrated to ethylene or dehydrogenated to acetaldehyde which subsequently decomposes to CH_4 and CO. These could react with water producing CO, CO_2, and H_2.

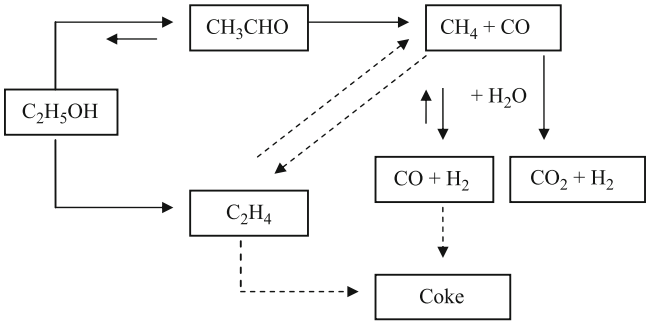

Kinetic evaluation and TPD experiments suggest a similar surface reaction mechanism involving the following steps [113]:

1. Ethanol dissociative adsorption on the catalyst surface form acetaldehyde intermediate.
2. Decarbonylation of it to produce mainly H_2, CH_4, and CO_2.
3. Water–gas shift reaction of CO adsorbed on metal sites to produce H_2 and CO_2.

Contrary to these theories the infrared spectra of adsorbed ethanol at higher temperature clearly show that mainly surface acetate, carbonates, and adsorbed CO are on the surface of the catalysts. DRIFT measurements revealed that surface acetate and adsorbed CO were detected during the catalytic reaction at 723 K on different supported Pt catalysts [31, 52, 135]. The intensities of the acetate bands increased linearly in the first hour of the reaction and then achieved a nearly steady-state value but that of CO decreased continuously (Fig. 4.4). The absorption characteristic of ethoxy species during the ethanol reforming at 723 K was commensurable with the noise. In the C–H stretching region bands characteristic of CH_x groups and of gaseous methane were also detected. These results mean that the formation rate of the acetate species is higher than their decomposition or further reaction.

Resini et al. [150] suggested that on Ni–Zn–Al catalyst the acetaldehyde formed on the surface as described above oxidized further with the surface oxygen to acetate

$$CH_3CHO_{(a)} + 2O^{2-} \rightarrow CH_3COO^-{}_{(a)} + {}^-OH_{(a)} + 2e^-. \tag{4.24}$$

and finally acetate species may give rise to acetic acid desorption or to decomposition

$$CH_3COO^-{}_{(a)} + {}^-OH_{(a)} \rightarrow CH_4 + CO_2 + O^{2-}, \tag{4.25}$$

$$CH_3COO^-{}_{(a)} + {}^-OH_{(a)} + 2e^- \rightarrow CH_4 + CO + 2O^{2-}. \tag{4.26}$$

CH_4 and CO could react further with water to produce CO_2 and hydrogen.

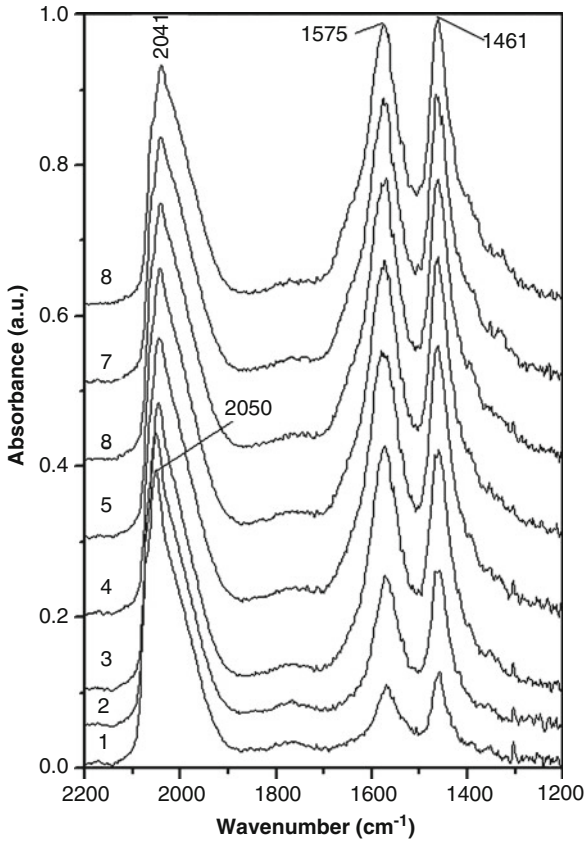

Fig. 4.4 Infrared spectra registered during ethanol reforming over Pt/Al_2O_3 catalysts at 723 K in the 30th second (1), first (2), fifth (3), 15th (4), 30th (5), 60th (6), 90th (7), 120th (8) minute of the reaction [51]

Most of the above described mechanisms of ethanol steam reforming assumed that both the metal and the support play an essential role in the behavior of the catalysts.

In the steam reforming of acetic acid on Pt/ZrO_2 a bifunctional mechanism was established where both Pt and ZrO_2 participate in the reaction. On Pt the bond breaking of acetic acid proceeds to form H_2, CO, CH_4, and CO_2. In situ IR data demonstrate that H_2O can be activated on ZrO_2 to create supplementary surface hydroxyl groups which react to gasify the species adsorbed on Pt, or CH_4 in a secondary reaction [151].

Similar conception was presented for the explanation of the efficiency of Pt/ZrO_2 in the water–gas shift reaction [152]. It was suggested that the reaction mechanism involves a redox mechanism. It means that the water is activated at an oxygen vacancy on the surface of zirconia adjacent to a Pt particle, followed by the transfer of $O_{(ads)}$ to Pt where it could react with CO.

Pt/Al_2O_3–ZrO_2 [153] was found to be an effective catalyst for the steam reforming of CH_4 which was related to its coking resistance that has been attributed to $Pt–Zr^{n+}$ interaction at the metal-support interface. The interfacial sites on $Pt–ZrO_y$ were active for CO and CO_2 adsorption with a decrease in the Pt–CO

bond strength inhibiting C–O bond breaking and consequently producing less carbon formation on the catalyst surface. Moreover zirconia is a well-known oxygen supplier and its oxygen mobility is fast which helps keep the metal surface free of carbon [151].

Taking into account the results found in the methane [153] and acetic acid reforming [151], in the water–gas shift reaction [152] on Pt/ZrO_2 we can suppose that the acetate groups formed in the ethanol reforming decompose at the metal–support interface and the products react with the OH groups activated on the partially reduced zirconia sites.

4.10.2 Deactivation of the Catalysts

Because several supported catalytic systems have high activity in ethanol conversion and have high selectivity for hydrogen formation, an interesting and important topic of research is the stability of the catalyst and the recognition of the changes of the catalytic activity and stability. Lot of papers reported that the selectivity and activity changed during the ethanol steam reforming especially at lower temperature, below 750 K.

The main processes of the catalytic deactivation are carbon or carbonaceous deposit formation and/or the changes in the oxidation state of the metal or that of support oxide.

There are some works which presented XPS results of the catalysts before and after the catalytic reaction and did not found any significant changes in the oxidation state of the components of the catalysts. This means that the changes in the activity or selectivity are caused by the formation of different carbon and carbonaceous deposits.

The deactivation of hydrogen formation in the ethanol steam reforming mainly on different supported Pt catalysts was attributed to the accumulation of acetate-like species on the support [31, 135]. Because of their relative high stability at 723 K these acetate species might block the migration of the ethoxy intermediate from the support to the metal particles where they can decompose and react with the surface OH groups. This theory was supported by the experimental results; namely when the stability of surface acetate was lower [53] or it was reduced by additives [51] the hydrogen selectivity increased in the reaction. On the other hand, Platon et al. [154] suggested that the intermediates like ethylene and acetone were the species responsible for the strong deactivation of the catalyst observed at low reforming temperatures (523 K).

It was found that the K additives stabilized the Ni/MgO catalyst but the mechanism of it was explained in another way. Frusteri and coworkers supposed that K suppresses the metal sintering and does not influence the coke formation [155]. When the Ni/Al_2O_3 was promoted with La and silver, La showed a positive effect while Ag did not concern the coke formation [156]. The effect of La was explained by Fatsikostas et al. [61] who supposed that under reaction conditions La_2O_3

species are formed, which decorate the Ni particles reacting with CO_2 to form $La_2O_3CO_3$. This lanthanum oxycarbonate reacts with the surface carbon to form CO and regenerates the La_2O_3.

Strong selectivity decay was also observed on Pt/Al_2O_3 [52] and stable acetate species were detected on the surface during the catalytic reaction. In spite of these observations it was supposed that the active sites responsible for the acetaldehyde decomposition are deactivated in the first minutes of the ethanol reforming by carbon deposits. A second reaction pathway was also supposed consisting of the decomposition of acetate intermediates formed over the surface of alumina which becomes the main reaction route operating in the steam reforming of ethanol. The species related with the formation of coke on the catalysts are probably methyl groups from C–C breaking reactions and ethylene formed by dehydration of ethanol on alumina [52].

The morphology of the carbon species formed during the reaction depends not only on the reaction conditions but also on the nature of both the support and the active metal and also on their chemical–physical interaction.

Cavallaro and coworkers [39] attribute the coke formation to the polymerization process of CH_x species formed during the reaction. The addition of a small amount of oxygen into the feed significantly decreased the catalyst deactivation but promoted the metal sintering.

Carbon deposition is considered to be the main cause for deactivation of the Rh- and Co-based catalysts. Catalyst support with high oxygen mobility and oxygen storage capacity helps minimize the carbon deposit [45, 87, 154].

Coke can destroy the catalyst structure and occupy catalyst surface resulting in the decay of the catalytic activity. Coke formation is faster on acidic support; on this surface the ethanol dehydration, i.e., ethylene formation occurs, which could polymerize or decompose. This effect could be reduced by using basic oxide as support or by adding alkali metal additives to the acidic support.

To avoid the coke formation and to improve catalytic stability recently double reactor was proposed. In this system ethanol passes through the first layer (Cu catalyst) at 573–673 K to perform dehydrogenation to acetaldehyde and hydrogen, followed by acetaldehyde steam reforming or decomposition on Ni sample [11]. The conversion of ethanol on the first layer at low temperature prevents ethylene and so the coke formation.

4.11 Conclusion

In this chapter the catalytic steam reforming of ethanol for hydrogen production is discoursed. Focus is given not only to the catalyst development but also to the surface interaction and to the mechanism of the reaction. From the comprehensive literature surveys it can be seen that the supported metals, among others, Rh, Ni, Co exhibited the best performance in ethanol conversion and hydrogen selectivity. The reaction pathway is complex and a number of undesirable side reactions could

also occur thereby affecting the selectivity of H_2. The results clearly show that the support has an essential role in the hydrogen formation; there are some explanations which suppose a bifunctional mechanism—in order to maximize hydrogen production suitable supports are required. For industrial use stable catalysts are necessary, but one of the big challenges of ethanol steam reforming is to decrease carbon or carbonaceous deposit formation on the catalyst, which can cause the catalyst deactivation. The use of suitable supports such as MgO, ZnO, CeO_2, ZrO_2, or mixed oxides can influence not only the catalytic effect of metal but also can inhibit carbon deposition to some extent. The results and the conclusions which one could be finding in the literature are not always unambiguous indicating that the mechanism of the reaction is much more complicated as it would be supposed in the first minute.

References

1. Brown LF (2001) A comparative study of fuels for on-board hydrogen production for fuel-cell-powered automobiles. Int J Hydrogen Energy 26:381–397
2. Manzolini G, Tosti S (2008) Hydrogen production from ethanol steam reforming: energy efficiencies analysis of traditional and membrane processes. Int J Hydrogen Energy 33:5571–5582
3. Lynd LR, Cushman JH, Nichols RJ, Wyman CE (1991) Fuel ethanol from cellulosic biomass. Science 251:1318–1323
4. Kim S, Dale BE (2004) Global potential bioethanol production from wasted crops and crop residues. Biomass Bioenergy 26:361–375
5. Stichnothe H, Azapagic A (2009) Bioethanol from waste: life cycle estimation of the greenhouse gas saving potential. Resour Conservat Recycl 53:624–630
6. Sanchez O, Cardona C (2008) Trends in biotechnological production of fuel ethanol from different feedstocks. Bioresour Technol 99:5270–5295
7. Lin Y, Tanaka S (2006) Ethanol fermentation from biomass resources: current state and prospects. Appl Microbiol Biotechnol 69:627–642
8. Navarro RM, Peña MA, Fierro JLG (2007) Hydrogen production reactions from carbon feedstocks: fossil fuels and biomass. Chem Rev 107:3952–3991
9. Haryanto A, Fernando S, Murali N, Adhikari S (2005) Current status of hydrogen production techniques by steam reforming of ethanol: a review. Energy Fuel 19:2098–2106
10. Ni M, Leung DYC, Leung MKH (2007) A review on reforming bio-ethanol for hydrogen production. Int J Hydrogen Energy 32:3238–3247
11. Vaidya PD, Rodrigues AE (2006) Insight into steam reforming of ethanol to produce hydrogen for fuel cells. Chem Eng J 117:39–49
12. Aupretre F, Descorme C, Duprez D, Casanave D, Uzio D (2005) Ethanol steam reforming over $Mg_xNil_{-x}Al_2O_3$ spinel oxide-supported Rh catalysts. J Catal 233:464–477
13. Rabenstein G, Hacker V (2008) Hydrogen for fuel cells from ethanol by steam-reforming, partial-oxidation and combined auto-thermal reforming: a thermodynamic analysis. J Power Sources 185:1293–1304
14. Aupretre F, Descorme C, Duprez D (2004) Hydrogen production for fuel cells from the catalytic ethanol steam reforming. Top Catal 30(31):487–492
15. Fishtik I, Alexander A, Datta R, Geana D (2000) A thermodynamic analysis of hydrogen production by steam reforming of ethanol via response reactions. Int J Hydrogen Energy 25:31–45

16. Vasudeva K, Mitra N, Umasankar P, Dhingra SC (1996) Steam reforming of ethanol for hydrogen production: thermodynamic analysis. Int J Hydrogen Energy 21:13–18
17. Rossi CCRS, Alonso CG, Antunes OAC, Guirardello R, Cardozo-Filho L (2009) Thermodynamic analysis of steam reforming of ethanol and glycerine for hydrogen production. Int J Hydrogen Energy 34:323–332
18. Haga F, Nakajima T, Miya H, Mishima S (1997) Catalytic properties of supported cobalt catalysts for steam reforming of ethanol. Catal Lett 48:223–227
19. García EY, Laborde MA (1991) Hydrogen production by the steam reforming of ethanol: thermodynamic analysis. Int J Hydrogen Energy 16:307–312
20. Ioannides T (2001) Thermodynamic analysis of ethanol processors for fuel cell applications. J Power Sources 92:17–25
21. Freni S, Maggio G, Cavallaro S (1996) Ethanol steam reforming in molten carbonate fuel cell: a thermodynamic approach. J Power Sources 62:67–73
22. Mas V, Kipreos R, Amadeo N, Laborde M (2006) Thermodynamic analysis of ethanol/water system with the stoichiometric method. Int J Hydrogen Energy 31:21–28
23. Arai H, Take JI, Saito Y, Yoneda Y (1967) Ethanol dehydration on alumina catalysts. J Catal 9:146–153
24. Freni S, Cavallaro S, Mondello N, Spadaro L, Frusteri F (2003) Production of hydrogen for MC fuel cell by steam reforming of ethanol over MgO supported Ni and Co catalysts. Catal Commun 4:259–268
25. Alberton AL, Souza MVM, Schmal M (2007) Carbon formation and its influence on the ethanol steam reforming over Ni/Al_2O_3 catalysts. Catal Today 123:257–264
26. Alvarado FD, Gracia F (2010) Steam reforming of ethanol for hydrogen production: thermodynamic analysis including different carbon deposits representation. Chem Eng J 165:649–657
27. Breen JP, Burch R, Coleman HM (2002) Metal-catalyzed steam reforming of ethanol in the production of hydrogen for fuel cell applications. Appl Catal B: Environ 39:65–74
28. Auprêtre F, Descrome C, Duprez D (2002) Bio-ethanol catalytic steam reforming over supported metal catalysts. Catal Commun 3:263–267
29. Liguras DK, Kondarides DI, Verykios XE (2003) Production of hydrogen for fuel cells by steam reforming of ethanol over supported noble metal catalysts. Appl Catal B: Environ 43:345–354
30. Frusteri F, Freni S, Spadaro L, Chiodo V, Bonura G, Donato S, Cavallaro S (2004) H_2 production for MC fuel cell by steam reforming of ethanol over MgO supported Pd, Rh, Ni and Co catalysts. Catal Commun 5:611–615
31. Erdőhelyi A, Raskó J, Kecskés T, Tóth M, Dömök M, Baán K (2006) Hydrogen formation in ethanol reforming on supported noble metal catalysts. Catal Today 116:367–376
32. Basagiannis AC, Panagiotopoulou P, Verykios XE (2008) Low temperature steam reforming of ethanol over supported noble metal catalysts. Top Catal 51:2–12
33. Zhang BC, Tang X, Li Y, Cai W, Xu Y, Shen W (2006) Steam reforming of bio-ethanol for the production of hydrogen over ceria-supported Co, Ir and Ni catalysts. Catal Commun 7:367–372
34. Benito M, Padilla R, Rodríguez L, Sanz JL, Daza L (2007) Zirconia supported catalysts for bioethanol steam reforming: effect of active phase and zirconia structure. J Power Sources 169:167–176
35. Homs N, Llorca J, de la Piscina PR (2006) Low-temperature steam-reforming of ethanol over ZnO-supported Ni and Cu catalysts. The effect of nickel and copper addition to ZnO-supported cobalt-based catalysts. Catal Today 116:361–366
36. Karim AM, Su Y, Sun J, Yang C, Strohm JJ, King DL, Wang Y (2010) A comparative study between Co and Rh for steam reforming of ethanol. Appl Catal B: Environ 96:441–448
37. Yaseneva P, Pavlova S, Sadykov V, Alikina G, Lykashevich A, Rogov V, Belochapkine S, Ross J (2008) Combinatorial approach to the preparation and characterization of catalysts for biomass steam reforming into syngas. Catal Today 137:23–28

38. Cavallaro S (2000) Ethanol steam reforming on Rh/Al_2O_3 catalysts. Energy Fuel 14:1195–1199
39. Cavallaro S, Chiodo V, Freni S, Mondello N, Frusteri F (2003) Performance of Rh/Al_2O_3 catalyst in the steam reforming of ethanol: H_2 production for MCFC. Appl Catal A: Gen 249:119–128
40. Diagne C, Idriss H, Kiennemann A (2002) Hydrogen production by ethanol reforming over Rh/CeO_2-ZrO_2 catalysts. Catal Commun 3:565–571
41. Zhong Z, Ang H, Choong C, Chen L, Huang L, Lin J (2009) The role of acidic sites and catalytic reaction pathways on the Rh/ZrO_2 catalysts for ethanol steam reforming. Phys Chem Chem Phys 11:872–880
42. Roh H-S, Wang Y, King DL, Platon A, Chin Y-H (2006) Low temperature and H_2 selective catalysts for ethanol steam reforming. Catal Lett 108:15–19
43. Roh H-S, Wang Y, King DL (2008) Selective production of H_2 from ethanol at low temperatures over Rh/ZrO_2-CeO_2 catalysts. Top Catal 49:32–37
44. Hsiao W-I, Lin Y-S, Chen Y-C, Lee C-S (2007) The effect of the morphology of nanocrystalline CeO_2 on ethanol steam reforming. Chem Phys Lett 441:294–299
45. Roh H-S, Platon A, Wang Y, King DL (2006) Catalyst deactivation and regeneration in low temperature ethanol steam reforming with Rh/CeO_2-ZrO_2 catalysts. Catal Lett 110:1–6
46. Diagne C, Idriss H, Pearson K, Gómez-García MA, Kiennemann A (2004) Efficient hydrogen production by ethanol reforming over Rh catalysts. Effect of addition of Zr on CeO_2 for the oxidation of CO to CO_2. C R Chimie 7:617–622
47. Scott M, Goeffroy M, Chiu W, Blackford MA, Idriss H (2008) Hydrogen production from ethanol over Rh-Pd/CeO_2 catalysts. Top Catal 51:13–21
48. Sheng PY, Yee A, Bowmaker GA, Idriss H (2002) H_2 Production from ethanol over Rh–Pt/CeO_2 catalysts: the role of Rh for the efficient dissociation of the carbon–carbon bond. J Catal 208:393–403
49. Sheng PY, Chiu WW, Yee A, Morrison SJ, Idriss H (2007) Hydrogen production from ethanol over bimetallic Rh-M/CeO_2 (M = Pd or Pt). Catal Today 129:313–321
50. Dömök M, Tóth M, Raskó J, Erdőhelyi A (2007) Adsorption and reactions of ethanol and ethanol-water mixture on alumina-supported Pt catalysts. Appl Catal B: Environ 69:262–272
51. Dömök M, Baán K, Kecskés T, Erdőhelyi A (2008) Promoting mechanism of potassium in the reforming of ethanol on Pt/Al_2O_3 catalyst. Catal Lett 126:49–57
52. Sanchez-Sanchez MC, Navarro Yerga RM, Kondarides DI, Verykios XE, Fierro JLG (2010) Mechanistic aspects of the ethanol steam reforming reaction for hydrogen production on Pt, Ni, and PtNi catalysts supported on γ-Al_2O_3. J Phys Chem A 114:3873–3882
53. Dömök M, Oszkó A, Baán K, Sarusi I, Erdőhelyi A (2010) Reforming of ethanol on Pt/Al_2O_3-ZrO_2 catalyst. Appl Catal A: Gen 383:33–42
54. Navarro RM, Álvarez-Galván MC, Sánchez-Sánchez MC, Rosa F, Fierro JLG (2005) Production of hydrogen by oxidative reforming of ethanol over Pt catalysts supported on Al_2O_3 modofied with Ce and La. Appl Catal B: Environ 55:229–241
55. Goula MA, Kontou SK, Tsiakaras PE (2004) Hydrogen production by ethanol steam reforming over commercial Pd/γ-Al_2O_3 catalyst. Appl Catal B: Environ 49:135–144
56. Goula MA, Kontou SK, Zhou W, Qin X, Tsiakaras PE (2003) Hydrogen production over commercial Pd/Al_2O_3 catalyst for fuel cell utilization. Ionics 9:248–252
57. Vaidya PD, Rodrigues AE (2006) Kinetics of steam reforming of ethanol over Ru/Al_2O_3 catalyst. Ind Eng Chem Res 45:6614–6618
58. Koh ACW, Chen L, Leong WK, Ang TP, Johnson BFG, Khimyak T, Lin J (2009) Ethanol steam reforming over supported ruthenium and ruthenium-platinum catalysts: comparison of organometallic clusters and inorganic salts as catalyst precursors. Int J Hydrogen Energy 34:5691–5703
59. Koh ACW, Leong WK, Chen L, Ang TP, Lin J, Johnson BFG, Khimyak T (2008) Highly efficient ruthenium and ruthenium-platinum cluster-derived nanocatalysts for hydrogen production via ethanol steam reforming. Catal Commun 9:170–175

60. Cai W, Wang F, Zhan E, Van Veen AC, Mirodatos C, Shen W (2008) Hydrogen production from ethanol over Ir/CeO_2 catalysts: a comparative study of steam reforming, partial oxidation and oxidative steam reforming. J Catal 257:96–107
61. Fatsikostas AN, Kondarides DI, Verykios XE (2002) Production of hydrogen for fuel cells by reformation of biomass-derived ethanol. Catal Today 75:145–155
62. Mas V, Bergamini ML, Baronetti G, Amadeo N, Laborde M (2008) A kinetic study of ethanol steam reforming using a nickel based catalyst. Top Catal 51:39–48
63. Mas V, Dienzeide ML, Jobbágy M, Baronetti G, Amadeo N, Laborde M (2008) Ethanol steam reforming using Ni(II)-Al(III) layered double hydroxide as catalyst precursor: kinetic study. Chem Eng J 138:602–607
64. Laosiripojana N, Assabumrungrat S (2006) Catalytic steam reforming of ethanol over high surface area CeO_2: the role of CeO_2 as an internal pre-reforming catalyst. Appl Catal B: Environ 66:29–39
65. Fatsikostas AN, Verykios XE (2004) Reaction network of steam reforming of ethanol over Ni-based catalysts. J Catal 225:439–452
66. Sánchez-Sánchez MC, Navarro RM, Fierro JLG (2007) Ethanol steam reforming over Ni/M_xO_y-Al_2O_3 (M = Ce, La, Zr and Mg) catalysts: influence of support on the hydrogen production. Int J Hydrogen Energy 32:1462–1471
67. Fatsikostas AN, Kondarides DI, Verykios XE (2001) Steam reforming of biomass-derived ethanol for the production of hydrogen for fuel cell applications. Chem Commun:851–852
68. Sun J, Qiu X-P, Wu F, Zhu W-T (2005) H_2 from steam reforming of ethanol at low temperature over Ni/Y_2O_3, Ni/La_2O_3 and Ni/Al_2O_3 catalysts for fuel-cell application. Int J Hydrogen Energy 30:437–445
69. Fierro V, Akalim MC (2003) On-board hydrogen production in hybrid electric vehicle by bio-ethanol oxidative steam reforming over Ni and noble metal based catalyst. Green Chem 5:20–24
70. Szijjártó GP, Tompos A, Margitfalvi JL (2011) High-throughput and combinatorial development of multicomponent catalysts for ethanol steam reforming. Appl Catal A: Gen 391:417–426
71. Llorca J, Homs N, de la Piscina PR (2004) In situ DRIFT-mass spectrometry study of ethanol steam-reforming reaction over carbonyl-derived Co/ZnO catalysts. J Catal 227:556–560
72. Llorca J, Homs N, Sales J, de la Pscina PR (2002) Efficient production of hydrogen over supported cobalt catalysts from ethanol steam reforming. J Catal 209:306–317
73. Llorca J, de la Piscina PR, Dalmon J-A, Sales J, Homs N (2003) CO-free hydrogen from steam-reforming of bioethanol over ZnO-supported cobalt catalysts. Effect of the metallic precursor. Appl Catal B: Environ 43:355–369
74. Llorca J, Homs N, Sales J, Fierro J-LG, de la Piscina PR (2004) Effect of sodium addition on the performance of Co-ZnO-based catalysts for hydrogen production from bioethanol. J Catal 222:470–480
75. Cavallaro S, Mondello N, Freni S (2001) Hydrogen produced from ethanol for internal reforming molten carbonate fuel cell. J Power Sources 102:198–204
76. Batista MS, Santos RKS, Assaf EM, Assaf JM, Ticianelli EA (2004) High efficiency steam reforming of ethanol by cobalt-based catalysts. J Power Sources 134:27–32
77. Huang L, Rongrong C, Chu D, Hsu AT (2010) Hydrogen production through auto-thermal reforming of bio-ethanol over Co-based catalysts: effect of iron in Co/Al_2O_3 catalysts. Int J Hydrogen Energy 35:1138–1146
78. Llorca J, Dalmon JA, de la Piscina PR, Homs N (2003) In situ magnetic characterisation of supported cobalt catalysts under steam-reforming of ethanol. Appl Catal A: Gen 243:261–269
79. Song H, Zhang L, Watson RB, Braden D, Ozkan US (2007) Investigation of bio-ethanol steam reforming over cobalt-based catalysts. Catal Today 129:346–354

80. Kaddouri A, Mazzocchia C (2004) A study of the influence of the synthesis conditions upon the catalytic properties of Co/SiO_2 or Co/Al_2O_3 catalyst used for ethanol steam reforming. Catal Commun 5:339–345
81. Sahoo DR, Vajpai S, Patel S, Pant KK (2007) Kinetic modelling of the steam reforming of ethanol for the production of hydrogen over Co/Al_2O_3 catalyst. Chem Eng J 125:139–147
82. Profeti LPR, Ticianelli EA, Assaf EM (2008) Production of hydrogen by ethanol steam reforming on Co/Al_2O_3 catalysts: effect of addition of small quantities of noble metals. J Power Sources 175:482–489
83. Song H, Mirkelamoglu B, Ozkan US (2010) Effect of cobalt precursor on the performance of ceria-supported cobalt catalysts for ethanol steam reforming. Appl Catal A: Gen 382:58–64
84. Haga F, Nakajima T, Yamashita K, Mishima S (1998) Effect of crystallite size on the catalysis of alumina-supported cobalt catalyst for steam reforming of ethanol. React Kinet Catal Lett 63:253–259
85. Song H, Ozkan US (2010) The role of impregnation medium on the activity of ceria-supported cobalt catalysts for ethanol steam reforming. J Mol Catal A: Chem 318:21–29
86. Lin SS-Y, Daimon H, Ha SY (2009) Co/CeO_2-ZrO_2 catalysts prepared by impregnation and coprecipitation for ethanol steam reforming. Appl Catal A: Gen 366:252–261
87. Song H, Ozkan US (2009) Ethanol steam reforming over Co-based catalysts: role of oxygen mobility. J Catal 261:66–74
88. Vargas JC, Libs S, Roger A-C, Kiennemann A (2005) Study of Ce-Zr-Co fluorite-type oxide as catalysts for hydrogen production by steam reforming of bioethanol. Catal Today 107–108:417–425
89. Virginie M, Araque M, Roger A-C, Vargas JC, Kiennemann A (2008) Comparative study of H2 production by ethanol steam reforming on Ce2Zr1.5Co0.5O8-δ: evidence of the Rh role on the deactivation process. Catal Today 138:21–27
90. Iwasa N, Takezawa N (1991) Reforming of ethanol: dehydrogenation to ethyl acetate and steam reforming to acetic acid over copper-based catalysts. J Chem Soc Japan 64:2619–2623
91. Cavallaro S, Freni S (1996) Ethanol steam reforming in a molten carbonate fuel cell a preliminary kinetic investigation. Int J Hydrogen Energy 21:465–469
92. Guarido CEM, Cesar DV, Souza MMVM, Schmal M (2009) Ethanol reforming and partial oxidation with Cu/Nb_2O_5 catalyst. Catal Today 142:252–257
93. Alonso CG, Furtado AC, Cantão MP, dos Santos OAA, Fernandes-Machado NRC (2009) Reactions over Cu/Nb_2O_5 catalysts promoted with Pd and Ru during hydrogen production from ethanol. Int J Hydrogen Energy 34:3333–3341
94. Nishiguchi T, Matsumoto T, Kanai H, Utani K, Matsumura Y, Shen W-J, Imamura S (2005) Catalytic steam reforming of ethanol to produce hydrogen and acetone. Appl Catal A: Gen 279:273–277
95. Wang F, Li Y, Cai W, Zhan E, Mu X, Shen W (2009) Ethanol steam reforming over Ni and Ni-Cu catalysts. Catal Today 146:31–36
96. Fierro V, Klouz V, Akdim O, Mirodatos C (2002) Oxidative reforming of biomass derived ethanol for hydrogen production in fuel cell applications. Catal Today 75:141–144
97. Furtado AC, Alonso CG, Cantão MP, Fernandes-Machado NRC (2009) Bimetallic catalysts performance during ethanol steam reforming: influence of support materials. Int J Hydrogen Energy 34:7189–7196
98. Velu S, Suzuki K, Vijayaraj M, Barman S, Gopinath CS (2005) In situ XPS investigations of $Cu_{1-x}Ni_xZnAl$-mixed metal oxide catalysts used in the oxidative steam reforming of bio-ethanol. Appl Catal B: Environ 55:287–299
99. Mariño F, Boveri M, Baronetti G, Laborde M (2004) Hydrogen production via catalytic gasification of ethanol. A mechanism proposal over copper-nickel catalysts. Int J Hydrogen Energy 29:67–71
100. Zhang L, Liu J, Li W, Guo C, Zhang J (2009) Ethanol steam reforming over Ni-Cu/Al_2O_3-M_yO_z (M = Si, La, Mg, and Zn) catalysts. J Nat Gas Chem 18:55–65

101. Klouz V, Fierro V, Denton P, Katz H, Lisse JP, Bouvot-Mauduit S, Mirodatos C (2002) Ethanol reforming for hydrogen production in a hybrid electric vehicle: process optimisation. J Power Sources 105:26–34
102. Vizcaíno AJ, Carrero A, Calles JA (2009) Ethanol steam reforming on Mg and Ca-modified Cu-Ni/SBA-15 catalysts. Catal Today 146:63–70
103. Mariño F, Boveri M, Baronetti G, Laborde M (2001) Hydrogen production from steam reforming of bioethanol using Cu/Ni/K/γ-Al_2O_3 catalysts. Effect of Ni. Int J Hydrogen Energy 26:665–668
104. Mariño F, Baronetti G, Jobbagy M, Laborde M (2003) Cu-Ni-K/γ-Al_2O_3 supported catalysts for ethanol steam reforming. Formation of hydrotalcite-type compounds as a result of metal-support interaction. Appl Catal A: Gen 238:41–54
105. Galetti AE, Gomez MF, Arrua LA, Marchi AJ, Abello MC (2008) Study of CuCoZnAl oxide as catalyst for the hydrogen production from ethanol reforming. Catal Commun 9:1201–1208
106. Llorca J, de la Piscina PR, Sales J, Homs N (2001) Direct production of hydrogen from ethanolic aqueous solutions over oxide catalysts. Chem Commun:641–642
107. Széchenyi A, Solymosi F (2007) Production of hydrogen in the decomposition of ethanol and methanol over unsupported Mo_2C catalysts. J Phys Chem 111:9509–9515
108. Barthos R, Széchenyi A, Solymosi F (2008) Efficient H_2 production from ethanol over Mo_2C/C nanotube catalyst. Catal Lett 120:161–165
109. Barthos R, Széchenyi A, Koos A, Solymosi F (2007) The decomposition of ethanol over Mo_2C/carbon catalysts. Appl Catal A: Gen 327:95–105
110. Akande A, Aboundheir A, Idem R, Dalai A (2006) Kinetic modelling of hydrogen production by the catalytic reforming of crude ethanol over a co-precipitated Ni-Al_2O_3 catalyst in a packed bed tubular reactor. Int J Hydrogen Energy 31:1707–1715
111. Morgenstern DA, Fornango JP (2005) Low-temperature reforming of ethanol over cupper plated Raney nickel: new rout to sustainable hydrogen for transportation. Energy Fuel 19:1708–1716
112. Akande AJ, Idem RO, Dalai AK (2005) Synthesis, characterization and performance evaluation of Ni/Al_2O_3 catalysts for reforming of crude ethanol for hydrogen production. Appl Catal A: Gen 287:159–175
113. Ciambelli P, Palma V, Ruggiero A (2010) Low temperature catalytic steam reforming of ethanol. 2. Preliminary kinetic investigation of Pt/CeO_2 catalysts. Appl Catal B: Environ 96:190–197
114. Akpan E, Akande A, Aboudheir A, Ibrahim H, Idem R (2007) Experimental, kinetic and 2-D reactor modelling for simulation of the production of hydrogen by the catalytic reforming of concentrated crude ethanol (CRCCE) over a Ni-based commercial catalyst in a packed–bed tubular reactor. Chem Eng Sci 62:3112–3126
115. Simson A, Waterman E, Farrauto R, Castaldi M (2009) Kinetic and process study for ethanol reforming using a Rh/Pt washcoated monolith catalyst. Appl Catal B: Environ 89:58–64
116. Görke O, Pfeifer P, Schubert K (2009) Kinetic study of ethanol reforming in a microreactor. Appl Catal A: Gen 360:232–241
117. Benito M, Sanz JL, Isabel R, Padilla R, Arjona R, Daza L (2005) Bio-ethanol steam reforming: insights on the mechanism for hydrogen production. J Power Sources 151:11–17
118. Panja C, Saliba N, Koel BE (1998) Adsorption of methanol, ethanol and water on well-characterized Pt-Sn surface alloys. Surf Sci 395:248–259
119. Sexton BA, Rendulic KD, Hughes AE (1982) Decomposition pathways of C1–C4 alcohols adsorbed on platinum (111). Surf Sci 121:181–198
120. Rajumon MK, Roberts MW, Wang F, Wells PB (1998) Chemisorption of ethanol at Pt(111) and Pt(111)-O surfaces. J Chem Soc Faraday Trans 94:3699–3703
121. Lee AF, Gawthrope DE, Hart NJ, Wilson K (2004) A fast XPS study of the surface chemistry of ethanol over Pt{111}. Surf Sci 548:200–208
122. Davis JL, Barteau MA (1990) Spectroscopic identification of alkoxide, aldehyde, and acyl intermediates in alcohol decomposition on Pd(111). Surf Sci 235:235–248

123. Gates SM, Russel JN, Yates JT Jr (1986) Bond activation sequence observed in the chemisorption and surface reaction of ethanol on Ni(111). Surf Sci 171:111–134
124. Resta A, Gustafson J, Westerström R, Mikkelsen A, Lundgren E, Andersen JN, Yang MM, Mab XF, Bao XH, Li WX (2008) Step enhanced dehydrogenation of ethanol on Rh. Surf Sci 602:3057–3063
125. Sexton BA (1979) Surface vibrations of adsorbed intermediates in the reaction of alcohols with Cu (100). Surf Sci 88:299–318
126. Greenler RG (1962) Infrared study of the adsorption of methanol and ethanol on aluminum oxide. J Chem Phys 37:2094–2099
127. Spitz RN, Barton JE, Barteau MA, Staley RH, Sleight AW (1968) Characterization of the surface acid-base properties of metal oxides by titration displacement reactions. J Phys Chem 90:4067–4075
128. Raskó J, Hancz A, Erdőhelyi A (2004) Surface species and gas phase products in steam reforming of ethanol on TiO_2 and Rh/TiO_2. Appl Catal A: Gen 269:13–25
129. Yee A, Morrison SJ, Idriss H (1999) A study of the reactions of ethanol on CeO_2 and Pd/CeO_2 by steady state reactions, temperature programmed desorption and in situ FT-IR. J Catal 186:279–295
130. Yee A, Morrison SJ, Idriss H (2000) A study of ethanol reaction over Pt/CeO_2 by temperature-programmed desorption and in situ FT-IR spectroscopy: evidence of benzene formation. J Catal 191:30–45
131. Golay S, Doepper R, Renken A (1998) In-situ characterization of the surface intermediates for the ethanol dehydration reaction over γ-alumina under dynamic conditions. Appl Catal Gen 172:97–106
132. de Lima SM, da Silva AM, da Costa LOO, Assaf JM, Jacobs G, Davis BH, Mattos LV, Noronha FB (2010) Evaluation of the performance of Ni/La_2O_2 catalyst prepared from $LaNiO_3$ perovskite-type oxides for the production of hydrogen through steam reforming and oxidative steam reforming of ethanol. Appl Catal A: Gen 377:181–190
133. Farkas AP, Solymosi F (2007) Adsorption and reaction of ethanol on Mo_2C/Mo(100). Surf Sci 601:193–200
134. Rachmadi W, Vannice MA (2002) Acetic acid reduction by H_2 over supported Pt catalysts: DRIFTS and TPD/TPR study. J Catal 207:317–330
135. Raskó J, Dömök M, Baán K, Erdőhelyi A (2006) FTIR and mass spectrometric study of the interaction of ethanol and ethanol-water with oxide-supported platinum catalysts. Appl Catal A: Gen 299:202–211
136. Hussein GAM, Sheppard N, Zaki MI, Fahim RB (1991) Infrared spectroscopic studies of the reactions of alcohols over group IVB metal oxide catalysts 3. Ethanol over TiO_2 ZrO_2 and HfO_2 and general conclusion from part 1 to part 3. J Chem Soc Faraday Trans 87:2661–2668
137. Cordi EM, Falconer JL (1996) Oxidation of volatile compounds on Al_2O_3, Pd/Al_2O_3 and PdO/Al_2O_3 catalysts. J Catal 162:104–117
138. Mavrikakis M, Barteau MA (1998) Oxygenate reaction pathways on transition metal surfaces. J Mol Catal A: Chem 131:135–147
139. Silva AM, Costa LOO, Barandas APMG, Borges LEP, Mattos LV, Noronha FB (2008) Effect of metal nature on the reaction mechanism of partial oxidation of ethanol over CeO_2-supported Pt and Rh catalysts. Catal Today 133–135:755–761
140. de Lima SM, da Silva AM, da Costa LOO, Graham UM, Jacobs G, Davis BH, Mattos LV, Noronha FB (2009) Study of catalyst deactivation and reaction mechanism of steam reforming, partial oxidation, and oxidative steam reforming of ethanol over Co/CeO_2 catalyst. J Catal 268:268–281
141. de Lima SM, Silva AM, Graham UM, Jacobs G, Davis BH, Mattos LV, Noronha FB (2009) Ethanol decomposition and steam reforming of ethanol over $CeZrO_2$ and Pt/$CeZrO_2$ catalysts: reaction mechanism and deactivation. Appl Catal A: Gen 352:95–113
142. Jacobs G, Keogh RA, Davis BH (2007) Steam reforming of ethanol over Pt/ceria with co-fed hydrogen. J Catal 245:326–337

143. de Lima SM, Silva AM, da Cruz IO, Jacobs G, Davis BH, Mattos LV, Noronha FB (2008) H_2 production through steam reforming of ethanol over Pt/ZrO_2, Pt/CeO_2 and $Pt/CeZrO_2$ catalysts. Catal Today 138:162–168
144. de Lima SM, Colman RC, Jacobs G, Davis BH, Souza KR, de Lima AFF, Appel LG, Mattos LV, Noronha FB (2009) Hydrogen production from ethanol for PEM fuel cells. An integrated fuel processor comprising ethanol steam reforming and preferential oxidation of CO. Catal Today 146:110–123
145. de Lima SM, da Silva AM, Jacobs G, Davis BH, Mattos LV, Noronha FB (2010) New approaches to improving catalyst stability over Pt/ceria during ethanol steam reforming: Sn addition and CO_2 co-feeding. Appl Catal B: Environ 96:387–398
146. Yee A, Morrison SJ, Idriss H (2000) The reactions of ethanol over M/CeO_2 catalysts. Evidence of carbon-carbon bond dissociation at low temperatures over Rh/CeO_2. Catal Today 63:327–335
147. Chen H-L, Liu S-H, Ho J-J (2006) Theoretical calculation of the dehydrogenation of ethanol on a $Rh/CeO_2(111)$ surface. J Phys Chem B 110:14816–14823
148. de Lima SM, da Cruz IO, Jacobs G, Davis BH, Mattos LV, Noronha FB (2008) Steam reforming, partial oxidation, and oxidative steam reforming of ethanol over $Pt/CeZrO_2$ catalyst. J Catal 257:356–368
149. Wang J-H, Lee CS, Lin MC (2009) Mechanism of ethanol reforming: theoretical foundations. J Phys Chem 113:6681–6688
150. Resini C, Montanari T, Barattini L, Ramis G, Busca G, Presto S, Riani P, Marazza R, Sisani M, Marmottini F, Costantino U (2009) Hydrogen production by ethanol steam reforming over Ni catalysts derived from hydrotalcite-like precursors: catalyst characterization, catalytic activity and reaction path. Appl Catal A: Gen 355:83–93
151. Takanabe K, Aika K-I, Inazu K, Baba T, Seshan K, Lefferts L (2006) Steam reforming of acetic acid as a biomass derived oxygenate: bifunctional pathway for hydrogen formation over Pt/ZrO_2 catalysts. J Catal 243:263–269
152. Tibiletti D, Meunier FC, Goguet A, Reid D, Burch R, Bosaro M, Vicario M, Trovarelli A (2006) An investigation of possible mechanisms for water—gas shift reaction over a ZrO_2 supported Pt catalyst. J Catal 244:183–191
153. Souza MVM, Schmal M (2005) Autothermal reforming of methane over $Pt/ZrO_2/Al_2O_3$ catalysts. Appl Catal A: Gen 281:19–24
154. Platon A, Roh HS, King DL, Wang Y (2007) Deactivation study of $Rh/Ce_{0.8}Zr_{0.2}O_2$ catalysts in low temperature ethanol steam reforming. Top Catal 46:374–379
155. Frusteri F, Freni S, Chiodo V, Spadaro L, Bonura G, Cavallaro S (2004) Potassium improved stability of Ni/MgO in the steam reforming of ethanol for the production of hydrogen for MCFC. J Power Sources 132:139–144
156. Liberatori JWC, Ribeiro RU, Zanchet D, Noronha FB, Bueno JMC (2007) Steam reforming of ethanol on supported nickel catalysts. Appl Catal A: Gen 327:197–204

Chapter 5
Methanol Steam Reforming

Malte Behrens and Marc Armbrüster

5.1 Introduction

The currently increasing interest in catalytic reactions of methanol, CH_3OH, is—in addition to its customary role as an important base chemical and feedstock for value-added molecules—due to its potential as a chemical storage molecule for hydrogen. Methanol is industrially produced from natural gas- or coal-derived syngas, but can in principle also be synthesized from CO_2 by hydrogenation [1]. It is suggested by Olah et al. [2] as a "CO_2-neutral" combustion fuel in the context of the so-called methanol economy or can be used in direct methanol fuel cells (DMFC) for generation of electric power. Methanol might thus play a key role in the transition toward a future energy scenario, which has to be more and more independent from fossil sources [3].

The main advantage of using methanol for chemical instead of physical storage of hydrogen is related to its decentralized use of hydrogen, e.g., in the transportation sector. Methanol is a very attractive onboard hydrogen source for polymer electrolyte membrane fuel cells (PEMFC) in mobile applications like automobiles, as it circumvents the problems of physical storage and distribution of hydrogen such as the necessity of pressurized or cryogenic containers. Methanol is liquid at ambient conditions and can be safely distributed using pipelines and conventional filling station infrastructure. It has a high H:C ratio of 4:1 and no C–C bond that has to be broken.

M. Behrens (✉)
Department of Inorganic Chemistry, Fritz-Haber-Institut der Max-Planck-Gesellschaft, Faradayweg 4-6, Berlin 14195, Germany
e-mail: behrens@fhi-berlin.mpg.de

M. Armbrüster
Max-Planck-Institut für Chemische Physik fester Stoffe, Nöthnitzer Strasse 40, Dresden 01187, Germany
e-mail: research@armbruester.net

L. Guczi and A. Erdőhelyi (eds.), *Catalysis for Alternative Energy Generation*,
DOI 10.1007/978-1-4614-0344-9_5,

There are several catalytic reactions available for liberating hydrogen from methanol:

Methanol decomposition (MD):

$$CH_3OH \rightarrow CO + 2H_2 \qquad \Delta H^0 = 90\,\text{kJ/mol} \tag{5.1}$$

Methanol steam reforming (MSR):

$$CH_3OH + H_2O \rightarrow CO_2 + 3H_2 \qquad \Delta H^0 = 49\,\text{kJ/mol} \tag{5.2}$$

Partial oxidation of methanol (POM):

$$CH_3OH + 0.5O_2 \rightarrow CO_2 + 2H_2 \qquad \Delta H^0 = -155\,\text{kJ/mol} \tag{5.3}$$

Furthermore, the water–gas shift (WGS) and reverse WGS (rWGS) reactions have to be considered:

$$CO + H_2O \rightleftharpoons CO_2 + H_2 \qquad \Delta H^0 = -41\,\text{kJ/mol}. \tag{5.4}$$

Among these reactions, MSR seems to be the most attractive as it generates the highest hydrogen concentration in the product stream, runs at relatively low temperatures of 500–600 K, and does not directly produce CO, which acts as a poison for the downstream PEMFC anode catalyst. MSR was first described in 1921 by J.A. Christiansen [4] and research on its application for hydrogen production has a long history [5]. The recently renewed interest was triggered by the development of fuel cell technology requiring clean and preferably renewable hydrogen. A number of general overview articles and reviews are available addressing the role of MSR in this context [5–11]. MSR is an endothermic reaction and requires external heating. It is sometimes used in combination with exothermic POM (autothermal reforming or oxidative steam reforming) [12, 13] or combustion of methanol [8] in order to generate the necessary heat. However, the endothermicity of MSR is much weaker compared to steam reforming of other hydrocarbons or higher alcohols [8] and reformer units can be relatively small enabling the onboard combination with PEMFCs. Several prototype vehicles that run on hydrogen fuel cell technology have already been developed by different companies. A comparison between methanol and other molecules as reactants for onboard hydrogen production can be found in the comprehensive review by Palo et al. and in the references therein [11].

This chapter will focus mainly on the challenges of catalyst development for MSR. The requirements for a good MSR catalyst to be used for onboard hydrogen production in combination with PEMFCs are the following:

- The catalyst should be highly selective to CO_2 and minimize the CO content in the hydrogen-rich product gas stream, which acts as a poison for PEMFC anodes.

- It should be active at low temperatures to be efficient and to disfavor the rWGS reaction as a source of CO.
- Its components should be abundant and of low cost and its preparation should be facile and scalable.
- It should be stable at extended time on stream, i.e., resistant to coke formation, stable against sintering, and tolerant toward catalyst poisons.
- In particular, it should be stable toward abrupt changes of the conditions of reforming, i.e., work reliably in transient situations like on–off operations as well as in steady state to produce sufficient amounts of hydrogen on demand.

The detrimental role of CO in the effluent for the downstream PEMFC is to be emphasized. CO chemisorbs irreversibly on the typically Pt-based fuel cell catalysts and causes irreversible site blocking. Its concentration has to be below ca. 20 ppm in order to prevent poisoning, which is usually not achieved in the reformer outlet gas. Thus, in technical applications, a gas purification step has to be introduced between reformer and fuel cell. The CO concentration in the gas stream can lowered by means of preferential oxidation (PROX) or using Pd membranes, which in both cases complicates the setup and generates costs [14]. Generally, a low selectivity to CO—in addition to high activity and stability—is, thus, a major and particular requirement for a successful MSR catalyst.

This chapter is divided into two parts treating different families of catalytic materials active in the MSR reaction. The first part covers the widely studied Cu-based catalysts, while the second part focuses on the role of intermetallic compounds in MSR. Some catalytic data from the literature for the MSR reaction over selected catalysts treated in this chapter are compiled in Table 5.1.

5.2 Cu-Based Catalysts for Methanol Steam Reforming

Cu-based catalysts are widely used in C1 chemistry. This is mostly due to the commercial interest in the most common industrial methanol synthesis catalyst, a complex $Cu/ZnO/Al_2O_3$ bulk catalyst, which is also active in MSR and fulfills many of the requirements mentioned above, such as high activity at low temperature, relatively low CO levels, and feasible and scalable—though complex—preparation at moderate costs. Commercial ternary $Cu/ZnO/Al_2O_3$ catalysts or the unpromoted binary Cu/ZnO model system was thus employed in many studies of MSR and this material will be discussed in detail below. While preparation and composition of the industrial catalyst $Cu/ZnO/Al_2O_3$ can be regarded as already highly optimized for application under methanol synthesis conditions, modifications of the Cu/ZnO/X system turned out to improve the properties of Cu-based catalysts for use in MSR. In particular, choosing another second oxide phase X, employing new catalyst precursors like layered double hydroxides (LDHs), or even changing to ZnO-free samples and using zirconia or ceria

Table 5.1 Comparison of catalytic performance in (oxidative) MSR of selected catalyst systems covered in this contribution

Catalyst	Pretreatment[a]	Conversion (%)	CO_x formation (%)	H_2 production rate (L g^{-1} h^{-1})	T (K)	Remarks[b]	References
43.8% Cu/ZnO	C623 R523	90	0.14[c]	–	582	(Co-ppt.)	[15]
39.4% $Cu/ZnO/Al_2O_3$	C623 R573	90	0.11[c]	–	579	(Co-ppt.)	[15]
32.3% $Cu/ZnO/ZrO_2$	C623 R573	90	0.05[c]	–	567	(Co-ppt.)	[15]
30.9% $Cu/ZnO/Al_2O_3/ZrO_2$	C623 R573	90	0.05[c]	–	551	(Co-ppt.)	[15]
$Cu/ZnO/Al_2O_3$	C723 R723	90	<0.05[c]	38.4	673	18 mol% Cu in LDH (Co-ppt.), oMSR	[16]
61.7% $Cu/ZnO/Al_2O_3$	R523	84.4	0.11[c]	1.4	523	(Commercial)	[17]
32.3% $Cu/ZnO/ZrO_2$	C723 R573	71.7	0.22[c]	8.7	503	(Co-ppt.), oMSR	[18]
35.5% $Cu/ZnO/CeO_2$	C723 R523	66.8	0.23[c]	8.2	503	(Co-ppt.), oMSR	[18]
8.5% Cu/ZrO_2	C773 R523	92	0.2[c]	–	523	(Templ. method)	[19]
16% Cu/ZrO_2	C673 R523	57	0.02[c]	–	523	(ME method)	[20]
3.9% Cu/CeO_2	C723 R673	90.7	2.3[d]	10.9	533	(Co-ppt.)	[21]
3.9% Cu/ZnO	C723 R673	66.8	0.9[d]	8.0	533	(Co-ppt.)	[21]
3.9% Cu/Al_2O_3	C723 R673	21.5	0.4[d]	2.6	533	(Co-ppt.)	[21]
QC-$Al_{63}Cu_{25}Fe_{12}$[e]	R523	–	–	14.1	573	L:NaOH	[22]
$CuAl_2$		–	–	3.81	513	L:NaOH/Na_2CrO_4	[23]

Ni_3Al	R523	10	6[f]	56[g]	793		[24]
A-$(Cu_{50}Zr_{50})_{90}Au_{10}$[e]	C550	80	100[f]	14.0	523		[25]
	R573						
10% Pd/SiO_2	C773	15.7	0[f]	2.82	493		[26]
	R773						
10% Pd/Al_2O_3	C773	67.4	0[f]	12.14	493		[26]
	R773						
10% Pd/ZnO	C773	55	99.8[f]	9.80	493		[26]
	R773						
10% Pt/SiO_2	C773	25.6	0.3[f]	4.61[h]	493[h]		[27]
	R773						
10% Pt/ZnO	C773	27.6	95.4[f]	4.96	493		[26]
	R773						
2% Pt–Zn/C	R873	100	83[f]	1.12	553	Zn/Pt = 5.0	[27]
2% Pt/C	R873	76	48[f]	0.84	553		[27]
10% Pt/In_2O_3	C773	30.6	98.3[f]	5.51	493		[28]
	R773						
10% Pt/Ga_2O_3	C773	5.4	75.5[f]	0.97	493		[28]
	R773						
10% Pd/Ga_2O_3	C773	21.2	94.6[f]	3.82	493		[26]
	R773						
10% Pd/In_2O_3	C773	28.3	95.5[f]	5.10	493		[26]
	R773						
15% Pd–In/Al_2O_3	C673	91	98.7[f]	68.25	698	In/Pd = 2	[26]
8.9% Pd–Zn/Al_2O_3	C623	46.5	99.4[f]	4.1	493	Zn/Pd = 2.6	[29]
	R673						
8.6% Pd/ZnO	C623	14.3	99.2[f]	1.6	493		[29]
	R673						

(continued)

Table 5.1 (continued)

Catalyst	Pretreatment[a]	Conversion (%)	CO_x formation (%)	H_2 production rate ($L\ g^{-1}\ h^{-1}$)	T (K)	Remarks[b]	References
10% Ni/ZnO	C773	15.7	4.7[f]	2.83[h]	493[h]		[27]
	R773						
10% Ni/SiO_2	C773	7.3	1.1[f]	1.31[c]	493[c]		[27]
	R773						
10% Co/ZnO	C773	20.3	8.9[f]	3.65[h]	493[h]		[27]
	R773						
Pd black	R513	7[i]	2[f]	13.3	533		[30]
ZnPd	R513	7[i]	100[f]	2.6	533		[30]
PtZn	R513	7[i]	50[f]	2.6	533		[30]
PdCd	R513	7[i]	100[f]	2.6	533		[30]
NiZn	R513	7[i]	15[f]	2.6	533		[30]

Note possible difference in feed gas composition and contact time of the experiments. Some values were recalculated from the data given in the original references

[a]Calcination (C) and reduction (R) temperatures in K

[b]Methods of preparation (*Co-ppt.* co-precipitation, *templ. method* template method, *ME method* microemulsion method, *LDH* layered double hydroxide, *L* leaching agent, *oMSR* oxidative MSR)

[c]Given as CO concentration in the product gas

[d]Given as selectivity toward CO

[e]*QC* quasicrystalline, *A* amorphous

[f]Given as selectivity toward CO_2

[g]In $L h^{-1}\ m^{-2}$

[h]Derived from comparison to data from [26]

[i]7–10% given

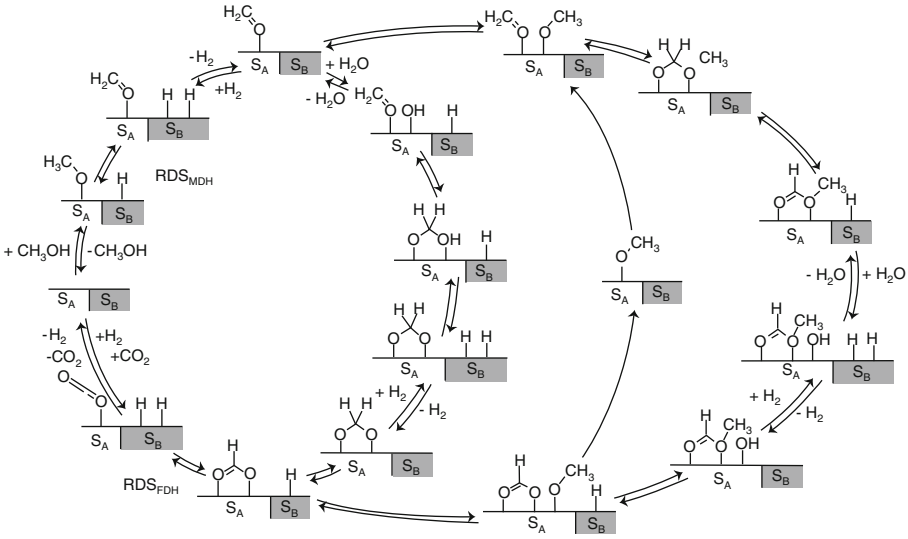

Fig. 5.1 Catalysis cycle for MSR over Cu-based catalysts based on the work in references [31–33], including two different kinds of reactive sites S_A and S_B. Reprinted from [37] with permission from Elsevier

for preparation of Cu-based catalysts was reported to lead to interesting MSR performance. The state of the active Cu surface under reaction conditions and the nature of the active sites are still debated in literature and will be discussed below.

Several studies are available addressing the mechanism and kinetics of the MSR reaction over Cu-based catalysts [31–37]. There seems to be agreement nowadays that CO_2 is a direct product of the MSR reaction and not of a sequence of MD and WGS reactions. The main source of CO is the rWGS reaction taking place as a secondary reaction after MSR. Frank et al. [37] presented a comprehensive microkinetic analysis of the MSR reaction based on the work of Peppley et al. [33]. They investigated several Cu-based catalysts with various oxide components showing considerably different activities. Similar activation energies support the idea that the surface chemistry is independent of the oxide material (with the exception of $Cu/Cr_2O_3/Fe_2O_3$, which behaved differently). Dehydrogenation of methoxy groups is the rate-limiting step and by means of DRIFTS experiments, methoxy and formate species were found to be the dominating species at the surface. Two distinct kinds of active sites were considered, S_A for the adsorption and desorption of oxygenates and S_B for hydrogen (Fig. 5.1), and two reaction pathways of the methoxy intermediate are discussed via dioxomethylene, the intermediate of the reverse methanol synthesis reaction, or methyl formate. On the basis of the kinetic data it was not possible to decide which route was dominant.

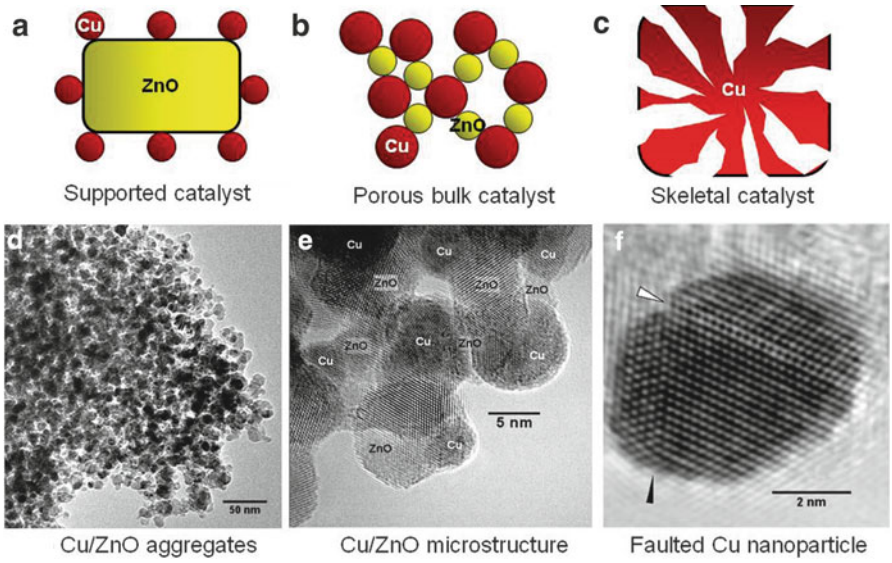

Fig. 5.2 Schemes of different catalyst microstructures (**a–c**) and transmission electron micrographs of a Cu/ZnO/(Al_2O_3) catalyst (**d** and **e**). In the high-resolution image (**f**) planar defects of the Cu-nanoparticles like twin boundaries (*black arrow*) and stacking faults (*white arrow*) can be seen

5.2.1 General Aspects of Cu/ZnO-Based Catalysts

Commercial Cu/ZnO/Al_2O_3 methanol synthesis catalysts are often mistaken as supported systems, but neither ZnO nor Al_2O_3 represents a classical extended oxidic support. This is obvious, when considering the typical composition of modern Cu/ZnO/(Al_2O_3) catalysts, which is characterized by a molar Cu:Zn ratio close to 70:30, while the amount of Al_2O_3 typically is significantly lower than that of ZnO. This Cu-rich composition manifests itself in a peculiar microstructure of the industrial Cu/ZnO/Al_2O_3 catalyst (Fig. 5.2) [38], which is composed of spherical Cu nanoparticles of a size <10 nm and often even smaller ZnO nanoparticles arranged in an alternating fashion. Thus, porous aggregates are formed (Fig. 5.2d) in which the oxide particles act as spacers between Cu particles (Fig. 5.2e). The presence of interparticle pores as seen in the HRTEM image allows some access to the "inner surface" of larger Cu/ZnO aggregates. This unique microstructure, represented in Fig. 5.2b, can be described as an intermediate stage between a supported catalyst, schematically drawn in Fig. 5.2a, and a bulk metallic sponge or skeletal Raney-type catalyst, represented in Fig. 5.2c.

It is this unique microstructure that enables a reasonably high dispersion of Cu and exposure of many Cu–ZnO interfaces at a high total Cu content. The specific Cu surface area (SA_{Cu}) of methanol catalysts can be determined by reactive N_2O titration [39], which causes surface oxidation of the Cu particles and allows estimation of SA_{Cu} from the amount of evolved N_2, as N_2O is decomposed at the

metallic Cu surface, or from the H_2 consumption upon re-reduction. Assuming the formation of an oxygen monolayer, a surface stoichiometry corresponding to Cu_2O and an abundance of 1.47×10^{19} copper atoms/m^2, SA_{Cu} can be calculated in $m^2\ g^{-1}$. This method has to be applied carefully, as for instance very high temperatures may cause a significant extent of bulk oxidation, which leads to an overestimation of SA_{Cu} [40, 41]. Also, the reaction of oxygen vacancies of the oxide components with N_2O or modified reactivity of a defective Cu surface toward N_2O may be a source of error. SA_{Cu} of the state-of-the-art methanol synthesis catalyst measured by this method amounts to 25–35 $m^2\ g^{-1}$. If reliable data of the average Cu particle size are available, e.g., by sufficient TEM observations [38], the degree of oxide coverage of the Cu particles, i.e., the average ratio of interface to surface area, can be calculated. For industrial $Cu/ZnO/Al_2O_3$ catalysts, this value is around 35% [42]. The high MSR activity of this type of $Cu/ZnO/(Al_2O_3)$ catalysts at relatively low temperatures can most likely be explained with the large SA_{Cu} due to this favorable microstructure and to the proper balance of Cu dispersion and loading.

Clearly, one role of ZnO is to act as spacer and stabilizer avoiding direct contact of the Cu particles and prevent them from sintering [43]. In addition to this geometrical function, a so-called Cu–ZnO synergy is described in literature for the methanol synthesis reaction [44]. The nature of this synergy is debated and several models have been proposed. Strong metal–support interactions (SMSI) between Cu and ZnO were observed at highly reducing conditions [45] and it was suggested that partially reduced ZnO_x migrates onto the surface of the Cu particles under methanol synthesis conditions [46]. On a supported Cu/ZnO model catalyst, reversible wetting/de-wetting was observed as the reduction potential of the gas phase was varied [47], which was not detected on Cu/SiO_2. While the role of surface decoration or morphology change for high-performance catalysts under industrial methanol synthesis conditions is still unclear, a correlation of the concentration of planar defects in the Cu particles with the catalytic activity in methanol synthesis was observed in a series of industrial $Cu/ZnO/Al_2O_3$ catalysts by Kasatkin et al. [38]. Planar defects like stacking faults and twin boundaries can also be observed by HRTEM and are marked with arrows in Fig. 5.2f. The origin of strain and defects is thought to be the interface of the Cu particles with the ZnO phase.

It is generally agreed that the role of ZnO in Cu-based methanol synthesis catalysts exceeds the function of a mere physical stabilizer and ZnO is a crucial component in high-performance methanol synthesis catalysts. In light of the fact that highly active Cu-based MSR catalysts can also be prepared in the absence of ZnO (e.g., as Cu/ZrO_2, see below), this type of Cu–ZnO synergy does not seem to be a critical factor in case of MSR compared to methanol synthesis or it is not as strictly limited to ZnO.

On the other hand, there are many similarities between methanol synthesis and MSR [34]. This is often accounted for by the concept of microscopic reversibility, as MSR formally is the reverse reaction of methanol synthesis. It has to be considered, however, that the different reactant gas mixtures used for MSR and methanol synthesis will affect the surface state of the catalyst, which consequently will be different under highly reducing methanol synthesis conditions compared to the much less reducing MSR feed. Thus, unlike forward and backward reactions at

equilibrium, methanol synthesis and MSR probably take place over practically different catalytic surfaces. This general limit of the application of the concept of microscopic reversibility has been pointed out by Spencer for WGS and rWGS [48] and is valid accordingly also for methanol synthesis and MSR [49]. One may conclude that an optimized methanol synthesis catalyst, for which the fine-tuning of preparation and operation conditions is far more advanced, will also be active in MSR due to its generally large SA_{Cu} and represents a powerful reference system, but will not necessarily represents the optimal catalyst for this reaction [49]. Finding Cu/ZnO/X systems with a composition and microstructure optimized for the MSR reaction is thus the major current challenge in the development of a MSR catalyst for energy applications.

5.2.2 Drawbacks of Cu/ZnO-Based Catalysts

The unique microstructure of modern Cu/ZnO/(Al_2O_3) methanol synthesis catalysts described above is responsible for many advantages of Cu-based catalysts and their application in MSR, such as high SA_{Cu}. However, a major drawback of Cu-based catalysts is their lack of long-term stability.

A loss of 30–40% of the initial MSR activity was observed by Frank et al. [37] for the selection of Cu-based catalysts in combination with different oxide components (Fig 5.3d). Deactivation proceeds faster during the first 100 h on stream and tends to level off afterwards. Deactivation of Cu/ZnO/Al_2O_3 catalysts in MSR has been reviewed by Twigg and Spencer [49]. A major aspect is the loss of SA_{Cu} due to Cu particle sintering. The melting point of elemental Cu is relatively low at T_M = 1,336 K resulting in low Tamann and Hüttig temperatures of 0.5 T_M and 0.3 T_M, respectively. The former refers to the approximated onset temperature of atom mobility leading to thermal sintering, while the latter is estimated to be the onset temperature of defect annealing. Compared to other metals, Cu is generally quite sensitive to sintering [50] and, as a rule of thumb, Cu-based catalysts should not be operated above ca. 600 K after activation. For the same reason, the pretreatment conditions of the catalysts have to be selected with care. Especially the exothermic reduction step during catalyst activation is crucial, as the heat of reduction may cause high local temperatures, thermal sintering, and a loss of SA_{Cu}. In spent Cu-rich commercial methanol synthesis catalysts, intermediate stages of sintering by coalescence can be identified by HRTEM (Fig. 5.3a, b) [51]. Interestingly, the formation of fivefold cyclic twins originating from the contact area of two Cu particles is observed in these images. The evolution of the Cu particle size distributions (Fig. 5.3c), determined by the evaluation of TEM micrographs of several thousand Cu particles, shows a clear widening and shift of the particle size distribution to larger particle diameters.

Rapid deactivation may not only be caused by external heat input during reaction alone but also considering the operating atmosphere of the catalyst. In methanol synthesis, which is operated at a similar temperature like MSR, modern Cu/ZnO/

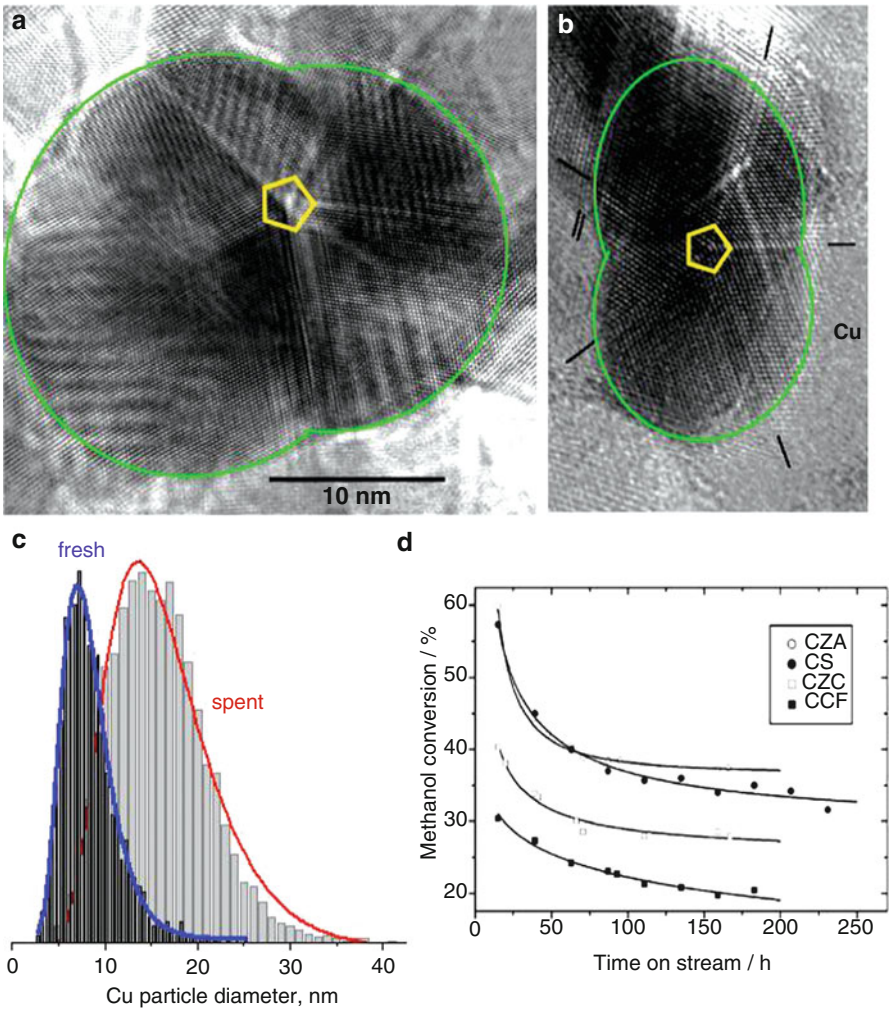

Fig. 5.3 HRTEM images of $Cu/ZnO/Al_2O_3$ catalyst used in methanol synthesis (**a** and **b**); evolution of the particle size distribution during reaction (**c**); and loss in methanol conversion with time on stream for different Cu-based catalysts during MSR at 493 K, 1 bar, MeOH: H_2O = 1:1 (**d**, CZA: 0.5 g $Cu/ZnO/Al_2O_3$, CS: 2.0 g Cu/SiO_2, CZC: 1.0 g $Cu/ZrO_2/CeO_2$, CCF: 2.5 g $Cu/Cr_2O_3/Fe_2O_3$, reprinted from [37] with permission from Elsevier)

Al_2O_3 catalysts can deliver stable performance over years on stream. The same catalyst may tend to deactivate more rapidly under MSR conditions suggesting a critical role of the gas-phase composition, most probably of water in the feed, on the sintering behavior. Löffler et al. [52] investigated the stability of several commercial WGS catalysts in the MSR reaction and fitted their data using a sintering model. $Cu/ZnO/Al_2O_3$ formulations were found to be the most active compared to other catalyst compositions, but were also most prone to deactivation by sintering.

In their analysis of catalyst deactivation of a commercial $Cu/ZnO/Al_2O_3$ catalyst during MSR, Thurgood et al. [53] revealed that in addition to the loss of surface area, also the site concentration at the catalyst's surface declined with time on stream.

The sensitivity of a given Cu/ZnO/X catalyst toward sintering under MSR conditions is determined by three main aspects: composition (Cu:Zn ratio), nature of promoting oxide X, and catalyst microstructure. Obviously, a high Cu:Zn ratio will lower the distance between neighboring Cu particles and favor the formation of direct contacts leading to sintering by particle coalescence. Lowering the Cu loading increases the stabilizer-to-metal ratio, and is thus expected to contribute to the stabilization of Cu particles. It is, however, usually not desired to significantly decrease the amount of active metal in a Cu/ZnO catalyst. In particular, it is noted that for preparation of the porous Cu–ZnO arrangement (Fig. 5.2) the Cu:Zn ratio is a crucial parameter, which has a clear optimum depending on the solid-state chemistry of the hydroxycarbonate precursor phase and cannot be varied freely without sacrificing SA_{Cu} and, thus, activity (see below).

It seems much more promising to try to stabilize a Cu/ZnO catalyst at a given (optimized) Cu:Zn ratio by adding a second oxidic species X and thus modify the Cu–ZnO interactions. In case of the methanol synthesis catalyst, these interactions seem to be significantly strengthened by the addition of small amounts of Al_2O_3 [49]. Ternary $Cu/ZnO/Al_2O_3$ catalysts are significantly more stable toward thermal sintering and consequently show a considerably longer lifetime in methanol synthesis than binary Cu/ZnO systems. In MSR also the hydrothermal stability of the oxide phase and its contact to the Cu particles has to be considered. Looking at Fig. 5.2e it becomes apparent that not only thermal sintering induced by mobility of Cu but also segregation or recrystallization of the ZnO component (e.g., induced by steam) will have the same detrimental effect on the porous Cu/ZnO arrangement and cause a loss of SA_{Cu}. Other ZnO/X combinations than ZnO/Al_2O_3, especially ZnO/ZrO_2 (see below) are promising candidates for the preparation of improved Cu-based MSR catalysts.

The third important consideration concerns the microstructure of the catalyst and is closely related to the Cu:Zn ratio and to the stabilizing interactions between Cu metal and the oxide. Modern $Cu/ZnO/Al_2O_3$ catalysts exhibit a unique and apparently fragile microstructure. The nanoscaled arrangement of metallic Cu and oxidic spacer particles seen in Fig. 5.2 is metastable and an irreversible gradual breakdown of the porous aggregates can be expected if the sample is submitted to thermal stress as the system lowers its free surface energy. Highly active $Cu/ZnO/Al_2O_3$ is pyrophoric and may even deactivate upon contact with air as the heat of oxidation of the highly reactive Cu nanoparticles is sufficient to cause sintering. A microstructure exhibiting larger and more stable Cu–ZnO interfaces may thus be desirable in order to stabilize the Cu particles. It is noted that the catalyst's microstructure heavily depends on its preparation history [17]. For example, at a given industrially relevant composition (Cu:Zn:Al = 60:25:15) the interface-to-surface ratio can be significantly increased to 50% for a $Cu/ZnO/Al_2O_3$ catalyst if the precursor preparation is modified by going from a batch process including

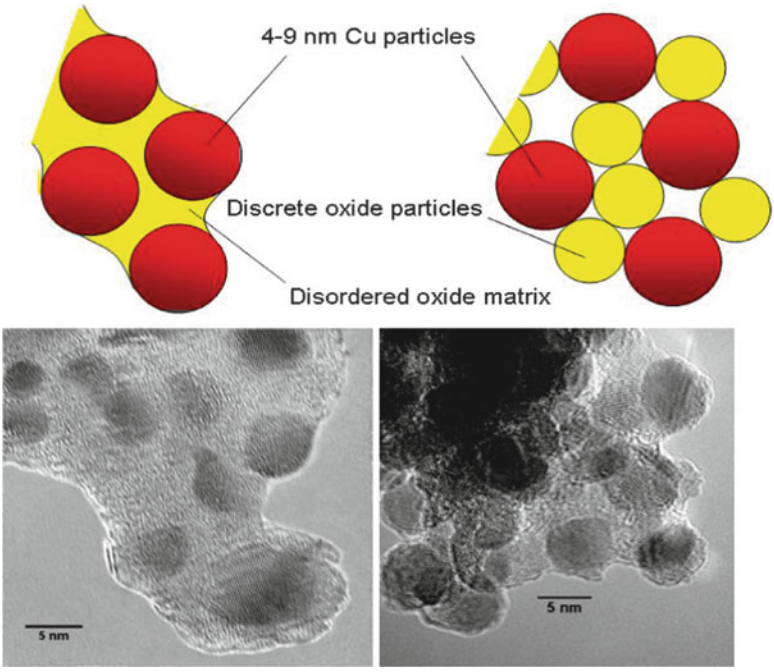

Fig. 5.4 Scheme and TEM micrographs of the microstructure of differently prepared Cu/ZnO/Al_2O_3 catalyst with the same composition and similar Cu particle sizes; adapted from [42]

precipitate aging to a continuous process suppressing the aging period [42]. In this example, the Cu particles have a similar size like in a conventional Cu/ZnO/Al_2O_3 catalyst, but are more deeply embedded into an amorphous oxide matrix and modified Cu–oxide interactions can be expected (Fig. 5.4). Generally, a low value of the interface-to-surface ratio of the Cu particles enables a large SA_{Cu}, while a larger value leads to a stronger embedment and different wetting behavior which may increase the stability of the catalyst toward thermal sintering. An intermediate value may represent a kind of compromise between both effects.

Other sources of catalyst deactivation are catalyst poisons like sulfur or chlorine [49]. These contaminations do typically not originate from the methanol feed, but may be present in steam or air used for MSR or oxidative MSR. Sulfur acts as a site-blocking poison for Cu and chlorine promotes sintering by formation of low-melting and mobile Cu and Zn chlorides. Agarwal et al. [54] reported coke formation as another source of deactivation of Cu/ZnO/Al_2O_3 catalysts in MSR.

The other major problem of Cu-based MSR catalysts is the formation of still too much CO during MSR, typically in the low % range. Agrell et al. [55] reported that the problem of CO formation over Cu/ZnO/Al_2O_3 catalysts can be attenuated by increasing the steam-to-methanol ratio or by the addition of oxygen or air (oxidative MSR). CO is formed at high methanol conversions most likely by the rWGS reaction consecutively to MSR as a secondary product. Decreasing the contact time

leads to lower CO selectivity. Lowering the reaction temperature is also helpful as it disfavors the rWGS equilibrium. Thus, probably the best way to make a Cu-based MSR catalyst less selective to CO would be to make it more active at lower temperatures.

5.2.3 *Preparation of Cu/ZnO-Based Catalysts*

The most studied member of the Cu/ZnO catalysts family for C1 chemistry is the commercial methanol synthesis catalyst, which can be seen as a reference system for Cu-based MSR catalysts (see above). It is prepared by co-precipitation, which is by far the most important method for synthesis of Cu/ZnO-based catalysts.

The industrially applied preparation of the low-temperature methanol synthesis catalyst was introduced by ICI company in 1966 and comprises co-precipitation and aging of a mixed Cu,Zn,(Al) hydroxycarbonate precursor material, thermal decomposition yielding an intimate mixture of the oxides, and finally activation of the catalyst by reduction of the Cu component [56]. The synthesis parameters have been studied in many academic and industrial groups and a high degree of optimization could be achieved over the last decades by mostly empirical fine-tuning of the conditions. The delicate nanoparticulate and porous microstructure of the industrial methanol synthesis catalyst (see above) can only be obtained if the optimized parameters are strictly obeyed during synthesis. Especially the synthesis conditions during the early co-precipitation and aging steps turned out to be crucial for the catalytic properties of the resulting methanol synthesis catalyst. This phenomenon, sometimes termed the "chemical memory" of the Cu/ZnO system [57], indicates the critical role of the preparation history of this catalyst system [17, 58, 59]. As was already mentioned above and is apparent from Fig. 5.2, the microstructural arrangement of Cu and ZnO in the final catalyst is metastable and tends to lower its free energy by sintering and segregation into macroscopic crystallites. Considering that the desired composite product is thus only kinetically stabilized and does not represent a deep minimum in the free energy landscape, it is not surprising that the precursor, i.e., the starting point of the path through the energy landscape during preparation, is of decisive importance for the exact position of our end point at which we wish to kinetically trap the system to obtain the arrangement like that seen in Fig. 5.2. Baltes et al. [58] elaborated a quantitative basis of the chemical memory in a systematic study and reported dramatic difference in SA_{Cu} of $Cu/ZnO/Al_2O_3$ catalysts of the same composition as pH or temperature of the co-precipitation step was varied. If self-made Cu/ZnO catalysts are employed as reference systems for MSR studies, it is thus very important to carefully prepare the catalyst as it is much easier to synthesize a poor Cu/ZnO catalyst than a good one, which could act as a conclusive reference for comparison with novel materials.

Preferred Cu:Zn ratios for ternary Cu,Zn,Al and binary Cu,Zn catalysts are near 70:30 [60] or 2:1 [61]. It was reported that the best catalysts can be obtained by constant pH co-precipitation with Na_2CO_3 solution at pH 6 or 7 and at elevated

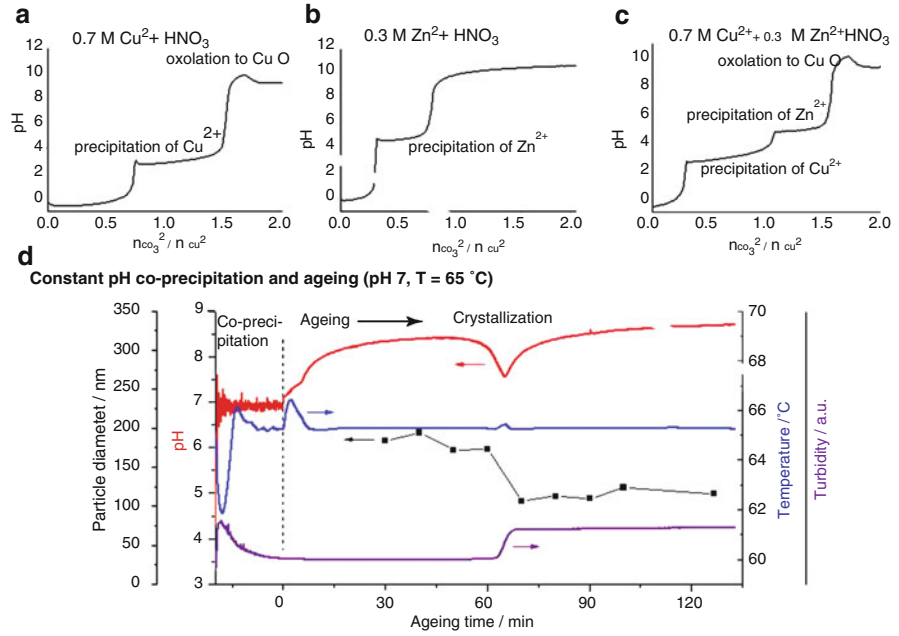

Fig. 5.5 Precipitation titration curves relevant for the co-precipitation of $Cu/ZnO/Al_2O_3$ catalyst precursors at 338 K using aqueous Na_2CO_3 as precipitation agent (**a**–**c**, adapted from [65]); preparation log of corresponding constant pH co-precipitation (**d**), adapted from [66]

temperatures around 333–343 K [58, 62]. Aging of the initial precipitate is crucial [61, 63, 64] and takes from around 30 min to several hours. Calcination is typically performed at relatively mild temperatures around 600–700 K. No doubt, this multistep preparation of Cu/ZnO catalysts is complex, but some progress in understanding the chemical memory has been made recently and helps to rationalize the benefit of exactly this setting of parameters.

It is clear that the target microstructure shown in Fig. 5.2 requires a homogeneous and maximized intermixing of the Cu and Zn species in order to stabilize the alternating arrangement of small Cu and ZnO nanoparticles. Thus, the main goal of the preparation is to carry over and maintain the perfectly homogeneous cation distribution in the mixed solution to a maximum extent via the precipitate to the final catalyst. The first step in this process is the solidification of the dissolved Cu and Zn cations by precipitation by elevation of pH. Precipitation titration is an elegant way to study the cation hydrolysis of Cu^{2+} and Zn^{2+} under conditions relevant for catalyst preparation [65]. Such experimental results are shown in Fig. 5.5a–c.

It can be seen in Fig. 5.5a that the hydrolysis of the pure Cu^{2+} solution is characterized by an underlying neutralization of the acidic starting solution with the basic precipitating agent. The S-shaped neutralization curve is interrupted by a precipitation plateau near pH 3, where Cu^{2+} forms a precipitate. If we now look at

the Zn^{2+} solution (Fig. 5.5b), a qualitatively similar picture emerges, but with the important difference that the Zn-precipitate is formed at pH 5 instead for pH 3. Such differences in hydrolysis behavior are of course not uncommon and are the basis for the traditional wet chemical ion separation techniques used for qualitative cation analysis. What is important, however, is that the precipitation titration curve of the binary system (Fig. 5.5c) is directly composed of those of the single systems. This fact indicates that there is no formation of a mixed binary precipitate under these conditions, but that Cu^{2+} is first completely precipitated at pH 3, which can be also seen from the vanishing of the blue color from the mother solution at pH 4, while Zn^{2+} is precipitated "on top" later at pH 5. Clearly, such increasing pH processes cannot yield a well-intermixed precipitate. The solution to this problem is the application of the constant pH co-precipitation technique [67, 68], meaning that the acidic metal solution and the precipitating agent are dosed simultaneously in a way that the average pH in the reaction vessel is maintained more or less constant. Using this mode of precipitation, it is possible to precipitate Cu and Zn very close in space and time as the curves shown in Fig. 5.5 are passed through not for the whole batch at once, but for every single droplet that hits the receiver solution. Thus, the cation distribution in the precipitate obtained by constant pH co-precipitation is much more homogeneous [65].

Also, the suitable pH for the precursor preparation can be deduced from the titration curves shown in Fig. 5.5. It should not be lower than 5 to guarantee complete precipitation of Zn^{2+} (and Al^{3+}), which otherwise would remain at least partially in solution. On the other hand, the pH should stay below 9, because in a very basic solution de-mixing of the Cu,Zn precipitate by oxolation of basic copper precipitates into stable tenorite, CuO, occurs [65]. This oxolation can be seen as a dip in the titration curves at high pH. Indeed, CuZn(Al) precursors are typically co-precipitated at neutral or even slightly acidic pH [58, 61, 62]. It is noted that the position of the precipitation plateaus are also a function of temperature [65]. An increase in the temperature of co-precipitation leads to a shift of the titration curves to lower pH values confirming that the proper selection of pH *and* temperature is crucial to guarantee the rapid and complete solidification of all components. Thus, pH 6–7 can only be regarded as optimal within a certain temperature window of 333–343 K [58, 65].

The initial Cu,Zn precipitate obtained by constant pH co-precipitation undergoes important changes during stirring in the mother liquor. This aging process is associated with crystallization, a change in color from blue to bluish green, and a change in particle size and morphology (Fig. 5.6d) [66]. Aging critically affects the microstructural as well as the catalytic properties of the resulting Cu/ZnO catalyst [69]. These changes occur rather steplike than gradually and are accompanied by a transient minimum in pH. The phase composition of the aging product is mostly determined by the Cu:Zn ratio [59, 71], but also by the mode of precipitation [71], and the speed of addition of the precipitating agent [72]. Typical phases obtained when going from Cu-rich to Zn-rich compositions are malachite $Cu_2(OH)_2CO_3$, zincian malachite $(Cu,Zn)_2(OH)_2CO_3$ (sometimes called rosasite, see [73]), aurichalcite $(Cu,Zn)_5(OH)_6(CO_3)_2$, hydrozincite $Zn_5(OH)_6(CO_3)_2$, and mixtures thereof.

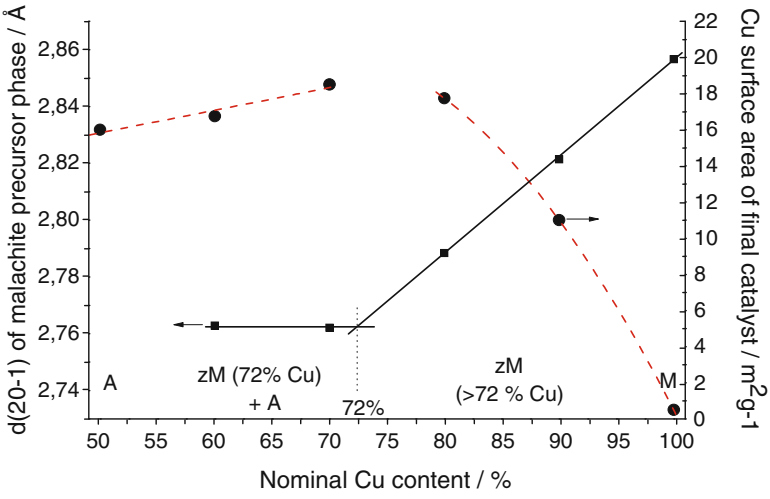

Fig. 5.6 Lattice contraction in the direction perpendicular to the $(20\bar{1})$ planes of zincian malachite as a measure of Zn incorporation in the precursor phase and SA_{Cu} of the final Cu/ZnO catalyst as a function Cu content (phase composition: *M* malachite, *zM* zincian malachite, *A* aurichalcite); adapted from [66]

In ternary Cu,Zn,Al systems, small amounts of LDHs may also be observed. This precursor phase is covered in detail in the next section. Due to the homogeneity ranges of the mixed phases, a comprehensive characterization of the precursor is difficult. Zincian malachite was suggested to be the relevant precursor phase for industrial catalysts [61], which is also confirmed by the industrially applied Cu-rich composition near Cu:Zn = 70:30, falling into the regime in which zincian malachite is the main product.

This view could be recently confirmed by a positive correlation of the Zn content in zincian malachite and the SA_{Cu} of the resulting catalyst [66]. The Zn fraction can be estimated from the angular position of the characteristic $(20\bar{1})$ XRD peak of the zincian malachite phase near 32° in 2θ using Cu K_α radiation [71]. This particular lattice plane distance contracts as Zn^{2+} is incorporated into zincian malachite and the corresponding peak is shifted to higher angles. This is due to the average lowering of Jahn–Teller distortions of the MO_6 building units in zincian malachite, whose elongated axes are aligned nearly perpendicular to this orientation. It is thus possible to measure the Zn content of this phase by conventional XRD despite the similar ionic radii and scattering factors of Cu and Zn. It is noted that due to the anisotropic contraction of the monoclinic unit cell the other strong XRD peaks at lower angles, which are often employed for phase identification, are only hardly affected by Cu,Zn substitution and do not give much diagnostic insight [73]. The decrease in the $(20\bar{1})$ lattice plane distance upon incorporation of Zn into malachite was measured for catalyst precursor phases obtained after aging of precipitates with different nominal Cu:Zn ratio (Fig. 5.6) [66]. It can be seen that, under the conditions applied in this study, the limit of Zn incorporation is found near 28%,

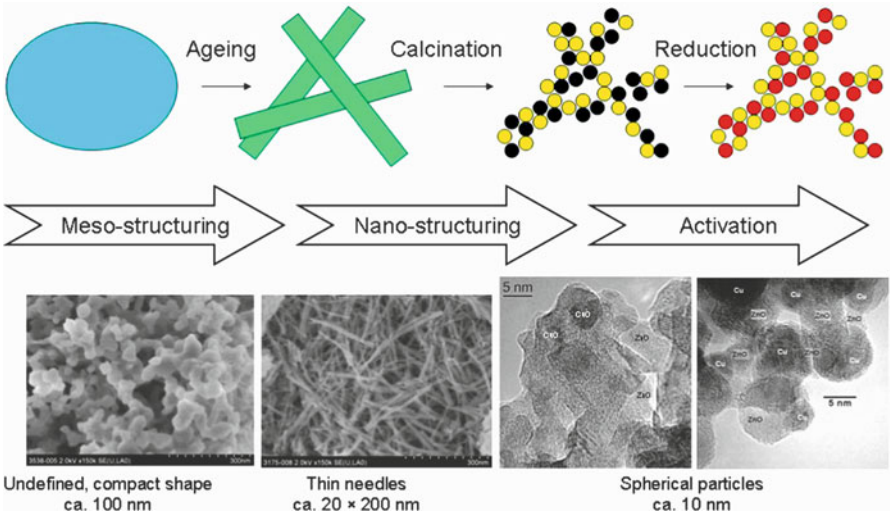

Fig. 5.7 Model for the chemical memory of Cu/ZnO/(Al_2O_3) catalyst preparation comprising two microstructure-directing steps

i.e., at a composition close to $(Cu_{0.72}Zn_{0.28})_2(OH)_2CO_3$. For higher nominal Zn content no further shift of the $(20\bar{1})$ reflection and crystallization of the Zn-richer aurichalcite phase as a side product were observed. The largest SA_{Cu} is observed for catalysts prepared from precursors near this critical composition (Fig. 5.6). This result strongly suggests that the desired porous microstructure of Cu/ZnO catalysts (Fig. 5.2) is formed from highly substituted zincian malachite precursors, and that the applied Cu:Zn ratio near 70:30 is beneficial, because it lies near the incorporation limit of Zn in the malachite phase.

This insight results in a simple geometrical model for the preparation of industrial Cu/ZnO catalysts comprising subsequent meso- and nanostructuring of the material (Fig. 5.7) [66]. In a first microstructure-directing step (meso-structuring) the homogeneous Cu,Zn precipitate obtained by constant-pH co-precipitation crystallizes in the form of thin needles of zincian malachite. Thin and interwoven needles are desired, because the porosity of the final catalyst is already predetermined at this step. In the second step, the individual needles are decomposed into CuO and ZnO and pseudomorphs of the precursor needles can be still observed after mild calcinations [58]. Because both phases are only poorly miscible, a de-mixing cannot be avoided at this stage and nanoparticles of the oxides, CuO and ZnO, are formed. The effectiveness of this nanostructuring step depends critically on the Zn content of the precursor. The closer we approach a 1:1 ratio of Cu^{2+} and Zn^{2+} in the zincian malachite phase, the smaller the newly formed oxide particles will be and the higher is the dispersion of the Cu phase [66]. A 1:1 ratio of Cu and Zn in synthetic zincian malachite, however, seems to be inaccessible by conventional co-precipitation and aging and due to solid-state chemical

constrains the limit is near 70:30 [73]. If we leave aside the synergetic effects of Cu and ZnO at this moment, the general benefit of using Zn^{2+} for the preparation of highly dispersed Cu-based catalysts is a geometric effect due to the chemical similarity of Cu^{2+} and Zn^{2+} concerning cation charge and size in aqueous solutions and in the precursor state. This similarity enables a common solid-state chemistry of Cu and Zn in one mixed precursor phase, may it be produced by co-precipitation or impregnation. Thus, highly intermixed precursors can be prepared easily in the Cu–Zn system, leading to highly dispersed Cu and ZnO particles upon decomposition.

This model of Cu/ZnO preparation can explain the "chemical memory" of the industrial system, because the important material properties of the final catalyst like porosity and dispersion are already predetermined by the properties of the precursor phase, like needle thickness and degree of Zn incorporation. It is also clear from this model that the synthesis conditions for industrial methanol synthesis catalysts were optimized in an unintended manner in order to improve the Zn incorporation into the zincian malachite precursor phase. This of course means that preparation of Cu/ZnO catalyst from other precursor phases requires a new and adjusted set of preparation conditions. The 70:30 ratio represents the optimal compromise between loading and dispersion of Cu only for catalysts prepared from zincian malachite precursors and each other precursor or preparation method requires an own optimization of the Cu:Zn ratio (and all other synthesis parameters). Catalysts of Cu:Zn ratio lower than 70:30 are often used for MSR. This usually leads to formation of the aurichalcite precursor phase instead of zincian malachite during co-precipitation of the precursor [57, 70, 74]. Aurichalcite crystallizes in form of platelets rather than needles [63] and yields a Cu/ZnO catalyst of different microstructure. SA_{Cu} usually is lower [60, 66], but the embedment and Cu–ZnO interactions may be more favorable for MSR. In contrast to zincian malachite, for aurichalcite, which usually does not require an extended aging period to crystallize, a homogeneous co-precipitation method using urea decomposition has been reported to lead to highly active Cu/ZnO MSR catalysts [75, 76]. Promoting oxides—Al_2O_3 in case of the industrial catalyst—usually have a higher charge than Cu^{2+} or Zn^{2+} and in case of M^{3+} ions LDHs are very interesting in the formation of $Cu/ZnO/Al_2O_3$ catalysts from a single precursor phase. Also, for academic purposes, it is generally desirable to prepare a Cu/ZnO-based catalyst from single-phase hydroxycarbonate precursor to obtain a homogenous microstructure, which enables drawing reliable conclusions regarding the intrinsic activity of differently prepared Cu/ZnO materials.

It is noted that $Cu/ZnO/(Al_2O_3)$ catalysts active in MSR can also be prepared from other precursors than hydroxycarbonates, like mixed oxalates [77], or following other recipes than co-precipitation, like reactive grinding [78] or CVD [79]. All these approaches will lead to different $Cu/ZnO/(Al_2O_3)$ catalytic materials, which have to prove their performance in comparison with the high-SA_{Cu} industrial reference catalysts. It is crucial to combine such comparative catalytic studies with comprehensive material characterization to establish structure–performance relationships and to learn about possible routes to further optimize the $Cu/ZnO/(Al_2O_3)$ system for application in MSR.

5.2.4 Ternary Cu/ZnO/X Catalysts ($X = Al_2O_3$, ZrO_2)

In contrast to the widely studied and debated role of ZnO, which can be separated into a geometric (spacer function) and an electronic (synergetic Cu–ZnO interactions) contribution (see above), only very little is known about the origin of the beneficial role of Al_2O_3. Its presence leads to an improved thermal stability and higher intrinsic activity in methanol synthesis [49, 80] and Al_2O_3 can be regarded as a structural promoter. As a porous oxide, alumina also provides a high surface area, but as mentioned earlier, cannot be seen as a classical support in commercial $Cu/ZnO/Al_2O_3$ catalysts. Many other oxides have been tested to find Cu/ZnO/X systems with improved catalytic properties, e.g., by combinatorial approaches [81]. In the field of MSR catalysts, Breen and Ross [82] compared a number of Cu/ZnO/X materials ($X = Al_2O_3$, ZrO_2, La_2O_3, Y_2O_3) of different composition and prepared by different precipitation sequences. They concluded that ZrO_2 is superior to Al_2O_3 as an oxide component in Cu/ZnO-based MSR catalysts. In addition to these $Cu/ZnO/ZrO_2$ catalysts, also $Cu/ZnO/Al_2O_3$ composites prepared from LDH precursors will be discussed in this section, since their microstructure and composition is markedly different from the commercial low-Al_2O_3-promoted Cu/ZnO system described above. It is noted that oxides other than Al_2O_3 or ZrO_2, for instance, SiO_2 [83], or also carbon [84, 85] were used to prepare active Cu/ZnO MSR catalysts.

LDHs or hydrotalcite-like compounds are hydroxycarbonate precursors, which can be derived from the naturally occurring Mg–Al salt hydrotalcite, $Mg_{1-x}Al_x(OH)_2(CO_3)_{2/x} \cdot mH_2O$ $(0.25 < x < 0.40)$. Mg and Al form layers of edge-sharing $(Mg,Al)(OH)_6$ octahedra. The H atoms point to the interlayer space, where the carbonate anions are also located. Carbonate ions (or other anions) are needed in the structure to compensate for the extra positive charge introduced by the trivalent Al^{3+} ions. LDHs are well-established precursor compounds for synthesis of various catalysts [86, 87]. They are especially interesting due to their ability to isomorphously substitute Mg^{2+} as well as Al^{3+} by other bi- or trivalent cations, in particular those from the first row of transition metals. Thus, they are highly attractive precursors for $Cu/ZnO/Al_2O_3$ catalysts as they can provide a perfect atomic distribution of all metal species in one single-phase precursor compound and should yield structurally uniform catalysts of high Cu dispersion and enhanced interaction between Cu metal and the Zn,Al oxide phase.

Several studies have shown that Cu,Zn,Al LDH precursors or precursor mixtures containing the LDH phase can indeed be decomposed into highly active MSR catalysts [18, 88, 89]. LDHs are typically and most easily prepared by co-precipitation, similar to the zincian malachite precursor of the methanol synthesis catalyst (see above). Preparation of phase-pure Cu,Zn,Al LDHs requires a modified metal composition with an increase in Al and a decrease in Cu content. The former is necessary to provide enough trivalent cations, which should exceed around one-fourth the total metal cations. Thus Al cannot be regarded as a structural promoter phase any more, but rather is an integral component of the oxide phase in the final catalyst.

The latter is to suppress formation of Cu-rich malachite-like phases (desired in case of the industrial methanol synthesis catalyst), which is favored by Cu^{2+} due to the tendency of the d^9 system to crystallize in Jahn–Teller distorted 4 + 2 coordination rather than in the more regular LDH environment. Usually, no extended aging period is needed to crystallize LDH phases from the precipitate.

Cu-rich phase-pure LDH precursors (up to 49 at.% Cu) can be prepared by such a modified direct co-precipitation and yield $Cu/ZnAl_2O_4$-type catalysts [90]. These catalysts exhibit a different microstructure from that of the industrial $Cu/ZnO/Al_2O_3$ catalyst shown in Fig. 5.2. Despite a smaller average Cu particle size observed in the ex-LDH material, which is a result of the lower total Cu content and the perfect cation distribution in the precursor, the accessible SA_{Cu} is considerably lower, around 5 $m^2\ g^{-1}$. This is a result of the much stronger embedment of the small metal particles in the $ZnAl_2O_4$ matrix. After calcination at 603 K and reduction, the interface-to-surface ratio was determined to be 89% compared to ca. 35% for the industrial system. The major challenge in the preparation of such ex-LDH $Cu/ZnAl_2O_4$ catalyst can thus be seen to optimize the "nuts-in-chocolate"-like morphology by adjusting the Cu particle size, the degree of embedment and the precursor platelet thickness in order to find the proper compromise between Cu metal–oxide interactions and Cu dispersion. Tang et al. [88] reported a surprisingly high accessible SA_{Cu} of 39 $m^2\ g^{-1}$ for a LDH-derived $Cu/ZnO/Al_2O_3$ catalyst (Cu:Zn:Al = 37:15:48) after calcination of the precursor at an elevated temperature of 873 K associated with the crystallization of spinel-type oxides and the complete decomposition of all carbonate on the sample. A microemulsion approach for the precipitation of the precursor to "nano-cast" the platelet morphology of the LDH phase has also been shown to be promising in this direction as it increases SA_{Cu} from 8 to 14 $m^2\ g^{-1}$ compared to a conventionally co-precipitated ex-LDH $Cu/ZnAl_2O_4$ catalyst (Cu:Zn:Al = 50:17:33) [91]. The MSR activity was improved, but did not scale linearly with SA_{Cu} and was still lower compared to a commercial $Cu/ZnO/Al_2O_3$ catalyst of the type described above.

Highly active ex-LDH $Cu/ZnO/Al_2O_3$ catalysts have been reported by Turco et al. [16, 92, 93] The authors applied a homogenous precipitation method of the chloride-containing LDH followed by anion exchange with carbonate and investigated the structural and catalytic properties of the resulting catalysts. Calcination at 723 K leads to the formation of CuO, ZnO, amorphous Al_2O_3, and probably also Cu and Zn aluminates. Cu contents were between 5 and 45% of all metal ions and SA_{Cu} of up to 17.5 $m^2\ g^{-1}$ could be achieved. The highest activity in oxidative MSR was observed for the composition Cu:Zn:Al = 18:33:49. This sample showed a conversion to CO near the detection limit of 0.01%, which did not increase significantly with temperature between 473 and 673 K.

Velu at al. [18, 94] have prepared Cu,Zn,Al-LDH precursors by co-precipitation and calcined at 723 K to obtain $Cu/ZnO/Al_2O_3$ catalysts. Among these, the sample of the molar composition Cu:Zn:Al = 33:43:24 showed the highest Cu dispersion. The high activity in oxidative MSR was stable over 25 h on stream. The authors also used ZrO_2 as a replacement for Al_2O_3 and as an additive to the $Cu/ZnO/Al_2O_3$ system. These $Cu/ZnO/ZrO_2$ and $Cu/ZnO/Al_2O_3/ZrO_2$ catalysts were prepared

from aurichalcite and mixed aurichalcite/LDH precursors, respectively. The samples containing ZrO_2 were more effective in oxidative MSR than the ZrO_2-free samples. Copper–zirconia interactions, in particular Cu–O–Zr bonding, were found in these materials [95, 96]. Cu was easier to reduce in the presence of ZrO_2 suggesting an effect of the promoter oxide on the redox chemistry of Cu. A Cu–ZrO_2 synergetic effect was proposed to be responsible for the better catalytic performance of the ZrO_2-containing samples probably by adjusting the Cu^0/Cu^+ ratio under working conditions (see below). Such an effect of the presence of ZrO_2 on the ratio of $Cu^0/Cu^{oxidized}$ at the catalyst surface was previously suggested by Breen and Ross on basis of modified redox chemistry of Cu detected by temperature-programmed reduction (TPR) [82]. Interestingly, a decreased reducibility of Cu was observed for their ZrO_2-containing catalysts and ascribed to the presence of the promoter. The authors observed in their study that Cu/ZnO/ZrO_2 catalysts were more active than Cu/ZnO/Al_2O_3 and the material could be further improved by addition of alumina and yttria. The interactions between Cu metal and zirconia are discussed in more detail below for ZnO-free Cu/ZrO_2 catalysts.

Agrell et al. [15] prepared and characterized several Cu/ZnO catalysts without and with the addition of Al_2O_3 and/or ZrO_2 by co-precipitation and used them in MSR. Among these samples, the ZrO_2-containing systems showed the highest Cu dispersions and best MSR performances. The Cu/ZnO/ZrO_2/Al_2O_3 catalyst also showed a high stability in POM activity upon redox cycling compared to the binary Cu/ZnO sample, suggesting again an influence of ZrO_2 on the redox properties of Cu.

Matsumura and Ishibe [97] used Cu/ZnO/ZrO_2 for high-temperature MSR at 673 K and compared it to binary Cu/ZnO and Cu/ZrO_2 (all 30 wt% CuO after calcination). They observed an increased BET surface area and smaller particles in their Cu/ZnO/ZrO_2 sample compared to binary Cu/ZnO. The catalytic activity was more stable than that of a commercial Cu/ZnO/Al_2O_3 catalyst. Interestingly, deactivation was found to be accompanied by the growth of the oxide particles rather than by Cu sintering.

An activity-promoting role of ZrO_2 was also reported by Jones and Hagelin-Weaver in a series of Cu/ZnO/X catalysts (X = ZrO_2, CeO_2, Al_2O_3) prepared by impregnation [98]. The best sample was a Cu/ZnO/ZrO_2/Al_2O_3 catalyst, which was most active and showed the least CO selectivity. This catalyst was prepared by co-impregnation of Cu and Zn onto a mixture of zirconia and alumina nanoparticles and the good catalytic properties were related to the presence of the monoclinic polymorph of ZrO_2.

5.2.5 *ZnO-Free Cu-Based Catalysts*

Among the ZnO-free Cu-based catalysts, those comprising ZrO_2 and CeO_2 are the most studied systems and will be in the focus of this section. Combinations of Cu with chromia [99–101] or manganese oxide [99] promoters or Cu on silica supports

[102] have also been used in MSR. Depending on the Cu content and the method of preparation—co-precipitation, sol–gel chemistry, or impregnation—these catalysts can be either obtained in the form of truly supported or bulk catalysts similar to the industrial $Cu/ZnO/Al_2O_3$ system. Also, skeletal Cu catalysts are known to be active in MSR, which can be prepared from Cu-containing alloys by selective leaching. These materials are prepared employing intermetallic compounds as precursor phases and are discussed in more detail in the second part of this chapter.

In the last few years there has been a growing interest in ZnO-free Cu/ZrO_2 as catalyst for the MSR reaction. Already in the 1980s, higher conversions of methanol were reported for Cu/ZrO_2 in comparison with Cu/SiO_2 prepared by impregnation methods [103, 104]. Cu/ZrO_2 catalysts prepared by precipitation showed turnover frequencies comparable to a Cu/ZnO catalyst [82]. The lower total activity for the Cu/ZrO_2 catalysts was ascribed to lower SA_{Cu} in these catalysts. Ritzkopf et al. [20] successfully applied a microemulsion technique using the water droplets of a water-in-oil system to confine the reaction space for co-precipitation. They obtained intimately mixed CuO/ZrO_2 particles with 4–16 wt% Cu and a particle size of less than 10 nm. At high temperatures, this catalyst showed activity levels identical to a commercial catalyst, but the level of produced CO was substantially reduced. At 573 K and ca. 90% conversion, the CO concentration in the effluent was only ca. one-fifth compared to the Cu/ZnO reference. In contrast to the commercial catalyst, oxidized Cu species were detected by X-ray photoelectron spectroscopy (XPS) on the surface of the Cu/ZrO_2 catalyst after reaction, supporting the stabilizing role of ZrO_2 on oxidized Cu species, which was also observed for ZrO_2-promoted $Cu/ZnO/(Al_2O_3)$ catalysts (see above). Such oxidized Cu^+ species are discussed to play an important role in the MSR reaction (see below).

Purnama et al. [19] reported about a Cu/ZrO_2 catalyst prepared by a templating procedure (8.5 wt% Cu), which showed higher activity as a function of W_{Cu}/F and better stability during MSR as well as a lower production of CO compared to a commercial $Cu/ZnO/Al_2O_3$ sample. This sample showed a complex activation behavior if oxygen pulses were added to the feed after certain periods of time on stream. Szizybalski et al. [105] prepared a Cu/ZrO_2 catalyst with 8.9 mol% Cu after calcination by a precipitation method and investigated this phenomenon more closely. The calcined catalyst contained small and disordered CuO particles rather than Cu^{2+} incorporated into the zirconia lattice. Again, a decreased reducibility was observed. By means of in situ Cu K-edge X-ray absorption spectroscopy, a significant amount of residual oxygen was detected in the Cu phase after reduction at 523 K, which could only be removed by treating the catalyst with hydrogen at 673 K. If oxygen was added to the feed during MSR, an increase in this residual oxygen concentration was detected after re-reduction in the feed, which was accompanied by an increase in MSR activity. Thus, a correlation of the amount of oxygen remaining in the copper particles and the catalytic activity was proposed leading to the conclusion that there must be a different metal–support interaction of Cu/ZrO_2 compared to Cu/ZnO catalysts, where such correlation was not observed.

Similar to the Cu/ZnO system, a high Cu loading of 80 wt% was reported to yield the most active material if co-precipitation and nitrate solutions were used for

preparation of Cu/ZrO_2 catalysts [106]. Yao et al. [107] prepared Cu/ZrO_2 catalysts with this composition by four different methods and showed that the catalysts prepared by co-precipitation revealed a higher conversion compared with the ones prepared by impregnation. The best results were obtained by an oxalate gel co-precipitation method and for a calcination temperature of 823 K [108]. In this catalyst, a thin layer of monoclinic ZrO_2 was detected on a bulk of tetragonal ZrO_2. With increasing calcination temperature the amount of monoclinic ZrO_2 increased accompanied by decreasing conversions.

Wu et al. [109] have studied the effect of ZnO and ZrO_2 on the catalytic properties of Cu in MSR by comparing pure Cu with inverse ZnO/Cu and ZrO_2/Cu model systems. Both oxides were found to enhance the activity of Cu and to stabilize the Cu particles against aggregation and sintering. Moreover, the presence of the oxides resulted in a stabilization of Cu^+ species at the surface of the catalyst. The authors concluded that ZrO_2 is the superior promoter oxide for the Cu-based MSR catalyst.

Also, CeO_2 turned out to be a promising oxide component for Cu-based MSR catalysts. Cu/CeO_2 catalysts were prepared by Liu et al. [21, 110, 111] using a co-precipitation method and calcination at 723 K. By this treatment, up to 20% Cu^{2+} could be incorporated into the ceria lattice. After reduction a Cu/CeO_2 catalyst was obtained (3.9 wt% Cu), which was more active than Cu/ZnO and $Cu/Zn/Al_2O_3$ catalysts of the same low Cu loading. After deactivation the initial activity could be regenerated by recalcination and reduction. The high activity was ascribed to strong Cu–oxide interactions and related to the high oxygen mobility of the ceria support. Also mixed CeO_2/ZrO_2 [112] or Zr- [113] or Gd-doped [114] ceria was used as support for Cu-based MSR catalysts.

The increasing Cu–oxide interactions when going from Cu/ZnO over Cu/ZrO_2 to Cu/CeO_2 are also reflected in a more and more enhanced substitution chemistry in the oxide phase at higher temperatures. While Zn^{2+} and Cu^{2+} show a common solid-state chemistry only on the stage of the precipitated catalyst precursor, e.g., in the form of a joint cationic lattice of hydroxycarbonate phases (see above), significant isomorphous substitution of Cu^{2+} in ZnO is, despite the match of cationic charge and similar ionic radii, hardly observed. The reason for this low degree of solid-state solubility is most likely the tetrahedral coordination environment of Zn^{2+} sites in ZnO, which is unfavorable for Cu^{2+}, which prefers a Jahn–Teller-distorted octahedral 4 + 2 coordination. Incorporation of M^{2+} cations, like Ca^{2+}, in the zirconia lattice on the other hand is well known and can stabilize the higher symmetric polymorphs of ZrO_2. It was also reported that Cu^{2+} can substitute Zr^{4+} and has an effect on the zirconia phase composition [115], but this effect may not play a role in the preparation of Cu-based MSR catalysts, where calcination temperatures are usually low and Cu was observed to be present rather in the form of highly dispersed CuO [105]. In case of CeO_2, however, clear evidence for the formation of a $Ce_{1-x}Cu_xO_2$ solid solution during catalyst preparation applying a calcination temperature of 723 K was presented by Liu et al. [21, 110, 111]. Both materials, ZrO_2 and CeO_2, are known to easily form sub-stoichiometric metal-to-oxygen ratios and the charge mismatch upon incorporation of Cu^{2+} can be

compensated by formation of oxygen vacancies. Although highly substituted bulk phases are not likely to form under MSR conditions or even in oxidative MSR atmosphere and thus themselves are probably not relevant for catalysis, these considerations still show that differences in the solid-state reactivity of Cu with different oxides exist. Under oxidative conditions the systems tend to form mixed oxides by beginning oxidation of the Cu metal, while under reducing conditions the systems tend to form an alloy by beginning reduction of the oxide. The connection of the redox chemistry of the Cu phase and its interaction with the oxide component was observed by many researchers. From the substitution chemistry of the bulk oxide phases, it is understandable that ZrO_2 and CeO_2 have a stabilizing effect on oxidized Cu leading to a higher reduction temperature, while this effect is not observed for ZnO [116].

Strengthened interactions between Cu metal and the oxide are probably important for the stability of the catalysts as they hinder mobility of the Cu particles and thus decrease the tendency for thermal sintering. Furthermore, these interactions may be important for the accessibility of higher Cu oxidation states at given conditions, or more generally for the ease of oxygen incorporation into the Cu lattice (see below). Another practical aspect is that the re-dispersion of the Cu phase by oxidative regeneration will work much better for those systems which can form mixed oxides like Cu/CeO_2 (stronger interactions) compared to those which cannot easily form mixed phases like Cu/ZnO.

In an optimized Cu-based catalyst for MSR, the beneficial effect of redox-promoting oxides on the Cu phase should be combined with the proven structure-promoting effects of the less redox active ZnO/Al_2O_3 components.

5.2.6 *The Active Form of Cu Under MSR Conditions*

The question to what is the active site of Cu-based catalysts in MSR is still open and debated in literature. Similar to the methanol synthesis reaction either metallic Cu^0 sites, oxidized Cu^+ sites dispersed on the oxide component or at the Cu–oxide interface, or a combination of both kinds of sites are discussed to contribute to the active ensembles at the Cu surface. Furthermore, the oxidic surface of the refractory component may take part in the catalytic reaction as well as providing adsorption sites for the oxygenate-bonded species [117], while hydrogen is probably adsorbed at the metallic Cu surface.

Clearly, SA_{Cu} is among the most important factors determining the activity of a Cu-based catalyst in MSR, indicating the importance of proper balance of Cu dispersion and loading, and thus of catalyst preparation. Sufficient SA_{Cu} is a prerequisite for a high-performance Cu-based MSR catalyst, but the metallic SA_{Cu} measured by N_2O decomposition does not scale linearly with activity in all cases, and turnover frequencies—which were calculated using SA_{Cu} as a count of active sites—vary even for the same sample after different pretreatments [118]. Thus, other factors intrinsic to the Cu phase and not detectable by the N_2O titration

method also contribute to the MSR activity. There are two major views discussed in literature relating these intrinsic factors either to the variable oxidation state of Cu, in particular to the in situ adjustment of the Cu^0/Cu^+ ratio at the catalyst's surface, or to the defect structure and varying amount of disorder in metallic Cu depending on the microstructure and preparation history of the catalyst. As we will see, these views are not necessarily contradicting each other.

Changes in the oxidation state of Cu are to be considered in particular in oxidative MSR due to the presence of gas-phase oxygen. It has been tried to answer the question of the oxidation state of Cu under (oxidative) MSR conditions by post-reaction characterization as well as by in situ investigations with sometimes different results depending on the feed gas compositions, the catalyst material studied, and the characterization method used. Near-surface sensitive techniques like X-ray photoelectron spectroscopy (XPS) are well suited to investigate the oxidation state of the near surface of a Cu-based MSR catalyst, although the discrimination of Cu^+ and Cu^0 may be challenging on the basis of the core level spectra. It is noted that contact with air has to be strictly avoided to obtain reliable results as highly dispersed Cu particles are prone to oxidation in air. Another drawback is that with laboratory XPS only ex situ investigations are possible and potential changes of the catalyst upon cooling and evacuation have to be taken into account. X-ray diffraction and X-ray absorption spectroscopy are also widely used to characterize the Cu phase in MSR catalysts. With these methods in situ investigations are possible, but they lack surface sensitivity. Another general aspect to be considered when reporting $Cu^0/Cu^{oxidized}$ ratios is the homogeneity of the catalyst studied. If different Cu species are present in the catalyst, e.g., larger Cu particles as well as highly dispersed Cu clusters, additional characterization information is needed to identify the effect of the individual Cu species on the results.

Agrell et al. [15] studied the near-surface region of a $Cu/ZnO/ZrO_2/Al_2O_3$ catalyst by XPS after simulating oxidative MSR reaction conditions in the pretreatment chamber. They reported the presence of metallic Cu^0 after reduction and formation of oxidized Cu^+ species after exposure to an O_2/MeOH atmosphere (1:2). In contrast, Goodby and Pemberton [119], who used pure MSR atmosphere without oxygen and a commercial $Cu/ZnO/Al_2O_3$ catalyst, found still about 7% Cu^+ at the surface after reduction in hydrogen, but the catalyst was fully reduced after using it in MSR. Raimondi et al. [120] used a similar method and found that the oxidation state of Cu in a commercial $Cu/ZnO/Al_2O_3$ catalyst is a function of feed gas composition. At a slightly sub-stoichiometric O_2:MeOH ratio Cu^+ was predominant only at temperatures below 510 K. At higher temperatures, Cu was reduced by MeOH to its metallic state. H_2 was produced only when Cu^+ or Cu^0 was detected, while Cu^{2+} formed at higher O_2 partial pressures was inactive and led to MeOH combustion. Using a sub-monolayer Cu on thin-oriented ZnO films as model catalyst, the same group showed that aggregation of the Cu islands is promoted by the presence of O_2 if Cu was in the metallic state at a O_2:MeOH ratio below 0.25 at 550 K. At higher O_2 concentrations, Cu is oxidized and the aggregation is less pronounced suggesting an effect of the oxidation state of Cu on the Cu–ZnO interactions [121]. Reitz at al. [122]

used bulk-sensitive in situ X-ray absorption spectroscopy to study the oxidation state of Cu under different conditions in the presence of methanol, steam, and oxygen. They observed MSR-inactive Cu^{2+} at low O_2 conversions and found H_2 production only if metallic Cu was detected. Cu^+ was detected as an intermediate during the reduction of Cu^{2+} to Cu^0.

It is not a surprise that the oxidation state of Cu is a function of the oxidation power of the gas feed, especially of the O_2 concentration if oxidative MSR is used. Knop-Gericke et al. [123] have shown the importance and complexity of the dynamic near-surface Cu–O chemistry by high-pressure in situ XPS for the MeOH oxidation reaction on Cu foil. With increasing O_2:MeOH ratio the in situ formed Cu surface could vary from metal via sub-oxide to Cu(I)-oxide like species. The most active and selective state (to formaldehyde) observed in this study was a disordered Cu^0 surface modified in situ by subsurface oxygen of a composition near $Cu_{\sim 10}O$ stressing that the pure Cu^0 metal and bulk Cu_2O phases are not sufficient to fully describe the surface chemistry of the Cu–O system. It is noted that the active surface phase was only observed in situ and did not form under UHV conditions.

It is not only the gas-phase composition that determines the oxidation state of Cu under MSR conditions, but the catalyst formulation that also plays a significant role. It was already mentioned above that the presence of ZrO_2 generally decreases the reducibility of CuO and can stabilize Cu^+ compared to ZrO_2-free systems at given MSR conditions. Such Cu^+ centers are often discussed to be the active sites of (oxidative) MSR in the context of a redox mechanism corresponding to the reverse of a reaction proposed for methanol synthesis by Klier [124], where Cu^+ centers incorporated into a ZnO matrix are suggested as active sites. The Busca group identified Cu^+ sites at the surface of LDH-derived $Cu/ZnO/Al_2O_3$ catalysts using IR spectroscopic methods and discussed their role in oxidative MSR [89, 125–127].

The second explanation for a varying intrinsic activity is the different amount of disorder in the metallic Cu phase. This disorder can manifest itself in the form of detectable lattice strain, e.g., by line profile analysis of XRD peaks [17], ^{63}Cu-NMR lines [64], or as an increased disorder parameter (Debye–Waller factor) derived from extended X-ray absorption fine structure (EXAFS) spectroscopy [118]. Strained copper has been shown theoretically [128] and experimentally [129] to have different adsorptive properties compared to unstrained surfaces. Strain, i.e., local variation in the lattice parameter, is known to shift the center of the d-band and alter the interactions of metal surface and absorbate [130]. Alternatively, a modification of the electronic structure of Cu was also discussed to take place at the interface between Cu metal and the semiconducting oxide forming a Schottky junction [131].

Günter at al. [118] used in situ XRD and EXAFS and found a correlation between the disorder in the Cu phase and the activity of a series of differently prepared Cu/ZnO catalysts in MSR. In addition, the selectivity toward CO_2 was affected. Kniep et al. [64] could show that the Cu phase in Cu/ZnO catalysts prepared under otherwise identical conditions was more strained and more active

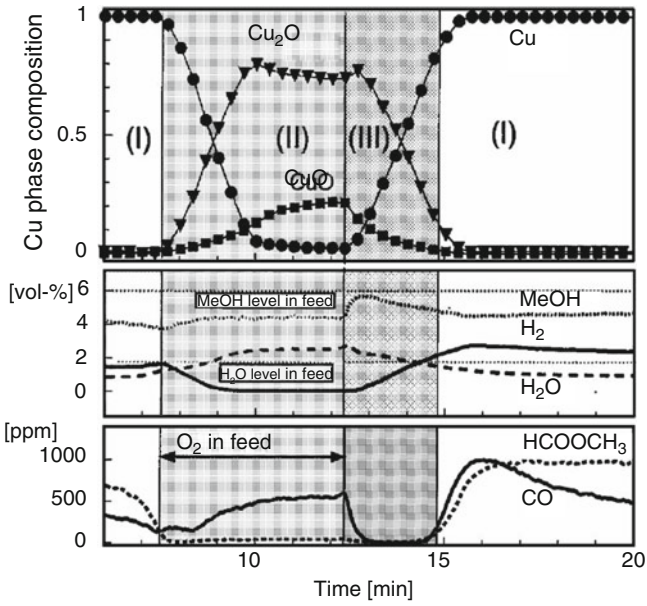

Fig. 5.8 Evolution of Cu phase composition of a Cu/ZnO catalyst during oxygen addition cycles into steam reforming feed at 523 K. Phase analysis was based on the corresponding X-ray absorption near edge structure (XANES) spectra. The two lower sections of the graph depict the evolution of the gas-phase in percent and ppm, respectively. Three transitions in bulk and gas-phase composition are marked: (I) copper metal during steam reforming, (II) oxidation of Cu, (III) and re-reduction of Cu oxide. Reprinted from [118] with permission from Elsevier

in MSR if the precipitate was aged. Also, the introduction of a microwave heating step [132] or reactive grinding [78] of the calcined CuO/ZnO material was used to prepare strained and disordered, and thus, intrinsically more active Cu particles in the final MSR catalyst. A certain increase in disorder seems to be also achievable by post-preparation treatment as could be shown by in situ investigations (Fig. 5.8) [118]. Addition of oxygen to the MSR feed led to a transient breakdown of MSR activity ascribed to the formation of CuO. After switching off the oxygen stream, the catalyst was re-reduced to Cu^0 in the MSR feed and exhibited a higher conversion of methanol as well as a lower selectivity to CO, which was ascribed to an increase in structural disorder. Bulk Cu_2O was observed only as an intermediate during reduction. The origin of structural disorder in highly active Cu/ZnO catalysts is thought to be the interface of the Cu^0 clusters with the ZnO particles. Thus, enhancement of this interface contact may be beneficial for the activity of the catalyst, if not much of SA_{Cu} is sacrificed.

Accordingly, the short addition of oxygen to a Cu/ZrO_2 MSR catalyst under working conditions was also shown to have an activating effect on the Cu phase, which is even more pronounced and stable compared to Cu/ZnO [19, 105]. In this case, no significant lattice strain of Cu could be detected, but incorporation of oxygen in metallic Cu was observed (see above). Considering similar effects on

the catalytic properties of Cu in these particular experiments but apparently different structural origins in Cu/ZnO and Cu/ZrO_2, and taking into account the work addressing the oxidation state of Cu, a general view on Cu in MSR emerges. The catalytic activity of Cu in MSR seems to be related to a nonequilibrium form of metallic Cu. The deviation of the catalytically active surface from its ordered equilibrium form can be triggered by redox chemistry as well as by a beneficial microstructural arrangement of the composite catalyst. The former relates to a distortion of the Cu lattice by oxygen dissolution and is a dynamic effect, which adjusts itself in situ. This effect can be measured by bulk methods as residual oxygen content in the Cu^0 phase and may well influence the Cu^0/Cu^+ ratio measured ex situ with surface-sensitive techniques. The extent of this distortion is a function of the gas-phase composition and the metal–oxide interactions. Oxygen incorporation is favored by increasing the oxidation power of the feed, e.g., by oxygen addition, and facilitated by strong (or synergetic) interactions of Cu and the oxide component like in Cu/ZrO_2. However, oxidation of Cu to a bulk oxide form (Cu_2O) by a too strongly oxidizing atmosphere as well as formation of a mixed oxide phase (e.g., inactive $CuAl_2O_4$) by too strong interactions of Cu with the oxide have to be avoided.

Deviation from equilibrium Cu due to static defects and lattice strain, on the other hand, can be introduced in the Cu particles by proper catalyst preparation aiming at kinetically trapping a distorted and defect-rich state of Cu. In a microstructure with small particles, many Cu^0–oxide interfaces like in the commercial $Cu/ZnO/(Al_2O_3)$ catalyst beneficially affect the Cu phase. In addition to the beneficial role of Zn^{2+} on Cu dispersion (see above), the interface of Cu metal and ZnO seems to be well suited to pin this favorable defect structure of Cu^0.

5.3 Intermetallic Compounds in Methanol Steam Reforming

Besides the Cu-based systems, different other systems, mainly based on palladium or platinum, have been explored as catalysts for the steam reforming of methanol. The driving force was to detect materials with higher stability against sintering and higher selectivity, i.e., lower CO partial pressures in the product [133].

Interestingly, the formation of intermetallic compounds is frequently observed in these metal–oxide supported systems and is very often connected with a significant increase in selectivity to CO_2 [27]. An "intermetallic compound" is composed of two or more metallic elements and possesses a crystal structure which is different from the constituting elements and at least partly ordered [134, 135]. "Compound" implies that it is single phase, which is not in contradiction to the often broad homogeneity ranges of intermetallic compounds. In contrast, the more familiar term "alloy" corresponds to a mixture of metals, intermetallic compounds, and/or nonmetals, and can consist of more than one phase.

Figure 5.9 demonstrates the huge consequences of an ordered intermetallic compound on the electronic structure of the catalytically active species. Opposed are the electronic densities of state (DOS) of Pd metal, Ag metal, and the

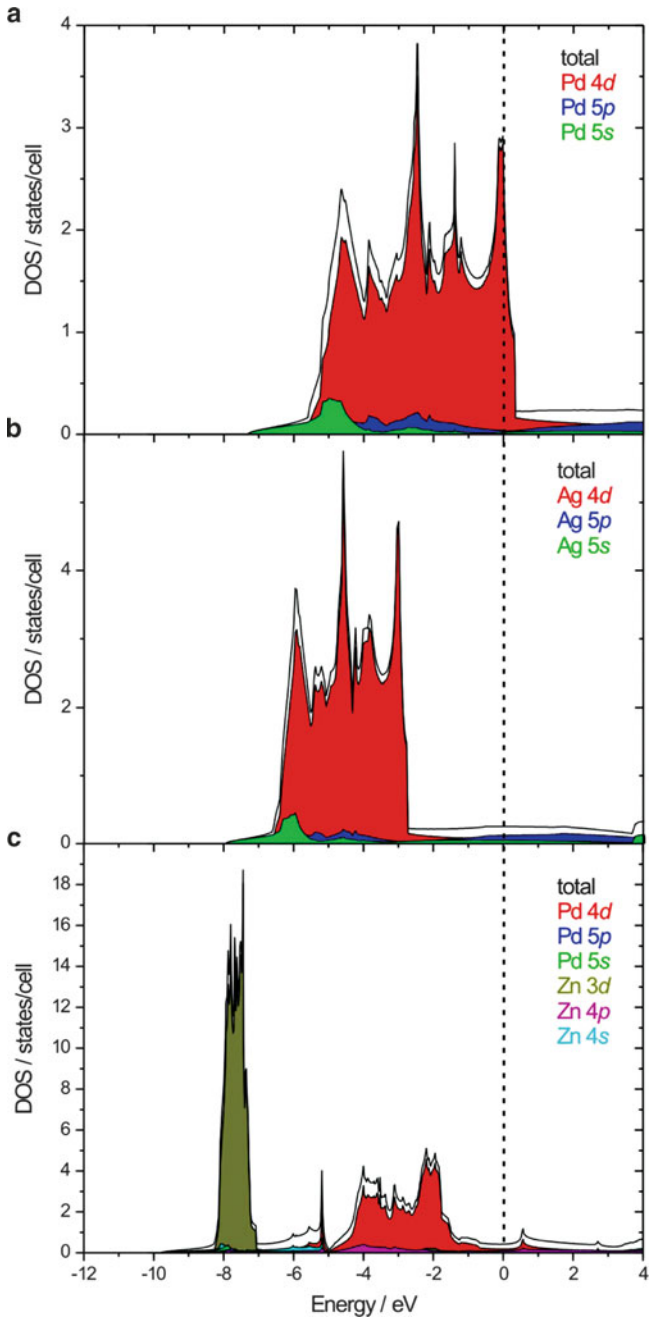

Fig. 5.9 Density of states of element Pd (**a**), Ag (**b**), and the intermetallic compound ZnPd (**c**). Ag–Pd alloy formation leads to d-band filling intermediate between elemental Pd and Ag. In contrast, huge differences are revealed at the Fermi energy as well as in the width of the Pd d-bands upon formation of the intermetallic compound ZnPd (**c**)

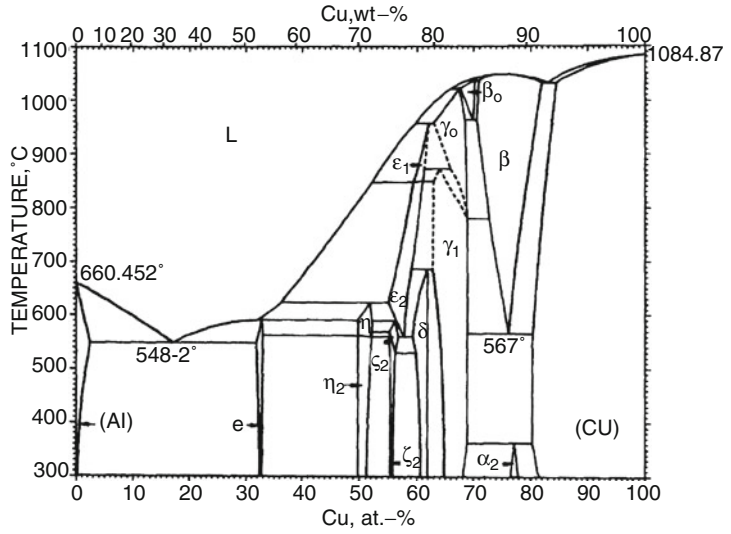

Fig. 5.10 Phase diagram of the system Al–Cu. Reprinted from [215], with permission from ASM International®. All rights reserved. http://www.asminternational.org

intermetallic compound ZnPd (often called PdZn but see [136]). By alloy formation of, e.g., Ag–Pd, the total electron concentration per atom increases with increasing Ag content, but the crystal structure does not change (Cu type of crystal structure, space group $Fm\bar{3}m$). As a consequence, the DOS remains very similar (so-called *rigid-band approach*) to that of elemental Pd but the d-bands are further populated until they reach the population of pure silver (Fig. 5.9b). On the other hand, the intermetallic compound ZnPd crystallizes in the ordered CuAu type of crystal structure (space group P4/*mmm*). The crystal structure is a direct consequence of the covalent chemical bonding within the intermetallic compound upon formation [136]. Interestingly, covalent interactions are quite common in intermetallic compounds, leading to a strong alteration of the electronic structure as seen in Fig. 5.9c. They are also displayed by the physical properties of the compounds [137–139]. Since a significant number of valence electrons are localized in the covalent bonds, the electrical conductivity is significantly reduced upon compound formation. An example is the well-investigated θ-phase, the intermetallic compound $CuAl_2$ [139] in the system Al–Cu shown in Fig. 5.10.

Both elements crystallize in the Cu-type of structure (cubic close packed). Alloy formation takes place on the Al- as well as the Cu-rich side. Up to 20 at.% of Al can be dissolved in Cu without changing the crystal structure. Between the two alloys, a number of intermetallic compounds with different structures are formed. In $CuAl_2$ the three-bonded Al atoms build covalent and interpenetrating 6^3 nets. The Cu atoms are located in tetragonal antiprismatic cavities and interconnect the 6^3 nets by 3-center bonds. This bonding situation dramatically influences the physical properties. In contrast to Cu and Al, $CuAl_2$ is no longer ductile, but brittle as glass—a property often observed for covalently bonded intermetallic compounds. Localization of the

electrons in the covalent bonds reduces the number of charge carriers and thus the electric resistivity is significantly increased to 7.6 μΩ cm [140] at 295 K compared to $\rho_{295\,K,\,Cu} = 1.55\,\mu\Omega\,cm$ and $\rho_{295\,K,\,Al} = 2.73\,\mu\Omega\,cm$. The strongly altered electronic and crystal structures determine the adsorption and the catalytic properties. Thus, it is necessary to keep the above-mentioned differences between an intermetallic compound and an alloy in mind when looking at bimetallic catalysts.

Staying with palladium, the direct consequences on the catalytic behavior upon compound formation can be demonstrated. While palladium possesses only a CO_2 selectivity of 0.9% in MSR, formation of the intermetallic compound ZnPd leads to 98% CO_2 selectivity [141]. In the following, the different roles played by intermetallic compounds in the steam reforming of methanol are discussed. Starting with the deliberate decomposition of intermetallic compounds to synthesize highly active catalysts and via the observation of intermetallic compounds formed during time on stream, this section ends with the use of well-defined intermetallic systems to systematically develop an understanding of the underlying principles of the steam reforming of methanol. The following sections do not aim at a complete review of the existing literature, but at revealing the different ideas concerning intermetallic compounds and the steam reforming of methanol present in literature.

5.3.1 *Catalysts Derived by Decomposition of Intermetallic Compounds*

Applying intermetallic compounds in MSR is still a young scientific subject. The first appearance was in 1994 when Miyao et al. [142] used Al–Cu, Cu–Zn, and Al–Cu–Zn alloys, which contained intermetallic compounds such as $CuAl_2$, CuZn, and Cu_5Zn_8 as precursors to synthesize highly active Cu-based Raney-type catalysts. During leaching with aqueous NaOH, the intermetallic compounds are decomposed and the observed catalytic properties cannot be correlated to the crystal and/or electronic structure of the starting materials. Typically, the leaching results in supported Cu particles with high surface area and thus higher activities than conventional Cu-based systems.

Also, single-phase intermetallic compounds like the well-investigated $CuAl_2$ [139] and even quasicrystalline phases, i.e., ordered but non-periodic intermetallic compounds, have been used as precursors for Raney-type catalysts (Fig. 5.11).

The group of Tsai leached powders of the quasicrystalline icosahedral i-Al–Cu–Fe phase, crystalline Al–Cu–Fe intermetallic compounds, and $CuAl_2$ with NaOH or Na_2CO_3 [22, 143–145]. This leads to a preferential dissolution of aluminum from the surface of the particles, leaving the intermetallic core untouched. The surface after leaching consists of transition metal particles which are dispersed on an aluminum hydroxide layer. As in the case of the above-mentioned materials, the H_2 production rate increased to 235 L/kg, but the presence of iron also leads to a higher stability of the Cu particles against sintering.

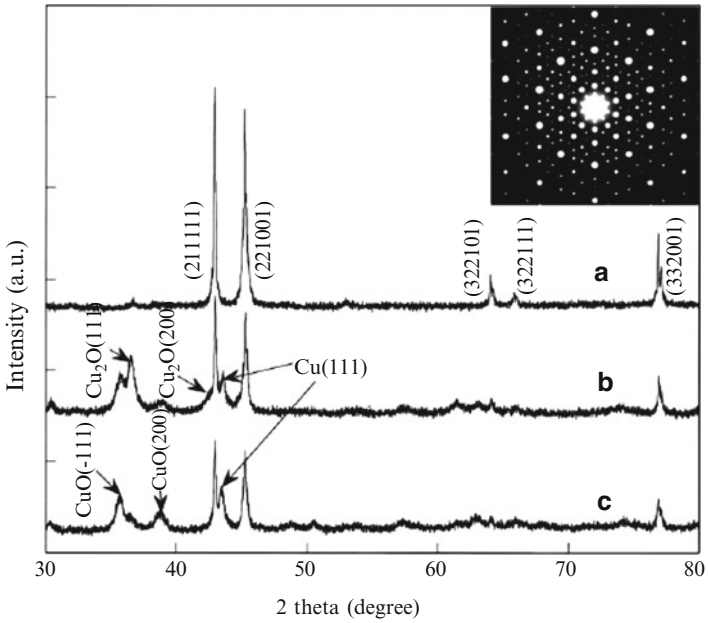

Fig. 5.11 XRD of quasicrystalline $Al_{63}Cu_{25}Fe_{12}$ (**a**), after leaching with 20 wt% NaOH at ambient temperature (**b**), and after use as MSR catalyst (**c**). The *inset* shows an electron diffraction pattern of (**a**), proving the existence of the icosahedral quasicrystal. Reprinted from [22], Copyright 2001, with permission from Elsevier

Interestingly, leaching of the quasicrystalline phase resulted in higher activity and stability compared to the crystalline intermetallic precursors—a phenomenon not understood as yet. Ma et al. modified the leaching solution for $CuAl_2$ with Na_2CrO_4 and discovered that this increases the activity by a factor of 2 [23]. Using XPS, they could show that the modification led to Cr_2O_3 promotion, which acts beneficial on the structural and catalytic properties. The presence of Cr_2O_3 results in higher BET surface areas due to higher porosity and smaller Cu particles. It was observed that Cr_2O_3 also increases the activity by itself, resulting in a higher activity compared to commercial copper chromite catalysts.

Another direction explored to generate highly specific SA_{Cu} is to oxidize intermetallic compounds or alloys prior to their use as catalysts. This approach is similar to the preparation of methanol synthesis catalysts which was developed in the 1970s by Wallace and Lambert [146, 147]. Here the oxidation of Cu–RE (RE, rare earth element) intermetallic compounds like $CeCu_2$ or $NdCu_5$ in the CO/H_2 feed leads to finely dispersed Cu particles which are supported on the rare earth oxides (Fig. 5.12).

Activation of Ni_3Al in the MSR feed leads to decomposition of the intermetallic compound to small Ni particles supported on oxidized/hydrolyzed aluminum [24]. While at a steam:carbon ratio of 1 both elements are oxidized, elemental Ni is preserved at a steam:carbon ratio of 0.1. The observed catalytic properties of the Ni_3Al-derived catalysts correspond to Ni-based catalysts and show CO_2

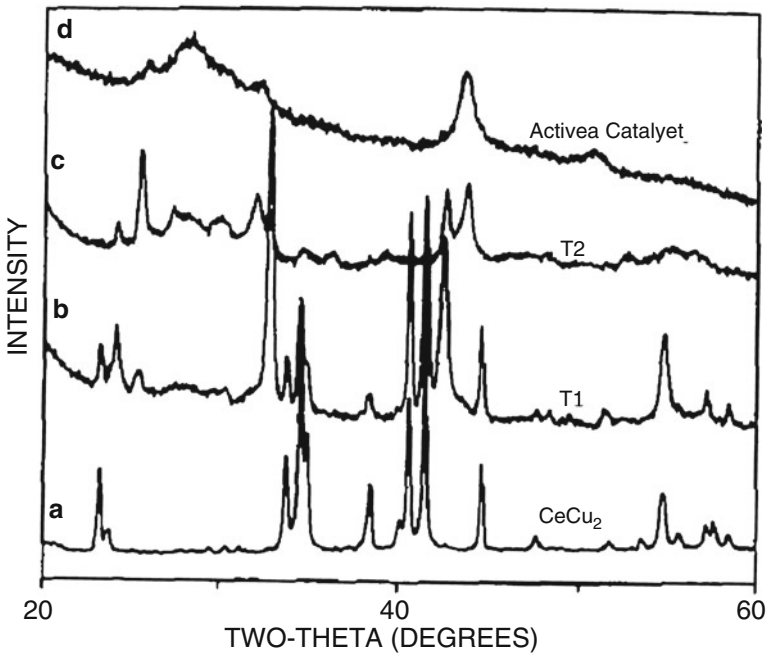

Fig. 5.12 X-ray diffraction of $CeCu_2$ in He (**a**) and during treatment in 15 bar CO/H_2 at 353 K (**b**) and 373 K (**c** and **d**). The active state of the catalyst consists of Cu particles supported on CeO_2, while T1 and T2 show the decomposition of the intermetallic compound during the treatment. Reprinted from [147], Copyright 1987, with permission from Elsevier

selectivities of only 10% since the main reaction—even under steam reforming conditions—is the decomposition of methanol.

To obtain highly specific transition metal surface areas, Takahashi et al. oxidized amorphous Cu–Zr alloys with small contents of Au, Pd, Pt, or Rh for 17 h in air at 570–587 K [25, 148]. By subsequent reduction at 573 K in hydrogen, the desired supported transition metal catalysts were obtained. The most active catalysts were obtained from alloys with Pt and Rh contents around 1%, while for Au the activity increased with increasing Au content. The selectivity toward CO_2 of these catalysts was around 100% and it was concluded that the main role of Pt, Rh, and Au is to increase the copper dispersion. The behavior of the Pd-modified Cu–Zr alloys differs significantly from the other alloys. While the activity is again increased, the selectivity to CO_2 is only around 60%. This can be attributed to the presence of elemental Pd which is an active catalyst for the decomposition of methanol to CO.

Besides being decomposed, intermetallic compounds are important in other ways in the steam reforming of methanol: On the one hand, they are often observed after the use of oxide-supported catalysts, which triggered research on their formation. On the other hand, unsupported intermetallic compounds are under investigation to reveal their part in the steam reforming of methanol. Research on these two topics is compiled below.

5.3.2 Supported Intermetallic Compounds

As seen above, intermetallic compounds can be changed by the reactive atmosphere applied—and conventional supported (monometallic) catalysts can be very dynamic systems. This is, for example, expressed by deactivation due to sintering of the supported metal or the deposition of carbonaceous species.

Especially under reducing conditions (e.g., in the last step of the preparation) two other effects can be present. One is the so-called strong metal–support interaction (SMSI), which can be defined by three characteristics [149]: (1) when reduced at low temperature, the catalyst shows a conventional chemical behavior, (2) high-temperature reduction strongly alters the chemisorption properties (SMSI state), and (3) the phenomenon is reversible by oxidation and mild reduction bringing the catalyst to state (1). While in the first publication by Tauster the involvement of intermetallic compounds was suggested [150], the SMSI is today assigned to a covering of the metallic particles by a mobile and partly reduced support [151–153], a view that was also taken by Tauster in later publications [154]. The other phenomenon is the formation of intermetallic compounds by partial reduction of the (oxidic) support and subsequent reaction with the supported metal, for which we propose the term "reductive metal–support interaction" (RMSI). The formation of the intermetallic compounds has to be differentiated from the SMSI, since it is usually not reversible unless the catalysts are treated under very strong oxidizing conditions.

Instead of being formed before the reaction, intermetallic compounds can also be formed under reaction conditions by RMSI. Commonly, this process is not complete unless very high reduction temperatures are applied, where the necessary temperature depends on the combination of metal and support. Figure 5.13 displays an example of the problem. Using only XRD, it is hard to identify the species present after reduction at low temperatures. The observed diffraction patterns could be due to partially reduced PdO, solid solutions of oxygen or hydrogen in Pd, or intermetallic compounds. If the process is not complete, different potentially catalytically active species can be present and the resulting complex systems (different metallic species, support, numerous interfaces) hinder the determination of the catalytic properties of each of the components. While the RMSI is usually only observed in catalytic systems involving an easily reducible support (e.g., ZnO, Ge_2O_3, In_2O_3)—unless very high temperatures are applied [155, 156]—the SMSI is not restricted to these systems and is also observed for ZrO_2 and Al_2O_3 [154].

Research for alternative MSR catalysts providing higher stability than the Cu-based systems led to the investigation of Pd- and Pt-based catalysts. In the first publication by Iwasa et al. Pd and Pt on different supports were evaluated [157]. Normally, elemental Pd selectively catalyzes the decomposition of methanol to CO, even in the presence of water, resulting in high CO contents in the product [32]. Surprisingly, Iwasa et al. observed that in the case of Pd/ZnO the CO_2 selectivity improved drastically from 0 to 97% with prior reduction of the catalyst.

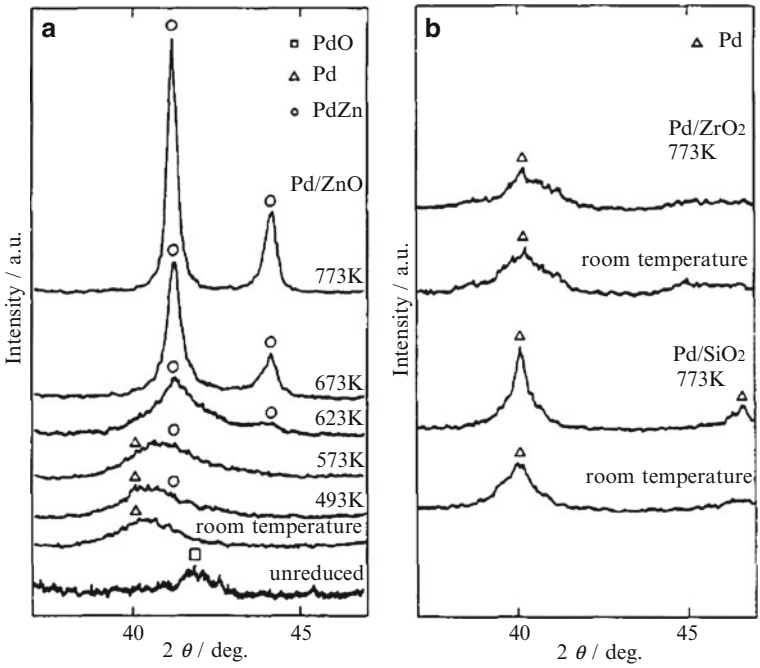

Fig. 5.13 Powder X-ray diffraction of 10 wt% Pd on ZnO (**a**) and ZrO_2 and SiO_2 (**b**), respectively. The temperatures at which the catalysts were reduced are given in the figure. Reprinted from [141], Copyright 1995, with permission from Elsevier

By comparison of Pd/ZnO with Pd/SiO_2 and Pd/ZrO_2 they could show that by RMSI the intermetallic compound ZnPd is formed on Pd/ZnO (Fig. 5.13), modifying strongly the catalytic selectivity of the Pd/ZnO catalyst [141]. On the other hand, no intermetallic compound was formed on Pd/SiO_2 or Pd/ZrO_2 at comparable temperatures, resulting in low selectivities of 0.9 and 35% toward CO_2, respectively.

In addition to XRD, the compound formation was also detected by X-ray photoelectron spectroscopy. The $Pd3d_{5/2}$ signal for elemental palladium is observed at 335.1 eV. The reductive treatment of Pd/ZnO at 673 K with hydrogen leads to a shift of 0.6 eV of the $Pd3d_{5/2}$ signal to higher binding energy.

The beneficial formation of ZnPd led to an increase in the conversion and selectivity from 33 to 62%, respectively, for Pd/ZnO catalysts reduced at 493 K to 58 and 98%, respectively, after reductive treatment at 673 K. For comparison, the conversion over Pd/SiO_2 was 10% with a selectivity of 0.9% and Pd/ZrO_2 showed a conversion of 87% and a selectivity of 20%. It was suggested that the reason for the selectivity increase is the different reaction pathways for the decomposition of formaldehyde species on Pd and ZnPd. While they are selectively decomposed to CO and H_2 on elemental Pd, the intermetallic compound ZnPd leads to an effective

attack by water and subsequent decomposition to CO_2 and H_2 similar to the reaction path suggested for Cu-based catalysts (Fig. 5.1).

These initial studies were followed by many others, making ZnPd/ZnO the best-investigated intermetallic system for the steam reforming of methanol. Special interest lies on how the intermetallic particles are formed and how the catalytic properties depend on the particle size and morphology. The formation of the intermetallic compound has been investigated by two approaches so far. Wang et al. studied 15.9% Pd/ZnO prepared by co-precipitation by TPR, desorption, electric conductivity, and XRD [158, 159]. The strong interaction between metallic palladium and the support leads to hydrogen spillover during reduction. This enables the reduction of the ZnO in the vicinity of the Pd particles and the formation of the intermetallic compound ZnPd at temperatures above 523 K. The suggested reduction process follows the sequence Pd/ZnO → $ZnPdO_{1-x}$/ZnO → ZnPd/ZnO. For this catalyst, the best catalytic performance (41% conversion, 94% selectivity, hydrogen yield 0.65 mol g^{-1} h^{-1} at 523 K and a WHSV of 17.2 h^{-1}) was obtained after reduction at 573 K for 1 h in pure hydrogen, which resulted in a crystallite size of 5–14 nm.

A different approach was followed by Penner et al. [160], who synthesized well-defined thin film model systems by embedding epitaxially grown Pd particles in an amorphous ZnO matrix which is mechanically stabilized by SiO_2. The advantage of this approach is the possibility to perform in-depth TEM characterization of these materials. The formation of well-ordered ZnPd was observed at temperatures as low as 473 K and it was stable up to 873 K, where it partially decomposed into Pd-rich silicides. The epitaxial growth of the Pd particles causes their alike crystallographic orientation. This enabled the observation that the ZnPd intermetallic compound is formed by a topochemical reaction [161] starting at the surface of the Pd particles. Comparison of a similar Pd/SiO_2 thin film model revealed amorphisation of the Pd particles by reduction, most likely due to hydride formation. This clearly does not happen in the presence of ZnO as otherwise the crystallographic orientation between the particles would be lost. Most likely, hydrogen is activated on the Pd surface or a crystalline α-Pd-hydride with low hydrogen content is formed. A low concentration of activated hydrogen is reasonable because the hydrogen is used up by the reduction of the ZnO in the vicinity of the Pd particles immediately. Thus, the most likely reaction sequence is Pd/ZnO → "PdH_x"/ZnO → ZnPd/ZnO, where "PdH_x" represents a crystalline Pd-hydride or activated hydrogen on the surface. Clarifying the intermediate in this reaction needs further investigation.

The influence of the ZnPd particle size (2–34 nm mean diameter) on the catalytic performance was studied by Dagle et al. and Karim et al. [162, 163]. They found that the intermetallic compound ZnPd is already formed at the relatively mild reduction temperature of 523 K. At these low temperatures, ZnPd and Pd coexist on the support. By varying the reduction temperature, the Pd/ZnPd ratio was changed, but no monotonic correlation between ZnPd content and the CO_2 selectivity was observed. Instead, small particles showed CO_2 selectivities of only 62% compared to 99% for the larger ones and highly selective catalysts could be obtained by elimination of the small and unselective particles of the intermetallic

compound. The loss in selectivity can be explained with a strong activity increase of small ZnPd particles in the rWGS reaction, thus, the production of CO by converting CO_2 and H_2 [164, 165]. Interestingly, large ZnPd particles (diameter of 34 nm) show the same catalytic activity as small particles with 9 nm diameter. This might indicate that not only the intermetallic compound ZnPd but also the ZnO support plays important roles during catalysis, e.g., by forming the catalytically active interface together.

The influence of ZnO on the catalytic properties has been studied in more detail by using catalytic systems consisting of Pd and Zn being present on an inert support like carbon or alumina. Suwa et al. compared the deactivation behavior of ZnPd–ZnO/C and ZnPd/ZnO catalysts [166]. After 50 h time on stream, both catalysts showed deactivation from 70 to 60% and 70 to 40%, respectively. XRD analysis revealed the presence of $Zn_4CO_3(OH)_6{\cdot}H_2O$ on the ZnPd/ZnO catalyst. It was concluded that the deactivation mechanism is due to $Zn_4CO_3(OH)_6{\cdot}H_2O$ covering the intermetallic surface. The stronger deactivation of ZnPd/ZnO compared to ZnPd–ZnO/C was explained by the higher amount on ZnO present on the former.

Another system on which the influence of ZnO has been studied is Pd–ZnO/Al_2O_3 [29]. A series of catalysts with different Pd loading and Pd:Zn molar ratios was prepared, characterized, and tested. The highest selectivity (98.6%) and activity (80% conversion at 523 K) was revealed at a loading of 8.9% Pd with a Pd:Zn ratio of 0.38. Doubling the ratio led to a six times higher CO content, whereas with half the ratio the CO content reached 1.7%. By XRD, ZnO was observed at low Pd:Zn ratios, while at high Pd:Zn ratios elemental Pd was observed. This clearly shows that an ideal Pd:Zn ratio exists. If enough Zn is not present, not all the Pd can be converted to ZnPd, thus catalytically decomposing the methanol to CO and H_2. Too high Zn contents on the other hand result in the formation of too much ZnO, which leads to lower selectivities and deactivation.

Pd/ZnO was also used in the oxidative steam reforming of methanol. Liu et al., who were the first to investigate this reaction/catalyst combination [167, 168], studied in a series of publications the effect of the Pd loading [169], the deactivation [170], and the influence of the presence of third metals [171]. In contrast to the steam reforming of methanol, the activity and selectivity increased with Pd loading, most probably due to the use of ZnO as support, thus not restricting the Pd:Zn ratio. Testing the catalysts over 25 h resulted in a deactivation behavior superior to Cu-based catalysts, but with increasing amounts of CO (up to 18%) produced with time on stream (Fig. 5.14).

By XPS investigations, it could be shown that the increasing CO content is due to a surface oxidation of the intermetallic compound ZnPd resulting in elemental palladium being present on the support, which leads to the decomposition of methanol. Modifying the Pd/ZnO co-precipitated catalysts with transition metals resulted in higher CO contents except in the cases of small amounts of Cr, Fe, or Cu, which increased the selectivity slightly. The promotional effect was assigned to the WGS activity of these transition metals. The intrinsically lower selectivity of unpromoted Pd/ZnO/Al_2O_3 was also observed for hydrotalcite derived catalysts, which showed

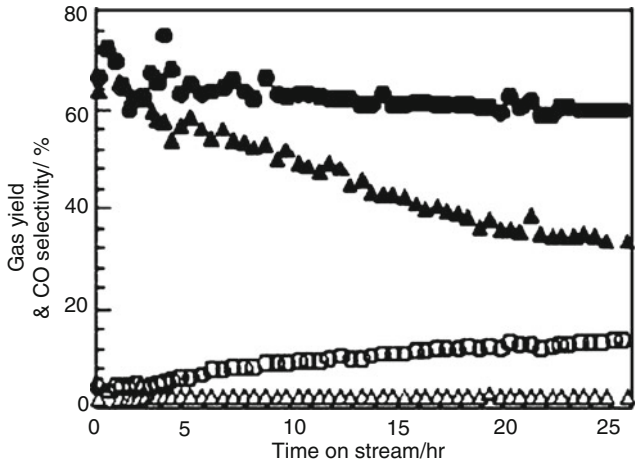

Fig. 5.14 Activity (*solid symbols*) and CO selectivity (*open symbols*) of Pd/ZnO (*circles*) and a commercial Cu/ZnO catalyst (*triangles*). Reprinted from [170], Copyright 2006, with permission from Elsevier

CO_2 selectivities of 74–89% [172]. Thus, it seems that using ZnPd in oxidative steam reforming is not a promising route to highly selective catalysts due to the decomposition of the selective intermetallic compound. In addition to methanol (oxidative) steam reforming, ZnPd has also been applied as catalyst for the POM [173–175], which is not in the focus of this chapter.

In summary, the catalytic system Pd/ZnO is quite complex. The different catalytic activities of ZnO, elemental Pd, ZnPd, and the resulting interfaces pose a hurdle for a knowledge-based development and the empirical database is not sufficient yet to draw final conclusions about the ongoing processes and the involved species. Large differences exist between different ZnPd/ZnO catalysts in the steam reforming of methanol (Table 5.1). These might be explained by different Pd:Zn ratios and varying ZnO contents as well as by particle size effects at two stages. First, the catalytic properties change with particle size as shown above. Second, the formation of Pd-hydrides depends on the particle size [176–178] and if the formation of ZnPd is proceeding via a palladium hydride, size dependence during formation is expected. As a consequence, each system and every preparation route involving ZnPd has its own ideal zinc content and reduction conditions which need to be explored and established.

Leaving the system Pd/ZnO and with it the intermetallic compound ZnPd, a number of other systems involving intermetallic compounds have been investigated for the steam reforming of methanol, albeit not yet in such depth as the aforementioned Pd/ZnO. Iwasa et al. were the first to explore other transition metals supported on ZnO [27]. Amongst Ni, Co, and Pt, only the latter formed an intermetallic compound (PtZn) during reduction. Compared to Pt/SiO_2 the CO_2 selectivity was enhanced from 25.6 to 95.6%. On the other hand, the Ni- and Co-

based systems showed selectivities of 4.7 and 8.9%, respectively. Testing Pt–Zn/C, Ito et al. also observed a selectivity increase after the formation of the intermetallic compound PtZn by reduction in H_2 at 873 K [179]. The resulting selectivity increase from 48% for Pt/C to 83% for PtZn/C was not as high as for PtZn/ZnO, probably indicating an uncompleted transformation of Pt.

In the next step, Iwasa et al. changed the support for the Pd- and Pt-based systems to Ga_2O_3 and In_2O_3 [26, 28, 180]. After reduction, the intermetallic compounds Pd_5Ga_2, $PdGa_5$, $Pd_{0.52}In_{0.48}$ (or PdIn), Pt_5Ga_3, $Pt_{10.6}Ga_{5.4}$ (or Pt_5Ga_3), and $PtIn_2$ were formed as observed by TPD, XRD, XPS, and AES. Using Ga_2O_3 as support resulted in a mixture of intermetallic compounds in contrast to ZnO- or In_2O_3-supported catalysts. As in the case of Pd/ZnO, the formation of the intermetallic compounds led to a large increase in the observed CO_2 selectivities. While the noncompound-forming systems Pd/SiO_2 and Pt/SiO_2 showed selectivities of 0 and 18.8%, respectively, the Ga–Pd and Ga–Pt intermetallic compounds raised the selectivity to 94.6 and 75.5%, respectively. In the case of the In_2O_3-supported catalysts, selectivities reached 95.5% for In–Pd intermetallic compounds and even 98.3% for In–Pt intermetallic compounds. Especially the latter nearly reaches that of ZnPd/ZnO catalysts, which possess a selectivity of 99.2% under the same conditions. $PdIn/Al_2O_3$ catalysts were applied in a microstructured reactor [26]. According to this study, $PdIn/Al_2O_3$ seems to be a more dynamic system than ZnPd/ZnO. By undergoing a self-optimization by reduction in the feed and reaching a highly selective steady state, a pre-reduction is superfluous. To address the question why these intermetallic compounds behave so differently, the decomposition of formaldehyde, which is often claimed as intermediate in the steam reforming of methanol, was studied on elemental Pd and Pt catalysts as well as on the intermetallic compound catalysts. Here, a marked difference was observed: while the elements decomposed formaldehyde to CO, the intermetallic compounds selectively produced CO_2 [141, 180]. This difference, as well as the different selectivities in the steam reforming of methanol, was assigned to the distinguished adsorption of the aldehyde in the η^1(O) structure on Cu, and the η^2(C,O) structure on Pd, Pt, and Ni. It was proposed that the very different catalytic properties of ZnPd and metallic Pd are due to the different structures of the HCHO intermediates on the metals. However, this view is not corroborated by theoretical calculations, which propose very similar adsorption geometries for the HCHO intermediate on Cu and Pd (η^1) but η^2 for ZnPd [181]. The support portfolio was enlarged by GeO_2 (both the tetragonal and the hexagonal modification) and SnO_2 [182]. Pd supported on these supports forms under reducing conditions Pd_2Ge at 473–673 K and a mixture of Pd_2Sn and Pd_2Sn_3 at 573 K, respectively. In both cases, decomposition of methanol is the prevailing reaction, resulting in very low CO_2 selectivities in the steam reforming of methanol.

The formation of the Pd-based intermetallic compounds by reaction of the noble metal and the support was investigated—as in the case of ZnPd—in detail by thin film models by the group of Klötzer very recently. For these XRD, TEM, and SEAD studies, small Pd particles were epitaxially grown on NaCl and this time covered with amorphous Ga_2O_3, In_2O_3, GeO_2, or SnO_2 [182, 183]. To mimic the conditions

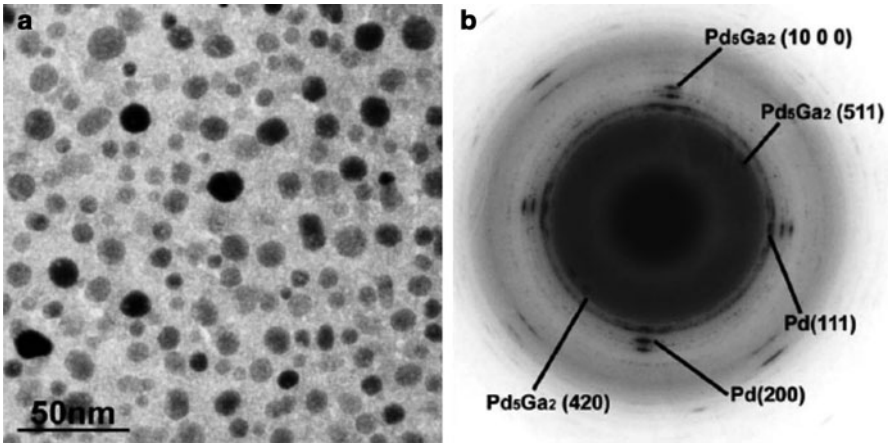

Fig. 5.15 TEM image of Pd/Ga_2O_3 thin film catalyst after reduction in 1 bar H_2 (**a**). The corresponding SAED pattern is shown in (**b**). Reprinted from [183], Copyright 2009, with permission from Elsevier

of the synthesis of the catalysts used above, the Pd/Ga_2O_3 particles were first oxidized to PdO before being reduced at different temperatures in H_2. Reducing the particles at 523 K resulted first in Pd particles, which subsequently were transformed to the intermetallic compound Pd_5Ga_2 (Fig. 5.15).

The transformation is not complete even when the reduction temperature is raised to 773 K. The remaining Pd is most probably located in the core of the particles, thus not taking part in the catalysis directly. Above 673 K pronounced sintering of the particles was observed in contrast to ZnPd/ZnO. The study was complemented by investigating an impregnated $Pd/\beta\text{-}Ga_2O_3$ powder catalyst. In contrast to the thin film studies, the formation of the intermetallic compound Pd_2Ga [184] was observed here by XRD at reduction temperatures above 573 K. As in the thin films, elemental Pd is still present, even if the reduction is carried out at 773 K. Above 923 K, the Pd_2Ga is transformed to the intermetallic compound PdGa by further reduction of the support. In difference to the work of Iwasa, the intermetallic compound $PdGa_5$ was neither observed on the thin film nor on the powder catalyst after reduction.

In the case of the In_2O_3-supported catalyst, a thin film sample and a Pd/In_2O_3 powder catalyst were also used to investigate the compound formation [185]. Two main differences to the former investigated systems occur in the Pd/In_2O_3 thin film samples: (1) the deposited In_2O_3 is partly crystalline and not fully amorphous and (2) already during the deposition the formation of the intermetallic compound PdIn is observed. Reducing the thin film samples in H_2 at 373 K resulted in higher PdIn contents and at 573 K the In_2O_3 film is fully crystallized. From the TEM investigation of the PdIn particles, it was concluded, that the topochemical reaction growth follows the scheme PdIn[001]||Pd[001] and PdIn[011]||Pd[011]. At 573 K all the Pd is transformed to PdIn and the orientation of the particles is lost due to the stability limit of the In_2O_3 in hydrogen atmosphere.

Reduction of the powder catalyst resulted in the complete transformation of Pd to PdIn at 573 K. As in the case of Ga_2O_3, higher temperatures lead to the formation of the main group metal-richer intermetallic compounds Pd_2In_3 (673 K) and $PdIn_3$ (773 K).

Pd particles in a GeO_2 matrix are converted to Pd_2Ge at 473–573 K [182]. This transformation does not depend on the use of the GeO_2 modifications if the particles are conventionally supported and furthermore, the only intermetallic compound observed on the amorphous thin films is Pd_2Ge. In contrast, the intermetallic compounds observed for Pd on SnO_2 depend on whether a thin film sample with amorphous SnO_2 or a conventionally supported system is reduced at 573 K. In the first case, Pd_2Sn and Pd_3Sn_2 are observed, while in the thin films the reduction yields Pd_2Sn and PdSn. Kamiuchi et al. investigated the interaction between the Pd particles and the SnO_2 support [186]. After reduction at 673 K only the intermetallic compound Pd_3Sn_2 is formed and the particles are intruding into the support as revealed by subsequent TEM studies. During the short time of air exposure, core–shell structures are formed by oxidation of the intermetallic tin on the surface. The core consists of the intermetallic compound Pd_3Sn_2 and the shell is an amorphous Sn-oxide corresponding to a SMSI state (see above). In contrast to the report by the group of Klötzer, Pd_2Sn was only observed after reoxidation of the sample in air at 673 K in the non-SMSI state.

Despite the thorough investigation of the formation processes of the intermetallic compounds, it is a disadvantage of all aforementioned systems that the intermetallic compound is at least mixed with the support and in most cases also with the corresponding noble metal in the elemental state. Sometimes even more than one intermetallic compound is present, bringing the complexity to an even higher level. In such systems, the number of possible catalytically active species hinders the assignment of the observed catalytic properties to a specific species and thus a knowledge-based development. The underlying processes might be complicated and most probably involve the support or the metal/support interfaces (at least in the case of ZnPd/ZnO, where this is indicated by the data available), but only reducing the complexity will allow to understand the role of the intermetallic compound. This approach can be followed either by theoretical calculations or by experiment and the progress achieved so far is summarized in the next section.

5.3.3 Unsupported Intermetallic Compounds

As seen in the large number of observations above, intermetallic compounds might play a pivotal role as catalysts for the steam reforming of methanol. However, the systems discussed so far do not allow an unambiguous correlation of the crystal and electronic structures of the intermetallic compounds and the observed catalytic properties for two reasons: (1) the intermetallic compounds are not the only species present, and the support, e.g., ZnO, might also influence the catalytic properties; (2) the stability of the compounds needs to be proven under reaction conditions. While

the impact of the first point is quite obvious, the second one can be exemplified by the subsurface carbon phase formation of palladium during the gas-phase hydrogenation of alkynes [187–189]. Here, the alkyne is decomposed on the surface and part of the carbon forms a metastable subsurface Pd–C phase. The electronic structure of the material is changed significantly, which can be detected, e.g., by XPS as a shift of the binding energy of the $Pd3d_{5/2}$ signal of 0.6 eV. As soon as the hydrocarbon supply is stopped, the subsurface Pd–C decomposes by segregation of the carbon to the surface. Before and after the reaction, only elemental palladium is observed (with carbon deposits after reaction), while the catalytically active phase actually is palladium modified by the subsurface carbon. Changes like this need to be detected and studied to allow valid correlations. Modifications by hydrocarbons might not play a major role in the steam reforming of methanol. But some intermetallic compounds are known to readily form hydrides in hydrogen-containing atmospheres. As in the case of carbon-modified palladium, this leads to a strong alteration of the electronic and sometimes the crystal structure as has, e.g., been studied in the case of $LaNi_5$ [190]. Besides hydride formation, decomposition of the intermetallic compounds can also occur as seen in the first section, demonstrating the need to prove the stability of the intermetallic compound in question under reaction conditions before correlating the electronic and crystal structure to the observed catalytic properties.

These requirements, i.e., to simplify the systems and prove their stability, can, e.g., be fulfilled by performing experiments and quantum theoretical calculations on unsupported single-phase intermetallic compounds. Experimentally, this allows to detect changes to the materials much easier, and, by proving the stability of the bulk and the surface, the resulting catalytic properties can be assigned directly to the intermetallic compound and thus to its crystal and electronic structure. Quantum chemical calculations can provide information about the surface, like adsorption properties and possible reaction pathways. In addition, bulk quantum chemical calculations of the electron localizability function allow studying the chemical bonding in real space [191–193]. These calculations give valuable insight and help to understand the stability under reaction conditions.

To investigate the intrinsic catalytic properties and stabilities experimentally, three different kinds of materials can be used. The first is the unsupported intermetallic compound, usually prepared by metallurgical synthesis or in nanoparticulate form. Large single crystals represent the second class of materials and so-called surface alloys the third. While the first is best suited in crushed form for reactor studies, the other two represent materials for surface science studies. Using unsupported intermetallic compounds as powders in a reactor and as single crystals in UHV studies allows to bridge the experimental "materials gap." Ideally, the usually brittle single crystals can be comminuted after being studied in UHV and then be used for reactor studies. In addition, unsupported intermetallic compounds also allow closing the gap between quantum chemical calculations and experimental studies.

Nevertheless, there are material restrictions that one has to bear in mind. Surface alloys can be synthesized under UHV conditions by depositing, e.g., Zn on a Pd

single crystal and allow the Zn to react with the first few Pd layers. Complications arise, because the substrate and the surface alloy are usually electronic conducting materials and the electronic structures influence each other. The surface alloy—even if it has the same crystal structure as the corresponding bulk phase—thus possesses a modified electronic structure, which might result in altered adsorption and catalytic properties. Similar considerations are true for intermetallic compounds in nanoparticulate form. Here, size-confinement effects can alter the electronic structure compared to the bulk. Since the influence is not known unless one compares bulk and nanoparticulate samples, nanoparticulate intermetallic compounds are not suitable to determine the intrinsic catalytic properties.

As could be shown in the case of Ga-Pd intermetallic compounds in the semi-hydrogenation of acetylene [134, 194–196], it is important to perform the experimental studies on well-characterized and single-phase materials, which can be obtained best by metallurgical synthesis routes. In contrast to alloys, intermetallic compounds are often brittle and allow easy comminution after synthesis, e.g., by grinding or milling. Changes of the materials by these treatments need to be investigated in order to find the best-suited route to generate higher active surface, while keeping the intrinsic structure.

The most-studied intermetallic compound with respect to MSR is ZnPd. These studies include the homogeneity range, chemical bonding and catalytic tests of the unsupported compound, and extensive surface quantum chemical calculations. The range of existence of the tetragonal intermetallic compound ZnPd (CuAu type of structure, space group *P4/mmm*, $a = 2.8931(1)$ Å and $c = 3.3426(2)$ Å, $c/a = 1.16$) reaches from $Zn_{37.1(4)}Pd_{62.9(4)}$ to $Zn_{50.9(1)}Pd_{49.1(1)}$ at 1,173 K [136]. In contrast to the published binary phase diagram, the existence of the cubic high-temperature structure could not be confirmed experimentally in this reinvestigation. Quantum chemical tight-binding linear-muffin-tin-orbital (TB-LMTO) and full-potential local-orbital (FPLO) calculations corroborated the experimental results and revealed a charge transfer from Zn to Pd of 0.4 e^-. Chemical bonding analysis by the electron localization indicator (ELI) revealed Pd–Pd interactions in the (001) plane as the driving force for the tetragonal distortion of ZnPd. The electronic DOS around the Fermi energy of ZnPd is very similar to the DOS of elemental copper and led to the suggestion that both should possess similar catalytic performance (Fig. 5.16) [30, 197, 198].

Further quantum chemical calculations show [199] that segregation is unlikely in accordance with the chemical bonding situation as described above. Out of the low-indexed surfaces, the (111) and (100) surface are calculated to be the most stable ones [197]. To elucidate the reaction mechanism, the group of Rösch performed surface quantum chemical calculations on ZnPd (111), (100), and stepped (221) surfaces with Pd $(221)^{Pd}$ and Zn $(221)^{Zn}$ steps. Assuming the decomposition of methoxide (CH_3O) as being the rate-limiting step in the steam reforming of methanol over Pd/ZnO, density functional calculations of the C–O and C–H bond breaking were performed. On all surfaces, the activation barrier of the C–H bond breaking is much lower than breaking the C–O bond, suggesting the first step in the decomposition is the abstraction of an H atom. Nevertheless, calculations on

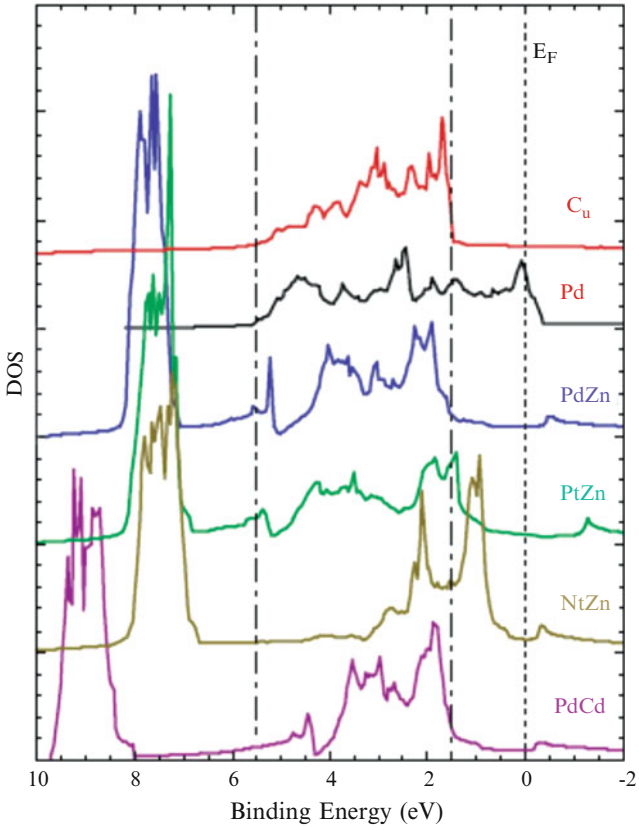

Fig. 5.16 Electronic density of states for elemental Cu and Pd as well as for the intermetallic compounds ZnPd, PtZn, NiZn, and PdCd. The *dotted line* represents the Fermi energy, while the two *broken lines* indicate the width of the Cu d states. Reprinted from [30], Copyright 2004, with permission from the Physical Society of Japan

defect-free ZnPd (111) and (100) surfaces revealed rather high activation barriers of 93 and 90 kJ mol^{-1} for the H-abstraction, respectively [200, 201]. In contrast, the activation energy is lowered to around 50 kJ mol^{-1} in the case of the ZnPd $(221)^{Pd}$ surface [202]. The reason for the lower activation energy is twofold: (1) the reactant CH_3O binds weaker to two Pd atoms of the step and (2) the resulting product CH_2O is bound stronger. For the abstraction of the H atom, two possible mechanisms have been identified. The first proceeds by tilting of the O-bound CH_3O toward the terrace followed by H-abstraction and possesses an activation energy of 49 kJ mol^{-1}. In the second case, the C–O bond of the molecule is tilted toward the Pd-terminated step in the transition state and the H atom is placed in an edge-bridge site, resulting in an activation barrier of 53 kJ mol^{-1}. Due to the large differences in activation energy of flat and stepped surfaces, it was concluded that the reaction is catalyzed by steps or other defects on the surface. A factor not considered in the calculations

so far is the presence of ZnO, which would result in a very complex system. Taking ZnO into account would be highly interesting, since the presence of ZnO could have an influence on the catalytic properties according to the experimental studies on supported systems.

The earliest work on Pd–Zn surface alloys in UHV was performed on Pd–Zn/Ru(001) and Pd/Zn(0001) [203, 204]. CO TDS on Pd–Zn/Ru(001) showed that already very small amounts of Zn decrease the CO desorption energy dramatically. The full complexity of the Pd–Zn surface alloy(s) has been investigated and is still under investigation by several groups applying a broad range of methods using Zn/Pd(111) as common model system.

Deposition of Zn on Pd(111) below 300 K leads to elemental Zn multilayers, diffusion into the subsurface layers of Pd(111) starts at temperatures above 300 K. Temperatures of 400–500 K lead to a metastable buckled surface alloy of several layers with a p(2×1) LEED pattern (surface alloy 1—SA1) [198, 205, 206]. Impact-collision ion scattering spectroscopy (ICISS) shows that the Zn atoms are sticking out of the surface with a 1:1 composition [198, 205, 207]. At temperatures above 550 K, the Zn of the subsurface layers starts to diffuse into the bulk Pd, but the depletion is only slightly affecting the topmost layer [207]. At 623 K the diffusion of the Zn in subsurface layers has further progressed and a subsurface Zn-diluted "monolayer" Pd–Zn surface alloy is obtained, which exhibits hardly any corrugation (SA2) [206–208]. The changes in the electronic structure by going from SA1 to SA2 are remarkable and result in a shift of the binding energy of the $Pd3d_{5/2}$ XPS signal of 335.3–335.6 eV and 335.9 eV for the 1 ML SA2 and a 3 ML SA1, respectively (Fig. 5.17).

If the deposition is performed at 300 K, ZnPd bilayer islands with a Pd:Zn ratio of 1:1 are formed, which are shown to be more stable than monolayer islands by DFT calculations [208, 209]. In contrast to SA1 and SA2, a p(2×2) LEED pattern is reported if the layer is annealed at 520 K [210]. STM investigations revealed that after deposition at 300 K, three energetically identical p(2×1) domains are formed (SA3) explaining the p(2×2) LEED pattern [208, 211]. As in the case of the multilayer alloy SA1, the surface of the bilayer islands of SA3 is not flat but buckled with the Zn atoms sticking out [205, 208]. If the whole surface is covered, additionally deposited Zn forms multilayers on top of SA3, which acts as a diffusion barrier at ambient temperature [208]. In difference to SA1, heating the Zn-covered sample to more than 600 K leads to partial Zn desorption and partial bulk diffusion of the additional Zn, before at 750 K the Zn of the SA3 starts to desorb [208]. As in the case of SA2, the buckling of the surface changes to Pd sticking out, as soon as the islands are reduced to one layer in thickness [208]. If the Zn deposition is carried out at 550 K, the p(2×1) LEED pattern characteristic for SA1 and SA2 is observed directly [198, 212]. This indicates that at this temperature the ordered domains are much larger than after deposition at 300 K [212]. More complex surface structures have been observed after deposition of >3 ML Zn at 750 K. This procedure leads to a well-ordered ZnPd surface alloy with a $(6\times4\sqrt{3}/3)$ rectangular LEED pattern (SA4) corresponding to an eightfold superstructure compared to the bulk structure [210].

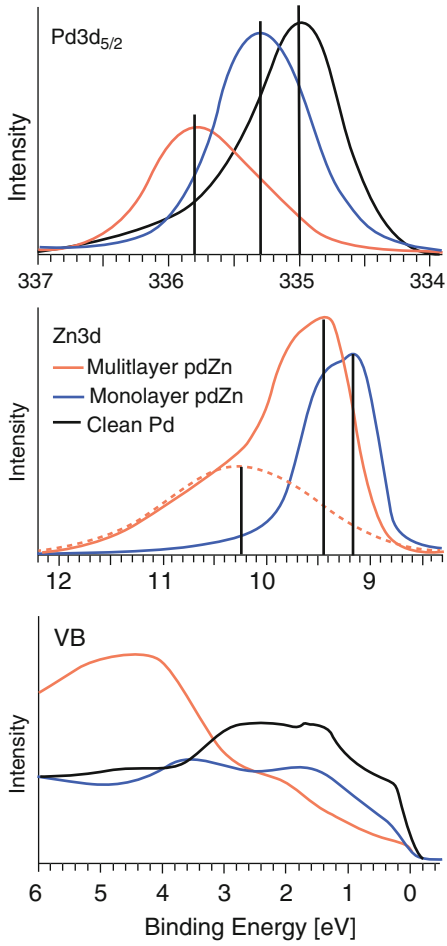

Fig. 5.17 In situ X-ray photoelectron spectra (Pd3d, Zn3d, and valence band (VB) regions) showing the large electronic differences between elemental Pd (*black*, ex situ), the monolayer surface alloy SA2 (*blue*) and the multilayer surface alloy SA1 (*red*). The *red dashed line* in the middle panel corresponds to an oxidized ZnO(H) component formed during the in situ spectra acquisition. Reprinted from [206], Copyright 2010, with permission from Wiley-VCH Verlag GmbH & Co. KGaA

The fcc structure of elemental Pd and the CuAu type of structure of ZnPd are closely related. Replacing Pd with Zn in an ordered manner would result in a c/a ratio of bulk ZnPd of 1.41. The experimentally determined ratio of 1.16 is significantly smaller caused by the covalent bonding [134]. A bulk-terminated (101) surface of ZnPd—corresponding to the Pd(111) surface—would result in a pseudo p(2x1) LEED pattern with $a' = 5.2833$ Å and $b' = 2.6416$ Å instead of the ideal values of $a = 5.4872$ Å and $b = 2.7436$ Å. Additionally, γ' would be 66.4° instead of the ideal 60.0° and the surface would be flat. However, no such deviations have been reported for the SA1 to SA4 yet. Since a comparison to the surface of bulk ZnPd is not possible yet, due to the challenges of growing such a crystal ($>$ 1,673 K are needed [213], which makes Zn very corrosive), the questions whether the underlying Pd(111) structure is causing a regular arrangement and the buckling, e.g., by modifying the electronic structure, is yet to be settled. The availability of a

large ZnPd single crystal would also enable to settle the question how representative the results obtained for Zn/Pd(111) are for other intermetallic surfaces, which are definitively present in supported ZnPd/ZnO catalysts and in polycrystalline unsupported material.

What becomes clear by CO desorption measurements is the strong alteration of the chemical properties of the surface by Zn deposition and surface alloy formation. The desorption-maximum temperature is decreased by 220 K for SA1 and SA4 compared to a clean Pd(111) surface [212, 213]. HREELS showed that the decrease in desorption goes hand in hand with a change of CO being adsorbed in threefold hollow and bridged sites to adsorption on-top for the surface alloy [212]. This has direct influences for the steam reforming of methanol, since not only is the adsorption of CO altered but the activity of methanol dehydrogenation is strongly decreased [211]. The dehydrogenation activity starts to decrease at as low Zn contents as 0.03 ML and is nearly absent at coverages above 0.5 ML [211]. This behavior has been assigned to the changes of the preferred adsorption sites for the intermediates CH_3O and CH_2O [211]. The former adsorbs on threefold hollow sites involving one or two Zn atoms, while the latter adsorbs in a bridging mode on a Pd–Zn dimer in such a way that the C atom is bonded to the Pd and the O is bonded to the Zn atom.

Even more striking is the different catalytic behavior of SA1 and SA2 in the steam reforming of methanol, which has recently been investigated [206]. With the electronic structure, also the catalytic properties in the steam reforming of methanol change dramatically (Fig. 5.17). While the thin surface alloy SA2 shows only very low selectivity toward CO_2 in the steam reforming of methanol, the multilayer surface alloy SA1 shows the expected high CO_2 selectivity. A thickness of SA1 of as little as five layers is sufficient to induce these strong changes of the catalytic properties. However, until the real structure of the working supported or bulk intermetallic catalyst is revealed, UHV studies on the clean surface–alloy material are helpful for comparison to, e.g., Pd, but the catalytically active supported or bulk material might be much more complex.

Experimental catalytic studies on the bulk intermetallic compound ZnPd are very limited. Iwasa et al. synthesized Pd–Zn samples by heat treatment of physical mixtures of Pd and Zn at 220–673 K [214]. The resulting materials were investigated by XRD, which revealed the presence of Pd, Zn, ZnPd, and/or $Zn_{6.1}Pd_{3.9}$ in the samples. Accordingly, the observed catalytic properties, e.g., the very low CO_2 selectivity of only 87.5%, cannot be assigned to the intermetallic compound ZnPd. Metallurgic single-phase samples of ZnPd, PtZn, PdCd, and NiZn were investigated by Tsai et al. [30]. The selection of the compounds was based on two considerations: (1) they are all isostructural and (2) possess electronic structures which differ from ZnPd in the order PdCd $<$ PtZn $<$ NiZn. Fulfilling these criteria, the compounds allow investigating the electronic influence on the catalytic properties, since the geometric parameters are very similar by going from one compound to the other. The observed selectivities correspond to the expectations from the similarity of the electronic structures. At 553 K ZnPd and PdCd show selectivities close to 100%, PtZn possesses a CO_2 selectivity of 45%

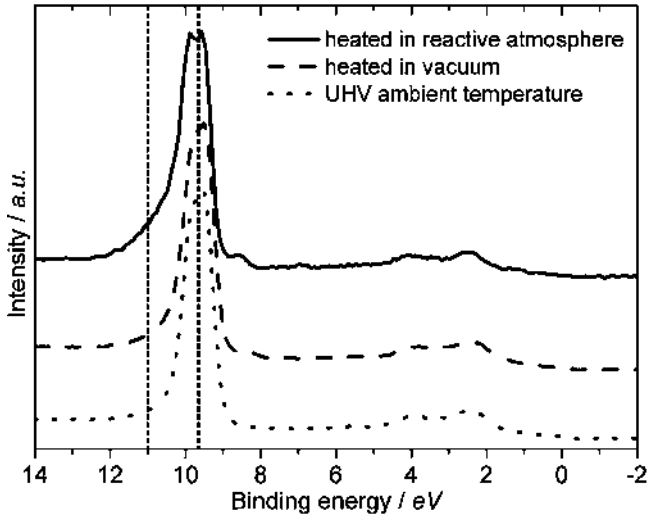

Fig. 5.18 XPS valence band spectra of ZnPd: UHV conditions at ambient temperature (*dotted line*), in situ after heating to 573 K in UHV and subsequent switching to reactive atmosphere (0.2 mbar methanol/H_2O at a 1:1 ratio, *dashed line*), and in situ after heating to 573 K in reactive atmosphere (*full line*). Photon energy is set to 237 eV for all spectra

and NiZn only 10%. From these results, a strong influence of the electronic structure could be derived, provided the compound is stable in situ.

The in situ stability of the unsupported intermetallic compounds NiZn, PtZn, and ZnPd has been investigated recently by our group applying high-pressure X-ray photoelectron spectroscopy in reactive atmosphere. When the intermetallic compound ZnPd is heated in vacuum to 573 K and a 1:1 M ratio MeOH:H_2O mixture is introduced subsequently, no changes occur in the Zn3d signal, as seen in the valence band spectra shown in Fig. 5.18.

On the other hand, heating ZnPd in MeOH/H_2O atmosphere from RT to 573 K leads to the development of a shoulder at 11 eV in the Zn3d signal, proving the formation of an oxidized Zn species on the surface (Fig. 5.18). For PtZn, very similar results are obtained. Interestingly, the intermetallic compound ZnPd without the oxidized Zn species on the surface is catalytically less active in reactor tests by a factor of more than 35 compared to the intermetallic compound heated in reactive atmosphere. These results show for the first time unambiguously that ZnPd is not the only component of the active sites and that the oxidized Zn species plays a crucial role. On the other hand, too much ZnO is detrimental to the catalytic performance as proven by studies on supported catalysts.

The intermetallic compound NiZn undergoes severe surface changes under reaction conditions. The untreated surface in UHV consists of intermetallic Ni and Zn, as well as oxidized Zn species as detected in the Zn3d region. As soon as the reactive gases are introduced into the XPS chamber (0.2 mbar methanol/H_2O, 1:1 M ratio, 573 K), the surface of the compound changes dramatically (Fig. 5.19).

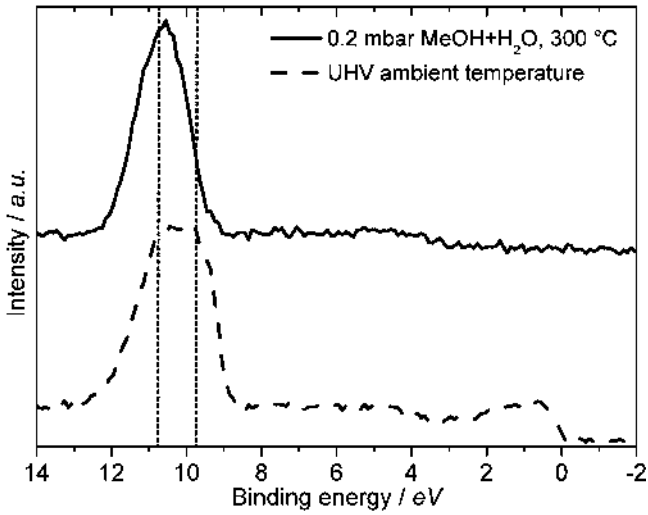

Fig. 5.19 UHV (*dashed*) and in situ (*full line*) XPS valence band spectra of the intermetallic compound NiZn. Under UHV conditions, the metallic character is clearly seen at the Fermi energy. In reactive atmosphere, the Zn is completely oxidized and the density of states at the Fermi level is lost, indicating an oxidic overlayer. The incident photon energy is 301 eV for both spectra

The intermetallic Zn on the surface is completely oxidized accompanied by a complete loss of the Ni core-level signals in the most surface-sensitive measurements. Thus, the methanol/H_2O mixture leads to segregation to and complete oxidation of the intermetallic Zn on the surface, forming a nonmetallic and Ni-free surface layer on the surface of the compound. In the case of the intermetallic compound NiZn, the observed catalytic properties cannot be attributed to the compound itself, but to the generated decomposition products.

The results of these investigations show that the intermetallic surface of these three compounds is altered under reaction conditions. It would also have been very hard to detect the changes on a supported catalyst due to the presence of large amounts of ZnO, disguising the newly formed oxidized Zn species. The investigations demonstrate the advantage of using unsupported intermetallic compounds to study the role they (or their decomposition products) play in MSR. These results also show that when investigating unsupported intermetallic compounds as catalysts, attention has to be paid to two issues: (a) analysis is simpler on single-phase samples and (b) the in situ stability should be confirmed. Otherwise the identification of the intrinsic catalytic properties is hindered.

Acknowledgments Robert Schlögl is greatly acknowledged for fruitful discussions and support. MB thanks the members of the Inorganic Chemistry Department of the Fritz-Haber Institute for their help, support, and discussions. MA thanks M. Friedrich for performing quantum chemical calculations and the Helmholtz Zentrum Berlin for providing BESSY beamtime 2009_1_80693

and continuing support during the XPS measurements. Networking within COST Action CM0904 "Network for Intermetallic Compounds as Catalysts in the Steam Reforming of Methanol" nurtured this publication.

References

1. Sato M (1998) R&D activities in Japan on methanol synthesis from CO_2 and H_2. Catal Surv Jpn 2:175–184
2. Olah GA, Goeppert A, Surya Prakash GK (2006) Beyond oil and gas: the methanol economy. Wiley-VCH, Weinheim
3. Schlögl R (2010) The role of chemistry in the energy challenge. ChemSusChem 3:209–222
4. Christiansen JA (1921) A reaction between methyl alcohol and water and some related reactions. J Am Chem Soc 43:1670–1672
5. Prigent M (1997) On board hydrogen generation for fuel cell powered electric cars—a review of various available techniques. Rev Inst Fr Pét 52:349–359
6. Navarro RM, Peña MA, Fierro JLG (2007) Hydrogen production reactions from carbon feedstocks: fossils fuels and biomass. Chem Rev 107:3952–3991
7. Sá S, Silva H, Brandão L, Sousa JM, Mendes A (2010) Catalysts for methanol steam reforming—a review. Appl Catal B 99:43–57
8. De Wild PJ, Verhaak MJFM (2000) Catalytic production of hydrogen from methanol. Catal Today 60:3–10
9. Joensen F, Rostrup-Nielsen JR (2002) Conversion of hydrocarbons and alcohols for fuel cells. J Power Sources 105:195–201
10. Cheekatamarla PK, Finnerty CM (2006) Reforming catalysts for hydrogen generation in fuel cell applications. J Power Sources 160:490–499
11. Palo DR, Dagle RA, Holladay JD (2007) Methanol steam reforming for hydrogen production. Chem Rev 107:3992–4021
12. Velu S, Suzuki K, Osaki T (1999) Oxidative steam reforming of methanol over CuZnAl(Zr)-oxide catalysts; a new and efficient method for the production of CO-free hydrogen for fuel cells. Chem Commun 2341–2342
13. Lattner JR, Harold MP (2007) Autothermal reforming of methanol: experiments and modeling. Catal Today 130:78–89
14. Park ED, Lee D, Lee HC (2009) Recent progress in selective CO removal in a H_2-rich stream. Catal Today 139:280–290
15. Agrell J, Birgersson H, Boutonnet M, Melián-Cabrera I, Navarro RM, Fierro JLG (2003) Production of hydrogen from methanol over Cu/ZnO catalysts promoted by ZrO_2 and Al_2O_3. J Catal 219:389–403
16. Turco M, Bagnasco G, Costantino U, Marmottini F, Montanari T, Ramis G, Busca G (2004) Production of hydrogen from oxidative steam reforming of methanol—II. catalytic activity and reaction mechanism on $Cu/ZnO/Al_2O_3$ hydrotalcite-derived catalysts. J Catal 228:56–65
17. Kurr P, Kasatkin I, Girgsdies F, Trunschke A, Schlögl R, Ressler T (2008) Microstructural characterization of $Cu/ZnO/Al_2O_3$ catalysts for methanol steam reforming—a comparative study. Appl Catal A 348:153–164
18. Velu S, Suzuki K (2003) Selective production of hydrogen for fuel cells via oxidative steam reforming of methanol over CuZnAl oxide catalysts: effect of substitution of zirconium and cerium on the catalytic performance. Top Catal 22:235–244
19. Purnama H, Girgsdies F, Ressler T, Schattka JH, Caruso RA, Schomäcker R, Schlögl R (2004) Activity and selectivity of a nanostructured CuO/ZrO_2 catalyst in the steam reforming of methanol. Catal Lett 94:61–68

20. Ritzkopf I, Vukojevic S, Weidenthaler C, Grunwaldt JD, Schüth F (2006) Decreased CO production in methanol steam reforming over Cu/ZrO_2 catalysts prepared by the microemulsion technique. Appl Catal A 302:215–223
21. Liu Y, Hayakawa T, Suzuki K, Hamakawa S, Tsunody T, Ishii T, Kumagai M (2002) Highly active copper/ceria catalysts for steam reforming of methanol. Appl Catal A 223:137–145
22. Tsai AP, Yoshimura M (2001) Highly active quasicrystalline Al-Cu-Fe catalyst for steam reforming of methanol. Appl Catal A 214:237–241
23. Ma L, Gong B, Tran T, Wainwright MS (2000) Cr_2O_3 promoted skeletal Cu catalysts for the reactions of methanol steam reforming and water gas shift. Catal Today 63:499–505
24. Jang JH, Xu Y, Chun DH, Demura M, Wee DM, Hirano T (2009) Effects of steam addition on the spontaneous activation in Ni_3Al Foil catalysts during methanol decomposition. J Mol Catal A 307:21–28
25. Takahashi T, Inoue M, Kai T (2001) Effect of metal composition on hydrogen selectivity in steam reforming of methanol over catalysts prepared from amorphous alloys. Appl Catal A 218:189–195
26. Iwasa N, Nomura W, Mayanagi T, Fujita SI, Arai M, Takezawa N (2004) Hydrogen production by steam reforming of methanol. J Chem Eng Jpn 37:286–293
27. Iwasa N, Masuda S, Takezawa N (1995) Steam reforming of methanol over Ni, Co, Pd and Pt supported on ZnO. React Kinet Catal Lett 55:349–353
28. Iwasa N, Mayanagi T, Ogawa N, Sakata K, Takezawa N (1998) New catalytic functions of Pd-Zn, Pd-Ga, Pd-In, Pt-Zn, Pt-Ga and Pt-In alloys in the conversion of methanol. Catal Lett 54:119–123
29. Xia G, Holladay JD, Dagle RA, Jones EO, Wang Y (2005) Development of highly active Pd-ZnO/Al_2O_3 catalysts for microscale fuel processor applications. Chem Eng Technol 28:515–519
30. Tsai AP, Kameoka S, Ishii Y (2004) PdZn=Cu: can an intermetallic compound replace an element? J Phys Soc Jpn 73:3270–3273
31. Jiang CJ, Trimm DL, Wainwright MS, Cant NW (1993) Kinetic mechanism for the reaction between methanol and water over A Cu-ZnO-Al_2O_3 catalyst. Appl Catal A 97:145–158
32. Takezawa N, Iwasa N (1997) Steam reforming and dehydrogenation of methanol: difference in the catalytic functions of copper and group VIII metals. Catal Today 36:45–56
33. Peppley BA, Amphlett JC, Kearns LM, Mann RF (1999) Methanol-steam reforming on $Cu/ZnO/Al_2O_3$ catalysts. Part 2. A comprehensive kinetic model. Appl Catal A 179:31–49
34. Rozovskii AY, Lin GI (2003) Fundamentals of methanol synthesis and decomposition. Top Catal 22:137–150
35. Lee JK, Ko JB, Kim DH (2004) Methanol steam reforming over $Cu/ZnO/Al_2O_3$ catalyst: kinetics and effectiveness factor. Appl Catal A 278:25–35
36. Peppley BA, Amphlett JC, Kearns LM, Mann RF (2005) Methanol steam reforming on $Cu/ZnO/Al_2O_3$. Part 1: the reaction network. Appl Catal A 179:21–29
37. Frank B, Jentoft FC, Soerijanto H, Kröhnert J, Schlögl R, Schomäcker R (2007) Steam reforming of methanol over copper-containing catalysts: influence of support material on microkinetics. J Catal 246:177–192
38. Kasatkin I, Kurr P, Kniep B, Trunschke A, Schlögl R (2007) Role of lattice strain and defects in copper particles on the activity of $Cu/ZnO/Al_2O_3$ catalysts for methanol synthesis. Angew Chem 119:7465–7468
39. Chinchen GC, Hay CM, Vanderwell HD, Waugh KC (1987) The measurement of copper surface areas by reactive frontal chromatography. J Catal 103:79–86
40. Hinrichsen O, Genger T, Muhler M (2000) Chemisorption of N_2O and H_2 for the surface determination of copper catalysts. Chem Eng Technol 11:956–959
41. Naumann d'Alnoncourt R, Graf B, Xia X, Muhler M (2008) The back-titration of chemisorbed atomic oxygen on copper by carbon monoxide investigated by microcalorimetry and transient kinetics. J Therm Anal Calor 91:173–179

42. Behrens M, Furche A, Kasatkin I, Trunschke A, Busser W, Muhler M, Kniep B, Fischer R, Schlögl R (2010) The potential of microstructural optimization in metal/oxide catalysts: higher intrinsic activity of copper by partial embedding of copper nanoparticles. ChemCatChem 2:816–818
43. Spencer MS (1999) The role of zinc oxide in Cu ZnO catalysts for methanol synthesis and the water-gas shift reaction. Top Catal 8:259–266
44. Hansen JB, Højlund Nielsen PE (2008) Methanol synthesis. In: Ertl G, Knözinger H, Schüth F, Weitkamp J (eds) Handbook of heterogenous catalysis, 2nd edn. Wiley-VCH, Weinheim, pp 2920–2949
45. Naumann d'Alnoncourt R, Xia X, Strunk J, Löffler E, Hinrichsen O, Muhler M (2006) The influence of strongly reducing conditions on strong metal-support interactions in Cu/ZnO catalysts used for methanol synthesis. Phys Chem Chem Phys 13:1525–1538
46. Grunwaldt JD, Molenbroek AM, Topsoe NY, Topsoe H, Clausen BS (2000) In situ investigations of structural changes in Cu/ZnO catalysts. J Catal 194:452–460
47. Hansen PL, Wagner JB, Helveg S, Rostrup-Nielsen JR, Clausen BS, Topsoe H (2002) Atom-resolved imaging of dynamic shape changes in supported copper nanocrystals. Science 295:2053–2055
48. Spencer MS (1995) On the activation energies of the forward and reverse water-gas shift reaction. Catal Lett 32:9–13
49. Twigg MV, Spencer MS (2003) Deactivation of copper metal catalysts for methanol decomposition, methanol steam reforming and methanol synthesis. Top Catal 22:191–203
50. Hughes R (1994) Deactivation of catalysts. Academic, New York
51. Kasatkin I et al., unpublished
52. Löffler DG, McDermott SD, Renn CN (2003) Activity and durability of water-gas shift catalysts used for the steam reforming of methanol. J Power Sources 114:15–20
53. Thurgood CP, Amphlett JC, Mann RF, Peppley BA (2003) Deactivation of $Cu/ZnO/Al_2O_3$ catalyst: evolution of site concentrations with time. Top Catal 22:253–259
54. Agarwal V, Patel S, Pant KK (2005) H_2 production by steam reforming of methanol over $Cu/ZnO/Al_2O_3$ catalysts: transient deactivation kinetics modeling. Appl Catal A 279:155–164
55. Agrell J, Birgersson H, Boutonnet M (2002) Steam reforming of methanol over a $Cu/ZnO/Al_2O_3$ catalyst: a kinetic analysis and strategies for suppression of CO formation. J Power Sources 106:249–257
56. Schimpf S, Muhler M (2009) Methanol catalysts. In: de Jong K (ed) Synthesis of solid catalysts. Wiley-VCH, Weinheim, pp 329–351
57. Bems B, Schur M, Dassenoy A, Junkes H, Herein D, Schlögl R (2003) Relations between synthesis and microstructural properties of copper/zinc hydroxycarbonates. Chemistry 9:2039–2052
58. Baltes C, Vukojevic S, Schüth F (2008) Correlations between synthesis, precursor, and catalyst structure and activity of a large set of $CuO/ZnO/Al_2O_3$ catalysts for methanol synthesis. J Catal 258:334–344
59. Shen GC, Fujita SI, Takezawa N (1992) Preparation of precursors for the Cu/ZnO methanol synthesis catalysis by coprecipitation methods—effects of The preparation conditions upon the structures of the precursors. J Catal 138:754–758
60. Günter MM, Ressler T, Bems B, Büscher C, Genger T, Hinrichsen O, Muhler M, Schlögl R (2001) Implication of the microstructure of binary Cu/ZnO catalysts for their catalytic activity in methanol synthesis. Catal Lett 71:37–44
61. Waller D, Stirling D, Stone FS, Spencer MS (1989) Copper–Zinc oxide catalysts. Activity in relation to precursor structure and morphology. Faraday Dissuss Chem Soc 87:107–120
62. Li JL, Inui T (1996) Characterization of precursors of methanol synthesis catalysts, copper/zinc/aluminum oxides, precipitated at different pHs and temperatures. Appl Catal A Gen 137:105–117
63. Whittle DM, Mirzaei AA, Hargreaves JSJ, Joyner RW, Kiely CJ, Taylor SH, Hutchings GJ (2002) Co-precipitated copper zinc oxide catalysts for ambient temperature carbon monoxide

oxidation: effect of precipitate ageing on catalyst activity. Phys Chem Chem Phys 4:5915–5920
64. Kniep BL, Ressler T, Rabis A, Girgsdies F, Baenitz M, Steglich F, Schlögl R (2003) Ratioal design of nanostructured copper-zinc oxide catalysts for the steam reforming of methanol. Angew Chem Int Ed Engl 43:112–115
65. Behrens M, Brennecke D, Girgsdies F, Kißner S, Trunschke A, Nasrudin N, Zakaria S, Fadilah Idris N, Bee Abd Hamid S, Kniep B, Fischer R, Busser W, Muhler M, Schlögl R (2011) Understanding the complexity of a catalyst synthesis: co-precipitation of mixed Cu, Zn, Al hydroxycarbonate precursors for $Cu/ZnO/Al_2O_3$ catalysts investigated by titration experiments. Appl Catal A 392:93–102
66. Behrens M (2009) Meso- and nano-structuring of industrial $Cu/ZnO/(Al_2O_3)$ catalysts. J Catal 267:24–29
67. Schüth F, Hesse M, Unger KK (2008) Precipitation and coprecipitation. In: Ertl G, Knözinger H, Schüth F, Weitkamp J (eds) Handbook of heterogeneous catalysis, 2nd edn. Wiley-VCH, Weinheim, pp 100–119
68. Lok M (2009) Coprecipitation. In: de Jong K (ed) Synthesis of solid catalysts. Wiley-VCH, Weinheim, pp 135–151
69. Kniep BL, Girgsdies F, Ressler T (2005) Effect of precipitate aging on the microstructural characteristics of Cu/ZnO catalysts for methanol steam reforming. J Catal 236:34–44
70. Millar GJ, Holm IH, Uwins PJR, Drennan J (1998) Characterization of precursors to methanol synthesis catalysts Cu/ZnO system. J Chem Soc Faraday Trans 94:593–600
71. Behrens M, Girgsdies F, Trunschke A, Schlögl R (2009) Minerals as model compounds for Cu/ZnO catalyst precursors: structural and thermal properties and IR spectra of mineral and synthetic (Zincian) malachite, rosasite and aurichalcite and a catalyst precursor mixture. Eur J Inorg Chem 10:1347–1357
72. Fujita S, Satriyo AM, Shen GC, Takezawa N (1995) Mechanism of the formation of precursors for the Cu/ZnO methanol synthesis catalysts by a coprecipitation method. Catal Lett 34:85–92
73. Behrens M, Girgsdies F (2010) Structural effects of Cu/Zn substitution in the malachite-rosasite system. Z Anorg Allg Chem 636:919–927
74. Shen GC, Fujita S, Matsumoto S, Takezawa N (1997) Steam reforming of methanol on binary Cu/ZnO catalysts: effects of preparation condition upon precursors, surface structure and catalytic activity. J Mol Catal A 124:123–136
75. Shishido T, Yamamoto Y, Morioka H, Takaki K, Takehira K (2004) Active Cu/ZnO and $Cu/ZnO/Al_2O_3$ catalysts prepared by homogeneous precipitation method in steam reforming of methanol. Appl Catal A 263:249–253
76. Shishido T, Yamamoto Y, Morioka H, Takehira K (2007) Production of hydrogen from methanol over Cu/ZnO and $Cu/ZnO/Al_2O_3$ catalysts prepared by homogeneous precipitation: steam reforming and oxidative steam reforming. J Mol Catal A 268:185–194
77. Zhang XR, Wang LC, Yao CZ, Cao Y, Dai WL, He HY, Fan KN (2005) A highly efficient $Cu/ZnO/Al_2O_3$ catalyst via gel-coprecipitation of oxalate precursors for low-temperature steam reforming of methanol. Catal Lett 102:183–190
78. Wang LC, Liu YM, Chen M, Cao Y, He HY, Wu GS, Dai WL, Fan KN (2007) Production of hydrogen by steam reforming of methanol over Cu/ZnO catalysts prepared via a practical soft reactive grinding route based on dry oxalate-precursor synthesis. J Catal 246:193–204
79. Becker M, Naumann d'Alnoncourt R, Kähler K, Sekulic J, Fischer RA, Muhler M (2010) The synthesis of highly loaded Cu/Al_2O_3 and $Cu/ZnO/Al_2O_3$ catalysts by the two-step CVD of Cu (II)diethylamino-2-propoxide in a fluidized-bed reactor. Chem Vap Deposition 16:85
80. Kurtz M, Bauer N, Büscher C, Wilmer H, Hinrichsen O, Becker R, Rabe S, Merz K, Driess M, Fischer RA, Muhler M (2004) New synthetic routes to more active Cu/ZnO catalysts used for methanol synthesis. Catal Lett 92:49–52

81. Omata K, Hashimoto M, Wanatabe Y, Umegaki T, Wagatsuma S, Ishiguro G, Yamada M (2004) Optimization of Cu oxide catalyst for methanol synthesis under high CO_2 partial pressure using combinatorial tools. Appl Catal A 262:207–214
82. Breen JP, Ross JRH (1999) Methanol reforming for fuel-cell applications: development of zirconia-containing Cu-Zn-Al catalysts. Catal Today 51:521–533
83. Matsumura Y, Ishibe H (2009) Suppression of CO by-production in steam reforming of methanol by addition of zinc oxide to silica-supported copper catalyst. J Catal 268:282–289
84. Yang HM, Liao PH (2007) Preparation and activity of Cu/ZnO-CNTs nano-catalyst on steam reforming of methanol. Appl Catal A 317:226–233
85. Kudo S, Maki T, Miura K, Mae K (2010) High porous carbon with Cu/ZnO nanoparticles made by the pyrolysis of carbon material as a catalyst for steam reforming of methanol and dimethyl ether. Carbon 48:1186–1195
86. Cavani F, Trifirò F, Vaccari A (1991) Hydrotalcite-type anionic clays: preparation, properties and applications. Catal Today 11:173–301
87. Takehira K, Shishido T (2007) Preparation of supported metal catalysts starting from hydrotalcites as the precursors and their improvements by adopting "memory effect". Catal Surv Asia 11:1–30
88. Tang Y, Liu Y, Zhu P, Xue Q, Chen L, Lu Y (2009) High-performance HTLcs-derived CuZnAl catalysts for hydrogen production via methanol steam reforming. Am Inst Chem Eng J 55:1217–1228
89. Busca G, Constatino U, Marmottini F, Montanari T, Patrono P, Pinari F, Ramis G (2006) Methanol steam reforming over ex-hydrotalcite Cu–Zn–Al catalysts. Appl Catal A 310:70–78
90. Behrens M, Kasatkin I, Kühl S, Weinberg G (2010) Phase-pure Cu, Zn, Al hydrotalcite-like materials as precursors for copper rich $Cu/ZnO/Al_2O_3$ catalysts. Chem Mater 22:386–397
91. Kühl S, Friedrich M, Armbrüster M, Behrens M, unpublished
92. Turco M, Bagnasco G, Costantino U, Marmottini F, Montanari T, Ramis G, Busca G (2004) Production of hydrogen from oxidative steam reforming of methanol - I. preparation and characterization of $Cu/ZnO/Al_2O_3$ catalysts from a hydrotalcite-like LDH precursor. J Catal 228:43–55
93. Turco M, Bagnasco G, Cammarano C, Senese P, Costantino U, Sisani M (2007) $Cu/ZnO/Al_2O_3$ catalysts for oxidative steam reforming of methanol: the role of Cu and the dispersing oxide matrix. Appl Catal B 77:46–57
94. Velu S, Suzuki K, Okazaki M, Kapoor MP, Osaki T, Ohashi F (2000) Oxidative steam reforming of methanol over CuZnAl(Zr)-oxide catalysts for the selective production of hydrogen for fuel cells: catalyst characterization and performance evaluation. J Catal 194:373–384
95. Velu S, Suzuki K, Kapoor MP, Ohashi F, Osaki T (2001) Selective production of hydrogen for fuel cells via oxidative steam reforming of methanol over CuZnAl(Zr)-oxide catalysts. Appl Catal A 213:47–63
96. Velu S, Suzuki K, Gopinath CS, Yoshida H, Hattori T (2002) XPS, XANES and EXAFS investigations of $CuO/ZnO/Al_2O_3/ZrO_2$ mixed oxide catalysts. Phys Chem Chem Phys 4:1990–1999
97. Matsumura Y, Ishibe H (2009) High temperature steam reforming of methanol over $Cu/ZnO/ZrO_2$ catalysts. Appl Catal B 91:524–532
98. Jones SD, Hagelin-Weaver HE (2009) Steam reforming of methanol over CeO_2- and ZrO_2-promoted Cu-ZnO catalysts supported on nanoparticle Al_2O_3. Appl Catal B 90:195–204
99. Idem RO, Bakhshi NN (1996) Characterization studies of calcined, promoted and non-promoted methanol-steam reforming catalysts. Can J Chem Eng 74:288–300
100. Lindström B, Pettersson LJ (2001) Hydrogen generation by steam reforming of methanol over copper-based catalysts for fuel cell applications. Int J Hydrogen Energy 26:923–933

101. Lindström B, Pettersson LJ, Menon PG (2002) Activity and characterization of Cu/Zn, Cu/Cr and Cu/Zr on gamma-alumina for methanol reforming for fuel cell vehicles. Appl Catal 234:111–125
102. Matsumura Y, Ishibe H (2009) Selective steam reforming of methanol over silica-supported copper catalyst prepared by sol-gel method. Appl Catal B 86:114–120
103. Kobayashi H, Takezawa N, Shimokawabe M, Takahashi K (1983) Preparation Of copper supported on metal oxides and methanol steam reforming reaction. Stud Surf Sci Catal 16:697–707
104. Takezawa N, Shimokawabe M, Hiramatsu H, Sugiura H, Asakawa T, Kobayashi H (1987) Steam reforming of methanol over Cu/ZrO_2—role of ZrO_2 support. React Kinet Catal Lett 33:191–196
105. Szizybalski A, Girgsdies F, Rabis A, Wang Y, Niederberger M, Ressler T (2005) In situ investigations of structure-activity relationships of a Cu/ZrO_2 catalyst for the steam reforming of methanol. J Catal 233:297–307
106. Oguchi H, Kanai H, Utani K, Matsumura Y, Imamura S (2005) Cu_2O as active species in the steam reforming of methanol by CuO/ZrO_2 catalysts. Appl Catal A 293:64–70
107. Yao C, Wang L, Liu Y, Wu G, Cao Y, Dai W, He H, Fan K (2006) Effect of preparation method on the hydrogen production from methanol steam reforming over binary Cu/ZrO_2 catalysts. Appl Catal A 297:151–158
108. Wang LC, Liu Q, Chen M, Liu YM, Cao Y, He HY, Fan KN (2007) Structural evolution and catalytic properties of nanostructured Cu/ZrO_2 catalysts prepared by oxalate gel-coprecipitation technique. J Phys Chem C 111:16549–16557
109. Wu GS, Mao DS, Lu GZ, Cao Y, Fan KN (2009) The role of the promoters in Cu based catalysts for methanol steam reforming. Catal Lett 130:177–184
110. Liu Y, Hayakawa T, Suzuki K, Hamakawa S (2001) Production of hydrogen by steam reforming of methanol over Cu/CeO_2 catalysts derived from $Ce_{1-x}Cu_xO_{2-x}$ precursors. Catal Comm 2:195–200
111. Liu Y, Hayakawa T, Tsunoda T, Suzuki K, Hamakawa S, Murato K, Shiozaki R, Ishii T, Kumagai M (2003) Steam reforming of methanol over Cu/CeO_2 catalysts studied in comparison with Cu/ZnO and Cu/Zn(Al)O catalysts. Top Catal 22:205–213
112. Mastalir A, Frank B, Szizybalski A, Soerijanto H, Deshpande A, Niederberger M, Schomäker R, Schlögl R, Ressler T (2005) Steam reforming of methanol over $Cu/ZrO_2/CeO_2$ catalysts: a kinetic study. J Catal 230:464–475
113. Oguchi H, Nishiguchi T, Matsumoto T, Kanai H, Utani K, Matsumura Y, Imamura S (2005) Steam reforming of methanol over $Cu/CeO_2/ZrO_2$ catalysts. Appl Catal A 281:69–73
114. Huang TJ, Chen HM (2010) Hydrogen production via steam reforming of methanol over $Cu/(Ce, Gd)O_{2-x}$ catalysts. Int J Hydrogen Energy 35:6218–6226
115. Bhagwat M, Ramaswamy AV, Tyagi AK, Ramaswamy V (2003) Rietveld refinement study of nanocrystalline copper doped zirconia. Mater Res Bull 38:1713–1724
116. Fierro G, Lo Jacono M, Inversi M, Porta P, Cioci F, Lavecchia R (1996) Study of the reducibility of copper in CuO–-ZnO catalysts by temperature-programmed reduction. Appl Catal A 137:327–348
117. Noei H, Qiu H, Wang Y, Löffler E, Wöll C, Muhler M (2008) The identification of hydroxyl groups on ZnO nanoparticles by infrared spectroscopy. Phys Chem Chem Phys 10:7092–7097
118. Günther MM, Ressler T, Jentoft RE, Bems B (2001) Redox behavior of copper oxide/zinc oxide catalysts in the steam reforming of methanol studied by *in situ* X-Ray diffraction and absorption spectroscopy. J Catal 203:133–149
119. Goddby BE, Pemberton JE (1988) XPS characterization of a commercial $Cu/ZnO/Al_2O_3$ catalyst: effects of oxidation, reduction, and the steam reformation of methanol. Appl Spectrosc 42:754–760

120. Raimondi F, Geissler K, Wambach J, Wokaun A (2002) Hydrogen production by methanol reforming: post-reaction characterisation of a $Cu/ZnO/Al_2O_3$ catalyst by XPS and TPD. Appl Surf Sci 189:59–71
121. Raimondi F, Schnyder B, Kötz R, Schelldorfer R, Jung T, Wambach J, Wokaun A (2003) Structural changes of model Cu/ZnO catalysts during exposure to methanol reforming conditions. Surf Sci 532–535:383–389
122. Reitz TL, Lee PL, Czaplewski KF, Lang JC, Popp KE, Kung HH (2001) Time-resolved XANES investigation of CuO/ZnO in the oxidative methanol reforming reaction. J Catal 199:193–201
123. Knop-Gericke A, Hävecker M, Schedel-Niedrig T, Schlögl R (2001) Characterisation of active phases of a copper catalyst for methanol oxidation under reaction conditions: an in situ X-ray absorption spectroscopy study in the soft energy range. Top Catal 15:27–34
124. Klier K (1982) Methanol synthesis. Adv Catal 31:243–313
125. Costantino U, Marmottini F, Sisani M, Montanari T, Ramis G, Busca G, Turco M, Bagnsco G (2005) Cu-Zn-Al hydrotalcites as precursors of catalysts for the production of hydrogen from methanol. Solid State Ionics 176:2917–2922
126. Larrubia Vargas MA, Busca G, Costantino U, Marmottini F, Montatnari T, Patrono P, Pinzari F, Ramis G (2007) An IR study of methanol steam reforming over ex-hydrotalcite Cu–Zn–Al catalysts. J Mol Catal A 266:188–197
127. Busca G, Montanari T, Resini C, Ramis G, Costantino U (2009) Hydrogen from alcohols: IR and flow reactor studies. Catal Today 143:2–8
128. Sakong S, Groß A (2003) Dissociative adsorption of hydrogen on strained Cu surfaces. Surf Sci 525:107–118
129. Girgsdies F, Ressler T, Wild U, Wübben T, Balk TJ, Dehm G, Zhou L, Günther S, Arzt E, Imbihl R, Schlögl R (2005) Strained thin copper films as model catalysts in the materials gap. Catal Lett 102:91–97
130. Hammer B, Nørskov JK (1995) Electronic factors determining the reactivity of metal surfaces. Surf Sci 343:211–220
131. Frost JC (1988) Junction effect interactions in methanol synthesis catalysts. Nature 334:577–580
132. Zhang XR, Wang LC, Cao Y, Dai WL, He HY, Fan KN (2005) A unique microwave effect on the microstructural modification of $Cu/ZnO/Al_2O_3$ catalysts for steam reforming of methanol. Chem Commun 4104–4106
133. Holladay JD, Wang Y, Jones E (2004) Review of developments in portable hydrogen production using microreactor technology. Chem Rev 104:4767–4790
134. Kovnir K, Armbrüster M, Teschner D, Venkov TV, Jentoft FC, Knop-Gericke A, Grin Yu, Schlögl R (2007) A new approach to well-defined, stable and site-isolated catalysts. Sci Tech Adv Mater 8:420–427
135. Kohlmann H (2002) Metal hydrides. In: Meyers RA (ed) Encyclopedia of physical science and technology, vol 9, 3rd edn. Academic, New York, pp 441–458
136. Friedrich M, Ormeci A, Grin Yu, Armbrüster M (2010) PdZn or ZnPd: charge transfer and Pd–Pd bonding as the driving force for the tetragonal distortion of the cubic crystal structure. Z Anorg Allg Chem 636:1735–1739
137. Armbrüster M, Schnelle W, Schwarz U, Grin Yu (2007) Chemical bonding in $TiSb_2$ and VSb_2: a quantum chemical and experimental study. Inorg Chem 46:6319–6328
138. Armbrüster M, Schnelle W, Cardoso-Gil R, Grin Yu (2010) Chemical bonding in the isostructural compounds $MnSn_2$, $FeSn_2$ and $CoSn_2$. Chem Eur J 16:10357–10365
139. Grin Yu, Wagner FR, Armbrüster M, Kohout M, Leithe-Jasper A, Schwarz U, Wedig U, von Schnering HG (2006) $CuAl_2$ revisisted: composition, crystal structure, chemical bonding compressibility and Raman spectroscopy. J Solid State Chem 179:1707–1719
140. Macchioni C, Rayne JA, Sen S, Bauer CL (1981) Low temperature resistivity of thin film and bulk samples of $CuAl_2$ and Cu_9Al_4. Thin Solid Films 81:71–78

141. Iwasa N, Masuda S, Ogawa N, Takezawa N (1995) Steam reforming of methanol over Pd/ZnO: effects of the formation of PdZn alloys upon the reaction. Appl Catal A 125:145–157
142. Miyao K, Onodera H, Takezawa N (1994) Highly active copper catalysts for steam reforming of methanol Catalysts Derived from Cu/Zn/Al Alloys. React Kinet Catal Lett 53:379–383
143. Kameoka S, Tanabe T, Tsai AP (2004) Al-Cu-Fe quasicrystals for steam reforming of methanol: a new form of copper catalyst. Catal Today 93–95:23–26
144. Tanabe T, Kameoka S, Tsai AP (2006) A novel catalyst fabricated from Al-Cu-Fe quasicrystal for steam reforming of methanol. Catal Today 111:153–157
145. Yoshimura M, Tsai AP (2002) Quasicrystal application on catalyst. J Alloy Comp 342:451–454
146. Wallace WE, Elattar A, Imamura H, Craig RS, Moldovan AG (1980) Intermetallic compounds: surface chemistry, hydrogen absorption and heterogeneous catalysis. In: Wallace WE, Rao ECS (eds) Science and technology of rare earth materials. Academic, New York, pp 329–351
147. Nix RM, Rayment T, Lambert RM, Jennings JR, Owen G (1987) An *in situ* X-Ray diffraction study of the activation and performance of methanol synthesis catalysts derived from rare-earth-copper alloys. J Catal 106:216–234
148. Takahashi T, Kawabata M, Kai T, Kimura H, Inoue A (2006) Preparation of highly active methanol steam reforming catalysts from glassy Cu-Zr Alloys with small amount of noble metals. Mater Trans 47:2081–2085
149. Bernal S, Calvino JJ, Cauqui MA, Gatica JM, Cartes CL, Omil JAP, Pintado JM (2003) Some contributions of electron microscopy to the characterisation of the strong metal-support interaction effect. Catal Today 77:385–406
150. Tauster SJ, Fung SC, Garten RL (1978) Strong metal-support interactions. Group 8 noble metals supported on TiO_2. J Am Chem Soc 100:170–175
151. Knözinger H, Taglauer E (2008) Spreading and wetting. In: Ertl G, Knözinger H, Schüth F, Weitkamp J (eds) Handbook of heterogeneous catalysis, 2nd edn. Wiley-VCH, Weinheim, pp 555–571
152. Simoens AJ, Baker RTK, Dwyer DJ, Lund CRF, Madon RJ (1984) A study of the nickel-titanium oxide interaction. J Catal 86:359–372
153. Centi G (2003) Metal-support interactions. In: Cornils B, Herrmann WA, Schlögl R, Wong CH (eds) Catalysis from A to Z, 2nd edn. Wiley-VCH, Weinheim, pp 490–491
154. Tauster SJ (1987) Strong metal-support interactions. Acc Chem Res 20:389–394
155. Penner S, Wang D, Su DS, Rupprechter G, Podloucky R, Schlögl R, Hayek K (2003) Platinum nanocrystals supported by silica, ceria and alumina: metal-support interactions due to high-temperature reduction in hydrogen. Surf Sci 532–535:276
156. Penner S, Wang D, Podloucky R, Schlögl R, Hayek K (2004) Rh and Pt nanoparticles supported by CeO_2: metal-support interaction upon high-temperature reduction observed by electron microscopy. Phys Chem Chem Phys 6:5244
157. Iwasa N, Kudo S, Takahashi H, Masuda S, Takezawa N (1993) Highly selective supported Pd catalysts for steam reforming of methanol. Catal Lett 19:211–216
158. Wang Y, Zhang J, Xu H (2006) Interaction between Pd and ZnO during reduction of Pd/ZnO catalyst for steam reforming of methanol to hydrogen. Chin J Catal 27:217–222
159. Wang Y, Zhang J, Xu H, Bai X (2007) Reduction of Pd/ZnO catalyst and its catalytic activity for steam reforming of methanol. Chin J Catal 28:234–238
160. Penner S, Jenewein B, Gabasch H, Klötzer B, Wang D, Knop-Gericke A, Schlögl R, Hayek K (2006) Growth and structural stability of well-ordered PdZn alloy nanoparticles. J Catal 241:14–19
161. Clark JB, Hastie JW, Kihlborg LHE, Metselaar R, Thackeray MM (1994) Definitions of terms relating to phase transitions of the solid state. Pure Appl Chem 66:577–594
162. Dagle RA, Chin YH, Wang Y (2007) The effects of PdZn crystallite size on methanol steam reforming. Top Catal 46:358–362

163. Karim A, Conant T, Datye A (2006) The Role of PdZn alloy formation and particle size on the selectivity for steam reforming of methanol. J Catal 243:420–427
164. Lebarbier V, Dagle R, Datye A, Wang Y (2010) The effect of PdZn particle size on reverse-water-gas-shift reaction. Appl Catal A 379:3–6
165. Bollmann L, Ratts JL, Joshi AM, Williams WD, Pazmino J, Joshi YV, Miller JT, Kropf AJ, Delgass WN, Ribeiro FH (2008) Effect of Zn addition on the water-gas shift reaction over supported palladium catalysts. J Catal 257:43–54
166. Suwa Y, Ito SI, Kameoka S, Tomishige K, Kunimori K (2004) Comparative study between Zn-Pd/C and Pd/ZnO Catalysts for steam reforming of methanol. Appl Catal A 267:9–16
167. Liu S, Takahashi K, Eguchi H, Uematsu K (2007) Hydrogen production by oxidative methanol reforming on Pd/ZnO: catalyst preparation and supporting materials. Catal Today 129:287–292
168. Liu S, Takahashi K, Uematsu K, Ayabe M (2005) Hydrogen production by oxidative methanol reforming on Pd/ZnO. Appl Catal A 283:125–135
169. Liu S, Takahashi K, Ayabe M (2003) Hydrogen production by oxidative methanol reforming on Pd/ZnO catalyst: effect of Pd loading. Catal Today 87:247–253
170. Liu S, Takajashi K, Fuchigami K, Uematsu K (2006) Hydrogen production by oxidative methanol reforming on Pd/ZnO: catalyst deactivation. Appl Catal A 299:58–65
171. Liu S, Takahashi K, Uematsu K, Ayabe M (2004) Hydrogen production by oxidative methanol reforming on Pd/ZnO catalyst: effects of the addition of a third metal component. Appl Catal A 277:265–270
172. Lenarda M, Storaro L, Frattini R, Casagrande M, Marchiori M, Capannelli G, Uliana C, Ferrari F, Ganzerla R (2007) Oxidative methanol steam reforming (OSRM) on a PdZnAl hydrotalcite derived catalyst. Catal Comm 8:467–470
173. Cubeiro ML, Fierro JLG (1998) Partial oxidation of methanol over supported palladium catalysts. Appl Catal A 168:307–322
174. Cubeiro ML, Fierro JLG (1998) Selective production of hydrogen by partial oxidation of methanol over ZnO-Supported palladium catalysts. J Catal 179:150–162
175. Agrell J, Germani G, Järås SG, Boutonnet M (2003) Production of hydrogen by partial oxidation of methanol over ZnO-supported palladium catalysts prepared by microemulsion technique. Appl Catal A 242:233–245
176. Eastman JA, Thompson LJ, Kestel BJ (1993) Narrowing the palladium-hydrogen miscibility gap in nanocrystalline palladium. Phys Rev B 48:84–92
177. Yamauchi M, Ikeda R, Kitagawa H, Takata M (2008) Nanosize effects on hydrogen storage in palladium. J Phys Chem C 112:3294–3299
178. Tew MW, Miller JT, van Bokhoven JA (2009) Particle size effect of hydride formation and surface hydrogen adsorption of nanosized palladium catalysts: L3 Edge vs K Edge X-Ray absorption spectroscopy. J Phys Chem C 113:15140–15147
179. Ito SI, Suwa Y, Kondo S, Kamoeka S, Timishige T, Kunimori K (2003) Steam reforming of methanol over Pt-Zn alloy catalyst supported on carbon black. Catal Comm 4:499–503
180. Iwasa N, Takezawa N (2003) New Supported Pd and Pt Alloy catalysts for steam reforming and dehydrogenation of methanol. Top Catal 22:215–224
181. Lim KH, Chen ZX, Neyman KM, Rösch N (2006) Comparative theoretical study of formaldehyde decomposition on PdZn, Cu, and Pd surfaces. J Phys Chem B 110:14890–14897
182. Lorenz H, Zhao Q, Turner S, Lebedev BL, Van Tendeloo G, Klötzer B, Rameshan C, Pfaller K, Konzett J, Penner S (2010) Origin of different deactivation of Pd/SnO_2 and Pd/GeO_2 catalysts in methanol dehydrogenation and reforming: a comparative study. Appl Catal A 381:242–252
183. Penner S, Lorenz H, Jochum W, Stöger-Pollach M, Wang D, Rameshan C, Klötzer B (2009) Pd/Ga_2O_3 methanol steam reforming catalysts: part I. Morphology, composition and structural aspects. Appl Catal A 358:193–202
184. Kovnir K, Schmidt M, Waurisch C, Armbrüster M, Prots Yu, Grin Yu (2008) Refinement of the crystal structure of dipalladium gallide, Pd_2Ga. Z Kristallogr New Cryst Struct 223:7–8

185. Lorenz H, Turner S, Lebedev OI, Van Tendeloo G, Klötzer B, Rameshan C, Pfaller K, Penner S (2010) Pd–In_2O_3 interaction due to reduction in hydrogen: consequences for methanol steam reforming. Appl Catal A 374:180–188
186. Kamiuchi N, Muroyama H, Matsui T, Kikuchi R, Eguchi K (2010) Nano-structural changes of SnO_2-supported palladium catalysts by redox treatments. Appl Catal A 379:148–154
187. Teschner D, Borsodi J, Wootsch A, Révay Z, Hävecker M, Knop-Gericke A, Jackson SD, Schlögl R (2008) The roles of subsurface carbon and hydrogen in palladium-catalyzed alkyne hydrogenation. Science 320:86–89
188. Teschner D, Révay Z, Borsodi J, Hävecker M, Knop-Gericke A, Schlögl R, Milroy D, Jackson SD, Torres D, Sautet P (2008) Understanding palladium hydrogenation catalysts: when the nature of the reactive molecule conrols the nature of the catalyst active phase. Angew Chem Int Ed 47:9274–9278
189. Seriani N, Mittendorfer F, Kresse G (2010) Carbon in palladium catalysts: a metastable carbide. J Chem Phys 132:024711
190. Al Alam AF, Matar SF, Nakhl M, Quaini N (2009) Investigations of changes in crystal and electronic structures by hydrogen within $LaNi_5$ from first-principles. Solid State Sci 11:1098–1106
191. Kohout M (2004) A measure of electron localizability. Int J Quant Chem 97:651–658
192. Kohout M, Wagner FR, Grin Yu (2006) Atomic shells from the electron localizability in momentum space. Int J Quant Chem 106:1499–1507
193. Kohout M (2007) Bonding indicators from electron pair density functionals. Faraday Discuss 135:43–54
194. Kovnir K, Armbrüster M, Teschner D, Venkov TV, Szentmiklósi L, Jentoft FC, Knop-Gericke A, Grin Yu, Schlögl R (2009) In situ surface characterization of the intermetallic compound pdga—a highly selective hydrogenation catalyst. Surf Sci 603:1784–1792
195. Osswald J, Giedigkeit R, Jentoft RE, Armbrüster M, Girgsdies F, Kovnir K, Grin Yu, Ressler T, Schlögl R (2008) Palladium gallium intermetallic compounds for the selective hydrogenation of acetylene. Part I: preparation and structural investigation under reaction conditions. J Catal 258:210–218
196. Osswald J, Kovnir K, Armbrüster M, Giedigkeit R, Jentoft RE, Wild U, Grin Yu, Schlögl R (2008) Palladium gallium intermetallic compounds for the selective hydrogenation of acetylene. Part II: surface characterization and catalytic performance. J Catal 258:219–227
197. Chen ZX, Neyman KM, Gordienko AB, Rösch N (2003) Surface structure and stability of PdZn and PtZn alloys: density functional slab model studies. Phys Rev B 68:075417
198. Bayer A, Flechtner K, Denecke R, Steinrück HP, Neyman KM, Rösch N (2006) Electronic properties of thin Zn layers on Pd(111) during growth and alloying. Surf Sci 600:78–94
199. Chen ZX, Neyman KM, Rösch N (2004) Theoretical study of segregation of Zn and Pd in Pd–Zn alloys. Surf Sci 548:291–300
200. Chen ZX, Neyman KM, Lim KH, Rösch N (2004) CH_3O Decomposition on PdZn(111), Pd (111), and Cu(111). A theoretical study. Langmuir 20:8068–8077
201. Chen ZX, Lim KH, Neyman KM, Rösch N (2004) Density functional study of methoxide decomposition on PdZn(100). Phys Chem Chem Phys 6:4499–4504
202. Chen ZX, Lim KH, Neyman KM, Rösch N (2005) Effect of steps on the decomposition of CH_3O at PdZn alloy surfaces. J Phys Chem B 109:4568–4574
203. Fasana A, Abbati I, Braicovich L (1982) Photoemission evidence of surface segregation at liquid-nitrogen temperature in Zn-Pd system. Phys Rev B 26:4749–4751
204. Rodriguez JA (1994) Interactions in bimetallic bonding: electronic and chemical properties of PdZn surfaces. J Phys Chem 98:5758–5764
205. Stadlmayr W, Penner S, Klötzer B, Memmel N (2009) Growth, thermal stability and structure of ultrathin Zn-layers on Pd(111). Surf Sci 603:251–255
206. Rameshan C, Stadlmayr W, Weilach C, Penner S, Lorenz H, Hävecker M, Blume R, Rocha T, Teschner D, Knop-Gericke A, Schlögl R, Memmel N, Zemlyanov D, Rupprechter G, Klötzer

B (2010) Subsurface-controlled CO_2 selectivity of PdZn near-surface alloys in H_2 generation by methanol steam reforming. Angew Chem Int Ed 49:3224–3227
207. Stadlmayr W, Rameshan C, Weilach C, Lorenz H, Hävecker M, Blume R, Rocha T, Teschner D, Knop-Gericke A, Zemlyanov D, Penner S, Schlögl R, Rupprechter G, Klötzer B, Memmel N (2010) Temperature-induced modifications of PdZn layers on Pd(111). J Phys Chem C 114:10850–10856
208. Weirum G, Kratzer M, Koch HP, Tamtögl A, Killmann J, Bako I, Winkler A, Surnev S, Netzer FP, Schennach R (2009) Growth and desorption kinetics of ultrathin Zn layers on Pd (111). J Phys Chem C 113:9788–9796
209. Koch HP, Bako I, Weirum G, Kratzer M, Schennach R (2010) A Theoretical study of Zn adsorption and desorption on a Pd(111) substrate. Surf Sci 604:926–931
210. Gabasch H, Knop-Gericke A, Schlögl R, Penner S, Jenewein B, Hayek K, Klötzer B (2006) Zn adsorption on Pd(111): ZnO and PdZn alloy formation. J Phys Chem B 110:11391–11398
211. Jeroro E, Vohs JM (2008) Zn Modification of the reactivity of Pd(111) toward methanol and formaldehyde. J Am Chem Soc 130:10199–10207
212. Jeroro E, Lebarbier V, Datye A, Wang Y, Vohs JM (2007) Interaction of CO with surface PdZn alloys. Surf Sci 601:5546–5554
213. Massalski TB (1990) Pd-Zn (palladium-zinc). In: Masaalski TB (ed) Binary alloy phase diagrams, 2nd edn. ASM International, Materials Park, pp 3068–3070
214. Iwasa N, Mayanagi T, Masuda S, Takezawa N (2000) Steam reforming of methanol over Pd-Zn catalysts. React Kinet Catal Lett 69:355–360
215. Murray JL (1985) The aluminium-copper system. Int Met Rev 30:211–233

Chapter 6
Biodiesel Production Using Homogeneous and Heterogeneous Catalysts: A Review

Ajay K. Dalai, Titipong Issariyakul, and Chinmoy Baroi

Abstract Biodiesel, which is an alternative renewable fuel, is defined as mono alkyl ester of long-chain fatty acids and has properties comparable to those of fossil-based diesel. Biodiesel can be produced from vegetable oils or animal fats. The most common method used to produce biodiesel is a reversible chemical reaction called transesterification. This reaction takes place either in the presence of catalysts at lower temperature and pressure or in the absence of catalysts at higher temperature and pressure in supercritical state. Catalyzed transesterification reaction is preferred in biodiesel production because of the moderate reaction conditions. Homogeneous base catalysis can be used in transesterification when fresh vegetable oil is used as a feedstock due to its low cost, high catalytic activity, and feasibility to operate at low temperatures. Homogeneous acid catalysis is a better choice when the feedstock contains higher amounts of free fatty acids (FFAs). Heterogeneous base and acid catalysis are preferred due to their easy separation from biodiesel, hence reducing number of product purification steps. However, heterogeneous catalysis is still under development and has a promising future in biodiesel industries. In this chapter, various acid- and base-catalyzed esterification and transesterification reactions are discussed, and recent trend in catalyst development is highlighted. It is recommended that a proper selection of catalyst is made in a transesterification reaction, depending largely on the type of feedstock.

6.1 Introduction

Increasing concerns on the depletion of conventional fossil-based fuels have caused a search for an alternative renewable fuel. Initially, vegetable oils, having colorific value comparable to that of fossil-based fuel, were used as fuel to operate diesel

A.K. Dalai (✉) • T. Issariyakul • C. Baroi
Catalysis and Chemical Reaction Engineering Laboratories, Department of Chemical Engineering, University of Saskatchewan, Saskatoon, SK, Canada S7N 5A9
e-mail: ajay.dalai@usask.ca

L. Guczi and A. Erdőhelyi (eds.), *Catalysis for Alternative Energy Generation*,
DOI 10.1007/978-1-4614-0344-9_6,

engine [1]. However, the use of neat vegetable oil for fueling diesel engine was questioned by early researchers. Triglyceride, the main component in vegetable oil, consists of glycerol backbone and fatty acid chains. It was proposed that the glycerol backbone has no calorific value and is likely to cause extra coke formation and therefore should be eliminated prior to its use in diesel engine [2]. In later years, it was reported that problems associated with using vegetable oil for fueling diesel engine were cold weather operating, plugging, and gumming and carbon deposits due to its high viscosity [3]. The most common method to reduce its viscosity is a chemical reaction called transesterification, in which the glycerol backbone part in triglyceride molecule is removed. The product fuel is known nowadays as "biodiesel."

Biodiesel is defined as mono alkyl ester of long-chain fatty acids. It has properties comparable to those of fossil-based diesel fuel and can be produced from vegetable oil or animal fats, thus is renewable. It can be used in diesel engine at all proportions (it can be blended with fossil-based diesel fuel or used as pure biodiesel) with no requirement for engine modification. The use of biodiesel also helps to reduce exhaust emissions such as particulate matters, total hydrocarbon (THC), CO, and aromatic and poly aromatic compounds [4].

6.2 Various Oils Available for Biodiesel Production

The vegetable oils used as lipid feedstock for biodiesel production highly depend on regional climate that is rapeseed oil in European countries and Canada, soybean oil in United States, and palm oil in tropical countries. Coconut oil is another lipid feedstock used for synthesis of biodiesel in coastal areas in tropical countries. Potential nonedible oils used as lipid feedstock in India include *Jatropha* oil (*Jatropha curcas*) and karanja oil (*Pongamia pinnata*) [5]. Table 6.1 summarizes oilseed price and availability. Soybean oil dominates the world oilseed production, while rapeseed production is second only to soybean oil. The oil content in soybean and rapeseed seeds is 21 and 35, respectively. Despite the lesser availability, palm oil is an interesting source of biodiesel feedstock due to its lower price and

Table 6.1 World oilseed production, average oil price, and oil content of various oilseeds

Plant	Oil content (%)	Oilseed production[a] (million metric tons)	Average oil price[a] (USD/metric ton)	Yield (kg/hector/year)	References
Rapeseed	35	46.72	852[b]	600–1,000	[6–8]
Soybean	21	235.77	684	300–450	[6, 7, 9]
Sunflower seed	44–51	30.15	n/a	280–700	[6, 7, 10]
Palm	40	10.27	655	2,500–4,000	[6–8]
Copra	65–68	5.28	n/a	n/a	[7, 11]
Coconut	63	n/a	812	600–1,500	[6–8]

[a]Data in 2006/2007
[b]Canola oil

relatively high oil content (40%). This oil also gives highest oil yield per hector per year as compared to other oils (see Table 6.1).

The major difference between various vegetable oils is type of fatty acids attached in the triglyceride molecule. Fatty acid compositions of various vegetable oils are shown in Table 6.2. Fatty acid composition is of utmost importance as it determines fuel properties of biodiesel derived from corresponding vegetable oils [23]. Fatty acid composition also determines degree of saturation/unsaturation and molecular weight of vegetable oils. The degree of saturation/unsaturation and molecular weight of vegetable oils can be calculated by iodine value and saponification value, respectively. The higher iodine and saponification values indicate the higher degree of unsaturation and lower molecular weight of the corresponding vegetable oils.

6.3 Biodiesel Quality

Fatty acid methyl ester or other esters of fatty acids can be used as diesel fuel or diesel fuel additive. The properties of diesel fuel blends do not change significantly at low biodiesel percentages. However, an addition of more than 30% biodiesel may affect the fuel properties of the blends [24]. Therefore, the properties of biodiesel after production are of great importance and needed to be controlled. The required properties are listed in Table 6.3. The heating value of biodiesel is approximately 10% less than that of fossil-based diesel fuel [25]. The viscosity of the fuel after transesterification should be reduced below 6 cSt. Water and sediments can cause fuel degradation and should not be present more than 500 ppm. Acid value reflects the percentage of free fatty acid (FFA) contained in the fuel. Acid value of biodiesel should be less than 0.5 mg KOH/g sample. Incomplete transesterification results in the high amounts of triglyceride, diglyceride, and monoglyceride, which lead to high values of total glycerin and boiling point distribution as acylglycerol boils at higher temperature compared to esters. It is reported that low-temperature properties and oxidation stability of biodiesel are inferior to fossil-based diesel fuel, and modification is required in order to improve these properties [26, 27]. Various types of antioxidant can be used to increase stability of biodiesel [28–31]. Biodiesel blends have improved lubricating properties as compared to fossil-based diesel fuel. It was reported that at 1% biodiesel addition, the lubricity of fuel was improved by 20% [32]. In general, the final biodiesel product should maintain fuel properties satisfying the specifications presented in Table 6.3.

6.4 Biodiesel Production via Transesterification and Esterification

Transesterification is a reaction in which triglyceride (TG) is reacted with alcohol (usually methanol) to form the corresponding alkyl ester (biodiesel) of FA mixtures that is found in the triglyceride feedstock. This reaction is commonly used to reduce

Table 6.2 Fatty acid compositions of vegetable oils

Vegetable oils		Fatty acid compositions (wt%)											
Common name	Species	12:0	14:0	16:0	16:1	18:0	18:1	18:2	18:3	20:0	22:0	22:1	References
Canola	*Brassica napus*	–	–	4.3	0.3	1.7	61.0	20.8	9.3	0.6	0.3	–	[12]
Black mustard	*Brassica nigra*	–	1.5	5.3	0.2	1.3	11.7	16.9	2.5	9.2	0.4	41.0	[13]
Oriental mustard	*Brassica juncea*	–	–	2.3	0.2	1.0	8.9	16.0	11.8	0.8	5.7	43.3	[14]
Soybean	*Glycine max*	–	–	10.1	–	4.3	22.3	53.7	8.1	–	–	–	[15]
Soybean	*GMO*[a]	–	–	3.5	0.1	2.8	22.7	60.3	9.8	0.2	0.2	–	[16]
Palm	*Elaeis oleifera*	–	0.2	18.7	1.6	0.9	56.1	21.1	–	–	–	–	[17]
Palm kernel	*Elaeis guineensis*	50.1	15.4	7.3	–	1.8	14.5	2.4	–	–	–	–	[17]
Palm olein	–	0.3	1.2	40.6	0.2	4.3	41.9	11.9	0.4	0.4	–	–	[18]
Sunflower	*Helianthus annuus*	–	–	5.2	0.1	3.7	33.7	56.5	–	–	–	–	[15]
Corn	*Zea mays*	–	–	11.6	–	2.5	38.7	44.7	1.4	–	–	–	[15]
Olive	*Olea europaea*	–	–	13.8	1.4	2.8	71.6	9.0	1.0	–	–	–	[15]
Linseed	*Linum usitatissimum*	–	–	5.6	–	3.2	17.7	15.7	57.8	–	–	–	[15]
Coconut	*Cocos nucifera*	50.9	21.1	9.5	–	4.9	8.4	0.6	–	–	–	–	[19]
Rice bran	*Oryza sativa*	–	–	22.1	–	2.0	38.9	29.4	0.9	–	–	–	[20]
Jatropha	*Jatropha curcas*	–	–	18.5	–	2.3	49.0	29.7	–	–	–	–	[21]
Karanja	*Pongamia glabra*	–	–	5.8	–	5.7	57.9	10.1	–	3.5	–	–	[22]

[a]Genetically modified oil

Table 6.3 Specification of fossil-based diesel and biodiesel

Fuel properties	Fossil-based diesel	Biodiesel
Specification	ASTM D975	ASTM D6751
Composition	C10–C21 HC	C12–C22 FAME
Calcium and magnesium (ppm)	–	5 max
Sodium and potassium (ppm)	–	5 max
Sulfated ash (% mass)	–	0.02 max
Sulfur (ppm)	500 max	15/500 max
Phosphorous (% mass)	–	0.001 max
Water and sediment	0.05 max (vol.%)	500 max (ppm)
Methanol (% mass)	–	0.02 max
Flash point (°C)	52 min	130 min
Cetane (°C)	40 min	–
Cetane index	40 min	
Kinematic viscosity, 40°C (cSt)	1.9–4.1	1.9–6.0
Acid number (mg KOH/g)	–	0.5 max
Free glycerin (% mass)	–	0.02 max
Total glycerin (% mass)	–	0.24 max
Distillation T90 (90%) (°C)	282–338	360 max
Oxidation stability (h)	–	3 min
HFRR, 60°C (μm)	520 max	–

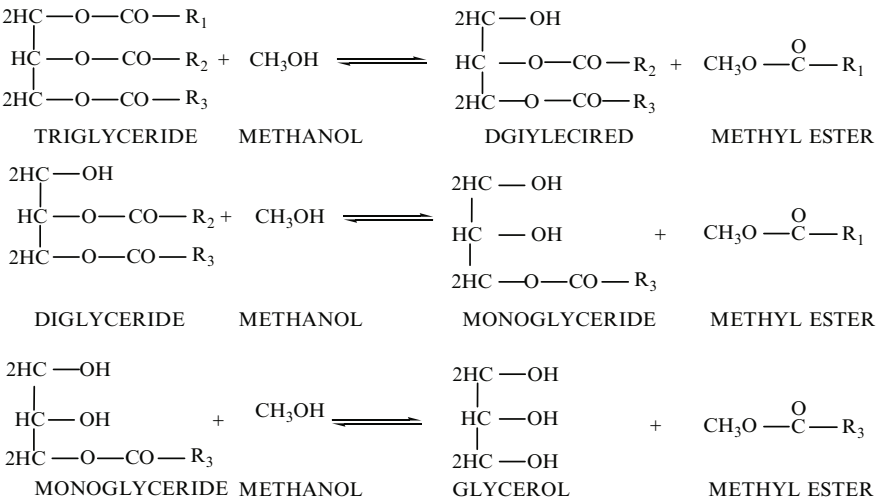

Fig. 6.1 Scheme for stepwise transesterification reaction

the viscosity of TG. Transesterification occurs in a series of consecutive, reversible reactions in which TG is reacted with alcohol to form DG, MG, and GL, respectively, as shown in Fig. 6.1. Stoichiometrically, each mole of TG requires 3 mol of alcohol to yield 3 mol of alkyl ester as shown in Fig. 6.2. Since the reaction is

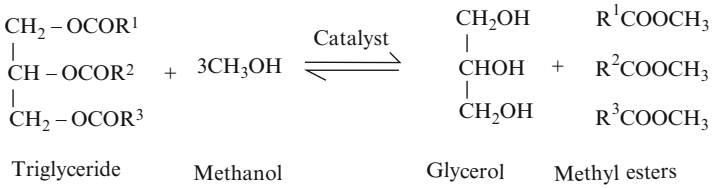

Fig. 6.2 Scheme for transesterification of triglyceride with methanol

reversible, an excess alcohol is usually required to shift the reaction equilibrium to the product side. The catalyst used in this reaction should possess either acid or base property. The mechanisms of both base- and acid-catalyzed reactions are discussed in Sects. 4.1 and 4.2, respectively.

6.4.1 Homogeneous Base Catalysis

In transesterification, a catalyst with base property catalyzes the reaction considerably faster than that of acid property [33, 34]. However, it is crucial for base-catalyzed transesterification that all reacting lipid and alcohol as well as catalyst must be substantially anhydrous [3]. Water, if present, could promote saponification to form soap. In addition, it can hydrolyze ester to form FFA. Subsequently, the FFA will irreversibly neutralize base catalyst and ultimately form alkaline salt. The mechanism for base-catalyzed transesterification is shown in Fig. 6.3. The first step is the attack of alkoxide ion (methoxide ion in the case of methanol as reacting alcohol) to carbonyl carbon of the triglyceride molecule to form a tetrahedral intermediate. In the second step, the tetrahedral intermediate reacts with alcohol to regenerate alkoxide ion. The last step involves the rearrangement of the tetrahedral intermediate to form alkyl ester and diglyceride. A small amount of water generated during transesterification may cause soap formation and subsequently lower ester yield. Examples of esterification and transesterification of various feedstocks using various homogeneous catalysts are given in Table 6.4.

The alcohols used in transesterification are those of primary and secondary monohydric aliphatic alcohols having 1–8 carbon atoms [3]. The reactivity of alcohol depends greatly on the type of alcohol as shown in Table 6.5. Since methanol is the most economical source of alcohol and has highest relative reactivity, it is commonly used as reacting alcohol in transesterification. However, it was found that the solubility of triglyceride in methanol is low; therefore, the mass transfer could make an adverse impact on the overall rate of methanolysis. The solubility of oil in methanol can be improved by an addition of ethers as a cosolvent such as tetrahydrofuran (THF) or methyl tertiary-butyl ether (MTBE) [60–62]. Alternatively, a mixture of methanol and ethanol can be used to increase the solubility of oil in alcohol due to the higher solubility of oil in ethanol. In this case, both methyl ester and ethyl ester are formed [25, 40]. The optimum alcohol to

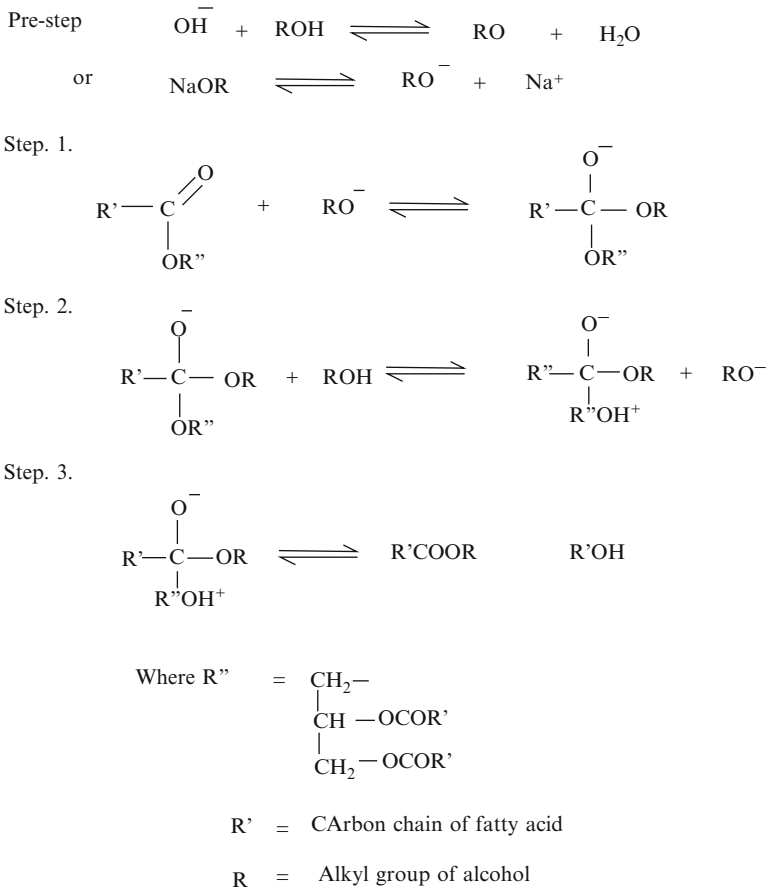

Fig. 6.3 Mechanism for base-catalyzed transesterification

oil molar ratio used in transesterification depends on type of lipid, alcohol, and catalyst. In general, at least 100% excess alcohol (6:1 alcohol to oil molar ratio) is used in order to shift the reaction to the product side. However, if too much methanol is added, the oil concentration will be too low which adversely affects the reaction rate. In addition, the glycerol either does not separate or move into the methanol-rich upper phase [60].

Temperature is another important parameter in transesterification reaction. Transesterification consists of the initial mass transfer-controlled region and kinetically controlled region [63, 64]. In the first region, triglyceride molecule moves into alcohol phase and collides with methoxide ion in order for the reaction to take place. When the higher temperature is used, the kinetic energy of TG molecule and methoxide ion are higher, hence, TG molecule and methoxide ion move faster, which leads to an increase in the rate of collision. In the kinetically controlled region, the higher temperature would favor the reaction due to endothermic nature

Table 6.4 Examples of esterification and transesterification reactions

Feedstock	Alcohol	Alcohol to oil ratio	Catalyst	Temperature (°C)	Duration	Conversion/ yield	References
Base catalysts							
Vegetable oils	C1–C4 alcohol	6:1	KOH 0.5% wt CH_3ONa 0.25% wt	25	40 min	87–96% yield	[26]
Vegetable oils	Methanol	6:1	KOH 1% wt	25	40 min	51–87% yield	[35]
Pongamia pinnata	Methanol	10:1	KOH 1% wt	105	1.5 h	92% conversion	[36]
Canola oil	Methanol	6:1	NaOH 1% wt	45	15 min	98% ester content	[37]
Used frying oil	Methanol	7:1	NaOH 1.1% wt	60	20 min	94.6% ester content	[37]
P. pinnata	Methanol	6:1	KOH 1% wt	65	2 h	97–98% yield	[38]
Soybean oil	Methanol	6:1	NaOH	45	10–20 min	100% yield	[39]
Canola oil	Methanol Ethanol	6:1	KOH 1% wt	25–70	2 h	>90% yield	[40]
Waste fryer grease	Methanol Ethanol	6:1	H_2SO_4 2% wt KOH 1% wt	50–60	5–6 h	97% ester content	[25]
Jatropha	Methanol	3:1	NaOH/KOH 1% wt	–	2–4 h	–	[41]
Mixed canola and used cooking oil	Methanol Ethanol	6:1	KOH 1% wt	50	2 h	98% ester content	[42]
Rapeseed	Methanol	6:1	KOH 1% wt	65	2 h	95–96% yield	[43]

Sunflower	Methanol	6:1	NaOH 1% wt	60	2 h	97.1% yield	[44]
Triolein	C1–C10 alcohol	6:1	KOH/NaOH 1% wt	Room	1 h	99% conversion	[45]
Greenseed canola oil	Methanol Ethanol	6:1	KOH 1% wt	60	90 min	97% ester content	[46]
Coconut oil	Ethanol	6:1	KOH 0.75% wt	–	7 min	98% yield	[47]
Coriander seed oil	Methanol	6:1	CH_3ONa 0.5% wt	60	90 min	94% yield	[48]
Acid catalysts							
Madhuca indica	Methanol	0.3–0.35 v/v	H_2SO_4 1% v/v	60	1 h	98% yield	[49]
Rubber seed oil	Methanol	6:1	H_2SO_4 0.5% by volume	45	20–30 min	–	[50]
Tobacco seed oil	Methanol	18:1	H_2SO_4 1–2%	60	25 min	91% yield	[51]
Waste frying oil	Methanol	24.5:1	H_2SO_4 3.8:1 mole ratio	70	4 h	99% yield	[52]
Calophyllum inophyllum	Methanol	6:1	H_2SO_4 0.65% by volume	65	90 min	85% yield	[53]
Zanthoxylum bungeanum	Methanol	24:1	H_2SO_4 2%	60	80 min	98% yield	[54]
Tallow	Methanol	30:1	H_2SO_4 2.5% wt	60	24 h	98.28% yield	[55]
Canola oil	Methanol	24:1	$AlCl_3$	110	18 h	98% conversion	[56]
Soybean oil	Methanol	20:1	CF_3CO_2H 2.0 M concentration	120	5 h	98.4% ester content	[57]
High AV oil	Methanol	20:1	H_2SO_4 4% wt	120	5 min residence time	99.5% yield	[58]

Table 6.5 Relative reactivity of alkyl group in the alcoholysis of acetates [59]

Alkyl group	Relative reactivity
Methyl	1.00
Ethyl	0.81
n-Propyl	0.79
n-Butyl	0.80
n-Heptyl	0.90

of transesterification [65]. However, when operated at atmospheric pressure, the reaction temperature should not exceed the boiling point of the alcohol, i.e., 64.7°C for methanol and 78.4°C for ethanol.

Many studies have shown that a longer reaction time results in higher ester yield [32, 33, 63, 64, 66, 67]. However, base-catalyzed transesterification occurs rapidly, and the reaction usually required less than 1 h to complete. In some cases, it is essential to terminate the reaction as soon as the free and bound glycerides meet the biodiesel specifications (see Table 6.3). If the reaction is prolonged, water produced during the reaction could hydrolyze ester to FFA. It is shown in a study that the acid value increases with reaction time when NaOH was used as a catalyst for methanolysis of soybean oil [68].

The most common homogeneous catalysts include KOH, NaOH, $KOCH_3$, and $NaOCH_3$. Alkaline metal alkoxides are believed to be a better catalyst as compared to those of hydroxides because they do not generate water during the reaction [33]. When water is generated, it can promote hydrolysis to form FFA, thus increasing acid value. Mahajan et al. [68] showed that when $NaOCH_3$ was used, the acid value of the reaction product was significantly lower than that when NaOH was used. However, due to their toxicity, higher price, and disposal problems, alkaline metal alkoxides are not commonly used in a large-scale production. When alkaline metal alkoxides and hydroxides are used as catalysts, the active catalytic species are the same, i.e., methoxide ion (CH_3O^-); therefore, it is concluded that these catalysts are equally effective for transesterification [26].

6.4.2 Homogeneous Acid Catalysis

When dealing with triglycerides that have relatively higher FFA content, alkaline catalysts are not suitable as they form soap with these acids. Therefore, acid catalyst is more suitable [3]. Acids used in this reaction can be sulfuric, phosphoric, hydrochloric, or organic sulfonic acids [69]. In addition to transesterification reaction, esterification takes place in which FFA reacts with methanol to form methyl ester (see Fig. 6.4). Unlike transesterification, 1 mol of FFA requires 1 mol of alcohol to form 1 mol of ester. It is noteworthy that the reverse reaction is hydrolysis, in which water reacts with ester to form FFA. One has to be aware of this reaction when synthesizing biodiesel in a system containing water. The mechanism of acid-catalyzed transesterification is shown in Fig. 6.5. The first step is protonation of carbonyl group in glyceride molecule which leads to the carbocation. Then the attack of alcohol produces tetrahedral intermediate. The elimination of

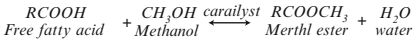

Fig. 6.4 Scheme for esterification of free fatty acid with methanol

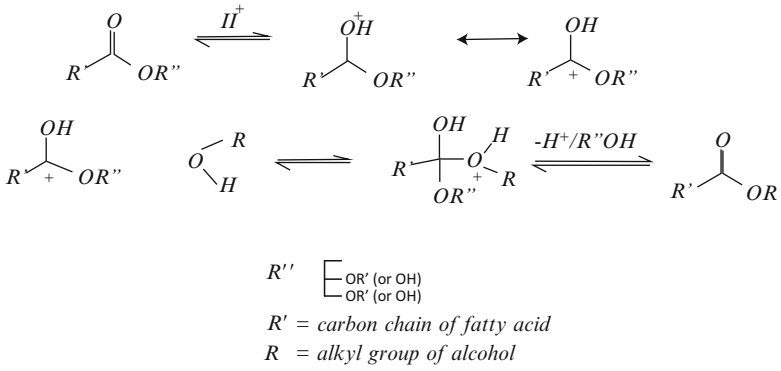

Fig. 6.5 Mechanism for acid-catalyzed transesterification

glycerol backbone from this intermediate regenerates the catalyst and forms an ester. Compared to base catalysis, acid-catalyzed reactions require higher alcohol to oil molar ratio, reaction temperature, and reaction time. If the reaction is operated at the temperature above the boiling point of the reacting alcohol, an elevated pressure is required in order to keep alcohol in liquid phase.

Although acid catalyst can handle feedstock with higher FFA content, it is crucial to keep water content below 0.5 wt% [70]. In this study, the addition of 5% water reduced ester yield from 95% (without water) to 5.6%. Water, if present, can surround proton (H^+) and form water-rich methanol proton complexes. These water-rich methanol proton complexes are less hydrophobic than methanol-only proton complexes, making the catalytic species (H^+) more difficult to approach triglyceride molecule which is hydrophobic. Therefore, the catalyst is deactivated when a significant amount of water is present in the feedstock [71]. In addition, it was found that the effects of water is more critical in acid-catalyzed transesterification than in base-catalyzed transesterification [72] and has more impacts on transesterification than esterification [71]. Due to the presence of carboxylic functional group in FFA, FFA is less hydrophobic than triglyceride molecule, rendering the polar water-rich methanol proton complexes easier to approach FFA than triglyceride.

6.4.3 Heterogeneous Base Catalysis

6.4.3.1 Alkaline Earth Metal Oxide Catalysts

Alkaline earth metal oxides have gained attraction to many researchers for transesterification to biodiesel production because of their less solubility and less

corrosiveness compared to other base catalysts. These catalysts are synthesized either as single metal oxides or mixed metal oxides.

It is believed that the basic sites are generated by the presence of M^{2+}–O^{2-} ion pairs in different coordination environments. The basic strength of group II metal oxides follows the order: MgO < CaO < SrO < BaO. The catalytic activity of these oxides in transesterification to biodiesel production also agrees with the same order, but their catalytic activity is less, compared to those of homogeneous base catalysts [73, 74]. BaO is not suitable for transesterification reaction to produce biodiesel because it dissolves in methanol and forms some noxious species. SrO is highly catalytically active and insoluble in water, but it reacts strongly with CO_2 and water in the air to form nonreactive $SrCO_3$ and $Sr(OH)_2$, and regeneration of SrO requires high temperature [73]. Ca-based bases are attractive as they are inexpensive and the least toxic, and they exhibit low methanol solubility tendency [75]. The problem of CaO is its low catalytic activity below the supercritical-state temperature of methanol (240°C) and methanol to oil molar ratio of 40:1, and 97–99% ester yield can be obtained above these conditions [76]. However, the rate of CaO catalysis can be accelerated in the presence of water because methoxide ions, which are the catalytic agents for transesterification reactions, are increased, but too much water (more than 2.8% by weight of oil) in the reaction medium cause Ca soap formation [77]. CaO has a drawback of undesired $Ca(OCH_3)_2$ formation on the CaO surface by reacting with triglycerides. Another drawback is its chemisorption tendency of H_2O and CO_2 on its active surface, which requires high temperature (700°C) to remove the poisonous species because of the chemisorption [76].

The purpose of synthesizing mixed metal oxides is to overcome the limitations of single metal oxide catalysts. It was demonstrated that mixed metal oxides (i.e., Mg–La oxide) have higher catalytic activity in transesterification for biodiesel production compared to that of single metal oxides (i.e., Ca, Ba, Mg oxides) because of superbasicity of the mixed oxides. This mixed metal oxide shows tolerable activities in the presence of water and FFAs, and 100% ester yield can be obtained within 2.2 h using room temperature, 20:1 methanol to oil molar ratio, and 5 wt% catalyst loading [78]. In a study of different metal oxides (A–B–O) where A = alkaline earth metal (Ca, Ba, Mg), alkaline metal, or rare earth metal (La) and B is the transition metal (Ti, Mn, Fe, Zr, Ce), it was found that Ca-based catalysts such as $CaMnO_3$, $Ca_2Fe_2O_3$, $CaZrO_3$, and $CaCeO_3$ have the highest base strength and catalytic activity in transesterification reactions, especially that more than 80% ester yield can be obtained using $CaZrO_3$ and $CaCeO_3$ within 10 h at 60°C with 6:1 methanol to oil molar ratio and the catalyst is reusable up to 5–7 times [79]. In another study, when CaO was loaded on different oxide supports (i.e., MgO, SiO_2, Al_2O_3), CaO/MgO was found to show the highest catalytic activity due to increased basicity. Highest 92% oil conversion was achieved within 3 h at 64.5°C with 6:1 methanol to oil molar ratio [80].

6.4.3.2 Supported Alkali Metal/Metal Salt Catalysts

Alkali (alkaline earth) metal is the most common source of superbasicity. Na, K, Li, Ba, and Mg are frequently used in the metallic form or as various salts such as halide, carbonate, hydroxide, and nitrate. The catalytic activity of the catalysts depends on the surface basicity rather than on the other properties such as surface area and pore volume. Supported halides (i.e., KF/Al_2O_3, KI/Al_2O_3) have higher catalytic activity in transesterification reaction compared to other supported salts (i.e., K_2CO_3/Al_2O_3, KNO_3/Al_2O_3). The catalytic activity of nitrates, hydroxides, and carbonates depends on the metal (i.e., K^+) loading on the support (i.e., Al_2O_3) by impregnation. The support for alkali or alkaline earth metal species can be CaO, BaO, MgO, and ZnO. In every case, it was found that supported alkali metals supported on alkali earth oxides are partially dissolved into the liquid phase, and the catalyst becomes homogeneous. It was also found that in rare cases, alkali earth oxide supports (i.e., BaO) leach into the ester phase more than the impregnated metal species [76]. D'Cruz et al. also found similar results when Li, Na, and K metals were loaded on CaO, MgO, BaO, and K_2CO_3 loaded on alumina. In their study, BaO-supported metals showed higher catalytic activity compared to other alkaline earth oxide-supported metals in transesterification reaction, but severe leaching of Ba was found in the reaction mixture, and K_2CO_3/Al_2O_3 was found to be a promising heterogeneous base catalyst [74].

6.4.3.3 Hydrotalcite

Hydrotalcite or layered double hydroxide is a naturally found anionic clay material, whose general formula is $[M_x{}^{z+}M'_y{}^{3+}(OH)_{2(x+y)}]^{b+}\,[(A^{n-})_{b/n}]\cdot nH_2O$. M is a monovalent (alkali metal) or divalent (alkaline earth metal) ion, M′ is a trivalent metal ion (usually Al^{3+}), and A^{n-} is an anion (usually $CO_3{}^{2-}$) neutralizing compound electronically. The Mg–Al hydrotalcite is a well-studied catalyst for transesterification for its higher catalytic activity. Li–Al hydrotalcite has stronger Bronsted basicity compared to Mg–Al, but the catalytic activity of Li–Al hydrotalcite in transesterification reaction has not been extensively studied yet [76]. The general composition of Mg–Al hydrotalcite is $[Mg_{(1-x)}Al_x(OH)_2]^{x+}[(CO_3)_{x/n}{}^{2-}]$ over the range of $x = 0.25$–0.55. Variations in the x content changes the basic properties [81]. For biodiesel synthesis, the Mg/Al molar ratio of hydrotalcites is usually set from 2 to 4. This Mg–Al hydrotalcite is attractive because of its negligible leaching tendency, high catalytic activity in the presence of water and FFA, and also activity up to 210°C. In a study, 99% conversion of triglycerides was obtained within 3 h at 200°C and a methanol to oil molar ratio of 6:1 with 1 wt% catalyst loading in the presence of 45 wt% water and 9.5 wt% FFA [82].

6.4.3.4 Zeolite

The acid–base properties of zeolites are controlled by the kind and quantities of ion-exchanged cations and by the Si/Al ratio in the main zeolite framework. The two general approaches taken to control the basicity are ion exchange with alkali metal ions and the impregnation of basic components on the inner surface of zeolite pores. Among these two approaches, the later one was found to create strong basic sites [76]. In case of alkali ion-exchanged zeolites, the basicity increases with the increasing electropositive nature of the exchanged cation. Among the zeolite family, the zeolites faujasite NaX and titanosilicate structure-10 (ETS-10) have been studied for transesterification for biodiesel production. The basicity of these zeolites was increased by ion exchange with higher electropositive metals such as K and Cs [81]. It was observed that ion exchange with K is more effective than with Cs, in terms of the basicity and transesterification activity [76]. In a study using partially Cs-exchanged NaX zeolite (34% Cs substituted), 70% conversion was achieved in 22 h using a methanol to oil molar ratio of 275:1 and catalyst loading of 10 wt% [83]. In another study, ester yield of 85% was obtained within 8 h at 65°C with a methanol to oil molar ratio of 8:1 using KOH/NaX, but severe leaching of KOH was found [84].

6.4.3.5 Organic Base Catalyst

Guanidine [$C(NH)(NH_2)_2$] is an organic compound which shows strong basicity. The basicity of alkylguanidine is comparable to that of NaOH, and it is a well-studied and effective base catalyst for transesterification for biodiesel production [76]. In a study, it was found that a commercial alkylguanidine, triazabicyclodecene (1,5,7-triazabicyclo[4.4.0]dec-5-ene or TBD), is a very effective catalyst in transesterification reaction, producing 90 ester yield within 1 h at 70°C with a 23:1 methanol to oil molar ratio [85]. The advantage of this organic base is that it forms a soluble complex with the FFA and does not form soap or emulsions. Several attempts have been taken to heterogenize the alkylguanidine on different supports, but severe leaching was found in all the cases [76]; thus, there is a necessity of further research on this. Anion-exchange polymer resins are of interest to many researchers for transesterification reactions because of their basicity, porosity, cheap price, and availability. In a study, it was found that Diaion® PA306s is an effective catalyst for transesterification to produce biodiesel. In the study, 80% ester yield was obtained within 1 h at 50°C with an ethanol to oil molar ratio of 20:1 and catalyst loading of 40%, and the catalysis was found to be free of saponification [86]. In another study, organic quaternary ammonium functionality (QN^+OH)-based anionic resin A26 (from Rohm and Haas) catalytic activity was compared to that of QN^+OH/SiO_2 for transesterification reaction. From that study, both the catalysts showed similar catalytic activity (60% conversion of the oil within 4 h at 60°C with a methanol to oil molar ratio of 6:1 and catalyst loading of 1.6 wt%), but anionic resin A26 showed negligible leaching tendency compared to that of QN^+OH/SiO_2 [87].

6.4.4 Heterogeneous Acid Catalysis

6.4.4.1 Sulfated Metal Oxides

Sulfated metal oxides show both Bronsted and Lewis acid sites, and their acidity is considered to be superacidity. Among different sulfated metal oxides, sulfated zirconia (SZ) shows superior catalytic activity due to its high acid strength. Schucharardt et al. [85] proposed a novel method of SZ preparation with improved catalytic activity, whereas conventional sulfated zirconia (SZ) shows lower activity in transesterification reaction and deactivation after the first run. In their study, 98.6% ester yield was obtained within 1 h at 120°C with a methanol to oil molar ratio of 20:1 and a catalyst loading of 5 wt%, whereas conventional SZ showed no activity, but the catalyst had poor reusability characteristics. The reason for these poor reusability characteristics is sulfur leaching as H_2SO_4 and HSO_4^- [81]. For this, Yadav and Murkute [88] proposed a novel method of SZ preparation with improved sulfate loading and resistance to leaching. Sulfated tin oxide (SO_4^{2-}/SnO_2) shows better catalytic activity in esterification reaction compared to that of sulfated zirconia (SZ) due to its superior acidity, but this catalyst has not been experimented yet for transesterification reaction because of inadequacies in preparation method [81]. Another superacidic sulfated metal oxide used in transesterification reaction was sulfated titania. It was found to be less active than sulfated zirconia but silica-supported sulfated titania was found to show better catalytic activity and stability compared to that of conventional sulfated zirconia. In the study, 90% ester yield was obtained within 6 h at 200°C with a methanol to oil molar ratio of 9:1 and catalyst loading of 3 wt% in the presence of 50% FFA [89].

6.4.4.2 Mixed Metal Oxides

Nonsulfated superacid material (i.e., tungstated zirconia) has attracted much attention because of the leaching and stability of sulfated zirconia. In a study, it was found that tungstated zirconia has lower catalytic activity compared to that of sulfated zirconia in transesterification reaction, but it has an advantage of easy regeneration, indicating that the catalytic deactivation in tungstated zirconia is because of coverage of the acid sites rather than leaching of the catalytic species [90]. Furuta et al. [91] found that doping of Al into the tungstated zirconia increases the catalytic activity much higher than tungstated zirconia in both transesterification and esterification reactions for biodiesel production. Amphoteric metal oxides are of interests to many researchers because of their adjusting acid–base properties. In a study, it was found that PbO and PbO_2 show high catalytic activity in transesterification reactions (89% ester yield within 2 h at 150°C with 7:1 methanol to oil molar ratio, 2 wt% catalyst loading), but they have a higher leaching tendency [92]. In this respect, ZnO-based catalysts are a point of interest. Zn–Al oxide developed by French Institute of Petroleum (IFP), shows higher catalytic

activity in transesterification reaction (91% biodiesel yield within 160 min, 250°C, 50 bar pressure), but the catalyst requires moisture-free feedstock. The composition of this mixed oxide is $ZnAl_2O_4{\cdot}xZnO{\cdot}yAl_2O_3$ (with x and y being in the range of 0–2) [73]. Zn–La mixed oxide is another attractive catalyst, which are composed of ZnO, La_2CO_3, and LaOOH. In series of studies, it was found that Zn3La1 (3:1 M ratio of zinc to lanthanum) has longer catalyst life (~17 recycling) and higher FFA (up to 30.5%) and water (up to 5%) tolerability. This catalyst is able to produce ester yield of ~96% in the presence of 30.5% FFA, 5% water within 150 min at 200°C, 36:1 methanol to oil molar ratio, and a catalyst loading of 2.3% based on the weight of the oil [93].

6.4.4.3 Heteropolyacids

Another important group of strongly acidic heterogeneous catalysts used in biodiesel production through transesterification and esterification of triglycerides is supported heteropolyacids and unsupported or supported heteropolyacid metal salts. Though sulfated metal oxides are more acidic than heteropolyacids, but the concern of sulfur leaching by sulfated metal oxides attracts the use of heteropolyacid-based solid catalysts to many researchers. Efforts made using supported/unsupported HPA and their salts especially as a catalyst for biodiesel production through transesterification reactions are summarized in a tabular form in Table 6.6. This table shows the comparative catalytic activity of different HPA and their salts.

6.4.4.4 Organically Functionalized Acid Catalyst

The purpose of synthesis and use of organically functionalized acid catalysts for biodiesel production is to overcome the shortcomings of other acid catalysts, such as leaching of active species, thermal stability, and low surface area. The activity of this class of catalysts is due to the presence of sulfonic acid sites, which can be considered as the heterogeneous counterpart of sulfuric acid. Sulfuric acid has excellent catalytic activity in the acid-catalyzed transesterification reaction, for this attempts have been made on its heterogenization to overcome the traditional drawbacks of homogeneous catalytic systems, such as equipment corrosion and difficult separation from the products. The carriers for sulfonic acid can be inorganic metal oxides such as zirconia oxide, tin oxide, mesostructured silica, and carbon materials such as multiwall carbon nanotubes and asphalt. Among these, sulfonic acid supported on asphalt showed promising catalytic activity and reusability (89.9% conversion within 3 h at 260°C using a methanol to oil molar ratio of 18.2 and catalyst loading of 0.2 wt%) [103, 104]. Attempts have also been taken with the sulfonic acid ionic-exchange resins, such as poly(DVB) resin sulfonated with H2SO4, Amberlyst-35(Rohm and Haas), Amberlyst-15 (Rohm and Haas), and Nafion SAC-13 for biodiesel production through transesterification reactions [73].

Table 6.6 Review on biodiesel production using HPA or supported HPA

Feedstock	Name of the catalyst and reactor used	Results and remarks	References
Canola oil containing up to 20% FFA	$H_3PW_{12}O_{40}$ (TPA) supported on hydrous zirconia (HZ), silica, alumina, and activated carbon	10% TPA/HZ, at 200°C, 9:1 methanol to oil molar ratio, 600 rpm, 3 w/w% catalyst loading could give maximum ester yield of 90% when the reaction was allowed to run for 10 h. The catalysts were recycled with negligible loss of activity	[94]
	500-cc Parr reactor	10% TPA/HZ surface area (S.A): 146 m^2/g, pore diameter (P.D.): 2.18 nm	
Eruca sativa Gars. Oils (ESG oil) with FFA 3.65%	$Cs_{2.5}H_5PW_{12}O_{40}$ 250-mL round reactor	A 99% ester conversion was obtained using a catalyst of 1.85×10^{-3} g/g of oil, 5.3:1 methanol to oil molar ratio, 55°C reaction temperature when the reaction was allowed to run for 45 min in the presence of a THF as a cosolvent. Catalyst structural properties were not analyzed	[95]
Rapeseed oil	$H_3PW_{12}O_{40}$, $Cs_2HPW_{12}O_{40}$, $H_3PW_{12}O_{40}/SiO_2$ 50-cm^3 Pyrex reactor	A 27% maximum conversion was obtained when 0.6 g unsupported $H_3PW_{12}O_{40}$ was used at a reaction temperature of 80°C stirring at 500 rpm, 6:1 ethanol to oil molar ratio for 3 h. Severer leaching was observed from the $H_3PW_{12}O_{40}/SiO_2$	[96]
Tripalmitin	$H_3PW_{12}O_{40}/Ta_2O_5$ 25-mL round bottom glass flask	Highest yield was achieved when 2% w/w $H_3PW_{12}O_{40}/Ta_2O_5$-10.8, 90:1 methanol to tripalmitin, 65°C reaction temperature was used for 6 h for simultaneous esterification and transesterification	[97]
Karanja, *Jatropha*, soybean, sunflower, and palm oil	$H_3PW_{12}O_{40}$/K-10, $H_3PMo_{12}O_{40}$/K-10, sodium tungstate hydrate/K-10 100-cm^3 Parr reactor	Highest conversion was achieved when 20% w/w $H_3PW_{12}O_{40}$/K-10, 5% w/w based on sunflower oil, 170 rpm, 15:1 methanol to sunflower oil ratio was used at a 170°C for 6 h	[98]

(continued)

Table 6.6 (continued)

Feedstock	Name of the catalyst and reactor used	Results and remarks	References
Triolein	$H_4PNbW_{11}O_{40}/WO_3$—Nb_2O_5, $H_4SiW_{12}O_{40}$, $H_4SiMo_{12}O_{40}$, $H_3PW_{12}O_{40}$, $Cs_{2.5}H_{.5}PW_{12}O_{40}$, $H_4PNbW_{11}O_{40}$ Batch reaction—autoclave and continuous-flow fixed-bed reactor	A highest ester yield of 87% was obtained when 0.2 g $H_3PW_{12}O_{40}$, 50:1 ethanol to triolein molar ratio, 100°C was used for 8 h	[99]
E. sativa Gars. oils (ESG oil) with FFA 3.65%	$Cs_{2.5}H_{0.5}PW_{12}O_{40}$ 500-mL round reactor	Maximum 98.1% conversion was achieved in 12 h using 65°C reaction temperature, 6:1 methanol to oil molar ratio, and 0.4 mmol of catalyst	[100]
Soybean oil with 20% myristic acid	Ta_2O_5/SiO_2—[$H_3PW_{12}O_{40}$/R] (R = Me or Ph), $H_3PW_{12}O_{40}/Ta_2O_5$-10.8, SiO_2—[$H_3PW_{12}O_{40}$(9.6)/Me(3)] 25-mL round bottom glass flask	The R (methyl or phenyl) group in the catalyst made the catalyst surface hydrophobic. Ta_2O_5/SiO_2—[$H_3PW_{12}O_{40}$(10.0)/Me(3)], (10 represents wt% loading, 3 is the molar ratio of Ta to Me/Ph group)—was obtained to be the most effective catalyst for simultaneous esterification and transesterification when 2 wt% catalyst, 65°C reaction temperature, 90:1 methanol to oil molar ratio were used for 24 h	[101]
Used cooking oil with 8% FFA	TPA($H_3PW_{12}O_{40}$)/Nb_2O_5, with TPA loading of 5–30% on Nb_2O_5	25 wt% TPA/Nb_2O_5 was the most promising one. Highest 92% ester yield was obtained at 200°C, 18:1 alcohol/oil molar ratio, and 3 wt% catalyst loading. The catalyst was recycled and reused with negligible loss in activity	[102]

These ion-exchange resins suffer from low thermal stability. Thus, in order to achieve high triglyceride conversion, high methanol to molar ratio (50:1 to 300:1) and high catalyst loading of 25–50% based on the oil are required [73, 105].

Recently, a novel approach has been developed by Hara et al. [106], where sulfonation of incompletely carbonized carbohydrates such as starch, cellulose, D-glucose, and sucrose occurred. The incomplete carbonization of the carbohydrates leads to a rigid carbon material consisting of small polycyclic

aromatic carbon sheets in a 3D *sp*3-bonded structure. Sulfonation of such carbon material has been demonstrated to afford a highly stable and physically robust solid with a high density of active sulfonic sites. Among other uses, such carbohydrate-derived acid catalysts have been successfully applied to biodiesel production. Using this type of catalyst, highest ester yield of 92% was obtained within 8 h using a reaction temperature of 80°C, 20:1 methanol to oil molar ratio, 10 wt% catalyst loading, and the feedstock containing ~28% FFA. An alternative approach of synthesis of sulfonic acid-based heterogeneous catalysts is the incorporation of organosulfonic groups over mesostructured silicas such as SBA-15. These materials have large uniform pores, high thermal stability due to its silica support, and the possibility to control their hydrophobicity and concentration of acid sites through organic functionalization. In a study, in the presence of 5.6 wt% FFA, ester yield of 98.4% was obtained within 2 h at 180°C, 10:1 methanol to oil molar ratio, and a catalyst loading of 6 wt% [105]. Supported organic metal salts also have heterogeneous acid catalysts property. In a study, Jacobson et al. [107] synthesized silica-supported zinc stearate and zinc acetate. Between these catalysts, silica-supported zinc stearates were able to produce ~98% ester yield, using a reaction temperature of 200°C, 18:1 methanol to oil molar ratio, and 3 wt% catalyst loading. These catalysts were reusable and had no leaching tendency.

6.5 Reaction Kinetics

Dossin et al. [108] proposed a type of Langmuir–Hinshelwood model for heterogeneous base-catalyzed transesterification reaction, which is based on a three-step "Eley–Rideal" type of mechanism. According to their proposed model, the rate-determining step is the adsorption of alcohol on the catalyst-free basic sites. As it is appropriate in the nonideal systems to use activities instead of the concentrations in the rate expression if the rate-determining step is an adsorption or desorption step, but according to Dossin et al. [108], it was observed that the effect of using concentrations instead of activities in the rate expressions was found to be small at all conditions considered and hence can be neglected, and a high initial reaction rate can be achieved by using smaller catalyst particle size, whereas temperature has only a minor effect. In another study by Veljkovic et al. [109], it was observed that the initial TG mass transfer limitation is due to the low active surface area of the base catalysts which are occupied by the adsorbed methanol. According to their study, that limitation disappears as the reaction progresses and the use of higher concentration of the catalysts and the overall transesterification reaction is the pseudo-first order [109]. Similar results were obtained by Li et al. [110], who proposed a model based on the overall transesterification reaction. In their study, internal diffusion was neglected by obtaining similar results using different particle sizes. According to their study, the overall reaction is irreversible and first order, and the model is applicable only for the initial stage of the reaction [110]. Singh and Fernando [92] studied different heterogeneous base-catalyzed transesterification

reaction, where they considered only the overall transesterification reaction. In their study, external and internal diffusion were believed to be eliminated, but the reasons are not discussed. The overall reaction order was varied from 1 to 3 depending on the catalysts [92].

Kulkarni et al. have explained the reaction mechanism of simultaneous transesterification and esterification [40]. Srilatha et al. analyzed reaction kinetics using used cooking oil with 8% FFA and 25 wt% TPA/Nb_2O_5 at 200°C, 18:1 alcohol/oil molar ratio, and 3 wt% catalyst loading. The overall reaction is a pseudo-first-order reaction with an activation energy of 34.4 kJ/mol, which is consistent with the reported values [102]. Lopez et al. [111] analyzed acidic Nafion® SAC-13 resin-catalyzed transesterification kinetics for biodiesel production. In their study, external and internal diffusion was avoided by adjusting the stirring speed and the catalyst particle size. They considered the first step of the transesterification reaction (Triglyceride to Diglycerides) instead of the overall reaction for their kinetic study. According to their findings, solid acid catalyst (Bronsted acidity) follows similar mechanistic pathway to that of homogeneous acid catalysts. The mechanism consists of protonation of the TG (by adsorbing on the catalyst surface—which acted as a single reaction site), followed by the surface reaction between the TG and the bulk liquid-phase alcohol (which is the rate-limiting step) and then a product desorption step. In their proposed mechanism, a deviation from the classical Eley–Rideal bimolecular mechanistic expression was observed due to the competitive adsorption of alcohol on the resin acid sites [111]. In that study, other possible reaction pathways for biodiesel production (i.e., hydrolysis followed by esterification) were neglected, and the overall reaction was second order with respect to the reactant concentrations. In another study, it was found by Lopez et al. [112] that triglyceride can react by two routes: hydrolysis followed by esterification and transesterification in the presence of solid acid catalysts. According to their study, the presence of FFAs in TG increases the reaction rate of transesterification because of the parallel faster hydrolysis followed by the esterification reaction rate. However, the esterification reaction rate of FFA in the TG mixture is slow compared to that of pure FFA. They found that the esterification reaction rate is almost 20 times faster than that of transesterification reaction [111].

6.6 Conclusions

When high-quality oil containing exceptionally low FFA and water is used to produce biodiesel, homogeneous base catalyst is preferred due to their high activity toward transesterification. However, most low-quality oils such as used cooking oil contain a significant amount of FFA, which could lead to saponification reactions and causes soap formation in base-catalyzed transesterification. In these low-quality oils where FFA percent is high, homogeneous acid catalysts are preferred. When acid catalyst is used, saponification can be avoided. Recently, heterogeneous catalysts have gained tremendous interests due to simplicity in purification process.

Unlike in homogeneous catalysts, an elimination of heterogeneous catalysts from biodiesel is simple and does not produce waste water. However, it is clear that the active species of almost all heterogeneous base catalysts leaches out into the reaction medium, lowers the selectivity of transesterification reaction, and produces soap if there is any FFA present in the feedstock. The solid base catalysts also lose its reusability. Comparatively, solid acid catalysts can catalyze esterification reaction to produce a similar type of ester from FFAs using alcohol along with transesterification reaction to produce biodiesel. Active species of many of the solid acid catalysts also leach out into the reaction medium, which affects only the reusability of the catalysts, but does not affect the selectivity. The reaction kinetics and mechanism of heterogeneous base- and acid-catalyzed reactions reveal that the first step in the base-catalyzed reaction is adsorption of alcohol (methanol) onto the catalyst active sites, whereas in case of acid-catalyzed reaction, the first step is adsorption of oil or triglycerides onto the catalyst active sites. In case of acid-catalyzed reaction, it is difficult to initiate the first step of the reaction because most of the supports and active sites are hydrophilic. Thus, the authors recommend further research on solid acid-catalyzed simultaneous esterification and transesterification reactions for biodiesel production and the development of a relationship between the catalyst type and vegetable oil used for biodiesel synthesis.

Acknowledgment The authors acknowledge the funding for this research from Natural Science and Engineering Research Council of Canada (NSERC), Agriculture and Bioproducts Innovation Program (ABIP), and Canada Research Chair (CRC) Program.

References

1. Knothe G, Gerpen JV, Krahl J (2005) The biodiesel handbook. AOCS Press, Champaign
2. Walton J (1938) The fuel possibilities of vegetable oils. Gas Oil Power 33:167–168
3. Ma F, Hanna MA (1999) Biodiesel production: a review. Bioresour Technol 70:1–15
4. Lapuerta M, Armas O, Rodr‚guez-Fernandez J (2008) Effect of biodiesel fuels on diesel engine emissions. Prog Energy Combust Sci 34:198–223
5. Sharma YC, Singh B (2009) Development of biodiesel: current scenario. Renew Sustain Energy Rev 13:1646–1651
6. Röbbelen G (1990) Mutation breeding for quality improvement: a case study for oilseed crops. Mutat Breed Rev 6:1–44
7. USDA-FAS (United States Department of Agriculture—Foreign Agricultural Service). Oilseeds: world markets and trade. http://www.fas.usda.gov/. Accessed 16 Nov 2009
8. Williams MA (2005) Recovery of oils and fats from oilseeds and fatty materials. In: Shahidi F (ed) Bailey's industrial oil and fat products, vol 5, 6th edn. Wiley, Hoboken, NJ
9. Wang T (2002) Soybean oil. In: Gunstone FD (ed) Vegetable oils in food technology composition, properties and uses. CRC Press LLC, Boca Raton, FL
10. Gupta MK (2002) Sunflower oil. In: Gunstone FD (ed) Vegetable oils in food technology composition, properties and uses. CRC Press LLC, Boca Raton, FL
11. Pantzaris TP, Basiron Y (2002) The lauric (coconut and palmkernel) oils. In: Gunstone FD (ed) Vegetable oils in food technology composition, properties and uses. CRC Press LLC, Boca Raton, FL

12. Ackman RG (1983) Chemical composition of rapeseed oil. In: Kramer JKG, Sauer FD, Pigden WJ (eds) High and low erucic acid rapeseed oils production, usage, chemistry, and toxicological evaluation. Academic, Toronto, ON
13. Basu AK, Ghosh A, Dutta S (1973) Fatty acid composition of mustard (Brassica nigra) seed oil by gas-liquid chromatography. J Chromatogr 86:232–233
14. Matthaus B, Vosmann K, Pham LQ, Aitzetmüller K (2003) FA and tocopherol composition of Vietnamese oilseeds. J Am Oil Chem Soc 80:1013–1020
15. Kamal-Eldin A, Andersson R (1997) A multivariate study of the correlation between tocopherol content and fatty acid composition in vegetable oils. J Am Oil Chem Soc 74:375–380
16. Reske J, Siebrecht J, Hazebroek J (1997) Triacylglycerol composition and structure in genetically modified sunflower and soybean oils. J Am Oil Chem Soc 74:989–998
17. Jalani BS, Cheah SC, Rajanaidu N, Darus A (1997) Improvement of palm oil through breeding and biotechnology. J Am Oil Chem Soc 74:1451–1455
18. Firestone D (2006) Physical and chemical characteristics of oils, fats, and waxes, 2nd edn. AOCS Press, Washington, DC
19. Pham LJ, Casa EP, Gregorio MA, Kwon DY (1998) Triacylglycerols and regiospecific fatty acid analyses of Philippine seed oils. J Am Oil Chem Soc 75:807–811
20. Bravi E, Perretti G, Montanari L (2006) Fatty acids by high-performance liquid chromatography and evaporative light-scattering detector. J Chromatogr A 1134:210–214
21. Banerji R, Chowdhury AR, Misra G, Sudarsanam G, Verma SC, Srivastava GS (1985) Jatropha seed oils for energy. Biomass 8:277–282
22. Bhattacharyya DK (2002) Lesser-known Indian plant sources for fats and oils. Inform 13:151–157
23. Ramos MJ, Fernández CM, Casas A, Rodríguez L, Pérez Á (2009) Influence of fatty acid composition of raw materials on biodiesel properties. Bioresour Technol 100:261–268
24. Reaney MJT, Hertz PB, McCalley WW (2005) Vegetable oils as biodiesel. In: Shahidi F (ed) Bailey's industrial oil and fat products, vol 6, 6th edn. Wiley, Hoboken, NJ
25. Issariyakul T, Kulkarni MG, Dalai AK, Bakhshi NN (2006) Production of biodiesel from waste fryer grease using mixed methanol/ethanol system. Fuel Process Technol 88:429–436
26. Lang X, Dalai AK, Bakhshi NN, Reaney MJT, Hertz PB (2001) Preparation and characterization of bio-diesels from various bio-oils. Bioresour Technol 80:53–62
27. Dinkov R, Hristov G, Stratiev D, Aldayri VB (2009) Effect of commercially available antioxidants over biodiesel/diesel blends stability. Fuel 88:732–737
28. Mittelbach M, Schober S (2003) The influence of antioxidants on the oxidation stability of biodiesel. J Am Oil Chem Soc 80(8):817–823
29. Knothe G, Dunn RO (2003) Dependence of oil stability index of fatty compounds on their structure and concentration and presence of metals. J Am Oil Chem Soc 80(10):1021–1026
30. Schober S, Mittelbach M (2004) The impact of antioxidants on biodiesel oxidation stability. Eur J Lipid Sci Technol 106:382–389
31. Dunn RO (2005) Oxidative stability of soybean oil fatty acid methyl esters by oil stability index (OSI). J Am Oil Chem Soc 82(5):381–387
32. Kulkarni MG, Dalai AK, Bakhshi NN (2006) Utilization of green seed canola oil for biodiesel production. J Chem Technol Biotechnol 81:1886–1893
33. Freedman B, Pryde EH, Mounts TL (1984) Variables affecting the yields of fatty esters from transesterified vegetable oils. J Am Oil Chem Soc 61(10):1638–1642
34. Freedman B, Butterfield RO, Pryde EH (1986) Transesterification kinetics of soybean oil. J Am Oil Chem Soc 63(10):1375–1380
35. Dmytryshyn SL, Dalai AK, Chaudhari ST, Mishra HK, Reaney MJ (2004) Synthesis and characterization of vegetable oil derived esters: evaluation for their diesel additive properties. Bioresour Technol 92:55–64
36. Karmee SK, Chadha A (2005) Preparation of biodiesel from crude oil of *Pongamia pinnata*. Bioresour Technol 96:1425–1429

37. Leung DYC, Guo Y (2006) Transesterification of neat and used frying oil: optimization for biodiesel production. Fuel Process Technol 87:883–890
38. Meher LC, Dharmagadda VSS, Naik SN (2006) Optimization of alkali-catalyzed transesterification of *Pongamia pinnata* oil for production of biodiesel. Bioresour Technol 97:1392–1397
39. Ji J, Wang J, Li Y, Yu Y, Xu Z (2006) Preparation of biodiesel with the help of ultrasonic and hydrodynamic cavitation. Ultrasonics 44:e411–e414
40. Kulkarni MG, Dalai AK, Bakhshi NN (2007) Transesterification of canola oil in mixed methanol/ethanol system and use of esters as lubricity additive. Bioresour Technol 98:2027–2033
41. Sarin R, Sharma M, Sinharay S, Malhotra RK (2007) Jatropha–Palm biodiesel blends: an optimum mix for Asia. Fuel 86:1365–1371
42. Issariyakul T, Kulkarni MG, Meher LC, Dalai AK, Bakhshi NN (2008) Biodiesel production from mixtures of canola oil and used cooking oil. Chem Eng J 140:77–85
43. Rashid U, Anwar F (2008) Production of biodiesel through optimized alkaline-catalyzed transesterification of rapeseed oil. Fuel 87:265–273
44. Rashid U, Anwar F, Moser BR, Ashraf S (2008) Production of sunflower oil methyl esters by optimized alkali-catalyzed methanolysis. Biomass Bioenergy 32:1202–1205
45. Hanh HD, Dong NT, Okitsu K, Nishimura R, Maeda Y (2009) Biodiesel production through transesterification of triolein with various alcohols in an ultrasonic field. Renew Energy 34:766–768
46. Issariyakul T, Dalai AK (2010) Biodiesel production from greenseed canola oil. Energy Fuel 24:4652–4658. doi:10.1021/ef901202b
47. Kumar D, Kumar G, Singh PCP (2010) Fast, easy ethanolysis of coconut oil for biodiesel production assisted by ultrasonication. Ultrason Sonochem 17:555–559
48. Moser BR, Vaughn SF (2010) Coriander seed oil methyl esters as biodiesel fuel: unique fatty acid composition and excellent oxidative stability. Biomass Bioenergy 34:550–558
49. Ghadge SV, Raheman H (2005) Biodiesel production from mahua (*Madhuca indica*) oil having high free fatty acids. Biomass Bioenergy 28:601–605
50. Ramadhas AS, Jayaraj S, Muraleedharan C (2005) Biodiesel production from high FFA rubber seed oil. Fuel 84:335–340
51. Veljkovic VB, Lakicevic SH, Stamenkovic OS, Todorovic ZB, Lazic ML (2006) Biodiesel production from tobacco (*Nicotiana tabacum* L.) seed oil with a high content of free fatty acids. Fuel 85:2671–2675
52. Zheng S, Kates M, Dubé MA, McLean DD (2006) Acid-catalyzed production of biodiesel from waste frying oil. Biomass Bioenergy 30:267–272
53. Sahoo PK, Das LM, Babu MKG, Naik SN (2007) Biodiesel development from high acid value polanga seed oil and performance evaluation in a CI engine. Fuel 86:448–454
54. Zhang J, Jiang L (2008) Acid-catalyzed esterification of *Zanthoxylum bungeanum* seed oil with high free fatty acids for biodiesel production. Bioresour Technol 99:8995–8998
55. Bhatti HN, Hanif MA, Qasim M, Rehman A-U (2008) Biodiesel production from waste tallow. Fuel 87:2961–2966
56. Soriano NU Jr, Venditti R, Argyropoulos DS (2009) Biodiesel synthesis via homogeneous Lewis acid-catalyzed transesterification. Fuel 88:560–565
57. Miao X, Li R, Yao H (2009) Effective acid-catalyzed transesterification for biodiesel production. Energy Convers Manage 50:2680–2684
58. Sun P, Sun J, Yao J, Zhang L, Xu N (2010) Continuous production of biodiesel from high acid value oils in microstructured reactor by acid-catalyzed reactions. Chem Eng J 162:364–370
59. Sridharan R, Mathai IM (1974) Transesterification reactions. J Sci Ind Res 33:178–186
60. Boocock DGB, Konar SK, Mao V, Lee C, Buligan S (1998) Fast formation of high-purity methyl esters from vegetable oils. J Am Oil Chem Soc 75(9):1167–1172
61. Boocock DGB, Konar SK, Mao V, Sidi H (1996) Fast one-phase oil-rich processes for the preparation of vegetable oil methyl esters. Biomass Bioenergy 11(1):43–50

62. Zhou W, Konar SK, Boocock DGB (2003) Ethyl esters from the single-phase base-catalyzed ethanolysis of vegetable oils. J Am Oil Chem Soc 80(4):367–371
63. Noureddini H, Zhu D (1997) Kinetics of transesterification of soybean oil. J Am Oil Chem Soc 74(11):1457–1462
64. Vicente G, Martinez M, Aracil J, Esteban A (2005) Kinetics of sunflower oil methanolysis. Ind Eng Chem Res 44:5447–5454
65. Ellis N, Guan F, Chen T, Poon C (2008) Monitoring biodiesel production (transesterification) using in situ viscometer. Chem Eng J 138(1–3):200–206
66. Mittelbach M, Trathningg B (1990) Kinetics of alkaline catalyzed methanolysis of sunflower oil. Fat Sci Technol 92(4):145–148
67. Komers K, Stloukal R, Machek J, Skopal F (2001) Biodiesel from rapeseed oil, methanol and KOH. 3. Analysis of composition of actual reaction mixture. Eur J Lipid Sci Technol 103 (6):363–371
68. Mahajan S, Konar SK, Boocock DGB (2007) Variables affecting the production of standard biodiesel. J Am Oil Chem Soc 84:189–195
69. Fukuda H, Kondo A, Noda H (2001) Review: biodiesel fuel production by transesterification of oils. J Biosci Bioeng 92(5):405–416
70. Canakci M, Van Gerpen J (1999) Biodiesel production via acid catalysis. Trans ASAE 42(5):1203–1210
71. Helwani Z, Othman MR, Aziz N, Fernando WJN, Kim J (2009) Technologies for production of biodiesel focusing on green catalytic techniques: a review. Fuel Process Technol 90 (12):1502–1514
72. Kusdiana D, Saka S (2004) Effects of water on biodiesel fuel production by supercritical methanol treatment. Bioresour Technol 91(3):289–295
73. Yan S, DiMaggio C, Mohan S, Kim M, Salley SO, Ng KYS (2010) Advancements in heterogeneous catalysis for biodiesel synthesis. Top Catal 53:721–736
74. D'Cruz A, Kulkarni MG, Meher LC, Dalai AK (2007) Synthesis of biodiesel from canola oil using heterogeneous base catalyst. J Am Oil Chem Soc 84:937–943
75. Helwani Z, Othman MR, Aziz N, Kim J, Fernando WJN (2009) Solid heterogeneous catalysts for transesterification of triglycerides with methanol: a review. Appl Catal A Gen 363:1–10
76. Lee DW, Park YM, Lee KY (2009) Heterogeneous base catalysts for transesterification in biodiesel synthesis. Catal Surv Asia 13:63–77
77. Liu X, He H, Wang Y, Zhu S, Piao X (2008) Transesterification of soybean oil to biodiesel using CaO as a solid base catalyst. Fuel 87:216–221
78. Babu NS, Sree R, Prasad PSS, Lingaiah N (2008) Room-temperature transesterification of edible and non-edible oils using a heterogeneous strong basic Mg/La catalyst. Energy Fuel 22:1965
79. Kawashima A, Matsubara K, Honda K (2008) Development of heterogeneous base catalysts for biodiesel production. Bioresour Technol 99:3439–3443
80. Yan S, Lu H, Liang B (2008) Supported CaO catalysts used in the transesterification of rapeseed oil for the purpose of biodiesel production. Energy Fuel 22:646–651
81. Jothiramalingam R, Wang MK (2009) Review of recent developments in solid acid, base, and enzyme catalysts (heterogeneous) for biodiesel production via transesterification. Ind Eng Chem Res 48:6162–6172
82. Barakos N, Pasias S, Papayannakos N (2008) Transesterification of triglycerides in high and low quality oil feeds over an HT2 hydrotalcite catalyst. Bioresour Technol 99:5037–5042
83. Leclercq E, Finiels A, Moreau A (2001) Transesterification of rapeseed oil in the presence of basic zeolites and related solid acids. J Am Oil Chem Soc 78:1161–1165
84. Xie W, Huang X, Li H (2007) Soybean oil methyl esters preparation using NaX zeolites loaded with KOH as a heterogeneous catalyst. Bioresour Technol 98:936–939
85. Schuchardt U, Vargas RM, Gelbard G (1995) Alkylguanidines as catalysts for the transesterification of rapeseed oil. J Mol Catal A Chem 99:65–70

86. Shibasaki-Kitakawa N, Honda H, Kuribayashi H, Toda T, Fukumura T, Yonemoto T (2007) Biodiesel production using anionic ion-exchange resin as heterogeneous catalyst. Bioresour Technol 98:416–421
87. Liu Y, Loreto E, Gordon JG Jr, Lu C (2007) Transesterification of triacetin using solid bronsted bases. J Catal 246:428–433
88. Yadav GD, Murkute AD (2004) Preparation of a novel catalyst UDCaT-5: enhancement in activity of acid-treated zirconia-effect of treatment with chlorosulfonic acid vis-à-vis sulphuric acid. J Catal 224:218–223
89. Peng BX, Shu JFQ, Wang GR, Wang DZ, Haan MH (2008) Biodiesel production from waste oil feedstocks by solid acid catalysis. Process Saf Environ Protect 86:441–447
90. Suwannakarn K, Loreto E, Ngaosuwan K, Goodwin JG Jr (2009) Simultaneous free fatty acid esterification and triglyceride transesterification using a solid acid catalyst with in situ removal of water and unreacted methanol. Ind Eng Chem Res 48:2810–2818
91. Furuta S, Matsuhashi H, Arata K (2004) Biodiesel fuel production with solid superacid catalysis in fixed bed reactor under atmospheric pressure. Catal Commun 5:721–723
92. Singh AK, Fernando SD (2007) Reaction kinetics of soybean oil transesterification using heterogeneous metal oxide catalysts. Chem Eng Technol 30(12):1716–1720
93. Yan S, Salley SO, Ng KYS (2009) Simultaneous transesterification and esterification of unrefined or waste oils over ZnO-La_2O_3 catalysts. Appl Catal A Gen 353:203–212
94. Kulkarni MG, Gopinath R, Meher LC, Dalai AK (2006) Solid acid catalyzed biodiesel production by simultaneous esterification and transesterification. Green Chem 8:1056–1062
95. Chai F, Cao F, Zhai F, Chen Y, Wang X (2007) Transesterification of vegetable oil to biodiesel using a heteropolyacid solid catalyst. Adv Synth Catal 349:1057–1065
96. Hamad B, Lopez de Souza RO, Sapaly G, Carneiro Rocha MG, Pries de Oliveira RG, Gonzalez WA, Andrade Sales E, Essayem N (2008) Transesterification of rapeseed oil with ethanol over heterogeneous heteropolyacids. Catal Commun 10:92–97
97. Xu L, Wang Y, Yang X, Yu X, Guo Y, Clark JH (2008) Preparation of mesoporous polyoxometalate-tantalum pentoxide composite catalyst and its application for biodiesel production. Green Chem 10:746–755
98. Bokade VV, Yadav GD (2009) Transesterification of edible and nonedible vegetable oils with alcohols over heteropolyacids supported on acid-treated clay. Ind Eng Chem Res 48 (21):9408–9415
99. Katada N, Hatanaka T, Ota M, Yamada K, Okumura K, Niwa M (2009) Biodiesel production using heteropoly acid-derived solid acid catalyst $H_4PNbW_{11}O_{40}/WO_3$—Nb_2O_5. Appl Catal A Gen 363:164–168
100. Li S, Wang Y, Dong S, Chen Y, Cao F, Chai F, Wang X (2009) Biodiesel production from Eruca sativa Gars vegetable oil and motor, emissions properties. Renew Energy 34:1871–1876
101. Xu L, Li W, Hu J, Yang X, Guo Y (2009) Biodiesel production from soybean oil catalyzed by multifunctionalized Ta_2O_5/SiO_2-[$H_3PW_{12}O_{40}$/R] (R = Me or Ph) hybrid catalyst. Appl Catal B Environ 90:587–594
102. Srilatha K, Issariyakul T, Lingaiah N, Sai Prasad PS, Kozinski J, Dalai AK (2010) Efficient esterification and transesterification of used cooking oil using 12-tungstophosphoric acid (TPA)/Nb_2O_5 catalyst. Energy Fuel 24:4748–4755. doi:10.1021/ef901307w
103. Melero JA, Bautista LF, Morales G, Iglesias J, Briones D (2009) Biodiesel production with heterogeneous sulfonic acid-functionalized mesostructured catalysts. Energy Fuel 23:539–547
104. Shu Q, Zhang Q, Xu G, Nawaz Z, Wang D, Wang J (2009) Synthesis of biodiesel from cottonseed oil and methanol using a carbon-based solid acid catalyst. Fuel Process Technol 90:1002–1008
105. Melero JA, Iglesias J, Morales G (2009) Heterogeneous acid catalysts for biodiesel production: current status and future challenges. Green Chem 11:1285–1308

106. Hara M, Yoshida T, Takagaki A, Takata T, Kondo JN, Hayashi S, Domen K (2004) A carbon material as a strong protonic acid. Angew Chem Int Ed 43:2955–2958
107. Jacobson K, Gopinath R, Meher LC, Dalai AK (2008) Solid acid catalyzed biodiesel production from waste cooking oil. Appl Catal B Environ 85:86–91
108. Dossin TF, Reyniers M, Berger RJ, Marin GB (2006) Simulation of heterogeneously MgO-catalyzed transesterification for fine-chemical and biodiesel industrial production. Appl Catal B Environ 67:136–148
109. Veljovic VB, Stamenkovic OS, Todorovic ZB, Lazic ML, Skala DU (2009) Kinetics of sunflower oil methanolysis catalyzed by calcium oxide. Fuel 88:1554–1562
110. Li E, Xu PZ, Rudolph V (2009) MgCoAl-LDH derived heterogeneous catalysts for the transesterification of canola oil to biodiesel. Appl Catal B Environ 88:42–49
111. Lopez DE, Goodwin JG Jr, Bruce DA (2007) Transesterification of triacetin with methanol on Nafion® acid resins. J Catal 245:381–391
112. Lopez DE, Goodwin JG Jr, Bruce DA, Furuta S (2008) Esterification and transesterification using modified-zirconia catalysts. Appl Catal A Gen 339:76–83

Chapter 7
Heterogeneous Catalysts for Converting Renewable Feedstocks to Fuels and Chemicals

Karen Wilson, Adam F. Lee, and Jean-Philippe Dacquin

Abstract The combination of dwindling oil reserves and growing concerns over carbon dioxide emissions and associated climate change is driving the urgent development of routes to utilise renewable feedstocks as sustainable sources of fuel and chemicals. Catalysis has a rich history of facilitating energy-efficient selective molecular transformations and contributes to 90% of chemical manufacturing processes and to more than 20% of all industrial products. In a post-petroleum era, catalysis will be central to overcoming the engineering and scientific barriers to economically feasible routes to biofuels and chemicals. This chapter will highlight some of the recent developments in heterogeneous catalytic technology for the synthesis of fuels and chemicals from renewable resources, derived from plant and aquatic oil sources as well as lignocellulosic feedstocks. Particular attention will be paid to the challenges faced when developing new catalysts and importance of considering the design of pore architectures and effect of tuning surface polarity to improve catalyst compatibility with highly polar bio-based substrates.

7.1 Introduction

The application of heterogeneous catalysis and use of renewable feedstocks in chemical synthesis are core themes behind the principles of Green Chemistry [1]. Worldwide concern over dwindling fossil fuel reserves and impact of CO_2 emissions on climate change means there is an urgent need to reduce our dependence on oil-based sources of fuels and chemicals. Oil is the most important source of energy worldwide, accounting for some 35% of primary energy consumption and the majority of the chemical feedstocks; the quest for sustainable resources to meet

K. Wilson (✉) • A.F. Lee • J.-P. Dacquin
Cardiff Catalysis Institute, School of Chemistry, Cardiff University, Cardiff, CF10 3AT, UK
e-mail: wilsonk5@cardiff.ac.uk

L. Guczi and A. Erdőhelyi (eds.), *Catalysis for Alternative Energy Generation*,
DOI 10.1007/978-1-4614-0344-9_7,

demands of a constantly rising global population is one of the main challenges for mankind this century [2]. To be truly viable, such alternative feedstocks must be sustainable, that is, "have the ability to meet twenty-first century energy needs without compromising those of future generations." While a number of sustainable technologies (e.g. wind, solar, hydroelectric and nuclear power) are currently receiving heavy investment for stationary energy sources [3], the most easily implemented and low-cost solutions for transportation needs are those based upon biomass-derived fuels [4]. Biomass also offers the only non-oil-based route to organic molecules for the manufacture of bulk, fine and speciality chemicals necessary to secure the future needs of society.

The choice of biomass is important for ensuring the sustainability of a renewable resource-based economy. Despite initial promise, first-generation bio-based fuels and chemicals derived from edible plant materials caused much anguish over competition between land use for fuel crops versus traditional agricultural cultivation. Of equal concern are deforestation practices underway, notably in Indonesia, wherein vast tracts of rainforest and peat land are being cleared to support palm oil plantations [5]. To be sustainable, so-called second generation bio-based fuels and chemicals should use biomass sourced from non-edible components of crops, such as stems, leaves and husks or cellulose from agricultural or forestry waste. Alternative non-food crops, such as switchgrass or *Jatropha curcas*, which require minimal cultivation can also be used. In addition, there is growing interest in using oil from aquatic biomass which can annually yield 80–180 times the volume of oil per hectare than that obtained from plants [6]. Second-generation biofuels are currently at a pre-commercial phase, and if they are to meet targets for implementation by 2015–2020, significant technical hurdles to the chemical transformation of biomass need to be overcome. Catalysis has a rich history of facilitating energy-efficient selective molecular transformations and contributes to 90% of chemical manufacturing processes and to more than 20% of all industrial products. In a post-petroleum era, catalysis will be central to overcoming the engineering and scientific barriers to economically feasible routes to bio-fuels and chemicals.

7.2 Sources of Biomass

Lignocellulosic biomass sourced from waste agricultural or forestry materials is considered a viable option for the production of fuels and chemicals by biochemical fermentation routes. Lignocellulose is a biopolymer comprised of polysaccharides, cellulose and hemicellulose, which are built up from C_6 and C_5 sugars, glucose, xylose and amylose, and lignin which is a polyphenolic compound (Scheme 7.1). However, cross-linking between the cellulose and hemicellulosic components with lignin via ester and ether linkages makes lignocellulose resistant towards hydrolysis, and thus, its simple chemical conversion is challenging. Processing of lignocellulose biomass first requires acid hydrolysis to separate the polysaccharides from lignin, which can subsequently be converted into monosaccharides for use in

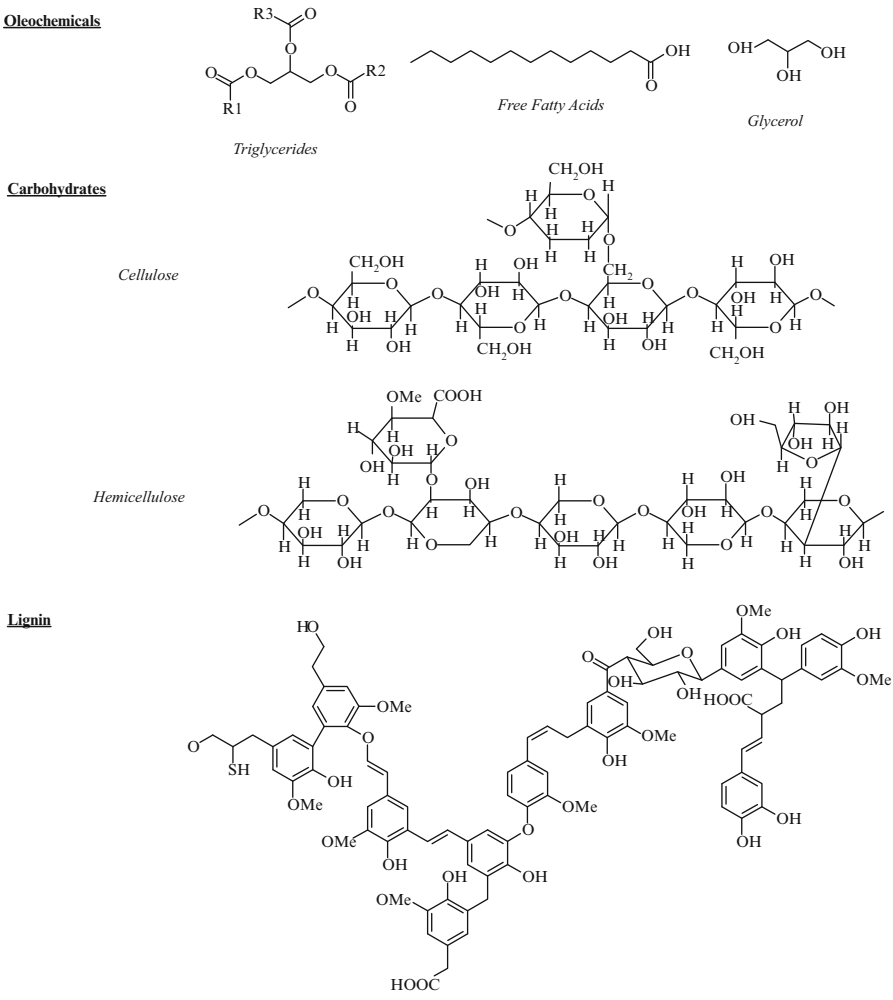

Scheme 7.1 Sources of biomass

fermentation. Thus, while the conversion of sugars such as glucose to chemical feedstocks by fermentation routes seems an attractive prospect, extensive preprocessing of the raw material is required [7].

Oleochemical feedstocks are obtained from triglycerides (TAGs) and free fatty acids (FFAs) found within plant oil seeds, animal fats and algae. Plant oils are conventionally obtained from seeds by pressing, or solvent extraction. Algal oil harvesting and extraction requires a combination of sedimentation, centrifugation, filtration, ultrafiltration, sometimes with an additional flocculation step to separate algae from water, followed by a drying and then solvent extraction step to remove the oil [6]. Cultivation of algal sources using wastewater and CO_2 from fuel gas cloud is proposed as a means to improve the energy efficiency of algal oil production [8].

Table 7.1 Oil contents of various plant and algae oil sources (adapted from [6])

Oil source	Seed oil content (% in dry biomass) [6]	Oil yield (L oil/ha year) [6]	FFA content/wt%
Soybean	18	636	2 [9]
Jatropha	28	741	14–14.9 [10, 11]
Rapeseed	41	974	2 [12]
Sunflower	40	1,070	0.3 [13]
Palm	36	5,366	2.3–6.6 [11, 14]
Microalgae (low oil content, e.g. *Pavlova salina*)	30	58,700	2 [15]
Microalgae (medium oil content, e.g. *Chlorella sp.*)	50	97,800	2
Microalgae (high oil content, e.g. *Botryococcus braunii*)	70	136,900	2

Table 7.1 shows a summary of the oil contents for various plant and algal oil sources from which it can be seen that algae offers significant increases in oil yield. However, there are a wide range of algal sources, and the optimum productivity will depend on both oil content and growth rate. While the *Botryococcus braunii* strain of algae has one of the highest oil contents, it is quite slow growing and it is proposed that the *Chlorella* family would be a better source for biodiesel applications [6]. The percentage of TAG or FFA, length of alkyl chain and degree of unsaturation are all found to vary depending on the oil source [16]. The choice of appropriate oils for fuel application is critical as alkyl chain length and degree of unsaturation affect pour and cloud points as well as stability of the final fuel [17].

There are a number of detailed reviews concerned with the conversion of biomass into chemicals [18, 19]; this chapter will highlight some of the recent developments in heterogeneous catalytic technology for the synthesis of fuels and chemicals from renewable resources derived from oil and lignocellulose feedstocks.

7.3 Oleochemical Feedstocks

7.3.1 Conversion of Plant and Aquatic Oils and Animal Fats to Fuels

7.3.1.1 Overview

Biodiesel spearheads the choice of renewable transportation fuels and is a biodegradable, non-toxic fuel synthesised from animal fats or plant oils extracted from cereal or non-food crops or aquatic biomass. From an application perspective, it is important to consider the oil composition when selecting a biomass source for producing fuels. Fatty acid properties such as chain length and degree of unsaturation can affect cloud points and miscibility with petroleum diesel [20] as well as overall fuel stability

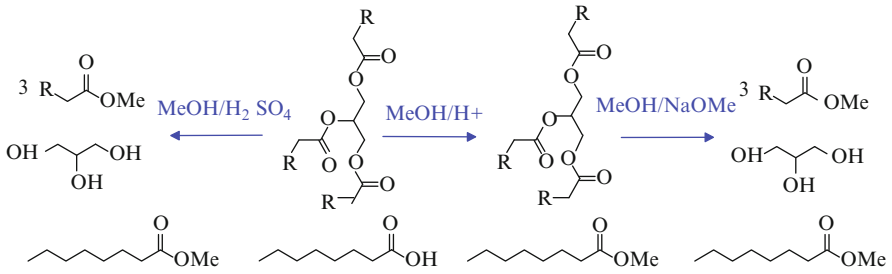

Scheme 7.2 Synthesis of biodiesel via acid or base-catalysed routes

towards oxidation during storage. Furthermore, incomplete combustion of trace amounts of longer chain FAMEs can result in long-term residue accumulation within engines. The combination of non-food oil seed crops, and a heterogeneously catalysed continuous esterification/transesterification process, could dramatically improve both the environmental impact and energy efficiency of biodiesel manufacture and dramatically improve public perception and the future development of biodiesel [21]. This section will give an overview of recent developments in inorganic solid acid and base catalysis for biodiesel synthesis.

TAGs and FFA contained within oil sources can be converted to biodiesel by either a single step acid catalysed process in which TAGs and FFA are respectively transesterified or esterified with methanol to FAME, or in a two step process involving an acid catalysed pretreatment to esterify FFA, followed by a basic catalysed transesterification of the purified TAGs to biodiesel [22]. FFAs in plant oils and animal fats are problematic for conventional biodiesel manufacturing routes [23, 24]. The negative influence of high FFA feedstocks on base-catalysed TAG transesterification is well known [16, 25, 26], with saponification resulting in viscous gels which hamper esterification and increase product separation costs. Consequently, there are tight specifications on feedstock compositions for transesterification, requiring FFA contents below $< 0.5\%$ [17]. Moreover, anhydrous alcohols (and catalysts) are required in order to avoid hydrolysis of the desired alkyl esters into FFAs and associated soap formation. Such traditional biodiesel synthesis involving soluble bases such as KOMe, NaOMe for the transesterification step, may also employ an acid-catalysed pre-esterification step to remove any FFAs (Scheme 7.2), before the oil is contacted with the soluble base catalyst.

While acid-catalysed transesterification is slower, requiring higher reaction temperatures than those typical for base catalysts, a single-step acid-catalysed route may be more economical for oils containing high levels of FFA such as those obtained from animal fats or waste oils. Unfortunately, these homogeneous acid and base catalysts can corrode reactors (and engine manifolds if carried through to the fuel), and their removal from the resulting biofuel is particularly problematic and energy intensive, requiring aqueous quench and neutralisation steps, which themselves result in stable emulsions and soap formation [27–30]. Furthermore, the glycerine by-product, which is of significant potential value to the

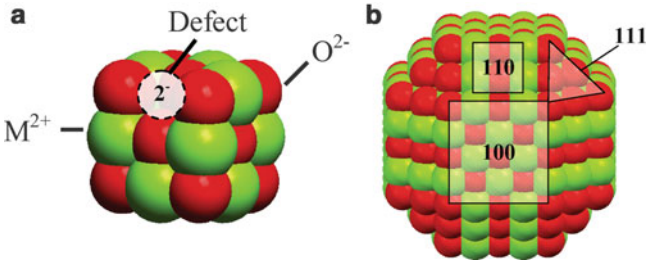

Scheme 7.3 Origin of base sites in alkaline earth oxides: (**a**) Generation of cationic defect sites. (**b**) Surface Mg^{2+}–O^{2-} ratio varies with crystallographic termination leading to increasing base strength across the series (100) < (110) < (111) [34]. *Reproduced by permission of the Royal Society of Chemistry*

pharmaceutical and cosmetic industries, is contained in a dilute aqueous phase that is heavily contaminated by inorganic salts. There is a tangible value for this glycerol as a number of derivatives used in the fine chemicals sector have a glycerol backbone, and its selective conversion to mono- or diglycerides is desirable for use in the cosmetics industry. However, its purification from current biodiesel processes is not economically viable. Development of a heterogeneous biodiesel process will make major improvements to the efficiency of fuel production by eliminating the need for quenching steps, allowing continuous operation while also improving the quality of the glycerol by-product, thus adding value overall to the process.

7.3.1.2 Solid Base Catalysts for Biodiesel Synthesis

Biodiesel synthesis using a solid base catalyst would facilitate separation of both catalyst (via a continuous flow, packed bed arrangement) and glycerol by-product from the final reaction mixture, thereby reducing production costs and enabling catalyst reuse. A variety of solid base catalysts are known, including alkali or alkaline earth oxides, supported alkali metals, basic zeolites and clay minerals (such as hydrotalcites) and supported organic bases [31]. The origin of basicity in alkaline earth oxides has been previously reviewed and is generally believed to arise from the presence of M^{2+}–O^{2-} ion pairs in different coordination environments [32], with the base strength of group two oxides and hydroxides increasing in the order Mg < Ca < Sr < Ba [33]. The strongest base site occurs at low coordination sites that exist at defects, corners, edges or on high Miller index surfaces as indicated in Scheme 7.3.

Such classic heterogeneous base catalysts have been extensively tested for TAG transesterification [35], and there are a number of reports of the application of CaO in the transesterification of rapeseed or sunflower oil by methanol [36–38]. The morphologies of such alkaline earth oxide catalysts and their corresponding basicities are very sensitive to their preparative route [32]. Since the active surface sites of fresh CaO catalysts are unavoidably poisoned by exposure to atmospheric

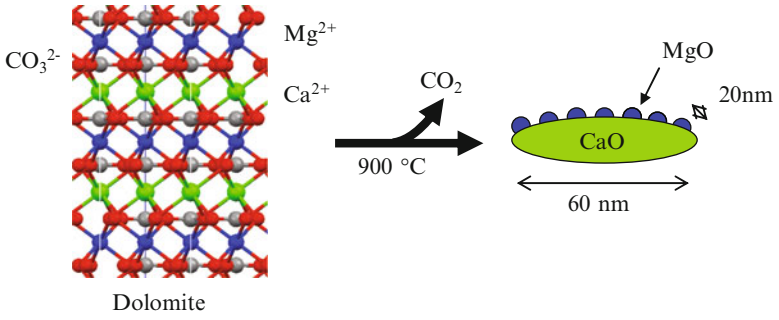

Scheme 7.4 Thermal decomposition of dolomite to MgO/CaO [34]. *Reproduced by permission of the Royal Society of Chemistry*

H_2O and CO_2, a thermal activation treatment is often required to remove surface $Ca(OH)_2$ and $CaCO_3$. Consequently, reported activities for CaO-catalysed transesterification are highly variable, with turnover frequencies (TOFs) for sunflower oil transesterification reported to range from 2.5 to 45 $g_{(oil)}h^{-1}g_{(cat)}{}^{-1}$, depending on sample pre-treatment and microcrystallinity [38]. CaO is generally found to be more active than MgO for rapeseed oil transesterification, with respective TOF of 1.66 $g_{(oil)}h^{-1}$ $g_{(cat)}{}^{-1}$ versus 0.14 $g_{(oil)}h^{-1}$ $g_{(cat)}{}^{-1}$ observed at 65°C [39]. However, care must be taken with such comparisons, as there is concern in the literature [40, 41] over partial leaching of Ca^{2+} from CaO under reaction conditions and associated homogeneous catalytic contributions, which could limit its utility in biodiesel production. Alkali-doped CaO and MgO have also been investigated for transesterification [42, 43]. These exhibit enhanced basicity which is generally associated with the formation of O^- centres when M^{2+} is replaced by M^+, resulting in charge imbalance and associated defect generation. In the case of Li-doped CaO, the optimum activity occurs for dopant levels sufficient to create a saturated Li^+ monolayer; however, care must be taken during catalyst synthesis to ensure that leaching of promoters does not occur [44].

Mixed CaO:MgO oxides prepared via thermal decomposition of natural dolomite have also shown promising activity and stability in the transesterification of a range of C_4–C_{18} TAGs under mild conditions [45]. Dolomitic rock comprises alternating layers of $Mg(CO_3)$–$Ca(CO_3)$ and is structurally very similar to calcite ($CaCO_3$). Calcination at 900°C transforms the mineral into a material comprising MgO nanocrystallites dispersed over larger (> 60 nm) CaO particles, Scheme 7.4. This calcined material exhibits very high activity, with a TOF of 2.9 $g_{(oil)}h^{-1}$ $g_{(cat)}{}^{-1}$ towards the transesterification of olive oil at only 60°C.

Literature suggests that such mixed MgO:CaO systems also show improved resistance to deactivation by CO_2 compared to CaO alone [46]. While the origin of this synergy requires further investigation, it may go some way to explaining why calcined dolomite exhibits a higher activity in plant oil transesterification than the separate CaO or MgO components. The genesis of highly dispersed MgO nanocrystallites on the surface of CaO may also contribute to the performance of calcined

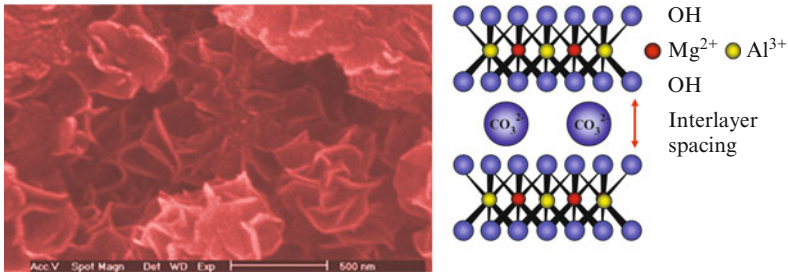

Scheme 7.5 Layered structure of hydrotalcite and "sand rose" structure observed by SEM

dolomite since recent reports reveal that the activity of MgO in TAG transesterification also shows a strong size dependency; nanocrystalline MgO significantly outperforms commercial microcrystalline forms [47, 48]. It is likely that this dependence reflects the correspondence between particle size and preferential surface termination. As prepared nanocrystalline, MgO is comprised of 3-nm (100) crystallites, which on calcination sinter to form larger crystallites ($\geq$ 7 nm) favouring (111) and (110) facets [48]. Such restructuring exposes higher surface densities of polarisable, electron-donating O^{2-} centres and creates bulk and surface defects, postulated as superbasic sites in solid base catalysts. In contrast, conventional commercial MgO samples are comprised of larger ~ 50-nm particles which are dominated by less basic (100) oriented facets. This study highlights the importance of correlating the surface structure and basicity of solid base materials with their catalytic activity; the absence of systematic materials characterisation has to date hampered catalyst optimisation and thus the implementation of new heterogeneous processes.

Amongst solid base catalysts, hydrotalcites have received considerable attention in recent years because of their high activity and robustness in the presence of water and FFA [49, 50]. Hydrotalcites of general formulae $[M^{2+}_{(1-x)}M^{3+}_{x}(OH)_2]^{x+}(A_{x/n})^{n-}\cdot yH_2O$ are another interesting class of solid base whose acid/basic properties can be easily controlled by varying their composition. The structure of hydrotalcites is based upon layered double hydroxides with brucite-like $[Mg(OH)_2]$ hydroxide layers containing octahedrally coordinated M^{2+} and M^{3+} cations; A^{n-} is the counter anion which resides in the interlayer space to balance the residual positive charge of the hydroxide layers which results from isomorphous substitution of M^{2+} by M^{3+} (Scheme 7.5). TAG transesterification has been reported in the literature over hydrotalcites using both poor and high-quality oil feeds; [51] in particular, Mg–Al–CO_3 hydrotalcite offers high transesterification rates in refined and acidic cottonseed oil and in a high water content animal fat feed. For acidified cottonseed oil (9.5 wt% FFA) and animal fat oil (45 wt% water), 99% TAG conversion was achieved within 3 h at 200°C in the presence of methanol (6:1 mole ratio of alcohol: TAG).

There remains some debate over the optimum Mg:Al ratio, which is an important factor when preparing hydrotalcites by precipitation from Na or K hydroxide/carbonate solutions. Complete removal of trace alkali residue from the hydrotalcite

surface is very difficult, resulting in uncontrolled and unquantifiable homogeneous activity from leached Na or K. We recently reported on structure-reactivity correlations within thermally activated Mg–Al hydrotalcites [52] synthesised via an alkali-free precipitation route. $[Mg_{(1-x)}Al_x(OH)_2]^{x+}$ $(CO_3)^{2-}{}_{x/n}$ materials were prepared with compositions spanning $x = 0.25$–0.55. Transesterification activity increased with Mg content in these Mg–Al hydrotalcites, which in turn tracked the intra-layer electron density and associated surface basicity. Davis et al. [53] investigated the influence of water on the activity and stability of activated Mg–Al hydrotalcites (Mg/Al molar ratio of 4) for the same chemistry. Brönsted base sites were active in the presence of water, but significant hydration was found to result in rapid catalyst deactivation, presumably through ester hydrolysis to butyric acid that subsequently irreversible neutralisation of surface base sites.

While solid base catalysts are very effective for transesterification, unfortunately, they cannot esterify any FFA in the oil to FAME and require pre-treatment by a solid acid to ensure that fuel compositions meet legislated standards.

7.3.1.3 Solid Acid Catalysts for Biodiesel Synthesis

Both transesterification and esterification reactions can be acid catalysed; however, despite the wide range of solid acids commercially available, the corresponding direct transesterification of oils into biodiesel by solid acid catalysts has not been extensively explored. This in part reflects the lower activities for acid-catalysed transesterification compared with base-catalysed routes [54] which in turn necessitates higher reaction temperatures to achieve acceptable reaction rates. While their activities are generally low, solid acids have the advantage that they are less sensitive to contaminants than their basic analogues and are able to function well with unrefined feedstocks containing 3–6 wt% FFAs [30]. In contrast to solid bases which require pre-treatments to remove FFA, solid acids are able to esterify FFAs impurities through FAME (see Scheme 7.2) while simultaneously transesterifying the major TAG oil components, all without risk of soap formation.

Vicente et al. [55] compared different types of acid–base catalysts (both homogeneous (NaOH) and heterogeneous (Amberlyst A26, A27)) for FAME synthesis from sunflower oil at 60°C. Unfortunately, under these conditions, the heterogeneous acid catalysts were almost inactive by comparison with NaOH. However, Lopez et al. [56] showed that various solid acid catalysts performed favourably relative to H_2SO_4 in the transesterification of a model C_2 TAG, triacetin. In the latter case, solid acids (inc. Amberlyst-15, sulphated zirconia, Nafion NR 50 and tungstated zirconia) showed reasonable activities at 60°C, indicating that they could act as alternatives to homogeneous acid catalysts without corrosion or saponification problems. The authors also highlighted the importance of internal mass transfer limitations, which impaired the performance of microporous heterogeneous catalysts such as ETS-10 (H) and zeolite H-beta.

Several studies have focused on sulphated zirconia in biodiesel synthesis, due to its strong (super) acidity and regeneration capacity [57–59]. Suwannakarn et al.

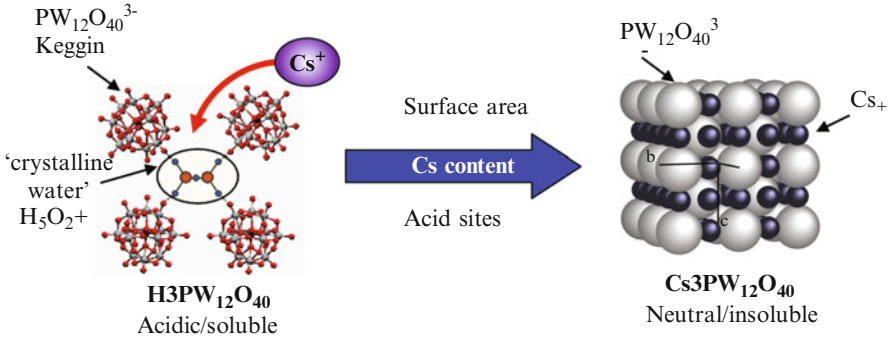

Scheme 7.6 Cs-exchanged $H_3PW_{12}O_{40}$ generates $Cs_xH_{(3-x)}PW_{12}O_{40}$ which is insoluble in polar media. Complete exchange yields neutral $Cs_3PW_{12}O_{40}$ [34]. *Reproduced by permission of the Royal Society of Chemistry*

studied the activity and stability of a commercial sulphated zirconia catalyst for tricaprylin transesterification at high temperature and pressure (120°C, 6.8 atm). While SO_4/ZrO_2 is very active towards tricaprylin, with 84% conversion observed in only 2 h, subsequent re-cycle tests suggest catalyst deactivation occurs due to sulphate loss into solution. Wider use of commercial SO_4/ZrO_2 catalysts may also be limited due to the large energy input (high temperature and pressure) required for both the transesterification reaction and catalyst reactivation.

Low-temperature transesterification requires robust solid acid catalyst with strong acidity. Heteropoly acids are an interesting class of well-defined superacids (materials with $pK_{H+} > 12$) [60], possessing flexible structures and tuneable (super) acidity. However, in their native form, heteropoly acids are unsuitable for biodiesel applications due to their high solubility in polar media [61], and although heteropoly acid dispersion onto high area supports can enhance the number of available acid sites [62–64], this cannot overcome the solubility issue. Ion-exchanged Keggin-type phospho- and silicotungstic acids [65] can however circumvent this problem, as the Cs^+- and NH_4^+-doped variants are found to be insoluble in water [66]. Cs salts of the general formulae $Cs_xH_{(3-x)}PW_{12}O_{40}$ and $Cs_yH_{(4-y)}SiW_{12}O_{40}$ also have the added benefit of dramatically boosted surface areas relative to their fully protonated forms (Scheme 7.6), enabling transesterification at ~ 60°C [67, 68].

Materials with Cs contents of $x = 2.1$–2.4 or $y = 2.8$–3.4 are efficient in both esterification and transesterification reactions. This optimal composition was rationalised in terms of a corresponding maximum in the density of *accessible* surface acid sites. In the case of $Cs_yH_{(4-y)}SiW_{12}O_{40}$, wherein C_4 and C_8 TAG transesterification were compared [68], the absolute reaction rates were faster for the shorter chain TAG, which may evidence either worse miscibility, or slower in-pore diffusion of the longer chain TAG in MeOH, in accordance with previous observations of C_8 transesterification by solid base catalysts [45]. Furthermore, the TOF for the optimum Cs-doped catalyst was greater than that of highly soluble

$H_4SiW_{12}O_{40}$, which operates homogeneously. This latter observation may reflect reports that $Cs_xSiW_{12}O_{40}$ salts are more hydrophobic than the parent $H_4SiW_{12}O_{40}$. Ester activation of the more lipophilic C_8 TAG (the first step in acid-catalysed transesterification) will thus be favoured over the more hydrophobic $Cs_xSiW_{12}O_{40}$ catalyst. Reactant/product polarity and associated mass transport to and from the active acid centres thus play an important role in controlling reactivity, even under homogeneous conditions, and molecular modelling may lead to a better understanding of such phenomena.

The use of solid acid catalysts for oil pre-treatment via FFA esterification would be desirable to avoid costly neutralisation/separation steps and reduce the overall number of processing steps in biodiesel synthesis [69]. Cs-doped [68] heteropoly acids are also very effective catalysts for palmitic acid esterification with methanol. Structure-activity relations were recently mapped for Cs-doped $H_4SiW_{12}O_{40}$ catalysts in palmitic acid esterification [68] which show a high activity for methyl palmitate production, associated with H^+ site accessibility within the stable mesopores. While the application of immobilised heteropoly acids has been reported for esterification [70], care must also be taken to avoid leaching of $H_3PW_{12}O_{40}$ which is very soluble in polar media.

A number of factors need to be considered when developing a solid acid for esterification including water tolerance [21], pore size and dimensionality of the channel system [30]. Mesoporous silicas from the MCM and SBA families have also been examined for FFA esterification. The intrinsically weak acidity of these materials has been enhanced via grafted sulphonic acid groups or surface coatings of SO_4/ZrO_2 to create stable and more active catalysts [71–74]. The synthesis of phenyl and propyl sulphonic acid SBA-15 catalysts, which are found to exhibit comparable activities to Nafion and Amberlyst acidic resins in palmitic acid esterification with methanol [72], is illustrated in Scheme 7.7. Phenyl sulphonic acid-functionalised catalysts were more active than the corresponding propyl systems, correlating with their respective acid strengths.

Further catalyst development and activity enhancement should prove possible through utilising tailored porous solids as high area supports to enhance TAG and FFA diffusion to the active acid/basic groups [75, 76]. Since the discovery of the M41S class of mesoporous materials by Mobil, there has been an explosion of interest in the preparation of such templated porous solids, the synthesis of which has been extensively reviewed [77–80]. In the case of silicates, the most widely investigated mesoporous inorganic supports, network morphology and stability reflect the templating conditions (ionic or neutral surfactant), silica precursor [e.g. fumed silica, tetraethyl orthosilicate (TEOS), Ludox or sodium silicate] and whether hydrothermal synthesis or co-solvents are employed. A general preparative route is shown in Scheme 7.8a in which a surfactant micellar array is used to direct the crystallisation of the SiO_2 framework. Subsequent calcination, to burn out the organic template, yields materials with well-defined meso-structured pores of 2–10 nm and surface areas up to 1,000 $m^2\ g^{-1}$. Macropores can also be introduced if an additional physical template, such as polystyrene microspheres, is added during templating of the mesopore network [81].

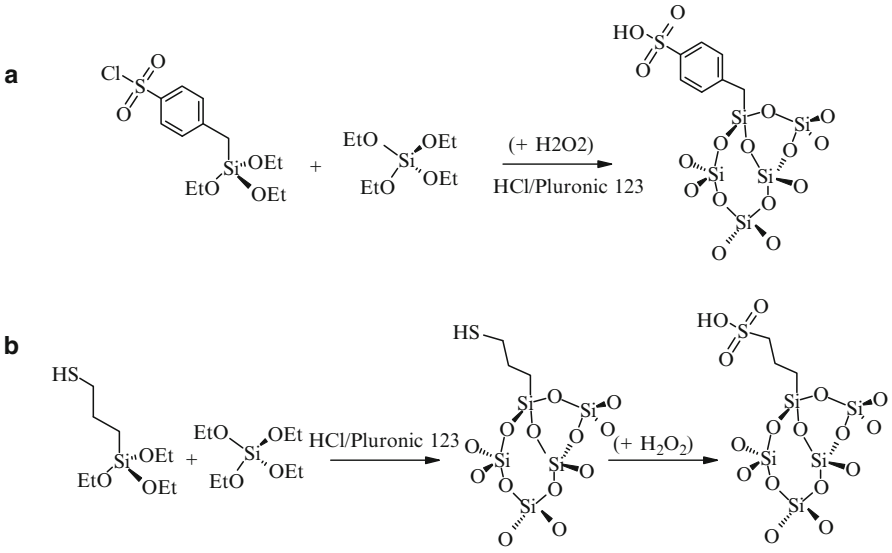

Scheme 7.7 Synthesis of sulphonic acid SBA-15 solid acids from either (**a**) phenyl or (**b**) propyl thiol precursors. Aromatic sulphonic acid centres provide stronger acid sites

Hierarchical macroporous–mesoporous sulphonic acid SBA-15 silicas have been synthesised via such dual-templating routes, employing liquid crystalline surfactants and polystyrene beads [82]. These materials offer high-surface areas and well-defined, interconnecting macro- and mesopore networks with respective narrow size 10 distributions around 300 nm and 3–5 nm. The enhanced mass transport properties of these new bimodal solid acid architectures were found to enhance both transesterification and esterification reactions, when compared to pure mesoporous analogues.

7.3.1.4 Hydrotreating of Plant Oils to Fuels

While transesterification routes to biodiesel are energetically efficient, the final fuel retains the general structure of the TAG hydrocarbon chain. Resulting fuel quality is thus highly dependent on oil source, with higher chain length ($> C_{18}$) molecules detrimental to engine performance. Refinement of renewable oils directly to transportation fuels by hydrotreating is a desirable alternative approach to yield high-grade fuels via processes that can use existing infrastructure from current petroleum-refining processes, thereby reducing capital costs [83]. While petroleum companies have a great understanding of crude fossil oil refining, the different physical properties of renewable oils present a new challenge for catalyst design and urgently require new classes of catalyst compatible with these viscous, bulky substrates. A combination of low sulphur content and a host of different impurities including sterols, phospholipids and a range of inorganics (e.g. Ca, Fe) [84] within

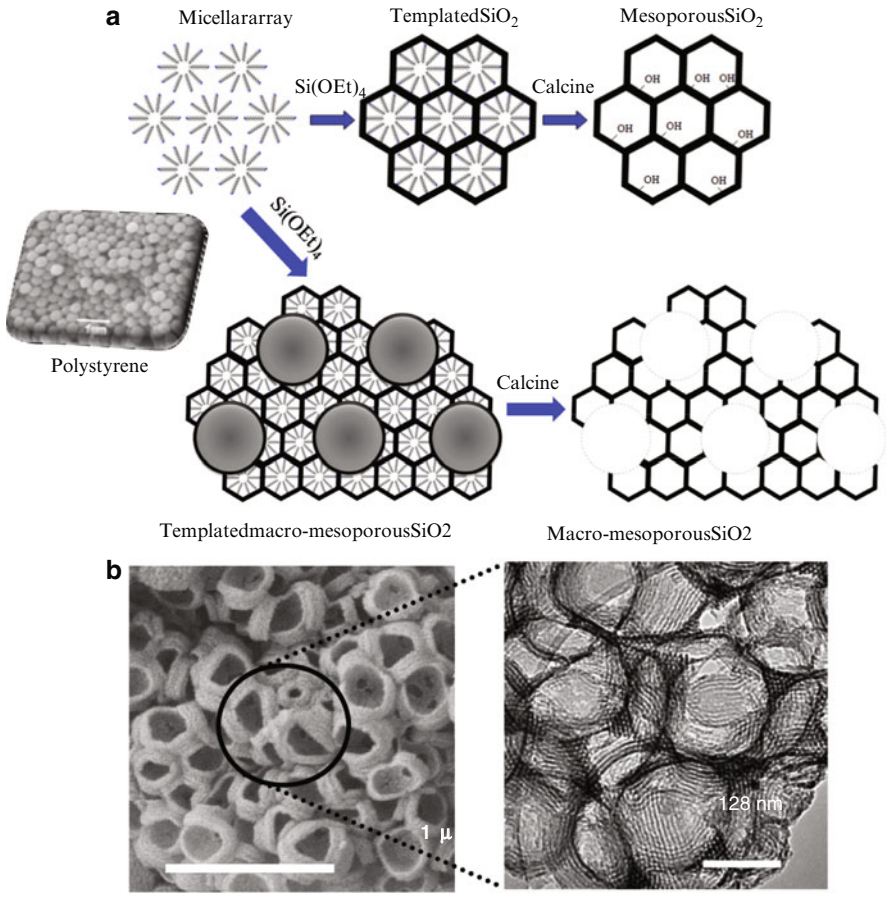

Scheme 7.8 (**a**) Liquid crystal templating route to form mesoporous silica and combined physical templating method using polystyrene microspheres to introduce a macropore network; (**b**) SEM of macroporous–mesoporous SBA-15 showing macropore network and TEM showing interconnecting mesopores

bio-oils necessitate development of a new family of catalysts that are either tolerant to these elements, or can selectively remove them from the feed. Hydrotreating thus utilises all the TAG for fuel [85] offering more flexibility in hydrocarbon chain length and fuel quality, while also being able to utilise existing infrastructure at petroleum refineries [86].

Hydrotreatment of TAGs proceeds by two reaction pathways (Scheme 7.9) [87]: hydrodeoxygenation (HDO) to yield *n*-alkanes, H_2O and propane or hydrodecarboxylation (HDC) which yields hydrocarbons with one carbon atom less than in the original fatty acid, with CO, CO_2 and propane formed as by-products. Initial investigations have focused on the use of conventional hydrotreating catalyst such as sulphided $NiMo/Al_2O_3$ catalysts used for hydrodesulphurisation [83, 88, 89].

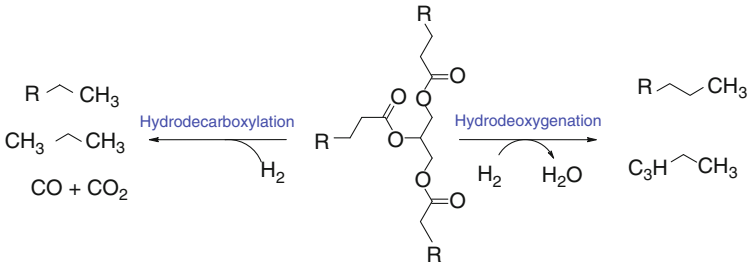

Scheme 7.9 Hydrotreating routes to convert triglycerides to alkanes

However, S loss from the catalyst is problematic, and generally, such catalysts are not optimised for deoxygenation processes. Many of the new catalysts investigated are based around Pd, Pt and Ru systems and are similar to those discussed in Sect. 3.3 for hydrotreating of bio-oil from lignocellulose. For example, Pt–Re supported on a range of zeolite supports including USY and HZSM-5 [90] has been used to hydrotreat vegetable and Jatropha oil to form $C_{15}-C_{18}$ alkanes, with Pt/USY found to offer the highest conversions of vegetable oil. Only ZSM-5-supported catalysts were investigated for Jatropha oil treatment, with Re found to promote hydrotreating of both Pt and Pd/ZSM-5 systems. Pd−Re/H-ZSM-5 was found to exhibit higher selectivity to C_{18} and C_{17} hydrocarbons than Pt/ZSM-5, indicating that C−C bond cleavage does not occur readily over Pd-based catalysts, and thus, HDO of the carboxyl group is favoured. In contrast, Ru-based catalysts exhibit high activity for C−C bond cleavage leading to a higher selectivity to methane and shorter chain C_{15} and C_{16} hydrocarbons. Comparison of 20 wt% Ni/C, 5 wt% Pd/C and 1 wt% Pt/C catalysts in the deoxygenation of tristearin, triolein and soybean oil has also been made [91]. Ni catalysts were found to give near quantitative conversion of the TAG with high yields of linear C_5 to C_{17} alkanes and alkenes obtained. Unsaturated fatty acid chains were found to be more sensitive towards cracking, yielding lighter hydrocarbons. In contrast, carbon-supported Pd or Pt catalysts showed lower activity for both TAG deoxygenation and cracking of the fatty acid chains.

7.3.2 Non-fuel Applications of Oleochemicals

7.3.2.1 Overview

TAGs and FFA from plant oils and animal fats contain a high degree of functionality making them ideal candidates for synthesising a wide range of chemical intermediates used in the production of surfactants, lubricants and personal care items. The reduced toxicity and higher biodegradability of saturated and polyunsaturated fatty acids also make them highly desirable alternatives to mineral oil lubricants. As with biodiesel, the use of soluble acid or base catalysts in the reaction of TAGs is problematic as it leads to low purity products. Pharmaceutical grade

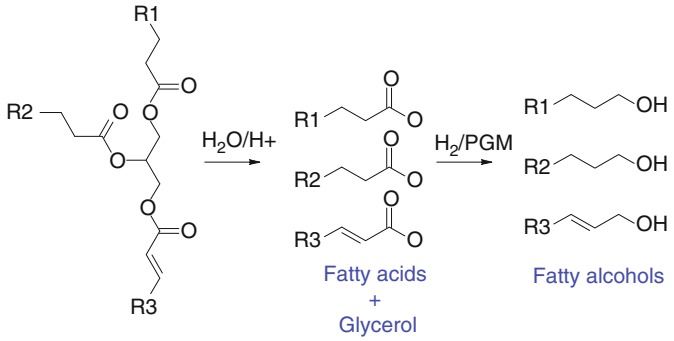

Scheme 7.10 Conversion of triglycerides to FFA and fatty alcohols

products are often prepared by thermal hydrolysis >210°C in the absence of catalysts; thus, the development of heterogeneous catalysts for non-fuel applications of plant oils and animal fats is also of great interest. This section will discuss the application of heterogeneous catalysts in transforming TAGs, FFA and glycerol into intermediates for fine and speciality chemicals.

7.3.2.2 Triglyceride and Fatty Acid Transformations

Current routes to obtain fatty acids for these applications involve the use of superheated steam to hydrolyse the ester bond in TAGs obtained from vegetable oils and/or animal fats (Scheme 7.10). The technology required to generate and handle supercritical and near critical water not only involves high capital and operating costs, but can also result in degradation of polyunsaturated fats, necessitating further purification by distillation [92].

A continuous, heterogeneously catalysed process to generate FFAs would thus be highly desirable. Fatty acids are readily obtained by hydrogenolysis of TAGs using basic or acid catalysts, including ZnO, CaO, MgO, sulphonated resins and heteropoly acids [93]. $H_3PW_{12}O_{40}$-impregnated ion-exchange resins were found to be most active [94] when compared to acid resins, $Cs_{2.5}H_{0.5}PW_{12}O_{40}$ and aluminosilicates. However, care should be taken when considering these catalysts given the high solubility of heteropoly acids in polar media and the fact that no leaching studies were reported. Tungstated zirconia (WZ) and a Nafion/silica composite (SAC-13) [95] have also been employed for the hydrolysis of tricaprylin and are found to operate at 110−150°C. WZ is initially found to be more active than SAC-13; however, both catalysts attain the same limiting TAG conversion of ~16–20% after 2-h reaction. Catalyst deactivation was attributed mainly to the adsorption and accumulation of organic species on the catalyst surface leading to catalytic site blockage. While WZ could be reactivated by calcination, however, this is not an option for SAC-13 due to poor thermal stability of the polymer component. Kinetic modelling of the hydrolysis reaction on WZ revealed it

proceeded via an Eley–Rideal single-site mechanism, with adsorbed TAG reacting with bulk-phase water [96].

Hydrogenation of unsaturated fatty acids and esters to the corresponding alcohols also finds application in the synthesis of surfactants and plasticisers and requires selective hydrogenation of COOH while retaining the C=C functionality (Scheme 7.10). A range of supported Ru, Pd and Rh catalysts have been employed for the hydrogenation of unsaturated fatty acids. Addition of Sn is found to enhance the selectivity of both Ru/Al_2O_3- [97] and Rh/Al_2O_3-catalysed [98] hydrogenation of fatty esters, methyl oleate, methyl laurate and methyl palmitate into the corresponding unsaturated alcohol. In both cases, the major side reaction involves formation of a heavy ester by-product via transesterification of the original ester with the alcohol and is found to occur in the absence of catalyst at the high temperatures (>200°C) employed. Catalysts prepared on low-surface area supports (e.g. α-Al_2O_3) were found to exhibit higher selectivity towards the alcohol [98], which reflects poor in-pore diffusion and increased side reactions in more microporous supports such as γ-Al_2O_3. The selective hydrogenation of methyl oleate to the corresponding unsaturated alcohol was achieved with $Ru–Sn–B/Al_2O_3$ [99], in which an optimum yield of alcohol was obtained for Sn:Ru ratios of 4:1. The reaction pathway is reported to be complex, involving a number of side reactions including hydrogenation of methyl oleate into oleyl alcohol, transesterification between methyl oleate and oleyl alcohol and hydrogenation of the resulting heavy ester back into oleyl alcohol. At low Sn content, formation of the saturated ester (methyl stearate) results from non-selective reduction of the C=C bond. The authors suggest incorporation of SnO_x inhibits C=C hydrogenation by favouring adsorption of the ester at Sn sites via the C=O group, thus orienting the molecule to increase selective hydrogenation to the alcohol.

Acetalisation of glucose with fatty alcohols is another important use of oleo feedstocks and is a desirable method to generate alkyl glucoside building blocks for the preparation of biodegradable non-ionic surfactants, which have a low degree of skin and oral toxicity. Typical reactions can give a complex mixture of products containing glucofuranoside or glucopyranoside rings and various amounts of oligomers (Scheme 7.11).

Acetalisation of glucose with butanol has been investigated as a model reaction over zeolites [100] and MCM-41 [101]. Zeolite crystal size is found to have a major effect on the activity, with diffusional effects limiting reaction rates over crystallite sizes larger than 0.35 μm. Activity, selectivity and tendency towards deactivation can however be controlled with the Si/Al ratio and surface hydrophobicity. The use of mesoporous MCM-41 solid acids is found to increase catalyst activity; however, development of larger pore acid catalysts would have significant additional benefits by reducing side reactions through increased in pore diffusion.

Fatty acids may also contain varying degrees of unsaturation, giving added functionality for conversion to, for example, epoxides or diols. The epoxidation of FAME from sunflower oil using *tert*-butyl hydroperoxide (TBHP) can be effectively catalysed using Ti-MCM-41 and Ti-silicates [102, 103]. Mesoporous niobium organosilicas have also been reported to effectively epoxidise methyl

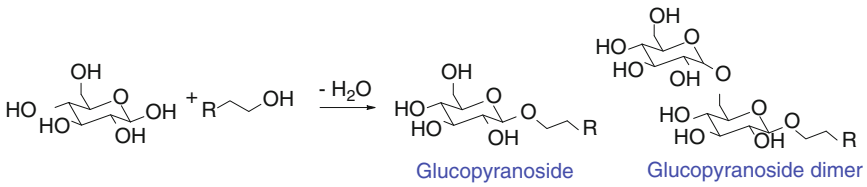

Scheme 7.11 Acetalisation of glucose with fatty alcohols

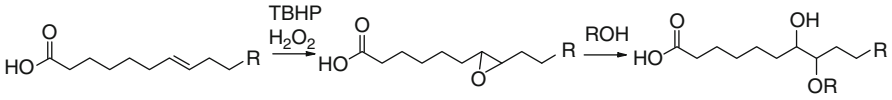

Scheme 7.12 Epoxidation of unsaturated FFA

oleate with H_2O_2 [104] (Scheme 7.12). Epoxidation of the C=C bond present in the fatty acid chains of TAGs present in soybean oil has also been reported using H_2O_2, acetic acid and acid-exchange resins [105].

7.3.2.3 Glycerol Utilisation

Glycerol is formed in vast quantities as a by-product of the biodiesel process. Current biodiesel processes generate dilute aqueous solutions of glycerol which are heavily contaminated with inorganic salts, so purification for its use in food, pharmaceutical or cosmetic applications is not cost effective. However, with a heterogeneously catalysed biodiesel process, the resulting glycerol will be of higher purity [16] and should be considered as a plentiful chemical feedstock. Glycerol can undergo a range of reactions including oxidation, esterification, etherification, oligomerisation and hydrogenolysis to yield to a range of valuable chemicals [106–110] shown in Scheme 7.13. The conversion of glycerol is however challenging as it is highly viscous and hydrophilic, resulting in diffusion and miscibility problems. Furthermore, all three hydroxyl groups have similar pK_a (~13.5) making selective catalytic transformation particularly demanding.

Oxidation alone can yield a wide range of products including dihydroxyacetone, hydroxypyruvic acid, glyceric acid and tartronic acid (2-hydroxypropanedioic acid). C_2 carboxylic acids, glycolic acid and oxalic acid can also form; thus, catalysts for the selective oxidation of glycerol are highly sought after [111]. Supported Pd, Pt and Au and corresponding bimetallic variants, which are capable of using molecular oxygen, are attracting much attention. The pH of the reaction is found to be critical for controlling selectivity towards reaction at the primary or secondary –OH position. Dihydroxyacetone [112] and hydroxypyruvic acid [113] are found to form under acidic conditions when using Pt and Pd catalysts, while under more basic conditions, glyceric acid is favoured [114]. Pd/C catalysts are also found to be promoted by Bi, with the rate of glucose oxidation found to increase by a factor of 20 compared to Pd/C alone [115, 116].

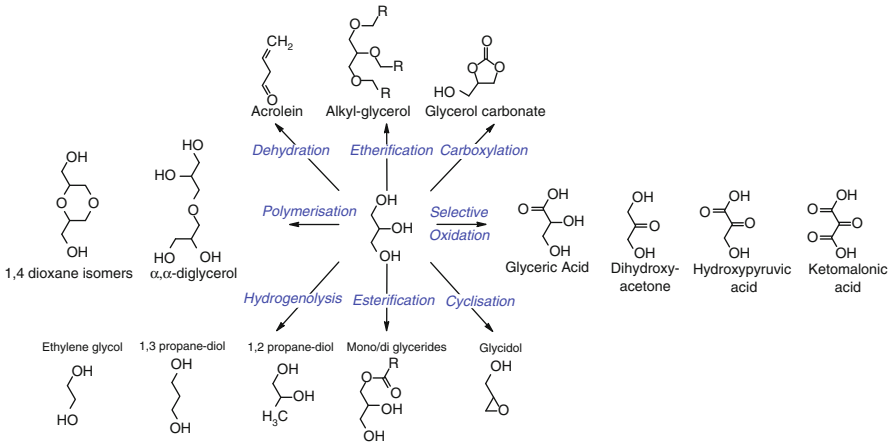

Scheme 7.13 Reaction products from catalytic conversion of glycerol

Comparison of 2.5 wt%Au–2.5%Pd/TiO_2 and 2.5%Au–2.5%Pd/C catalysts revealed that TiO_2-supported catalysts were more active for glycerol oxidation [109]. At low conversions, the TiO_2-supported system is more selective than the carbon-supported catalyst for glyceric acid formation. However, as the reaction proceeds, selectivity to tartronic acid increases at the expense of glyceric acid, indicating a consecutive over-oxidation reaction occurs. In contrast, the carbon-supported catalyst appears to maintain a steady selectivity towards glyceric acid, indicating it is less prone to subsequent oxidation.

Glycerol dimerisation has been investigated over alkali earth oxide solid base catalysts [117], with glycerol conversion found to correlate with increased catalyst basicity in the order MgO < CaO < SrO < BaO. High (>90%) selectivity to di- and trimers is observed over CaO, SrO, and BaO, with no significant acrolein formation observed. Lewis acidity was also found to affect catalytic activity, suggesting Lewis acid sites at the M^{n+} centre play an important role in the catalytic cycle as illustrated in Scheme 7.14. Colloidal CaO particles of about 50–100 nm were found to form during the reaction which are highly active for etherification.

Acid-catalysed transformations of glycerol can also be used for its dehydration to acrolein, as well as for etherification and esterification reactions with short chain alcohols, alkenes or carboxylic acids to generate esters and ethers for utilisation as fuel additives [118]. Silica-supported sulphonic catalysts were found to be promising catalysts for esterifying glycerol with acetic acid [119], which were found to form di- and triacylglycerols with comparable activity to H_2SO_4, Amberlyst 15 and Nafion–silica composite SAC-13 solid acids. Mono- or diglycerides formed during esterification of glycerol with fatty acids are also of interest for cosmetic applications and have been synthesised using a range of solid acid catalysts including H-beta, H-USY, sulphonic acid silicas [71, 120, 121] and ion-exchange resins [122].

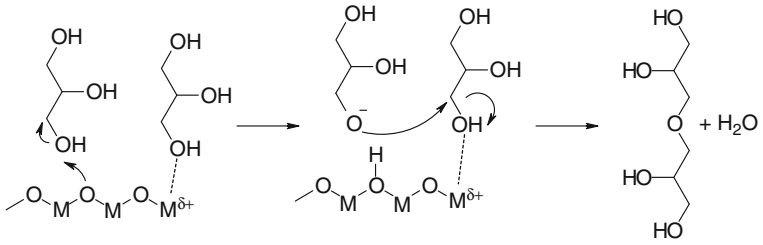

Scheme 7.14 Role of Lewis base and acid sites in the dimerisation of glycerol over solid-base catalysts

The synthesis of monoglycerides can also be achieved by the base-catalysed transesterification of fatty acid methyl esters and glycerol. Transesterification of glycerol with methyl stearate [123] has been investigated over MgO, CeO_2, La_2O_3 and ZnO. While the order of activity was found to follow $La_2O_3 > MgO >> ZnO > CeO_2$, which is accord with the trend in basicity, selectivity to the monoglyceride was independent of the catalyst type and only dependent on conversion. Typical selectivities at 80% conversion were similar to that obtained from a homogenous basic catalyst, with 40% monoester, 50% diester and 10% triester produced. These observations were attributed to catalysts being essentially non-porous and thus unable to impart any "shape selectivity" on the reaction pathway. If however porous catalysts are used, namely, Mg-doped MCM, then increased selectivity to the monoglyceride could be achieved, with transesterification of glycerol with methyl dodecanoate found to yield glycerol monolaurate with a selectivity and yield of ~80% [124]. Selectivity to the monoglyceride was found to depend on catalyst pore size and hydrocarbon chain length of the methyl ester. Hydrotalcites can likewise be used to produce monoglycerides from reaction of oleic acid methyl ester with glycerol [125]. In this instance, rehydrated hydrotalcite catalysts containing Brönsted basic sites are more active and selective towards monoglyceride formation than the corresponding calcined Lewis basic variant.

Reaction of isobutene or isobutanol with glycerol over sulphonic acid resins and zeolites [126–128] can be used to produce glycerol ethers. Isobutanol was however found to be a problematic reagent to due to water formed during reaction deactivating the solid acid catalyst. While early studies reported highest conversions of glycerol over H-β zeolite, pore-size constraints limited the formation of tri-tertiary-butyl glycerol (TTBG). Macroreticular resins such as Amberlyst 35 were found to be very effective catalysts for etherification with isobutylene. The large pore diameters of these resins were found to facilitate 100% conversion of glycerol, with 92% selectivity to di- and tri-ethers. Reaction selectivity was found to be highly sensitive to reaction temperature, with formation of undesirable isobutylene dimers (which would require separating from the fuel additive), observed to increase with temperature [129]. Mesoporous sulphonic acid silicas are found to be superior to sulphonic acid resins [130] in the etherification of glycerol with isobutylene. Arene sulphonic acid-modified SBA-15 silica

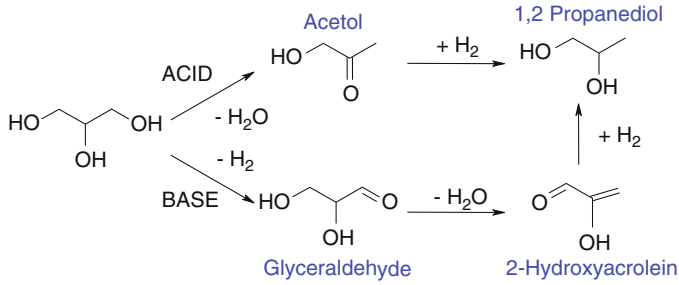

Scheme 7.15 Effect of acid or basic conditions on hydrogenolysis pathways

(Ar-SO_3H-SBA-15) was found to give the highest production of di- and tri-tert-butyl glycerol, with 92% selectivity to these two products observed, with no undesirable oligomerisation products detected.

Etherification of glycerol with longer chain alkenes can be used to generate intermediates for the pharmaceutical industry, agrochemicals or synthesise surfactants [106, 131]. Etherification of glycerol with 1-octene 1-dodecene and 1-hexadecene has been investigated over Amberlyst resins and various zeolites including H-Y, H-Beta and ZSM-5 [132]. Hydrophilicity and pore structure were the critical parameters identified as controlling catalyst performance, with H-β observed to be the most selective zeolite, which could also be successfully be recycled. Etherification of glycerol with alkyl alcohols, olefins and dibenzyl ethers has also been reported using a range of sulphonated carbons, resins and sulphonic acid silicas [133]. Conventional syntheses of mono-alkyl-glyceryl ethers use toxic reagents such as epichlorohydrin, 3-chloro-1,2-propanediol or glycidol; thus, the use of solid acids offer a desirable more benign synthetic route.

The selective hydrogenolysis of glycerol in the presence of metallic catalysts and hydrogen can be used to synthesise 1,2-propanediol (1,2-PDO), 1,3-propanediol (1,3-PDO) or ethylene glycol (EG) (Scheme 7.15). Typical reactions have employed a range of metal catalysts including Raney Ni, Pd, Ru, Rh, Cr, Au and Ir [107] which operate at 453–513 K and hydrogen pressures of around 6–10 MPa. Ni, Pt, Cu and Cu–Cr catalysts are all selective for the conversion of glycerol to propylene glycol. In contrast, Ru and Pd exhibit competitive hydrogenolysis of C–C and C–O bonds leading to formation of shorter chain alcohols and gases. Ru/C catalysts are found to be structure sensitive for glycerol hydrogenolysis, with activity found to increase with Ru crystallite size [134], which was attributed to the tendency for small particles become heavily oxidised. Selectivity towards C–O or C–C bond cleavage is however found to be independent of particle size. Copper-based catalysts are poor for C–C cleavage while being efficient catalyst for C–O bond hydrogenation and dehydrogenation, so generally show highest selectivity towards propanediol formation. Both Raney Cu and Cu/C catalysts [135] are however found to deactivate, due to a combination of sintering, oxidation and loss of Cu(I)OH. A detailed study of Cu/MgO catalysts found them to be efficient for hydrogenolysis of glycerol to 1,2-PDO [136], with catalyst activity increasing with decreased Cu particle size.

Co-precipitated samples with 15 wt% Cu, having particle sizes ~4 nm, were found to exhibit highest activity and selectivity. Addition of Cr is found to promote Cu hydrogenolysis catalysts, with enhanced yields of propanediol (>73%) observed at low H_2 pressures [137]. The mechanism of promotion was proposed to involve the formation of $CuCr_2O_4$ spinel species containing tetrahedral Cu^{2+} sites which helps stabilise highly dispersed Cu clusters [138].

The reaction pathway for glycerol hydrogenolysis is pH dependent with acid or base conditions directing dehydration or reduction pathways of the hydroxyl group respectively (Scheme 7.15). This is illustrated by studies of the effect of support (γ-Al_2O_3, SiO_2, ZrO_2) and Ru precursor used to synthesise Ru-based catalysts. These studies indicate hydrogenolysis activity correlates with acid strength of the support which decreases from $Ru(Cl_3)/\gamma$-Al_2O_3 > $Ru(NO_3)/ZrO_2$ > $Ru(NO_3)/\gamma$-Al_2O_3 > $Ru(Cl_3)/SiO_2$ > $Ru(NO_3)/SiO_2$. While $Ru(Cl_3)/\gamma$-Al_2O_3 was most active for glycerol conversion, selectivity to 1,2-PDO was poor due to sequential hydrogenolysis to 1-propanol [139]. Selectivity to 1,2-PDO was found to follow the order $Ru(NO_3)/SiO_2$ (65%) > $Ru(NO_3)/ZrO_2$ (62.4%) > $Ru(Cl_3)/SiO_2$ (54.6%) > $Ru(NO_3)/\gamma$-Al_2O_3 (52%) > $Ru(Cl_3)/\gamma$-Al_2O_3 (39.4%). The use of chloride precursors was believed to have a detrimental effect on the selectivity of final Ru catalysts due to retention of Cl^- ions by the support.

The effect of acidity on hydrogenolysis reactions has also been investigated through use of Ru/C in conjunction with an acidic Amberlyst resin [140] to allow tandem dehydration + hydrogenation (i.e. hydrogenolysis) of glycerol under mild reaction conditions (393 K, 8.0 MPa). While promising results were obtained, the undesired formation of cracking products was rather high over Ru/C, with the dehydration of glycerol to 1-hydroxyacetone being catalysed by the acid catalysts. Care must be taken however with this approach as the resins were found to decompose under the hydrolysis reaction conditions. When coupling a range of inorganic solid acid co-catalysts with Ru/C, the rate of hydrogenolysis was found to follow the order Nb_2O_5 > $H_3PW_{12}O_{40}/ZrO_2$ > $Cs_2HPW_{12}O_{40}$ > $Cs_2HPW_{12}O_{40}/ZrO_2$ [141]. Ru-doped (5 wt%) $Cs_{2.5}H_{0.5}[PW_{12}O_{40}]$ also functions as an effective bifunctional catalyst for glycerol hydrogenolysis to 1,2-PDO, offering 96% selectivity to 1,2-PDO at 21% glycerol conversion [142].

The activity of Ru/C, Pt/C, Au/C and bimetallic PtRu/C and AuRu/C [143] has been compared for glycerol hydrogenolysis under neutral conditions. Ru/C is found to be more active than both Pt/C and Au/C, the latter being completely inactive for the hydrogenolysis of glycerol. Metal-catalysed C–C cleavage was found to be favoured over Ru leading to ethylene glycol formation, whereas over Pt [144] propanediol production was predominant. Although monometallic Pt and Ru exhibit different activities and selectivities in hydrogenolysis, the bimetallic PtRu catalyst showed a similar activity to Ru/C. Thus, it was proposed that the presence of Pt provided sites for dissociative adsorption of H_2, while C–C cleavage occurred over Ru sites. In the presence of base, lactate and propylene glycol formation was favoured; however, the overall product selectivity for the bimetallic catalysts were quantitatively similar to those for Ru/C alone, indicating no apparent benefit of using bimetallic systems in this instance. However, subsequent studies revealed that

the method used to prepare bimetallic catalysts is critical to ensure phase separation does not occur. Ru–Cu bimetallic catalysts prepared via an ionic liquid-assisted route have been shown to exhibit superior performance to conventionally prepared materials [145], with a 3:1 Ru:Cu catalyst found to give 100% glycerol conversion and 85% yield of 1,2-PDO. The presence of the ionic liquid is proposed to inhibit nanoparticle sintering during reaction, while conventional Ru–Cu particle clusters are found to increase in size to 50 nm after reaction and the IL-stabilised particles remain unchanged at 5–8 nm.

Sulphonic acid silicas have been utilised for the acetalisation of glycerol with acetone to yield 2,2-dimethyl-1,3-dioxolane-4-methanol, which can be used as a fuel additive. Arene sulphonic acid-functionalised silica exhibits comparable activity to Amberlyst-15, with reaction using both technical (91.6 wt%) and crude (85.8 wt%) glycerol found to result in 84 and 81% conversion, respectively. For refined and technical glycerol, the catalysts could be reused, without any regeneration treatment, up to three times while maintaining the initial high activity. The high sodium content in crude glycerol however deactivates the sulphonic acid sites by cation exchange; this is, however, readily reversed by simple acidification of the catalyst after reaction [146].

Glycerol carbonate has potential as a new precursor for incorporation into polymeric materials such as polycarbonates and polyurethanes [147]. While direct addition of CO_2 would be desirable, most approaches use a reagent, such as urea, or an organic carbonate as a carbonating agent (Scheme 7.16). The reaction of ethylene carbonate and glycerol using supercritical CO_2 coupled with resin catalysts and zeolites [148] reveals that basic resins give the best conversions of glycerol. Detailed investigation of a range of solid bases [149] (CaO, MgO, CaO/Al_2O_3, Al–Mg and Al–Li hydrotalcites) reveals that when using ethylene glycol carbonate as the carbonating reagent, strong bases and low temperature are required in order to achieve highest selectivity to glycerol carbonate. CaO/Al_2O_3 was found to offer high glycerol conversions with 98% selectivity to glycerol carbonate while operating at low (0.5 wt%) catalyst loadings. More recently, the application of uncalcined Mg–Al hydrotalcite catalyst [150] revealed glycerol carbonate could be synthesised from glycerol and dimethyl carbonate to give 98% glycerol carbonate yield under solvent-free conditions.

The use of basic ZnO or MgO catalysts has also been employed to synthesise glycerol carbonate from urea as the CO_2 source [151]. A number of issues need to be addressed for this system, however, including the recovery of NH_3 and stability of the catalyst, with common single component bases often found to dissolve under reaction conditions. γ-Zirconium phosphate has also been reported as an effective heterogeneous catalyst for glycerol carbonate formation using urea, with 80% of conversion of glycerol under mild reaction conditions and low catalyst loadings of ~0.6–1.5 wt% [152]. Similarly, it has recently been discovered that bifunctional acid–base catalysts such as Zn–Al-mixed oxides are also stable catalysts for glycerol carbonate formation. A mechanism is proposed in which Lewis acid sites activate the carbonyl of urea, while the conjugated base site activates the hydroxyl group of the glycerol [149].

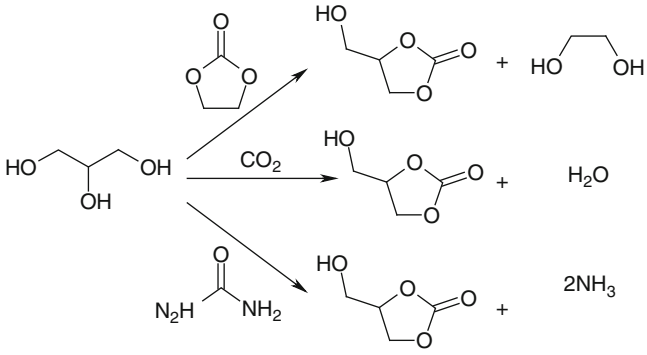

Scheme 7.16 Routes to synthesise glycerol carbonate from ethylene glycol carbonate, CO_2 or urea

Direct conversion of glycerol and CO_2 to glycerol carbonate has so far only been reported using homogeneous tin catalysts [153, 154] such as *n*-$Bu_2Sn(OMe)_2$, *n*-Bu_2SnO or $Sn(OMe)_2$, with the most active catalysts for glycerol conversion found to be *n*-$Bu_2Sn(OCH_3)_2$. The use of Sn-exchanged mesoporous inorganic [155, 156] or polymeric materials [157, 158] would seem a logical progression to improve product separation in this system.

7.4 Cellulosic and Lignocellulosic Feedstocks

7.4.1 Thermo and Biochemical Conversion of Lignocellulose

There are a number of ways to utilise lignocellulosic biomass for fuels and chemicals synthesis, ranging from sugar fermentation to ethanol, gasification to syngas (CO/H_2) and liquefaction or pyrolysis to form bio-oil (Scheme 7.17).

In the biochemical route, sugars extracted from raw lignocellulosic material by acid hydrolysis are fermented through to platform chemicals and ethanol. In the thermochemical route, raw material is either pyrolysed or gasified through bio-oil [159] or syngas, respectively, which can be further transformed into fuels. Pyrolysis involves heating the biomass feedstock in the absence of air, to convert ~50–90% of the biomass energy into a liquid form. Fast pyrolysis favours liquids, whereas slow pyrolysis tends to produce more solid material which can be used as a solid fuel [160]. Syngas formed from gasification can be used in well-established catalytic processes such as Fischer–Tropsch and methanol synthesis routes to convert CO/H_2 mixes to fuels and methanol. While this initial gasification/pyrolysis step is energetically costly, less initial biomass processing is required, so with efficient heat recovery modules, these routes are attractive for their compatibility with existing industrial processes.

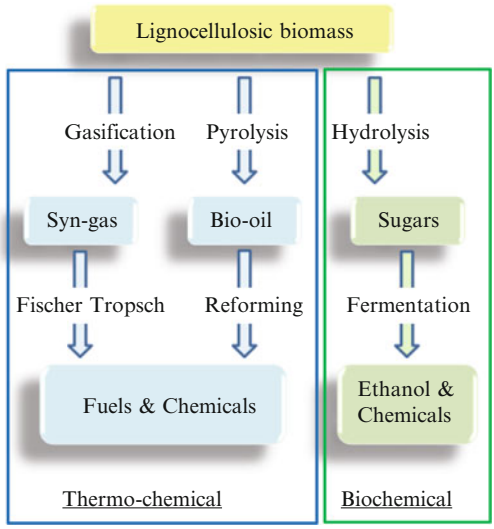

Scheme 7.17 Biochemical and thermochemical routes for the conversion of lignocellulosic biomass to chemicals and fuels

While bio-oil is a promising renewable energy source, it cannot be used directly as a fuel due to its high oxygen content, acidity and instability [161]. Bio oil is comprised of a aqueous, acidic (containing 15–30 wt% H_2O, pH 2.5) highly oxygenated complex mixture of aldehydes, alcohols, aromatics, esters, sugars and phenolic compounds [162–164] (Scheme 7.18) which require converting to alkanes before being used as a fuel.

The composition of bio-oil is dependent on the source of biomass with the presence of inorganic impurities affecting the pyrolysis product distribution. Pyrolysis of pure cellulose tends to produce levoglucosan in high yields (~60%), via an intermolecular condensation of two adjacent glucose units; however, glycolaldehyde is found as the major product if K, Li or Na is added during the pyrolysis step [165]. Refinement of bio-oils directly to transportation fuels by hydrotreating is a particularly desirable approach which could yield high-grade fuels via processes akin to those used in current petroleum refining. The high energy density and liquid nature of these oils make them desirable feedstocks for use in existing infrastructure thereby reducing capital costs [83, 85]. Bio-oils have lower sulphur and higher oxygen contents than conventional petroleum feeds; thus, current sulphided hydrotreating catalysts used for refining fossil fuels may not be suitable, and new catalyst technology for bio-oil refining is required.

The use of enzymes in the biochemical route allows more selective conversion of biomass via fermentation. Recent reports have identified several building block chemicals that can be produced via biological or chemical conversion of biomass. Examples of these include ethanol (C_2), glycerol (C_3), fumaric acid (C_4), xylitol (C_5), and sorbitol (C_6), which are all highly oxygenated [typically $C_x(H_2O)_y$] and thus very different to traditional hydrocarbon sources from petrochemical sources. The use of biomass-derived chemicals represents an area with extensive R&D

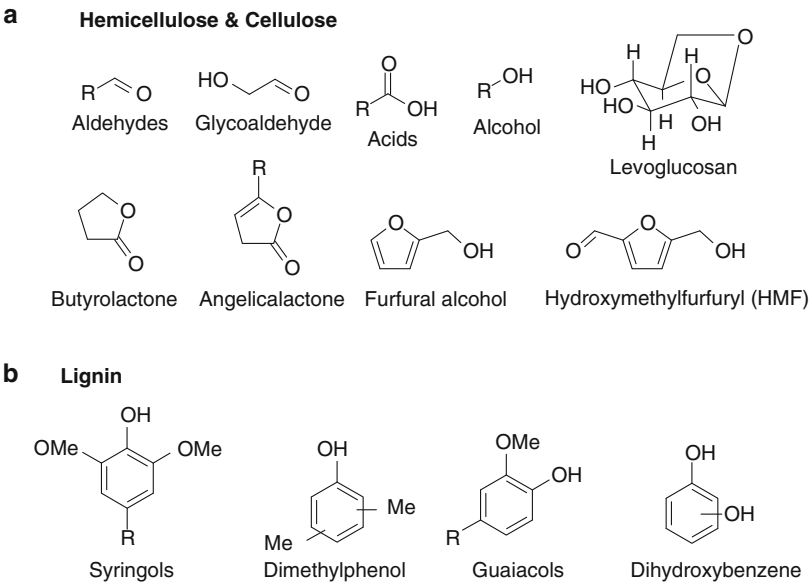

Scheme 7.18 Major components of bio-oil resulting from fast pyrolysis of (**a**) hemicellulose, cellulose and (**b**) lignin components of lignocellulosic biomass

potential for the development of a renewable feedstock-based technology platform. However, the presence of high percentages of pentoses from hemicelluloses in extracted biomass feeds can prove problematic for the biochemical route, as unlike hexoses, such as glucose, pentoses are difficult to ferment. Another difficulty/challenge for use of chemicals obtained via fermentation is that they also produced as dilute aqueous mixtures. It is not energetically efficient to distil these feeds, so catalysts compatible with aqueous media are required for the subsequent conversion of these impure feedstocks. The technology required for handling biomass-derived building blocks will thus be very different and requires reverse chemical transformations, whereby these highly functional molecules are "deoxygenated" to reach the target molecule rather than being "oxygenated" as would be the case starting from crude oil resources. Scheme 7.19 illustrates a possible scenario of adipic acid synthesis, where current petrochemical routes follow the selective oxidation of cyclohexane, whereas a biomass route starting from glucose would require selective reduction. To facilitate a transition from a society reliant on petrochemical-derived products, new classes of catalyst are urgently required which are compatible with these hydrophilic, bulky substrates. Improvements and innovations in catalyst and processes design are thus required for the production of high-value chemicals from these biomass-derived building blocks.

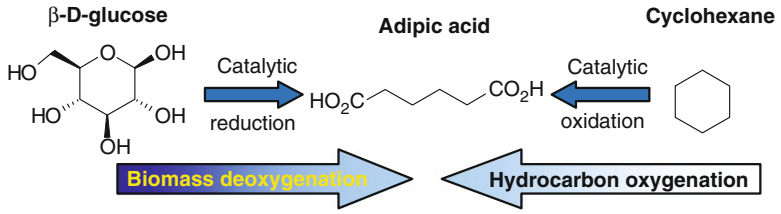

Scheme 7.19 Routes to adipic acid from biomass or petroleum feedstocks

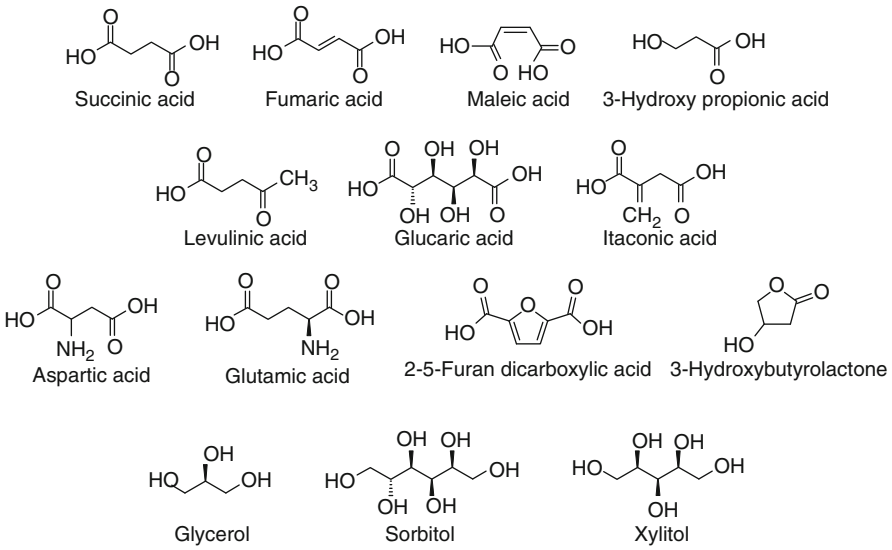

Scheme 7.20 Possible platform chemicals produced from biomass

7.4.2 Platform Chemicals

The US DoE identified 12 Platform Chemicals that can be produced from sugars via chemical or biochemical transformation of lignocellulosic biomass (Scheme 7.20) [166]. When generated from fermentation processes, these molecules are often present at low concentrations (typically $<10\%$) in aqueous solutions in the presence of other polar molecules. Purification of such fermentation broths is particularly difficult and not energetically feasible; thus, an ability to directly transform the aqueous solution is desirable [167]. As outlined above, there is a need to therefore develop catalysts, capable of performing organic chemistry in water, that are resistant to impurities present in the fermentation broth [168] while selectively transforming these platform molecules to a wide range of useful chemical feedstocks [169].

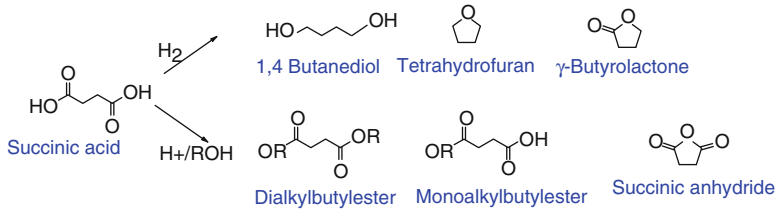

Scheme 7.21 Selected acid-catalysed or hydrogenation products of succinic acid

Such catalysts will need to be hydrophilic, stable over a wide pH range and resistant towards leaching under reaction conditions [170]. The porosity of the catalyst is also important to enable diffusion of bulky, viscous reactants to the active sites; support materials such as those described earlier in Scheme 7.8 may be promising materials to generate catalysts for converting platform chemicals. The use of organic–inorganic hybrid catalysts may also be interesting as these allow the hydrophobicity of the catalyst to be tuned: by changing the hydrophobicity, it is possible to tune the adsorption properties of polar molecules [171]. Mesoporous carbons [172] may also prove suitable for use with biomass conversion, as carbon supports tend to be highly resistant to acidic and chelating media. To transform the functional groups on platform chemicals, catalysts capable of performing dehydration, hydrogenolysis (already discussed in the context of glycerol utilisation) and hydrogenation will be required. Suitable catalysts will thus contain acid sites or even be bifunctional having acid sites for dehydration and metallic sites to initiate hydrogenation catalysis. Corma et al. have produced an extensive review of current proposed methods for transforming platform molecules into chemicals [18], many of which employ conventional homogeneous reagents or commercial catalysts. There is thus enormous scope for research and development into designing improved heterogeneously catalysed processes that are tailored for use with biomass-derived feedstocks.

A number of reports have described pathways to obtain important chemical intermediates from platform molecules [169]. Succinic acid is proposed to be a valuable platform chemical, from which a range of chemical intermediates can be derived, as illustrated in Scheme 7.21 for acid-catalysed esterification, or metal-catalysed reductions. Carbon-based solid acid catalysts have proven effective materials for the esterification of succinic acid with ethanol [173, 174]. New biopolymers produced from polyesters, polyamides and polyesteramides which can all be derived from succinic acid are also promising new materials [175].

The purity of crude biorefinery feeds often presents a major challenge for catalyst development, with the fermentation broth typically produced as a salty medium which would contain diammonium succinate rather than pure succinic acid. This however can be exploited for the production of 2-pyrrolidone or *N*-methylpyrrolidone by hydrogenation of diammonium succinate [175, 176] using catalysts such as $Pd/ZrO_2/C$ and 2.5%Rh–2.5%Re on C, with reaction in the presence of methanol found to favour *N*-methylpyrrolidone formation.

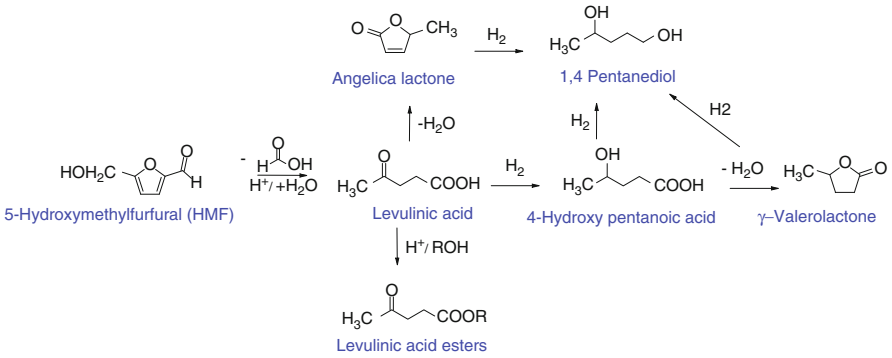

Scheme 7.22 Selected acid-catalysed or hydrogenation products from levulinic acid

Another popular platform molecule is 5-hydroxymethylfurfural (HMF) which is produced by the dehydration of hexoses. HMF has potential as an important bio-based commodity chemical for the synthesis of a variety of useful acids, aldehydes, alcohols and amines, as well as the promising fuel 2,5-dimethylfuran (DMF). There are only a few reports of sucrose dehydration over solid acids including acidic resins [177] and HY-zeolite [178], aluminium-pillared montmorillonite, MCM-20 and MCM-41 [179]. Overall HMF yields are found to be enhanced over mesoporous catalysts with pore diameters of 1–3 nm. In contrast, zeolites were found to produce lower DMF yields, which were attributed to significant coke formation and deactivation during reaction. Porosity was also observed to have a significant effect on HMF and levulinic acid yields obtained from sucrose dehydration over acid-exchange resins [177]. Larger pore materials were found to favour HMF, with slow diffusion of HMF out of smaller pores suggested to favour subsequent reaction and higher selectivity to levulinic acid. The kinetics of acid-catalysed dehydration of HMF to generate levulinic and formic acid has largely been investigated using mineral acids; however, there are a few reports examining the use of solid catalysts such as polymer resins and zeolites [180]. Application of solid acids in the dehydration of xylose to the analogous cyclic compound, furfural, is also restricted to a few examples where heteropoly acids [181] and MCM sulphonic acid [182] have been employed.

Levulinic acid is another valuable precursor to a range of chemical intermediates (Scheme 7.22) which can be generated by a combination of acid-catalysed dehydration, esterification or metal-catalysed reduction processes [183].

While there are a number of studies investigating reduction, there is surprisingly little work concerning the esterification of platform molecules using solid acid catalysts. To date, levulinic acid esterification is mostly performed using H_2SO_4 [184], and only a few studies exist which employ solid acids such as SO_4/TiO_2 and acid resins [18]. Clearly, there much scope for the development of new catalytic systems for the conversion of bio-refinery feedstocks to chemicals. However, efforts must focus on developing water-tolerant catalysts for the direct reaction of aqueous feeds, with a focus also on the development of tailored pore materials capable of operating in continuous flow conditions.

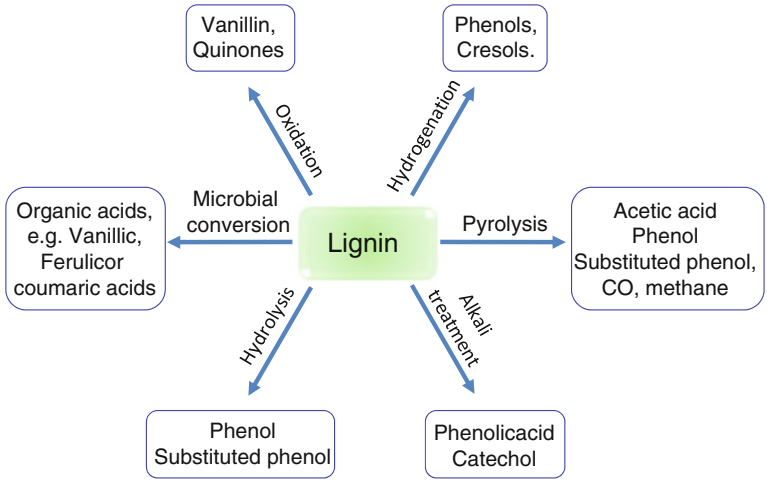

Scheme 7.23 Summary of routes to convert lignin to chemical precursors

7.4.3 Chemicals from Lignin

Lignin is another product from biomass-based processes which still contains a lot of useful functionality. Unfortunately, lignin is harder to convert than cellulose, and at the moment is mainly used to produce process heat by combustion. The main building blocks of lignin are *p*-coumaryl alcohol, coniferyl alcohol and sinapyl alcohol which are polymerised to form the complex structure shown earlier in Scheme 7.1.

However, lignin does have the potential to be a chemical feedstock via gasification to producing syngas (CO/H_2), which can be transformed into methanol, dimethyl ether, olefins and mixed alcohols (ethanol and higher value alcohol chemicals). Alternatively, there are a number of hydrocracking [185], hydrogenation [186, 187] or oxidation [188] methods that can be used to convert lignin into aromatic hydrocarbon species such as phenol guaiacol, syringol or vanillin. During thermal degradation, phenol derivatives are formed by the elimination of carbonyl groups in the side chain alkyl linkers of lignin. Addition of a range of inorganic catalysts including NaOH, K_2CO_3 and Na_2CO_3 or Zn(II), Cu (II) Mn (III), Co (III) and Fe (III) salts as well as Rh complexes can alter the resulting product distributions [189]. Scheme 7.23 shows a summary of routes that can be used to convert lignin to chemical precursors. Because of the complexity of the feedstocks obtained from lignin processing, most catalyst development and optimisation has focused on using model compounds, the details of which have recently been comprehensively reviewed [190].

The application of heterogeneous catalysts in lignin utilisation has generally focused on cracking, hydrogenolysis and oxidative routes. Lignin can undergo direct oxidative decomposition to aldehydes, and while most investigations focus on homogeneous catalysts, there are a few heterogeneous examples using Pd/Al_2O_3

[188] or perovskite-type oxide catalyst $LaFe_{1-x}Cu_xO_3$ ($x = 0$, 0.1, 0.2) [191] catalysts which operate under 2–20 bar O_2 pressure to yield vanillin, syringaldehyde and *p*-hydroxybenzaldehyde as the main products.

Hydrogenolysis reactions have generally been investigated by following the conversion of phenol, *o*-cresol, anisole and guaiacol model compounds to aromatics or alkanes via simultaneous hydrodeoxygenation and ring hydrogenation. The position of substituents on the ring is critical, with *ortho*-substituted molecules found to be least reactive, which is attributed to steric hindrance [192]. Catalysts for HDO are however frequently focussed on materials used for hydrodesulphurisation such as sulphided CoMo and NiMo catalysts [193]. As remarked in Sect. 7.3.1.4, these may not be most appropriate catalysts due to the different compositions of fossil and biomass-derived feedstocks; thus, non-sulphided catalysts would be preferable [194]. Alternative catalytic systems are however also being investigated including Ni–W/SiO_2–Al_2O_3 [185] and Ni–Cu on CeO_2 and ZrO_2 [195], Ru/C [196] and Pd/C [197]. Hydrocracking catalysts are generally bifunctional materials comprising a solid acid component and a metal for the hydrogenation reaction [184]; typical materials include H ZSM-5 [198–200] and Pt/Al_2O_3/SiO_2 [201]. The mechanism of operation for these bifunctional catalysts is dealt with extensively in the context of refining bio-oils for fuels [87] and will be considered in more detail in the next section.

7.4.4 Bio-Oil Utilisation

The conversion of biomass-derived oxygenates to H_2 and alkanes involves a multi-step reaction consisting of hydrogenation, hydrolysis, and dehydration. The ideal heterogeneous catalyst for a single-step aqueous-phase catalytic reforming process should employ bifunctional catalysts based on platinum group metal nanoparticles which are immobilised on an acidic support to promote hydrogenolysis and dehydration of the oxygenate, respectively [202]. Bio-oil conversion to alkanes has also been reported [203], using a commercial 5 wt% Pd/C catalyst in combination with the mineral acid H_3PO_4 to facilitate "one-pot" HDO. Production of alkanes by aqueous-phase reforming of sorbitol has been reported over SiO_2–Al_2O_3-supported Pt or Pd [204] catalysts. Sorbitol is first dehydrated by the acidic aluminosilicate support and then hydrogenated on the supported Pt crystallites. H_2 can be either co-fed with the sorbitol or produced in situ by aqueous-phase reforming of sorbitol or ethylene glycol to CO_2 and H_2 using Sn-promoted Raney Ni or Pt/Al_2O_3 catalysts [205, 206]. Sn-promoted Raney Ni gives higher H_2 selectivities by suppressing CH_4 formation under reaction conditions. Future advances in the development of new types of solid-acid and metal alloys catalysts are required to lead to further bio-oil reforming process improvements. Studies of reforming of model bio-oils (containing 5% methanol, 12% acetaldehyde, 14% acetic acid, 4% glyoxal, 8% acetol, 8% glucose, 17% guaiacol, 4% furfural, 8% vanillin and 20 wt% de-ionised water) using supported Pt catalysts reveal that the choice of support is important,

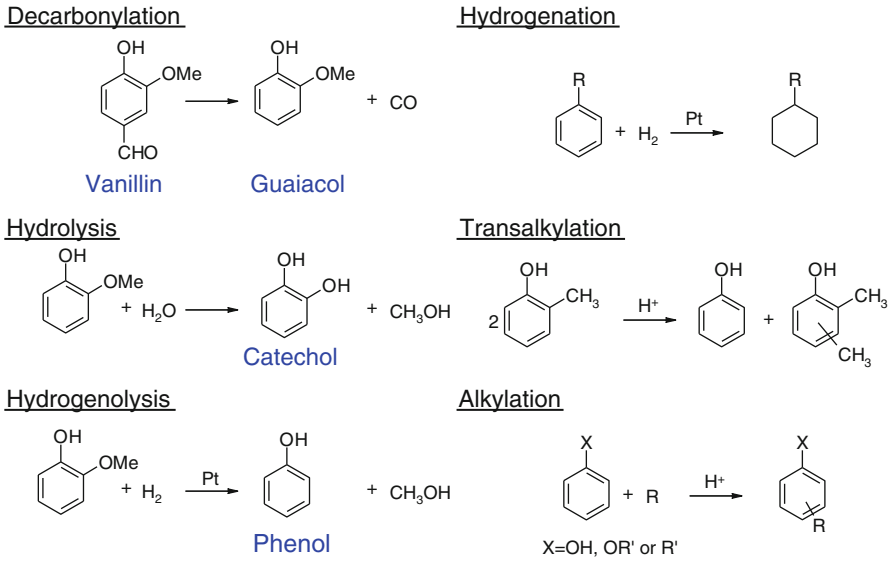

Scheme 7.24 Model reactions to study bio-oil upgrading [207]

with the degree of deoxygenation found to be most effective over Al_2O_3 > SiO_2–Al_2O_3 > TiO_2 > $CeZrO_2$ > ZrO_2 > CeO_2 [207]. Again, model compounds [161] are often studied to gain mechanistic insight into catalyst operation and deactivation, examples of which are shown in Scheme 7.24.

7.5 Future Challenges

This review highlights the significant progress made in recent years towards developing heterogeneous catalysts for converting renewable feedstocks to chemicals and fuels. The development of commercial heterogeneously catalysed processes requires a better understanding of how each reactant interacts with the active catalyst phase, particularly when dealing with bulky polar molecules such as those found in biorefinery feeds.

While traditional biodiesel synthesis via transesterification is a cheap and effective route to synthesise fuel, there are concerns over long-term biodiesel use and associated engine wear due to the build up of less volatile components in high-performance diesel vehicles [17]. However, longer chain (~C_{18}) FAMEs should be easier to implement in heavy duty diesel engines. Genetic modification, though controversial, may also assist by enabling plant biologists to engineer new higher yielding seed crops [208] that are also rich in the optimum TAG chain length and degree of saturation and matched to the catalyst of choice and desired fuel

properties. Crucially, widespread uptake and development of next-generation biodiesel fuels requires progressive government policies and incentive schemes to place biodiesel on a comparative footing with cheaper fossil-based fuels [209]. Plant oil viscosity and poor miscibility with light alcohols continues to hamper the use of new heterogeneous catalysts for continuous biodiesel production from both materials and engineering perspectives.

The initial acid hydrolysis/extraction step in preparation of sugars from lignocellulose is one of the most wasteful steps in the process. The stability of cellulose presents major problems, and finding an environmentally friendly and energetically efficient means to break up the biopolymer is a current challenge. In contrast to oils, conventional heterogeneous catalysts cannot be employed alone as this would involve working with a solid–solid mixture. Recent reports have however reported the use of ball milling as an effective means to [210] induce "mechanocatalysis" between cellulose and clay-based catalysts with layered structures. Alternative approaches are also building on the exciting discovery that ionic liquids can dissolve cellulose and when coupled with acidic reagents also generate selected platform chemicals [211, 212]. Recently, this approach has been coupled with solid catalysts [213, 214]; the combined ease of separation of a solid catalyst with the dissolving power of the ionic liquid offers exciting prospects for cleaner conversion of cellulose to chemicals.

Bio-oil obtained from pyrolysis of biomass is a complex liquid that is only partially soluble in either water or hydrocarbon solvents [85]. In order to overcome problems of working with such mixtures, materials with tunable hydrophobicity or even use of micellar catalyst systems should be considered. This has recently been exploited by the group of Resasco [215] in which a phase transfer system based upon Pd nanoparticles immobilised on carbon nanotube/silica composite support is employed. These materials are able to catalyse the transformation of both hydrophilic and hydrophobic substrates to fuels at the oil:water interface, without the need for multiple separation steps or addition of surfactants.

Development of new catalysts and overall process optimisation requires collaboration between catalytic chemists, chemical engineers and experts in molecular simulation to take advantage of innovative reactor designs; the future of renewable feedstock utilisation requires a concerted effort from chemists and engineers to develop catalysts and reactors in tandem. Current political concerns over the "food versus fuel" debate also requires urgent development of non-edible oil feedstocks as well as necessary technical advances in order to ensure that biofuels remains a key player in the renewable energy sector for the twenty-first century.

Acknowledgements Financial support from the EPSRC under grants EP/F063423/1 and EP/G007594/1, and the Royal Society for the award of an Industrial Fellowship to KW is gratefully acknowledged.

References

1. Anastas PT, Warner JC (1998) Green chemistry: theory and practice. Oxford University Press, New York
2. Walter B, Gruson JF, Monnier G (2008) Diesel engines and fuels: a wide range of evolutions to come. Oil Gas Sci Technol 63:387–393
3. Armaroli N, Balzani V (2007) The future of energy supply: challenges and opportunities. Angew Chem Int Ed 46:1–2
4. http://www.hm-treasury.gov.uk/independent_reviews/stern_review_economicsclimate_change/stern_review_report.cfm. Accessed Jul 2010
5. Danielsen F, Beukema H, Burgess ND, Parish F, Brühl CA, Donald PF, Murdiyarso D, Phalan B, Reijnders L, Struebig M, Fitzherbert EB (2009) Biofuel plantations on forested lands: double jeopardy for biodiversity and climate. Conserv Biol 23:348–358
6. Mata TM, Martins AA, Caetano NS (2010) Microalgae for biodiesel production and other applications: a review. Renew Sustain Energy Rev 14:217–232
7. Mosier N, Wyman C, Dale B, Elander R, Lee YY, Holtzapple M, Ladisch M (2005) Features of promising technologies for pretreatment of lignocellulosic biomass. Bioresour Technol 96:673–686
8. Clarens AF, Resurreccion EP, White MA, Colosi LM (2010) Environmental life cycle comparison of algae to other bioenergy feedstocks. Environ Sci Technol 44:1813–1819
9. Lanser AC, List GR, Holloway RK, Mounts YL (1991) FTIR estimation of free fatty acid content in crude oils extracted from damaged soybeans. J Am Oil Chem Soc 68:448–449
10. Sharma YC, Singh B, Upadhyay SN (2008) Advancements in development and characterization of biodiesel: a review. Fuel 87:2355–2373
11. Berchmans HJ, Hirata S (2008) Biodiesel production from crude *Jatropha curcas* seed oil with a high content of free fatty acids. Bioresour Technol 99:1716–1721
12. Kulkarni MG, Dalai AK (2006) Waste cooking oil—an economical source of biodiesel: a review. Ind Eng Chem Res 45:2901–2913
13. Bensmira M, Jiang B, Nsabimana C, Jian T (2007) Effect of lavender and thyme incorporation in sunflower seed oil on its resistance to frying temperatures. Food Res Int 40:341–346
14. Saad B, Ling CW, Jab MS, Lim BP, Ali ASM, Wai WT, Saleh MI (2007) Determination of free fatty acids in palm oil samples using non-aqueous flow injection titrimetric method. Food Chem 102:1407–1414
15. Paik M-J, Kim H, Lee J, Brand J, Kim K-R (2009) Separation of triacylglycerols and free fatty acids in microalgal lipids by solid-phase extraction for separate fatty acid profiling analysis by gas chromatography. J Chromatogr A 1216:5917–5923
16. Narasimharao K, Lee AF, Wilson K (2007) Catalysts in production of biodiesel: a review. J Biobased Mater Bioenergy 1:19–30
17. Knothe G (2009) Improving biodiesel fuel properties by modifying fatty ester composition. Energy Environ Sci 2:759–766
18. Corma A, Iborra S, Velty A (2007) Chemical routes for the transformation of biomass into chemicals. Chem Rev 107:2411–2502
19. Gallezot P (2007) Catalytic routes from renewables to fine chemicals. Catal Today 121:76–91
20. Imahara H, Minami E, Saka S (2006) Thermodynamic study on cloud point of biodiesel with its fatty acid composition. Fuel 85:1666–1670
21. Hoydonckx HE, De Vos DE, Chavan SA, Jacobs PA (2004) Esterification and transesterification of renewable chemicals. Top Catal 27:83–96
22. Freedman B, Pryde EH, Mounts TL (1984) Variables affecting the yields of fatty esters from transesterified vegetable oils. J Am Oil Chem Soc 61:1638–1643

23. Canakci M, Gerpen JV (1999) Biodiesel production via acid catalysis. Trans ASAE 42:1203–1210
24. Ma F, Hanna MA (1999) Biodiesel production: a review. Bioresour Technol 70:1–15
25. Dorado MP, Ballesteros E, Almeida JA, Shellet C, Lohrlein HP, Krause R (2002) An alkali-catalysed transesterification process for high free fatty acid waste oils. Trans ASAE 45:525–529
26. Turck R (2002) US patent, 0156305B
27. Ma FR, Clements LD, Hanna MA (1999) The effect of mixing on transesterification of beef tallow. Bioresour Technol 69:289–293
28. Demirbas A (2003) Biodiesel fuels from vegetable oils via catalytic and non catalytic supercritical alcohol transesterifications and other methods: a survey. Energy Convers Manage 44:2093–2109
29. Demirbas A (2007) Importance of biodiesel as transportation fuel. Energy Policy 35:4661–4670
30. Lotero E, Liu Y, Lopez DE, Suwannakarn K, Bruce DA, Goodwin JG Jr (2005) Synthesis of biodiesel via acid catalysis. Ind Eng Chem Res 44:5353–5363
31. Tanabe K, Misono M, Ono Y, Hattori H (1989) Preface. Stud Surf Sci Catal 51:1
32. Hattori H (1995) Heterogeneous basic catalysts. Chem Rev 95:537–558
33. Greenwood NN, Earnshaw A (1989) Chemistry of the elements. Pergamon Press, Oxford
34. Dacquin JP, Lee AF, Wilson K (2010) Heterogeneous catalysts for biodiesel production. In: Crocker M (ed) Thermochemical conversion of biomass to liquid fuels and chemicals. RSC Publishing, Cambridge
35. Albuquerque MCG, Azevedo DCS, Cavalcante CL Jr, Gonsalez JS, Robles JMM, Tost RM, Castellon ER, Lopez AJ, Torres PM (2009) Transesterification of ethyl butyrate with methanol using MgO/CaO catalysts. J Mol Catal A Chem 300:19–24
36. Paterson GR, Scarrah WP (1984) Rapeseed oil transesterification by heterogeneous catalysis. J Am Oil Chem Soc 61:1593–1597
37. Gryglewicz S (1999) Rapeseed oil methyl esters preparation using heterogeneous catalysts. Bioresour Technol 79:249–253
38. Granados ML, Poves MDZ, Alonso DM, Mariscal R, Galisteo FC, Tost RM, Santamaria J, Fierro JLG (2007) Biodiesel from sunflower oil by using activated calcium oxide. Appl Catal B Environ 73:317–326
39. Yan S, Lu H, Liang B (2008) Supported CaO catalysts used in the transesterification of rapeseed oil for the purpose of biodiesel production. Energy Fuel 22:646–651
40. Granados ML, Alonso DM, Sadaba I, Mariscal R, Ocon P (2009) Leaching and homogeneous contribution in liquid phase reaction catalysed by solids: the case of triglycerides methanolysis using CaO. Appl Catal B Environ 89:265–272
41. Demirbas A (2007) Biodiesel from sunflower oil in supercritical methanol with calcium oxide. Energy Convers Manag 48:937–941
42. Watkins RS, Lee AF, Wilson K (2004) Li-CaO catalysed tri-glycerides transesterification for biodiesel applications. Green Chem 6:335–340
43. MacLeod CS, Harvey AP, Lee AF, Wilson K (2008) Evaluation of the activity and stability of alkali-doped metal oxide catalysts for application to an intensified method of biodiesel production. Chem Eng J 135:63–70
44. Alonso DM, Mariscal R, Granados ML, Torres PM (2009) Biodiesel preparation using Li/CaO catalysts: activation process and homogeneous contribution. Catal Today 143:167
45. Wilson K, Hardacre C, Lee AF, Montero JM, Shellard L (2008) The application of calcined natural dolomitic rock as a solid base catalyst in triglyceride transesterification for biodiesel synthesis. Green Chem 10:654–659
46. Philipp R, Fujimoto K (1992) FTIR spectroscopic study of CO_2 adsorption/desorption on MgO/CaO catalysts. J Phys Chem 96:9035–9038

47. Verziu M, Cojocara B, Hu J, Richards R, Ciuculescu C, Filip P, Parvulescu VI (2008) Sunflower and rapeseed oil transesterification to biodiesel over different nanocrystalline MgO catalysts. Green Chem 10:373–381
48. Montero JM, Gai P, Wilson K, Lee AF (2009) Structure-sensitive biodiesel synthesis over MgO nanocrystals. Green Chem 11:265–268
49. Di Serio M, Ledda M, Cozzolino M, Minutillo G, Tesser R, Santacesaria E (2006) Transesterification of soybean oil to biodiesel by using heterogeneous basic catalysts. Ind Eng Chem Res 45:3009–3014
50. Siano D, Nastasi M, Santacesaria E, Di Serio M, Tesser R, Minutillo G, Ledda M, Tenore T (2006) PCT application no. WO2006/050925
51. Barakos N, Pasias S, Papayannakos N (2008) Transesterification of triglycerides in high and low quality oil feeds over an HT2 hydrotalcite catalyst. Bioresour Technol 99:5037–5042
52. Cantrell DG, Gillie LJ, Lee AF, Wilson K (2005) Structure-reactivity correlations in MgAl hydrotalcite catalysts for biodiesel synthesis. Appl Catal A Gen 287:183–190
53. Xi X, Davis RJ (2008) Influence of water on the activity and stability of activated Mg-Al hydrotalcites for the transesterification of tributyrin with methanol. J Catal 254:190–197
54. Fukuda H, Kondo A, Noda H (2001) Effect of methanol and water contents on production of biodiesel fuel from plant oil catalysed by various lipases in a solvent-free system. J Biosci Bioeng 91:12–15
55. Vicente G, Coteron A, Martinez M, Aracil J (1998) Application of the factorial design of experiments and response surface methodology to optimize biodiesel production. Ind Crops Prod 8:29–35
56. Lopez DE, Goodwin JG, Bruce DA, Lotero E (2005) Transesterification of triacetin with methanol on solid acid and base catalysts. Appl Catal A Gen 295:97–105
57. Peters TA, Benes NE, Holmen A, Keurentjes JTF (2006) Comparison of commercial solid acid catalysts for the esterification of acetic acid with butanol. Appl Catal A Gen 297:182
58. Suwannakarn K, Lotero E, Goodwin JG Jr, Lu C (2008) Stability of sulfated zirconia and the nature of the catalytically active species in the transesterification of triglycerides. J Catal 255:279–286
59. Kiss AA, Dimian AC, Rothenberg G (2006) Solid acid catalysts for biodiesel production—towards sustainable energy. Adv Synth Catal 348:75–81
60. Mizuno N, Misono M (1998) Heterogeneous catalysis. Chem Rev 98:199–217
61. Okuhara T, Mizuno N, Misono M (1996) Catalytic chemistry of heteropoly compounds. Adv Catal 41:113–252
62. Misono M (1987) Heterogeneous catalysis by heteropoly compounds of molybdenum and tungsten. Catal Rev 29:269–321
63. Newman AD, Brown DR, Siril P, Lee AF, Wilson K (2006) Structural studies of high dispersion $H_3PW_{12}O$ 40/SiO_2 solid acid catalysts. Phys Chem Chem Phys 8:2893–2902
64. Newman AD, Lee AF, Wilson K, Young NA (2005) On the active site in $H_3PW_{12}O_{40}/SiO_2$ catalysts for fine chemical synthesis. Catal Lett 102:45–50
65. Okuhara T, Nishimura T, Watanabe H, Misono M (1992) Insoluble heteropoly compounds as highly active catalysts for liquid-phase reactions. J Mol Catal 74:247–256
66. Okuhara T, Arai T, Ichiki T, Lee KY, Misono M (1989) Dehydration mechanism of ethanol in the pseudoliquid phase of $H_{3-x}Cs_xPW_{12}O_{40}$. J Mol Catal 55:293–301
67. Narasimharao K, Brown DR, Lee AF, Siril PF, Wilson K (2007) Structure-activity relations in Cs-doped heteropolyacid catalysts for biodiesel production. J Catal 248:226–234
68. Pesaresi L, Brown DR, Lee AF, Montero JM, Williams H, Wilson K (2009) Cs-doped $H_4SiW_{12}O_{40}$ catalysts for biodiesel applications. Appl Catal A Gen 360:50–58
69. Peterson GR, Sacarrah WP (1984) Rapeseed oil transesterification by heterogeneous catalysis. J Am Oil Chem Soc 61:1593–1597
70. Pizzio LR, Vazquez PG, Caceres CV, Blanco MN, Alesso EN, Erlich MI, Torviso R, Finkielsztein L, Lantano B, Moltrasio GY, Aguirre JM (2004) Influence of the alcohol

molecular size in the dehydration reaction catalyzed by carbon-supported heteropolyacids. Catal Lett 93:67–73
71. Bossaert WD, De Vos DE, Van Rhijn W, Bullen J, Grobet PJ, Jacobs PA (1999) Mesoporous sulfonic acids as selective heterogeneous catalysts for the synthesis of monoglycerides. J Catal 182:156–164
72. Wilson K, Lee AF, Macquarrie DJ, Clark JH (2002) Structure and reactivity of sol-gel sulphonic acid silicas. Appl Catal A Gen 228:127–133
73. Chen XR, Ju YH, Mou CY (2007) Direct synthesis of mesoporous sulfated silica-zirconia catalysts with high catalytic activity for biodiesel via esterification. J Phys Chem C 111:18731–18737
74. Mbaraka IK, Radu DR, Lin VS-Y, Shanks BH (2003) Organosulfonic acid-functionalized mesoporous silicas for the esterification of fatty acid. J Catal 219:329–336
75. Shah P, Ramaswamy AV, Lazar K, Ramaswamy V (2004) Synthesis and characterization of tin oxide-modified mesoporous SBA-15 molecular sieves and catalytic activity in trans-esterification reaction. Appl Catal A Gen 1–2:239–248
76. Gaudino MC, Valentin R, Brunel D, Fajula F, Quignard F, Riondel A (2005) Titanium-based solid catalysts for transesterification of methyl-methacrylate by 1-butanol: the homogeneous catalysis contribution. Appl Catal A Gen 2:157–164
77. Ying JY, Mehnert CP, Wong MS (1999) Synthesis and applications of supramolecular-templated mesoporous materials. Angew Chem Int Ed 38:56–77
78. Linssen T, Cassiers K, Cool P, Vansant EF (2003) Mesoporous template silicates: an overview of their synthesis, catalytic activation and evaluation of the stability. Adv Colloid Interface Sci 103:121–147
79. Davidson A (2002) Modifying the walls of mesoporous silicas prepared by supramolecular-templating. Curr Opin Colloid Interface Sci 7:92–106
80. Galarneau A, Iapichella J, Bonhomme K, Di Renzo F, Kooyman P, Terasaki O, Fajula F (2006) Controlling the morphology of mesostructured silicas by pseudomorphic transformation: a route towards applications. Adv Funct Mater 16:1657–1667
81. Dacquin JP, Dhainaut J, Duprez D, Royer S, Lee AF, Wilson K (2009) An efficient route to highly organized, tunable macroporous-mesoporous alumina. J Am Chem Soc 131: 12896–12897
82. Dhainaut J, Dacquin JP, Lee AF, Wilson K (2010) Hierarchical macroporous-mesoporous SBA-15 sulfonic acid catalysts for biodiesel synthesis. Green Chem 12:296–303
83. Donnis B, Egeberg RG, Blom P, Knudsen KG (2009) Hydroprocessing of bio-oils and oxygenates to hydrocarbons: understanding the reaction routes. Top Catal 52:229–240
84. Czernik S, French RJ, Magrini-Bair KA, Chornet E (2004) The production of hydrogen by steam reforming of trap grease-progress in catalyst performance. Energy Fuel 18:1738–1743
85. Huber GW, Iborra S, Corma A (2006) Synthesis of transportation fuels from biomass: chemistry, catalysts, and engineering. Chem Rev 106:4044–4098
86. Huber GW, O'Connor P, Corma A (2007) Processing biomass in conventional oil refineries: production of high quality diesel by hydrotreating vegetable oils in heavy vacuum oil mixtures. Appl Catal A Gen 329:120–129
87. Huber GW, Corma A (2007) Synergies between bio- and oil refineries for the production of fuels from biomass. Angew Chem Int Ed 46:7184–7201
88. Stumborg M, Wong A, Hogan E (1996) Hydroprocessed vegetable oils for diesel fuel improvement. Bioresour Technol 56:13–18
89. Kubicka D, Kaluza L (2010) Deoxygenation of vegetable oils over sulfided Ni, Mo and NiMo catalysts. Appl Catal A Gen 372:199–208
90. Murata K, Liu YY, Inaba M, Takahara I (2010) Production of synthetic diesel by hydrotreatment of Jatropha oils using Pt-Re/H-ZSM-5 catalyst. Energy Fuel 24:2404–2409
91. Morgan T, Grubb D, Santillan-Jimenez E, Crocker M (2010) Conversion of triglycerides to hydrocarbons over supported metal catalysts. Top Catal 53:820–829

92. Patil TA, Raghunathan TS, Shankar HS (1988) Thermal hydrolysis of vegetable oils and fats. 2. Hydrolysis in continuous stirred tank reactor. Ind Eng Chem Res 27:735–739
93. Yow CJ, Liew KY (1999) Hydrolysis of palm oil catalyzed by macroporous cation-exchanged resin. J Am Oil Chem Soc 76:529–533
94. Yow CJ, Liew KY (2002) Hydrolysis of palm olein catalyzed by solid heteropolyacids. J Am Oil Chem Soc 79:357–361
95. Ngaosuwan K, Lotero E, Suwannakarn K, Goodwin JG Jr, Praserthdam P (2009) Hydrolysis of triglycerides using solid acid catalysts. Ind Eng Chem Res 48:4757–4767
96. Ngaosuwan K, Mo XH, Goodwin JG Jr, Praserthdam P (2010) Reaction kinetics and mechanisms for hydrolysis and transesterification of triglycerides on tungstated zirconia. Top Catal 53:783–794
97. Pouilloux Y, Piccirilli A, Barrault J (1996) Selective hydrogenation into oleyl alcohol of methyl oleate in the presence of Ru-Sn/Al_2O_3 catalysts. J Mol Catal A 108:161–166
98. Miyake T, Makino T, Taniguchi S, Watanuki H, Niki T, Shimizu S, Kojima Y, Sano M (2009) Alcohol synthesis by hydrogenation of fatty acid methyl esters on supported Ru-Sn and Rh-Sn catalysts. Appl Catal A Gen 364:108–112
99. Pouilloux Y, Auin F, Guimon C, Barrault J (1998) Hydrogenation of fatty esters over ruthenium–tin catalysts; characterization and identification of active centers. J Catal 176:215–224
100. Camblor MA, Corma A, Iborra A, Miquel A, Primo J, Valencia S (1997) Beta zeolite as a catalyst for the preparation of alkyl glucoside surfactants: the role of crystal size and hydrophobicity. J Catal 172:76–84
101. Climent MJ, Corma A, Iborra A, Miquel S, Primo J, Rey F (1999) Mesoporous materials as catalysts for the production of chemicals: synthesis of alkyl glucosides on MCM-41. J Catal 183:76–82
102. Guidotti M, Ravasio N, Psaro R, Gianotti E, Marchese L, Coluccia S (2003) Heterogeneous catalytic epoxidation of fatty acid methyl esters on titanium-grafted silicas. Green Chem 5:421–424
103. Rios LA, Weckes P, Schuster H, Hoelderich WF (2005) Mesoporous and amorphous Ti-silicas on the epoxidation of vegetable oils. J Catal 232:19–26
104. Feliczak A, Walczak K, Wawrzyńczak A, Nowak I (2009) The use of mesoporous molecular sieves containing niobium for the synthesis of vegetable oil-based products. Catal Today 140:23–29
105. Sinadinović-Fišer S, Janković M, Petrović ZS (2001) Kinetics of in situ epoxidation of soybean oil in bulk catalyzed by ion exchange resin. J Am Oil Chem Soc 78:725–731
106. Barrault J, Jerome F (2008) Design of new solid catalysts for the selective conversion of glycerol. Eur J Lipid Sci Technol 110:825–830
107. Zhou C-H, Beltramini JN, Fan Y-X, Lu GQ (2008) Chemoselective catalytic conversion of glycerol as a biorenewable source to valuable commodity chemicals. Chem Soc Rev 37:527–549
108. Barrault J, Pouilloux Y, Clacens JM, Vanhove C, Bancquart S (2002) Catalysis and fine chemistry. Catal Today 75:177–181
109. Pagliaro M, Ciriminna R, Kimura H, Rossi M, Della Pina C (2007) From glycerol to value-added products. Angew Chem Int Ed 46:4434–4440
110. Behr A, Eilting J, Irawadi K, Leschinski J, Lindner F (2008) Improved utilisation of renewable resources: new important derivatives of glycerol. Green Chem 10:13–30
111. Dimitratos N, Lopez-Sanchez JA, Hutchings GJ (2009) Green catalysis with alternative feedstocks. Top Catal 52:258–268
112. Kimura H, Tsuto K, Wakisaka T, Kazumi Y, Inaya Y (1993) Selective oxidation of glycerol on a platinum-bismuth catalyst. Appl Catal A Gen 96:217–228
113. Abbadi A, Bekkum HV (1996) Selective chemo-catalytic routes for the preparation of β-hydroxypyruvic acid. Appl Catal A Gen 148:113–122

114. Garcia R, Besson M, Gallezot P (1995) Chemoselective catalytic oxidation of glycerol with air on platinum metals. Appl Catal A Gen 127:165
115. Fordham P, Garcia R, Besson M, Gallezot P (1995) Selective catalytic oxidation of glyceric acid to tartronic and hydroxypyruvic acids. Appl Catal A Gen 133:L179–L184
116. Besson M, Gallezot P (2000) Selective oxidation of alcohols and aldehydes on metal catalysts. Catal Today 57:127–141
117. Ruppert AM, Meeldijk JD, Kuipers BWM, Ern BH, Weckhuysen BM (2008) Glycerol etherification over highly active CaO-based materials: new mechanistic aspects and related colloidal particle formation. Chem Eur J 14:2016–2024
118. Melero JA, Iglesias J, Morales G (2009) Heterogeneous acid catalysts for biodiesel production: current status and future challenges. Green Chem 11:1285–1308
119. Melero JA, van Grieken R, Morales G, Paniagua M (2007) Acidic mesoporous silica for the acetylation of glycerol: synthesis of bioadditives to petrol fuel. Energy Fuel 21:1782–1791
120. Diaz I, Marquez-Alvarez C, Mohino F, Perez-Pariente J, Sastre E (2000) Combined alkyl and sulfonic acid functionalization of MCM-41-type silica: part 2. Esterification of glycerol with fatty acids. J Catal 193:295–302
121. Diaz I, Mohino F, Perez-Pariente J, Sastre E (2003) Synthesis of MCM-41 materials functionalised with dialkylsilane groups and their catalytic activity in the esterification of glycerol with fatty acids. Appl Catal A Gen 242:161–169
122. Pouilloux Y, Abro S, Vanhove C, Barrault J (1999) Reaction of glycerol with fatty acids in the presence of ion-exchange resins: preparation of monoglycerides. J Mol Catal A 149:243–254
123. Bancquart S, Vanhove C, Pouilloux Y, Barrault J (2001) Glycerol transesterification with methyl stearate over solid basic catalysts: I. Relationship between activity and basicity. Appl Catal A Gen 218:1–11
124. Barrault J, Bancquart S, Pouilloux Y (2004) Selective glycerol transesterification over mesoporous basic catalysts. Comptes Rendus Chimie 7:593–599
125. Corma A, Abd Hamid SB, Iborra S, Velty A (2005) Lewis and Brönsted basic active sites on solid catalysts and their role in the synthesis of monoglycerides. J Catal 234:340–347
126. Kiatkittipong W, Suwanmanee S, Laosiripojana N, Praserthdam P, Assabumrungrat S (2010) Cleaner gasoline production by using glycerol as fuel extender. Fuel Proc Technol 91:456–460
127. Klepacova K, Mravec D, Bajus M (2005) Tert-butylation of glycerol catalysed by ion-exchange resins. Appl Catal A Gen 294:141–147
128. Frusteri F, Arena F, Bonura G, Cannilla C, Spadaro L, Di Blasi O (2009) Catalytic etherification of glycerol by tert-butyl alcohol to produce oxygenated additives for diesel fuel. Appl Catal A Gen 367:77–83
129. Klepacova K, Mravec D, Kaszonyi A, Bajus M (2007) Etherification of glycerol and ethylene glycol by isobutylene. Appl Catal A Gen 328:1–13
130. Melero JA, Vicente G, Morales G, Paniagua M, Moreno JM, Roldan R, Ezquerro A, Perez C (2008) Acid-catalyzed etherification of bio-glycerol and isobutylene over sulfonic mesostructured silicas. Appl Catal A Gen 346:44–51
131. Clacens JM, Pouilloux Y, Barrault J (2002) Selective etherification of glycerol to polyglycerols over impregnated basic MCM-41 type mesoporous catalysts. Appl Catal A Gen 227:181–190
132. Ruppert AM, Parvulescu AN, Arias M, Hausoul PJC, Bruijnincx PCX, Gebbink RJMK, Weckhuysen BM (2009) Synthesis of long alkyl chain ethers through direct etherification of biomass-based alcohols with 1-octene over heterogeneous acid catalysts. J Catal 268:251–259
133. Gu Y, Azzouzi A, Pouilloux Y, Jerome F, Barrault J (2008) Heterogeneously catalyzed etherification of glycerol: new pathways for transformation of glycerol to more valuable chemicals. Green Chem 10:164–167

134. Montassier C, Ménézo JC, Hoang LC, Renaud C, Barbier J (1991) Aqueous polyol conversions on ruthenium and on sulfur-modified ruthenium. J Mol Catal 70:99–110
135. Montassier C, Dumas JM, Granger P, Barbier J (1995) Deactivation of supported copper based catalysts during polyol conversion in aqueous phase. Appl Catal A Gen 121:231–244
136. Yuan Z, Wang J, Wang L, Xie W, Chen P, Hou Z, Zheng X (2010) Biodiesel derived glycerol hydrogenolysis to 1,2-propanediol on Cu/MgO catalysts. Bioresour Technol 101:7088–7092
137. Dasari MA, Kiatsimkul PP, Sutterlin WR, Suppes GJ (2005) Low-pressure hydrogenolysis of glycerol to propylene glycol. Appl Catal A Gen 281:225–231
138. Ma Z, Xiao Z, Van Bokhoven JA, Liang C (2010) A non-alkoxide sol-gel route to highly active and selective Cu-Cr catalysts for glycerol conversion. J Mater Chem 20:755–760
139. Vasiliadou ES, Heracleous E, Vasalos IA, Lemonidou AA (2009) Ru-based catalysts for glycerol hydrogenolysis—effect of support and metal precursor. Appl Catal B Environ 92:90–99
140. Miyazawa T, Kusunoki Y, Kunimori K, Tomishige K (2006) Glycerol conversion in the aqueous solution under hydrogen over Ru/C + an ion-exchange resin and its reaction mechanism. J Catal 240:213–221
141. Balaraju M, Rekha V, Sai Prasad PS, Prabhavathi Devi BLA, Prasad RBN, Lingaiah N (2009) Influence of solid acids as co-catalysts on glycerol hydrogenolysis to propylene glycol over Ru/C catalysts. Appl Catal A Gen 354:82–87
142. Alhanash A, Kozhevnikova EF, Kozhevnikov IV (2008) Hydrogenolysis of glycerol to propanediol over Ru: polyoxometalate bifunctional catalyst. Catal Lett 120:307–311
143. Maris EP, Ketchie WC, Murayama M, Davis RJ (2007) Glycerol hydrogenolysis on carbon-supported PtRu and AuRu bimetallic catalysts. J Catal 251:281–294
144. Maris EP, Davis RJ (2007) Hydrogenolysis of glycerol over carbon-supported Ru and Pt. J Catal 249:328–337
145. Jiang T, Zhou Y, Liang S, Liu H, Han B (2009) Hydrogenolysis of glycerol catalyzed by Ru-Cu bimetallic catalysts supported on clay with the aid of ionic liquids. Green Chem 11:1000–1006
146. Vicente G, Melero JA, Morales G, Paniagua M, Martín E (2010) Acetalisation of bio-glycerol with acetone to produce solketal over sulfonic mesostructured silicas. Green Chem 12:899–907
147. Plasman V, Caulier T, Boulos N (2005) Polyglycerol esters demonstrate superior antifogging properties for films. Plast Addit Compd 7:30–33
148. Vieville C, Yoo JW, Pelet S, Mouloungui Z (1998) Synthesis of glycerol carbonate by direct carbonatation of glycerol in supercritical CO_2 in the presence of zeolites and ion exchange resins. Catal Lett 56:245–247
149. Climent MJ, Corma A, De Frutos P, Iborra S, Noy M, Velty A, Concepción P (2010) Chemicals from biomass: synthesis of glycerol carbonate by transesterification and carbonylation with urea with hydrotalcite catalysts. The role of acid-base pairs. J Catal 269:140–149
150. Takagaki A, Iwatani K, Nishimura S, Ebitani K (2010) Synthesis of glycerol carbonate from glycerol and dialkyl carbonates using hydrotalcite as a reusable heterogeneous base catalyst. Green Chem 12:578–581
151. Yoo JW, Mouloungui Z (2003) Catalytic carbonylation of glycerin by urea in the presence of zinc mesoporous system for the synthesis of glycerol carbonate. Stud Surf Sci Catal 146:757–760
152. Aresta M, Dibenedetto A, Nocito F, Ferragina C (2009) Valorization of bio-glycerol: new catalytic materials for the synthesis of glycerol carbonate via glycerolysis of urea. J Catal 268:106–114
153. Aresta M, Dibenedetto A, Nocito F, Pastore C (2006) A study on the carboxylation of glycerol to glycerol carbonate with carbon dioxide: the role of the catalyst, solvent and reaction conditions. J Mol Catal A 257:149–153

154. Patel Y, George J, Pillai SM, Munshi P (2009) Effect of lipophilicity of catalyst in cyclic carbonate formation by transesterification of polyhydric alcohols. Green Chem 11:1056–1060
155. Corma A, Navarro MT, Renz M (2003) Lewis acidic Sn(IV) centers—grafted onto MCM-41—as catalytic sites for the Baeyer-Villiger oxidation with hydrogen peroxide. J Catal 219:242–246
156. Selvaraj M, Kawi S (2007) Effect of tin precursors and crystallization temperatures on the synthesis of SBA-15 with high levels of tetrahedral tin. J Mater Chem 17:3610–3621
157. Deshayes G, Poelmans K, Verbruggen I, Camacho-Camacho C, Dege P, Pinoie V, Martins JC, Piotto M, Biesemans M, Willem R, Dubois P (2005) Polystyrene-supported organotin dichloride as a recyclable catalyst in lactone ring-opening polymerization: assessment and catalysis monitoring by high-resolution magic-angle-spinning NMR spectroscopy. Chemistry 11:4552–4561
158. Kerric G, Le Grognec E, Fargeas V, Zammattio F, Quintard JP, Biesemans M, Willem R (2010) Synthesis, characterization and primary evaluation of the synthetic efficiency of supported vinyltins and allyltins. J Organomet Chem 695:1414–1424
159. Mohan D, Pittman CU, Steele PH (2006) Pyrolysis of wood/biomass for bio-oil: a critical review. Energy Fuel 20:848–889
160. Bridgwater AV, Peacocke GVC (2000) Fast pyrolysis processes for biomass. Renew Sustain Energy Rev 4:1–73
161. Furimsky E (2000) Catalytic hydrodeoxygenation. Appl Catal A Gen 199:147–190
162. Czernik S, Bridgwater AV (2004) Overview of applications of biomass fast pyrolysis oil. Energy Fuel 18:590–598
163. Catoire L, Yahyaoui M, Osmont A, Gokalp I (2008) Thermochemistry of compounds formed during fast pyrolysis of lignocellulosic biomass. Energy Fuel 22:4265–4273
164. Fernando S, Adhikari A, Chandrapaul C, Murali N (2006) Biorefineries: current status, challenges, and future direction. Energy Fuel 20:1727–1737
165. Evans RJ, Milne TA (1987) Molecular characterization of the pyrolysis of biomass. 1. Fundamentals. Energy Fuel 1:123–137
166. Bozell JJ, Petersen GR (2010) Technology development for the production of biobased products from biorefinery carbohydrates—the US department of energy's "top 10" revisited. Green Chem 12:539–554
167. Huh YS, Jun YS, Hong YK, Song H, Lee SY, Hong WH (2006) Effective purification of succinic acid from fermentation broth produced by Mannheimia succiniciproducens. Process Biochem 41:1461–1465
168. Clark JH (2007) Green chemistry for the second generation biorefinery—sustainable chemical manufacturing based on biomass. J Chem Technol Biotechnol 82:603–609
169. Werpy T, Petersen G, Aden A, Bozell J, Holladay J, White J, Manheim A (2004) Top value added chemicals from biomass volume I: results of screening for potential candidates from sugars and synthesis gas. U.S. Department of Energy (DOE) report by the National Renewable Energy Laboratory. DOE/GO-102004-1992
170. Rinaldi R, Schuth F (2009) Design of solid catalysts for the conversion of biomass. Energy Environ Sci 2:610–626
171. Dacquin JP, Cross HE, Brown DR, Düren T, Williams J, Lee AF, Wilson K (2010) Interdependent lateral interactions, hydrophobicity and acid strength and their influence on the catalytic activity of nanoporous sulfonic acid silicas. Green Chem 12:1383–1391
172. Lin WC, Lu AH, Schuth F (2005) Preparation of monolithic carbon aerogels and investigation of their pore interconnectivity by a nanocasting pathway. Chem Mater 17:3620–3626
173. Zhang B, Ren J, Liu X, Guo Y, Guo Y, Lu G, Wang Y (2010) Novel sulfonated carbonaceous materials from p-toluenesulfonic acid/glucose as a high-performance solid-acid catalyst. Catal Commun 11:629–632

174. Clark JH, Budarin V, Dugmore T, Luque R, Macquarrie DJ, Strelko V (2008) Catalytic performance of carbonaceous materials in the esterification of succinic acid. Catal Commun 9:1709–1714
175. Bechthold I, Bretz K, Kabasci S, Kopitzky R, Springer A (2008) Succinic acid: a new platform chemical for biobased polymers from renewable resources. Chem Eng Technol 31:647–654
176. Delhomme C, Weuster-Botza D, Kuhn FE (2009) Succinic acid from renewable resources as a C4 building-block chemical—a review of the catalytic possibilities in aqueous media. Green Chem 11:13–26
177. Schraufnagel RA, Rase HF (1975) Levulinic acid from sucrose using acidic ion-exchange resins. Ind Eng Chem Prod Res Dev 14:40–44
178. Lourvanij K, Rorrer GL (1993) Reactions of aqueous glucose solutions over solid-acid Y-zeolite catalyst at 110–160°C. Ind Eng Chem Res 32:11–19
179. Lourvanij K, Rorrer GL (1997) Reaction rates for the partial dehydration of glucose to organic acids in solid-acid, molecular-sieving catalyst powders. J Chem Technol Biotechnol 69:35–44
180. Moreau C, Durand R, Razigade S, Duhamet J, Rivalier P, Ros P, Avignon G (1996) Dehydration of fructose to 5-hydroxymethylfurfural over H-mordenites. Appl Catal A Gen 145:211–224
181. Dias AS, Pillinger M, Valente AA (2005) Liquid phase dehydration of D-xylose in the presence of keggin-type heteropolyacids. Appl Catal A Gen 285:126–131
182. Dias AS, Pillinger M, Valente AA (2005) Dehydration of xylose into furfural over micro-mesoporous sulfonic acid catalysts. J Catal 229:414–423
183. Reid L (1956) Levulinic Acid as a Basic Chemical Raw Material. Ind Eng Chem 48:1330–1341
184. Bart HJ, Reidetschlager J, Schatka K, Lehmann A (1994) Kinetics of esterification of levulinic acid with *n*-butanol by homogeneous catalysis. Ind Eng Chem Res 33:21–25
185. Thring RW, Breau J (1996) Hydrocracking of solvolysis lignin in a batch reactor. Fuel 75:795–800
186. Saeman JF, Harris DEE (1946) Hydrogenation of lignin over Raney nickel. J Am Chem Soc 68:2507–2509
187. Harris EE, Saeman JF, Bergstrom CB (1949) Lignin hydrogenation products. Ind Eng Chem 41:2063–2067
188. Sales FG, Maranhão LCA, Lima Filho NM, Abreu CAM (2007) Experimental evaluation and continuous catalytic process for fine aldehyde production from lignin. Chem Eng Sci 62:5386–5391
189. Amen-Chen C, Pakdel H, Roy C (2001) Production of monomeric phenols by thermochemical conversion of biomass: a review. Bioresour Technol 79:277–299
190. Zakzeski J, Bruijnincx PCA, Jongerius AL, Weckhuysen BM (2010) The catalytic valorization of lignin for the production of renewable chemicals. Chem Rev 110:3552–3599
191. Zhang J, Deng H, Lin L (2009) Wet aerobic oxidation of lignin into aromatic aldehydes catalysed by a perovskite-type oxide: $LaFe_{1-x}Cu_xO_3$ ($x = 0$, 0.1, 0.2). Molecules 14:2747–2757
192. Gevert BS, Otterstedt JE, Massoth FE (1987) Kinetics of the HDO of methyl-substituted phenols. Appl Catal 31:119–131
193. Laurent E, Delmon B (1994) Study of the hydrodeoxygenation of carbonyl, carboxylic and guaiacyl groups over sulfided $CoMo/\gamma\text{-}Al_2O_3$ and $NiMo/\gamma\text{-}Al_2O_3$ catalysts. I. Catalytic reaction schemes. Appl Catal A Gen 109:77–96
194. Ferrari M, Delmon B, Grange P (2002) Influence of the impregnation order of molybdenum and cobalt in carbon-supported catalysts for hydrodeoxygenation reactions. Carbon 40:497–511

195. Yakovlev VA, Khromova SA, Sherstyuk OV, Dundich VO, Ermakov DY, Novopashina VM, Lebedev MY, Bulavchenko O, Parmon VN (2009) Development of new catalytic systems for upgraded bio-fuels production from bio-crude-oil and biodiesel. Catal Today 144:362–366
196. De Wild P, Van der Laan R, Kloekhorst A, Heeres E (2009) Lignin valorisation for chemicals and (transportation) fuels via (catalytic) pyrolysis and hydrodeoxygenation. Environ Prog Sustain Energy 28:461–469
197. Elliott DC, Hart TR (2009) Catalytic hydroprocessing of chemical models for bio-oil. Energy Fuel 23:631–637
198. Sharma RK, Bakhshi NN (1993) Catalytic upgrading of pyrolysis oil. Energy Fuel 7:306–314
199. Vitolo S, Bresci B, Seggiani M, Gallo MG (2001) Catalytic upgrading of pyrolytic oils over HZSM-5 zeolite: behaviour of the catalyst when used in repeated upgrading-regenerating cycles. Fuel 80:17
200. Corma A, Huber GW, Sauvanaud L, O'Connor P (2007) Processing biomass-derived oxygenates in the oil refinery: catalytic cracking (FCC) reaction pathways and role of catalyst. J Catal 247:307–327
201. Sheu YHE, Anthony RG, Soltes EJ (1988) Kinetic studies of upgrading pine pyrolytic oil by hydrotreatment. Fuel Proc Technol 19:31–50
202. Cortright RD, Davda RR, Dumesic JA (2002) Hydrogen from catalytic reforming of biomass-derived hydrocarbons in liquid water. Nature 418:964–967
203. Zhao C, Kou Y, Lemonidou AA, Li X, Lercher JA (2009) Highly selective catalytic conversion of phenolic bio-oil to alkanes. Angew Chem Int Ed 48:3987–3990
204. Huber GW, Cortright RD, Dumesic JA (2004) Renewable alkanes by aqueous-phase reforming of biomass-derived oxygenates. Angew Chem Int Ed 43:1549–1551
205. Huber GW, Shabaker JW, Dumesic JA (2003) Raney Ni-Sn catalyst for H_2 production from biomass-derived hydrocarbons. Science 300:2075–2077
206. Shabaker JW, Dumesic JA (2004) Kinetics of aqueous-phase reforming of oxygenated hydrocarbons: Pt/Al_2O_3 and Sn-modified Ni catalysts. Ind Eng Chem Res 43:3105–3112
207. Fisk CA, Morgan T, Ji Y, Crocker M, Crofcheck C, Lewis SA (2009) Bio-oil upgrading over platinum catalysts using in situ generated hydrogen. Appl Catal A Gen 358:150–156
208. Knothe G (2005) Dependence of biodiesel fuel properties on the structure of fatty acid alkyl esters. Fuel Proc Technol 86:1059–1070
209. Pinzi S, Garcia IL, Lopez-Gimenez FJ, Luque de Castro MD, Dorado G, Dorado MP (2009) The ideal vegetable oil-based biodiesel composition: a review of social, economical and technical implications. Energy Fuel 23:2325–2341
210. Hick SM, Griebel C, Restrepo DT, Truitt JH, Buker EJ, Bylda C, Blair RG (2010) Mechanocatalysis for biomass-derived chemicals and fuels. Green Chem 12:468–474
211. Binder JB, Raines RT (2009) Simple chemical transformation of lignocellulosic biomass into furans for fuels and chemicals. J Am Chem Soc 131:1979
212. Zhao H, Holladay JE, Brown H, Zhang ZC (2007) Metal chlorides in ionic liquid solvents convert sugars to 5-hydroxymethylfurfural. Science 316:1597–1600
213. Roberto Rinaldi R, Palkovits R, Schüth F (2008) Depolymerization of cellulose using solid catalysts in ionic liquids. Angew Chem Int Ed 47:8047–8050
214. Villandier N, Corma A (2010) One pot catalytic conversion of cellulose into biodegradable surfactants. Chem Commun 46:4408–4410
215. Crossley S, Faria J, Shen M, Resasco DE (2010) Solid nanoparticles that catalyze biofuel upgrade reactions at the water/oil interface. Science 327:68–72

Chapter 8
Catalytic Combustion of Methane

Naoto Kamiuchi and Koichi Eguchi

Abstract The combustion of methane has been investigated for production of heat and for removal of unburnt fuel. Achievement of complete methane oxidation at lower temperatures has been desired in every application. In this chapter, studies for methane combustion over catalyst are summarized from a perspective of catalyst materials. The development of catalysts with high activity at low temperatures and long-term durability under reaction conditions is required. Therefore, this chapter deals with the studies on low-temperature catalytic combustion of methane, while the hexaaluminate-related compounds for high-temperature combustion are described. In the case of low-temperature combustion, a large number of previous researches are classified into four kinds of catalysts: Pd, Pt, CeO_2–ZrO_2 mixed oxide, and perovskite-type oxide. The catalytic activities, durabilities, reaction mechanism, and degradation phenomena, the influence of support material, the effect of addition of other components, and so on are discussed.

8.1 Introduction

Catalytic combustion of hydrocarbons has been extensively investigated so far for the various applications to environmental protection and thermal energy production because of the clean exhaust, low pollutant emission, and high efficiency, as compared with conventional flame-combustion systems [1]. Although the operating condition of a combustor strongly depends on the catalyst activity and the air/fuel ratio, even a lean-fuel mixture can be stably burned over a wide range of temperatures. For applications to low-temperature combustion, e.g., in direct drying

N. Kamiuchi • K. Eguchi (✉)
Department of Energy and Hydrocarbon Chemistry, Graduate School of Engineering, Kyoto University, Nishikyo-ku Kyoto 615-8510, Japan
e-mail: eguchi@scl.kyoto-u.ac.jp

L. Guczi and A. Erdőhelyi (eds.), *Catalysis for Alternative Energy Generation*,
DOI 10.1007/978-1-4614-0344-9_8,

of foods and polymers, the required heat can be supplied by the combustion of very lean mixtures over a highly active catalyst. Low-temperature catalytic combustion can also be applied for the cleaning of car exhaust, removing volatile organic compounds (VOCs), flameless heaters, household appliances, and other systems utilizing heat-radiation applications operated below 1,000°C.

Some precious metal catalysts have been known to be active for ignition reactions. Platinum has been known as the most active catalyst component for various fuels including hydrocarbons and VOCs [2, 3]. On the other hand, methane is sometimes contained in the exhaust as this molecule is most difficult to achieve complete combustion. Palladium has been known to be the most active component for the combustion of methane. The activities of supported Pd catalysts are higher than Pt-based catalysts unlike other fuels. Modification of the catalytic activity of precious metal catalysts in combination with oxide supports has been discussed based on morphological and chemical effects, such as the dispersion and surface reconstruction of metal particles, and chemisorbed oxygen on active sites. The nature of the interaction between oxide and a precious metal and the resultant activation of surface has been the subject of extensive studies.

Mixed metal oxide catalysts are attractive because of their low cost and abundant resources. Catalytic activity and combustion characteristics are dependent on the components, concentration of metal species, and crystal structure. Some mixed oxides with specific crystal structures, such as perovskite, spinel, and hexaaluminate, are active for oxidation of hydrocarbons. One of the advantages for series of the mixed oxides is the possibility to control the oxidation activity by appropriate selection of components and compositions without a change in the crystal structure. The activity and chemical and morphological stability should be comparable to precious metal catalysts to be used for practical application. In this chapter, various catalysts for combustion of methane have been investigated.

8.2 Catalytic Combustion

Catalytic combustion is the oxidation reaction of organic compounds such as hydrocarbons by using solid catalysts [*reaction* (8.1)].

$$C_lH_mO_n + \left(l + \frac{1}{4m} - \frac{1}{2n}\right)O_2 \rightarrow lCO_2 + \frac{1}{2m}H_2O. \tag{8.1}$$

Although ignition of flame initiates homogeneous combustion, flame and radical formation is unnecessary for the surface catalytic reaction. Therefore, the combustion reaction proceeds at lower temperatures because of its small activation energy than conventional flame combustion. Stable combustion on the catalyst surface is effectively achieved even for lean-fuel gases. Consequently, emission of toxic substances under incomplete combustion is inhibited. Because of these advantages,

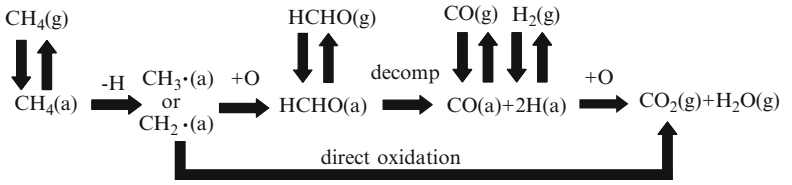

Fig. 8.1 Proposed mechanism for methane oxidation. Adsorbed (a) and gas phase (g) [14]

catalytic combustion has been applied in many fields as a clean and efficient method. Although the catalytic oxidation is often employed for production of useful chemicals, the partial oxidation of organic compounds is not dealt with in this chapter.

Catalytic combustion is generally classified into three categories according to the temperature zones of the combustion systems. Low-temperature combustion is operated below 300°C, the intermediate temperature combustion from 300 to 800°C, and the high-temperature combustion over 800°C. The low-temperature catalytic combustion has been applied to oil heaters, gas sensors, abatement of harmful compounds such as VOCs [4–11], and so on. The catalytic combustion at intermediate temperatures has been utilized for the purification of automobile exhaust emissions [12], the energy recovery systems in industrial plants, the catalytic heaters, etc. Meanwhile, the practical applications of high-temperature combustion are represented by the gas turbine and boiler [13]. Catalytic combustion has two attractive features in its practical use. They are the high combustion efficiency and the reduction of thermal NO_x emission. In the conventional flame combustion, thermal NO_x and prompt NO_x are produced via radical chain reaction operated in the middle- and high-temperature regions and the rich-fuel region, respectively. However, the catalytic combustion proceeds without formation of NO_x due to the low operation temperature and absence of radical species. Thus, the NO_x emission is extremely low in comparison with the flame combustion. In every application of catalytic combustion, a low light-off temperature is requested for effective utilization of catalysts. The preheating of catalysts is minimized by using active catalysts with low light-off temperature. Therefore, the design of catalyst is significant to the practical application.

In the case of methane combustion over Pd catalyst, the reaction mechanism was proposed as shown in Fig. 8.1 [14]. At first, the methane molecule chemisorbed onto the surface of the catalyst dissociates into methyl or methylene radicals by the removal of hydrogen atoms. In one process, CO_2 and H_2O are directly produced due to the reaction of radicals and adsorbed oxygen. In another process, chemisorbed formaldehyde is produced by the reaction of radicals and oxygen. The adsorbed formaldehyde decomposes into adsorbed CO and hydrogen, and subsequently CO and hydrogen react with adsorbed oxygen. Consequently, the adsorbed formaldehyde changes into CO_2 and H_2O.

8.3 Precious Metal Catalysts

8.3.1 Palladium Catalysts

The supported precious metal catalysts generally exhibit high catalytic activities for the oxidation reaction of hydrocarbon. Among them, the catalysts composed of platinum and palladium with high d-electron density are well known as most active species. Platinum catalysts are generally most active for the oxidation of various fuels such as saturated hydrocarbons. For complete methane oxidation, however, the activity of palladium catalysts is superior to that of platinum catalysts. Therefore, Pd catalysts for methane combustion have been investigated by many researchers so far. In many reports, alumina has been chosen as the support material because of its high surface area, relatively high thermal stability, and low cost.

Farrauto et al. evaluated the catalytic activities of PdO/Al_2O_3 for methane oxidation [15]. The typical result of methane conversion test is shown in Fig. 8.2. The conversion was recorded in heating and cooling courses. During heating course, the oxidation of methane started around 300°C, and the complete oxidation was achieved at ca. 700°C. After the temperature of furnace was increased up to 1,000°C, the sample was cooled at a rate of 20°C/min as shown by the dashed line. The peak of conversion appeared at ca. 600°C. This significant hysteresis indicates that at least two distinct species with different activities are operative depending on the temperature range. Groppi et al. investigated the O_2 concentration profile of PdO/La-doped Al_2O_3 by temperature-programmed decomposition–temperature-programmed oxidation (TPD–TPO) experiments, and the obtained profile was compared with the catalytic activity [16]. From these experiments, a $PdO \leftrightarrow Pd^0$ transition plays the decisive role in the catalytic activity. In other words, the activity hysteresis should be related with the property of palladium species, i.e., the PdO species are more active and dominated in the reaction at 300–400°C, whereas the decomposition to metallic palladium provides less active surface above ca. 800°C.

The mechanism of methane combustion is not thoroughly understood, whereas many researchers have tried to reveal the reaction process of methane oxidation. In the case of reduced Pd/Al_2O_3 catalyst, Firth and Holland proposed the mechanism of methane oxidation between adsorbed oxygen and adsorbed methane at the top surface of catalyst below 310°C [17]. On the other hand, it was suggested that the adsorbed oxygen reacts with methane on the layer of adsorbed oxygen, because the oxygen coverage reaches maximum above 310°C. Seimanides et al. suggested the mechanism of methane oxidation followed the well-known Eley–Rideal model by the experimental support of solid electrolyte potentiometry (SEP) [18]. The controversial mechanisms are partly because of the difference in the surface properties and the oxidation state of palladium under investigation. However, the Mars and van Krevelen mechanism (redox mechanism) is widely accepted [19–21]. In this model, the PdO is reduced by the adsorbed methane, followed by the reoxidation of the reduced Pd with gaseous oxygen. This model well explains the previous discussion that transformation of $PdO \leftrightarrow Pd^0$ is confirmed by the ^{18}O isotope

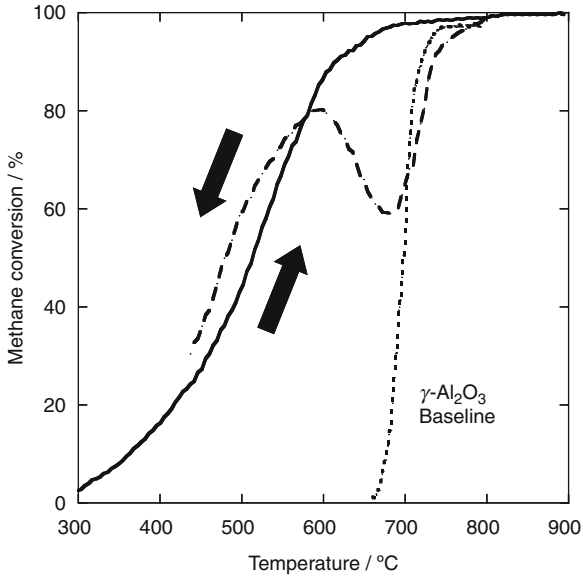

Fig. 8.2 Methane conversion by 4% $PdO/A1_2O_3$ as a function of temperature from 300 to 900°C; (*line*) heating, (*dashed line*) cooling, and (*dotted line*) baseline [15]

labeling [22]. Furthermore, Fujimoto et al. proposed the significant contribution of oxygen vacancies [23, 24]. The methane oxidation over Pd catalyst proceeds at the coexisting sites for adsorbed oxygen and adsorbed methane on oxygen vacancies. However, more investigation about the reaction process should be continued because the mechanism is still unclear in most of the catalysts.

The transition of $PdO \leftrightarrow Pd^0$ was verified by several instrumental observations. Datye et al. studied the microstructural changes of 5 wt% $Pd/\theta\text{-}Al_2O_3$ catalyst during the transition of oxidation states by transmission electron microscopy (TEM), X-ray diffraction (XRD), and X-ray photoelectron spectroscopy (XPS) [25]. In the TEM image of the catalyst after methane oxidation at 1,133 K, the coexisting phases of Pd metal and PdO were observed. Furthermore, the surface of polycrystalline particles was roughened for the sample heat-treated in air. After a series of experiments, they proposed mechanisms about the morphological changes during a transformation of $PdO \leftrightarrow Pd^0$. The most possible mechanism for the microstructural changes is the partial oxidation of Pd particles without significant volume change of the particles and redispersion of PdO particles.

As mentioned above, the palladium catalysts supported on Al_2O_3 generally exhibit high activities for methane combustion. However, the degradation of catalytic activities is induced by several factors such as sintering and poisoning. Sintering proceeds in both precious metal and metal oxide supports at high temperatures. This process is usually irreversible, as the lowered surface energy will not be recovered. Therefore, the choice of support material and preparation methods [26] are important as well as the precious metal species in order to prepare the catalyst with high dispersion and thermal stability. From this viewpoint, hexaaluminate-related compounds with high thermal stabilities and high catalytic activities have been proposed as a heat-resistant support.

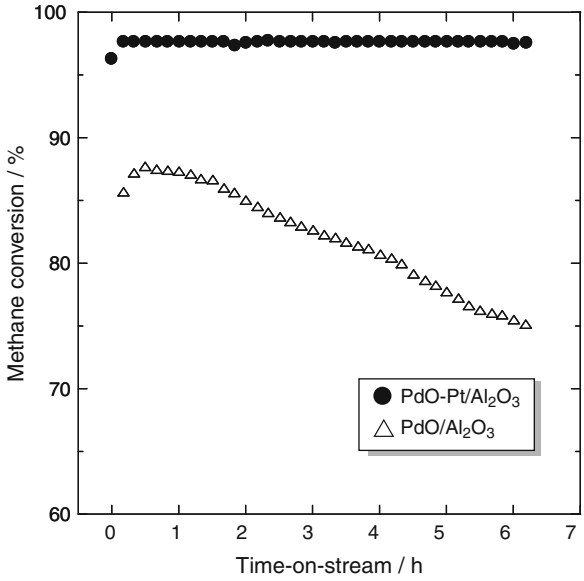

Fig. 8.3 Time-on-stream activity of $PdO/\alpha\text{-}Al_2O_3$ and $PdO–Pt/\alpha\text{-}Al_2O_3$ catalysts in the methane combustion at 623 K (reaction conditions: 0.5% CH_4 in air, space velocity: 18,000 h^{-1}) [30]

The adsorption of sulfur, which is the impurity of natural gas, or reaction products (water, CO, and CO_2) may also lead to deactivation of catalysts as a result of the modification of electronic state and structural properties of surface by the adsorbed species. The poisoning effect on the activity of the Pd/Al_2O_3 catalyst in methane combustion was investigated with and without the supply of H_2S in the reaction gas [27]. The ignition temperature of methane was raised from 500 to 600°C in the presence of H_2S. The sulfur species inhibit the adsorption and dissociation of methane and oxygen, and the reaction between adsorbed species is limited. Venezia et al. also investigated the sulfur poisoning effect for Pd and PdAu catalysts supported on mesoporous silica (HMS) [28] and Pd/TiO_2-doped SiO_2 catalyst [29]. The Pd/HMS catalyst was highly tolerant to SO_2 in addition to its high activity in methane oxidation. Moreover, the degraded activity of Pd/HMS by a SO_2 treatment at 350°C was recovered by the subsequent cycle of methane oxidation reaction. From the XPS measurements for PdAu/HMS catalyst, it was ascertained that the surface of palladium was reduced during methane oxidation in the presence of SO_2. In the case of Pd on TiO_2-doped SiO_2, the high SO_2 tolerance was achieved for the Pd catalyst supported on the silica modified by a small amount of titania (5–10 wt%). It was suggested that the Si–O–Ti linkages were responsible for the improvement of catalytic activity. In addition, the superior SO_2 tolerance resulted from the interaction between TiO_2 and the sulfur molecule and the easy desorption of SO_x from silica with a high surface area. As mentioned above, the support material is significant for the catalytic activity and sulfur tolerance.

The catalytic properties of bimetallic systems have been investigated so far. Narui et al. reported that the catalytic activities of $Pd–Pt/\alpha\text{-}Al_2O_3$ at 350°C were significantly gained as compared with $Pd/\alpha\text{-}Al_2O_3$ (Fig. 8.3) [30]. The catalytic

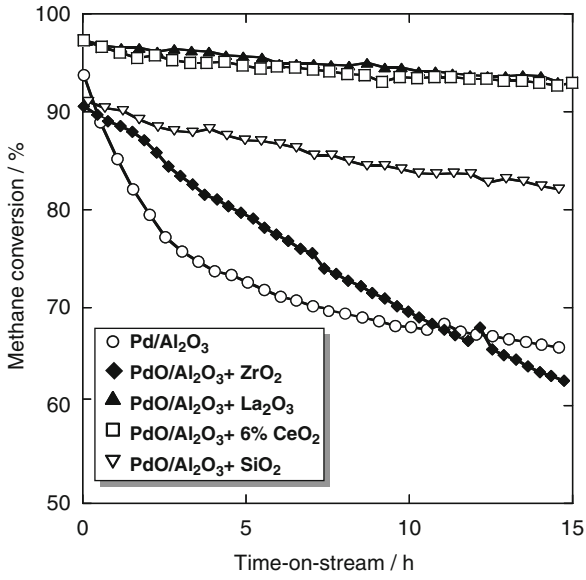

Fig. 8.4 Influence of promoters on catalyst durability—conversion versus time on stream [32]

activities were enhanced from 90 to 98% by the addition of platinum, which also accompanied the high thermal durability of Pd–Pt/α-Al_2O_3. This result was attributed to the high dispersion of Pd and Pt particles and the inhibition of sintering at 350°C because of the interaction between two precious metal components. Recently, Persson et al. also studied the catalytic oxidation of methane over Pd/γ-Al_2O_3 and Pd–Pt/γ-Al_2O_3 [31]. In their experiments, the activity over Pd–Pt/γ-Al_2O_3 was higher than that of Pd/γ-Al_2O_3. From the TEM observation for Pd/γ-Al_2O_3, it was revealed that the palladium particles composed of small PdO and Pd became more oxidized with a larger particle size under an oxidative atmosphere. In the case of Pd–Pt/γ-Al_2O_3, two kinds of particles with PdO and alloy between Pd and Pt were observed. The composition of Pd/Pt in alloy decreased during methane oxidation. The Pd particles excluded from alloy were oxidized and became small PdO particles. As a result, Pd–Pt/γ-Al_2O_3 catalyst exhibited higher activity and thermal durability.

The deactivation of palladium catalysts could be sometimes avoided by appropriate selection of support such as modified metal oxides. Among several promoters investigated (ZrO_2, La_2O_3, CeO_2, and SiO_2), Euzen et al. found that ceria and lantana added to alumina especially improved its catalytic activity and durability (Fig. 8.4) [32]. It was suggested that the role of CeO_2 is to gain the sintering resistance of PdO or to stabilize the active oxidation state of PdO.

The properties of support material are of great significance in order to achieve high activities and durability, as well as the state of palladium particles. Thus, the metal oxides except Al_2O_3 have been also used as the support. The catalytic activities of Pd catalyst supported on various metal oxides were evaluated for the methane oxidation by Widjaja et al. [33, 34]. As can be seen in Fig. 8.5, Pd/SnO_2

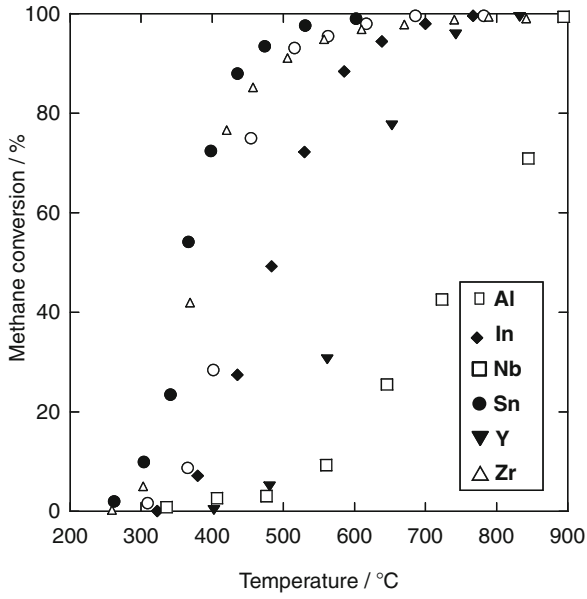

Fig. 8.5 Catalytic combustion of methane over 1 wt% Pd/MO_x (M = Al, In, Nb, Sn, Y, and Zr) (reaction conditions: CH_4, 1 vol.%; air, 99 vol.%; space velocity: 48,000 h^{-1}) [33]

and Pd/ZrO_2 catalysts exhibited higher activities than Pd/Al_2O_3, even though their surface areas were extremely lower than that of Pd/Al_2O_3. Furthermore, the activity of Pd/SnO_2 in the heating and cooling courses agreed with each other, whereas significant hysteresis was observed in Pd/Al_2O_3 as mentioned. It is considered that the reaction products of H_2O and CO_2 have little influence on the activity of Pd/SnO_2. In addition, it is noted that palladium oxide was observed as a surface layer which uniformly covered SnO_2 particles from TEM observation, and the eggshell structure originated from strong metal–support interaction results in the large active surface of palladium.

The catalytic activities over unsupported Pd catalysts have been also examined by some researchers. For instance, palladium cation-exchanged zeolites (ZSM-5, mordenite, and ferrierite) were studied by Li et al. [35]. As a result, Pd-zeolites exhibited much higher activities than PdO/Al_2O_3. Methane oxidation over Pd–ZSM-5 was started at ca. 200°C, even though the ignition temperature of conventional PdO/Al_2O_3 catalyst was around 250°C. It was concluded that the high activities of Pd-zeolite were related to the high dispersion of palladium in atomic scale and abundant lattice oxygen.

8.3.2 Supported Pt Catalysts

The platinum catalysts have been investigated for combustion of methane similar to the palladium catalysts. Platinum catalysts generally demonstrate high catalytic activities for the oxidation of paraffins with carbon number of 3 or higher, whereas

Table 8.1 Comparison of methane conversions over 4% Pt/Al_2O_3 and 4% Pd/Al_2O_3 catalysts at different temperatures [36]

	O_2/CH_4 5:1		O_2/CH_4 1:1	
Temperature/°C	Pt	Pd	Pt	Pd
300	1.2	23.0	0.6	9.1
325	2.2	40.6	1.2	18.2
350	4.2	–	4.0	33.0
375	6.6	82.5	59.0	50.7
400	14.0	94.5	67.9	59.2
425	22.0	98.5	78.8	68.1
450	35.3	100	88.1	77.6
475	49.2	–	94.6	86.2
500	65.8	–	97.9	91.1
525	81.6	–	99.0	93.1
550	93.8	–	99.4	94.5

palladium catalysts are more active for the oxidation of methane, CO, and olefins. In addition, the oxidation states of two precious metals are also different. The active platinum phase for complete oxidation of methane is the metallic Pt (0). On the other hand, the active phase of palladium is the oxidized state of PdO. The catalytic activities for methane oxidation over Pt-based catalysts are generally inferior to those over Pd-based catalysts. However, some exceptional examples of higher activities of Pt catalysts than Pd catalysts for methane combustion have been reported. Burch et al. carried out the methane combustion under lean and rich conditions over Pt/Al_2O_3 and Pd/Al_2O_3 [36]. Under the oxygen-rich condition (O_2:CH_4 = 5:1), the 4% Pt/Al_2O_3 catalyst gave only 1.2% conversion at 300°C compared to 23% for the 4% Pd/Al_2O_3 (Table 8.1). The conversion over Pt/Al_2O_3 was 35% at 450°C, whereas methane was completely oxidized at this temperature over Pd/Al_2O_3. Meanwhile, Pt/Al_2O_3 showed higher activity above 350°C under the fuel-rich condition (O_2:CH_4 = 1:1). They assumed that the light-off over Pt/Al_2O_3 under the fuel-rich condition is ascribed to the local heating or the concentration unbalance of methane and oxygen adsorbed at the surface of the catalyst. Under the oxygen-rich condition, on the other hand, the adsorbed oxygen inhibits the adsorption of methane.

Garetto et al. studied the difference of the catalytic activities of Pt/Al_2O_3 for complete oxidation of cyclopentane and methane [37]. The ignition temperature of methane was significantly higher than that of cyclopentane as shown in Fig. 8.6. As just described, Pt catalysts are usually more active for the oxidation of higher alkanes and alkenes. Therefore, many experiments have been conducted so as to prepare platinum catalysts with higher activities for methane oxidation. Corro et al. studied the effect of Sn addition to Pt/Al_2O_3 catalyst, sulfation, and the presence of C_3H_8 gas [38, 39]. The catalysts of 1% Pt/γ-Al_2O_3 and 1% Pt–2% Sn/γ-Al_2O_3 were prepared by the impregnation method. Then, a part of the catalysts was presulfated for 10 h at 500°C in a gaseous mixture composed of 50-ppm SO_2, 5% O_2. Figure 8.7 shows the methane conversion over 1% Pt/γ-Al_2O_3 and 1% Pt–2% Sn/γ-Al_2O_3 [39]. From the results of combustion test, the ignition temperature could be reduced either by the addition of Sn or by sulfation. This promoted reaction by the Sn

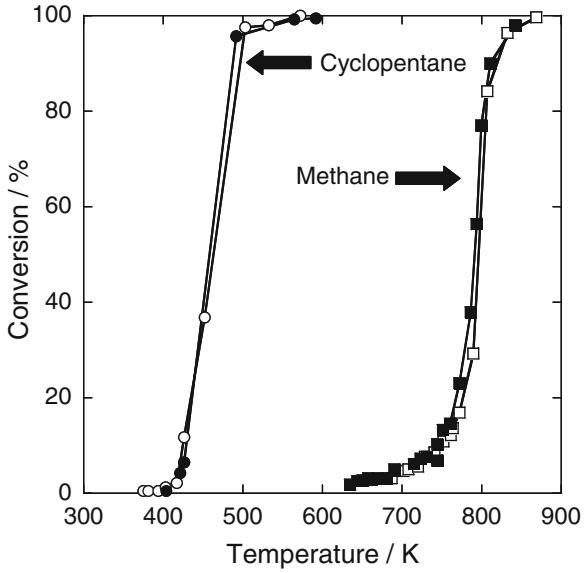

Fig. 8.6 Consecutive light-off curves: (*filled circle*, *filed square*) first run; (*open circle*, *open square*) second run. Cyclopentane combustion: $W/F_{CP}{}^{0} = 54$ g catalyst h/mol cyclopentane, $P = 1$ atm, CP:O_2:N_2 = 0.65:10:90. Methane combustion: $W/F_{CH4}{}^{0} = 20$ g catalyst h/mol methane, $P = 1$ atm, CH_4:O_2:N_2 = 2:9.8:88.2 [37]

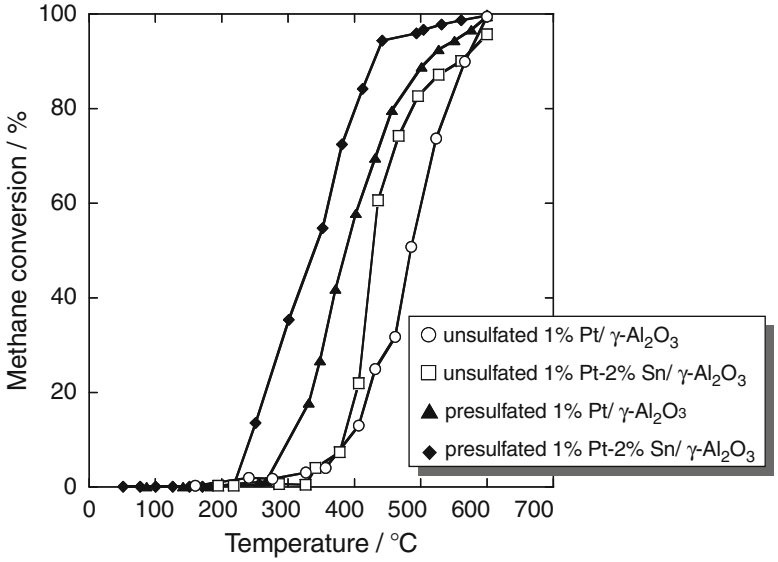

Fig. 8.7 Methane conversion as a function of temperature on the CH_4–O_2 reaction. Effect of 1,000-ppmV C_3H_8 in the reaction feed on the CH_4–O_2 reaction over (*open circle*): unsulfated 1% Pt/γ-Al_2O_3, (*open square*): unsulfated 1% Pt–2% Sn/γ-Al_2O_3, (*filled triangle*): presulfated 1% Pt/ γ-Al_2O_3, and (*filled diamond*): presulfated 1% Pt–2% Sn/γ-Al_2O_3. Reaction feed: 4% CH_4, 20% O_2, 1,000-ppmV C_3H_8, balance He [39]

addition and sulfation is attributed to the inhibition of Pt particles from sintering. It is also noteworthy that the ignition temperature for methane oxidation was lowered in the presence of C_3H_8. The propane combustion, initiating at a lower temperature, provides local heat to activate Pt sites for adsorption of methane.

It was reported that several support materials such as SiO_2 and SnO_2 also played an important role in enhancing the catalytic properties [40–42]. Niwa et al. investigated the catalytic activities of methane oxidation over Pt/Al_2O_3, $Pt/SiO_2–Al_2O_3$, and Pt/SiO_2 [40]. It was revealed that $Pt/SiO_2–Al_2O_3$ exhibited the highest activities among them. They confirmed that the dispersion of Pt particles on support strongly affected the catalytic activities. Roth et al. [42] reported higher activity of Pt/SnO_2 catalyst despite the lower surface area than Pt/Al_2O_3.

As in the case of Pd catalysts, it is commonly known that the chloride or sulfur deactivates the catalytic activities of Pt-based catalysts. For example, Marceau et al. studied the influence of residual chloride ions in Pt/Al_2O_3 catalysts by using the platinum precursor of H_2PtCl and $Pt(NH_3)_4(OH)_2$ [43]. It was found that chloride ion deteriorated the activities of total methane oxidation over Pt/Al_2O_3. The inhibitory effect was gradually weakened as chloride ions were eliminated with an elapse of time on stream.

8.4 $CeO_2–ZrO_2$-Based Catalysts

Supported precious metal catalysts are well known for their high catalytic activities in methane combustion. Palladium and platinum catalysts especially exhibit high activities as mentioned above. However, most precious metal catalysts are deactivated under the severe operating conditions. Furthermore, precious metals have the problem of their cost and resource. From this perspective, the development of the catalysts consisting of other materials has been desired. Generally, transition metal oxides are inexpensive as compared with precious metals, and the number of combination of transition metals is possible for the design of active catalysts. The catalysts consisting of transition metal oxides exhibit higher activities for the oxidation of hydrocarbons, though the activities were generally inferior to those of precious metal catalysts. Therefore, the transition metal oxide catalysts have been widely investigated so far. Among them, cerium, zirconium, and cobalt are the promising components for combustion catalysts. Pengpanich et al. investigated the activities of $CeO_2–ZrO_2$ mixed oxide catalysts as well as the dependence on the Ce/Zr ratio [44]. Figure 8.8 shows the methane conversion profile over $Ce_{1-x}Zr_xO_2$ mixed oxide catalysts calcined at 500°C. It is noteworthy that the $Ce_{1-x}Zr_xO_2$ mixed oxide catalysts were more active than either pure CeO_2 or ZrO_2. The activity of $Ce_{0.75}Zr_{0.25}O_2$ was highest in this binary oxide system despite its lower surface area than that of $Ce_{0.5}Zr_{0.5}O_2$ and $Ce_{0.25}Zr_{0.75}O_2$. It was found from CO-TPR profiles that $Ce_{0.75}Zr_{0.25}O_2$ was most reducible at low temperatures in relation with its high catalytic activities in the $CeO_2–ZrO_2$ catalysts.

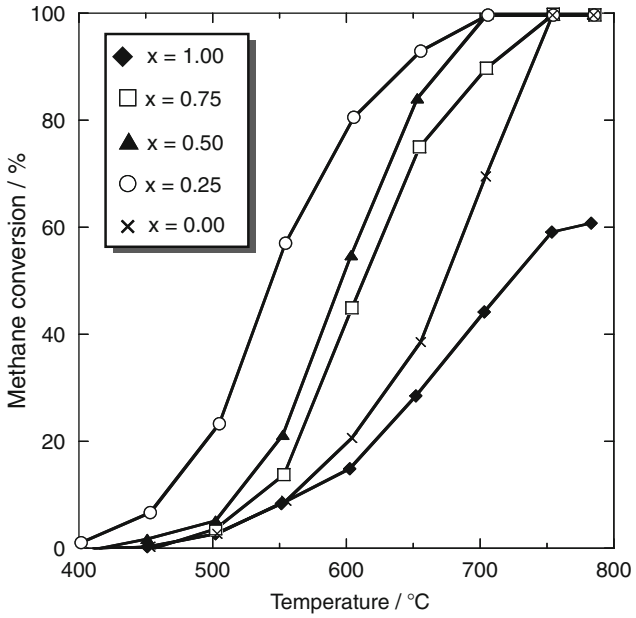

Fig. 8.8 Light-off curves over $Ce_{1-x}Zr_xO_2$ mixed oxide catalysts prepared via sol–gel technique with aging time = 50 h calcined at 500°C. Gas mixture contains 2.0% CH_4, 21.0% O_2, and balance He. Total flow 100 ml/min [44]

The CeO_2–ZrO_2 mixed oxides prepared from coprecipitation method were investigated by Bozo et al. [45]. Their conclusion was that the $Ce_{0.67}Zr_{0.33}O_2$ had a superior thermal stability from the comparison of TPR profiles of a series of $Ce_{1-x}Zr_xO_2$ before and after aging at 1,000°C in $O_2 + H_2O$. In addition, $Ce_{0.67}Zr_{0.33}O_2$ which contained a small amount of zirconium showed the highest activity [46].

The CeO_2–ZrO_2 catalysts containing an additional active component such as Pt [45, 46], Pd [46–48], Mn [45, 49], Cu [49, 50], and Co [51, 52] have been also reported. Subsequently, Bozo et al. compared the catalytic activities of Pt or MnO_x supported on $Ce_{0.67}Zr_{0.33}O_2$ for methane combustion with those of Pt/Al_2O_3 or MnO_x/Al_2O_3 catalyst. The initial temperature of combustion over $Pt/Ce_{0.67}Zr_{0.33}O_2$, being ca. 200°C, was much lower than the temperature over Pt/Al_2O_3 catalyst (ca. 450°C). On the other hand, $MnO_x/Ce_{0.67}Zr_{0.33}O_2$ was slightly more active than MnO_x/Al_2O_3. The promoting effect of $Ce_{0.67}Zr_{0.33}O_2$, however, disappeared after aging treatment at 1,000°C, accompanied with the dramatic decrease in the BET surface area of $Pt/Ce_{0.67}Zr_{0.33}O_2$ and $MnO_x/Ce_{0.67}Zr_{0.33}O_2$. In the case of $Pt/Ce_{0.67}Zr_{0.33}O_2$ and $Pd/Ce_{0.67}Zr_{0.33}O_2$ [46], the degraded activities under methane combustion for 10 h were recovered by the in situ reduction treatment in H_2, whereas the activity was not restored by in situ oxidation treatment.

Terribile et al. analyzed the catalytic activities and the influence of dopants in Mn- or Cu-doped CeO_2–ZrO_2 catalysts [49]. It was found that a small amount of

MnO_x and CuO dissolved into the lattice of CeO_2–ZrO_2 catalysts, and then the redox behavior of catalyst was strongly affected. Thereby, the catalytic activity and stability were promoted by the addition of MnO_x and CuO.

The cobalt containing catalysts are also very active components for CO and methane oxidation [53, 54]. Therefore, Liotta et al. prepared Co_3O_4/CeO_2 and Co_3O_4/CeO_2–ZrO_2 composite catalysts by coprecipitation method, and conducted methane combustion tests [51, 52]. The catalytic activities of CeO_2 and CeO_2–ZrO_2 were drastically improved by the presence of 30 wt% Co_3O_4 species. Moreover, the activity of 30 wt% Co_3O_4/CeO_2 was not deteriorated even after calcination at 750°C for 7 h. From a series of experiments, it was indicated that the reducibility of the Co_3O_4 species or the oxygen mobility in the catalysts strongly affected the methane combustion activity. Furthermore, it was concluded that CeO_2 and CeO_2–ZrO_2 were effective in dispersing the active Co_3O_4 phase and stabilizing it against decomposition into the less active CoO phase.

8.5 Perovskite Catalysts

The catalytic combustion of methane over perovskite-type catalysts has been investigated extensively by many researchers, because of its several advantages. Among the variety of mixed oxides with ABO_3-type perovskite structure, appropriate components for A and B sites and compositions can be selected to achieve high thermal stability and high activity. Activities of some perovskite-type oxides are comparable to those of platinum-based catalysts [55–58]. Among them, oxide systems based on $LaCoO_3$, $LaFeO_3$, and $LaMnO_3$ are active and thermally stable as to be the candidates for combustion catalysts at high temperatures [59].

Arai et al. reported the catalytic combustion of CH_4 over various perovskite-type oxides ($LaMO_3$, M = Co, Mn, Fe, Cu, Ni, Cr) [60]. The catalytic activities, surface area, and apparent activation energies of those perovskite-type oxides and 1 wt% Pt/Al_2O_3 catalyst are summarized in Table 8.2. Combustion of methane was promoted and the apparent activation energy was lowered by the presence of metal and oxide catalysts, as compared with non-catalytic thermal reaction. The activities of $LaCoO_3$, $LaMnO_3$, and $LaFeO_3$ catalysts were quite close to that of Pt/Al_2O_3 catalyst, whereas Pt/Al_2O_3 catalyst exhibited highest activities due to its larger surface area.

The cation sites in the perovskite lattice (ABO_3) can be easily substituted by foreign cations for A and/or B sites, and the substitution sometimes brings about promotion of the catalytic activity of perovskite-type oxides. The partial substitution of A and/or B sites often gives rise to vacancy formation, lattice distortion, valence shift, etc., and thereby affects the catalytic activity.

Partial substitution of A-site in perovskite-type oxide has been demonstrated by many researchers so far [60–66]. The perovskite-type oxides of $La_{1-x}A_xMnO_3$ (A = Sr, Eu, and Ce) were investigated by Marchetti et al. [62]. The temperature of complete oxidation of methane over all catalysts was ca. 500–600°C (Fig. 8.9),

Table 8.2 Methane oxidation activity of perovskite-type oxides, ABO_3, and Pt/alumina catalysts [60]

Catalyst	Surface area (m^2/g)	$T_{50\%}$(°C)	E_a (kcal/mol)
$LaCoO_3$	3.0	525	22.1
$LaMnO_3$	4.0	579	21.8
$LaFeO_3$	3.1	571	18.2
$LaCuO_3$	0.6	672	23.8
$LaNiO_3$	4.8	702	19.4
$LaCrO_3$	1.9	780	28.8
1 wt% Pt/Al_2O_3	146.5	518	27.6
Thermal data		834	61.5

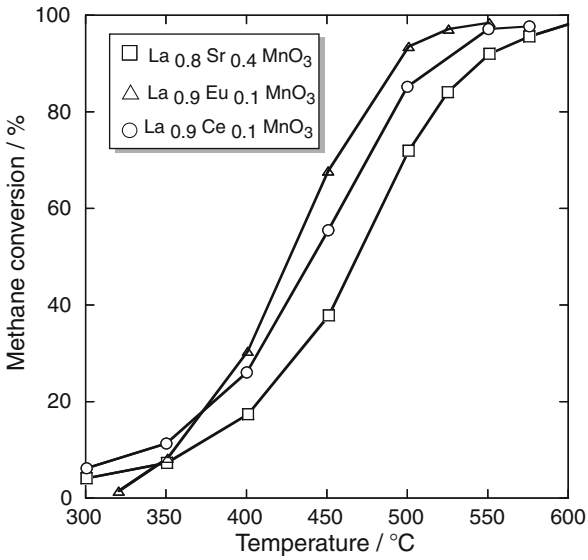

Fig. 8.9 Activity comparison data under standard reaction conditions [62]

and the high catalytic activities were not deteriorated for 100 h on stream. From the O_2 TPD measurements, it was found that two kinds of oxygen species desorbing in different temperature regions were active in these catalysts. They were an adsorbed oxygen species and a lattice oxygen species. The former reacts at lower temperatures, and the latter becomes active at higher temperatures. Thereby, the order of activities of $La_{0.6}Sr_{0.4}MnO_3$, $La_{0.9}Eu_{0.1}MnO_3$, and $La_{0.9}Ce_{0.1}MnO_3$ in the low-temperature region was different from the order in the high-temperature region.

Voorhoeve et al. proposed that the oxidation over perovskite-type oxides is classified into suprafacial and intrafacial reactions [67]. The reaction between adsorbed species on the surface proceeds at relatively low temperatures for the suprafacial reaction, whereas the intrafacial reaction is a high-temperature process

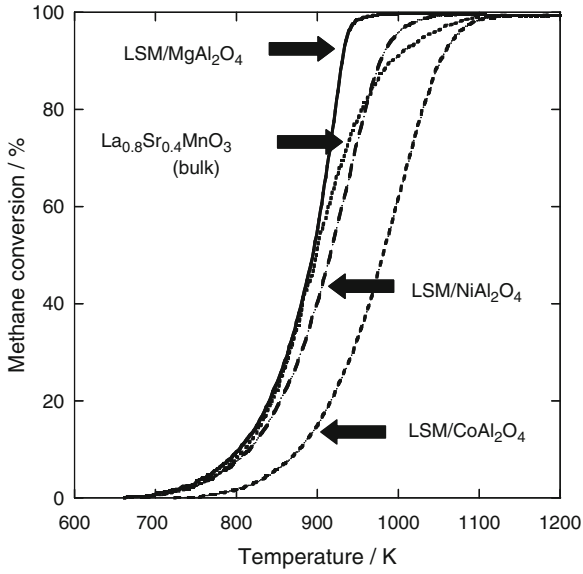

Fig. 8.10 Comparison of methane combustion activities of supported $La_{0.8}Sr_{0.2}MnO_{3+x}$ and pure $La_{0.8}Sr_{0.2}MnO_{3+x}$. Sample weight: 0.100 g; reactant gas composition: 1% CH_4, 4% O_2, and He (balance); GHSV: 135,000 h^{-1} [71]

in which the reaction rate is correlated with the thermodynamic stability of lattice oxygen bonded to transition metal ions.

The partial substitution of the B-site has also influenced the methane combustion activity [68–70]. For example, $LaCr_{1-x}Mg_xO_3$ ($x = 0$–0.5) by the citrate method [69] shows that catalytic activities were promoted by Mg doping. This promoting effect of the Cr/Mg substitution was ascribed to the co-formation of perovskite and MgO crystals. The presence of MgO should result in the high dispersion of perovskite.

Although the perovskite phase is thermodynamically stable for most of the systems, the thermal stability of catalysts, especially sintering resistance at elevated temperatures, is required as well as high activity for methane oxidation for practical applications. The support materials have been studied so as to suppress the sintering at high temperatures [71, 72]. Marti et al. investigated the effect of spinel support (MAl_2O_4, M = Mg, Ni, and Co) for the activities over $La_{0.8}Sr_{0.2}MnO_{3+x}$ (LSM) [71]. The overall activities of the three kinds of catalysts ($LSM/MgAl_2O_4$, $LSM/NiAl_2O_4$, and $LSM/CoAl_2O_4$) are compared with the activity of unsupported LSM, as shown in Fig. 8.10. The activity of $LSM/MgAl_2O_4$ was higher than that of unsupported LSM, whereas $LSM/NiAl_2O_4$ and $LSM/CoAl_2O_4$ were not so active. It was revealed that the amount of active oxygen species increased in the order $LSM/CoAl_2O_4 < LSM/NiAl_2O_4 < LSM/MgAl_2O_4$. This result of TPD measurements indicated that the $LSM/MgAl_2O_4$ catalyst was most active due to its large amount of oxygen species available for catalytic oxidation.

Cimino et al. also studied the effect of metal oxide supports. The perovskite of $LaMnO_3$ was supported on La-stabilized γ-Al_2O_3 and MgO by the deposition precipitation (DP) method. Although these two catalysts treated at 800°C exhibited

high catalytic activities for methane combustion, the catalytic activity of $LaMnO_3$/La/Al_2O_3 treated at 1,100°C was dramatically degraded. On the other hand, $LaMnO_3$/MgO catalysts were thermally stable as far as the dispersion state of $LaMnO_3$ was concerned.

The sensitivity to sulfur poisoning of perovskite oxides ($La_{1-x}Ce_xMn_{1-y}Co_yO_3$) was investigated by Alifanti et al. [73]. Although all perovskite-type catalysts were deactivated under the combustion test in the presence of 20-ppm SO_2, the catalysts substituted by a small amount of cerium ($La_{0.9}Ce_{0.1}CoO_3$, $La_{0.8}Ce_{0.2}CoO_3$, $La_{0.8}Ce_{0.2}MnO_3$) were less sensitive to the poisoning process. They concluded by XPS measurements that the deactivation was caused by the formation of sulfate species such as $La_2(SO_4)_3$ at the surface of catalysts.

Recently, the effects of preparation methods of perovskite catalysts have been investigated for methane combustion. For example, the urea decomposition method [74, 75], ultrasonic spray combustion method [76], spray pyrolysis [77], and microwave irradiation method [78] have been reported. Gao et al. compared the catalytic activities of $La_{0.9}Sr_{0.1}CoO_{3-\delta}$ catalysts prepared by urea decomposition method, citrate method, precipitation method with aqueous ammonia as precipitant, and precipitation method with ammonium carbonate solution [74]. The activities of methane combustion were in order of $La_{0.9}Sr_{0.1}CoO_{3-\delta}$ prepared by urea decomposition method > citrate method > precipitation with ammonia > precipitation with carbonate. The surface molar ratios of lattice oxygen/cobalt ion ($3-\delta$) in catalysts prepared by urea decomposition and citrate methods were 3.4 and 4.0, respectively, whereas the ratios of the other two catalysts prepared by precipitation with ammonia and carbonate were smaller than the nominal ratio of 3. Moreover, the BET surface area of the catalyst prepared by urea decomposition was larger than that of the catalyst by citrate method. Therefore, the high activity of the catalyst prepared by urea decomposition method was attributed to the appropriate surface structure which allowed the release and regeneration of surface active oxygen species.

8.6 Hexaaluminate-Related Compounds

The hexaaluminate-related compounds are also attractive catalysts for methane combustion especially at high temperatures around or above 1,000°C, since the precious metal components in supported catalysts volatilize as PdO or PtO_2 at ca. 1,000°C. The hexaaluminate compounds are represented by the general formula $MO_x{\cdot}6Al_2O_3$, where the component of M is usually the metal with large ion diameter such as an alkaline, alkaline-earth, or rare-earth metal. The crystal structure of hexaaluminate compound is illustrated as β-alumina or magnetoplumbite-type structures (Fig. 8.11) [79], and the hexaaluminate compounds with two kinds of structure are ideally represented as $MAl_{11}O_{17}$ and $MAl_{12}O_{19}$. However, most hexaaluminate compounds are described as $MAl_{12}O_{19-x}$, because they have some defects to satisfy the electroneutrality.

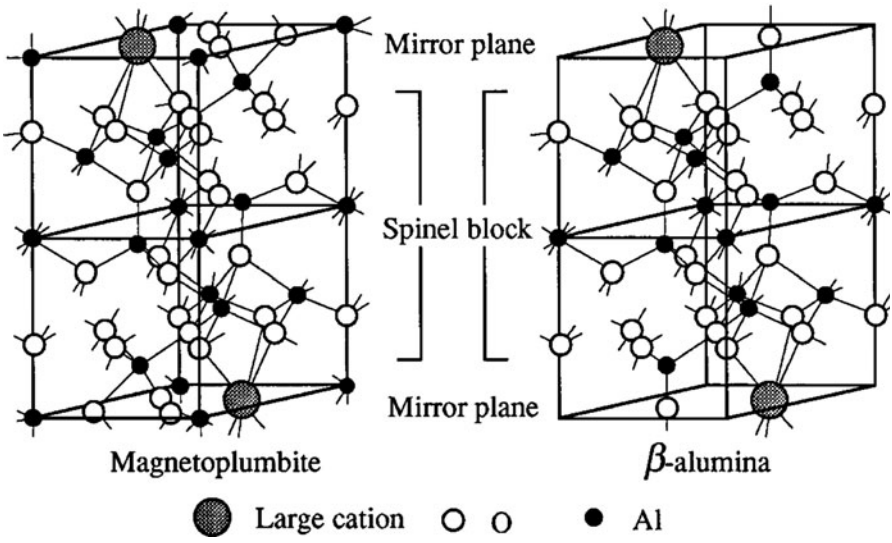

Fig. 8.11 Crystal structure of magnetoplumbite and β-alumina [79]

The unsubstituted hexaaluminate compounds are extremely thermally stabile, but the catalytic activities for methane combustion are insufficient for practical use. Therefore, substituted hexaaluminate compounds such as Ba–Mn–Al–O [80, 81], Ba–Fe–(Mn)–Al–O [81], Sr–La–Mn–Al–O [82], and Sr–(Ce, Pr, Nd, Sm, Gd)–Mn–Al–O [79] have been investigated in which transition metal species serve as active components. Figure 8.12 shows the methane combustion profile over $Sr_{0.8}La_{0.2}MnAl_{11}O_{19}$ (SLMA), $BaMnAl_{11}O_{19}$ (BMA), $Sr_{0.8}La_{0.2}Al_{12}O_{19}$ (SLA), and α-Al_2O_3 [82]. The enhancement of catalytic activities by the substitution was clearly observed. The surface area of SLMA, BMA, SLA, and α-Al_2O_3 were 17.5, 14.9, 25.8, and 3.1 $m^2\ g^{-1}$, respectively. This relatively high surface area after heat treatment at 1,200°C should be closely related to the catalytic activities. In addition, since Mn is known as redox-active species for CH_4 combustion, SLA and α-Al_2O_3 will be inactive in comparison with SLMA and BMA.

The hexaaluminate-related compounds are also used as support materials [83–85]. Jang et al. compared the activities of 2% Pd/$LaMnAl_{11}O_{19-\alpha}$ and $LaMnAl_{11}O_{19-\alpha}$ [83]. The light-off over Pd-supported $LaMnAl_{11}O_{19-\alpha}$ started at an extremely low temperature of 360°C, while the thermal stability was still insufficient for practical use.

The hexaaluminate compounds are generally synthesized by the hydrolysis of metal alkoxide, sol–gel methods, coprecipitation methods, and solid-state reaction of powders. Zarur and Ying prepared nanocrystalline barium hexaaluminate (BHA) by reverse microemulsion synthesis [86, 87]. Figure 8.13 shows the catalytic activities for methane oxidation over three kinds of preparation methods, conventional BHA, nanocrystalline BHA by the reverse microemulsion synthesis, and

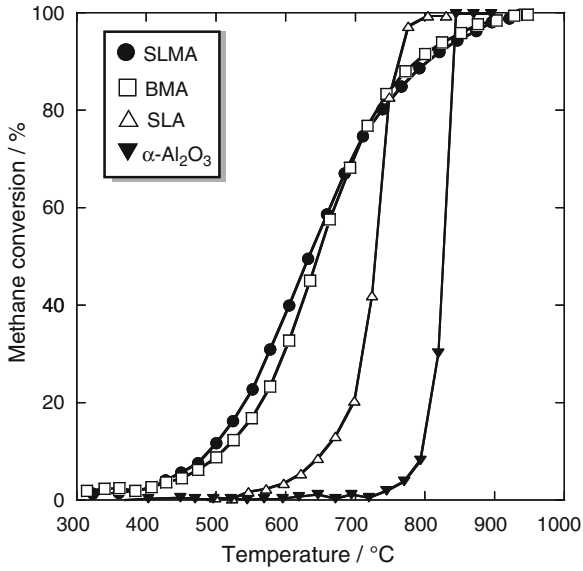

Fig. 8.12 Catalytic combustion of methane over hexaaluminate materials and α-Al_2O_3: (*filled circle*) $Sr_{0.8}La_{0.2}MnAl_{11}O_{19-\alpha}$ prepared via alkoxide hydrolysis (SLMA); (*open square*) $BaMnAl_{11}O_{19-\alpha}$ (BMA); (*open triangle*) $Sr_{0.8}La_{0.2}Al_{12}O_{19-\alpha}$ (SLA); and (*filled inverted triangle*) α-Al_2O_3. Reaction conditions: CH_4, 1 vol.%; air 99 vol.%; space velocity: 48,000 h^{-1} [82]

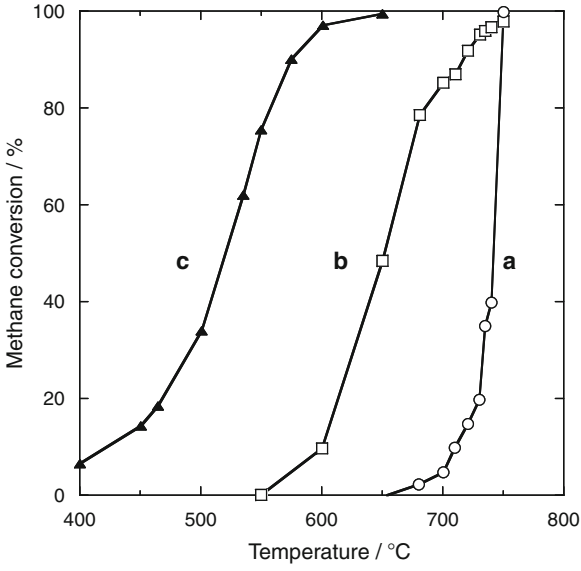

Fig. 8.13 Catalytic methane combustion experiments. Catalytic methane oxidation activity: (*a*) sol–gel-derived conventional BHA, (*b*) reverse microemulsion-derived BHA nanoparticles, (*c*) reverse microemulsion-derived CeO_2–BHA nanocomposite. The reactant stream consisted of 1 vol.% CH_4 in air; space velocity: 60,000 h^{-1} [86]

25 wt% CeO_2 deposited nanocrystalline BHA particles. The nanocrystalline BHA exhibited much higher activities in comparison to BHA prepared by the sol–gel method. Moreover, it was confirmed that the addition of CeO_2 resulted in the further activation of BHA. The high activities should be ascribable to the high surface area (40–60 m^2 g^{-1}) even after calcination at 1,300°C.

Wang et al. proposed supercritical drying (SCD) method as the preparation method of $LaMn_xAl_{12-x}O_{19}$ [88]. After the mixture of NH_4OH and metal nitrate solutions, the SCD method is used to extract water in the hydrogel. In the case of SCD method, the homogeneous $LaMn_xAl_{12-x}O_{19}$ aerogel with high pore volumes and pore diameters was prepared, unlike in conventional oven drying (CD) method. Therefore, $LaMn_xAl_{12-x}O_{19}$ catalyst with small crystal size and high surface area was prepared and exhibited the high activities for methane combustion. The effect of preparation methods may be ascribable to the textural modification and homogeneous phase formation which are especially strongly affected in the case of hexaaluminate compounds.

8.7 Conclusions

Methane combustion over various catalysts based on Pd, Pt, CeO_2–ZrO_2, perovskite-type metal oxides, and hexaaluminate compounds is summarized in this chapter. In particular, Pd catalysts have been generally known as most active for methane oxidation. However, other catalyst systems demonstrated unique activity and characteristics for this reaction by modification with additives and other factors. The catalytic properties of activities and catalyst lifetime are strongly affected by many factors such as components of catalyst, support material, preparation method, reaction temperature, and atmosphere. Therefore, the precise optimization of the conditions is significant in order to put catalysts into practical use. The degradation and regeneration of combustion catalysts have not been thoroughly understood, though the researches for regeneration in addition to the development of catalysts with higher durability should be increasingly important.

References

1. Forzatti P, Groppi G (1999) Catalytic combustion for the production of energy. Catal Today 54:165–180
2. Mitsui T, Tsutsui K, Matsui T, Kikuchi R, Eguchi K (2008) Catalytic abatement of acetaldehyde over oxide-supported precious metal catalysts. Appl Catal B Environ 78:158–165
3. Mitsui T, Matsui T, Kikuchi R, Eguchi K (2009) Low-temperature complete oxidation of ethyl acetate over CeO_2-supported precious metal catalysts. Top Catal 52:464–469
4. Papaefthimiou P, Ioannides T, Verykios XE (1997) Combustion of non-halogenated volatile organic compounds over group VIII metal catalysts. Appl Catal B Environ 13:175–184
5. Larsson P, Andersson A (1998) Complete oxidation of CO, ethanol, and ethyl acetate over copper oxide supported on titania and ceria modified titania. J Catal 179:72–89
6. Larsson P, Andersson A (2000) Oxides of copper, ceria promoted copper, manganese and copper manganese on Al_2O_3 for the combustion of CO, ethyl acetate and ethanol. Appl Catal B Environ 24:175–192
7. Kim SC (2002) Reverse microemulsion synthesis of nanostructured complex oxides for catalytic combustion. J Hazard Mater 91:285–299

8. Takeguchi T, Aoyama S, Ueda J, Kikuchi R, Eguchi K (2003) Catalytic combustion of volatile organic compounds on supported precious metal catalysts. Top Catal 23:159–162
9. Okumura K, Kobayashi T, Tanaka H, Niwa M (2003) Toluene combustion over palladium supported on various metal oxide supports. Appl Catal B Environ 44:325–331
10. Perkas N, Rotter H, Vradman L, Landau MV, Gedanken A (2006) Sonochemically prepared Pt/CeO_2 and its application as a catalyst in ethyl acetate combustion. Langmuir 22:7072–7077
11. Cellier C, Lambert S, Gaigneaux EM, Poleunis C, Ruaux V, Eloy P, Lahousse C, Bertrand P, Pirard J-P, Grange P (2007) Investigation of the preparation and activity of gold catalysts in the total oxidation of *n*-hexane. Appl Catal B Environ 70:406–416
12. Heck RM, Farrauto RJ (2001) Automobile exhaust catalysts. Appl Catal A Gen 221:443–457
13. Eguchi K, Arai H (1996) Recent advances in high temperature catalytic combustion. Catal Today 29:379–386
14. Oh SH, Mitchell PJ, Siewert RM (1991) Methane oxidation over alumina-supported noble metal catalysts with and without cerium additives. J Catal 132:287–301
15. Farrauto RJ, Hobson MC, Kennelly T, Waterman EM (1992) Catalytic chemistry of supported palladium for combustion of methane. Appl Catal A Gen 81:227–237
16. Groppi G, Cristiani C, Lietti L, Forzatti P (2000) Study of PdO/Pd transformation over alumina supported catalysts for natural gas combustion. Stud Surf Sci Catal 130:3801–3806
17. Firth JG, Holland HB (1969) Catalytic oxidation of methane over noble metals. Trans Faraday Soc 65:1121–1127
18. Seimanides S, Stoukides M (1986) Catalytic oxidation of methane on polycrystalline palladium supported on stabilized zirconia. J Catal 98:540–549
19. Muller CA, Maciejewski M, Koeppel RA, Baiker A (1997) Catalytic oxidation of methane on polycrystalline palladium supported on stabilized zirconia. J Catal 166:36–43
20. Muller CA, Maciejewski M, Koeppel RA, Baiker A (1999) Oxidation of benzyl alcohol using supported gold–palladium nanoparticles. Catal Today 47:245–252
21. Epling WS, Hoflund GB (1999) Catalytic oxidation of methane over ZrO_2-supported Pd catalysts. J Catal 182:5–12
22. Mueller CA, Maciejewski M, Koeppel RA, Tschan R, Baiker A (1996) Role of lattice oxygen in the combustion of methane over PdO/ZrO_2: combined pulse TG/DTA and MS study with ^{18}O-labelled catalyst. J Phys Chem 100:20006–20014
23. Fujimoto K, Ribeiro FH, Iglesia E, Avalos-Borja M (1997) Preprint Paper Am Chem Soc Div Petrol Chem 42:190
24. Fujimoto K, Ribeiro FH, Avalos-Borja M, Iglesia E (1998) Structure and reactivity of PdO_x/Zro_2 catalysts for methane oxidation at low temperatures. J Catal 179:431–442
25. Datye AK, Bravo J, Nelson TR, Atanasova P, Lyubovsky M, Pfefferle L (2000) Catalyst microstructure and methane oxidation reactivity during the Pd ↔ PdO transformation on alumina supports. Appl Catal A Gen 198:179–196
26. Kinnunen NM, Suvanto M, Moreno MA, Savimaki A, Kallinen K, Kinnunen T-JJ, Pakkanen TA (2009) Methane oxidation on alumina supported palladium catalysts: effect of Pd precursor and solvent. Appl Catal A Gen 370:78–87
27. Hoyos LJ, Praliaud H, Primet M (1993) Catalytic combustion of methane over palladium supported on alumina and silica in presence of hydrogen sulfide. Appl Catal A Gen 98:125–138
28. Venezia AM, Murania R, Pantaleo G, Deganello G (2007) Pd and PdAu on mesoporous silica for methane oxidation: effect of SO_2. J Catal 251:94–102
29. Venezia AM, Di Carlo G, Pantaleo G, Liotta LF, Melaet G, Kruse N (2009) Oxidation of CH_4 over Pd supported on TiO_2-doped SiO_2: effect of Ti(IV) loading and influence of SO_2. Appl Catal B Environ 88:430–437
30. Narui K, Yata H, Furuta K, Nishida A, Kohtoku Y, Matsuzaki T (1999) Effects of addition of Pt to PdO/Al_2O_3 catalyst on catalytic activity for methane combustion and TEM observations of supported particles. Appl Catal A Gen 179:165–173

31. Persson K, Jansson K, Jaras SG (2007) Characterisation and microstructure of Pd and bimetallic Pd–Pt catalysts during methane oxidation. J Catal 245:401–414
32. Euzen P, Le Gal J-H, Rebours B, Martin G (1999) Deactivation of palladium catalyst in catalytic combustion of methane. Catal Today 47:19–27
33. Widjaja H, Sekizawa K, Eguchi K (1999) Low-temperature oxidation of methane over Pd supported on SnO_2-based oxides. Bull Chem Soc Jpn 72:313–320
34. Widjaja H, Sekizawa K, Eguchi K (1998) Catalytic combustion of methane over Pd supported on metal oxides. Chem Lett 6:481–482
35. Li Y, Armor JN (1994) Catalytic combustion of methane over palladium exchanged zeolites. Appl Catal B Environ 3:275–282
36. Burch R, Loader PK (1994) Investigation of Pt/Al_2O_3 and Pd/Al_2O_3 catalysts for the combustion of methane at low concentrations. Appl Catal B Environ 5:149–164
37. Garetto TF, Apesteguia CR (2000) Oxidative catalytic removal of hydrocarbons over Pt/Al_2O_3 catalysts. Catal Today 62:189–199
38. Corro G, Fierro JLG, Odilón Vazquez C (2005) Strong improvement on CH_4 oxidation over $Pt/\gamma\text{-}Al_2O_3$ catalysts. Catal Comm 6:287–292
39. Corro G, Fierro JLG, Odilón Vazquez C (2006) Promotional effect of Sn addition to sulfated $Pt/\gamma\text{-}Al_2O_3$ catalysts on CH_4 combustion. Effect of C_3H_8 addition. Catal Comm 7:436–442
40. Niwa M, Awano K, Murakami Y (1983) Activity of supported platinum catalysts for methane oxidation. Appl Catal 7:317–325
41. Cullis CF, Willatt BM (1983) Oxidation of methane over supported precious metal catalysts. J Catal 83:267–285
42. Roth D, Gelin P, Tena E, Primet M (2001) Combustion of methane at low temperature over Pd and Pt catalysts supported on Al_2O_3, SnO_2 and Al_2O_3-grafted SnO_2. Top Catal 16:77–82
43. Marceau E, Che M, Saint-Just J, Tatibouet JM (1996) Influence of chloride ions in $Pt/A1_2O_3$ catalysts for methane total oxidation. Catal Today 29:415–419
44. Pengpanich S, Meeyoo V, Rirksomboon T, Bunyakiat K (2002) Catalytic oxidation of methane over CeO_2–ZrO_2 mixed oxide solid solution catalysts prepared via urea hydrolysis. Appl Catal A Gen 234:221–233
45. Bozo C, Guilhaume N, Garbowski E, Primet M (2000) Combustion of methane on CeO_2–ZrO_2 based catalysts. Catal Today 59:33–45
46. Bozo C, Guilhaume N, Herrmann JM (2001) Role of the ceria–zirconia support in the reactivity of platinum and palladium catalysts for methane total oxidation under lean conditions. J Catal 203:393–406
47. Zhou R, Zhao B, Yue B (2008) Effects of CeO_2–ZrO_2 present in Pd/Al_2O_3 catalysts on the redox behavior of PdO_x and their combustion activity. Appl Surf Sci 254:4701–4707
48. Specchia S, Finocchio E, Busca G, Palmisano P, Specchia V (2009) Surface chemistry and reactivity of ceria–zirconia-supported palladium oxide catalysts for natural gas combustion. J Catal 263:134–145
49. Terribile D, Trovarelli A, Leitenburg C, Primavera A, Dolcetti G (1999) Catalytic combustion of hydrocarbons with Mn and Cu-doped ceria–zirconia solid solutions. Catal Today 47:133–140
50. Liu W, Flytzani-Stephanopoulos M (1995) Total oxidation of carbon monoxide and methane over transition metal fluorite oxide composite catalysts: I. Catalyst composition and activity. J Catal 153:304–316
51. Liotta LF, Carlo GD, Pantaleo G, Deganello G (2005) Co_3O_4/CeO_2 and Co_3O_4/CeO_2–ZrO_2 composite catalysts for methane combustion: correlation between morphology reduction properties and catalytic activity. Catal Comm 6:329–336
52. Liotta LF, Carlo GD, Pantaleo G, Deganello G (2007) Catalytic performance of Co_3O_4/CeO_2 and Co_3O_4/CeO_2–ZrO_2 composite oxides for methane combustion: influence of catalyst pretreatment temperature and oxygen concentration in the reaction mixture. Appl Catal B Environ 70:314–322

53. Xiao T, Ji S, Wang H, Coleman KS, Green MLH (2001) Methane combustion over supported cobalt catalysts. J Mol Catal A Chem 175:111–123
54. Kirchnerova J, Alifanti M, Delmon B (2002) Evidence of phase cooperation in the $LaCoO_3$–CeO_2–Co_3O_4 catalytic system in relation to activity in methane combustion. Appl Catal A Gen 231:65–80
55. Libby WF (1971) Promising catalyst for auto exhaust. Science 171:499–500
56. Voorhoeve RJH, Remeika JP, Trimble LE (1976) Ann N Y Acad Sci 272:3–21
57. Yao HC, Shelef M (1973) The surface interaction of O_2 and NO with manganous oxide. J Catal 31:377–383
58. Gallagher PK, Johnson DW, Schrey F (1974) Studies of some supported perovskite oxidation catalysts. Mater Res Bull 9:1345–1352
59. Coutures JP, Badie JM, Berjoan R (1980) High Temp Sci 13:331–336
60. Arai H, Yamada T, Eguchi K, Seiyama T (1986) Effect of substitution by cerium on the activity of $LaMnO_3$ perovskite in methane combustion. Appl Catal 26:265–276
61. Voorhoeve RJH, Remeika JP, Johnson DW (1973) Rare-earth manganites: catalysts with low ammonia yield in the reduction of nitrogen oxides. Science 180:62–64
62. Marchetti L, Forni L (1998) Catalytic combustion of methane over perovskites. Appl Catal B Environ 15:179–187
63. Ferri D, Forni L (1998) Methane combustion on some perovskite-like mixed oxides. Appl Catal B Environ 16:119–126
64. Ciambelli P, Cimino S, Rossi SD, Faticanti M, Lisi L, Minelli G, Pettiti I, Porta P, Russo G, Turco M (2000) $AMnO_3$ (A = La, Nd, Sm) and $Sm_{1-x}Sr_xMnO_3$ perovskites as combustion catalysts: structural, redox and catalytic properties. Appl Catal B Environ 24:243–253
65. Ciambelli P, Cimino S, Lisi L, Faticanti M, Minelli G, Pettiti I, Porta P (2001) La, Ca and Fe oxide perovskites: preparation, characterization and catalytic properties for methane combustion. Appl Catal B Environ 33:193–203
66. Alifanti M, Kirchnerova J, Delmon B (2003) Effect of substitution by cerium on the activity of $LaMnO_3$ perovskite in methane combustion. Appl Catal A Gen 245:231–243
67. Voorhoeve RJH (1977) Perovskite-related oxides as oxidation-reduction catalysts. In: Burton JJ, Garten RL (eds) Advanced materials in catalysis. Academic, New York
68. Saracco G, Geobaldo F, Baldi G (1999) Methane combustion on Mg-doped $LaMnO_3$ perovskite catalysts. Appl Catal B Environ 20:277–288
69. Saracco G, Scibilia G, Iannibello A, Baldi G (1996) Methane combustion on Mg-doped $LaCrO_3$ perovskite catalysts. Appl Catal B Environ 8:229–244
70. Zhong Z, Chen K, Ji Y, Yan Q (1997) Methane combustion over B-site partially substituted perovskite-type $LaFeO_3$ prepared by sol-gel method. Appl Catal A Gen 156:29–41
71. Marti PE, Maciejewski M, Baiker A (1994) Methane combustion on Mg-doped $LaCrO_3$ perovskite catalysts. Appl Catal B Environ 4:225–235
72. Cimino S, Lisi L, Pirone R, Russo G, Turco M (2000) Methane combustion on perovskites-based structured catalysts. Catal Today 59:19–31
73. Alifanti M, Auer R, Kirchnerova J, Thyrion F, Grange P, Delmon B (2003) Activity in methane combustion and sensitivity to sulfur poisoning of $La_{1-x}Ce_xMn_{1-y}Co_yO_3$ perovskite oxide. Appl Catal B Environ 41:71–81
74. Gao Z, Wang R (2010) Catalytic activity for methane combustion of the perovskite-type $La_{1-x}Sr_xCoO_{3-\delta}$ oxide prepared by the urea decomposition method. Appl Catal B Environ 98:147–153
75. Civera A, Pavese M, Saracco G, Specchia V (2003) Combustion synthesis of perovskite-type catalysts for natural gas combustion. Catal Today 83:199–211
76. Wei X, Hug P, Figi R, Trottmann M, Weidenkaff A, Ferri D (2010) Catalytic combustion of methane on nano-structured perovskite-type oxides fabricated by ultrasonic spray combustion. Appl Catal B Environ 94:27–37

77. Yanqing Z, Jieming X, Cuiqing L, Xin X, Guohua L (2010) Influence of preparation method on performance of a metal supported perovskite catalyst for combustion of methane. J Rare Earth 28:54–58
78. Zhu Y, Sun Y, Niu X, Yuan F, Fu H (2010) Preparation of La–Mn–O perovskite catalyst by microwave irradiation method and its application to methane combustion. Catal Lett 135:152–158
79. Inoue H, Sekizawa K, Eguchi K, Arai H (1996) Changes of crystalline phase and catalytic properties by cation substitution in mirror plane of hexaaluminate compounds. J Solid State Chem 121:190–196
80. Groppi G, Bellotto M, Cristiani C, Forzatti P, Villa PL (1993) Preparation and characterization of hexaaluminate-based materials for catalytic combustion. Appl Catal A Gen 104:101–108
81. Artizzu-Duart P, Millet JM, Guilhaume N, Garbowski E, Primet M (2000) Catalytic combustion of methane on substituted barium hexaaluminates. Catal Today 59:163–177
82. Kikuchi R, Tanaka Y, Sasaki K, Eguchi K (2003) High temperature catalytic combustion of methane and propane over hexaaluminate catalysts: NO_x emission characteristics. Catal Today 83:223–231
83. Jang BW-L, Nelson RM, Spivey JJ, Ocal M, Oukaci R, Marcelin G (1999) Catalytic oxidation of methane over hexaaluminates and hexaaluminate-supported Pd catalysts. Catal Today 47:103–113
84. McCarty JG (1995) Kinetics of PdO combustion catalysis. Catal Today 26:283–293
85. Sekizawa K, Machida M, Eguchi K, Arai H (1993) Catalytic properties of Pd-supported hexaaluminate catalysts for high-temperature catalytic combustion. J Catal 142:655–663
86. Zarur AJ, Ying JY (2000) Reverse microemulsion synthesis of nanostructured complex oxides for catalytic combustion. Nature 403:65–67
87. Zarur AJ, Hwu HH, Ying JY (2000) Reverse microemulsion-mediated synthesis and structural evolution of barium hexaaluminated nanopartices. Langmuir 16:3042–3049
88. Wang J, Tian Z, Xu J, Xu Y, Xu Z, Lin L (2003) Preparation of Mn substituted La-hexaaluminate catalysts by using supercritical drying. Catal Today 83:213–222

Chapter 9
The Status of Catalysts in PEMFC Technology

M. Aulice Scibioh and B. Viswanathan

Abstract Polymer electrolyte membrane fuel cells (PEMFCs), which convert the chemical energy stored in the fuel hydrogen directly and efficiently into electrical energy and water, have the potential to eliminate our fossil energy dependency and emissions, when the hydrogen is derived from renewable energy sources such as solar, wind, biomass, among other possibilities. PEMFCs are being developed as electrical power sources for vehicular, stationary, and portable power applications. In spite of tremendous R&D efforts in the advancements of PEMFC technology, the commercialization is still a long way to go due to the prohibitively high cost of platinum-based catalysts used in the electrodes. However, attempts were made to reduce the quantity of platinum-based catalyst and to extract the maximum activity from a given quantity of platinum in various ways including the development of supported system, employing binary or ternary Pt-based or non-Pt alloy systems, and finding alternate catalysts of various kinds with no platinum in them. In this chapter, we set to examine various logistics and underpinning science in PEMFC catalyst development in one frame analysis, and further, we propose future directions to push the frontiers ahead in order to realize PEMFC commercialization in aspects of both anode and in cathode catalysts of PEMFC.

M.A. Scibioh
NASA-URC Centre for Advanced Nanoscale Materials, University of Puerto Rico-Rio Piedras, P.O. Box 70377, San Juan, PR 00936-8377, USA

National Centre for Catalysis Research (NCCR), Indian Institute of Technology Madras (IITM), Chennai 600 036, India
e-mail: maria.aulice1@upr.edu

B. Viswanathan (✉)
National Centre for Catalysis Research (NCCR), Indian Institute of Technology Madras (IITM), Chennai 600 036, India
e-mail: bvnathan@iitm.ac.in

L. Guczi and A. Erdőhelyi (eds.), *Catalysis for Alternative Energy Generation*,
DOI 10.1007/978-1-4614-0344-9_9,

9.1 Introduction

Energy is a prime propellant for growth and modernization, power and prestige, progress and prosperity. Hence, the quality of life is dependent on the access to a bountiful supply of cheap energy. For a sustainable future, energy should be derived from nonfossil materials: ideally, it should be reliable, safe, flexible for use, affordable, and limitless. Hydrogen exhibits unique potentialities for an ideal fuel which would produce electricity and drinking water when it combines with oxygen with zero emissions, and it is the simplest and most abundant element of the universe. Interest in hydrogen is rising due to significant advancements in fuel cells as power sources. Proton exchange membrane fuel cell, also known as polymer electrolyte membrane fuel cell (PEMFC), employs hydrogen as fuel in the anode, and it is considered as the most attractive power sources for a wide spectrum of applications ranging from stationary, vehicular, and portable electronic equipments due to its high efficiency, low-temperature operations, rapid start-up, and environmentally benign technology for energy conversion avoiding the Carnot limitations associated with combustion engines. Initially, the PEMFC technology was developed for military and spacecraft applications at General Electric, USA in 1960s. However, it was abandoned in 1970s, mainly due to high cost. The period 1980s and 1990s witnessed renewed interests of several companies, notably by Ballard Power Systems, Canada, for portable electronics and vehicular applications. In the present days, PEMFC is extensively demonstrated for wide applications. In spite of several of its attractive features, the commercialization of PEMFC is hampered by prohibitively high cost. Till date, only platinum and platinum-based catalysts have been employed to drive the electrochemical reactions in PEMFCs. Platinum accounts for a large portion of the cost of the PEMFC unit due to its high price and limited availability in the planet. The catalyst accounts for 55% of the total cost, while 7% belongs to the membrane, 10% to bipolar plates, and 10% to gas diffusion layers. Present proton exchange membrane fuel cell prototypes employ catalysts selected almost five decades ago. Hence, developing high-performance, cost-effective, and durable electrocatalysts is the utmost priority of PEMFC research and development. This chapter would examine and place on record the contribution of 50 years catalyst research to the present status of PEMFC development. Various aspects of catalyst development and the underpinning science would be addressed, assessed, and evaluated. The progress and advancement made in search of innovative catalyst materials are systematically summarized, and the problems and successes are analyzed. Directions and novel approaches for furthering the advancement in this technology are suggested.

9.2 Working Principle of PEMFC

A fuel cell generates electrical power by converting chemical energy of a fuel into electrical energy through an electrochemical reaction. PEMFC typically uses hydrogen as a fuel at the anode and the oxidant oxygen, which usually comes from air is supplied to the cathode. When hydrogen gas is fed into the system, at the catalyst surface of the membrane, it splits in to protons and electrons. The protons pass through the membrane to react with oxygen (oxide ion) in the cathode, forming water. The electrons which cannot pass through the membrane flow through the external circuit, producing electricity. The working principle of a PEMFC is shown in Fig. 9.1 [1]. Individual fuel cells can be combined to form a fuel cell stack. The number of cells in the fuel cell stack thus determines the total voltage; the surface area of each cell determines the total current.

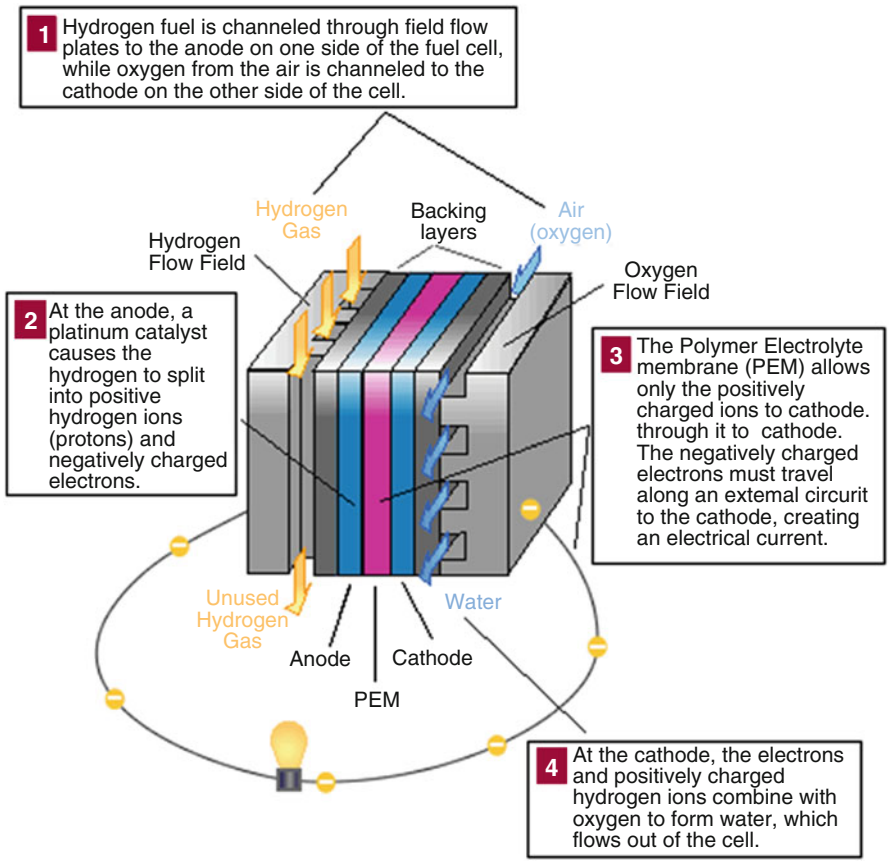

Fig. 9.1 Schematics of a PEMFC [reproduced from with permission http://www.fueleconomy.gov/feg/fcv_pem.shtml]

The typical cell reactions are as follows.
At the anode:

$$H_2 \rightarrow 2H^+ + 2e^- \quad E^o = 0.00\,V \text{ versus NHE} \tag{9.1}$$

At the cathode:

$$\frac{1}{2}O_2 + 2H^+ + 2e^- \rightarrow 2H_2O \quad E^o = 1.23\,V \text{ versus NHE} \tag{9.2}$$

Overall reaction:

$$H_2 + \frac{1}{2}O_2 \rightarrow 2H_2O \quad E^o = 1.23\,V \text{ versus NHE} \tag{9.3}$$

9.3 Operational Aspects of PEMFC

Under reversible conditions, the electromotive force of the cell (EMF, E^o_{cell}) can be defined as the difference between the standard potentials of the anode and cathode (E^o_{anode}, $E^o_{cathode}$). In hydrogen/oxygen polymer electrolyte fuel cell operating at standard conditions, the reversible cell EMF is 1.23 V. The standard free energy change (ΔG^o) of the overall reaction of the fuel cell is given as

$$\Delta G^o = -nFE^o_{cell} \tag{9.4}$$

where n is the number of electrons transferred and F is the Faraday's constant, 96,745 C/equiv. Since, n, F, and E^o_{cell} are positive integers, the total free energy change of the overall reaction is negative, indicating the spontaneity of the reaction. This is the underpinning thermodynamics in the fuel cell operation. In an ideal, reversible fuel cell, the cell voltage is independent of the current drawn. But, in practice, the reversible cell voltage is not realized even under open-circuit conditions, when no current is drawn from the system. This is due to various irreversibilities which arise during the functioning of a fuel cell. The difference between the actual cell voltage at a given current density and the reversible cell voltage of the reaction is termed as over voltage (when referring to a single electrode, it is termed as overpotential of the electrode).

The origin of various loses arise during the operation of a PEMFC can be seen in a polarization curve, a plot of cell potential against current density under a set of constant operating conditions. An ideal polarization curve for a single hydrogen/air fuel cell has three major regions, which are shown in Fig. 9.2 [2, 3]. At low current densities, considered as the region of activation polarization, the cell potential drops sharply, and majority of these losses are due to the sluggish kinetics of

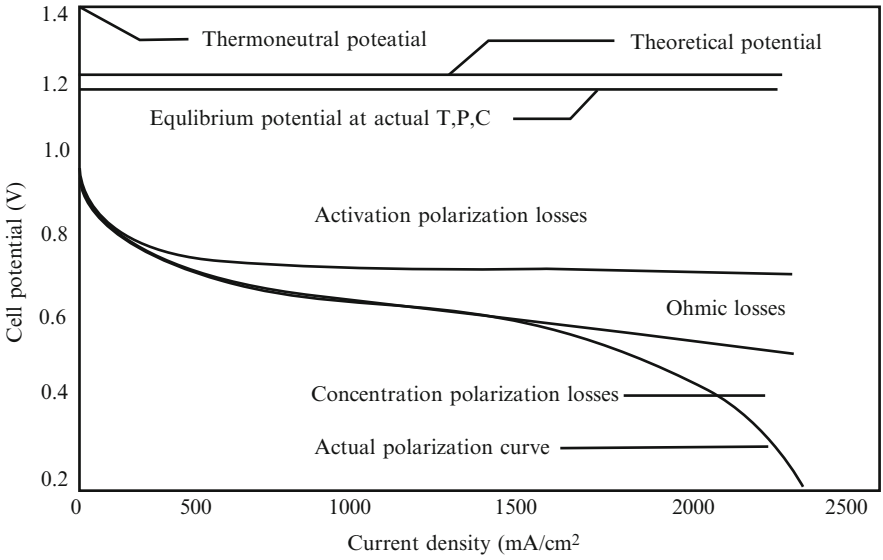

Fig. 9.2 Schematic of an ideal polarization curve with the corresponding regions and overpotentials. (Reproduced with permission from [2])

oxygen-reduction reaction (ORR). Regarding the anode reaction in PEMFC, the overpotential for the hydrogen oxidation reaction (HOR) is negligibly small when pure hydrogen is used as a fuel gas. At the intermediate current densities, known as the region of ohmic polarization, the voltage loss caused by ohmic resistance becomes significant and originates mainly from the resistance to the flow of ions in the electrolyte and resistance to the flow of electrons through the electrode [4]. In this region, the cell potential decreases nearly linearly with the current densities, while the activation overpotential attains relatively a constant value. At high-current densities, the region of concentration polarization, the cell performance drops drastically, due to the dominant mass transport effects arising from transport limitations of the reactant gas through the porous structures of the gas diffusion layers and electrocatalyst layers. One can also see in Fig. 9.2 the difference between the theoretical cell potential (1.23 V) and thermoneutral voltage (1.4 V) showing the energy loss under reversible conditions [5]. The thermoneutral cell voltage is the voltage at which no exchange of heat with the surrounding occurs. A cell operated at thermoneutral cell voltage remains at the temperature of the surroundings by consumption or production of (electrical) energy not used for electrochemical reaction. Yet another prominent loss which is not well discussed in the literature arises from mixed potentials at the electrodes arising from the unavoidable parasitic reactions which tend to lower the equilibrium electrode potential. The main cause of mixed potential is due to the crossover of fuel through the electrolyte from anode to cathode compartments and vice versa. This is a primary source of losses at open-circuit conditions.

9.4 Challenges in Key Components of Membrane Electrode Assembly in PEMFC

Membrane electrode assembly is considered as the heart of the fuel cell. In spite of remarkable advancement in technological developments in the past decades, the reliable and durable performance and commercialization of PEMFC are still facing challenges posed by its key components of membrane electrode assembly [6]. The major material challenges are listed below.

- High cost of Nafion (perfluorosulfonic acid) membrane and platinum-based catalysts
- Hydrogen and oxygen crossover through the membrane leading to mixed potentials and the consequent performance decay
- Physical instability of Nafion at high-temperature operations
- Chemical instability of Nafion membrane by peroxide and superoxide intermediates formed during the fuel cell reactions
- Sluggish ORR at the cathode
- Dissolution and growth of electrocatalyst particulates during prolonged operations
- Ready poisoning of the anode Pt catalyst due to impurities that may be present in the hydrogen gas and other contaminants in the components
- Inaccessibility of catalyst particles which are deposited in the micropores of carbon support by the reactants
- Corrosion and instability of carbon supports

These critical issues are the major concerns and objectives of material developments in PEMFC technology. Among various challenges, the contribution of catalyst scientist in the development of appropriate catalysts and supported materials for the advancement of PEMFC technology are discussed and documented below.

9.5 Challenges in PEMFC Electrocatalysis

In a PEMFC, Pt and Pt alloys are considered as the best electrocatalysts, to date, for both hydrogen oxidation and ORRs. Apart from the high cost and scarcity of platinum, in this section, we discuss the challenges posed by inherent nature of the electrochemical reactions at the electrodes of the PEMFC. The overpotential for the HOR is considerably lower than that for the ORR. For instance, in a PEMFC operating at current densities of 1 A cm^{-2}, the overpotential at the hydrogen electrode is around 200 mV, while at the oxygen electrode, it is around 400 mV. Mainly, one half of the overpotential at the oxygen electrode is due to its loss at open-circuit potential. The deviation of the practical cell potential of the PEMFC from the reversible value is due to the extremely low exchange current density (i_o)

for oxygen reduction (about 10^{-9} A cm^{-2}, very low compared to that for the electrooxidation of hydrogen, 10^{-3} A cm^{-2}) on smooth platinum electrodes. Due to such a low i_o value, competing anodic reactions (oxide formation, oxidation of organic impurities) are responsible for setting up a mixed potential of about 1.0 V for the oxygen electrode at open circuit. Oxygen reduction is considerably more complex than hydrogen oxidation due to (1) the strong O–O bond and the formation of highly stable Pt–O or Pt–OH species, (2) it being a four-electron transfer reaction, and (3) the possible formation of a partially oxidized species (H_2O_2). Being a four-electron transfer reaction, there are at least four intermediate steps proposed:

$$O_2 + H^+ + M + e^- \rightarrow MHO_2 \tag{9.5}$$

$$MHO_2 + e^- \rightarrow MO + H_2O \tag{9.6}$$

$$MO + H^+ + e^- \rightarrow MOH \tag{9.7}$$

$$MOH + H^+ + e^- \rightarrow M + H_2O \tag{9.8}$$

Even after over five decades of research, still no conclusive mechanism has been arrived at for the intermediate and the rate-determining steps for this reaction on different types of electrocatalysts. This is unlike the case of the two-electron transfer HOR, where there is definitive evidence for the reaction pathway:

$$H_2 + 2M \rightarrow 2MH \tag{9.9}$$

$$2MH \rightarrow 2M + 2H^+ + 2e^- \tag{9.10}$$

In HOR, the first step (9.9) is rate determining on platinum.

Regarding anode reaction in PEMFC, the overpotential for the HOR at the Pt anode is significantly small when pure hydrogen is used as the fuel. But the major problem with the Pt electrocatalysis for hydrogen electrode is its low tolerance to CO in H_2 from reformed fuels. According to the US Department of Energy (DOE), an increase of the cell potential to about 0.75–0.8 V is necessary for PEMFCs to compete with compression-ignition direct-injection (CIDI) engines in order to meet the goal of an efficiency of 45% for fuel consumption in the partnership for a new generation vehicle (PNGV) program. The improvement can only be possible by decreasing the oxygen overpotential by 50–100 mV. Investigations have demonstrated that such an improvement is possible by using intermetallic electrocatalysts of platinum with a transition metal. One of the challenges in acid fuel cell research is to find non-platinum electrocatalysts for the fuel cell reaction. Platinum and/or platinum alloys are still the best electrocatalysts and are used in the state-of-the-art fuel cells.

9.6 Materials Choices for PEMFC Electrodes: R&D Approaches in Catalysis

This section is not merely aiming at summarizing the works in the field of PEMFC electrocatalysis, but to critically evaluate some of the vital issues in the development of PEMFC in terms of formulation, design, and fabrication of anode and cathode catalyst materials and support systems. We would emphasize the areas where improvements would be highly desired:

- The activities of both anodes and cathodes must be improved by identifying suitable catalysts.
- In order to reduce the usage of precious metals and thus the cost, the current loadings of noble metals are to be reduced by extracting best possible performance from a given amount of the catalyst.
- Identification of suitable support materials are needed with improved metal-support interactions.

Generally, the PEMFC catalysts can be classified into three groups based on the active component: Pt-based catalyst, where Pt is used as unsupported or supported on high surface area materials such as carbon, polymer, or other supports; Pt-modified with other noble and non-noble metal combinations; and Pt-free non-noble metal catalysts and organometallic complexes. Table 9.1 lists the commonly used catalysts as well as their advantages and limitations.

9.6.1 Anodes for PEMFC

9.6.1.1 CO Poisoning of Pt Catalyst

Pure hydrogen is an ideal fuel for the HOR in order to realize an optimal performance in PEMFC at low-temperature operations (70–80°C). However, the H_2 produced from steam reforming or partial oxidation routes has an adverse influence on the kinetics of anodic oxidation of H_2 because it contains CO which poisons the Pt anode catalyst even at a 10 ppm level, decreasing the cell performance. The CO poisoning of Pt has been ascribed to the preferential adsorption of CO on Pt sites, as

Table 9.1 General classification of three types of catalysts for PEMFC

Catalyst type	Advantage	Limitation
Pt-based catalysts	Excellent characteristics of high activities for fuel cell reactions	High cost and relatively low stabilities
Modified Pt-based catalyst	Low cost and high durability under optimized conditions	Uncertainty for long-term applications
Pt-free non-noble catalysts	Low-cost and extensive resources	Relatively low activities

the Pt–CO bond strength is greater than that of the Pt–H, so that CO inhibits the dissociative absorption of H_2 on Pt and its subsequent oxidation. The mechanism by which a platinum catalyst surface is poisoned by CO is well established. As given below in (9.11)–(9.13), the CO competes with the adsorption of hydrogen on active sites of Pt at normal operating potentials of anode [7]. In the year 2002, there was an interesting report by Papageorgopoulos and de Bruijn [8] on quantitative results of CO poisoning for a 1% CO/hydrogen mixture showing that 98% of active sites are blocked by CO at 25°C.

$$H_2 + 2Pt \rightarrow 2\left(\frac{H}{Pt}\right) \tag{9.11}$$

$$2\left(\frac{H}{Pt}\right) \rightarrow 2H^+ + 2e^- + 2Pt \tag{9.12}$$

$$CO + Pt \rightarrow \frac{CO}{Pt} \tag{9.13}$$

The adsorbed CO on a catalytic site can be removed by increasing the anode potential to about 0.7 V versus RHE. At this potential, the CO reacts with the hydroxyl species which are adsorbed on the platinum surface to form CO_2 as shown in the following: (9.14) and (9.15). But, this approach leads to a serious loss of efficiency and thus is not practical [7].

$$H_2O + Pt \leftrightarrow \frac{OH}{Pt} + H^+ + e^- \tag{9.14}$$

$$\frac{CO}{Pt} + \frac{OH}{Pt} \rightarrow 2Pt + CO_2 + H^+ + e^- \tag{9.15}$$

9.6.1.2 Strategies to Decrease CO Poisoning

Generally, four methods are presently being adopted to decrease the CO poisoning of Pt anode catalyst. These include bleeding of O_2 or oxygen-evolving compounds into the H_2 fuel, operating the cell at elevated temperatures, employing reformers with advanced designs, and using Pt alloys which are CO tolerant for H_2 oxidation. The first approach, oxygen bleeding, was originally proposed in the 1990s, which involved the injection of 0.4–2% O_2 into the CO-contaminated H_2 stream to oxidize the CO adsorbed on the catalyst. In this method, however, the utilization of the fuel will certainly be decreased, and safety issues must also be considered [9–12]. A related technique is the oxidative removal of CO by nascent O_2 from H_2O_2, which is introduced in the humidification system.

The second approach involves the operation of fuel cells at temperatures above 150°C which would diminish CO adsorption on Pt catalysts versus adsorption of hydrogen and, therefore, its adverse influence on the performance of the Pt anode; this concept has indeed been demonstrated in phosphoric acid fuel cells. However, implementation in PEM fuel cells requires development of membranes that are stable in the temperature range of 120–200°C. The third approach involves the advanced reformer designing. Most of the reformers, including auxiliary processors which are currently employed, are capable of producing the CO content to an extent of 50 ppm or less after a warm-up period up to 2 h. To actualize the oxidant bleeding effect by modifying the reformer, several researchers have considered the possibility of new designing of reformer in which auxiliary processors for cleanup steps, such as shift converters and a selective oxidizer, can be fitted [13–15]. These approaches would obviously increase the complexity of the overall system and hence the cost of the fuel cell system. In spite of these additional stages, it is still difficult to maintain low CO levels during start-up and transient operations without the addition of an air bleed into the fuel stream [16–19].

Employing CO-tolerant electrocatalysts would be an appealing approach in terms of system efficiency since it causes less associated problems with decreased parasitic power losses of the overall fuel cell system. Most efforts have been directed to developing CO-tolerant Pt alloys or composites based on the concept of so-called bifunctional catalysis that provide some sites at which CO can be oxidized along with others where H_2 dissociative chemisorption can take place. There are several reports which employ a second element with Pt, such as Ru, Sn, Co, Cr, Fe, Ni, Pd, Os, Mo, and Mn, in the form of an alloy, composite or co-deposit, yielding significant improvement in the CO-tolerance capacities compared to pure Pt systems [20–26]. Several investigations were carried out employing ternary catalyst systems, mainly based on a Pt–Ru alloy, and their performances have been compared with that of Pt/C and PtRu/C systems. Specifically, Pt–Ru alloy systems with several transition metal elements such as Ni, Pd, Co, Rh, Ir, Mn, Cr, W, Zr, and Nb have been studied [22–24, 26, 27]. However, there are still unsettled issues over the preparation methods and the enhancement of electrochemical performances. The primary focus of these investigations is toward realizing high activity for the HOR in the presence of CO. Mechanistic and kinetic studies related to the HOR on these Pt alloy catalysts are, however, few.

9.6.1.3 Pt-Based CO-Tolerant Anodes

In the initial stages of catalyst development, pure Pt was used as the anode fuel cell catalyst. In spite of its best activity for HOR, platinum is unfortunately readily susceptible to CO. An ideal catalyst for the anode would be fully tolerant to CO poisoning, while maintaining its activity for the oxidation of hydrogen.

Among these various Pt-based binary systems, the most commonly used catalyst is the PtRu supported on carbon. This material is known to enhance CO tolerance, which can be ascribed to electronic modification of Pt in Pt–Ru alloys that

Table 9.2 Oxidation potentials of CO at Pt and Pt/Ru surfaces [32]

Anode catalyst	Fuel	Fuel cell voltage	η_v (%)	$\Delta\eta_v$ (%)
Pt	Hydrogen	0.682	55.4	–
Pt	100 ppm CO	0.231	18.8	−66.1
Pt–Ru	100 ppm CO	0.482	39.2	−29.2

decreases the CO binding energy on Pt as in (9.13) and also binds OH strongly on the Ru active sites in the Pt–Ru alloys [28]. Within this system, the performance of PEMFCs has been improved for fuel streams containing CO [29, 30]. However, it has to be noted as from the studies of Acres et al. [31] that a PEMFC with a Pt–Ru/C performs less active than pure Pt catalyst when pure hydrogen is employed as a fuel. Investigations by Iorio et al. reveal that the Pt–Ru anode catalyst leads to a substantial loss in the cell potential as can be seen from data presented in Table 9.2 [31]. The results reveal that when Pt–Ru is used as anode catalyst, the potential of the cell is 250 mV less compared with the cell with pure Pt. In the presence of 100 ppm CO, there is a further loss of about 200 mV with 30% voltage efficiency compared with the use of pure hydrogen as the fuel.

While the researches are underway to suppress the adsorption and formation of surface-bound CO, there are ways to decrease the surface CO through alloying Pt with Ru and other transition metals such as Sn which can be stable in acid media [33, 34]. However, till date, the Pt–Ru alloys are still commonly employed as the best and most stable anode electrocatalyst for the oxidation of H_2/CO in PEMFCs. In Pt–Ru, the enhanced tolerance could be ascribed to a decrease in CO binding energy on platinum due to electronic effects and to the oxidation of chemisorbed CO being catalyzed at low potentials by the activation of H_2O [28, 35]. The latter is due to the facile formation of the oxygen-containing species, in the form of adsorbed hydroxyl species (OH_{ads}), on oxophilic ruthenium. The water-induced oxide formation has been found with metals of the early transition series, and a high water dissociation capability has been predicted for these metals [36]. A decade ago, Ticianelli et al. found a two- to threefold enhancement of CO tolerance in a PEM fuel cell with carbon-supported alloy nanocrystalline Pt–Mo (4:1)/C, as compared to Pt–Ru/C anode catalyst [37, 38]. The increased CO tolerance was attributed to the ability of Pt–Mo to promote the CO oxidation reaction at very low electrode potentials. This behavior was explained based on oxygen transfer from Mo oxyhydroxide species with only the OH species of the oxyhydroxide states, mainly $MoO(OH)_2$ being reactive with adsorbed CO [39, 40]. This is considered as the reactive moiety, and due to its size, it has the potential for reducing the availability of adjacent Pt sites for molecular hydrogen dissociation. A Pt–Mo catalyst with an atomic ratio of 4:1 was shown to give the best performance. Furthermore, molybdenum hydrogen bronze H_yMoO_x could be formed by the "spillover" of hydrogen from Pt sites to Mo, suggesting a plausible enhanced catalytic activity toward CO [41].

9.6.1.4 Pt Metal-Based CO-Tolerant Unsupported Systems

A series of binary Pt alloy electrocatalyst with non-precious metals of various compositions has been tested for the electrocatalytic activity for hydrogen oxidation in the presence of trace amounts of CO (100 ppm). Igarashi et al. [42] examined various compositions of PtFe, PtNi, PtCo, PtMo, PtMn, PtSn, PtAg, PtZn, PtCr, PtCu, PtGe, PtNb, PtPd, PtIn, PtSb, PtW, PtAu, PtPb, and PtBi prepared through Ar-sputtering Pt, and the second metal targets simultaneously onto a Pyrex glass substrate to study the electrocatalytic activity. It has been found that regardless of the composition, the PtFe, PtNi, PtCo, and PtMo exhibited CO tolerance in a fashion similar to that of the PtRu alloy. The mechanism of CO tolerance was explained by "detoxification mechanism" in which the surface of all non-precious metal alloys is composed of a thin Pt layer with an electronic structure different from that of pure Pt, indicating an increased 5d vacancy of Pt in the layers of the CO-tolerant alloys. The CO coverage mainly with multiple bonding was decreased due to decreased electron donation from the Pt 5d band to the $2\pi^*$ orbital of CO. With these CO-tolerant Pt alloys, the equilibrium CO coverage was suppressed to values less than 0.6. Markovic and Ross [43] compared the polarization curves for the oxidation of H_2 containing 0.1% CO on Pt and Ir electrodes, and their alloys in sulfuric acid solution at 60°C and observed that the Ir electrode is more active than the Pt electrode. Since the heat of adsorption of OH_{ads} is higher on Ir than on Pt, it is plausible that some CO_{ads} may be displaced by OH_{ads} from the Ir surface even at very low potentials. This, in turn, will increase the rate of oxidation of CO_{ads}, so the transition from an inactive, i.e., poisoned, surface to an active surface during the electrooxidation of H_2/CO mixture on Ir is observed at a lower potential than on Pt. Although under potentiodynamic conditions at low potentials Ir has a better ability to oxidize CO_{ads} than Pt, a continuous supply of CO can easily deactivate Ir electrode. The catalytic activities of Ir and Pt were notably increased by alloying these metals with Ru, Sn, Re, or Mo, with the order of activities, at low overpotential increasing in the sequence Pt–Sn, Ir–Sn $<$ Pt–Ru $\leq$ Pt–Mo [44]. The surface composition of these alloys is different from the average composition of the bulk. These differences arise due to the phenomenon of segregation of these systems. The term surface segregation in bimetallic systems refers to the enrichment of one component of the mixture in the surface region relative to the bulk composition.

It appears that the process with the platinum-based bimetallic systems seems to be the bifunctional mechanism of action. The alloying metal serves to nucleate OH_{ads} species at lower potentials from water than on a pure Pt electrode, leading to the oxidative removal of CO_{ads} on Pt sites nearby, freeing Pt sites for the HOR. Based on this reaction mechanism, two classes of CO-tolerant catalysts can be distinguished: (1) the first class has a pseudo-bifunctional mechanism of action, as in the case of Pt–Ru and Pt–Re, where CO is adsorbed on both the Pt and Ru(Re) sites, thereby second metal does not serve exclusively to nucleate OH_{ads}; (2) the second class has a pure bifunctional mechanism of action, as in the case of the

Table 9.3 CO-tolerant ternary catalysts examined for H_2/CO oxidation

Ternary catalyst	Electrochemical test conditions	Major finding	References
Pt–Ru–WO_3/C	0.5 M H_2SO_4, H_2/100 ppm CO, 80°C	No effect of WO_3 addition to Pt–Ru at 220 mA/cm^2 over a test period of 6 h	[31]
Pt–Ru–M/C (M = Sn, Mo, W) 1:1:1	PEM full cell, H_2/150 ppm CO, 75°C	Pt–Ru–W shows highest activity at current densities lower than 220 mA/cm^2; Pt–Ru–Sn shows highest activity at current densities higher than 200–300 mA/cm^2	[48]
Pt–Ru–M/C (M = Nb, Mo) 9:9:2	PEM full cell, H_2/CO	Mo addition improves the cell performance; Nb addition promotes CO poisoning and hence decreases cell performance	[51]
Pt–Ru–Ag/C 1:1:1, Pt–Ru–Au/C 1:1:1, Pt–Ru–Rh/C 1:1:0.4, Pt–Ru–W_2C/C 1:1:0.4	PEM full cell, H_2/104 ppm CO, 80°C	Pt–Ru–W_2C shows higher CO tolerance than Pt–Ru. Others exhibit lower CO tolerance than Pt–Ru	[52]
Pt–Ru–Au/C 1:1:1, Pt–Ru–Os/C 1:1:1, Pt–Ru–SnO_x/C 1:1:1, Pt–Ru–WO_x/C 1:1:1	PEM full cell, H_2/1% CO	Pt–Ru–Os and Pt–Ru similar activity for CO tolerance; Pt–Ru–WO_2 more active than Pt–Ru; Pt–Ru–SnO_x shows lowest onset potential for CO oxidation	[53]
Pt–Ru–Ir/C, Pt–Ru–Ni/C	PEM full cell	Both catalysts show higher CO tolerance than Pt–Ru	[54, 55]

Pt–Sn and Pt–Mo systems at low overpotentials, where CO is exclusively adsorbed on the platinum sites, and oxygen-containing species are attached to the second element. A detailed discussion of the mechanism can be found in Refs. [39, 45–47].

9.6.1.5 CO-Tolerant Pt-Based Ternary Catalysts

There are efforts to improve the catalytic behavior of the Pt–Ru binary system by incorporating a third metal in order to achieve facile oxide formation characteristics. The inclusion of W was found to be beneficial [48, 49], while partial substitution of Ru in Pt–Ru by Cr, Zr, or Nb resulted in a decrease in activity for H_2 oxidation in the presence of 10 or 100 ppm CO [50]. The results of various investigations in the past two decades on electrochemical tests of HOR in the presence of trace amounts of CO carried out by employing various ternary catalysts are summarized in Table 9.3.

9.6.1.6 Pt-Free CO-Tolerant Catalyst

Analysis of the literature reveals that in the last few decades, there have been extensive studies on the improvement in activity and stability of non-platinum cathode catalysts, whereas the studies on the replacement of platinum or platinum alloys from anode side of PEMFC are limited. The possibility of employing transition metal carbides as catalysts for HOR was explored at the end of 1960s by Bohm and Pohl [56], showing that WC/C can be used in fuel cell operated with pure hydrogen and CO-rich hydrogen. Later, several research groups investigated tungsten-based materials for HOR and found that these catalysts showed significant activity and high tolerance for CO and H_2S [57–61], hence making WC system as a more preferable anode catalyst for PEMFC compared with Pt, which is easily deactivated even by the presence of trace amounts of CO and sulfur compounds.

In 2002, Mclntyre et al. [62] prepared WC and WMC (M = Co, Ni) by various chemical methods and tested these catalysts for hydrogen oxidation in the presence of CO. WC showed a small and reversible reduction in the rate and magnitude of rise in hydrogen oxidation current when 1% CO was added to the hydrogen fuel. The effect of CO on WC is attributed to the very weak surface adsorption, temporarily blocking the most active sites for hydrogen oxidation.

In 2008, Izhar and Nagai [63] prepared and evaluated cobalt molybdenum (Co–Mo) carbides using a single fuel cell and three-electrode cell and found high activities for the anodic electrooxidation of hydrogen over the Co–Mo catalysts carburized at 873 and 923 K. The Co–Mo catalyst carburized at 873 K had the highest activity and achieved 10.9% of the performance of a commercial Pt/C catalyst in a full cell. The low performance of the carbide catalysts was attributed to two factors: the intrinsic activity and low surface area of the carbide materials. Though these materials exhibit activities lower than that of Pt/C catalysts, the results exhibit a positive step in the development of low-cost Pt-free catalysts. Later, the same group [64, 65] investigated CoWC and MoWC supported on high surface area carbon and obtained 14 and 11% activity compared to that of 20 wt% Pt/C.

Tasik et al. [66] employed Co electrodeposited on a carbon paper as anode for PEMFC single cell and found satisfactory performance levels though the activity is lesser than that of pure Pt anode catalyst. Li et al. [67] recently achieved an exciting result of high cell performance with a loading of 40% Ir–10% V/C, exhibiting a power density of 1,008 mW cm^{-2} at 0.6 V, 70°C, which is 50% higher performance than that obtained with Pt/C anode catalyst.

9.6.2 Cathode Catalysts for PEMFC: Materials and Challenges

The main focus of this section is on the electroreduction of oxygen in the acid environment, a crucial component in the PEMFC system. The reason that the present day PEMFCs do not exhibit its theoretical thermodynamic efficiencies is

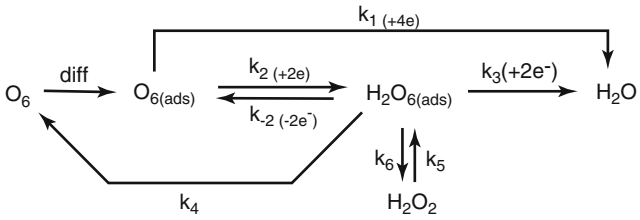

Scheme 9.1 Canonical mechanism for ORR in acid medium showing both direct and indirect pathways. (Reproduced from [68] with permission)

attributed to the sluggishness of ORR. This can be understood with the following equation showing a direct relationship between the cell overpotential and fuel cell electrical efficiency, ζ.

$$\zeta = 1 - \frac{\eta_a + \eta_b}{\Delta E^o} \tag{9.16}$$

where η_a and η_b are the overpotentials at the anode and cathode, respectively, and ΔE^o is the total cell potential (mass transfer of the oxygen is not included). Since the early 1960s, scientists recognized that the slow kinetics of the ORR in an acid solution presents a major challenge for the PEMFC development. The difficulty in oxygen reduction stems from the strong O=O bond (498 kJ/mol), making the activation of this bond typically kinetically slow. The elucidation of the mechanism associated with ORR has been the subject of both an experimental and theoretical components for several decades, mainly they center around platinum. ORR process includes several individual reactions, as given in Scheme 9.1 [68].

Two different processes are operative simultaneously, and each of them contains a few discrete steps. First, the "direct" pathway (k_1), a concerted four-electron transfer, reducing oxygen to water. Second, "series" mechanism showing a series of one- or two-electron transfers forming peroxo species. Incomplete reduction of oxygen to hydrogen peroxide not only leads to lower energy conversion efficiency, but this species further produces harmful free radical species. Hence, a desired feature of ORR catalyst is that it should reduce oxygen to water through the four electron route. Even in the present days, there is still no clear consensus regarding the primary steps of the ORR on platinum or indeed on any other metal surface. One particular approach in elucidating ORR kinetics on metal surface has been through the "d-band model" proposed by Norskov et al. [69] and later used as the basis for new catalyst development by several groups. This model involves the coupling of adsorbate states with metal d states on the electrode. By examining the strength of coupling between O, O_2, or OH species on different metals, the well-known "volcano plots" relating this strength to reactivity can be developed [70]. These plots are the manifestations of the well-known principles of Sabatier in heterogeneous catalysis [71]. Figure 9.3 shows one of these plots showing that among pure metals, platinum has the highest reactivity. The strength of coupling between O or

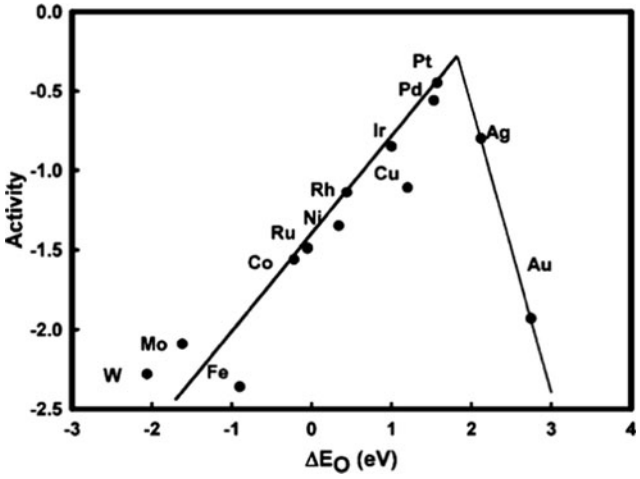

Fig. 9.3 Trends in oxygen-reduction activity plotted as a function of the oxygen binding energy. (Reproduced with permission from [75])

OH and the surface of the metal can be altered by alloying. An extension of this model is the multiparameter correlation proposed by Norskov for the formulation and design of alloy systems for selection of catalysts for fuel cell applications.

9.6.2.1 ORR Catalyzed by Platinum

Metallic platinum has been the oxygen-reduction catalyst of choice since the development of the PEMFC by General Electric Company in the early 1960s, and it still remains as the benchmark catalyst against which the newly developed ORR catalysts are evaluated. Current state-of-the-art PEMFC cathodes employ Pt loadings of 0.4 mg_{Pt}/cm^2 and exhibit mass activities of 0.16 A/mg_{Pt} at 0.9 V_{RHE}. A reduction of the Pt loading of 0.16 mg_{Pt}/cm^2 corresponding to a target mass activity of 0.45 A/mg_{Pt} at 0.9 V_{RHE} is desired for large-scale applications [72]. These catalysts are generally of 40 wt% Pt/C with Pt diameters of 3–4 nm with active Pt surface areas of 90 m^2/g. Catalysts with less than 3-nm platinum particulates and increased active surface areas do not exhibit increased mass activities over the state-of-the-art commercial Pt/C catalysts. This is due to the size effect of Pt particles in ORR, showing best activities in optimum Pt size; because when the Pt size becomes too small, the adsorption strength of OH_{ads} increases, blocking the active sites. Currently, the carbon-supported Pt catalysts are prepared mostly via impregnation route. Such catalysts typically do not have the uniformity in size and shape in comparison to those made by colloidal synthesis. Control over the structural parameters of Pt nanoparticles is essential in order to harvest excellent properties demonstrated on selective crystal surfaces. Hence, yet another route to reduce the Pt loading is to prepare Pt nanoparticles with designer morphologies [73]

and the references cited therein. While some of the structures such as polyhedral, nanowires, and branched structures exhibit higher specific activities than 40% Pt/C, these improvements are more than compensated for by the reduced surface areas of these materials, resulting in no net gain in mass activities [74]. Given these understandings, it is not likely that the target mass activities can be accomplished with pure Pt catalyst.

In addition, there are several limitations to employ Pt catalysts for ORR, beside the issue of its high cost. The main reasons are the following: at first, Pt-catalyzed ORR is not a complete four-electron reaction. Therefore, it is necessary to find an effective catalyst that can promote the direct four-electron reduction of oxygen to give water in order to improve the efficiency of the PEMFC. Secondly, Pt catalysts are very sensitive to the contaminants in the feed system. These contaminations occur through the impurities in the feed stream such as CO, H_2S, NH_3, organic sulfur–carbon and carbon–hydrogen compounds in H_2 stream and NOx and SOx species in the airstream. These impurities can easily poison the Pt catalyst, leading to degradation in performance. Further, the platinum catalysts gradually degrade upon potential cycling via sintering, dissolution, and corrosion of the carbon support, resulting in lack of durability for reliable applications.

9.6.2.2 ORR Catalyzed by Pt Alloys

In 1990s, investigators who worked on phosphoric acid fuel cells (PAFCs) reported higher ORR activity and stability with several binary and ternary platinum alloy catalysts than pure platinum catalyst. Diverse explanations were invoked in explaining the enhanced activities of those alloy catalysts including structural and electronic factors as documented in [72]. The reviews [73, 75] have addressed the growth mechanism and structure of Pt alloy particles. In PAFCs, the gradual leaching of the base metal is not a matter of concern; but in PEMFCs, the leached cations poison the ionomer membrane, displacing the protonic sites and catalyze the degradation of the membrane [72]. There are at least three possible causes for the leaching of the base metal catalysts in PEMFCs: firstly, excess base metal deposited onto carbon support during preparation; secondly, incomplete alloying of the base metal to Pt due to a low alloying temperature employed during the formation of the alloy; even a well-alloyed base metal may leach out during PEMFC operations, leaving a platinum-enriched surface or skin since thermodynamically base metals are unstable under PEMFC operating conditions in acid electrolytes. The preleaching of Pt_xCo_{1-x} alloys with acid can be carried out to prevent further leaching and the consequent contamination of the membrane electrode assembly. Activity as high as 0.28 A/mg_{Pt} at 0.9 V_{RHE} reported using commercial materials is regarded as benchmark for alloy catalysts.

The results of various investigations in the past two decades on electrochemical tests of ORR by employing various binary and ternary platinum alloy catalysts are presented in Table 9.4. In the second half of this table, emphasis was placed on the most recent and promising advancements utilizing various strategies to control

Table 9.4 Binary and ternary platinum catalysts for ORR in PEMFC

Pt alloy catalyst	Electrochemical test conditions	Major findings	References
Carbon-supported Pt_3Cr, Pt_3Co, Pt_3Ni	PEMFC life test	Negligible losses in the performance over 400–1,200 h. High stability of Pt and alloying components	[76]
Pt with Ni, Co, and Fe	Anodic potential of 1.1 V in dilute acid	From XPS, most of Ni, Co, and Fe easily disappeared from Pt alloy surface layers by dissolution; XRD indicates no difference before and after experiments. Inference: loss of base metal occurs only within few monolayers of alloy surface. Modification of electronic structure of the Pt layer with respect to bulk alloys results in enhanced ORR	[77]
Pt/C, Pt_3Ni/C	Accelerated durability test	Pt_3Ni alloy shows better resistance to sintering than pure Pt catalyst	[78]
Pt–Fe alloy on C	Accelerated durability test	Sintering effect of Pt is suppressed	[79]
Pt–Co alloy on C	Accelerated durability test	Sintering effect of Pt is suppressed	[80]
Pt–M (M = Fe, Co, and Ni)	Accelerated durability test	For 1:1 Pt and non-noble metal ratio, highest metal loss was observed; for 3:1 Pt and non-noble metal ratio, lowest metal loss was observed; electron microprobe cross-section analysis: Co dissolution found on membrane	[81]
Pt–Co, 2.5:1 atomic ratio on C	Dynamic fuel cell with continuous water fluxing in the cathode	13.9 mol% Co dissolved in first 400 cycles; 6% after 800 cycles. Overall performance loss with PtCo/C was less than Pt/C after 2,400 cycles. Performance loss in Pt/C after 1,200 cycles—due to loss of active surface area of Pt; In PtCo/C case, Co dissolution is the cause	[82]
Pt–Co on C	PEMFC durability test 1,000 h	Performance offset 15–25 mV was between Pt/C and	[72]

(continued)

Table 9.4 (continued)

Pt alloy catalyst	Electrochemical test conditions	Major findings	References
		Pt–Co/C was maintained throughout 1,000 h. Pt alloys starts life with larger size and does not sinter as rapidly as Pt/C	
$Pt_{1-x}M_x/C$ (M = Fe, Ni)	Simulated PEMFC operating conditions	Transition metals are removed from all compositions during acid treatment, and the amount of metal removed increases with x, acid strength, and temperature	[83]
Pt/C, Pt–Co/C, PtIrCo/C	PEMFC full cell	Alloys showed better activity and remarkable stability over Pt/C. The loss of real surface area after 1,800 cycles at 120°C was 45% for Pt/C, 18% for PtCo/C, and 8% for PtIrCo/C	[84]
Pt–M, 1:1 M = Fe, Mn, Ni, Cr, Ti	PEMFC full cell	The Cr and Ni showed no apparent leaching while Fe, Mn, and Ni showed leaching of base metal into MEA but no performance loss over 200 cycles	[85, 86]
Pt–M, M = Fe, Mn, Ni, Cu	PEMFC full cell	No significant loss for 2 continuous days of operation	[87]
Pt–Ni/C	Polarization at 0.80 V for 1 h in $HClO_4$	Stability of alloy catalyst is good; No Pt surface enrichments	[88]
Pt–Ni, Pt–Co on C	Thin film RRDE in 0.1 M $HClO_4$ at 25, 60°C	Pt–Co 3:1, 1:1 and Pt–Ni 3:1 are stable, while Pt–Ni 1:1 changed sustainability	[89]
Pt_3Cr	Hydrogen-air PEMFC	Pt was less stable than Pt_3Cr under high-current density and high-humidity conditions	[90]
Most recent promising advancements to control morphology of the nanoparticles—Pt skins, nanoparticles decorated with smaller particles or dendritic structures			
Pd nanocrystals of 9 nm as seeds for the formation of dendritic Pt nanoparticles	Hydrogen-air PEMFC	Pt mass activities as high as 0.43 A/mg_{Pt} at 0.9 V_{RHE}	[91]
3 nm Pt particles grown on 5 nm Pd particles	Hydrogen-air PEMFC	12% decay after 30,000 potential cycles compared to a 39% decay with Pt/C	[92]
Deposits of small Au clusters on Pt/C	Hydrogen-air PEMFC	Dramatic improvement in durability without	[93]

(continued)

Table 9.4 (continued)

Pt alloy catalyst	Electrochemical test conditions	Major findings	References
		significant decrease in initial activity	
Pt_3M, M = Ni, Co, Fe, V, Ti annealed to form Pt skin on the alloy surface	Hydrogen-air PEMFC	$Pt_3Ni(111)$ surface is approximately tenfold more active than Pt(111), 90-fold more active than Pt nanoparticles on a mass activity basis, and has the highest ORR activity of any alloy reported to date	[94, 95]
Pt skin formation on another metal by electrochemical underpotential deposition of Cu, followed by displacement of Cu with Pt	Hydrogen-air PEMFC	ORR mass activity 20 times higher than that of platinum particles	[96–101]
C supported nanoparticles with non-noble metal core and noble metal shells	Hydrogen-air PEMFC	Pt monolayer on C supported Co@Pd with 3–4-nm core-shell nanoparticles show total noble metal mass activity of 0.4 A/mg_{Pt} at 0.9 V_{RHE} which is very close to the target for traction applications	[101]
Pt alloy nanoparticles with Pt-enriched surface layers by electrochemical dealloying $Pt_{20}Cu_{20}Co_{60}$	Hydrogen-air PEMFC	0.5 A/mg_{Pt} at 0.9 V_{RHE} exceeding the activity benchmark for practical applications	[102]

the morphology of the nanocatalyst particulates and the formation of heterogeneous structures like platinum skin, nanoparticles decorated with smaller particles, and dendritic structures. This part would demonstrate to the reader the contribution of catalyst development and designing in the recent years, accomplishing impressive performance improvement in PEMFCs, enhancing the activity and stability of conventional Pt/C catalysts and Pt alloys that are commonly employed.

From the various observations of the investigations given in Table 9.4, one can find both high and low stability of platinum-based alloys in acid medium in the literature. There are some investigations which showed the high stability of the catalysts even after 1,000 h of life test in PEMFCs [72, 76]. In certain cases as in [88], poor stability of materials was found in short durations with measurements in half cells. It should be noted that the half-cell results can lead to different results compared to full-cell tests. In addition, parameters such as temperature, pressure, pH, and acid type can also affect the behavior of the alloy catalysts.

According to certain reports [85, 86, 89], the stability of non-noble metals in acid environment depends on the kind of metal. Pt–Cr and Pt–Co are considered as more stable ones than Pt–V, Pt–Ni, and Pt–Fe. But, the stability of these catalysts depends

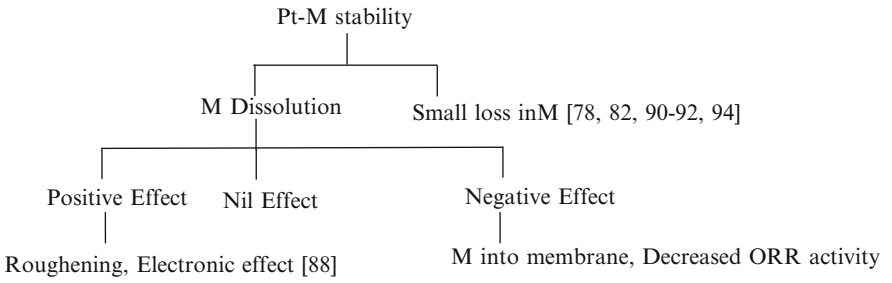

Scheme 9.2 Pt–M stability in acid environment and consequences

on the degree of alloying and, to a lesser extent, on the size of the metal particle and not on the type of metal. In general, Cr and Co exhibit higher degree of alloying with Pt than V, Ni, and Fe. This could explain the higher stability of Pt–Cr and Pt–Co than Pt–V, Pt–Ni, and Pt–Fe. The various studies show that most part of M dissolved came from non-alloyed M. Another interesting finding is that the alloy particles showed better resistance to sintering than pure platinum particles [78–80]. The presence of the non-precious metal particles appears to hinder the mobility of platinum on carbon. The major findings of various investigations on ORR studies employing Pt–M catalysts and the stability and activity issues are shown in Scheme 9.2.

It can be stated that the dissolution of base metal affects the characteristics of the catalyst in two different ways. The non-precious metal dissolution may lead to increase in ORR activity by surface roughening, and this phenomenon leads to increased platinum surface area and/or by modification of the electronic structure of the Pt skin originating from the loss of base metal. On the other hand, the non-noble metal dissolution leads to a decrease in ORR activity due to disruption of beneficial structure.

9.6.2.3 ORR Catalyzed by Non-noble Metals

In the effort to reduce the cost and improve the reliability of platinum-based fuel cell catalysts, a non-Pt catalysis approach greatly attracted the investigators. ORR on metal surfaces such as Cu (001), Cu (111), and Ni (100) has been examined by different investigators [103–105]. Oxygen molecules were adsorbed and migrated on Cu (001) surface as revealed by a STM study. The hydrogenation of adsorbed O on Cu (111) surface was studied with TDS and Auger spectroscopy, revealing that the formation of gaseous water is following two consecutive steps of formation of OH_{ads} followed by hydrogenation to H_2O_{ad}. In Ni (100) surface, fast formation and desorption of water molecules were observed.

Other than pure metals, metal oxides and alloys have also been investigated. ORR activity was found on anodically formed TiO_2 on Ti surface [106]. From rotating disk experiments, it has been found that the ORR on TiO_2 proceeds through a two-electron process in acidic solutions and four-electron process in basic solutions.

Polyoxometallates are a huge class of transition metal–oxygen cluster compounds that have unique properties such as stability, easy synthetic route, and commercial availability. Vanadium oxide was examined for its ORR activity [107] and exhibited one order of magnitude more current as cathode catalyst than anode catalyst in PEMFCs. Tungsten carbide has been a good HOR catalyst and tested for ORR reaction also. But it is not stable enough under ORR conditions, and hence, tantalum was added to enhance its cathodic activity. The corrosion resistance of WC was notably increased by the addition of Ta, and the electrocatalytic activity of ORR with WC + Ta was observed at 0.8 V, which is 0.35 V more positive than with pure WC catalyst [108]. Another study employed the perovskite-type oxide, lanthanum manganite for ORR in basic media [109].

Ruthenium-based bimetallic electrocatalysts with non-noble metals such as Ti, Cr, Fe, Co, and Pb on carbon support were prepared using chelation process [110] and examined for ORR activity. Rotating ring-disk electrode measurements showed that RuFeNx/C exhibits the activity and selectivity toward four-electron reduction of oxygen to water comparable to conventional Pt/C catalysts. The MEA prepared with RuFeNx/C for PEMFC exhibited the maximum power density of 0.18 Wcm^{-2} and no performance degradation for continuous 150 h of operation.

9.6.2.4 ORR Catalyzed by Transition Metal Chalcogenides

Since, Vante and Tributsch [111] proposed semiconducting Chevrel phase Ru–Mo chalcogenides (sulfides, selenides), a spurt of research activities employing various transition metal chalcogenides is investigated for ORR in acid media and, in some cases, reported their PEMFC full-cell activities. The attractive behavior of chalcogenides is their high stability in an acid environment, especially when in combination with other transition metals. Further, delocalization of electrons in a metal cluster can lead to high electron conductivity and attenuate relaxation of the electronic states. The availability of reservoir of charges for multielectron charge transfer is essential for enhanced catalytic activity. A summary of the results of ORR studies, employing chalcogenides in half cell using liquid electrolyte and PEMFC studies carried out by various investigators is given in Table 9.5. Mostly Ru-based chalcogenides [111–117] were employed, and there is a recent report using Pd chalcogenide [118] for ORR. A very few investigations were found on non-noble metal chalcogenide tested for ORR in acid medium [119, 120].

9.6.2.5 ORR Catalyzed by Transition Metal Complexes

A variety of carbon-supported transition metal macrocyclic complexes such as N_4-, N_2O_2-, N_2S_2-, O_4- and S_4-systems all showed certain extent of catalytic activity for oxygen reduction. Especially the N_4-macrocycles such as phthalocyanines, porphyrins, Schiff bases, and related derivatives and the metal, M, usually Fe, Co, and Ni ([68, 121, 122] and the references cited therein) showed significant

Table 9.5 ORR reactions on metal chalcogenides

Metal chalcogenide	Electrochemical test conditions	Major finding	References
Noble metal chalcogenides			
$Mo_{4.2}Ru_{1.8}Se_8$, $Mo_{3.7}Ru_{2.3}Se_8$, $Ni_{0.85}Mo_{1.8}Se_8$	Half cell, O_2 saturated 0.5 M H_2SO_4	$Mo_{4.2}Ru_{1.8}Se_8$ closely approached Pt catalysts. Further optimization of catalyst structure was recommended	[111]
$Ru_xCr_ySe_z$	Half cell, O_2 saturated 0.5 M H_2SO_4 H_2/O_2 PEMFC full cell 25, 80°C	High activity, facilitating 4 e^- transfer; Tafel slope for the ORR remains constant with T at -0.117 V dec^{-1}, and the charge transfer coefficient increases in $d\alpha/dT = 1.8 \times 10^{-3}$, attributed to entropy turnover contribution similar to Ru-based Se catalysts	[112]
S, Se, Te-modified Ru catalysts	Half cell, O_2 saturated 0.5 M H_2SO_4	ORR activity: Ru–Te > Ru–Se > Ru–S; $RuTe_2$/C showed high-cathodic current compared to Pt/C, but exhibited about 0.2 V overpotential for the ORR compared to Pt/C	[113]
$Ru_xMo_ySe_z$ on C	Half cell, O_2 saturated 0.5 M H_2SO_4 H_2/O_2 PEMFC full cell	Best performance with 20% $Ru_xMo_ySe_z$/C, 240 mW cm^{-2} at 0.30 V. This value is the half of the performance obtained with Pt under the same conditions	[114]
$Ru_xM_ySe_z$ (M = Cr, Mo, W)	Half cell, O_2 saturated 0.5 M H_2SO_4 H_2/O_2 PEMFC full cell	ORR activity: $Ru_xMo_ySe_z > Ru_xW_ySe_z > Ru_xCr_ySe_z$	[115]
$RuSe_x$/C ($x = 0.35$–2)	Half cell, O_2 saturated 0.5 M H_2SO_4	$RuSe_x$/C with a pyrite structure and Se/Ru ratio near two exhibits a high ORR activity and superior stability compared to $RuSe_x$/C with Se/Ru ratio less than one and the $RuSe_{cluster}$/C	[116]
$Ru_{1-x}Fe_xSe_y$/C ($x = 0.0$–0.46, $y = 0.4$–1.9)	Half cell, O_2 saturated 0.5 M H_2SO_4	ORR activity increases with increasing Fe and Se contents. Fe substitution enhances activity and reduces material cost, but increases H_2O_2 yield of 3.0% between 0.7 and 0.9 V in contrast to 1.0% of catalyst without Fe. High activity of $Ru_{0.54}Fe_{0.46}Se_{1.9}$/C decays rapidly than $RuSe_{2.0}$/C may be due to Fe and Se leaching at potential cycling up to 1.2 V. Catalysts with pyrite structure exhibit higher durability than cluster-type catalyst of $RuSe_{cluster}$/C (Ru:Se = 1:0.3)	[117]
$Pd_{0.5}Ni_xSe_{(0.5-x)}$	Half cell, O_2 saturated 0.5 M H_2SO_4	Low Se content improves catalytic activity and selectivity toward the 4 e^- process of ORR to water formation, with less than 2% of H_2O_2 formation	[118]
Non-noble metal chalcogenides			
Co–Se	Half cell, O_2 saturated 0.5 M H_2SO_4	Co–Se thin films with varying Se are active for ORR although the open-circuit potential (OCP) is lower than for Pt	[119]
W–Co–Se	Half cell, O_2 saturated 0.5 M H_2SO_4	Significant ORR activity with onset potential 0.755 V_{NHE}	[120]

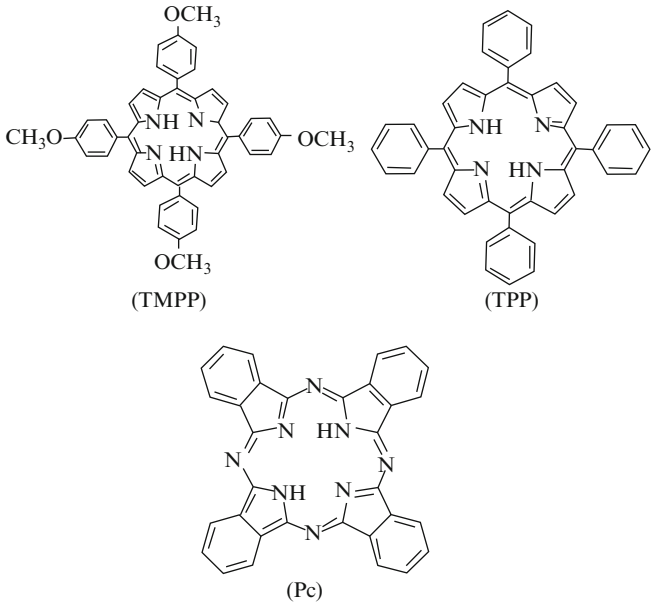

Fig. 9.4 Molecular structures of metal tetramethoxyphenylporphyrin (TMPP), tetraphenylporphyrin (TPP), and phthalocyanine (Pc)

ORR activities in acid medium. The molecular structure of some of the extensively studied macrocyclic ligands such as tetramethoxyphenylporphyrin (TMPP), tetraphenylporphyrin (TPP), and phthalocyanine (Pc) for ORR is shown in Fig. 9.4. Beck [123] predicted that the mechanism of ORR on N_4-chelates of transition metal mainly associated with a modified redox catalysis. In ORR, the first step was the adsorption of oxygen on the catalyst metal center to form an oxygen-catalyst adduct, followed by an electron transfer from a metal center to bound O_2 and the regeneration of the reduced N_4-chelates.

The central metal ion in the macrocycle seems to play a key role in the oxygen-reduction mechanism. Depending on the nature of the metal, the ORR could take place via four-electron reduction to water (Fe complexes), two-electron reduction to H_2O_2 (Co complex). For N_4 chelates, phthalocyanines, the influence of metal ion showed the ORR activities in the following order [124]: Fe > Co > Ni > Cu ~ Mn. The sequence of activity was explained by molecular orbital theory based on oxygen adsorption [125]. Though Fe complexes of phthalocyanine (Pc) and porphyrin (PP) can promote four-electron reduction pathway, they are not stable. Cobalt complexes exhibit higher stability than those of Fe; they can only catalyze two-electron reduction of oxygen. The electrochemical stability sequence of metal macrocyclic complexes toward ORR is Co > Fe > Mn [126].

For the N_4-macrocycle such as porphyrin metal complexes, the formation of H_2O_2 is believed to be responsible for the deterioration of electrode performance over time. Heat treatment of such complexes is found to overcome these shortcomings. van Veen et al. [127] proposed four models to explain the heat-treatment effect: (1) improving the dispersion of the supported chelate, (2) catalyzing the formation of a special type of carbon, (3) generating the M–N species, and (4) promoting a reaction between chelate and adjacent carbon in such a way as to modify the electronic structure of the central metal ion with retentions of its N_4 coordination environment. In order to combine the advantages of four-electron reduction of Fe complexes with the higher electrochemical stabilities of Co complexes, Chu and Jiang [128] studied the effect of the heat-treated mixture of two transition metalloporphyrins (V/Fe, Co/Fe, Ni/Fe, and Cu/Fe) for ORR and compared with that of heat-treated single transition metalloporphyrin. They found that the heat-treated binary Fe and Co tertaphenylporphyrins could give higher ORR current compared with their single constituents when employed individually.

The electrocatalytic activities are determined from rotating ring-disk electrode in half-cell reactions for selected Co and Fe-N/C which are synthesized at the best heat-treatment temperature, and metal loading of catalysts are listed in Table 9.6 [122].

PEMFC full-cell tests were also investigated using CoPPY, CoTMPP [129], FeTMPP [145], FeAc/NH_3 [148], and CoPc [153], in the presence of either air or oxygen in the cathodes. It has to be mentioned that the E_p, E_{onset}, and E_{ocp} values for ORR at the benchmark Pt/C were reported to be 0.71 V [134], 1.0 V [131], and 0.99 V (vs. NHE) [129], respectively. By comparing the listed parameters in Table 9.6 and information from PEMFC full-cell studies, two important inferences can be derived. Firstly, the electrocatalytic activities of these catalysts toward the ORR are not too far from those of Pt-based catalysts, as many of the catalysts exhibited very close values of E_p, E_{onset}, and E_{ocp}. Secondly, the turnover rates of these non-noble metal catalysts are low compared to Pt/C catalyst.

9.6.3 Supports for PEMFC Catalysts

9.6.3.1 Carbon Supports

The PEMFC catalyst research and development involves the development of suitable support materials. Support plays an important role in enhancing the catalytic activity and stability through its appropriate morphology, metal-support interactions, and through synergetic effects in certain materials. Carbon in its various forms is extensively employed as a support material in fuel cell electrodes. The attractive characteristics of carbon are:

- High surface area (ranging from 60 to 1,750 m^2/g)
- Good electrical conductivity and stability in wide potential window
- Adequate dimensional and mechanical stability

Table 9.6 ORR activity of some Co and Fe macrocycles in half-cell reactions

Catalyst/C	Test conditions	Activity/NHE $\left(E_p^a/\text{mV}\right)$	References
CoTMPP	0.5 M H_2SO_4	850[a]	[129]
FeTMPP	1.0 M H_2SO_4	890[a]	[130]
CoTPP/FeTPP	0.5 M H_2SO_4	900[b]	[131]
FePhen/NH_3	0.5 M H_2SO_4	500	[132]
FeTMPP	0.5 M H_2SO_4	–	[133]
FePAN	0.5 M H_2SO_4	600	[134]
CoPAN	0.5 M H_2SO_4	550	[135]
FeAc/AN	0.5 M H_2SO_4	555	[136]
CoTMPP	0.5 M H_2SO_4	660	[137]
FeTTP	H_2SO_4 pH 0.5	–	[138]
CoTTP	H_2SO_4 pH 0.5	–	[138]
$FeCl_2$/AN	H_2SO_4 pH 0.5	504	[139]
$FeCl_3$/AN	H_2SO_4 pH 0.5	594	[139]
$Fe(OH)_2$/AN	H_2SO_4 pH 0.5	494	[139]
$Fe(OH)_2$/AN	H_2SO_4 pH 0.5	594	[139]
$Fe(OH)_2$/TCNQ	H_2SO_4 pH 0.5	624	[140]
$Fe(OH)_2/H_2Pc$	H_2SO_4 pH 0.5	644	[141]
$Fe(OH)_2$/AN	H_2SO_4 pH 0.5	429	[142]
FeTPP	H_2SO_4 pH 0.5	684	[142]
FeAc/NH_3	H_2SO_4 pH 0.5	694	[143]
FeAc/NH_3	1.17 M H_2SO_4	694	[144, 145]
FeTMPP	0.5 M H_2SO_4	659	[144, 145]
FeTMPPCl	0.5 M H_2SO_4	711	[146]
FeAc/NH_3	0.5 M H_2SO_4	719	[147]
FeAc/NH_3	0.5 M H_2SO_4	744	[148]
FeAc/NH_3	0.5 M H_2SO_4	687	[149]
CoAc	0.5 M H_2SO_4	544	[150]
CoTMPP	0.5 M H_2SO_4	544	[151]
$FeSO_4/NH_3$	H_2SO_4 pH 1.0	684	[151]
CoTMPP	0.5 M pH 3.0 phosphate buffer	599	[152]

Ac acetate, *PAN* polyacrylonitrile, *PPY* 2-phenyl pyridinato, *TMPPCl* tetramethoxyphenyl porphyrin chloride, *TCNQ* tetracyanoquinodimethane, E_{ocp} open-circuit potential, E_{onset} onset potential, E_p^a potential at which cathodic peak height of oxygen reduction is maximum

[a] E_{ocp}/mV

[b] E_{onset}/mV

- Lightweight
- Porosity which helps in dispersion, activity enhancement, and stability of metal catalyst by preventing agglomeration
- Rich surface chemistry and versatile for functional group modifications
- Facile mass transport due to its hydrophobic characteristics

The most commonly used carbon supports in fuel cell electrodes together with their characteristics are given in Table 9.7.

The effect of carbon black characteristics on the dispersion of supported metals and on their electrocatalytic activity is well studied in literature. In case of metal

Table 9.7 Carbon supports for fuel cell electrodes

Carbon support	Maker	Surface area (m^2/g)	Particle size (nm)
Carbon black			
Vulcan XC-72R	Cabot	254	30
BLACK PEARLS® 2000	Cabot	1,475	15
Ketjenblack, 300J	Akzo Noble	829	30–40
Acetylene black	Cabot	70	–
Exp. Sample AB	Denki Kagaku Kogyo	835	30
Shavinigan AB	Gulf Oil	70–90	40–50
Denka black AB	Denki Kagaku Kogyo	58	40
3950 FB	Mitsubishi Kasei	1,500	16
Printex XE-2	Evonik	950	–
SRC	–	–	–
Condutex 975 FB	Columbian	250	24
Active carbon			
NORIT SX ULTRA	Norit	1,076	5–400
P33	–	15.5	–
RB carbon	–		–

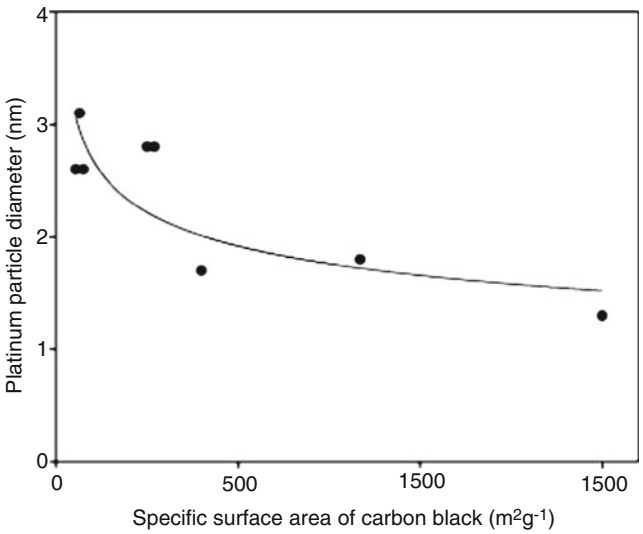

Fig. 9.5 Dependence of Pt particle diameter on specific surface area of carbon blacks [160]. (Reproduced with permission)

deposition on carbon support by impregnation methods, the specific surface area of the carbon appears to have little effect on Pt dispersion [153]. Uchida et al. [154] evaluated the effect of specific surface area of different carbons on Pt particle size in Pt/C prepared by colloidal method. The Pt particle size decreased with increasing specific surface area of the carbon as shown in Fig. 9.5. McBreen et al. [155]

examined the Pt deposited by colloidal method on five-carbon supports such as Vulcan XC-72R, Regal 600R, Monarch 1300, CSX98, and Mogul L. Vulcan XC-72R and Regal 600R exhibited higher Pt dispersion than that on other carbons. The high dispersion on Vulcan XC-72R was attributed to the high internal porosity, which that on Regal 600R was ascribed to the surface property of the carbon, resulting in strong metal-support interaction.

In order to enhance their electrochemical active surface area, the catalyst particles supported on high surface area carbon materials are widely used in PEMFCs. The physical and chemical properties of carbon support greatly influence the electrochemical properties of the fuel cell catalyst. The carbon materials with high surface area and good crystallinity facilitate electron transfer in addition to high dispersion of catalyst particles. In this direction, novel nonconventional carbon materials are architectured with desired physicochemical properties in numerous morphologies, and the examples include ordered mesoporous carbons, carbon aerogels, carbon nanotubes, carbon nanofibers, carbon nanohorns, and carbon nanocoils. The challenge before the scientists is to develop carbon supports with appropriate pore sizes, high surface area, good electrical conductivity, and chemical stability in harsh fuel cell environments to achieve reliable durability through simple, energy efficient ways. Among carbon materials, carbon nanotubes appear to be promising material with desirable characteristics such as high crystallinity, stability, high electrical conductivity for their employment in fuel cell electrodes. As seen from literature, several researchers reported ([156] and the reference cited therein) that when used as anode and/or cathode materials, Pt and Pt–M catalysts supported on carbon nanotubes exhibited higher catalytic activity and stability than that observed with the same catalysts supported on conventional carbon blacks. The higher activity of catalyst particles supported on CNT compared to carbon black can be attributed to several factors:

- The hollow cavity and graphitic layer interspaces offer facile access to reactant gases than conventional supports. For instance, the extensively employed Vulcan XC-72 R has randomly distributed pores of different sizes, hindering the facile mass transport of reactants and products, where as the tubular morphology of the CNTs makes the diffusion of reactant easier.
- The morphology of the CNTs can give rise to edge sites on which Pt particles can deposit, and these sites may be more active than the sites in planar carbon black.
- The crystalline nature of CNTs makes them as good conductive substrates.
- The chemical differences between CNTs and carbon black induce flat deposition of Pt on CNTs. This configuration of Pt crystallite results in decrease of the hydrogen adsorption energy as inferred from temperature-programmed decomposition (TPD) studies. This might arise from lowering of d-band center induced by the reduction of Pt lattice constant and/or charge transfer from anchoring sites of Pt. Such changes in electronic property may be responsible for the enhanced electrochemical activity of Pt on CNT [157].

The specific characteristics of various new forms of carbon and conventional carbons along with the characteristics of supported catalysts are listed in Table 9.8.

Table 9.8 Specific characteristics of different carbon materials and properties of supported catalysts [150]

Carbon material	Surface area (m^2/g)	Porosity	Electronic conductivity ($S\ cm^{-1}$)	Supported catalyst properties	References
Vulcan XC-72R	254	Microporous	4.0	Good metal dispersion, low gas flow	([156] and reference cited therein)
Ordered mesoporous carbon	400–1,800	Mesoporous	$0.3 \times 10^{-2} - 1.4$	High metal dispersion, high gas flow, low metal accessibility	
Carbon gels	400–900	Mesoporous	>1	High metal dispersion, high gas flow, high metal accessibility	
CNT (SWCNT)	400–900	Microporous	$10–10^4$ depending on alignment	Good metal dispersion, high gas flow	
CNT (MWCNT)	200–400	Mesoporous	0.3–3 function-alized	Low metal accessibility, high metal stability	
Carbon nanohorn, carbon nanocoil	150	Micro/ mesoporous	3–200	High metal dispersion, high gas flow	
Activated carbon nanofiber	>1,000	Microporous	13	High metal dispersion, low gas flow, high metal stability	
Carbon nanofiber	10–300	Mesoporous	$10^2–10^4$	High metal dispersion, high gas flow, high metal stability	
Boron-doped diamond	2	–	1.5	Low metal dispersion, low metal stability	

9.6.3.2 Alternate Support Materials

Ceramic materials such as titanium, tin, ruthenium and tungsten metal oxides, and carbides ([158] and the references cited therein) are explored as alternate support materials for low-temperature fuel cell applications in order to overcome two major limitations posed by carbon materials: the corrosion of carbon at cathodic potentials and Pt dissolution during long-term operations. Zhang et al. [159] employed Pt/C

and Pt/W_xC_y catalysts prepared by using Vulcan XC-72 R and tungsten carbide supports, respectively, as both anode and cathode materials in PEMFC single cell to compare their performance degradation. It has been found that before stability test, the PEMFC with Pt/C performed better than that with Pt/W_xC_y. After stability test, in contrast, Pt/W_xC_y catalyst showed a better performance than with Pt/C, indicating high oxidation resistance of Pt/W_xC_y catalyst. The initial electrochemical surface area of Pt/C and Pt/W_xC_y was 16.1 and 10.2 m^2/g, respectively. This difference has been ascribed to higher surface area of carbon than that of calcined tungsten carbide. It is desirable to find ways to synthesize high surface area tungsten carbide materials for fuel cell applications. Chhina et al. [160, 161] compared the stability of Pt supported on commercial WC (BET = 1.6 m^2/g) with that of homemade Pt supported on Vulcan XC-72 R and commercial Pt/C. In both works, the stability of Pt/WC was higher than that of Pt/C.

Several conducting polymers such as polyaniline, polypyrrole, polythiophene, and their derivatives ([162] and the references cited therein) exhibit greater advantages as fuel cell catalyst supports due to their high surface areas, suitable porosities, high electronic and protonic conducting properties, mechanical properties, and the simple and rapid ways of preparing them. The main interest in conducting polymers is due to the three-dimensional availability of catalyst metal deposits, whereas the conventional carbon supports employed in fuel cell systems at the present days inhibit the accessibility of the catalyst particles due their complicated pore morphologies.

9.7 Perspectives

The challenge of the research and technological development of fuel cells especially that of the PEMFCs centered on the catalytic materials for both the anode and cathode. A major impediment for commercialization of PEMFC is the cost and scarcity of platinum because the PEMFC employ platinum in both anodes and cathodes in order to attain satisfactory performance. Durability is another issue because Pt catalysts are easily poisoned by the impurities and intermediates in the fuel cell reactions. The first question is, have we learnt enough to reduce the quantity of required Pt in the electrodes and what does catalysis do to this? The second question is, have we learned to move away from the Pt catalysts which were proposed 50 years ago and in fact from day one of the genealogy of hydrogen-air fuel cell? The third question is, are the electrocatalytic materials possess appropriate durability?

We would like to answer these questions pictorially through Figs. 9.6 and 9.7.

Yes, we see the light, but not too far away! High power densities and efficiencies are being realized, due to the dispersion of nanosized, tailor-made metal structures, on high surface area alternative support materials. The loading of platinum or platinum alloy metals applied as gas diffusion electrodes is significantly reduced to a relatively few milligrams per geometric area compared to the efforts done during the past decades. We also start detaching ourselves from complete reliability on platinum by searching for Pt-free, cost-effective nonmetals with abundance of

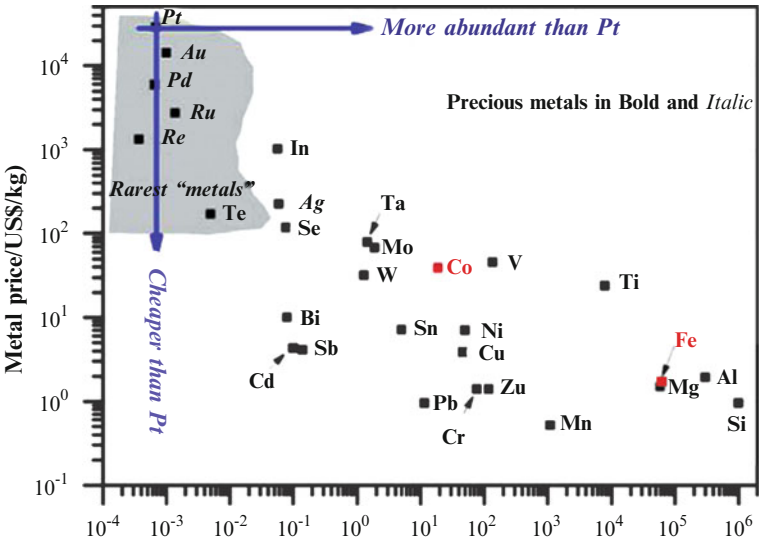

Fig. 9.6 Relationship between metal prices and relative abundance of the chemical elements in Earth's upper continental crust based on the abundance of Si with 10^6 atoms. The corresponding metal price data on September 02, 2005 are from http://www.metalprices.com [163]

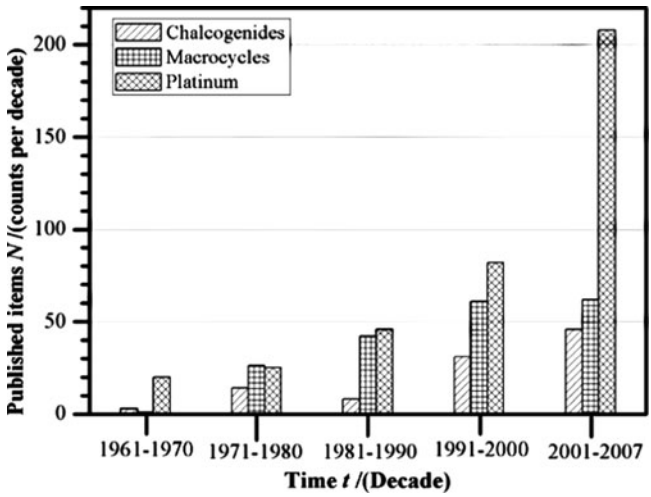

Fig. 9.7 Number of publications regarding chalcogenides, macrocycles, and platinum for oxygen-reduction reaction each decade from 1961 to 2007 [163]

supply and sustainability. Nature is a good teacher! We started taking our lessons from it by opting for materials which are structural and functional mimics of macrocyclic complexes, in ORR. Indeed, in spite of their little lower activities for ORR, the transition metal complexes appear to be promising ones, due to their

stability and their efficiencies involving reactions with multielectron transfers. New synthetic approaches are to be developed for designing the catalysts with molecular level assembling. To realize the full potentiality of the PEMFC technology, the fuel hydrogen needs to be derived by energy economic pathways.

In an earlier communication [164], the challenges that are ahead of the adaptation of fuel cell technology for large-scale commercialization and utilization have been outlined both from the academic as well as technological points of view. It has been pointed that the successful advancement of fuel cell technology will require a sustained, long-term commitment to fundamental research, commercial development, and incremental market entry. Depending on the sector of the market like portable communications and stationary and transportation applications, the number and magnitude of the challenges to be addressed change and various estimates are available on these [165].

Acknowledgments The authors wish to thank Department of Science and Technology and the Ministry of New and Renewable Energy, Government of India for the support of our research programs.

References

1. http://www.fueleconomy.gov/feg/fcv_pem.shtml
2. Wu J, Yuan XZ, Wang H, Blanco M, Martin JJ, Zhang J (2008) Diagnostic tools in PEM fuel cell research: part I electrochemical techniques. Int J Hydrogen Energy 33:1735–1746. doi:10.1016/j.ijhydene.2008.01.013
3. Barbir F (2005) PEM fuel cells: theory and practice. Elsevier/Academic Press, New York
4. Ju H, Wang CY (2004) Experimental validation of a PEM fuel cell model by current distribution data. J Electrochem Soc 151:A1954–A1960. doi:10.1149/1.1805523
5. Li X (2006) Principle of fuel cells. Taylor & Francis, New York
6. Viswanathan B, Aulice Scibioh M (2008) Fuel cells: principles and applications. Taylor & Francis, New York
7. Adams WA, Blair J, Bullock KR, Gardner CL (2005) Enhancement of the performance and reliability of CO poisoned PEM fuel cells. J Power Sources 145:55–61. doi:10.1016/j.jpowsour.2004.12.049
8. Papageorgopoulos DC, de Bruijn FA (2002) Examining a potential fuel cell poison: a voltammetry study of the influence of carbon dioxide on the hydrogen oxidation capability of carbon-supported Pt and PtRu anodes. J Electrochem Soc 149:140–145. doi:doi.org/10.1149/1.1430413
9. Gottesfeld S, Pafford JJ (1988) A new approach to the problem of carbon monoxide poisoning in fuel cells operating at low temperatures. J Electrochem Soc 135:2651–2652. doi:doi.org/10.1149/1.2095401
10. Schmidt VM, Oetjen H-F, Divisek J (1997) Performance improvement of a PEMFC using fuels with CO by addition of oxygen-evolving compounds. J Electrochem Soc 144: L237–L238. doi:doi.org/10.1149/1.1837928
11. Batista MS, Santiago EI, Assaf EM, Ticianelli EA (2005) Evaluation of the water-gas shift and CO methanation processes for purification of reformate gases and the coupling to a PEM fuel cell system. J Power Sources 145:50–54. doi:10.1016/j.jpowsour.2004.12.032
12. Bellows RJ, Marucchi-Soos E, Reynolds RP (1998) The mechanism of CO mitigation in proton exchange membrane fuel cells using dilute H_2O_2 in the anode humidifier. Electrochem Solid State Lett 1:69–70. doi:S1099-0062(97)12-131-9

13. Choudhary TV, Goodman DW (1999) Stepwise methane steam reforming: a route to CO-free hydrogen. Catal Lett 59:93–94. doi:10.1023/A:1019008202235
14. Lee S-H, Han J-S, Lee K-Y (2002) Development of PROX (preferential oxidation of CO) system for 1 kW_e PEMFC. Kor J Chem Eng 19:431–433. doi:10.1007/BF02697152
15. Lee S-H, Han J-S, Lee K-Y (2002) Development of 10-kWe preferential oxidation for fuel cell vehicles. J Power Sources 109:394–402. doi:10.1016/S0378-7753(02)00096-4
16. Batista MS, Santiago EI, Assaf EM, Ticianelli EA (2004) High efficiency steam reforming of ethanol by cobalt-based catalysts. J Power Sources 134:27–32. doi:10.1016/j.jpowsour.2004.01.052
17. Heinzel A, Vogel B, Hubner P (2002) Reforming of natural gas-hydrogen generation for small scale stationary fuel cell systems. J Power Sources 105:202–207. doi:10.1016/S0378-7753(01)00940-5
18. Zalc JM, Loffler DG (2002) Fuel processing for PEM fuel cells: transport and kinetic issues of system design. J Power Sources 111:58–64. doi:10.1016/S0378-7753(02)00269-0
19. Chen G, Yuan Q, Li H, Li S (2004) CO selective oxidation in a microchannel reactor for PEM fuel cell. Chem Eng J 101:101–106. doi:10.1016/j.cej.2004.01.020
20. Gasteiger HA, Markovic NM, Ross PN Jr, Cairns EJ (1994) Carbon monoxide electrooxidation on well-characterized platinum-ruthenium alloys. J Phys Chem 98:617–625. doi:10.1021/j100053a042
21. Gasteiger HA, Markovic NM, Ross PN Jr (1995) H_2 and CO electrooxidation on well-characterized Pt, Ru, and Pt–Ru. 2. Rotating disk electrode studies of CO/H_2 mixtures at 62 degree C. J Phys Chem 99:16757–16767. doi:10.1021/j100045a042
22. Grgur BN, Zhuang G, Markovic NM, Ross PN Jr (1997) Electrooxidation of H_2/CO mixtures on a well-characterized $Pt_{75}Mo_{25}$ alloy surface. J Phys Chem B 101:3910–3913. doi:10.1021/jp9704168
23. Ley KL, Liu R, Pu C, Fan Q, Leyarovska N, Segree C, Smotkin ES (1997) Methanol oxidation on single-phase Pt–Ru–Os ternary alloys. J Electrochem Soc 144:1543–1548. doi:doi.org/10.1149/1.1837638
24. Chen KY, Shen PK, Tseung ACC (1995) Anodic oxidation of impure H_2 on teflon-bonded Pt–Ru/WO_3/C electrodes. J Electrochem Soc 142:L185–L187. doi:doi.org/10.1149/1.2050038
25. Mukerjee S, Srinivasan S, Soriaga MP (1995) Role of structural and electronic properties of Pt and Pt alloys on electrocatalysis of oxygen reduction. J Electrochem Soc 142:1409–1422. doi:doi.org/10.1149/1.2048590
26. Wang K, Gasteiger HA, Markovic NM, Ross PN Jr (1996) On the reaction pathway for methanol and carbon monoxide electrooxidation on Pt–Sn alloy versus Pt–Ru alloy surfaces. Electrochim Acta 41:2587–2593. doi:10.1016/0013-4686(96)00079-5
27. Gasteiger HA, Markovic NM, Ross PN Jr (1995) H_2 and CO electrooxidation on well-characterized Pt, Ru, and Pt–Ru. 1. Rotating disk electrode studies of the pure gases including temperature effects. J Phys Chem 99:8290–8301. doi:10.1021/j100020a063
28. Koper MTM, Shubina TE, van Santen RA (2002) Periodic density functional study of CO and OH adsorption on Pt–Ru alloy surfaces: implications for CO tolerant fuel cell catalysts. J Phys Chem B 106:686–692. doi:10.1021/jp0134188
29. Schmidt VM, Bröckerhoff P, Höhlein B, Menzer R, Stimming U (1994) Utilization of methanol for polymer electrolyte fuel cells in mobile systems. J Power Sources 49:299–313. doi:10.1016/0378-7753(93)01830-B
30. Lin SD, Hsiao TC (1999) Morphology of carbon supported Pt–Ru electrocatalyst and the co tolerance of anodes for PEM fuel cells. J Phys Chem B 103:97–103. doi:10.1021/jp982296p
31. Acres GJK, Frost JC, Hards GA, Potter RJ, Ralph TR, Thompsett D, Burstein GT, Hutchings GJ (1997) Electrocatalysts for fuel cells. Catal Today 38:393–400. doi:10.1016/S0920-5861(97)00050-3
32. Iorio T, Yasuda K, Siroma Z, Fujiwara N, Miyazaki Y (2003) Enhanced CO-tolerance of carbon-supported platinum and molybdenum oxide anode catalyst. J Electrochem Soc 150: A1225–A1230, http://dx.doi.org/10.1149/1.1598211
33. Lipkowski J, Ross PN (1998) Electrocatalysis. Wiley-VCH, New York

34. Markovic NM, Ross PN (2002) Surface science studies of model fuel cell electrocatalysts. Surf Sci Rep 45:117–230. doi:10.1016/S0167-5729(01)00022-X
35. Watanabe M, Moto S (1975) Electrocatalysis by ad-atoms part II. Enhancement of the oxidation of methanol on platinum by ruthenium ad-atoms. J Electroanal Chem 60:267–273. doi:10.1016/S0022-0728(75)80261-0
36. Anderson AB, Grantscharova E, Seong S (1996) Systematic theoretical study of alloys of platinum for enhanced methanol fuel cell performance. J Electrochem Soc 143:2075–2082, http://dx.doi.org/10.1149/1.1836952
37. Mukerjee S, Lee SJ, Ticianelli EA, McBreen J, Grger BN, Markovic NM, Ross PN Jr, Giallombardo PN, DeCatro ES (1999) Investigation of enhanced CO tolerance in proton exchange membrane fuel cells by carbon supported PtMo alloy catalyst. Electrochem Solid State Lett 2:12–15, http://dx.doi.org/10.1149/1.1390718
38. Ticianelli EA, Mukerjee S, Lee SJ, McBreen J, Giallombardo JR, De Castro ES (1998) In: Gottesfeld S, Fuller TF, Halpert G (eds) Proton conducting membrane fuel cells, PV 98-27, The electrochemical society proceedings series, Pennington, NJ, p 162
39. Grgur BN, Markovic NM, Ross PN (1999) The electro-oxidation of H_2 and H_2/CO mixtures on carbon-supported Pt_xMo_y alloy catalysts. J Electrochem Soc 146:1613–1619, http://dx.doi.org/10.1149/1.1391815
40. Grgur BN, Markovic NM, Ross PN (1999) In: Gottesfeld S, Fuller TF, Halpert G (eds) Proton conducting membrane fuel cells, PV 98-27, The electrochemical society proceedings series, Pennington, NJ, p 177
41. Zhang H, Wang Y, Fachini ER, Cabrera CR (1999) Electrochemically codeposited platinum/molybdenum oxide electrode for catalytic oxidation of methanol in acid solution. Electrochem Solid State Lett 2:437–439. doi:doi.org/10.1149/1.1390863
42. Igarashi H, Fujino T, Zhu Y, Uchida H, Watanabe M (2001) CO tolerance of Pt alloy electrocatalysts for polymer electrolyte fuel cells and the detoxification mechanism. Phys Chem Chem Phys 3:306–314. doi:10.1039/B007768M
43. Markovic NM, Ross PN (2000) Electrocatalysts by design: from the tailored surface to a commercial catalyst. Electrochim Acta 45:4101–4115. doi:10.1016/S0013-4686(00)00526-0
44. Gasteiger HA, Markovic NM, Ross PN (1996) Structural effects in electrocatalysis: electrooxidation of carbon monoxide on Pt_3Sn single-crystal alloy surfaces. Catal Lett 36:1–8. doi:10.1007/BF00807197
45. Markovic NM, Widelov A, Ross PN, Monteiro OR, Brown IG (1997) Electrooxidation of CO and CO/H_2 mixtures on a Pt–Sn catalyst prepared by an implantation method. Catal Lett 43:161–166. doi:10.1023/A:1018907110025
46. Ocko BM, Wang J, Davenport A, Isaacs H (1990) In situ X-ray reflectivity and diffraction studies of the Au(001) reconstruction in an electrochemical cell. Phys Rev Lett 65:1466–1469. doi:10.1103/PhysRevLett.65.1466
47. Tidswell IM, Markovic NM, Ross PN (1993) Potential dependent surface relaxation of the Pt (001)/electrolyte interface. Phys Rev Lett 71:1601–1604. doi:10.1103/PhysRevLett.71.1601
48. Lima A, Coutanceau C, Leger JM, Lamy C (2001) Investigation of ternary catalysts for methanol electrooxidation. J Appl Electrochem 31:379–386. doi:10.1023/A:1017578918569
49. Gotz M, Wendt H (1998) Binary and ternary anode catalyst formulations including the elements W, Sn and Mo for PEMFCs operated on methanol or reformate gas. Electrochim Acta 43:3637–3644. doi:10.1016/S0013-4686(98)00121-2
50. Holleck GL, Pasquariello DM, Clauson SL (1999) In: Gottesfeld S, Fuller TF, Halpert G (eds) Proton conducting membrane fuel cells, PV 98-27, The electrochemical society proceedings series, Pennington, NJ, p 150
51. Papageorgopoulos DC, Keijzer M, de Bruijn FA (2002) The inclusion of Mo, Nb and Ta in Pt and PtRu carbon supported electrocatalysts in the quest for improved CO tolerant PEMFC anodes. Electrochim Acta 48:197–204. doi:10.1016/S0013-4686(02)00602-3
52. Venkataraman R, Kunz HR, Fenton JM (2003) Development of new CO tolerant ternary anode catalysts for proton exchange membrane fuel cells. J Electrochem Soc 150: A278–A284. doi:doi.org/10.1149/1.1543567

53. He C, Kunz HR, Fenton JM (2003) Electro-oxidation of hydrogen with carbon monoxide on Pt/Ru-based ternary catalysts. J Electrochem Soc 150:A1017–A1024. doi:doi.org/10.1149/1.1583714
54. Liang Y, Zhang H, Zhong H, Zhou X, Tian Z, Xu D, Yi B (2006) Preparation and characterization of carbon-supported PtRuIr catalyst with excellent CO-tolerant performance for proton-exchange membrane fuel cells. J Catal 238:468–476. doi:10.1016/j.jcat.2006.01.005
55. Liang Y, Zhang H, Tian Z, Zhu X, Wang X, Yi B (2006) Synthesis and structure-activity relationship exploration of carbon-supported PtRuNi nanocomposite as a CO-tolerant electrocatalyst for proton exchange membrane fuel cells. J Phys Chem B 110:7828–7834. doi:10.1021/jp0602732
56. Bohm H, Pohl FA (1968) Wiss. Ber, AEG-Telefunken, (Allg. Elektricitaets-Ges)-Telefunken 41: 46
57. von Benda K, Binder H, Köhling A, Sandstede G (1972) Electrocatalysis to fuel cells. University of Washington Press, Seattle
58. von Benda SP (1975) Surface characterization of catalytically active tungsten carbide. J Catal 39:298–301. doi:10.1016/0021-9517(75)90335-8
59. Ross PN, Stonehart P (1977) The relation of surface structure to the electrocatalytic activity of tungsten carbide. J Catal 48:42–59. doi:10.1016/0021-9517(77)90076-8
60. Christian JB, Mendenhall RG (2003) Tungsten containing fuel cell catalyst and method of making them. US Patent 6,656,870
61. Christian JB, Mendenhall RG (2006) Tungsten containing fuel cell catalyst and method of making them. US Patent 7,060,648
62. McIntyre DR, Burstein GT, Vossen A (2002) Effect of carbon monoxide on the electrooxidation of hydrogen by tungsten carbide. J Power Sources 107:67–73. doi:10.1016/S0378-7753(01)00987-9
63. Izhar S, Nagai M (2008) Cobalt molybdenum carbides as anode electrocatalyst for proton exchange membrane fuel cell. J Power Sources 182:52–60. doi:10.1016/j.jpowsour.2008.03.084
64. Nagai M, Yoshida M, Tominaga H (2007) Tungsten and nickel tungsten carbides as anode electrocatalysts. Electrochim Acta 52:5430–5436. doi:10.1016/j.electacta.2007.02.065
65. Izhar S, Yoshida M, Nagai M (2009) Characterization and performances of cobalt-tungsten and molybdenum–tungsten carbides as anode catalyst for PEFC. Electrochim Acta 54:1255–1262. doi:10.1016/j.electacta.2008.08.049
66. Tasik GS, Miljanic SS, Kaninski MPM, Saponjic DP, Nikolic VL (2009) Non-noble metal catalyst for a future Pt free PEMFC. Electrochem Commun 11:2097–2100. doi:10.1016/j.elecom.2009.09.003
67. Li B, Qiao J, Zheng J, Yang D, Ma J (2009) Carbon-supported Ir-V nanoparticle as novel platinum-free anodic catalysts in proton exchange membrane fuel cell. Int J Hydrogen Energy 34:5144–5151. doi:10.1016/j.ijhydene.2009.04.013
68. Wang B (2005) Recent development of non-platinum catalysts for oxygen reduction reaction. J Power Sources 152:1–15. doi:10.1016/j.jpowsour.2005.05.098
69. Norskov JK, Rossmeisl J, Logadottir A, Lindqvist L, Kitchin JR, Bligaard T, Jonsson H (2004) Origin of the overpotential for oxygen reduction at a fuel-cell cathode. J Phys Chem B 108:17886–17892. doi:10.1021/jp047349j
70. Gewirth AA, Thorum MS (2010) Electroreduction of dioxygen for fuel-cell applications: materials and challenges. Inorg Chem 49:3557–3566. doi:10.1021/ic9022486
71. Masel RI (1995) Principles of adsorption and reaction on solid surfaces. Wiley, New York
72. Gasteiger HA, Kocha SS, Sompalli B, Wagner FT (2005) Activity benchmarks and requirements for Pt, Pt-alloy, and non-Pt oxygen reduction catalysts for PEMFCs. Appl Catal B 56:9–35. doi:10.1016/j.apcatb.2004.06.021

73. Peng Z, Yang H (2009) Designer platinum nanoparticles: control of shape, composition in alloy, nanostructure and electrocatalytic property. Nano Today 4:143–164. doi:10.1016/j.nantod.2008.10.010
74. Chen JY, Lim B, Lee EP, Xia YN (2009) Shape-controlled synthesis of platinum nanocrystals for catalytic and electrocatalytic applications. Nano Today 4:81–95. doi:10.1016/j.nantod.2008.09.002
75. Zhang CJ, Luo J, Njoki PN, Mott D, Wanjala B, Loukrakpam R, Lim S, Wang L, Fang B, Xu ZC (2008) Fuel cell technology: nano-engineered multimetallic catalysts. Energy Environ Sci 1:454–466. doi:10.1039/B810734N
76. Mukerjee S, Srinivasan S (1993) Enhanced electrocatalysis of oxygen reduction on platinum alloys in proton exchange membrane fuel cells. J Electroanal Chem 357:201–224. doi:10.1016/0022-0728(93)80380-Z
77. Toda T, Igarashi H, Uchida H, Watanabe M (1999) Enhancement of the electroreduction of oxygen on Pt alloys with Fe, Ni, and Co. J Electrochem Soc 146:3750–3756. doi:doi.org/10.1149/1.1392544
78. Colon-Mercado HR, Kim H, Popov BN (2004) Durability study of Pt_3Ni_1 catalysts as cathode in PEM fuel cells. Electrochem Commun 6:795–799. doi:10.1016/j.elecom.2004.05.028
79. Wei Z, Guo H, Tang Z (1996) Heat treatment of carbon-based powders carrying platinum alloy catalysts for oxygen reduction: influence on corrosion resistance and particle size. J Power Sources 62:233–236. doi:10.1016/S0378-7753(96)02425-1
80. Salgado JRC, Antolini E, Gonzalez ER (2004) Structure and activity of carbon-supported Pt-Co electrocatalysts for oxygen reduction. J Phys Chem B 108:17767–17774. doi:10.1021/jp0486649
81. Colon-Mercado HR, Popov BN (2006) Stability of platinum based alloy cathode catalysts in PEM fuel cells. J Power Sources 155:253–263. doi:10.1016/j.jpowsour.2005.05.011
82. Yu P, Pemberton M, Plasse P (2005) PtCo/C cathode catalyst for improved durability in PEMFCs. J Power Sources 144:11–20. doi:10.1016/j.jpowsour.2004.11.067
83. Bonakdarpour A, Wenzel J, Stevens DA, Sheng S, Monchesky TI, Lobel R, Atanasoski RT, Schmoeckel AK, Vernstrom GD, Debe MK, Dahn JR (2005) Studies of transition metal dissolution from combinatorially sputtered, nanostructured $Pt_{1-x}M_x$ ($M = Fe, Ni$; $0 < x < 1$) electrocatalysts for PEM fuel cells. J Electrochem Soc 152:A61–A72. doi:doi.org/10.1149/1.1828971
84. Protsailo L, Haug A (2005) Electrochemical society meeting abstracts, 208th ECS Meeting, Los Angeles, CA
85. Thompsett D (2003) In: Vielstich W, Gasteiger H, Lamm A (eds) Handbook of fuel cells—fundamentals, technology and applications vol. 3, Wiley, Chichester, UK
86. Ralph TR, Keating JE, Collis NJ, Hyde TI (1997) ETSU Contract Report F/02/00038
87. Xiong L, Manthiram A (2005) Effect of atomic ordering on the catalytic activity of carbon supported PtM (M = Fe, Co, Ni, and Cu) alloys for oxygen reduction in PEMFCs. J Electrochem Soc 152:A697–A703. doi:doi.org/10.1149/1.1862256
88. Yang H, Vogel W, Lamy C, Alonso-Vante N (2004) Structure and electrocatalytic activity of carbon-supported Pt−Ni alloy nanoparticles toward the oxygen reduction reaction. J Phys Chem B 108:11024–11034. doi:10.1021/jp049034+
89. Paulus UA, Wokaun A, Scherer GG, Schmidt TJ, Stamenkovic V, Markovic NM, Ross PN (2002) Oxygen reduction on carbon-supported Pt−Ni and Pt−Co alloy catalysts. J Phys Chem B 106:4181–4191. doi:10.1021/jp013442l
90. Xie J, Wood DL, Wayne DM, Zawodzinski TA, Atanassov P, Borup RL (2005) Durability of PEFCs at high humidity conditions. J Electrochem Soc 152:A104–A113. doi:doi.org/10.1149/1.1830355
91. Lim B, Jiang MJ, Camargo PHC, Cho EC, Tao J, Lu XM, Zhu YM, Xia YA (2009) Pd–Pt bimetallic nanodendrites with high activity for oxygen reduction. Science 324:1302–1305. doi:10.1126/science.1170377

92. Peng ZM, Yang H (2009) Synthesis and oxygen reduction electrocatalytic property of Pt-on-Pd bimetallic heteronanostructures. J Am Chem Soc 131:7542–7543. doi:10.1021/ja902256a
93. Zhang J, Sasaki K, Sutter E, Adzic RR (2007) Stabilization of platinum oxygen-reduction electrocatalysts using gold clusters. Science 315:220–222. doi:10.1126/science.1134569
94. Stamenkovic VR, Flower B, Mun BS, Wang GF, Ross PN, Lucas CA, Markovic NM (2007) Improved oxygen reduction activity on $Pt_3Ni(111)$ via increased surface site availability. Science 315:493–497. doi:10.1126/science.1135941
95. Stamenkovic VR, Mun BS, Arenz M, Mayrhofer KJJ, Lucas CA, Wang G, Ross PN, Markovic NM (2007) Trends in electrocatalysis on extended and nanoscale Pt-bimetallic alloy surfaces. Nat Mater 6:241–247. doi:10.1038/nmat1840
96. Zhang JL, Vukmirovic MB, Xu Y, Mavrikakis M, Adzic RR (2005) Controlling the catalytic activity of platinum-monolayer electrocatalysts for oxygen reduction with different substrates. Angew Chem Int Ed 44:2132–2135. doi:10.1002/anie.200462335
97. Adzic R, Zhang J, Sasaki K, Vukmirovic M, Shao M, Wang J, Nilekar A, Mavrikakis M, Valero J, Uribe F (2007) Platinum monolayer fuel cell electrocatalysts. Top Catal 46:249–262. doi:10.1007/s11244-007-9003-x
98. Zhang J, Mo Y, Vukmirovic MB, Klie R, Sasaki K, Adzic RR (2004) Platinum monolayer electrocatalysts for O_2 Reduction: Pt monolayer on Pd(111) and on carbon-supported Pd nanoparticles. J Phys Chem B 108:10955–10964. doi:10.1021/jp0379953
99. Zhang J, Lima FHB, Shao MH, Sasaki K, Wang JX, Hanson J, Adzic RR (2005) Platinum monolayer on nonnoble metal-noble metal core-shell nanoparticle electrocatalysts for O_2 reduction. J Phys Chem B 109:22701–22704. doi:10.1021/jp055634c
100. Zhang J, Vukmirovic MB, Sasaki K, Nilekar AU, Mavrikakis M, Adzic RR (2005) Mixed-metal Pt monolayer electrocatalysts for enhanced oxygen reduction kinetics. J Am Chem Soc 127:12480–12481. doi:10.1021/ja053695i
101. Shao M, Sasaki K, Marinkovic NS, Zhang L, Adzic RR (2007) Synthesis and characterization of platinum monolayer oxygen-reduction electrocatalysts with Co–Pd core-shell nanoparticle supports. Electrochem Commun 9:2848–2853. doi:10.1016/j.elecom.2007.10.009
102. Srivastava R, Mani P, Hahn N, Strasser P (2007) Efficient oxygen reduction fuel cell electrocatalysis on voltammetrically dealloyed Pt–Cu–Co nanoparticles. Angew Chem Int Ed 46:8988–8991. doi:10.1002/anie.200703331
103. Ohno S, Yagyuu K, Nakatsuji K, Komori F (2004) Dissociation preference of oxygen molecules on an inhomogeneously strained Cu(0 0 1) surface. Surf Sci 554:183–192. doi:10.1016/j.susc.2004.01.063
104. Kammler Th, Küppers J (2001) The kinetics of the reaction of gaseous hydrogen atoms with oxygen on Cu(1 1 1) surfaces toward water. J Phys Chem B 105:8369–8374. doi:10.1021/jp0112222
105. Vellianitis DK, Kammler Th, Küppers J (2001) Interaction of gaseous hydrogen atoms with oxygen covered Cu(1 0 0) surfaces. Surf Sci 482–485:166–170. doi:10.1016/S0039-6028(01)00855-X
106. Mentus SV (2004) Oxygen reduction on anodically formed titanium dioxide. Electrochim Acta 50:27–32. doi:10.1016/j.electacta.2004.07.009
107. Limoges BR, Stanis RJ, Turner JA, Herring AM (2005) Electrocatalyst materials for fuel cells based on the polyoxometalates $[PMo_{(12-n)}V_nO_{40}]^{(3+n)-}$ ($n = 0$–3). Electrochim Acta 50:1169–1179. doi:10.1016/j.electacta.2004.08.014
108. Lee K, Ishihara A, Mitsushima S, Kamiya N, Ota K (2004) Stability and electrocatalytic activity for oxygen reduction in WC + Ta catalyst. Electrochim Acta 49:3479–3485. doi:10.1016/j.electacta.2004.03.018
109. Hayashi M, Uemura H, Shimanoe K, Miura N, Yamazoe N (2004) Reverse micelle assisted dispersion of lanthanum manganite on carbon support for oxygen reduction cathode. J Electrochem Soc 151:A158–A163. doi:doi.org/10.1149/1.1633266

110. Liu L, Lee JW, Popov BN (2006) Development of ruthenium-based bimetallic electrocatalysts for oxygen reduction reaction. J Power Sources 162:1099–1103. doi:10.1016/j.jpowsour.2006.08.003
111. Vante A, Tributsch H (1986) Energy conversion catalysis using semiconducting transition metal cluster compounds. Nature 323:431–432. doi:10.1038/323431a0
112. Alcantara KS, Castellanos AR, Dante R, Feria OS (2006) $Ru_xCr_ySe_z$ electrocatalyst for oxygen reduction in a polymer electrolyte membrane fuel cell. J Power Sources 157:114–120. doi:10.1016/j.jpowsour.2005.07.065
113. Hara Y, Minami N, Itagaki H (2008) Electrocatalytic properties of ruthenium modified with Te metal for the oxygen reduction reaction. Appl Catal A 340:59–66. doi:10.1016/j.apcata.2008.01.036
114. Alkantara KS, Feria OS (2008) Kinetics and PEMFC performance of $Ru_xMo_ySe_z$ nanoparticles as a cathode catalyst. Electrochim Acta 53:4981–4989. doi:10.1016/j.electacta.2008.02.025
115. Alkantara KS, Feria OS (2009) Comparative study of oxygen reduction reaction on $Ru_xM_ySe_z$ (M = Cr, Mo, W) electrocatalysts for polymer exchange membrane fuel cell. J Power Sources 192:165–169. doi:10.1016/j.jpowsour.2008.10.118
116. Shen MY, Chiao SP, Tsai DS, Wilkinson DP, Jiang JC (2009) Preparation and oxygen reduction activity of stable $RuSe_x$/C catalyst with pyrite structure. Electrochim Acta 54:4297–4304. doi:10.1016/j.electacta.2009.02.081
117. Chiao SP, Tsai DS, Wilkinson DP, Chen YM, Huang YS (2010) Carbon supported $Ru_{1-x}Fe_xSe_y$ electrocatalysts of pyrite structure for oxygen reduction reaction. Int J Hydrogen Energy 35:6508–6517. doi:10.1016/j.ijhydene.2010.04.032
118. Sánchez GR, Feria OS (2010) Int J Hydrogen Energy, #5, 12105
119. Lee K, Zhang L, Zhang J (2007) Ternary non-noble metal chalcogenide (W–Co–Se) as electrocatalyst for oxygen reduction reaction. Electrochem Commun 9:1704–1708. doi:10.1016/j.elecom.2007.03.025
120. Susac D, Sode A, Zhu L, Wong PC, Teo M, Bizzotto D, Mitchell KAR, Parsons RR, Campbell SA (2006) A methodology for investigating new nonprecious metal catalysts for PEM fuel cells. J Phys Chem B 110:10762–10770. doi:10.1021/jp057468e
121. Zhang L, Zhang J, Wilkinson DP, Wang H (2006) Progress in preparation of non-noble electrocatalysts for PEM fuel cell reactions. J Power Sources 156:171–182. doi:10.1016/j.jpowsour.2005.05.069
122. Bezerra CWB, Zhang L, Lee K, Liu H, Marques ALB, Marques EP, Wang H, Zhang J (2008) A review of Fe–N/C and Co–N/C catalysts for the oxygen reduction reaction. Electrochim Acta 53:4937–4951. doi:10.1016/j.electacta.2008.02.012
123. Beck F (1977) The redox mechanism of the chelate-catalysed oxygen cathode. J Appl Electrochem 7:239–245. doi:10.1007/BF00618991
124. Wiesener K (1989) N_4 macrocycles as electrocatalysts for the cathodic reduction of oxygen. Mater Chem Phys 22:457–475. doi:10.1016/0254-0584(89)90010-2
125. Alt H, Binder M, Sandstede G (1973) Mechanism of the electrocatalytic reduction of oxygen on metal chelates. J Catal 28:8–19. doi:10.1016/0021-9517(73)90173-5
126. Jiang R, Xu L, Jin R, Dong S (1985) Fenxi huaxue. Anal Chem 13:270
127. van Veen JAR, Colijn HA, van Baar JF (1988) On the effect of a heat treatment on the structure of carbon-supported metalloporphyrins and phthalocyanines. Electrochim Acta 33:801–804. doi:10.1016/S0013-4686(98)80010-8
128. Chu D, Jiang R (2002) Novel electrocatalysts for direct methanol fuel cells. Solid State Ionics 148:591–599. doi:10.1016/S0167-2738(02)00124-8
129. Liu H, Song C, Tang Y, Zhang J (2007) High-surface-area CoTMPP/C synthesized by ultrasonic spray pyrolysis for PEM fuel cell electrocatalysts. Electrochim Acta 52:4532–4538. doi:10.1016/j.electacta.2006.12.056

130. Gojkovic SL, Gupta S, Savinell RF (1998) Heat-treated iron(III) tetramethoxyphenyl porphyrin supported on high-area carbon as an electrocatalyst for oxygen reduction. J Electrochem Soc 145:3493–3499. doi:doi.org/10.1149/1.1838833
131. Jiang R, Chu D (2000) Remarkably active catalysts for the electroreduction of O_2 to H_2O for use in an acidic electrolyte containing concentrated methanol. J Electrochem Soc 147:4605–4609. doi:doi.org/10.1149/1.1394109
132. Bron M, Fiechter S, Hilgendorff M, Bogdanoff P (2002) Catalysts for oxygen reduction from heat-treated carbon-supported iron phenanthroline complexes. J Appl Electrochem 32:211–216. doi:10.1023/A:1014753613345
133. Schulenburg H, Stankov S, Schünemann V, Radnik J, Dorbandt I, Fiechter S, Bogdanoff P, Tributsch H (2003) Catalysts for the oxygen reduction from heat-treated Iron(III) tetramethoxyphenylporphyrin chloride: structure and stability of active sites. J Phys Chem B 107:9034–9041. doi:10.1021/jp030349j
134. Ye S, Vijh AK (2003) Non-noble metal-carbonized aerogel composites as electrocatalysts for the oxygen reduction reaction. Electrochem Commun 5:272–275. doi:10.1016/S1388-2481(03)00043-2
135. Ye S, Vijh AK (2005) Cobalt-carbonized aerogel nanocomposites electrocatalysts for the oxygen reduction reaction. Int J Hydrogen Energy 30:1011–1015. doi:10.1016/j.ijhydene.2005.01.004
136. Matter PH, Zhang L, Ozkan US (2006) The role of nanostructure in nitrogen-containing carbon catalysts for the oxygen reduction reaction. J Catal 239:83–96. doi:10.1016/j.jcat.2006.01.022
137. Ma ZF, Xie XY, Ma XX, Zhang DY, Ren Q, Mohr NH, Schimidt VM (2006) A review of heat-treatment effects on activity and stability of PEM fuel cell catalysts for oxygen reduction reaction. Electrochem Commun 8:389–394. doi:10.1016/j.jpowsour.2007.08.028
138. Faubert G, Lalande G, Cote R, Guay D, Dodelet DP, Weng LT, Bertrand P, Dénès G (1996) Heat-treated iron and cobalt tetraphenylporphyrins adsorbed on carbon black: physical characterization and catalytic properties of these materials for the reduction of oxygen in polymer electrolyte fuel cells. Electrochim Acta 41:1689–1701. doi:10.1016/0013-4686(95)00423-8
139. Fournier J, Lalande G, Cote R, Guay D, Dodelet JP (1997) Activation of various Fe-based precursors on carbon black and graphite supports to obtain catalysts for the reduction of oxygen in fuel cells. J Electrochem Soc 144:218–226. doi:doi.org/10.1149/1.1837388
140. Faubert G, Cote R, Guay D, Dodelet JP, Denes G, Poleunis C, Bertrand P (1998) Activation and characterization of Fe-based catalysts for the reduction of oxygen in polymer electrolyte fuel cells. Electrochim Acta 43:1969–1984. doi:10.1016/S0013-4686(97)10120-7
141. Cote R, Lalande G, Faubert G, Guay D, Dodelet JP, Denes G (1998) Influence of nitrogen-containing precursors on the electrocatalytic activity of heat-treated $Fe(OH)_2$ on carbon black for O_2 reduction. J Electrochem Soc 145:2411–2418. doi:doi.org/10.1149/1.1838651
142. Faubert G, Cote R, Guay D, Dodelet JP, Denes G, Bertrand P (1998) Iron catalysts prepared by high-temperature pyrolysis of tetraphenylporphyrins adsorbed on carbon black for oxygen reduction in polymer electrolyte fuel cells. Electrochim Acta 43:341–353. doi:10.1016/S0013-4686(97)00087-X
143. Faubert G, Cote R, Dodelet JP, Lefevre M, Bertrand P (1999) Oxygen reduction catalysts for polymer electrolyte fuel cells from the pyrolysis of Fe^{II} acetate adsorbed on 3,4,9,10-perylenetetracarboxylic dianhydride. Electrochim Acta 44:2589–2603. doi:10.1016/S0013-4686(98)00382-X
144. Lefevre M, Dodelet JP, Bertrand J (2000) O_2 reduction in PEM fuel cells: activity and active site structural information for catalysts obtained by the pyrolysis at high temperature of Fe precursors. J Phys Chem B 104:11238–11247. doi:10.1021/jp002444n
145. Lefèvre M, Dodelet JP, Bertrand P (2002) Molecular oxygen reduction in PEM fuel cells: evidence for the simultaneous presence of two active sites in Fe-based catalysts. J Phys Chem B 106:8705–8713. doi:10.1021/jp020267f

146. Medard C, Lefevre M, Dodelet JP, Jaouen F, Lindbergh G (2006) Oxygen reduction by Fe-based catalysts in PEM fuel cell conditions: activity and selectivity of the catalysts obtained with two Fe precursors and various carbon supports. Electrochim Acta 51:3202–3213. doi:10.1016/j.electacta.2005.09.012
147. Jaouen F, Charraterour F, Dodelet JP (2006) Fe-based catalysts for oxygen reduction in PEMFCS. J Electrochem Soc 153:A689–A698. doi:doi.org/10.1149/1.2168418
148. Villers D, Jacques-Bedard X, Dodelet JP (2004) Fe-based catalysts for oxygen reduction in PEM fuel cells. J Electrochem Soc 151:A1507–A1515. doi:doi.org/10.1149/1.1781611
149. Jaouen F, Marcotte S, Dodelet JP, Lindbergh G (2003) Oxygen reduction catalysts for polymer electrolyte fuel cells from the pyrolysis of iron acetate adsorbed on various carbon supports. J Phys Chem B 107:1376–1386. doi:10.1021/jp021634q
150. Lefevre M, Dodelet JP, Bertrand P (2005) Molecular oxygen reduction in PEM fuel cell conditions: ToF-SIMS analysis of Co-based electrocatalysts. J Phys Chem B 109:16718–16724. doi:10.1021/jp0529265
151. Wang H, Cote R, Faubert G, Guay D, Dodelet JP (1999) Effect of the pre-treatment of carbon black supports on the activity of Fe-based electrocatalysts for the reduction of oxygen. J Phys Chem B 103:2042–2049. doi:10.1021/jp9821735
152. Zhao F, Harnisch F, Schroder W, Scholz F, Bogdanoff P, Herrmann I (2005) Application of pyrolysed iron(II) phthalocyanine and CoTMPP based oxygen reduction catalysts as cathode materials in microbial fuel cells. Electrochem Commun 7:1405–1410. doi:10.1016/j.elecom.2005.09.032
153. Fraga MA, Jordao E, Mendes MJ, Freita MMA, Faria JL, Figueredo JL (2002) Properties of carbon-supported platinum catalysts: role of carbon surface sites. J Catal 209:355–364. doi:10.1006/jcat.2002.3637
154. Uchida M, Aoyama Y, Tanabe M, Yanagihara N, Eda N, Ohta A (1995) Influences of both carbon supports and heat-treatment of supported catalyst on electrochemical oxidation of methanol. J Electrochem Soc 142:2572–2576. doi:doi.org/10.1149/1.2050055
155. McBreen J, Olender H, Srinivasan S, Kordesch K (1981) Carbon supports for phosphoric acid fuel cell electrocatalysts: alternative materials and methods of evaluation. J Appl Electrochem 11:787–796. doi:10.1007/BF00615184
156. Antolini E (2009) Polymer supports for low-temperature fuel cell catalysts. Appl Catal B 88:1–19. doi:10.1016/j.apcata.2009.05.045
157. Yoo E, Okada T, Kizuka T, Nakamura J (2008) Effect of carbon substrate materials as a Pt–Ru catalyst support on the performance of direct methanol fuel cells. J Power Sources 180:221–226. doi:10.1016/j.jpowsour.2008.01.065
158. Antolini E, Gonzalez ER (2009) Ceramic materials as supports for low-temperature fuel cell catalysts. Solid State Ionics 180:746–763. doi:10.1016/j.ssi.2009.03.007
159. Zhang S, Zhu H, Yu H, Hou J, Yi B, Ming P (2007) The oxidation resistance of tungsten carbide as catalyst support for proton exchange membrane fuel cells. Chin J Catal 28:109–111. doi:10.1016/S1872-2067(07)60014-X
160. Chhina H, Campbell S, Kesler O (2007) Thermal and electrochemical stability of tungsten carbide catalyst supports. J Power Sources 164:431–440. doi:10.1016/j.jpowsour.2006.11.003
161. Chhina H, Campbell S, Kesler O (2008) High surface area synthesis, electrochemical activity, and stability of tungsten carbide supported Pt during oxygen reduction in proton exchange membrane fuel cells. J Power Sources 179:50–59. doi:10.1016/j.jpowsour.2007.12.105
162. Antolini E, Gonzalez ER (2009) Polymer supports for low-temperature fuel cell catalysts. Appl Catal B 365:1–19. doi:10.1016/j.apcata.2009.05.045
163. Feng Y, Alonso-Vante N (2008) Nonprecious metal catalysts for the molecular oxygen-reduction reaction. Phys Status Solidi B 245:1792–1806. doi:doi. 10.1002/pssb.200879537
164. Viswanathan B (2009) In: Kaneco S, Viswanathan B, Katsumata H (eds) Photo/electrochemistry and photobiology in the environment, energy and fuel, Research signpost, pp 1–14
165. http://www.evworld.com/news.cfm?newsid=888

Chapter 10
Catalysis for Direct Methanol Fuel Cells

C. Bock, B. MacDougall, and C.-L. Sun

Abstract The direct methanol fuel cell (DMFC) is a particular case of a low-temperature proton exchange membrane (PEM) fuel cell (FC). A DMFC utilizes CH_3OH as anode fuel and O_2 as cathode fuel. Depending on the application, a DMFC is typically operated in the range of 40–80°C. DMFCs are very attractive due to the high energy density of CH_3OH, thus making them lightweight devices. In fact, DMFCs can have 15 times the energy density of a Li-ion battery. Other advantages are that DMFCs can be refueled on the fly within seconds, and CH_3OH is an inexpensive and readily available fuel. Furthermore, CH_3OH is a liquid, thus facilitating its distribution, and it can be taken on airplanes in designated cartridges. The impact of the eventual successful commercialization of DMFCs is estimated to be large and expands into the microelectronics industry. However, significant obstacles need to be overcome before DMFCs can be truly considered to be a viable technology. Some of these challenges are related to the anode catalyst such as lowering the cost of the catalyst used by lowering the amount of the noble metal component, as well as extending the lifetime of both the anode and cathode catalysts.

A number of reviews describing the technical aspects of DMFCs as an entire device are available (Scott et al. J Power Sources 79:43–59, 1999; Lamm and Müller System design for transport applications. In: Vielstich et al. (ed) Handbook of fuel cells fundamentals technology and applications, Wiley, New York, 2003; Narayanan et al. DMFC system design for portable applications. In: Vielstich et al. (ed) Handbook of fuel cells fundamentals technology and applications, Wiley, New York, 2003; Gottesfeld Design concepts and durability challenges for mini fuel

C. Bock (✉) • B. MacDougall
Institute for Chemical Processes and Environmental Technologies,
National Research Council of Canada, Montreal Road, Ottawa, ON, Canada K1A 0R6,
e-mail: Christina.Bock@nrc-cnrc.gc.ca

C.-L. Sun
Department of Chemical and Materials Engineering, Chang Gung University,
Taoyuan 333, Taiwan

L. Guczi and A. Erdőhelyi (eds.), *Catalysis for Alternative Energy Generation*,
DOI 10.1007/978-1-4614-0344-9_10,

cells. In: Vielstich et al. (ed) Handbook of fuel cells fundamentals technology and applications, Wiley, New York, 2009). Therefore, these aspects are not covered in this chapter, which instead focuses on the catalysis aspects of the electrochemical CH_3OH oxidation reaction. However, cross-references to proton electrolyte fuel cells (PEMFCs) and related reactions are given where appropriate.

10.1 Brief History of the Development and Applications of Fuel Cells

The discovery of fuel cells (FCs) dates back to the late 1830s. In 1839, the work of Christian Friedrich Schoenbein was published that reported an experiment describing the so-called fuel cell effect [5]. He filled tubes immersed in dilute sulfuric acid with H_2 and O_2 gases and using Pt foil electrodes reported the H_2/O_2 voltage difference and the fact that a current is measured. Schoenbein's work focused on the fundamentals of the electrochemical reactions. However, he did suggest that the combination of the H_2 and O_2 reactions could potentially be useful to generate electricity. His work was published just 1 month before Sir Walter Grove's report entitled the "On Voltaic Series and the Combination of Gases by Platinum" [6]. Sir Walter Grove continued this work and was the first to demonstrate actual working devices in the 1840s [7]. The first studies of these "low"-temperature FC devices utilized bulk metal Pt foils as electrodes. It was quickly recognized that the use of these smooth and low-surface area electrodes did not provide sufficiently high interfacial areas for the reactions, and hence, the devices did neither produce high currents nor high power densities. Therefore, Grove explored the use of platinized Pt, i.e., higher-surface area catalyst electrodes. This resulted in distinct improvements; however, the pores of the electrodes were filled with electrolyte, thus limiting the access of the reactant gases to the catalyst sites. It was eventually recognized that the optimization of the so-called triple zone, which consists of the gas, liquid, and solid phase, is needed for FC optimization. Experiments were conducted using a hydrophobic phase to improve "triple zone" characteristics [8]. Furthermore, dispersed Pt catalysts and porous electrodes were used to achieve higher catalyst surface areas [8, 9]. The now widespread use of nanosized Pt catalysts that are deposited onto high-surface area supports, i.e., Pt/C catalysts, followed some years later [10].

The utilization of other anode fuels than H_2 attracted attention shortly after Schoenbein's and Walter Grove's reports. Up to now, fuels capable of supplying hydrogen like ammonia, various alcohols, and hydrocarbons have been explored. Alkaline as well as acidic electrolyte media have been considered, although the latter appears more attractive as it offers fewer disadvantages. The many decades of research on FCs has led to the conclusion that proton electrolyte fuel cells (PEMFCs) are potentially suitable for transportation and stationary applications. PEMFCs run on H_2 and O_2 as anode and cathode fuels, respectively, and use a proton-conductive polymer as anode and cathode separator. These systems are typically in the larger than 10 kW range. The direct methanol fuel cell (DMFC) has been recognized as an

interesting system for a long period of time. However, it is now recognized that DMFCs are more suitable for the lower power generation range ($\ll$10 kW) [11]. Also the use of DMFCs with batteries, e.g., for scooter applications, appears attractive as the combined operation of a DMFC and a battery significantly (7–10 times) increases the operation range of the system. DMFCs are also of interest for electronic devices such as cell phones. Again, DMFCs are attractive for this type of application due to their high charge density. In a DMFC, the CH_3OH serves as the hydrogen source and is directly fed into the anode compartment and converted into electricity. Direct feed of the CH_3OH fuel saves on weight and system design, as an external reformer for CH_3OH to H_2 is not needed. It should be noted that the electrochemical CH_3OH oxidation reaction is much more sluggish than the very rapid H_2 electrooxidation reaction. This requires that larger amounts of the expensive Pt-based catalysts are used for DMFCs than for PEMFCs (provided that the latter are operated with neat H_2). The slower CH_3OH than H_2 oxidation kinetics results in lower currents, and hence, lower power outputs of a DMFC vs. a PEMFC. Based on these facts, it is generally recognized that DMFCs are not suitable for high power applications such as, e.g., needed in the automotive industry. Nevertheless, DMFCs are of high technological interest due to many attractive properties CH_3OH offers as a fuel. These are, for example, the high power storage density of CH_3OH, the fact that CH_3OH is a liquid, it is readily available, and a DMFC can be refueled on the fly. Despite the fact that the working principles of FCs are now relatively well known, many challenges still need to be overcome to make PEMFCs and DMFCs economically viable. However, this type of FCs offer many positive aspects as power generating devices such as their high power densities, ease of use in remote areas, and extended range of operation.

In this chapter, the aspects of electrocatalysis of the CH_3OH oxidation reaction for DMFCs are discussed. Many research and review articles have been published covering various aspects of FCs. This chapter focuses on the electrocatalysis of the CH_3OH oxidation reaction and related reactions. It expands into the topic of high-surface area and three-dimensional electrode processes.

10.2 Introduction: Direct Methanol Fuel Cells

10.2.1 Basics of DMFCs: Choice of Media and Fuels

In a DMFC, CH_3OH is oxidized to CO_2 and O_2 is reduced. Either air or pure O_2 can be used as source of fuel for the O_2 reduction reaction (ORR). This is shown in the reaction scheme in (10.1–10.3). It should be noted that (10.1–10.3) show an overall reaction scheme and not a detailed mechanism, which will be discussed later. The oxidation of CH_3OH takes place at the anode (10.1), while the reduction of O_2 takes place at the cathode (10.2):

$$CH_3OH + H_2O = CO_2 + 6H^+ + 6e^-. \quad (10.1)$$

$$3O_2 + 6H^+ + 6e^- = 3H_2O. \quad (10.2)$$

Net:

$$CH_3OH + 3O_2 = CO_2 + 3H_2O. \quad (10.3)$$

The details of the CH_3OH oxidation, as well the ORR, have attracted a lot of attention over many decades of research. Improvements made in regard to catalyst utilization in the electrode structure of an actual cell, as well as improvements in the activities of both the anode and the cathode catalysts, will enhance the performance of a DMFC. However, it should be noted that for the case of a DMFC, where CH_3OH rather than neat H_2 is used as fuel, major improvements on the anode side are needed. Of course, other improvements in the system such as better ORR catalysts and electrodes, better water management, and lower CH_3OH crossover will also improve the performance of a DMFC. However, it is essential to improve the anode catalysts in terms of catalytic activity and to improve their stability, i.e., protect them against dissolution during operation of a device. For practical DMFC applications, an acidic environment is generally preferred in order to achieve the complete oxidation of CH_3OH to CO_2 (see Sect. 11.5.1.1). Furthermore, system problems that result from carbonate formation in alkaline media are avoided using acidic environments, and more stable anode–cathode separators (membranes) are available for acid-based FCs. Therefore, the reactions discussed in this chapter are in general for acid-based systems, unless otherwise noted. It is, however, noteworthy that alkaline FC systems, which utilize, e.g., NH_3, ethanol, ethylene glycol, or methanol as anode fuel, have attracted a lot of attention. Also, alkaline systems may be of interest for, e.g., power generation in space, where the formation of carbonate is not an issue. They are also appealing based on the fact that both the anode and cathode reactions are more rapid in alkaline than in acidic environments. This allows for the reduction, or even avoids (in the case of the ORR), the use of expensive noble metal catalysts. It is very important to note that the use of Pt-based catalysts is essential for acidic "low" temperature FC applications in order to achieve the required high power output. Furthermore, if carbon-based anode fuels are used, it is essential to ensure the complete oxidation of the fuel to CO_2. Complete oxidation to CO_2 avoids not only catalyst coking problems but also the production of other undesired and frequently toxic side products [12, 13].

Figure 10.1 shows a schematic explaining the principles of a DMFC. These basic principles apply to FCs in general. The main difference between a DMFC and a PEMFC is that H_2 rather than CH_3OH is used as anode fuel for the latter. The schematic in Fig. 10.1 shows the heart of an FC that consists of the anode, the cathode, and the proton-conductive membrane. The latter is also the anode and cathode separator and must be electronically nonconductive in order to not short the two electrodes. Protons are formed at the anode as shown in (10.1) and are transported to the cathode, where they react to form H_2O, with the O^{2-} formed by reducing O_2, as summarized in (10.2). This closes the electrical circuit and

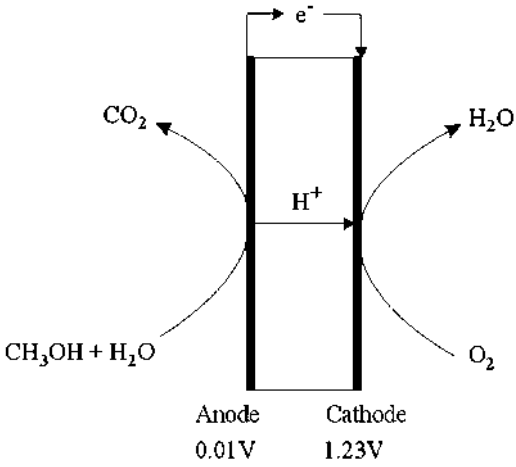

Fig. 10.1 Schematic demonstrating the principles of a DMFC

fulfills the conditions of electroneutrality. The transport of the protons across the membrane from the anode to the cathode can take place by the usual means of counterion transport, which is induced by concentration gradients, i.e., diffusion as well as ohmic migration (the latter being dominating in an FC [14, 15]). Furthermore, the protons are hydrated, and water is dragged from the anode to the cathode, which is not depicted in the schematic in Fig. 10.1.

It is clear that the membrane must be a proton conductor. Furthermore, the anode and cathode catalyst layers are generally relatively thick, in the several-μm range, and a proton-conductive phase is also needed in the catalyst layers. Another FC schematic demonstrating the more detailed making of the membrane electrode assembly (MEA) and electrode structures is shown in Fig. 10.2. Much research has been devoted to the development of proton-conductive, low-CH_3OH crossover, inexpensive, and stable membranes that also show low crossover to CH_3OH [16]. Crossover of CH_3OH from the anode to the cathode is not desired as CH_3OH anode fuel is lost, and the CH_3OH fuel is oxidized at the cathode, which results in a lower cathode potential, and hence lower DMFC performance. The membrane must be "compatible" with the catalyst layer, to the extent that one must be able to form a stable MEA by hot pressing in a straightforward manner and to also not swell during operation. The latter could lead to cracking of the catalyst layer and result in subsequent delamination between the catalyst layer and membrane. Most commonly Nafion is used as a membrane as well as H^+ conductor in the catalyst layers. Nafion suffers the disadvantage of high CH_3OH crossover when used as membrane, while the high CH_3OH permeability turns out to be an advantage in the anode catalyst layer. Access of the CH_3OH fuel to the catalyst sites is not hindered by the presence of Nafion in the anode catalyst layer, as a thin layer of Nafion allows for the permeation of CH_3OH. Despite the crossover issues, Nafion is currently still the membrane of choice for DMFCs. It seems that issues such as the manufacturing of the MEAs and their stability during operation present somewhat of a challenge if non-Nafion membranes are used. It should also be noted that crossover of CH_3OH is

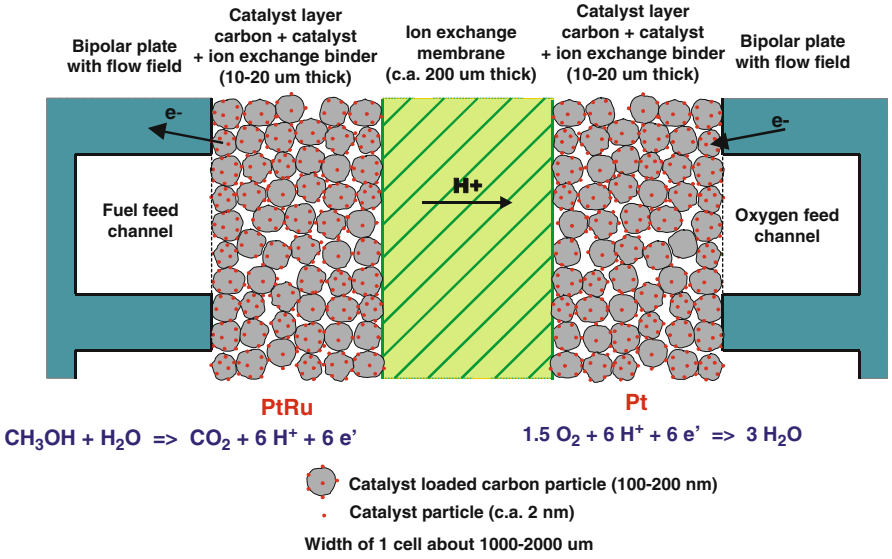

Fig. 10.2 Schematic showing the making of the heart of a fuel cell and the membrane electrode assembly (MEA)

not always considered as negative. Based on DMFC field studies, it was suggested that the problem of CH_3OH crossover is academic and that it can be counteracted by oversizing the FC [11]. Furthermore, the following three beneficial factors were listed as a benefit in operating DMFC systems [11]. Crossover of CH_3OH is suggested to be a way to deal with water management problems in dry conditions. It is beneficial during start-up conditions, as the CH_3OH electrooxidation is exothermic and apparently the heat release is the most efficient way to increase the stack temperature. Furthermore, methanol diffusion within the MEA results in a distribution of antifreeze substances that are probably used in a real system to allow for the use of DMFCs in lower temperature environments.

Figure 10.2 shows the assembly of a single cell of an FC. A practical device consists of an FC stack, i.e., of several of these single units connected together.

10.2.2 Introduction to Reaction Rates and the Nature of the Catalysts for Low-Temperature DMFCs

The oxidation rate of methanol increases with increasing temperature according to the Arrhenius relationship, as follows:

$$k = A \times \exp^{(-E_a/RT)}. \tag{10.4}$$

In (10.4), k is a rate coefficient, A a constant, E_a the activation energy (kJ mole^{-1}), R the universal gas constant (8.314 $\times$ 10^{-3} kJ mol^{-1} K^{-1}), and T the temperature (in Kelvin). Equation (10.4) suggests that the reaction rate increases, and accordingly, the performance of a DMFC increases when the cell is operated at higher Ts. As a rule of thumb, the reaction rate of a simple reaction doubles with a temperature increase of 10°C. The electrochemical CH_3OH oxidation reaction is a multistep reaction involving adsorption and diffusion of reactant and intermediates on the catalyst surface. Therefore, a simple relationship like doubling of the CH_3OH reaction rate per 10°C raise in temperature is not observed. Nevertheless, an increase in the CH_3OH reaction rate with temperature is observed [17, 18]. For example, a change from 60 to 80°C results in a ca. 2 times increase in the CH_3OH oxidation current in a DMFC at an anode potential of 0.5 V vs. the reversible hydrogen electrode (RHE) [17]. Obviously, this is less than two times increase predicted per 10°C increase.

It should be noted that the typical operating range for DMFCs is between 40 and 80°C, and liquid feed of CH_3OH vs. vapor feed seems to be preferable [18, 19]. Higher DMFC performances can be achieved at higher temperatures and using vapor feed [1]. However, the vaporization process consumes energy and adds complication to the system. It is also essential to separate unused CH_3OH fuel from the gaseous CO_2 product if vapor feed CH_3OH is used. For such "low"-temperature FC applications, catalysts containing Pt metal are needed. Pt is unique and has the capability of abstracting the H-atoms from the carbon of the $–CH_3$ group of CH_3OH. This results in the formation of a –CO-type species adsorbed ($–CO_{ads}$) on the catalyst surface. This species can further be oxidized to CO_2 with the assistance of an oxygen atom donated from H_2O. The identification of the intermediate species and the products of the CH_3OH electrooxidation reaction has been the subject of numerous studies [20–32]. The exact details of the CH_3OH oxidation reaction are still the subject of much discussion. However, it can be said that the general mechanism of the CH_3OH electrooxidation reaction has now been accepted. The general mechanism applies to both Pt-only and bimetallic Pt-based catalysts, although the exact pathways and product yields frequently depend on the catalyst. The yields and reaction products of the CH_3OH oxidation reaction may depend not only on the crystal and chemical structure of the electrodes but also on the roughness factor of the Pt-based electrodes. Studies for Pt-only electrodes have already been carried out decades ago and have shown that the yield for the CO_2 production is much higher for anode catalysts of increased surface roughness than for smooth Pt electrodes [33]. The established views about the influence of the electrode roughness and structure on the CH_3OH oxidation reaction are discussed in separate Sects. 10.4.1.2 and 10.5.4.1 These parameters appear to be of relevance for the CH_3OH oxidation reaction pathway on Pt-only electrodes.

Due to the high cost of Pt and other possible noble metal components of the catalysts such as ruthenium, the Pt-based catalysts are typically dispersed onto high-surface area supports [34–39]. To date, high-surface area carbons are typically used as they are electronically conductive and also offer the advantage of being inexpensive. It should, however, be noted that there are several issues using carbon

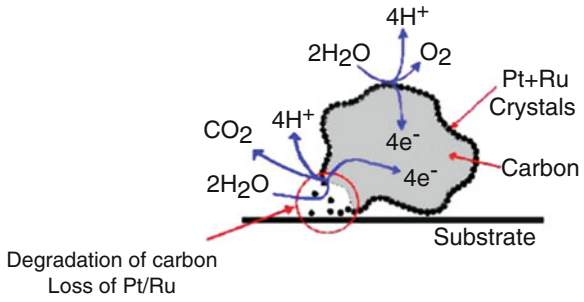

Fig. 10.3 Schematic demonstrating the oxidation of carbon to CO_2 possibly taking place under fuel starving conditions in the anode layer of a DMFC. Reprinted from [40] with permission from Elsevier

as a support, such as its stability to corrosion. This, of course, is a very pronounced issue for the cathode, as the cathode in an FC experiences positive polarizations and an oxidative environment, namely the presence of O_2. Nevertheless, carbon corrosion can also be an issue for the anode. It is known that parts of the anode can experience fuel starving conditions. Fuel starving conditions can drive parts of the anode to evolve O_2, which then also results in very positive local anode potentials that can favor the corrosion of carbon and its oxidation to, e.g., CO_2 [40]. This is demonstrated in the schematic shown in Fig. 10.3. Therefore, non-carbon-based catalyst support materials have been sought for many years [37, 41]. However, nanosized catalysts on high-surface area carbon blacks are still the most commonly used catalysts. Over the past decades, significant efforts have also been devoted to develop improved catalyst structures such as Pt alloys (see [42–58] for examples). This is done with the goal to establish better catalytic activities. In the case of DMFC anodes, so-called bimetallic Pt-based catalysts are utilized. The usefulness of bimetallic Pt-based catalysts dates back to the 1960s when reports of adding another metal to Pt, most effectively Ru, showed that the onset potential of the CH_3OH oxidation reaction can be substantially lowered. The so-called bimetallic Pt-based catalysts are needed to achieve a lower anode overpotential (η_{an}). This, in turn, results in a higher cell voltage (E_{cell}) and hence also a higher power (P) output [see (10.8) and (10.9) in Sect. 10.3.1]. The bimetallic mechanism is viewed to involve the formation of active $–OH_{ads}$ species on the admetal at lower anode potentials (E_{anode}) than observed for Pt-only catalysts. The $–OH_{ads}$ species are formed through the electrochemical discharge reaction of H_2O, as further discussed in this chapter. This allows for the oxidation of CH_3OH at lower E_{anode} values, hence resulting in a higher cell voltage (E_{cell}) and higher P values. Other effects such as electronic (also called ligand) and so-called third body effects can also influence the electrochemical CH_3OH and CO oxidation reaction. Some reports suggest the electronic effect to be very strong, namely in the range of half of an electron volt [59]. However, it should be noted that a lot of the studies suggesting beneficial electronic effects are based on theoretical calculations utilizing model

catalyst systems. The bimetallic effect has been clearly accepted to be capable of lowering the onset potential of both the electrooxidation reactions of CH_3OH and CO_{ads} of up to 0.3 V compared to Pt-only catalysts.

10.3 Thermodynamics

10.3.1 Equilibrium (E^o) and Cell (E_{cell}) Potentials

The standard potential (E^o) of the CH_3OH oxidation reaction, summarized in (10.1), is 0.01 V vs. RHE. The E^o value for the ORR (10.2) is 1.23 V. Therefore, the maximal E_{cell} value of a DMFC is 1.22 V, as the E_{cell} value is the difference between the potential of the cathode and the anode, as follows:

$$E_{cell} = E_{cathode} - E_{anode}. \tag{10.5}$$

The theoretical value of 1.22 V for a DMFC is only slightly lower than the maximal E_{cell} value of 1.23 V that is theoretically achievable for a PEMFC. The E^o value for the H_2 to $2H^+$ oxidation reaction is 0 V vs. RHE. Furthermore, the E^o values for the CH_3OH oxidation reaction and the ORR reveal that the voltage of the anode is less positive than the voltage of the cathode, thus driving the electrochemical conversion reactions of CH_3OH and O_2 due to the favored free energy values. In real FC applications, effects such as current–resistance (IR) drops, overpotentials at the anode (η_{an}) and cathode (η_{cat}), and methanol crossover from the anode to the cathode lower the E_{cell} value. Some of these effects are seen under load, i.e., when power is thrown from the FC, while others are already observed when the cell is at equilibrium, i.e., under zero load and when no net current is measured. The schematic shown in Fig. 10.4 demonstrates how the E_{cell} value changes when current is drawn from the system. At zero load, i.e., when no current

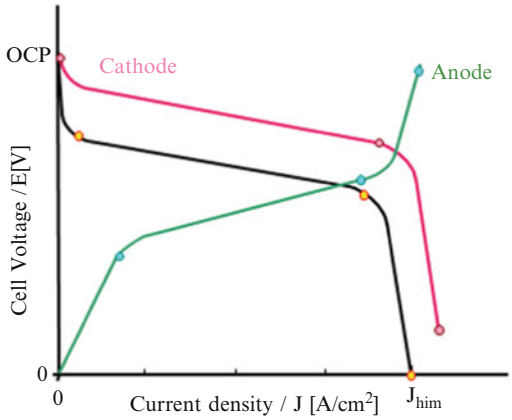

Fig. 10.4 Schematic demonstrating the makeup of the E_{cell} value as a function of the current density (J) drawn from the FC

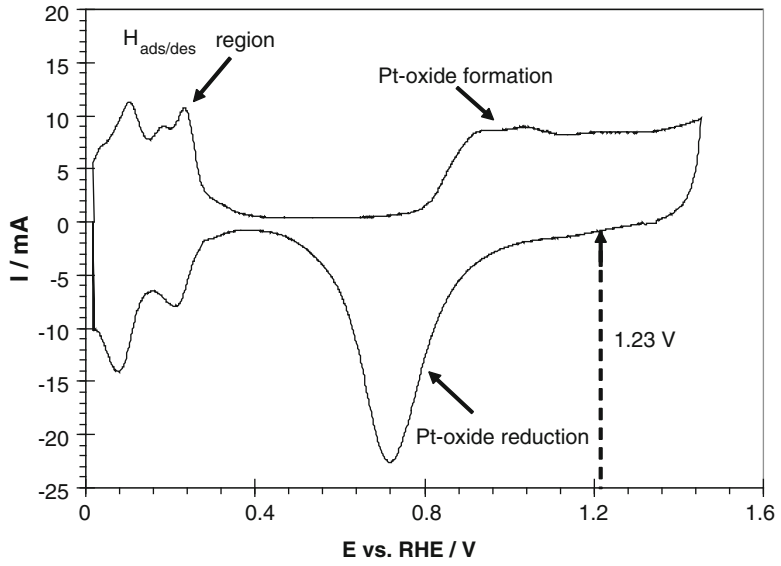

Fig. 10.5 Cyclic voltammogram (CV) of a polycrystalline Pt foil recorded in 0.5M H_2SO_4. The CV demonstrates the typically electrochemistry of polycrystalline Pt. The *y*-axis is the current (*I*) in mA and the *x*-axis the potential (*V*) vs. a reversible hydrogen electrode (RHE)

flows, the maximal E_{cell} value of a particular FC is measured. Under these conditions, the cell is at its open-circuit potential. As stated above, the maximal E_{cell} value of a DMFC is 1.22 V. However, E_{cell} values of less than 1.22 V are typically measured at open-circuit potential for a practical FC. This is due to a number of factors such as crossover of CH_3OH from the anode to the cathode, which results in depolarization of the cathode, i.e., a lower $E_{cathode}$ value. The lower $E_{cathode}$ value results from a mixed potential at the cathode. In the case of CH_3OH crossover, parts of the three-dimensional cathode respond to the presence of CH_3OH, i.e., act as "anode," while other parts respond to O_2. Furthermore, the state-of-the art cathode catalysts used for low-temperature FC applications are Pt-based catalysts. An E^o value of 1.23 V for the cathode can only be achieved for oxide-free Pt catalysts, i.e., metallic Pt. In the presence of H_2O and O_2, hydroxides and oxides are formed on the Pt surface at positive potentials. The formation and reduction of PtOH and PtO are demonstrated in Fig. 10.5 that shows a so-called cyclic voltammogram (CV) of a bulk polycrystalline Pt foil in 0.5M H_2SO_4. The potential (E) is recorded vs. a RHE, and the current (*y*-axis) is recorded by changing the potential of the Pt electrode at a constant rate, e.g., at 100 mV s^{-1}. The latter is called the sweep rate. The electrochemical characteristics of Pt are well documented in the literature [21, 59]. At low potentials, between ~0 and ~0.3 V vs. RHE, the so-called butterfly peaks are observed. They are characteristic for the adsorption and desorption of atomic H ($H_{ads/des}$) on Pt metal. During the positive potential scan, an increase in current is observed indicating the formation of Pt oxide.

Pt oxide formation takes place in several steps [60]. First, a monolayer of Pt–OH_{ads} is formed, followed by the formation of a monolayer of PtO according to (10.6) and (10.7):

$$Pt + H_2O \rightarrow Pt - OH_{ads} + H^+ + e^-, \tag{10.6}$$

$$Pt - OH_{ads} + H_2O \rightarrow PtO + H^+ + e^-. \tag{10.7}$$

(At potentials more positive than needed for the formation of a PtO monolayer [at 1.335 V vs. RHE in 0.5M H_2SO_4], multilayer Pt oxide formation takes place.) The formation of Pt–OH_{ads} and PtO are surface processes. Therefore, they are independent of the sweep rate, i.e., the same CV characteristics and charge for Pt–OH_{ads} and PtO formation are obtained for the different sweep rates ($<$100 mV s^{-1}). During the negative potential scan, the Pt oxides are reduced, as indicated in Fig. 10.5. The Pt oxide reduction process is strongly dependent on the amount of Pt oxides formed during the positive scan, i.e., it is influenced by the upper potential limit used in the CV scan. For the conditions used in Fig. 10.5, Pt oxide reduction is initiated and completed at ca. 1.1 and 0.4 V, respectively. From the CV shown in Fig. 10.5, it is clear that at 1.23 V, the surface of the Pt electrode is covered with oxide, thus blocking access of the O_2 fuel to the catalyst sites. The incapability of the O_2 to adsorb onto the oxide covered Pt catalyst surface results in lower E_{cathode} values than 1.23 V at open-circuit conditions of FCs. Therefore, the theoretical E_{cell} values of 1.22 and 1.23 V for a DMFC and a PEMFC, respectively, are not achieved for a real system. Complete reduction of the Pt oxides is not needed for the ORR to take place. However, a smaller active Pt(0) area is available for a Pt electrode that is partially covered with oxide, thus reducing the turnover rate for O_2. Both high E_{cell} and current (I) values are desirable as the value of P generated by an FC is the product of E_{cell} and I, i.e.:

$$P = E_{cell} \times I. \tag{10.8}$$

Or, in terms of the power density (P^*) and J, the current density:

$$P^* = E_{cell} \times J. \tag{10.9}$$

However, as shown in Fig. 10.4, the E_{cell} value decreases as current is drawn from the system. The change in the E values can be divided into three regions. They are the region dominated by (1) activation polarization, (2) cell impedance, and (3) mass transport control. As shown in (10.5), the E_{cell} value is the difference between the values of E_{cathode} and E_{anode}. Both the E_{anode} and E_{cathode} values change in a similar fashion when current is drawn from the system, i.e., they are governed by the same three influences, namely activation polarization, cell impedance, and mass transport control. Practical E_{cell}, E_{anode}, and E_{cathode} vs. current density (J) curves for an FC show a pronounced change in the E values at low J's, as demonstrated in Fig. 10.4. The changes in this region are dominated by the current–potential (I–V)

relationship of electrochemical reactions that are under activation control. In the activation-controlled region, the E_{cell} value is equal to the difference between the E^{o} values of the cathode and the anode, which are corrected for losses in the corresponding activation overpotential (η_{act}). Changes in the activation-controlled region are due to slowness of the electrochemical reactions taking place at the electrode/reactant interface. These loses take place in an exponential manner, as described by the Butler–Volmer equation (10.10) for the faradaic reaction taking place at a particular electrode:

$$I = AJ_o\left\{\exp\left[\frac{(1-\alpha)nF}{RT}\left(E - E_{eq}\right)\right] - \exp\left[-\frac{\alpha nF}{RT}\left(E - E_{eq}\right)\right]\right\}. \tag{10.10}$$

In (10.10), A is the electrode surface area, J_{o} the exchange current density, E_{eq} the equilibrium potential, and α is the symmetry factor. All other symbols have their usual meaning. Furthermore, $E - E_{\text{eq}}$ equals η_{act}. There are two limiting cases to the Butler–Volmer equation, namely the low field case for the case of η_{act} values $<$~25 mV. For the low field case, changes in the η_{act} value are small, and hence, the exponential terms in (10.10) can be approximated by a linear relationship, thus simplifying (10.10) to:

$$\frac{I}{A} = J_o\frac{nF}{RT}\left(E - E_{eq}\right) = J_o\frac{nF}{RT}\eta_{act}. \tag{10.11}$$

The second case is the high field case that applies to η_{act} values >30–100 mV. For this case, the electrode is sufficiently polarized that the kinetics of the forward reaction are much faster than the kinetics of the backward reaction. For example, for the case of the CH_3OH oxidation reaction, only the oxidation reaction of CH_3OH needs to be considered, and the reverse reaction, the "reduction" of "CH_3OH oxidation products," can be ignored. Similarly, for the case of the cathode only, the reduction reaction of O_2 needs to be considered, and the oxidation reaction of, e.g., O^{2-} or H_2O_2, can be neglected for the high field case. Equation (10.10) can be simplified, as shown in (10.12), for the case of the anode:

$$E_{anode} - E_{eq} = \eta_a = a + b\log(I). \tag{10.12}$$

The simplified form shown in (10.12) is written in the form of the well-known Tafel equation. The symbols a and b are constants that are specific for a particular reaction and a particular temperature. Also, the symbol η_{a}, which stands for the overpotential of the anode, is used specifying that (10.12) describes the E–I relationship of the anode.

In the second region, observed at intermediate J's, ohmic loses also contribute to the decrease in the E_{cell} value. The ohmic loss or IR drop is the product of I and the resistance R of the cell. In this region, the E_{cell} value follows the following relationship:

$$E_{cell} = \eta_{act} - R \times I. \tag{10.13}$$

In (10.13), I represents the total current flowing through the cell, and η_{act} describes the losses due to activation control at the anode and the cathode. Different methods are used to obtain the R value of a particular cell. Often the current interrupt method is used. However, it has been shown [61, 62] that this method yields higher R values than other methods such as AC resistance, high-frequency resistance, or AC impedance spectroscopy. The R value obtained from the high-frequency resistance and AC impedance measurements should be the same. Furthermore, both these methods involve the application of a small AC perturbation of several frequencies. Therefore, they are preferable to the one data point measurements of the current interrupt method and the single AC frequency applied in the AC resistance method. Typical R values are in the 0.1–0.15-Ω cm^2 range [61, 62].

Figure 10.4 shows that at higher J's, which correspond to faster electron transfer rates and faster fuel consumption, a rapid drop in the E_{cell} value is observed. This drop is related to a limiting current (I_{lim}) or a limiting current density (J_{lim}). This effect results from limited mass transport processes taking place in the FC structure, for example, associated with limited access of fuel or proton transport to or within the catalyst layer. In this region, concentration gradients build up in the FC. The loss in potential introduced by mass transport limitations (η_{lim}) is defined as follows:

$$\eta_{lim} = \frac{RT}{nF} \ln\left(\frac{I_{lim}}{I_{lim} - I}\right). \tag{10.14}$$

In (10.14), I_{lim} is the limiting current arising from the concentration gradient. The value of I_{lim} is defined by the rate the reactant that can be transported to the catalyst surface, i.e., by Fick's law. Examination of Fig. 10.4 also demonstrates that I_{lim} is the maximal current that can be drawn from a particular FC.

10.3.1.1 Examples of DMFC Performance Values and Catalyst Loadings

Improvements in the performance of DMFCs have been made over the last years. In a proof-of-concept study carried out in 2002, it was shown that DMFCs can be operated over 2,000 h with only a small loss in performance [18]. The amount of catalyst needed was also discussed in this study. Pt–Ru/C and Pt/C catalysts were used at the anode and at the cathode, respectively, and a Nafion 117 membrane was used. A 5 cm^2 DMFC was operated at 80°C on 1M CH_3OH at the anode and air at the cathode. A total amount of 3 mg Pt per cm^2 FC area was used, and a maximal power density (P_{max}) of ca. 110 mW cm^{-2} was achieved. This was a proof-of-concept study to show that a DMFC can indeed run for 2,000 h. To date, typically lower anode and cathode catalyst loadings per cm^2 FC area are used, and the catalysts are supported on high-surface area carbons. For example, a study reported by a research laboratory in Juelich utilized Pt–Ru/C as anode catalyst and Pt/C as cathode catalyst. The total metal loadings are 2 + 2 mg per cm^2 FC area. Operation of a single cell of 18 cm^2 area at 80°C and ambient pressure, air at the cathode and

1M CH_3OH at the anode, was shown to yield an initial maximal power P_{max} of 85 mW cm^{-2}. A 30% decrease in the P_{max} value was observed after 5,000 h of operation of the single cell [63].

10.3.2 The Driving Force of an FC: The ΔG and ΔE Value

The net reaction of a DMFC is discussed above. As shown in (10.3), it is:

$$CH_3OH + 3O_2 = CO_2 + 3H_2O. \tag{10.3}$$

The anode and cathode reactions of an FC are driven by the negative difference in free energy (ΔG) of the reactions, i.e.:

$$\Delta G = \Delta G^{o} + RT \ln K. \tag{10.15}$$

In (10.15), ΔG^{o} is the free energy at standard conditions, K is the equilibrium constant of the overall reaction, and all other symbols have their usual meaning. For a DMFC:

$$K = \frac{pCO_2}{[CH_3OH][pO_2]^3}. \tag{10.16}$$

ΔG^{o} can be expressed in terms of the difference in the standard electrode potential (ΔE^{o}), namely:

$$\Delta G^{o} = nF\Delta E^{o}. \tag{10.17}$$

Inserting (10.17) into (10.15) then results in the following relationship:

$$\Delta G = nF\Delta E^{o} + RT \ln K. \tag{10.18}$$

Furthermore, at equilibrium, when ΔG is 0 (10.18) can be reorganized and ΔE^{o} can be expressed as:

$$\Delta E^{o} = -\frac{RT}{nF} \ln K. \tag{10.19}$$

As previously stated, at equilibrium, $\Delta E^{o} = E^{o}_{cathode} - E^{o}_{anode}$, i.e., $E^{o}_{O2/H2O} - E^{o}_{CH3OH/CO2}$, thus $\Delta E^{o} = 1.23 - 0.01$ V $= 1.22$ V $\cong 1.2$ V. This is the E_{cell} value at zero load, hence reflecting the theoretical open-circuit potential value. As discussed in Sect. 10.3.1 above, ΔE^{o} values significantly lower than 1.2 V are observed for DMFCs due to problems such as CH_3OH crossover and the presence of oxides on the Pt catalyst surface. This behavior is also observed for PEMFCs.

An advantage of a DMFC operated using liquid anode fuels is the fact that the transition between gaseous and liquid products and reactants is not needed. In the case of the PEMFCs operated on H_2, the anode gas H_2 is oxidized to protons that will be hydrated, i.e., H_3O^+. The protons are transported across the membrane to the cathode, where they form H_2O with the O_2^- ions generated by the electrochemical reduction reaction of O_2. Hence, in the case of PEMFCs run on H_2 and O_2, two gaseous products are converted to a liquid. This involves changes of products of higher entropy state (1 mol H_2 + ½ mol O_2) to an eventually liquid product (1 mol of H_2O).

10.4 Mechanism and Rate of the CH_3OH and of the CO_{ads} Electrooxidation Reaction on Pt-Only Electrodes

As stated previously, PEMFCs and DMFCs require Pt-based catalyst. For the case of a PEMFC run on neat H_2, the Pt loadings of the anode catalyst layer are very low (typically less than 0.1 mg Pt per cm^2 FC area). Therefore, the amount of Pt used at the anode of a PEMFC operated on neat H_2 is not a significant issue. For the case of FCs that utilize CH_3OH or H_2 feed containing CO impurities, much higher loadings of the Pt catalysts are needed in the anode catalyst layer. The loadings in the latter two cases are in the several mg Pt per cm^2 FC area range. Many studies have been carried out to understand the kinetics and mechanism of the CH_3OH oxidation reaction for Pt-only electrodes, which will be discussed below. Studies are also carried out that report the development of non-Pt-containing catalysts for the CH_3OH electrooxidation reaction. Frequently, only the CH_3OH oxidation current is measured in these studies, i.e., the nature of the reaction products and whether the CH_3OH is completely oxidized to CO_2 is not always established. In some cases, non-Pt metal anode catalysts are promoted on the basis that they are less expensive, even though the CH_3OH oxidation currents can be much lower than observed for state-of-the art Pt-based catalysts. Such a view is not valid, as the requirement of complete oxidation of CH_3OH to CO_2 needs to be fulfilled for a DMFC anode catalyst. In order for the CH_3OH to CO_2 reaction to take place, an H-atom adsorption and abstraction mechanism from the methyl ($–CH_3$) group of CH_3OH needs to take place, as discussed below.

10.4.1 General Mechanism for Low-Surface Area Pt Electrodes in Acidic Solutions

The electrooxidation of CH_3OH has been studied extensively since the 1960s [20–32]. The electrooxidation reaction of CH_3OH to CO_2 is a 6-e^- reaction and involves the need for an external oxygen species. This oxygen species is donated from H_2O.

The CH_3OH electrooxidation reaction is a multistep reaction. The actual reaction yields and the distribution of the reaction products depend on several factors as for example, on the concentration of CH_3OH and the reaction temperature [26]. Many studies have been carried out using bulk Pt metal electrodes such as polycrystalline Pt and Pt single crystal electrodes. The overall oxidation mechanism for "smooth" Pt-based electrodes has been established many years ago. (The term "smooth" used here refers to an electrode with a low roughness factor, i.e., to an electrode of similar electrochemical and geometrical surface area.) It is well known that even bulk metal electrodes are not completely smooth and have edge and kink sites that can indeed be important for electrocatalysis. However, discussion about the detailed mechanism of the CH_3OH electrooxidation reaction on Pt bulk metal electrodes is still ongoing. In particular, details about the reaction products and current efficiencies of the CH_3OH to CO_2 electrooxidation reaction are being discussed. Studies are somewhat complicated by the fact that accurate reaction kinetic measurements require a significant generation of reaction products and thus a reasonably high magnitude of the current. It follows that for practical reasons, such measurements on smooth and hence low-surface area Pt electrodes are often carried out at relatively positive potentials typically higher than 0.5 V vs. RHE. It needs to be noted that these conditions do not reflect the target value of E_{anode} for DMFC operating conditions, which is more negative than 0.5 V vs. RHE. The oxidation of CH_3OH, a single carbon and H-rich molecule, involves multiple steps. In acidic solutions, the first steps involve the adsorption of CH_3OH onto the Pt surface, followed by the abstraction of the H-atoms from the C atom, as, e.g., shown in (10.20–10.22):

$$Pt_3 + H_3COH \rightarrow Pt_2 - H_2COH + Pt + H^+ + e^-. \tag{10.20}$$

$$Pt_2 - H_2COH \rightarrow Pt - HCOH + Pt + H^+ + e^-. \tag{10.21}$$

$$Pt - HCOH \rightarrow Pt - COH + H^+ + e^-. \tag{10.22}$$

There has been much debate about the exact nature and orientation of the intermediate of the reaction shown in (10.22). In early studies, it has been suggested that the final H-abstraction steps results in an aldehyde (–COH) species, as indeed shown in (10.22). Various radiochemical and electrochemical methods have been used to study the adsorption and formation of intermediate species from numerous organic molecules [28–32]. It is now generally accepted that a Pt–CO_{ads}-type species is formed. The Pt–CO_{ads} species is also referred to as a poisoning intermediate formed during the CH_3OH oxidation reaction. It is important to note that these conclusions are based on the detection of Pt–CO_{ads} by in situ electrochemical infrared spectroscopy (in situ IR) measurements [29, 30, 32]. These measurements are useful to study the nature of adsorbed surface species as a function of the electrode potential. However, the collection of an IR spectrum requires a relative "long" time scale of several seconds. Species that are shorter lived are not detected by this method. Therefore, it is not known whether the Pt–CO_{ads} species detected by

in situ IR is formed rapidly or by a slower transformation reaction of an initially formed –COH species, as, e.g., illustrated in (10.23):

$$Pt - COH \rightarrow Pt - CO_{ads} + H^+ + e^-. \tag{10.23}$$

Indeed, NMR studies have added support to the transformation reaction and the view that the $–CO_{ads}$ species is formed at a longer (several seconds) time scale [64]. The complete oxidation of CH_3OH to CO_2 requires an external O-atom. The latter is donated by the oxidative adsorption reaction of H_2O onto the Pt surface forming an $–OH_{ads}$ species, shown in (10.24). The latter can then oxidize the Pt–CO_{ads}-type species completely to CO_2, thus freeing up Pt catalyst sites, as shown in (10.25):

$$Pt + H_2O \rightarrow Pt - OH_{ads} + H^+ + e^-. \tag{10.24}$$

$$Pt - OH_{ads} + Pt - CO_{ads} \rightarrow 2Pt + CO_2 + H^+ + e^-. \tag{10.25}$$

According to this reaction mechanism, three Pt sites are needed for the adsorption of the CH_3OH molecule [see (10.20)] and an additional Pt molecule is needed for the formation of $–OH_{ads}$ from H_2O (10.24). According to (10.25), the catalyst sites active for the CH_3OH adsorption reaction should preferably be in close contact with the catalyst sites that are active for the $–OH_{ads}$ reaction. The $–CO_{ads}$ molecules can diffuse across the catalyst surface to an active $–OH_{ads}$ site. However, this is not desirable as the surface diffusion process can take time, thus resulting in a slower overall oxidation rate (see also Sect. 7.3.1). The surface diffusion process and oxidation of $–CO_{ads}$ formed through the formation of the adsorption of gaseous CO at low potentials have been studied extensively. For example, diffusion rate constants for $–CO_{ads}$ in the range of 10^{-14} cm s^{-1} have been estimated [65]. It needs to be noted that the $–CO_{ads}$ surface diffusion rates are dependent on factors such as the potential of the working electrode and the catalyst particle size.

It is noteworthy that DMFC anode catalysts are frequently characterized using the electrooxidation reaction of $–CO_{ads}$ [66, 67]. Therefore, the characteristics of the $–CO_{ads}$ electrooxidation reaction are also discussed in this chapter. The $–CO_{ads}$ is formed by bubbling CO gas through the electrolyte solution, in which the catalyst electrode is immersed. The potential of the catalyst-working electrode is typically controlled at a value at which close to a monolayer of $–CO_{ads}$ can be formed onto a metallic catalyst surface. Useful information can be extracted about the catalyst surface, even though the $–CO_{ads}$ formed from gaseous CO and the poisoning intermediate ($–CO_{ads}$ type) species formed during the CH_3OH oxidation reaction are viewed to be different. The bonding of the $–CO_{ads}$ onto Pt electrode surfaces has been the subject of some discussions. There are many studies on in situ IR spectroscopy [29, 30, 32, 68, 69]. However, in situ IR measurements most frequently suggest that the $–CO_{ads}$ is linearly bonded onto the Pt electrode for both CO_{ads} formed through the adsorption of CO from "CO gas" dissolved in the electrolyte solution and formed during the CH_3OH oxidation reaction [68]. The wave number of the $–CO_{ads}$ peak yields a measurement of the bonding strength of

the CO_{ads} with the electrode surface. Typically, a shift in the CO_{ads} peak position is observed with changes in the electrode potential. Some of the observed shift in wave number position can be assigned to changes in the potential of the working electrode (i.e., changes in the external static field around the working electrode) rather than solely by a change in bonding strength. These changes are associated with a phenomenon known as the Stark effect.

10.4.1.1 Comments to the CH_3OH Electrooxidation Mechanism in Alkaline and "Dry" Media

Equations 10.20–10.25 describe the CH_3OH electrooxidation reaction in acidic media, but studies in alkaline media are also frequently carried out. The use of an alkaline media has advantages and a number of disadvantages. The latter are substantial, thus making alkaline DMFCs devices not practical for most applications. The advantages of the alkaline media are that both the ORR and the oxidation reaction of methanol are enhanced compared to the electrochemical reaction rates observed in acids. In the case of the ORR, Pt catalysts are not needed, and much less expensive catalysts can be used. The oxidation rate enhancement of CH_3OH in alkaline solutions arises from the fact that strictly speaking CH_3OH is an acid, i.e.:

$$CH_3OH + H_2O \leftrightarrow CH_3O^- + H_3O^+. \tag{10.26}$$

The pK_a of CH_3OH is 15, and hence, in an alkaline environment, a fraction of the CH_3OH is present in the deprotonated, i.e., the CH_3O^-, form. For example, for 0.01M NaOH solution, 0.1% of the CH_3OH molecules are present as CH_3O^- anions. The pathways of the oxidation reactions of CH_3OH and CH_3O^- are different. The oxidation of the deprotonated CH_3O^- species is also more rapid. The oxidation of CH_3O^- does not proceed via the abstraction of H-atoms from the $–CH_3$ group. The CH_3O^- anion adsorbs through its oxygen group at the Pt catalyst surface. The throwback of the oxidation via this mechanism is that CO_2 is not the final oxidation product, but dimerization or coupling products can be formed. This can take place through the formation of CH_3O^* radicals and a Kolbe-type reaction, i.e., by a radical reaction mechanism of two nearby radical molecules. The coupling products can be, e.g., methanaldimethylacetal $[H_2C(OCH_3)_2]$ and methylformate $[HCOOCH_3]$. Furthermore, even a 6-e^- oxidation reaction of CH_3OH does not result in the formation of CO_2 in alkaline media but rather in the formation of carbonate, CO_3^{2-}. Formation of CO_3^{2-} is not desirable as it forms solid products, which can block the pathways for the fuel and products in the FC. It should be noted that other organic species that have been explored as potential anode fuels such as ethanol and ethylene glycol are also acids. Therefore, the same issues apply to them in alkaline solutions as for CH_3OH.

The exact oxidation mechanism, and product distribution, of course depends on the oxidation conditions, namely potential range, electrode, and CH_3OH to water ratio [12, 13, 26]. In fact, the CH_3OH to water ratio can be very important for the CH_3OH oxidation reaction [12]. In the absence of water, i.e., in "dry" media, the CH_3OH oxidation reaction takes place via the methanolic O–H splitting, i.e.:

$$CH_3OH \rightarrow (CH_3O)_{ads} + H_{ads}. \tag{10.27}$$

This is similar to the initial CH_3OH oxidation pathway taking place in alkaline solutions. Due to the complicating issues arising in alkaline solutions, this chapter focuses on CH_3OH oxidation reactions in acidic media, generally of a CH_3OH to water ratio of at least 1 to 1. However, it needs to be emphasized that the final product generation needs to be identified when new fuels, different media, new catalyst formulations, or any other new experimental conditions are explored. The complete oxidation reaction, e.g., the 6-e^- reaction of CH_3OH to CO_2, is essential for practical fuel cell applications as well as for safety reasons.

10.4.1.2 Reaction Rates on Clean and Single Crystal Surfaces: Kink, Edge, and Terrace Sites

Both the CH_3OH and CO_{ads} oxidation reactions depend on the surface of the catalyst. Therefore, considerable efforts have been devoted to gain insight into the fundamentals of these reactions using very clean and well-defined Pt surfaces [70–72]. In summary, the results have shown that the dehydrogenation reaction of CH_3OH results in the formation of a $–CO_{ads}$ type species. It is often referred to as poisoning intermediate species to emphasize that it is a $–CO_{ads}$-type species, which may be different from CO_{ads} formed by bubbling CO gas through an electrolyte solution, as discussed in Sect. 10.4.1 [70]. Previous studies clearly established that the structure of the Pt surface influences the CH_3OH dissociation reaction and the bonding and further oxidation of the $–CO_{ads}$-type species. Sun et al. carried out an extensive study for the formation and oxidation of the poisoning intermediate $–CO_{ads}$-type species [70]. They utilized a large number of Pt single crystals, namely low index planes [Pt(100), Pt(111), and Pt(110)] and stepped surfaces [Pt(310), Pt(511), Pt(610), Pt(211), Pt(311), Pt(332), Pt(320), Pt (210)]. Polycrystalline Pt was also studied. Based on their results, it was concluded that the CH_3OH oxidation reaction is facilitated on stepped surface sites as compared to terrace sites. They also proposed that the poisoning intermediate species formed from the dissociation reaction of CH_3OH is similar to the poisoning species formed from HCOOH. Herrero et al. [73] carried out a detailed study of the CH_3OH oxidation reaction for low index plane Pt surfaces, i.e., Pt (111), Pt(100), and Pt(110). They carried out CV, chronoamperometric, and Tafel plot studies for the CH_3OH oxidation reaction on all three surfaces. The CH_3OH oxidation reaction was clearly observed to be dependent on the surface structure

and also reported to be influenced by the anion of the electrolyte solution. The CV results reveal that the onset potential for the CH_3OH oxidation reaction can be up to 0.2 V lower for the Pt(111) surface than for the Pt(110) surface. The CH_3OH onset potential was the highest for the Pt(100) electrode. The CH_3OH onset oxidation potentials were also different in the different electrolyte solutions. Nevertheless, the influence of the surface structure was sufficiently substantial that the onset potential values can be grouped as follows: Pt(111) < Pt(110) < Pt (100). Furthermore, the H_3PO_4 solution appeared to show the lowest onset potential in general. However, it needs to be stated that an Ag/AgCl electrode was used as the reference. The Ag/AgCl electrode is a pH-independent electrode, and hence, differences in the electrolyte solution pH values are not accounted for. Furthermore, the onset potential for the CH_3OH oxidation reaction is the lowest for the Pt(111) surface. However, the CH_3OH oxidation currents are the lowest for the Pt(111) electrode. The Pt(110) surface yields the highest CH_3OH current. The authors calculated a turnover number of 163 molecules per Pt site s^{-1} from chronoamperometric data at 0.2 V vs. Ag/AgCl for the Pt(110) electrode, which is a high turnover number for Pt-only electrodes.

The turnover rates for the Pt(111) surface are the lowest for the three electrodes. The fact that a low overpotential is observed for this electrode indicates that the initial dissociative adsorption reaction of CH_3OH onto the Pt(111) surface is fast. However, further oxidation to CO_2 is slow, indicating that further oxidation of the poisoning intermediate species to CO_2 is difficult on the Pt(111) surface. Indeed, in situ IR studies show the formation of CO_{ads} on the three electrode surfaces and suggest a CO_{ads} to CO_2 oxidation rate as follows: Pt(110) > (100) ≫ (111) [75]. Therefore, the adsorption and dehydrogenation reaction of CH_3OH is fast (takes place at low potentials) on the Pt(111) surface, but the Pt–OH_{ads} formation and complete oxidation of –CO_{ads} to CO_2 [see (10.25)] require positive electrode potentials. Based on these results, it is clear that the utilization of pure single crystal Pt(111) catalysts for the CH_3OH oxidation reaction is not an advantage. Furthermore, it should be noted that the use of low Miller index Pt surfaces is limited to model studies rather than to real applications. It is well known that the structure of single crystal surfaces are altered under real FC applications that can involve very large changes in electrode potentials, which can be equivalent to potential cycling conditions.

As mentioned above, the anion of the electrolyte solution can influence the CH_3OH oxidation reaction. However, it should be noted that $HClO_4$ and H_2SO_4 are considered good electrolytes. H_2SO_4 appears to be preferred for the CH_3OH oxidation reaction, as it is considered closer to the Nafion environment in the FC. Electrolytes like HCl should be avoided as Cl^- is much more strongly adsorbing and also has the propensity to react with intermediate species formed during the CH_3OH oxidation reaction. Anion adsorption effects are of high relevance for the ORR. The ORR electrode operates at more positive potentials than the CH_3OH anode, and hence, anion adsorption can be very pronounced for the ORR cathode. Anion effects cannot be ignored when kinetics of the ORR are studied.

In summary, it can be said that the studies carried out using single crystal Pt electrodes show that the adsorption and dehydrogenation reaction of CH_3OH strongly depends on the Pt surface structure. The activity of kink, edge, and defect sites is much higher than compared to the low activity of terrace sites [70, 73]. The number of kink vs. terrace sites can be important in the case of nanosized Pt catalysts. Kinoshita calculated the dependence of the number of Pt surface atoms located at edge and terrace sites on the Pt particle size for cubo-octahedral shapes [74]. The latter is the theoretically thermodynamically stable form of Pt particles. The calculations showed that the dependence of the number and ratio of these sites on the Pt particle size is strong. This could explain the observed dependence of reaction rates on the size of Pt particles of less than 5 nm. It needs to be noted that different explanations have also been offered to explain particle size effects. Furthermore, it is possible that Pt nanoparticles undergo shape changes as a result of the electrochemical test conditions. Furthermore, the actual shape of the as-prepared Pt nanoparticles depends on their preparation method; the resulting particles may or may not be cubo-octahedral.

10.5 Promotion of the CH_3OH and CO_{ads} Electrooxidation Reaction: The Addition of Reaction Promoters to Pt

10.5.1 The Bifunctional Mechanism of the CH_3OH and CO_{ads} Electrooxidation Reaction

As discussed above, the complete oxidation of CH_3OH to CO_2 requires the assistance of an external oxygen species. This can be an $–OH_{ads}$ species formed from the anodic discharge reaction of water, as shown in (10.24) and (10.25) for the example of $Pt–OH_{ads}$ formation on Pt. However, the water activation reaction on Pt takes place at relatively positive potentials. For smooth polycrystalline Pt electrodes, the $Pt–OH_{ads}$ formation reaction is clearly observed at E_{anode} values more positive than 0.72 V vs. RHE, as seen in the CV in Fig. 10.5. Consequently, the complete oxidation reactions of CH_3OH and $–CO_{ads}$ to CO_2 on Pt-only catalysts take place at very positive potentials. As early as the 1960s, Frumkin et al. recognized that Pt–Ru catalysts display a catalytic benefit for the CH_3OH oxidation reaction over Pt-only catalysts [24]. The Pt–Ru catalysts [which are now typically referred to as bimetallic catalysts] allow for the complete oxidation of CH_3OH and $–CO_{ads}$ to CO_2 at lower potentials. In fact, a lowering of the CH_3OH oxidation potential of up to 0.3 V can be observed for Pt–Ru over Pt-only catalysts [66, 75]. The catalytic benefit of Pt_xRu_y catalysts is shown in Fig. 10.6. Figure 10.6 shows CVs recorded in 0.5M CH_3OH + 0.5M H_2SO_4 solutions. The Pt_xRu_y alloy is seen to show the lowest onset potential for the CH_3OH oxidation reaction. The catalytic benefit of the bimetallic systems is assigned to a so-called bifunctional mechanism, which is

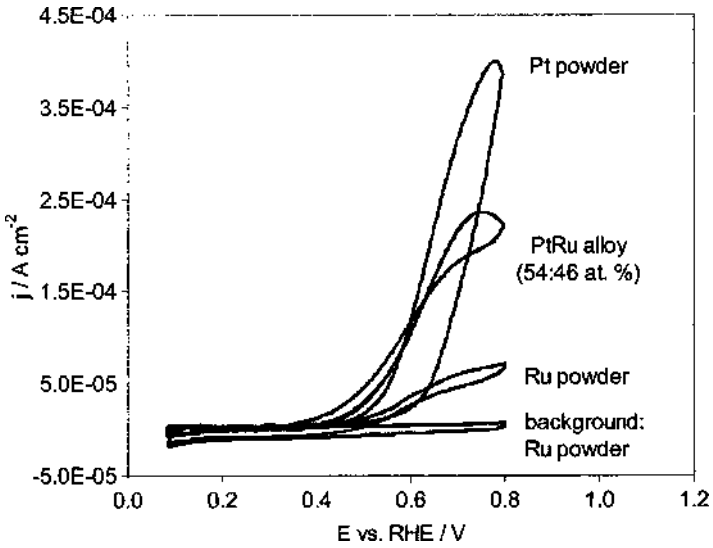

Fig. 10.6 CVs recorded at 10 mV s^{-1} in 0.5M CH_3OH + 0.5M H_2SO_4 solutions for various catalyst powder electrodes, as indicated in the figure. The current scales are normalized for the Pt and Ru surface areas. Reprinted from [47] with permission of the Electrochemical Society, Inc.

related to the fact that Ru adsorbs water at low potentials. This is summarized in the reaction scheme shown in the following equations [45]:

$$Pt + CH_3OH = Pt - (CH_3OH)_{ads}. \tag{10.28}$$

$$Pt - (CH_3OH)_{ads} = Pt - (CO)_{ads} + 4H^+ + 4e^-. \tag{10.29}$$

$$M + H_2O \rightarrow M - OH + H^+ + 1e^-. \tag{10.30}$$

$$Pt - (CO)_{ads} + M - OH \rightarrow Pt + M + CO_2 + H^+ + 1e^-. \tag{10.31}$$

It should be noted that (10.28–10.31) are meant as a schematic to demonstrate the basics of the overall CH_3OH oxidation reaction rather than suggesting a detailed reaction mechanism. Equations 10.30 and 10.31 are similar to (10.23) and (10.24) above. However, in (10.30) and (10.31), M rather than just Pt is used. M stands for the admetal that acts as the site to form active $–OH_{ads}$. For the case of Ru metal electrodes, it is known that the formation of surface oxides, e.g., $Ru–OH_{ads}$, already takes place in the 0–0.2-V range vs. RHE [76]. Many admetals and even metal oxide species have been explored as potential bifunctional catalysts for the oxidation reaction of CH_3OH and $–CO_{ads}$. However, the best catalysts for the electrochemical CH_3OH oxidation reaction are still based on Pt–Ru. In the case of the electrochemical oxidation reactions of solution CO and CO_{ads} from gaseous CO, systems like $Pt–MoO_x$ and Pt–Sn have also shown considerable catalytic benefits.

However, the electrochemical stabilities of the adcomponents of the latter two systems are problematic. According to their Pourbaix diagrams, both Sn and Mo dissolve at low potentials and in acidic solutions. The stability of Ru is also an issue (see Sect. 10.5.1.3), although to a lower extend than for adcomponents like Sn and Mo. It is clear from (10.17) that the admetal M, that provides an adsorption site for the formation of active $-OH_{ads}$ groups, needs to be in close proximity with the $Pt–CO_{ads}$ in order to have a catalyst system that has a fast recombination reaction, (10.31), and hence fast CO_2 formation reaction. Therefore, a catalyst surface that consists of homogenously distributed Pt to Ru sites on the atomic scale appears to be preferable. Pt and Ru are known to form disordered alloys of fcc structure up to large (>60 at.%) Ru contents [77]. Therefore, a random distribution of the Pt and Ru atoms on the atomic scale is achieved in the bulk of Pt_xRu_y alloys. However, a random distribution of Pt and Ru atoms on the atomic scale on the surface of even Pt_xRu_y alloys is likely not the case. In fact, according to theoretical studies, Pt surface segregation takes place for most Pt_xM_y combinations except for Pt_xAu_y alloys [78]. This has been supported by experimental evidence [47, 79, 80]. The actual makeup of the catalyst and the catalyst surface depends on the preparation method. For example, annealing in an O_2 atm at temperatures as low as 100°C results in the binding of the O-atoms with Ru, thus bringing Ru to the surface in the form of Ru oxides [79]. Furthermore, if chemical reduction methods are used to make the catalysts, differences in the rate of reduction of the corresponding precursor salts influence the actual make of the final catalyst. The reduction of Pt is typically faster than the reduction of metal salts that are less noble. If this is the case, a catalyst made of a Pt-enriched core and a surface enriched with the adcomponent results. The general view has become accepted that practical Pt–Ru systems consist of Ru oxide islands formed on the surface of Pt or Pt_xRu_y alloys [81].

Many reports discuss the turnover rates for the CH_3OH oxidation reaction for Ru or Ru oxide islands formed on Pt metal electrodes [81–84]. Other studies discuss the CH_3OH turnover rates for Pt_xRu_y alloys [43–45, 47, 85]. However, to the best of our knowledge, there is not a single study that allows for a comparison between the CH_3OH oxidation rates of Pt_xRu_y alloys and Ru oxide islands formed on Pt bulk electrodes. It needs to be noted that often different experimental conditions are used in the individual studies, thus complicating the comparison of the data. Small differences in the potential of the working electrode, the temperature, the electrolyte, and the CH_3OH concentration, as well as the sampling time, can have a significant influence on the resulting CH_3OH turnover rate.

10.5.1.1 The Active Form of Ru and Its Influence on the CH_3OH Turnover Number

There has been some discussion as to what form of Ru is the most active in bimetallic Pt–Ru catalysts. Some studies propose that Ru oxides (preferably a hydrous form) are much more active for the CH_3OH oxidation catalysts rather than Pt_xRu_y alloys [86]. Other studies favor the view that Ru in its reduced form

[Ru(0)] provides the most active catalyst sites for formation of active $-OH_{ads}$ [81, 87, 88]. The chemistry and electrochemistry of Ru are complex. For example, the surface oxidation of Ru metal takes place over a wide potential range. Surface oxidation is initiated at potentials as low as 0 V vs. RHE [76]. RuOH and RuO species (possibly hydrous) are already formed at very low potentials. The electrochemistry of these species is reversible, i.e., they are reduced in the cathodic scan. Further oxidation to Ru(+III) and Ru(+IV) species takes place at more positive potentials.

Long et al. [86] strongly proposed to avoid bimetallic Pt_xRu_y alloys for the CH_3OH electrooxidation reaction. They proposed an effective CH_3OH oxidation catalyst to consist of separate Pt and Ru oxide phases. They reported that a mixed phase Pt metal and hydrous Ru oxide (RuO_xH_y) catalyst has orders of magnitudes higher activity than a Pt_xRu_y alloy catalyst. They reported differences in mass-normalized CH_3OH exchange current densities ($J_{o,mass}$) of 250 times for the mixed phase Pt and RuO_xH_y catalysts vs. their so-called Pt^0Ru^0 equivalent catalyst powder. They used a commercial Pt–Ru black catalyst powder for their study. The powder was used as-received and referred to as mixed phase Pt and RuO_xH_y powder. The as-received powder was also subjected to heat treatments in different atmospheres, thus achieving the reduced forms of the Ru oxide, i.e., their so-called Pt^0Ru^0 powder among other catalyst powders. The CH_3OH oxidation activities were extracted from Tafel plots. Five to six points were obtained for each catalyst studied, over a potential range of 100–125 mV. The $J_{o,mass}$ values were then estimated from this data by extrapolating to the E^o value of the CH_3OH oxidation reaction. This involved the extrapolation from five to six experimental data measured in the 0.3 and 0.4 V vs. RHE range down to close to 0 V vs. the RHE. Examination of their data suggests very similar Tafel slope values for all powders except for the as-received powder that shows a higher Tafel slope. An explanation for the difference in the Tafel slope value for the one powder, namely the as-received powder, is not offered. Furthermore, error calculations for the $J_{o,mass}$ values estimated by extrapolation from a few data points over a fairly narrow potential range are not reported. The Pt^0Ru^0 powder used and made in their study shows the poorest performance. This powder is made by reducing the as-received mixed phase Pt metal and RuO_xH_y catalyst powder in a H_2 atm at 100°C. These conditions are known to be sufficient to reduce the hydrous Ru oxide to Ru^0; however, it is questionable whether indeed a Pt_xRu_y alloy is formed from a mixed phase powder at 100°C. Therefore, their study does not seem to provide sufficient evidence to conclude that Pt_xRu_y alloys should be avoided as DMFC anode catalysts.

In another study, a range of unsupported Pt–Ru powders were made and characterized [88]. Pt_xRu_y alloy powders were made by rapid reduction of Pt and Ru precursor salts at low temperatures. RuO_2 was also deposited onto preformed unsupported Pt powders. Part of the latter powder, the RuO_2, was reduced to Ru(0) in a H_2 atm at 100°C. The CH_3OH oxidation rates were then obtained for these powders over a wide potential range of 0.2–0.7 V vs. RHE. The CH_3OH oxidation currents were normalized for the electroactive Pt area of the corresponding electrodes; hence, true electrocatalytic currents were obtained. CO_{ads} stripping voltammetry and CO_{ads}

stripping transients at constant potentials were studied to obtain information about the site distribution of Pt and active Ru sites. Information about the nucleation and ease of formation of active $–OH_{ads}$ on the Ru sites were also obtained from the transients. The results of this study suggest that the distribution of Pt and Ru sites on the Pt–Ru catalysts surface strongly influences the CH_3OH oxidation rate. Highest CH_3OH oxidation activities were found for the catalyst powders with the best distribution of Pt to Ru surface sites, namely Pt_xRu_y alloys.

It is noteworthy that the stability of the Pt–Ru catalyst also needs to be considered for the selection of a DMFC anode catalyst. Recent studies indicate a lower susceptibility of Pt_xRu_y alloy powders for the dissolution of Ru at open-circuit potential as compared to Pt–Ru catalysts that contain a separate Ru/Ru oxide phase (Sect. 10.5.1.3).

10.5.1.2 The Optimal Ratio of Pt to Ru

Equations 10.14–10.17 suggest that the distribution of the Pt to Ru sites on the catalyst surface plays a major role for the CH_3OH and $–CO_{ads}$ oxidation reaction. According to the reaction scheme, specific assemblies of catalyst sites consisting of an optimized number of neighboring Pt to Ru sites are expected to yield the best catalyst performance. For the case of the $–CO_{ads}$ oxidation reaction, the view is that one CO molecule adsorbs on one Pt site. A Ru site, that provides the active form of $–OH_{ads}$, is then needed for the oxidation of the $–CO_{ads}$ molecule to CO_2. Therefore, an atomically homogenously distributed surface composition of Pt to Ru of 1 to 1 is believed to give the best activity for the oxidation reaction of $–CO_{ads}$. In fact, Pt_xRu_y alloys of $x = y$ (1:1 Pt:Ru atomic ratio) are typically used for CO oxidation catalysts [43]. For the case of the CH_3OH electrooxidation reaction, the adsorptive dehydrogenation reaction of CH_3OH is believed to require three Pt sites and one Ru site active for the formation of $–OH_{ads}$ [26]. Based on this, an optimal Pt to Ru atomic site ratio of 3 to 1 has been proposed and supported by experimental data [43, 47]. In earlier studies, it has been proposed that the optimal Pt to Ru ratio changes from 3 to 1 to a 1 to 1 Pt:Ru ratio when the temperature is increased from 25 to 60°C [43]. The proposed change in the optimal Pt to Ru ratio with temperature was rationalized to be due to an activation of surface Ru at the elevated T's, namely that Ru is also able to adsorb CH_3OH at, e.g., 60°C. However, closer inspection of the reported experimental data suggests that the optimal Pt to Ru ratio for the CH_3OH oxidation reaction is independent of the reaction temperature [43, 44, 47, 83] and that the optimal Pt to Ru ratio is 3 to 1 for both 25 and 60°C [47]. However, it should be noted that the optimal 3 to 1 Pt:Ru ratio is proposed for Pt_xRu_y alloys. It is possible that a different apparent optimal Pt to Ru atomic ratio may be determined for non-Pt_xRu_y alloy catalysts. It should also be noted that the above studies of the optimal Pt to Ru ratio were carried out for bulk metal type catalysts and unsupported Pt–Ru catalyst powders. Therefore, the catalysts are relatively large consisting of a much larger bulk to surface atom ratio. For the case of nanosized catalysts, studies that yield a conclusive answer about the optimal Pt to

Ru surface ratio are not available. This is due to the fact that the synthesis and characterization of nanosized Pt–Ru systems of defined composition are more complicated. The detailed characterization of nanosized bimetallic catalyst particles that are less than 5 nm in size is not trivial. Furthermore, it is more challenging to control the Pt_xRu_y alloy content and form nanoparticles of small (<5 nm) and narrow size distribution than bulk Pt_xRu_y alloys. Also, for the case of catalyst nanoparticles, large stabilizers that subsequently block access of the fuel to the catalyst site need to be avoided.

It needs to be noted that the optimal Pt to Ru ratio of 3 to 1 has been determined for bulk Pt_xRu_y alloys and for the anode potential range of interest to practical DMFC operating conditions, which is between 0.3 and 0.5 V vs. RHE [47]. Within this anode potential range, the formation reaction of $–OH_{ads}$, (10.30), is the rate-determining step [45], while at more positive potentials, the rate-determining step becomes the adsorption reaction of CH_3OH (10.28). Activation enthalpy values for the CH_3OH oxidation reaction of ~30 kJ mol^{-1} have been reported for an electrode potential of 0.68 V vs. RHE [43]. This is lower than the E_{cat} value of ~60 kJ mol^{-1} reported for less positive potentials of <0.5 V vs. RHE [47]. This difference may be related to a change in the rate-determining step of the CH_3OH oxidation reaction.

10.5.1.3 Stability of Pt–Ru Anode Catalysts

Recent studies have shown that the dissolution of Ru from the anode catalyst can have a significant detrimental influence on the performance of a DMFC [89–91]. After operation of DMFC single cells or stacks, significant amounts of Ru have been found in the cathode compartment [89]. This suggests that dissolved Ru species are transported across the Nafion membrane from the anode to the cathode. Furthermore, the performance of the cathode has been measured to be lower for Ru-contaminated cathodes [90]. It is further known that electrochemical Ru dissolution takes place under fuel starving conditions. Fuel starving conditions can occur locally in the anode compartment, thus driving parts of the anode into the evolution of O_2. Dissolution of Ru can also take place at open-circuit potentials. However, in this case, Ru dissolution takes place from separate Ru oxide phases, while Pt_xRu_y alloys are not susceptible to Ru dissolution at open-circuit potentials [91]. There are many unanswered questions about the dissolution of Ru from Pt–Ru catalysts. For example, the exact nature of the Ru species that is dissolved and transported across the membrane anode is not known. It is to expect that a charged Ru-complex species is formed, although some studies also speculate about the possible formation of Ru oxide nanoparticles. Studies carried out for Ru metal electrodes in acidic solutions (typically 0.5M H_2SO_4) have shown that electrochemical dissolution of Ru(+III) and Ru(+IV) species takes place at potentials more positive than 0.6 V vs. RHE. An estimate of the amount of Ru lost from a Ru metal electrode as a function of the potential is shown in Fig. 10.7 [92]. The results are obtained from electrochemical quartz crystal microbalance measurements.

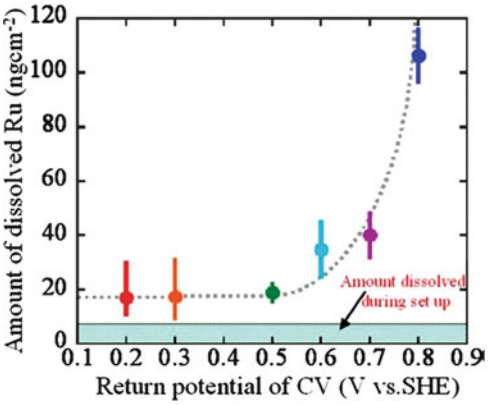

Fig. 10.7 Amount of Ru dissolved from a Ru metal electrode as a function of the potential measured vs. the standard hydrogen electrode (SHE). The amounts of Ru dissolved are estimated from electrochemical quartz crystal microbalance measurements. Reprinted from [92] with the permission of the Electrochemical Society, Inc.

It is seen that the electrochemical dissolution of Ru follows an exponential relationship with the potential. Ru dissolution reaches a significant level at potentials more positive than 0.7 V vs. the standard hydrogen electrode (SHE).

Based on the Ru dissolution studies carried out to date, it can be concluded that Pt_xRu_y alloys show little susceptibility toward Ru dissolution at open-circuit potential. Furthermore, fuel starving conditions in the anode compartment result in electrochemical dissolution of Ru, which is accompanied by irreversible detrimental effects on the performance of a DMFC. As a rule of thumb, catalysts containing separate Ru components and potential excursions within the anode more positive than 0.7 V vs. SHE should be avoided in order to minimize the dissolution of Ru.

10.5.2 The Third Body (Ensemble) Effect: Suppressing the Formation of Poisoning Surface Species

Mechanisms other than the bifunctional effect have also been shown to result in catalytic benefits for electrooxidation reactions such as the CH_3OH oxidation reaction. Such an effect is the so-called third body effect [93–95]. This effect, which has already been reported several decades ago, seems to have been extensively studied for the electrooxidation of HCOOH. In the case of CH_3OH, the catalytic effect of the third body is much smaller than observed for the bifunctional mechanism of the Pt–Ru systems and is hence less pursued for the CH_3OH oxidation reaction. The third body effect involves the adsorption of a foreign metal (or oxide) on the Pt electrode surface, such as the metal or oxides of Pb, Sb, or Bi. The presence of the third body can change the adsorption reaction of the organic

molecule, thus hindering the formation of a surface species that is difficult to completely oxidize to CO_2 [93]. As stated previously, the stability of the third body for many metal and metal oxides can be poor at the potential range of interest for DMFC operation in acidic conditions. Furthermore, the toxicity of the metal and metal oxides needs to be considered.

10.5.3 Electronic (Ligand) Effect

The so-called electronic (sometimes also referred to as the ligand) effect has also attracted a lot of attention for the electrooxidation reaction of CH_3OH and $–CO_{ads}$ [59, 96, 97]. In fact, this mechanism appears to have attracted more attention than the bifunctional mechanism by some research groups over the past few years [97]. Electronic effects have been discussed as an essential element for the ORR reaction for many years. A lot of the interest in the electronic effect for CH_3OH and $–CO_{ads}$ oxidation catalysis appears to stem from reports that are based on theoretical work [96]. The reports by the groups of Koper and Norskov are probably the best known studies for the theoretical exploration of electrocatalysts for $–CO_{ads}$ and CH_3OH oxidation reaction carried out in recent years [59, 96]. The surfaces of various Pt–Ru catalysts and the resulting impact of the catalyst "structure" on the electrooxidation reaction of CO were modeled. Different models of catalyst surfaces such as perfect monolayers of Pt on Ru (0001), as well as catalyst surfaces consisting of perfect Pt_xRu_y alloys, were studied for the oxidation reaction of CO and the adsorption reaction of –OH. The catalysts were viewed as bulk materials. Their surfaces are considered flat showing no curvature. The calculations suggest that a catalyst surface made of a perfect monolayer of Pt formed on Ru (0001) changes the binding energies of $–CO_{ads}$ more favorably in the 0.5-eV range as compared to Pt [59]. Based on these results, many attempts have been made to construct practical catalysts consisting of a monolayer of Pt on bulk metal Ru. However, the catalyst surfaces used in the theoretical study are model surfaces. It has now been generally accepted that neither a catalyst consisting of a perfect monolayer of Pt on Ru nor, vice versa, a perfect monolayer of Ru on Pt can be formed. Similarly, the surface of a practical Pt_xRu_y alloy catalyst is not made of a perfect alloy but rather consists of clusters of either Ru or Pt depending on the catalyst preparation method, as discussed in Sect. 10.5.1 Therefore, it needs to be noted that the practical and theoretical catalyst systems show fundamental differences that can influence the resulting electrocatalytic effects. The lack of the practical ability of forming such "perfectly" structured catalyst surfaces on the monolayer or atomic level is consistent with the fact that Pt tends to surface segregate with most elements, and three-dimensional clusters rather than single layers are formed. The only exception appears to be the Pt–Au system, where the formation of a monolayer structure and surface alloy formation appears to be possible [78].

It should also be noted that electronic effects of the substrate are most pronounced in the first monolayer for any system. The influence of the substrate decays exponentially, i.e., rapidly in the following layers. This and the fact that Pt and Ru strongly surface segregate make it questionable if practical Pt–Ru systems that show substantial catalytic benefits due to electronic alterations induced by the underlying substrate can be made in reality.

10.5.4 Three-Dimensional and High-Surface Area Electrode Structures

10.5.4.1 Product Distribution and CO_2 Yields for Smooth vs. High-Surface Area and Porous Electrodes

Much of the above discussion and reaction mechanism studies apply to smooth or thin layer catalyst systems. The actual real surface area of such electrodes is small, and overall reaction rates are relatively low. The anode catalyst layer in a real DMFC system consists of thick, several tenths of micrometers, electrodes that are porous and provide a high interfacial area between the reactant and the catalyst sites. The reaction mechanism, product distribution, and yield for CO_2 production of the CH_3OH oxidation reaction can be different for smooth vs. high-surface area electrodes. This has been shown by, e.g., Ota et al. [33] for the case of platinized Pt electrodes and is of course also highlighted by studies using Pt(hkl) electrodes. The effects are due to the fact that the adsorption of CH_3OH, CO, and H_2O is influenced by edge and kink sites of the Pt catalysts. As shown by Ota et al., the yield for CO_2 production for the CH_3OH oxidation reaction on high-surface area Pt electrodes may not be a 100% during the initial period of electrolysis. Depending on the temperature, the potential and the CH_3OH concentration products like HCOOH and HCOH can be formed. Ota et al. further showed that after a couple of tenths of minutes of electrolysis, the current efficiency for the CO_2 production approaches 100%. It is noteworthy that this influence of the surface roughness on the initial product distribution of the CH_3OH oxidation reaction is very pronounced for Pt catalysts. It is not observed to the same extend for Pt–Ru catalysts (provided that a sufficient amount of water is present in the study) and is hence not further discussed in this chapter.

CH_3OH oxidation activities have also been studied as a function of the Pt particle size for catalysts supported on high-surface area carbons. A dependence of the CH_3OH oxidation current on the Pt particle size is observed for mass and specific activities [98]. (The mass activity is the current measured per mass of Pt, while the specific activity is the current normalized per Pt surface area. The latter represents a true measurement of the catalytic activity.) The observed increase in mass activity with decreasing Pt particle size is expected. The CH_3OH oxidation reaction takes place at the catalyst surface, and a decrease in Pt particle size results in a larger number of Pt surface vs. the inactive Pt atoms located in the bulk.

The specific activity shows a maximum in the 4–5-nm range for the CH_3OH oxidation reaction on supported Pt nanoparticles [98]. This could be due to changes in the ratio of surface vs. edge atoms on the Pt nanoparticles (see Sect. 10.4.1.2). For the case of Pt–Ru catalysts, experimental data show an influence of the particle size on the mass activity of the CH_3OH oxidation reaction, while an influence on the specific activity appears not to be observed.

10.5.4.2 Proposed Use of Ru Oxides as Proton-Conductive Phase in the Electrode Structure

There are a number of studies that explore the fact that Ru oxides are proton conductors. In the catalyst layer of a PEMFC and a DMFC, the conduction of protons is a crucial parameter. In fact, it has been reported that for anode catalyst layers exceeding 10-μm thickness, the conduction of protons is likely the performance-limiting factor [99, 100]. The exact limiting thickness, of course, depends on the operating conditions of the DMFC, as well as the exact composition of the anode layer and its preparation method. In order to improve the proton conductivity and to possibly also allow better catalyst utilization, anode catalyst layers have been prepared by depositing Pt-based catalysts onto layers of Ru oxides. Such catalyst layers have a potential advantage over anode catalyst layers made using carbon-supported catalysts formed in combination with, e.g., Nafion as proton conductor, as likely thinner electrode layers can be made if the low-density carbon components are eliminated. Both the proton conductivity and the surface area of the Ru oxide are a function of the preparation method. Treatment and/or the involvement of higher temperatures results in the dehydration of the Ru oxide, which is accompanied by a loss in proton conductivity. Furthermore, the use of a single Ru oxide phase in large quantities in the anode catalyst layer raises the question of the stability of Ru (Sect. 10.5.1.3). To the best of our knowledge, the stability of the Ru oxide in these types of catalyst layers has only been referred to in one study [100]. The stability of so-called RuO_2 nanosheets used for support of Pt particles was studied by potential cycling experiments [100]. Completion of 1,000 potential cycles between 0.05 and 1.2 V vs. RHE resulted in a decay of 30% of the initial CH_3OH mass activity for the Pt catalyst supported on RuO_2 nanosheets. This was, in fact, taken as being a "positive" for the RuO_2 nanosheets since the corresponding decay observed for a Pt/C catalyst is ~86%, i.e., considerably smaller. Based on the studies presented up to date, it appears premature to draw conclusions if such catalyst layers are indeed better than catalysts made using an organic ionomer (typically Nafion) as proton conductor.

10.5.4.3 Notes on the Preparation of Electrode Catalyst Layers

The actual preparation of catalyst layers for PEMFCs and DMFCs is somewhat of a black art. Many different methods exist. Most of them involve the formation of an ink made of at least the supported or unsupported catalyst, the ionomer

(Nafion), and a solvent. The effectiveness of a catalyst layer strongly depends on the preparation method, its porosity, and actual composition. For example, an excessive amount of Nafion can block reactant access, while an insufficient amount of Nafion can result in a low proton conductivity of the layer. It appears that improvements can be made in regard to the design, the preparation, and the characterization of the actual catalyst layers for DMFCs.

10.5.5 Summary Pt-Based Catalysts

The work carried out to date on catalysts for the electrooxidation reaction of CH_3OH suggests that Pt–Ru catalysts are still the most active. Pt_xRu_y alloy catalysts appear to be the best performing for the CH_3OH electrooxidation reaction. Furthermore, recent studies also suggest that Pt_xRu_y alloys have a better stability than catalysts that also contain a single Ru phase [91]. The better performance of the Pt–Ru catalysts is viewed as being linked to the facilitation of Ru to form an active $–OH_{ads}$ species, i.e., to a so-called bifunctional mechanism. Some studies have also promoted Pt-based catalysts that contain a metal oxide phase such as MoO_x, WO_x, or H_xWO_y [101–103]. The addition of MoO_x has shown some promise in the case of the electrooxidation reaction of CO and $–CO_{ads}$ [102]. However, the potential range of an anode containing MoO_x is limited due to stability issues of MoO_x. The originally reported enhanced effects of the addition of H_xWO_y and WO_x to Pt and PtRu catalyst can probably be assigned to a beneficial influence on the catalyst size (i.e., resulting in a higher number of noble metal catalyst sites on the surface vs. the bulk), rather than a true catalytic effect [104]. Studies have been carried out preparing ternary and even quaternary Pt-based catalysts [45]. The addition of third and fourth metal or metal oxide components, of course, likely increases the challenges in the synthesis of a catalyst of a specific makeup (e.g., uniform distribution of all components) as well as the characterization of the catalyst. Full characterization of newly made or modified catalysts is essential in order to understand whether observed differences in CH_3OH oxidation currents are indeed due to a real catalytic effect. Information at the atomic level for the bulk and the surface of the catalysts should be obtained. Gathering reliable information about the latter is work intensive and challenging. Therefore, combinatorial methods have not yet provided any real breakthroughs in the area of catalyst development for CH_3OH electrooxidation reaction catalysts.

There are a number of challenges that remain to be solved for CH_3OH electrooxidation catalysts. These are full characterization and characterization tools for nanosized bimetallic catalysts, controlled synthesis methods for nanosized Pt_xRu_y alloy catalysts, and the stability of the Pt–Ru catalysts. The preparation, construction, and characterization of the catalyst layers for actual DMFC devices also need more work.

10.6 "Pure" Electrochemical Methods for the Evaluation of Catalysts

In the last sections of this chapter, "pure" electrochemical methods are described that are useful for evaluating catalyst characteristics on a laboratory scale. Methods that allow one to distinguish whether true or mass activities of the CH_3OH oxidation catalysts are measured are discussed. The method involves basic electrochemical equipment typically available in research laboratories concerned with electrocatalytic studies.

10.6.1 Distinguishing Real Catalytic vs. Mass Activities

Measurements of true catalytic activities require the knowledge of the electroactive surface area of the particular catalyst electrode studied and the determination of the onset potential of the CH_3OH electrooxidation reaction.

10.6.1.1 Catalyst Surface Area Measurements

The evaluation of practical catalysts requires some care in order to evaluate if the newly prepared catalysts are indeed showing better catalytic activities or if possible observed differences between tested catalysts are due to differences in purely physical properties, e.g., due to differences in mass activity. The true catalytic activity measures the turnover rate or CH_3OH oxidation current per cm^2 of real catalyst surface area. Therefore, in order to estimate true catalytic activities, the electroactive catalyst surface area needs to be known. For the case of Pt-only catalysts, the $H_{ads/des}$ reaction can be used to calculate the catalyst surface area, i.e., the charge observed for the $H_{ads/des}$ ($Q_{Hads/des}$) is calculated from the corresponding CV; see, e.g., Fig. 10.4. For bimetallic catalysts, the $H_{ads/des}$ region is often distorted by the presence of the admetal or admetal oxide. For example, Ru metal also adsorbs H in the same potential region as observed for Pt. However, unlike Pt, the $H_{ads/des}$ charge is not proportional to the Ru surface area. Furthermore, the Ru or a portion of the Ru may not be present in the metallic state, but rather covered with an oxide even in the $H_{ads/des}$ region. Therefore, the use of the $H_{ads/des}$ region for the estimation of practical catalysts like Pt–Ru is typically not suitable. The electrochemical oxidation reaction of $–CO_{ads}$ has also been applied to study Pt and Pt-based catalyst surfaces. It is considered as a useful in situ probe to gain information about a catalyst surface [67]. It has been shown to be potentially useful to yield information about the catalyst surface area in combination with the electrochemical oxidation reaction of $(COOH)_2$ [105]. The latter needs to be carried out as an activation-controlled electrochemical oxidation reaction and has been applied to unsupported, i.e., bulk powder type Pt–Ru and Pt–Ru oxide catalysts [105].

However, the application of the $(COOH)_2$ oxidation method to nanosized catalysts has never been probed. The $(COOH)_2$ oxidation method has been applied to Pt–Ru powder catalysts. The adsorption and oxidation of $(COOH)_2$ takes place on Pt metal surfaces. Its oxidation to CO_2 does not follow a bifunctional mechanism, as the donation of an additional O-atom is not needed to form CO_2. Therefore, the activation-controlled $(COOH)_2$ oxidation current is proportional to the Pt surface area. Another useful method is the underpotential deposition of Cu [106]. Cu undergoes underpotential deposition onto Pt and Ru metal surfaces and can subsequently be stripped from the surface. It has been shown that one Cu atom is deposited per Pt(0) and Ru(0) atom. However, this Cu underpotential deposition method requires the knowledge of the fraction of surface Ru present as Ru(0) vs. the Ru oxide form in the underpotential region of Cu.

10.6.1.2 The Onset Potential of the CH_3OH Oxidation Reaction

The onset potential of the CH_3OH oxidation reaction is a key parameter describing a catalyst. An estimate of the onset potential can be obtained from, e.g., CV studies. A positive potential scan should be used for the evaluation. The actual characteristics of the negative scan are strongly influenced by the positive potential limit used. For a polycrystalline bulk Pt electrode, Pt oxide formation starts at potentials more positive than 0.7 V vs. RHE. The Pt oxides hinder the CH_3OH adsorption reaction (10.28). This results in a hysteresis between the positive and negative potential scan. The onset potential for the CH_3OH oxidation reaction is determined by extrapolation of the CH_3OH oxidation current in the positive scan to zero currents. A lower onset potential for the CH_3OH oxidation reaction reflects a true electrocatalytic benefit, while an increase in the CH_3OH oxidation current at a particular potential, and for the same mass of catalyst, may simply be due to changes in catalyst surface area. State-of-the art Pt–Ru catalysts show a significant decrease in the CH_3OH oxidation overpotential of ca. 0.3 V as compared to Pt catalysts.

Some studies examine the hysteresis between the positive and negative potential scan in the CVs recorded in CH_3OH solutions in an attempt to gain further inside into a catalyst surface. It should be noted that the hysteresis is strongly dependent on the degree of oxidation of the catalyst surface. The latter is very susceptible to the positive potential limit used. Even small changes in the positive potential limit typically exhibit an influence on the hysteresis, thus making the interpretation of the data very complex.

10.6.2 Determining the Rate-Determining Step and Tafel Plots

Knowledge of the rate-determining step of the CH_3OH electrooxidation reaction is also of importance. Depending on the potential range of the anode, the rate-determining step can change. The rate-determining step is determined by studying

the CH_3OH oxidation current of a particular catalyst electrode at different CH_3OH concentration. If the current is independent of the CH_3OH concentration, then the $–OH_{ads}$ formation reaction, (10.30), is the rate-determining step. If the current is dependent on the CH_3OH concentration, then the adsorption reaction of CH_3OH is rate determining (10.28). In the anode potential range of interest for practical DMFC applications, which is more negative than 0.5 V vs. RHE, typically a zero order in the CH_3OH electrooxidation reaction is observed [45]. This suggests that the formation reaction of $–OH_{ads}$ rather than the CH_3OH adsorption reaction is the rate-determining step in this potential range.

Tafel slope measurements are also very important for electrocatalytic studies. The measurements should be carried out over a wide potential range and collecting as many data points as possible. More than one Tafel slope can be obtained depending on the catalyst system. The value of the Tafel slope also yields information about the rate-determining step of the reaction of interest. For example, a Tafel slope of 120 mV dec^{-1} suggests that an initial 1-e^- transfer reaction is the rate-determining step in the CH_3OH oxidation reaction, i.e., [73]:

$$CH_3OH \xrightarrow{rds} (CH_2OH)_{ads} + H^+ + e^-. \tag{10.32}$$

A Tafel slope value can be less than 120 mV dec^{-1}. However, a true Tafel slope value cannot be larger than 120 mV dec^{-1}. Nevertheless, values >120 mV dec^{-1} can be observed, which could reflect the formation of surface oxides and/or a resistive effect. A change in the Tafel slope value indicates a change in the rate-determining step. Generally, a low Tafel slope value is preferred for a catalyst. A higher Tafel slope indicates that for the same incremental increase in current, the anode potential is shifted to more positive values. This is equivalent to a loss in P, see (10.8).

10.6.3 Current Transients Collected at a Constant Potential

10.6.3.1 CO_{ads} Stripping Transients

CO_{ads} stripping transients recorded at constant potential can yield very valuable information about a catalyst surface. Also, the information gathered from such transients is reflective of a particular state of an electrode, as the transients are collected at a constant potential. This is unlike the case of CV studies, during which the surface of an electrode is altered. This method has only been applied in a few studies [107–110]. Prior to the recording of the transient, the CO is adsorbed onto the catalyst surface by bubbling CO gas through the electrolyte solution, while the electrode potential is held at a low value, e.g., 0.1 V vs. RHE. This process is essentially the same as carried out prior to the recording of CO_{ads} stripping voltammograms. The procedure for the latter is well described in the literature. After removal of the solution CO, the potential is stepped to a value of interest, and the current is recorded as a function of time. Initially, a large positive current is

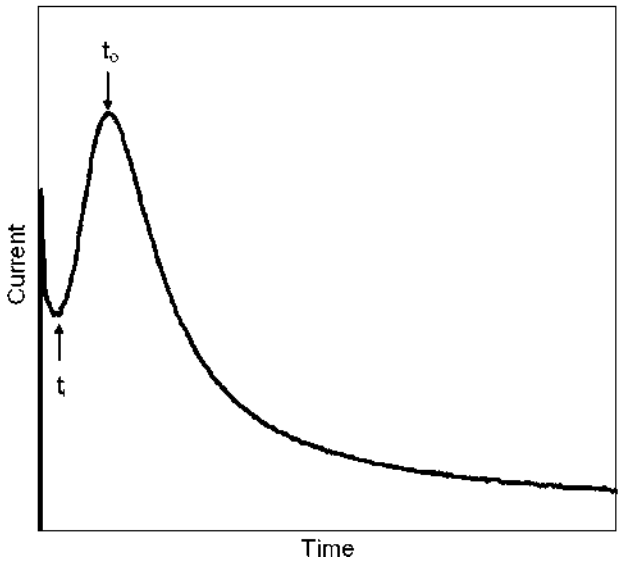

Fig. 10.8 Example of a CO_{ads} stripping time transient recorded at a constant potential for a Pt-based catalyst

observed, which reflects the double layer charging current. This current decays rapidly. Afterward, the current resulting from the $–CO_{ads}$ oxidation reaction to CO_2 is observed. A typical CO_{ads} stripping transient is shown in Fig. 10.8. The time, t_i, needed to observe the increase in the CO_{ads} stripping current reflects the time needed to initiate the recombination reaction between $–CO_{ads}$ and $–OH_{ads}$ sites, i.e.:

$$X - CO_{\text{ads}} + M - OH_{ads} \rightarrow X + \text{M} + CO_2 + H^+ + e^-. \tag{10.33}$$

In (10.33), X stands for the site at which CO is adsorbed. X can be either a Pt or Ru metal site, and M stands for the catalyst site that allows for the formation of $–OH_{ads}$. Depending on the working electrode potential, M is either Ru or Pt. If a potential lower than 0.5 V vs. RHE is used, Pt can be ruled out as a source of active $–OH_{ads}$ sites. After t_i, the current increases reaching a maximum at the time t_o. During the period between t_i and t_o, $–CO_{ads}$ molecules close to an active $–OH_{ads}$ site are oxidized. It is also possible that additional $–OH_{ads}$ sites are formed during this period. After t_o, a decay in current is observed. After t_o, $–CO_{ads}$ molecules near an active $–OH_{ads}$ site have been oxidized, and the recombination reaction (10.33) is limited by the rate, the remaining $–CO_{ads}$ molecules can be transported across the catalyst surface to an active $–OH_{ads}$ site. It is well known that CO_{ads} can be transported across the Pt-based catalyst surface involving free catalyst surface sites, X*, as follows:

$$X - CO_{ads} + X^* \leftrightarrow X + X^* - CO_{ads}. \tag{10.34}$$

It is likely that only Pt catalyst surface sites act as X*. CO does not adsorb on oxide covered Ru, and a free Ru(0) site is likely to act as an $–OH_{ads}$ site. The time between t_o and the total time needed to approach a zero current, hence, reflects a measurement of the separation distance between the remaining $–CO_{ads}$ molecules and the active $–OH_{ads}$ sites. If the surface diffusion coefficient of $–CO_{ads}$ (D_{COads}) is known, this time can be used to estimate the separation distance from the furthest $X–CO_{ads}$ site to an active $–OH_{ads}$ site, as described in [110]. However, not many methods are available for accurate measurements of D_{COads}, and the numbers are often estimates.

The charge, Q_o, passed between t_i and t_o reflects the number of $–CO_{ads}$ and active $–OH_{ads}$ sites that are in close vicinity. The percentage of Q_o over the total CO_{ads} charge of the electrode studied (% Q_o) divided by t_o (% Q_o/t_o) reflects a measurement of the quality of a particular catalyst. A larger % Q_o value indicates a higher the number of $–CO_{ads}$ and$–OH_{ads}$ sites that are in close vicinity. A good catalyst yields a large % Q_o value obtained during a short period of t_o. It follows that a catalyst that shows a large % Q_o/t_o value is a good CO_{ads} oxidation catalyst. This type of analysis has been applied to various Pt–Ru powder catalysts [110].

10.6.3.2 CH_3OH Oxidation Transients

CH_3OH oxidation activities for particular catalysts are typically extracted from current–time transients recorded at a constant potential. As discussed above, the CH_3OH oxidation currents need to be normalized for the electroactive catalyst surface area in order to extract true catalytic activities. It is essential to describe the details of the experiment, as to the potential of the working electrode prior to the recording of the transient, and of course the potential used to record the transient, the CH_3OH concentration and electrolyte solution, and at what time in the transient the CH_3OH oxidation current is recorded. The latter is important, as a CH_3OH oxidation transient does not reach an actual steady-state value. It reaches a so-called pseudo-steady state value after a few minutes. However, the actual CH_3OH oxidation current value decreases at a slow rate over time. This is believed to be due to a slow poisoning of the catalyst surface.

Presumably, a similar analysis of current–time transients as carried out for the CO_{ads} stripping reaction (Sect. 10.6.3.1) could be carried out for the stripping reaction of adsorbed CH_3OH (CH_3OH_{ads}). The CH_3OH is adsorbed from CH_3OH containing electrolyte solutions at low potentials, where the subsequent oxidation reaction of CH_3OH_{ads} is slow. The CH_3OH electrolyte solution can then be replaced by flushing with a CH_3OH free electrolyte solution, while the potential of the working electrode is maintained at the low potential, prior to stepping the potential to more positive values to record the CH_3OH_{ads} stripping transients. This type of study may be somewhat complicated by the fact that less than a monolayer of CH_3OH_{ads} is formed on this catalyst surface. The surface fraction of CH_3OH_{ads} on bulk Pt metal electrodes has been studied decades ago [26]. The CH_3OH was adsorbed as described above. However, instead of stepping the potential positive

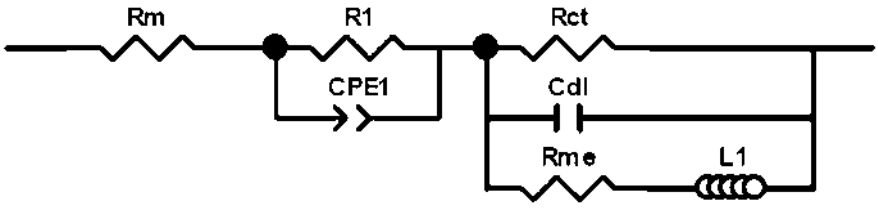

Fig. 10.9 Equivalent circuit (EQC) for the CH_3OH oxidation reaction in the anode layer of a DMFC

to oxidize the CH_3OH_{ads}, the potential was scanned negative into the H_{ads} region, and subsequently in a positive direction across the H_{des} region of the Pt electrode. The CH_3OH_{ads} suppresses the H_{ads} reaction. Therefore, the difference in the $Q_{Hads/des}$ values between a CV scan carried out with and without CH_3OH_{ads} yields a measurement of the fraction of the surface covered with CH_3OH_{ads}.

10.6.4 AC Impedance Spectroscopy

AC impedance spectroscopy has been applied in several studies to either investigate the CH_3OH electrooxidation reaction in electrolyte solutions or in a catalyst layer of an MEA [111, 112]. AC impedance is a very useful technique as it allows for the extraction of a large number of parameters. In the case of the CH_3OH electrooxidation reaction, the charge transfer resistance for the CH_3OH electrooxidation reaction, R_{ct}, has been extracted. The impedance spectra recorded for the CH_3OH electrooxidation reaction also shows an inductance at low frequencies. The inductance (L) has been explained as reflecting the poisoning of the catalyst surface by CH_3OH, e.g., $–CO_{ads}$ formation. The $–CO_{ads}$ is then oxidized at a longer time scale, i.e., at lower frequencies seen in the current lagging the potential, i.e., the inductance. It appears that a very similar equivalent circuit (EQC) describes the AC impedance spectra for the electrooxidation reaction of CH_3OH in electrolyte solutions and in anode catalyst layers of DMFCs. Figure 10.9 shows the EQC describing the CH_3OH oxidation reaction in the anode layer of a DMFC [112]. R_m is the membrane resistance, which is the solution resistance when the CH_3OH oxidation reaction is studied in electrolyte solutions. The origin of R_1 and the constant phase element (CPE_1) have been debated. However, they are specific to AC spectra of a CH_3OH anode measured in a DMFC. C_{dl} is the double layer capacitance and R_{me} and L_1 arise from the $–CO_{ads}$ surface poisoning species seen at lower frequencies in the AC spectra [111].

Acknowledgments The authors wish to thank the editors who have provided them with the opportunity to write this chapter.

Glossary

A	Surface area [cm^2]
AC	Alternating current
α	Symmetry factor
C_{dl}	Double layer capacitance [F]
CPE	Constant phase element
CV	Cyclic voltammogram
D_{COads}	Surface diffusion coefficient of $-CO_{ads}$ [$cm^2\ s^{-1}$]
$DMFC$	Direct methanol fuel cell
E^o	Standard potential [V]
E_a	Activation energy [kJ $mole^{-1}$]
E_{anode}	Anode potential [V]
$E_{cathode}$	Cathode potential [V]
E_{cell}	Cell potential [V]
E_{eq}	Equilibrium potential [V]
EQC	Equivalent circuit
FC	Fuel cell
F	Faraday's constant [A s mol_{e-}^{-1}]
ΔG	Gibb's free energy [J mol^{-1}]
ΔG^o	Gibb's free energy at standard conditions [J mol^{-1}]
$H_{ads/des}$	H adsorption and desorption
I	Current [A]
I_{lim}	Limiting current [A]
IR	IR [Current–resistance, i.e., voltage] drop or Infrared spectroscopy
J	Current density [A cm^{-2}]
J_{lim}	Limiting current density [A cm^{-2}]
J_o	Exchange current density [A cm^{-2}]
$J_{o,mass}$	Exchange current density per catalyst mass limiting current density [A mg_{Pt}^{-1}]
K	Equilibrium constant
L	Inductance [H]
MEA	Membrane electrode assembly
η_{act}	Activation overpotential [V]
η_{an}	Anode activation overpotential [V]
η_{cat}	Cathode activation overpotential [V]
η_{lim}	Potential losses introduced by mass transport limitations [V]
ORR	O_2 reduction reaction
P	Power [W]
P^*	Power density [W cm^{-2}]
P_{max}	Maximal power density [W cm^{-2}]
PEM	Proton exchange membrane
$PEMFC$	Proton electrolyte fuel cell
p	Partial Pressure

pK_a	Negative logarithms of the acid–base constant
R	Gas constant [kJ mol^{-1} K^{-1}] or Resistance [ohm]
rds	Rate-determining step
$Q_{H\text{ads/des}}$	Charge for the $H_{ads/des}$ reaction [C]
Q_o	Charge passed between t_i and t_o in a $–CO_{ads}$ stripping transient [C]
% Q_o	Indication of the number of $–CO_{ads}$ and $–OH_{ads}$ sites in close vicinity [%]
% Q_o/t_o	Measurement of the quality of a particular catalyst [% s^{-1}]
T	Temperature [°C or K]
t_i	Initiation time for $–CO_{ads}$ and $–OH_{ads}$ recombination reaction [s]
t_o	Time needed to reach maximal current in $–CO_{ads}$ stripping transient [s]
R_{ct}	Charge transfer resistance [R]
RHE	Reversible hydrogen electrode
R_m	Resistance of membrane [R]
R_{me}	Resistance related to poisoning of the catalyst surface [R]
SHE	Standard hydrogen electrode

References

1. Scott K, Taama WM, Argyropoulos P (1999) Engineering aspects of the direct methanol fuel cell system. J Power Sources 79:43–59
2. Lamm A, Müller J (2003) System design for transport applications. In: Vielstich W, Lamm A, Gasteiger HA (eds) Handbook of fuel cells fundamentals technology and applications, vol. 4, fuel cell technology and applications: part 2, 1st edn. Wiley, New York
3. Narayanan SR, Valdez TI, Rohatgi N (2003) DMFC system design for portable applications. In: Vielstich W, Lamm A, Gasteiger HA (eds) Handbook of fuel cells fundamentals technology and applications, vol. 4, fuel cell technology and applications: part 2, 1st edn. Wiley, New York
4. Gottesfeld S (2009) Design concepts and durability challenges for mini fuel cells. In: Vielstich W, Lamm A, Gasteiger HA (eds) Handbook of fuel cells fundamentals technology and applications, vol. 6, advances in electrocatalysis, materials, diagnostics and durability: part 2, 1st edn. Wiley, New York
5. Schoenbein FC (1838) Experimental researches in electricity. Phil Trans R Soc Lond 114:1–5
6. Grove WR (1839) On voltaic series and the combination of gases by platinum. Phil Mag J Sci 149:127–130
7. Grove WR (1842) On a gaseous voltaic battery. Phil Mag J Sci 201:417–420
8. Junger EW (1919) Hydrophobieren von potassium hydroxidele mit paraffin. German Patent DRP 348'293
9. Schmid A (1923) Die diffusionsgaselektrode. Ferdinand Enke, Stuttgart
10. Lowde DR, Williams JO, Attwood PA, Bird RJ, McNicol BD, Short RT (1979) Characterization of electro-oxidation catalysts prepared by ion-exchange of platinum salts with surface oxide groups on carbon. J Chem Soc Faraday Trans 1 75:2312–2324
11. Müller J (2009) Field experience with portable DMFC products. In: Vielstich W, Lamm A, Gasteiger HA (eds) Handbook of fuel cells fundamentals technology and applications, vol. 6, advances in electrocatalysis, materials, diagnostics and durability: part 2, 1st edn. Wiley, New York

12. Wasmus S, Wang J-T, Savinell RF (1995) Real-time mass spectrometric investigation to methanol oxidation in a direct methanol fuel cell. J Electrochem Soc 142:3825–3833
13. Fan Q, Pu C, Smotkin ES (1996) In situ Fourier transform infrared-diffuse reflection spectroscopy of direct methanol fuel cell anodes and cathodes. J Electrochem Soc 143:3053–3057
14. Eikerling M, Kornyshev AA (1998) Modelling the performance of the cathode catalyst layer of polymer electrolyte fuel cells. J Electroanal Chem 453:89–106
15. Eikerling M, Kornyshev AA, Kuznetsov AM, Ulstrup J, Walbran S (2001) Mechanisms of proton conductance in polymer electrolyte membranes. J Phys Chem B 105:3646–3662
16. Kim YS, Pivovar BS (2007) Polymer electrolyte membranes for direct methanol fuel cells. In: Zhao T, Kreuer K-D, Nguyen TV (eds) Advances in fuel cells, vol. 1, 1st edn. Elsevier, Oxford
17. Gurau B, Smotkin ES (2002) Methanol crossover in direct methanol fuel cells: a link between power and energy density. J Power Sources 112:339–352
18. Thomas SC, Ren X, Gottesfeld S, Zelenay P (2002) Direct methanol fuel cells: progress in cell performance and cathode research. Electrochim Acta 47:3741–3748
19. Ren X, Zelenay P, Thomas S, Davey J, Gottesfeld S (2000) Recent advances in direct methanol fuel cells at Los Alamos National Laboratory. J Power Sources 86:111–116
20. Breiter MW, Gilman S (1962) Anodic oxidation of methanol on platinum II. Interpretation of potentiostatic current-potential curves in acidic solutions. J Electrochem Soc 109:1009–1104
21. Buck RP, Griffith LR (1962) Voltammetric and chronopotentiometric study of the anodic oxidation of methanol, formaldehyde, and formic acid. J Electrochem Soc 109:1009–1104
22. Giner J (1964) The anodic oxidation of methanol and formic acid and the reductive adsorption of CO_2. Electrochim Acta 9:63–77
23. Liang C, Franklin TC (1964) The electrolytic oxidation of simple aldehydes and alcohols at platinum electrodes. Electrochim Acta 9:517–530
24. Petry OA, Podlovchenko BI, Frumkin AN, Lal H (1965) The behaviour of a platinized-platinum and platinum-ruthenium electrodes in methanol solutions. J Electroanal Chem 10:253–269
25. Podlovchenko BI, Petry A, Frumkin AN, Lal H (1966) The behaviour of a platinized-platinum electrode in solutions of alcohols containing more than one carbon atom, aldehydes and formic acid. J Electroanal Chem 11:12–25
26. Bagotzky VS, Vassilyev YB (1967) Mechanism of electro-oxidation of methanol on the platinum electrode. Electrochim Acta 12:1323–1343
27. Bagotzky VS, Vassilyev YB, Khazova OA (1967) Generalized scheme of chemisorption, electrooxidation and electroreduction of simple organic compounds on platinum group metals. J Electroanal Chem 81:229–238
28. Wieckowski A, Sobkowski J (1975) Comparative study of adsorption and oxidation of formic acid and methanol on platinized electrodes in acidic solutions. J Electroanal Chem 63:365–377
29. Beden B, Lamy C, Bewick A, Kunimatsu K (1981) Electrosorption of methanol on platinum electrodes. IR spectroscopic evidence for adsorbed CO species. J Electroanal Chem 121:343–347
30. Wilhelm S, Iwasita T, Vielstich W (1987) COH and CO as adsorbed intermediates during methanol oxidation on platinum. J Electroanal Chem 238:383–391
31. Christensen PA, Hamnett A, Troughton GL (1993) The role of morphology in the methanol electro-oxidation reaction. J Electroanal Chem 362:207–218
32. Hamnett A (1997) Mechanism and electrocatalysis in the direct methanol fuel cell. Catal Today 38:445–457
33. Ota K, Nakagaway Y, Takahashi M (1984) Reaction products of anodic oxidation of methanol in sulfuric acid solution. J Electroanal Chem 179:179–186

34. Goodenough JB, Hamnett A, Kennedy BJ, Manoharan R, Weeks SA (1988) Methanol oxidation on unsupported and carbon supported Pt + Ru anodes. J Electroanal Chem 240:133–145
35. Bett J, Lundquist J, Washington E, Stonehart P (1973) Platinum crystallite size consideration for electrocatalytic oxygen reduction-I. Electrochim Acta 18:343–348
36. Petrow HG, Allen RJ (1977) Finely particulated colloidal platinum compound and sol for producing the same, and method of preparation of fuel cell electrodes and the like employing the same. US Patent 4,044,193
37. McNicol BD (1981) Electrocatalytic problems associated with the development of direct methanol-air fuel cells. J Electroanal Chem 118:71–118
38. Watanabe M, Uchida M, Motoo S (1986) Applications of the gas diffusion electrode to a backward feed and exhaust (BFE) type methanol anode. J Electroanal Chem 199:311–322
39. Goodenough JB, Hamnett A, Kennedy BJ, Weeks SA (1987) XPS investigation of platinized carbon electrodes for the direct methanol air fuel cell. Electrochim Acta 32:1233–1238
40. Knights SD, Colbow KM, St-Pierre J, Wilkinson D (2004) Aging mechanisms and lifetime of PEFC and DMFC. J Power Sources 127:127–134
41. Fuentes RE, Garcia BL (2008) A Nb-doped TiO_2 electrocatalyst for use in direct methanol fuel cells. ECS Trans 12:239–248
42. Watanabe M, Makoto U, Motoo S (1987) Preparation of highly dispersed Pt + Ru alloy clusters and the activity for the electrooxidation of methanol. J Electroanal Chem 229:395–406
43. Gasteiger HA, Markovic N, Ross PN, Cairns EJ (1994) Temperature-dependent methanol electro-oxidation on well-characterized Pt–Ru alloys. J Electrochem Soc 147:1795–1803
44. Kabbabi A, Faure R, Durand R, Beden B, Hahn F, Leger J-M, Lamy C (1998) In situ FTIRS study of the electrocatalytic oxidation of carbon monoxide and methanol at platinum–ruthenium bulk alloy electrodes. J Electroanal Chem 444:41–53
45. Gurau B, Viswanathan R, Liu R, Lafrenz TJ, Ley KL, Smotkin ES, Reddington E, Sapienza A, Chan BC, Mallouk TE, Sarangapani S (1998) Structural and electrochemical characterization of binary, ternary, and quaternary platinum alloy catalysts for methanol electro-oxidation. J Phys Chem B 102:9997–10003
46. Laine RM, Sellinger A (2003) preparation of supported nano-sized catalyst particles via a polyol process. US Patent 6,551,960 B1
47. Bock C, MacDougall B, LePage Y (2004) Dependence of CH_3OH oxidation activity for a wide range of PtRu alloys. J Electrochem Soc 151:A1269–A1278
48. Wang ZB, Yin GP, Shi PF (2005) Stable Pt–Ru/C catalysts prepared from new precursors by thermal reduction for direct methanol fuel cell. J Electrochem Soc 152:A2406–A2412
49. Raman RK, Shukla AK, Gayen A, Hedge MS, Priolkar KR, Sarode PR, Emura S (2006) Tailoring a Pt–Ru catalyst for enhanced methanol electro-oxidation. J Power Sources 157:45–55
50. Chen L, Guo M, Zhang H-F, Wang Z-D (2006) Characterization and electrocatalytic properties of PtRu/C catalysts prepared by impregnation-reduction method using Nd_2O_3 as dispersing reagent. Electrochim Acta 52:1191–1198
51. Basnayake R, Li Z, Katar S, Zhou W, Rivera H, Smotkin ES, Casadonte DJ Jr, Korzeniewski C (2006) PtRu nanoparticle electrocatalyst with bulk alloy properties prepared through a sonochemical method. Langmuir 22:10446–10450
52. Silva DF, Neto AO, Pino ES, Linardi M, Spinace EV (2007) PtRu/C electrocatalysts prepared using γ-irradiation. J Power Sources 170:303–307
53. Wang D, Zhuang L, Lu J (2007) An alloying-degree-controlling step in the impregnation synthesis of PtRu/C catalysts. J Phys Chem C 111:16416–16422
54. Xu C, Wang L, Mu X, Ding Y (2010) Nanoporous PtRu alloys for electrocatalysis. Langmuir 26:7437–7443
55. Kim MS, Fang B, Chaudhari NK, Song M, Bae T-S, Yu J-S (2010) A highly efficient synthesis approach of supported Pt–Ru catalyst for direct methanol fuel cell. Electrochim Acta 55:4543–4550

56. Onodera T, Suzuki S, Takamori Y, Daimon H (2010) Improved methanol oxidation activity and stability of well-mixed PtRu catalysts synthesized by electroless plating method with addition of chelate ligands. Appl Catal A Gen 379:69–76
57. Avila-Garcia I, Ramirez C, Hallen Lopez JM, Arce Estrada EM (2010) Electrocatalytic activity of nanosized Pt alloys in the methanol oxidation reaction. J Alloys Compd 495:462–465
58. Bonnemann H, Khelashvili G (2010) Efficient fuel cell catalysts emerging from organometallic chemistry. Appl Organomet Chem 24:257–268
59. Davies JC, Bonde J, Logadottir A, Norskov JK, Chorkendorff I (2005) The ligand effect: CO desorption from Pt/Ru catalysts. Fuel Cells 5:429–439
60. Laitinen HA, Enke CK (1960) The electrolytic formation and dissolution of oxide films on platinum. J Electrochem Soc 107:773–781
61. Smith M, Cooper K, Johnson D, Scribner L (2005) Comparison of fuel cell electrolyte resistance measurement. Fuel Cell Mag 5:26–31
62. Cooper KR, Smith M (2006) Electrical test methods for on-line fuel cell ohmic resistance measurement. J Power Sources 160:1088–1095
63. Wippermann K (2008) Topic 5: alcohol fuel Cells-Germany. Performance and durability enhancement for power DMFC, Canadian-German Corporation, NRC-ICPET, Ottawa, ON 4th + 5th Feb
64. Slezak PJ, Wieckowski A (1993) Interfacing surface electrochemistry with solid-state NMR. Characterization of surface CO on polycrystalline platinum. J Magn Reson Ser 102:166–172
65. Friedrich KA, Geyzers KP, Marmann A, Stimming U, Vogel R (1999) Bulk metal electrodeposition in the sub-monolayer regime: Ru on Pt(111). Z Phys Chem 208:137–150
66. Gasteiger HA, Markovic N, Ross PN, Cairns EJ Jr (1994) CO electrooxidation on well-characterized Pt–Ru alloys. J Phys Chem 98:617–625
67. Dinh HN, Ren X, Garzon FH, Zelenay P, Gottesfeld S (2000) Electrocatalysis in direct methanol fuel cells: in-situ probing of PtRu anode catalyst surfaces. J Electroanal Chem 491:222–233
68. Markovic NM, Gasteiger HA, Ross PN Jr, Jiang X, Villegas I, Weaver MJ (1995) Electrooxidation mechanisms of methanol and formic acid on Pt–Ru alloy surfaces. Electrochim Acta 40:91–98
69. Leger J (2001) Mechanistic aspects of methanol oxidation on platinum-based electrocatalysts. J Appl Electrochem 31:767–771
70. Sun SG, Clavilier J (1987) Electrochemical study on the poisoning intermediate formed from methanol dissociation at low index and stepped platinum surfaces. J Electroanal Chem 236:95–112
71. Markovic N, Ross PN (1992) The effect of specific adsorption of ions and underpotential deposition of copper on the electro-oxidation of methanol on platinum single-crystal surfaces. J Electroanal Chem 330:499–520
72. Kita H, Gao Y, Nakato T, Hattori H (1994) Effect of hydrogen sulphate ion on the hydrogen ionization and methanol oxidation reactions on platinum single-crystal electrodes. J Electroanal Chem 373:177–183
73. Herrero E, Franaszczuk WA (1994) Electrochemistry of methanol at low index crystal planes of platinum: an integrated voltammetric and chronoamperometric study. J Phys Chem 98:5074–5083
74. Kinoshita K (1990) Particle size effects for oxygen reduction on highly dispersed platinum in acid electrolytes. J Electrochem Soc 137:845–848
75. Watanabe M, Motoo S (1975) Electrocatalysis by ad-atoms part II. Enhancement of the oxidation of methanol on platinum by ruthenium Ad-atoms. J Electroanal Chem 60:267–273
76. Hadzi-Jordanov KHA, Conway BE (1975) Surface oxidation and H deposition at ruthenium electrodes: resolution of component processes in potential-sweep experiments. J Electroanal Chem 60:359–362

77. LePage Y, Bock C, Rodgers JR (2006) Small step graphs of cell data vs. composition for ccp solid-solution binary alloys: application to the (Pt, Ir), (Pt, Re) and (Pt, Ru) systems. J Alloys Compd 422:164–172
78. Ruban AV, Skriver HL, Norskov JK (1999) Surface segregation energies in transition-metal alloys. Phys Rev B 59:15990–16000
79. Nashner MS, Frenkel AI, Adler DL, Shapley JR, Nuzzo RG (1997) Structural characterization of carbon-supported platinum-ruthenium nanoparticles from the molecular cluster precursor $PtRu_5C(CO)_{16}$. J Am Chem Soc 119(33):7760–7771
80. Hwang BJ, Chen C-H, Sarma LS, Chen J-M, Wang G-R, Tang M-T, Liu D-G, Lee J-F (2006) Probing the formation mechanism and chemical states of carbon-supported Pt–Ru nanoparticles by in situ X-ray absorption spectroscopy. J Phys Chem B 110:6475–6482
81. Kim H, Rabelo de Moraes I, Tremiliosi-Filho G, Haasch R, Wieckowski A (2001) Chemical state of ruthenium submonolayers on a Pt(111) electrode. Surf Sci 474:L203–L212
82. Lee CE, Bergens SH (1998) Deposition of Ru adatoms on Pt using organometallic chemistry. J Electrochem Soc 145:4182–4185
83. Iwasita T, Hoster H, John-Anacker A, Lin WF, Vielstich W (2000) Methanol oxidation on PtRu electrodes. Influence of surface structure and Pt–Ru atom distribution. Langmuir 16:522–529
84. El-Shafei AA, Hoyer R, Kibler LA, Kolb DM (2004) Methanol oxidation on Ru-modified preferentially oriented Pt electrodes in acidic medium. J Electrochem Soc 151:F141–F145
85. Chu D, Gilman S (1996) Methanol electro-oxidation on unsupported Pt–Ru alloys at different temperatures. J Electrochem Soc 143:1685–1690
86. Long JW, Sroud RM, Swider-Lyons KE, Rolison DR (2000) How to make electrocatalysts more active for direct methanol oxidations avoid PtRu bimetallic alloys! J Phys Chem B 104:9772–9776
87. Frelink T, Visscher W, van Veen JAR (1996) Measurement of the Ru surface content of electrocodeposited PtRu electrodes with the electrochemical quartz crystal microbalance: implications for methanol and CO electrooxidation. Langmuir 12:3702–3708
88. Bock C, Collier A, MacDougall B (2005) Active form of Ru for the CH_3OH electro-oxidation reaction: introduction of a simple electrochemical in-situ method. J Electrochem Soc 152 (12):A2291–A2299
89. Piela P, Eickes C, Brosha E, Garzon F, Zelenay P (2004) Ruthenium crossover in direct methanol fuel cell with Pt–Ru black anode. J Electrochem Soc 151:A2053–A2059
90. Valdez TI, Firdosy S, Koel B, Narayanan SR (2006) Investigation of ruthenium dissolution in advanced membrane electrode assemblies for direct methanol based fuel cell stacks. ECS Trans 1:293–303
91. Gancs L, Hakim N, Hult BN, Mukerjee S (2006) Dissolution of Ru from PtRu electrocatalysts and its consequences in DMFCs. ECS Trans 3:607–618
92. Sugawara Y, Yadav AP, Nishikata A, Tsuru T (2008) EQCM study on dissolution of ruthenium in sulfuric acid. J Electrochem Soc 155:B897–B902
93. Capon A, Parsons R (1973) The oxidation of formic acid at noble metal electrodes. Part III: intermediates and mechanism on platinum electrodes. J Electroanal Chem 45:205–231
94. Watanabe M, Motoo S (1975) Electrocatalysis by Ad-atoms. Part I. Enhancement of the oxidation of methanol on platinum and palladium by gold Ad-atoms. J Electroanal Chem 60:259–266
95. Motoo S, Watanabe M (1979) Electrocatalysis by Ad-atoms. Part IV. Enhancement of the oxidation of formic acid on PtAu and AuPt electrodes by bismuth Ad-atoms. J Electroanal Chem 98:203–211
96. Koper MTM, Shubina TE, van Santen RA (2002) Periodic density functional study of CO and OH adsorption on Pt–Ru alloy surfaces: implications for CO tolerant fuel cell catalysts. J Phys Chem B 106:686–692
97. Stolbov S, Ortigoza MA, Adzic R, Rahman TS (2009) High CO tolerance of Pt/Ru nanocatalyst: insight from first principles calculations. J Chem Phys 130:124714

98. Frelink T, Visscher W, van Veen JAR (1995) Particle size effect of carbon-supported platinum catalysts for the electrooxidation of methanol. J Electroanal Chem 382:65–72
99. Rolison DR, Hangans PL, Swider-Lyons KE, Long JW (1999) Role of hydrous ruthenium oxide in Pt–Ru direct methanol fuel cell anode electrocatalysts: the importance of mixed electron/proton conductivity. Langmuir 15:774–779
100. Saida T, Sugimoto W, Takasu Y (2010) Enhanced activity and stability of Pt/C fuel cell anodes by the modification with ruthenium-oxide nanosheets. Electrochim Acta 55:857–864
101. Shen PK, Tseung ACC (1994) Anodic oxidation of methanol on Pt/WO_3 in acidic media. J Electrochem Soc 141:3082–3090
102. Mukerjee S, Urian RC (2002) Bifunctionality in Pt alloy nanocluster electrocatalysts for enhanced methanol oxidation and CO tolerance in PEM fuel cells: electrochemical and in situ synchrotron spectroscopy. Electrochim Acta 47:3219–3231
103. Barczuk PJ, Tsuchiya H, Macak JM, Schmuki P, Szymanska D, Makowski O, Miecznikowski K, Kulesza PJ (2006) Enhancement of the electrocatalytic oxidation of methanol at Pt/Ru nanoparticles immobilized in different WO_3 matrices. Electrochem Solid State Lett 9: E13–E16
104. Yang LX, Bock C, MacDougall B, Park J (2004) The role of the WO_x Ad-component to Pt and PtRu catalysts in the electrochemical CH_3OH oxidation reaction. J Appl Electrochem 34:427–438
105. Bock C, MacDougall B (2003) Novel method for the estimation of the electroactive Pt area. J Electrochem Soc 150:E377–E383
106. Green CL, Kucernak A (2002) Determination of the platinum and ruthenium surface areas in platinum-ruthenium electrocatalysts by underpotential deposition of copper. 2: effect of surface composition on activity. J Phys Chem B 106:11446–11456
107. Metikoš-Huković M, Omanovic S (1998) Electrocatalytic oxidation of preadsorbed monolayer of CO on polycrystalline Pt_{60}-Ru_{40} electrocatalyst: nucleation and growth of oxygen-containing species. J Mol Catal A Chem 136:75–84
108. Jiang J, Kucernak A (2003) Electrooxidation of small organic molecules on mesoporous precious metal catalysts II: CO and methanol on platinum-/ruthenium alloy. J Electroanal Chem 543:187–199
109. Maillard F, Eikerling M, Cherstiouk OV, Schreier S, Savinova E, Stimming U (2004) Size effects on reactivity of Pt nanoparticles in CO monolayer oxidation: the role of surface mobility. Faraday Discuss 125:357–377
110. Bock C, Blakely MA, MacDougall B (2005) Characteristics of adsorbed CO and CH_3OH oxidation reactions for complex Pt/Ru catalyst systems. Electrochim Acta 50:2401–2414
111. Seland F, Tunold R, Harrington DA (2006) Impedance study of methanol oxidation on platinum electrodes. Electrochim Acta 51:3827–3840
112. Hsu N-Y, Yen S-C, Jeng K-T, Chien C-C (2006) Impedance studies and modeling of direct methanol fuel cell anode with interface and porous structure perspectives. J Power Sources 161:232–239

Chapter 11
Some Colloidal Routes to Synthesize Metal Nanoparticle-Based Catalysts

Szilvia Papp, László Kőrösi, Rita Patakfalvi, and Imre Dékány

Abstract Inorganic colloids and especially metal nanoparticles (NPs) have been in the focus of interest for a long time. Their valuable characteristics due to their small size, such as their unique electron structure and extremely large specific surface area, open the way for their practical utilization. By virtue of their high activity and selectivity, they have become widely known as novel type catalysts. Various methods are developed for their preparation, from which colloidal chemical routes became more and more widespread. In this study, some colloidal methods for preparation of metal (Pd, Rh, Au, Ag) NPs and NP-based catalysts are presented. The effects of various polymer molecules, clay lamellae, and reducing agents on the kinetic of NPs formation were investigated. The formation of NPs was followed by transmission electron microscopy (TEM), UV–Vis spectroscopy, isothermal titration calorimetry (ITC), and dynamic light scattering (DLS). NPs were also prepared on clay mineral surface. Interlamellar space of clay minerals is capable of stabilizing colloid particles. Influence of the NPs into the original lamellar structures was examined by X-ray diffraction and small-angle X-ray scattering. The surface oxidation state of the particles sitting on the support in the metal-containing catalysts was determined by XPS.

S. Papp • L. Kőrösi • R. Patakfalvi
Supramolecular and Nanostructured Materials Research Group of the Hungarian Academy of Sciences, University of Szeged, Aradi vértanúk tere 1, H-6720 Szeged, Hungary

I. Dékány (✉)
Supramolecular and Nanostructured Materials Research Group of the Hungarian Academy of Sciences, University of Szeged, Aradi vértanúk tere 1, H-6720 Szeged, Hungary

Department of Physical Chemistry and Materials Science, University of Szeged, Aradi vértanúk tere 1, H-6720 Szeged, Hungary

L. Guczi and A. Erdőhelyi (eds.), *Catalysis for Alternative Energy Generation*,
DOI 10.1007/978-1-4614-0344-9_11,

11.1 Introduction

Scientists have recognized that the physical properties and the chemical reactivity of nanosize particles (NPs) in the various reactions differ from those of macroscopic material. The preparation and characterization of noble metal NPs with outstanding practical importance have moved into the focus of cutting-edge research. A variety of catalytic reactions have been carried out successfully with metal NPs. They are effective catalysts due to their large surface area and a unique combination of reactivity, stability, and selectivity. Their preparation processes are very different depending on the application of catalyst composites. The main expectation from each process is to produce uniform NPs with desired size and shape. Through the careful control of reaction conditions such as time, temperature, and the concentration of reagents and stabilizers, these requirements can be achieved.

Various methods are available for their preparation. It is essential that aggregation be prevented in the course of preparation; in this way, the synthesis of NPs becomes possible. The most widely used techniques make use of the physical limitations of the preparation environment, like in reactions staged inside inverse micelles [1, 2], porous solid materials [3], gels [4], polymers [5], or dendrimers [6]. John Bradley classified reactions that have so far been utilized for the preparation of metal NPs into four groups corresponding to four types of methods [7]. Due to its simplicity, the currently most preferred preparation method is liquid-phase reduction of metal salts. The reducing agent employed is mainly hydrogen gas [8, 9], hydrazine [10, 11], or sodium borohydride [12, 13], but citrate [14, 15], hypophosphorous acid [16], and oxidizable solvents such as alcohols [17, 18] have also been successfully used in synthetic reactions.

In order to be able to control the NPs size and geometry, it is necessary to be acquainted with the mechanism of NPs formation, which is therefore studied by an ever-increasing number of research groups [19–30]. NPs formation can be monitored by a number of different experimental methods. NPs have a characteristic absorption maximum in the visible wavelength range; the simplest method for monitoring their formation is UV–Vis spectroscopy. The Mie theory and its developed versions even allow calculation the size of NPs [31].

According to a mechanism proposed by Watzky and Finke at the end of the 1990s, slow continuous nucleation followed by fast autocatalytic surface growth results in nearly monodisperse size distribution [23]. It has been experimentally proven that stronger reducing agents promote the formation of nuclei with smaller diameters, which then continue to grow [24]. Growth may proceed in two different ways. According to one conception, nuclei formed in the first stage join together, whereas another theory proposes that already solidified particles are further enlarged by collisions with freshly reduced metal ions. The notion accepted in the special literature is that the final size is determined by the relative rates of nucleation and growth. Henglein monitored the stepwise growth of silver clusters by spectroscopic methods [25]. According to his results, growth follows an

autocatalytic reaction pathway that includes adsorption of metal ions and their subsequent reduction on the surface of the zerovalent metal cluster. Caia et al. [26] studied the formation of silver NPs stabilized by hexanethiol as revealed by their UV–Vis absorbance spectra. The characteristic absorption peak of silver was first shifted toward lower wavelengths and later, as the reaction progressed, toward higher wavelengths. It was deduced from these observations that in the first part of the reaction, large particles were formed, which later fell apart to give rise to smaller ones, and later those in turn also started to grow. The reaction could be described by a first-order rate equation. Hoogsteen and Fokkink prepared polymer-stabilized Pd hydrosols, using hypophosphorous acid (H_3PO_2) as reductant [16]. The presence of polyvinyl alcohol (PVA), a compound weakly adsorbing to the surface of palladium had no effect on the kinetics of NPs formation, and particle size was not controllable either. However, polyvinyl pyrrolidone (PVP), a polymer strongly binding to metal surfaces did affect the kinetics of NPs formation and particle size: in its presence, smaller particles were formed. Poly-2-vinyl pyrrolidone (P2VP) affects the process of sol formation not only by its high affinity to metal surfaces, but also, by virtue of its cationic character, through complex formation with the precursor salt $PdCl_4^{2-}$. These authors also established that particle size decreases with increasing the concentrations of the stabilizing polymer and the reducing agent. Ayyappan et al. later made similar observations on other metal sols [27]. Busser et al. studied the strength of the coordination between rhodium ions and various polymers [28]. They found that precursor ions cannot be reduced when the interaction is too strong, whereas a weak coordination leads to the formation of large particles. It was observed in the course of photochemical preparation of silver NPs stabilized by PVP [29] that higher PVP concentrations bring about a faster photochemical reaction: Ag NPs interact with excited C=O* groups, which reduce Ag^+ ions to metallic silver. Esumi et al. investigated the effect of the precursor molecules on the NPs formation [30]. They found that the size distribution of NPs generated by reduction of $Pd(OAc)_2$ was nearly monodisperse (2–4 nm), whereas slow reduction of $Pd(AcAc)_2$ resulted with a relatively wide size distribution.

Block copolymers are widely utilized for the synthesis of metal NPs [32–37]. In selective solvents, amphiphilic diblock copolymers are known to form colloid-sized aggregates or micelles, within which NPs can be synthesized. The size and geometry of the micelles can be controlled through variation of the copolymer composition and block length. A prerequisite for the successful synthesis of metal NPs is that the metal salt should be insoluble in the solvent and enter into interaction (usually of coordination type) with the polymer block forming the micelle core. NP size can be controlled through selection of the block copolymer used, the strength of the reducing agent, and the concentration of the precursor. Antonietti et al. reported that for the slowly reacting triethylsilane (TES), a single NP is usually formed in each micelle, whereas rapid reduction (with $NaBH_4$, superhydrides) leads to the formation of many small NPs per micelle [33]; the former situation was termed cherry morphology, and the latter, raspberry morphology. Spatz et al. stated that slow reduction allows the exchange of polymers during the collision of micelles, leading to an uneven distribution of the NP [34].

Liveri et al. performed calorimetric measurements for thermodynamic studies on the formation of NPs [38–41]. They used microemulsions for the preparation of NPs because they could synthesize NPs of controlled size within the aqueous droplets of w/o microemulsions. For example, they studied the formation of micellar microphases in Aerosol OT reverse microemulsions [38] and synthesized palladium NPs in water/AOT/*n*-heptane microemulsions [39]. They established that the energetic state of Pd NPs in microemulsions is entirely different from that in the aqueous phase. According to their experiments, the heat of formation is a function of particle size and the enthalpy of formation is dependent on the diameter of the microemulsion droplet. They also determined that the duration of nucleation is a few seconds; NPs growth, however, takes place on a time scale of minutes. Enthalpies of formation are exothermic, i.e., the formation of NPs; in other words, the reduction of Pd^{2+} ions is an exothermic process. The extent of exothermicity increases with the crystal size of the NPs. The highest heat of formation was measured in pure water (ca. −400 to −500 kJ/mol).

There is nowadays an ever-increasing need for metal catalysts on solid supports. Many different physical methods (pulse laser evaporation, electron beam lithography) and chemical procedures are available for the preparation of supported catalysts. These are mainly prepared by the impregnation technique, preferred due to its simplicity. In the course of the procedure, the metallic precursor is first impregnated on the support and later reduced. The impregnation technique, however, does not allow control of the size, morphology, and surface distribution of NPs. Preparation of NPs by colloidal chemical methods is becoming more and more widespread. One of the most practical of these is the preparation of metal sols and their deposition on supports. At the first stage of the procedure, a stabilized suspension of metal NPs is produced by reduction, the NPs are next bound to a support, and, finally, the product is washed. Bönnemann et al. synthesized supported bimetal Pd–Pt catalyst by adsorption of metal organosol stabilized by quaternary ammonium salts on activated carbon [42]. Pd–organoclay was prepared by the cation-exchange reaction between sodium montmorillonite and tetradecyltrimethylammonium-stabilized palladium hydrosol [43]. Reetz et al. applied electrochemically obtained colloids on charcoal, silica, and alumina supports using two different methods [44, 45]. He added the support to the reaction medium either in the course of NPs formation or after the completion of the electrochemical reaction. He established by transmission electron microscopy (TEM) of the support-bound particles that neither their structure nor their size was altered during adsorption in either case. Wang et al. bound PVP- and PVA-stabilized Pd, Pt, and Rh NPs to silica surfaces [46, 47]. They interpret binding as joint adsorption of the polymer and the metal NPs. Polymer adsorption is due to hydrogen bonding with the hydroxyl groups of silica.

The so-called solid–liquid interface nanoreactor technique [also known as "controlled colloidal synthesis" (CCS)] enables in situ formation and stabilization of metal NPs on the surface of the support [48–51]. The procedure consists of adsorbing the precursor ions of the nanocrystalline material in the interfacial adsorption layer of solid particles (i.e., about 1-nm-thick lamellae) dispersed in

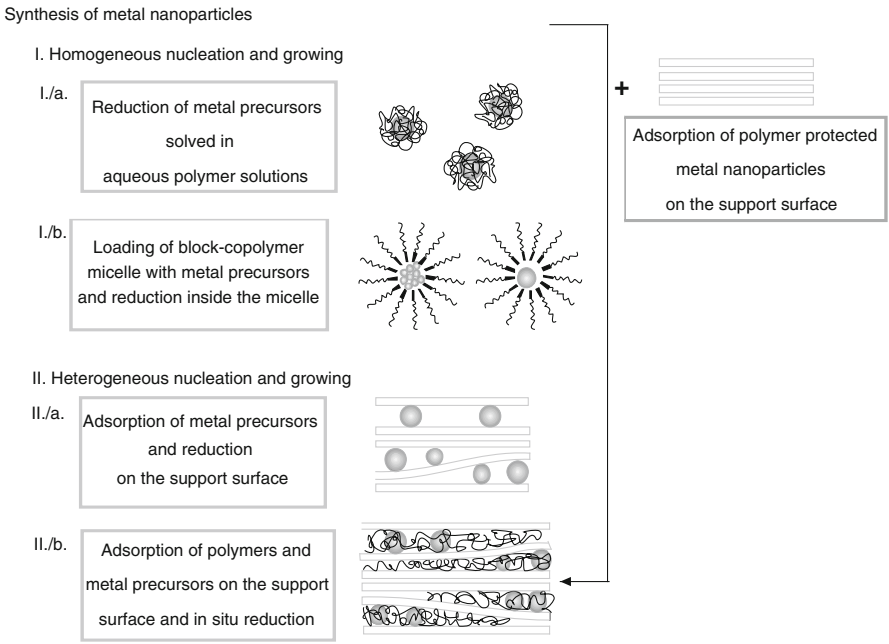

Fig. 11.1 Applied synthesis methods for metal NPs preparation

liquid phase, and the synthesis is carried out at the solid–liquid interface by introducing the reducing agent. Layer silicate minerals with large internal surfaces, readily swelling in aqueous media, lend themselves well to the preparation of particles with diameters of a few nanometers not only on their surfaces but—under suitable conditions—also within their interlamellar space. The NPs can be grown attached to the surface, in well controllable number and size between the silicate layers. Király et al. synthesized Pd NPs (2–14 nm) in situ in organophilized montmorillonite (HDAM) in an ethanol–toluene binary mixture [50]. After the establishment of the adsorption equilibrium, 1% $Pd(OAc)_2$ toluene solution was added to the system. At the appropriate ethanol/toluene ratio, ethanol is preferentially adsorbed in the interlamellar space (acting as a nanophase reactor) and reduces Pd^{2+} ions transported there by diffusion. A similar procedure was used for the preparation of Pd subcolloids measuring 4–10 nm in diameter on pillared clay minerals [51].

In the work described here, we studied the formation of noble metal NPs in homogeneous phase and on the surface of supports. Our aim was to study the effects of metal ion and reducing agent concentrations and of the presence of polymers on the ratio of the rates of nucleation and nucleus growth by spectrophotometrically monitoring the formation of polymer-stabilized sols in aqueous media. In addition, we also investigated the kinetics of heterogeneous nucleation in optically transparent hectorite suspensions. The applied synthesis methods for metal NPs are presented in Fig. 11.1.

11.2 Metal NPs Formation in Polymer Solution

11.2.1 Kinetic Analysis of the Formation of Palladium NPs by Homogeneous Nucleation in Polymer Solution

Polymer-stabilized particles with a diameter of a few nanometers were grown in aqueous medium. Our aim was to study the effect of polymer and metal ion concentrations on the ratio of the rates of nucleation and particle growth. Palladium ions were reduced with hydrazine, and the NPs formation was followed by UV–Vis spectroscopy. Two different polymers were used to stabilize the Pd nanoparticles: [poly(*N*-vinyl-2-pyrrolidone) (PVP, Mw $= 4 \times 10^4$)] and [poly(sodium 4-styrenesulfonate) (PSSNa, Mw $= 7 \times 10^4$)]. Hydrazine solution was injected to the appropriate mixture of polymer and $PdCl_2$ (acidic) solution under constant stirring [52]. Changes in the spectrum was recorded by the diode array detector every 1–2 s for 10 min.

Since there is no peak characteristic of palladium NPs, their formation can be monitored by following the decrease in precursor ion concentration or the increase in absorbance at higher wavelengths. The increase in absorbance indicates an increase in the number and size of the NPs formed. Because of the noise at the maximum, we chose the latter method. Accordingly, we characterized NPs formation by the increase in absorbance values measured at $\lambda = 600$ nm. Kinetic curves do not allow differentiation of nucleation and nucleus growth. We characterized the rate of the process as a whole by the slope of the initial section of the absorbance versus time function, which we term apparent kinetic constant (k^*). The calculated kinetic parameters are presented in Table 11.1.

The reduction of palladium ions is completed instantaneously in the absence of polymer, and later, the spectrum shows hardly any change. Absorbance at wavelengths above 250 nm is significantly increased, indicating the formation of aggregated palladium NPs. The apparent kinetic constant of NPs formation is $k^* = 0{,}098\ s^{-1}$. TEM images show 6–20-nm aggregates consisting of individual NPs with an average diameter of 2.1 nm.

When using PVP as stabilizer, the spectrum displayed in Fig. 11.2 is obtained. Figure 11.3 shows that the initial rate is much lower than that of reduction without stabilizer. Absorbance does not increase after 40 s ($A = 0.104$) and stays below the value measured without stabilizer ($A = 0.137$). Average particle diameter calculated from TEM analysis is 3.8 nm (Fig. 11.4). This means that the PVP molecule is capable of strongly binding to the metal surface and inhibits growth by collision.

Table 11.1 Composition of polymer-stabilized Pd sols, kinetic parameters, and particle diameter

Stabilizer and concentration ($g/100\ cm^3$)		$c^0_{Pd^{2+}}$ ($mmol/dm^3$)	Polymer/Pd ratio	k^* (s^{-1})	$\tau_{1/2}$ (s)
–	–	0.075	–	0.098	7.07
PVP	0.5	0.075	4.67×10^4	0.0065	106.64
PSSNa	0.5	0.075	2.52×10^4	0.0028	247.55

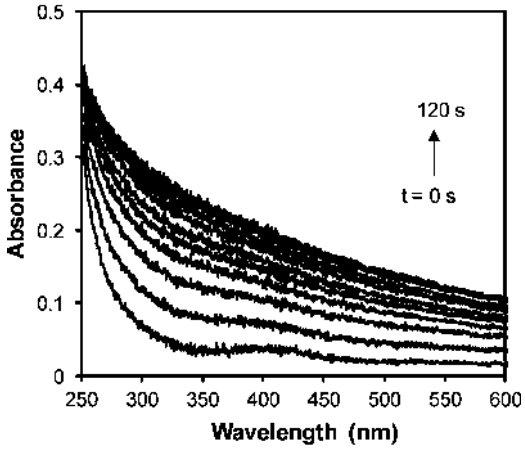

Fig. 11.2 Formation of Pd NPs stabilized with PVP followed up by UV–Vis spectroscopy (see [52])

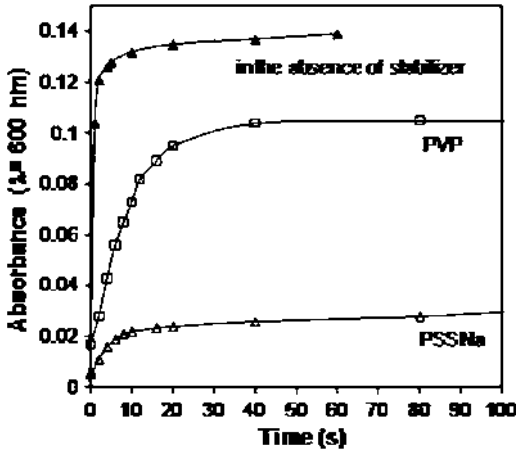

Fig. 11.3 Absorbance ($\lambda = 600$ nm) versus time curves of Pd NPs stabilized by PVP and PSSNa ($c_{\text{stabilizer}} = 0.5$ g/100 cm^3 and $c_{Pd^{2+}} = 0.038$ mmol/dm^3) (see [52])

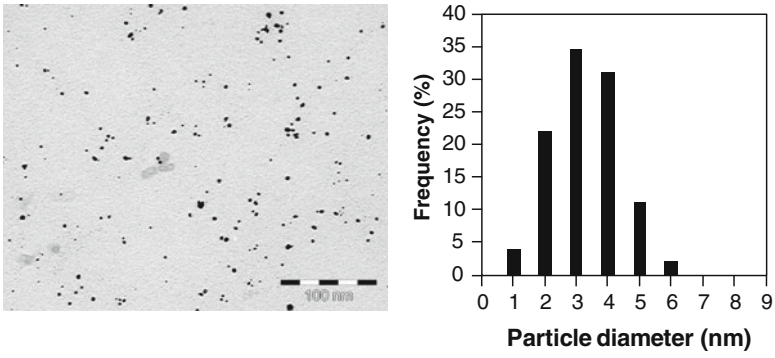

Fig. 11.4 TEM image and particle-size distribution of PVP-stabilized Pd nanosol

The effect of the negatively charged PSS^- molecules on the kinetics of NPs formation was also assessed. The initial spectrum was similar to that obtained with PVP, but reduction was much slower. The value of the apparent rate constant was considerably lower ($k^* = 0.0065 \rightarrow 0.0028\ s^{-1}$). The rise of the spectrum at higher wavelengths was less pronounced, i.e., fewer and smaller NPs were formed.

The role of polymers (PVP and PSSNa) was studied in homogeneous nucleation experiments. The polymers studied are capable of stabilizing the nascent metal particles. PSSNa is more effective than PVP in decreasing the rate of reduction.

11.2.2 Kinetic Analysis of the Homogeneous Nucleation of Silver NPs

The formation of Ag nanoparticles synthesized by homogeneous nucleation, stabilized by polymer (PVP), was monitored by UV–Vis spectrophotometry and TEM. Our aim was to differentiate between the two main phases of particle formation, i.e., nucleation and growth and to characterize their rates with the help of appropriate kinetic equations.

Hydroquinone is one of the relatively milder reductants used for the reduction of silver ions. At appropriately selected hydroquinone concentrations, the rate of NPs formation and thereby the size of the generated NPs can be controlled. We used Na citrate and PVP to slow the reaction and to act as stabilizer.

From the moment of adding hydroquinone to the reaction mixture of $AgNO_3$, Na citrate, and polymer solution, the absorption spectra were recorded [53, 54]. Absorption spectra of an Ag sol containing 0.07 g/100 cm^3 PVP recorded every minute for 20 min are shown in Fig. 11.5. The initial phase of the reaction is very fast; after about 20 min, particle formation slows down. The wavelength of the maximum of the absorption band of silver ($\lambda = 420$ nm) is not altered in the course of the reaction.

It can also be observed that the spectra of Ag sols prepared in PVP solutions are less symmetrical (Fig. 11.6). The spectrum of the sol prepared in 0.5 g/100 cm^3 PVP displays a shoulder in the higher wavelength range, indicating the presence of larger, aggregated particles. Polymer molecules join individual particles into larger aggregates.

For a kinetic characterization of NPs formation, absorbances measured at 420 nm were plotted against time at several polymer concentrations (Fig. 11.7). The course of the functions reveals that a slow induction process takes place first and later the process is accelerated. In the case of PVP, the process can be considered as complete in about 25 min for each sol. We assume that the first, relatively slow stage corresponds to nucleation, which does not bring about any considerable increase in absorbance. After 5–8 min, the faster process already involves nucleus growth. This assumption is also in accordance with the effect of polymer concentration. It is clear that, due to kinetic and steric inhibition by polymer chains present in the solution, polymer addition slows down both the formation and the growth of NPs.

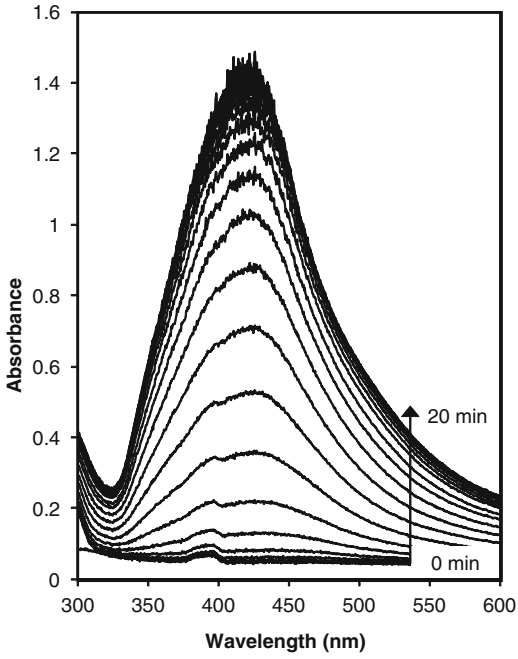

Fig. 11.5 UV–Vis spectra during the synthesis of Ag NPs stabilized by 0.07 g/100 cm^3 PVP solution. The spectra were recorded every minute (see [53])

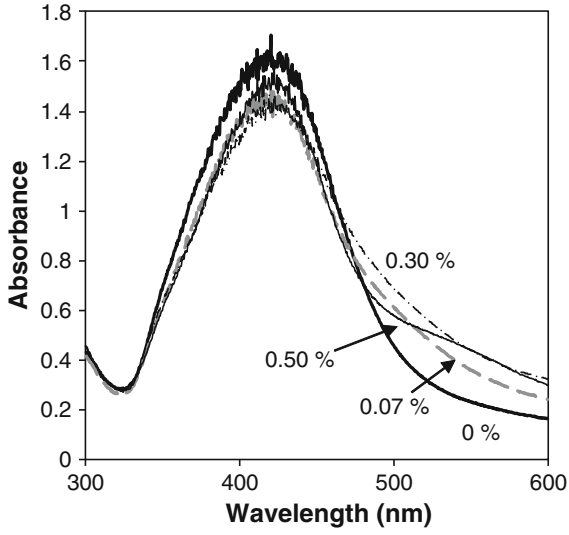

Fig. 11.6 UV–Vis spectra of Ag NPs stabilized at different PVP concentrations after 30 min reaction time (see [53])

Average particle sizes determined from electron micrographs are listed in Table 11.2. In the absence of polymer, aggregated particles with an average diameter of 9.3 nm are observed (Fig. 11.8). The sol is quite polydisperse. In the presence of polymer stabilizer, the average particle size decreases and the distribution is less polydisperse. The size of Ag NPs decreases with increasing polymer

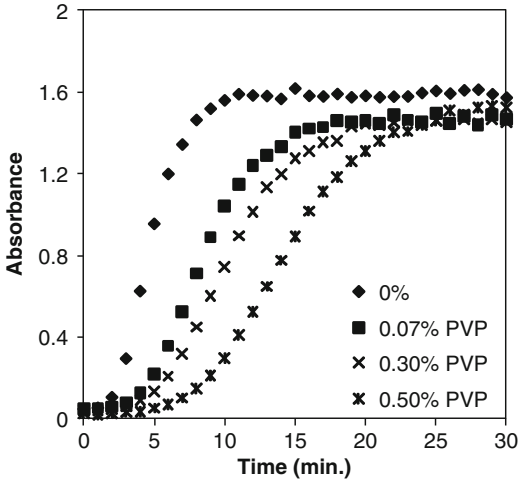

Fig. 11.7 Time course of absorbance at $\lambda = 422$ nm: Ag NPs stabilized at various PVP concentrations (see [53])

Table 11.2 Average particle size and apparent rate constants of Ag NPs formation at different polymer concentrations (k_a, k_1, k_2)

PVP concentration (%)	d_{TEM} (nm)	$k_a \times 10^3$ (s^{-1})	$k_1 \times 10^4$ (s^{-1})	k_2 ($M^{-1}\ s^{-1}$)	$(k_2/k_1) \times 10^{-4}$ (M^{-1})
0	9.3 ± 3.9	15.2	2.19	96.99	44
0.07	3.5 ± 1.5	8.3	2.22	50.37	23
0.19	2.9 ± 0.7	8.8	1.74	55.64	32
0.3	2.7 ± 0.8	7.1	1.6	45.86	29
0.5	5.0 ± 2.1	6.2	0.45	41.35	91.8

concentrations, although aggregated particles are also observed. This aggregation could already be predicted from the absorption spectra (Fig. 11.6).

The sigmoid course of the kinetic curves in Fig. 11.7, starting with a slow induction period, sharply rising, and finally reaching saturation, indicates an autocatalytic reaction [55]. If, in our case, the process is indeed autocatalytic, it follows that the function quantitatively describing the progress of reduction, $\ln[a/(1-a)]$ (where $a = A_t/A_\infty$ and A_t and A_∞ are maximum absorbances at t and ∞, respectively), changes in a linear fashion in time [55]. The functions $\ln[a/(1-a)]$ versus t are presented in Fig. 11.9. Thus, the formation of Ag NPs is indeed autocatalytic up to a certain conversion ratio.

The apparent rate constant of the autocatalytic process (k_a) was determined from the slopes of the $\ln[a/(1-a)]$ versus t functions (k_a) (Table 11.2). The value of the rate constant is the highest in the case of the sol without polymer ($15.2 \times 10^{-3}\ s^{-1}$), as already shown by the absorbance versus time function. The values of k_a for PVP-containing sols are lower than that for the polymer-free sol. Increasing polymer concentration results in a decrease in the rate constant ($8.3 \times 10^{-3}\ s^{-1} \rightarrow 6.2 \times 10^{-3}\ s^{-1}$).

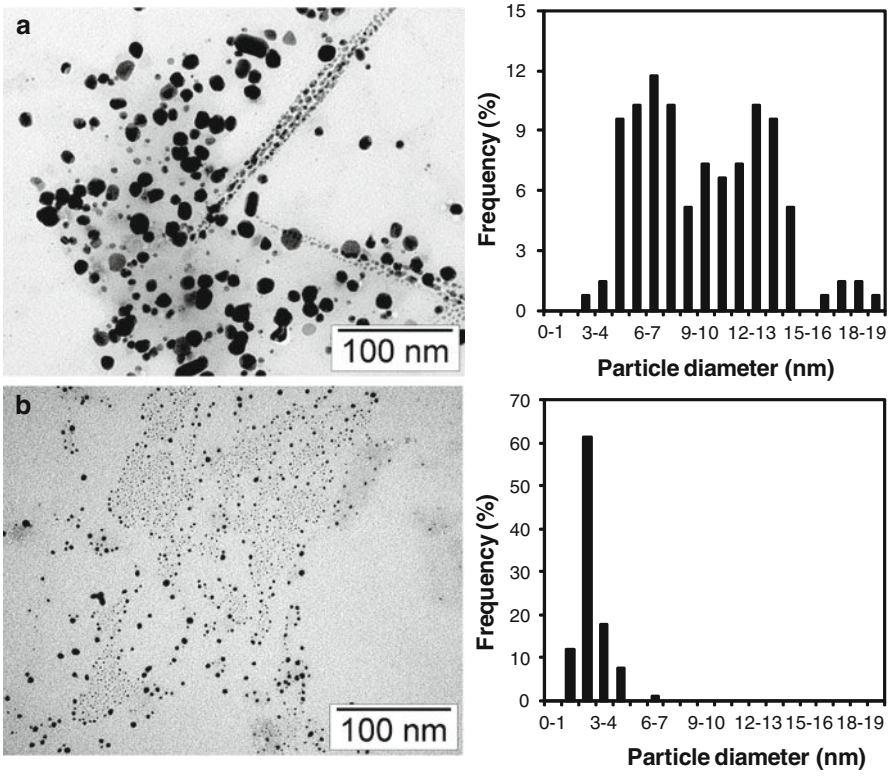

Fig. 11.8 Transmission electron micrographs and particle size distributions of Ag NPs prepared (**a**) without polymer, (**b**) stabilized with 0.3 g/100 cm^3 PVP (see [53])

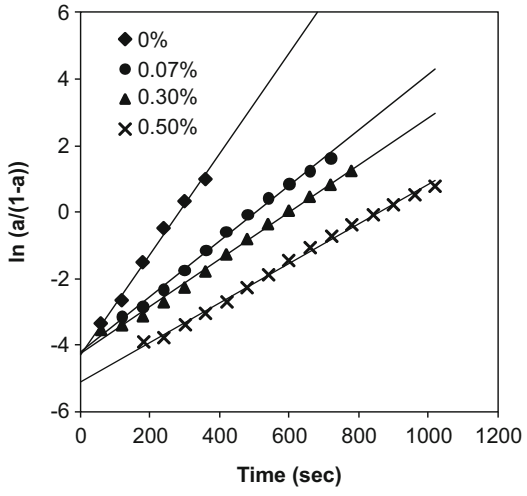

Fig. 11.9 Plots of $\ln[a/(1-a)]$ as a function of reaction time (see [54])

In the case of sols, the size, the size distribution, and the structure of the particles formed depend on the relative rates of nucleation and growth. Although the calculations above yield information on the kinetics of particle formation, the two main phases could not be differentiated. Watzky and Finke [23] prepared Ir nanoclusters by H_2 reduction. The kinetic curve of the reaction was also sigmoid, i.e., an autocatalytic process took place. The authors proposed two important pseudo-first-rate steps for the interpretation of their result:

$$A \xrightarrow{k_1} B,$$

corresponding to a slow, continuous nucleation. This is followed by rapid, autocatalytic surface growth:

$$A + B \xrightarrow{k_2} 2B.$$

A kinetic equation including the two rate constants (k_1, k_2) and the concentrations of A, A_0, and B can be formulated for the description of the entire process [54]. Derivation and linearization of the rate equation yields the following relationship:

$$f(t) = \ln\left[\frac{[A]_0 - [A]}{[A]}\right] = \ln\left[\frac{k_1}{k_2[A]}\right] + k_2[A]_0 t.$$

Thus, representation of $f(t) = \ln\left[\frac{[A]_0 - [A]}{[A]}\right]$ as a function of time allows calculation of the apparent rate constants from the intersection and the slope.

In our case, the nucleation process was $nAg \rightarrow Ag_n$ and growth was $Ag + Ag_n \rightarrow Ag_{n+1}$. The apparent rate constants (k_1 and k_2, respectively) are listed in Table 11.2 [54].

The rate of nucleation was decreased by PVP. The value of the rate constant k_2 is the highest in the absence of polymer; in other words, growth was inhibited by the presence of polymer. The ratio of the two rate constants allows estimation of particle size and size distribution. When growth rate was considerably higher than nucleation rate, the size distribution of the particles will probably be polydisperse.

In order to demonstrate that nucleation and growth can indeed be differentiated on the basis of absorption spectra, the reaction was frozen at certain time points and particle size was determined by TEM. In order to verify that the process monitored by spectrophotometry was indeed nucleation and nucleus growth, we plotted the kinetic curve of the formation of a sol containing 0.5 g/100 cm^3 PVP and average particle sizes on the same diagram (Fig. 11.10). At first glance, the result is surprising: the increase in particle size corresponds to the increase in absorbance.

Based on the kinetic functions, it was established that reduction is an autocatalytic process: a slow, continuous nucleation is followed by rapid, autocatalytic particle growth. The presence of polymer hindered the nucleation and decreased the rate of growth. Slower nucleation and faster growth indicated larger particle size and polydisperse size distribution.

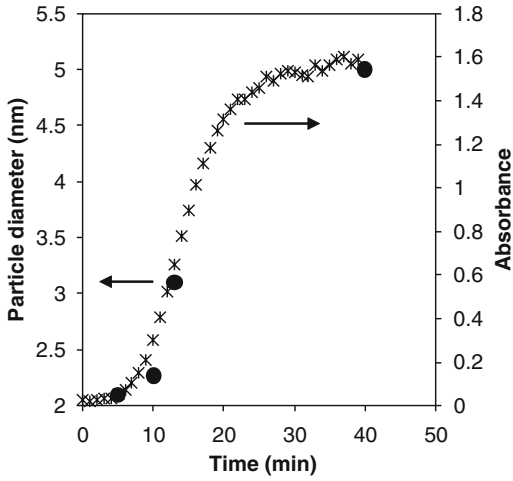

Fig. 11.10 Average particle diameters (*filled circle*) and absorbance values at $\lambda = 422$ nm (*asterisk*) as a function of reaction time. Ag sol stabilized by 0.50 g/100 cm^3 PVP (see [54])

11.2.3 Nucleation and Growth of Silver NPs Monitored by Titration Microcalorimetry

The nucleation and the growth of Ag NPs were followed by titration microcalorimeter. Silver ions were reduced with hydroquinone in aqueous media, and the NPs were stabilized by Na citrate. We examined how changes in the concentrations of the Ag^+ precursor ions and the reducing agent affect the enthalpy of formation.

In our experiments, the reducing agent hydroquinone was added to $AgNO_3$ solutions of various concentrations in order to observe whether the formation of Ag NPs was an energetically favored process. Figure 11.11a shows the enthalpogram of 4 mM $AgNO_3$ solution during the addition of 10×50 µl of reducing agent ($[Ag^+]/[\text{hydroquinone}] = 14$). When the reducing agent was added gradually, in hourly portions under constant stirring, increasingly larger endothermic heat effects were observed. The enthalpogram of mixing was recorded by titration experiment of Na citrate and hydroquinone (Fig. 11.11b).

When $AgNO_3$ solution of a higher concentration (e.g., 10 mM) was titrated in the calorimeter with 40 mM hydroquinone ($[Ag^+]/[\text{hydroquinone}] = 0.875$), exothermic heat effects were obtained already at the initial stages of the experiment (Fig. 11.12).

The total enthalpy changes measured by calorimetry were fulfilled in the following way:

$$\Delta H_{\text{total}} = \Delta H_{\text{nucl}} + \Delta H_{\text{mix}},$$

where ΔH_{nucl} is the enthalpy of particle formation (nucleation) and ΔH_{mix} is the enthalpy of mixing in the reduction (titration) process. When the values of ΔH_{mix} are known from separate measurements, the value of $\Delta H_{\text{nucl}} = \Delta H_{\text{total}} - \Delta H_{\text{mix}}$ can be calculated in every reduction step. After adding these enthalpy values, the

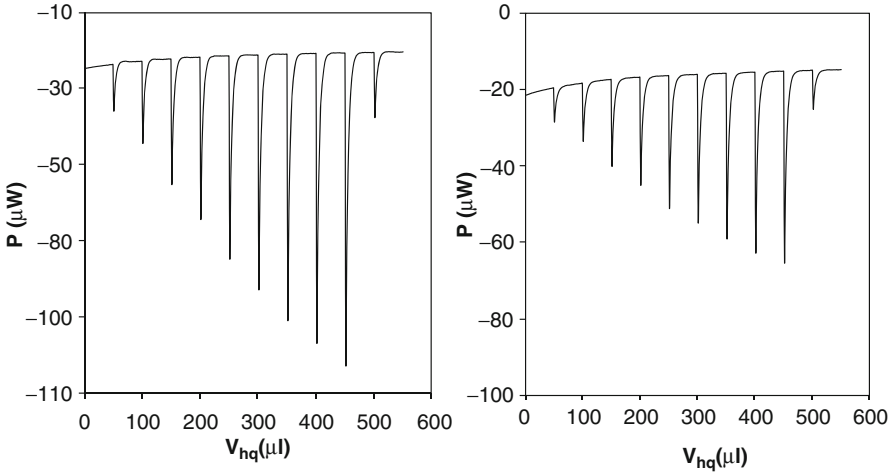

Fig. 11.11 (**a**) Typical enthalpogram of the formation of Ag NPs, $[Ag^+]/[hq] = 14$ (10×50 μl 1 mM hydroquinone solution is added to 1.75 cm^3 4 mM $AgNO_3$ and 0.25 cm^3 10 mM Na citrate) (see [41]). (**b**) Typical enthalpogram of the mixing of the components (10×50 μl 1 mM hydroquinone solution is added to 1.75 cm^3 water and 0.25 cm^3 10 mM Na citrate) (see [41])

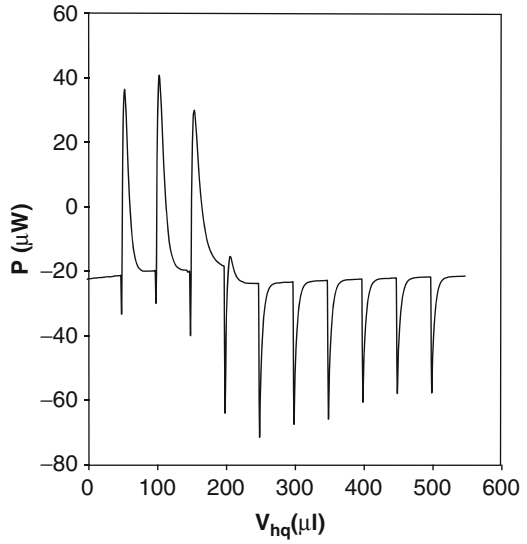

Fig. 11.12 Enthalpogram of the formation of larger, aggregated NPs, $[Ag^+]/[hq] = 0.875$ (10×50 μl 40 mM hydroquinone solution is added to 1.75 cm^3 10 mM $AgNO_3$ and 0.25 cm^3 10 mM Na citrate) (see [41])

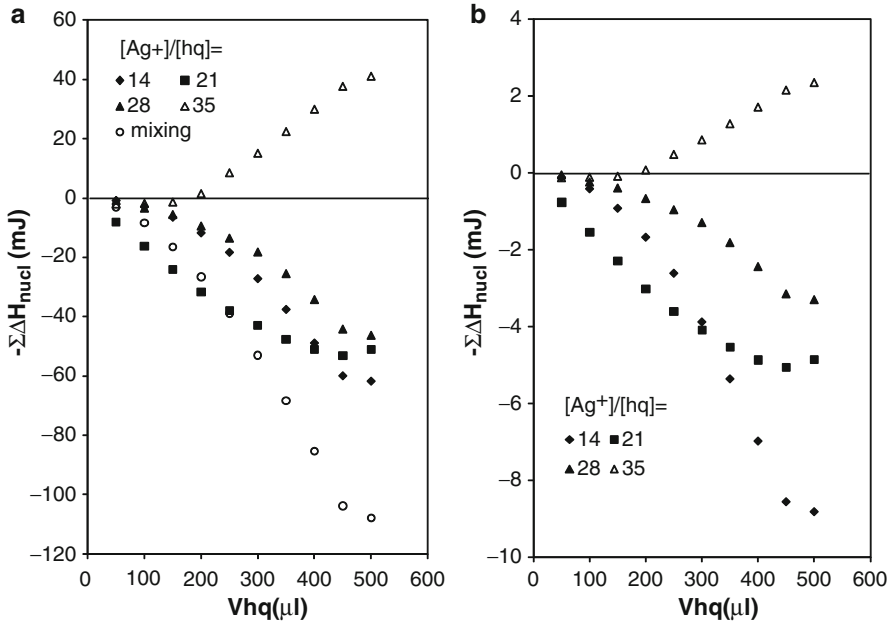

Fig. 11.13 (**a**) The nucleation enthalpy as a function of addition of hydroquinone (see [41]). (**b**) The molar enthalpy of reduction of Ag NPs as a function of the reducing agent (see [41])

integral enthalpy $\Sigma\Delta H_{\text{nucl}} = \text{f}\,(V_{\text{hq}})$ functions showing the change in enthalpy due to the addition of hydroquinone can be drawn up (Fig. 11.15). It is clearly seen that if a maximum of 0.5 cm^3 of 1 mM hydroquinone is added to 10 mM Na-citrate solution, the enthalpy of mixing (ΔH_{mix}) brings about a maximally endothermic change in enthalpy, −110 mJ, in the calorimeter. When samples with increasing $AgNO_3$ concentrations were reduced, the integral enthalpy of reduction increased with the addition of hydroquinone; however, the magnitude of the endothermic effects decreased. When 10 mM $AgNO_3$ solution was reduced ($[Ag^+]$/[hydroquinone] = 35), the values of the net integral enthalpy of reduction already fell into the exothermic range, indicating that at higher hydroquinone concentrations, the process of reduction produced an exothermic heat effect. When the data measured were normalized to the amount of silver ions presented in the solution, the resulting curve showed the molar enthalpy of reduction of silver as a function of the concentration of the reducing agent (Fig. 11.13b).

As shown in Fig. 11.14, this ratio (whose value varies in the range of 1–35) as a function of Ag^+ precursor concentration had a minimum with increasing Ag^+ precursor concentration and reached into the exothermic range. At precursor/reducing agent ratio = 28–35, aggregates of large Ag NPs (particle diameter 15–20 nm) were already formed.

Based on the experimental evidence above, the formation of NPs as monitored by calorimetry can be divided into three stages. In stage 1, silver ions were turned

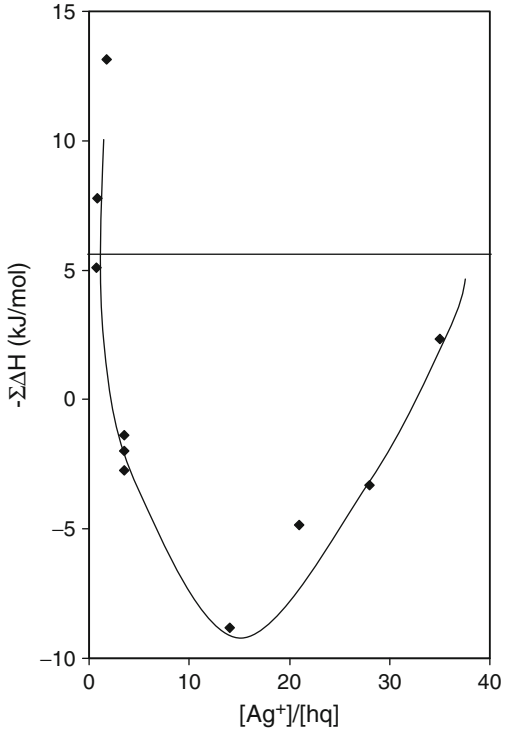

Fig. 11.14 The molar enthalpy as a function of the $[Ag^+]/[hq]$ ratio (see [41])

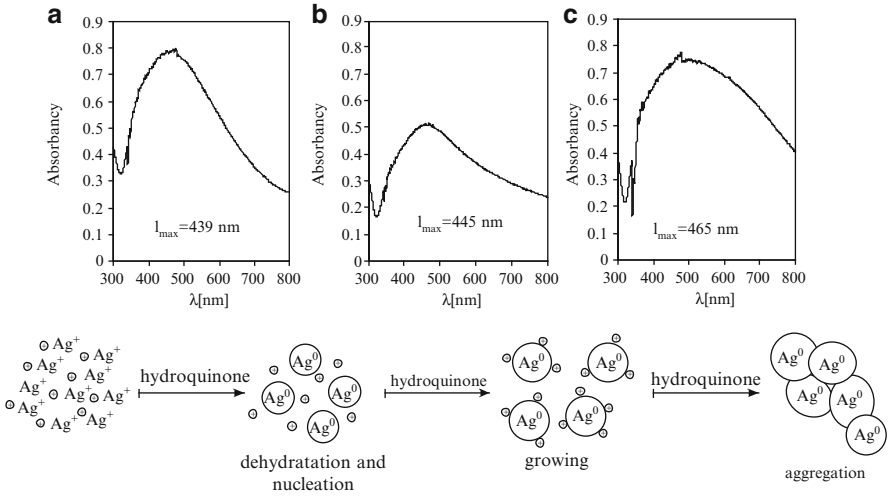

Fig. 11.15 Schematic picture and UV–Vis spectra of the formation of Ag NPs (**a**) $[Ag^+]/[hq] = 14$, (**b**) $[Ag^+]/[hq] = 21$, and (**c**) $[Ag^+]/[hq] = 35$ (see [41])

into metallic silver clusters by the effect of the reducing agent, a process that can be considered as nucleation (Fig. 11.15a). The nucleation was associated with the dehydration of silver ions and the enthalpy change of which was endothermic. This heat effect was insignificant; however, the enthalpy requirement of dehydration, 451.9 kJ/mol [56], also had to be taken into consideration. When the concentration of precursor ions was further increased, nucleation was followed by particle growth and heat effects detectable by calorimetry were shifted to the endothermic direction (Fig. 11.5b). This was also demonstrated by the UV–Vis absorption spectra recorded at various concentrations. When the Ag/hydroquinone ratio was further increased, the particles began to aggregate in spite of the fact that in every case, the stabilizer Na citrate was present in the solution (Fig. 11.5c, $\lambda = 465$ nm). Coagulation of Ag NPs leading to the appearance of larger aggregates causes heat release; the process was exothermic, which means that this effect again overcompensated the endothermic effect associated with the dehydration of the large amount of Ag^+ ions present (10 mM). The processes of nucleation, growth, and aggregation brought about by the addition of the reducing agent hydroquinone can be observed within a given experimental sequence. TEM pictures show that nucleation dominated after the addition of up to 2×50 µl hydroquinone and the average particle diameter was $d = 2.6$ nm. Next, the addition of 6×50 µl hydroquinone initiated particle growth, and $d = 4.1$ nm. After the addition of 8×50 µl reducing agent, the particles were aggregated, and $d = 7.8$ nm.

From microcalorimetrical experiment, it was established that nucleation is an exothermic process and heat effects are basically determined by the ratio of silver ions to hydroquinone. The process of nanoparticle formation was divided to three phases: the nucleation phase is exothermic, the growth phase is endothermic, and further addition of the reducing agent results in the aggregation of silver nanoparticles, which produces a second exothermic heat effect.

11.2.4 *Formation of Gold NPs in Diblock Copolymer Micelles with Various Reducing Agents*

In selective solvents, amphiphilic diblock copolymers can form micelles, within which NPs can be synthesized. Au NPs were prepared by the reduction of $HAuCl_4$ acid incorporated into the polar core of poly(styrene)-*block*-poly(2-vinylpyridine) (PS-*b*-P2VP) copolymer micelles dissolved in toluene. The formation of Au NPs was controlled by using three reducing agents with different strengths: hydrazine (HA), triethylsilane (TES), and potassium triethylborohydride (PTB). The formation of Au NPs was followed by TEM, UV–Vis spectroscopy, isothermal titration calorimetry (ITC), and dynamic light scattering (DLS) [57].

The stock solution of the block copolymer micelles loaded with tetrachloroauric acid (gold ion-loaded micellar solution: GILMS) was prepared as described by Mössmer et al. [37]. A 0.5 wt% solution of PS(350)-*b*-P2VP(50) block copolymer

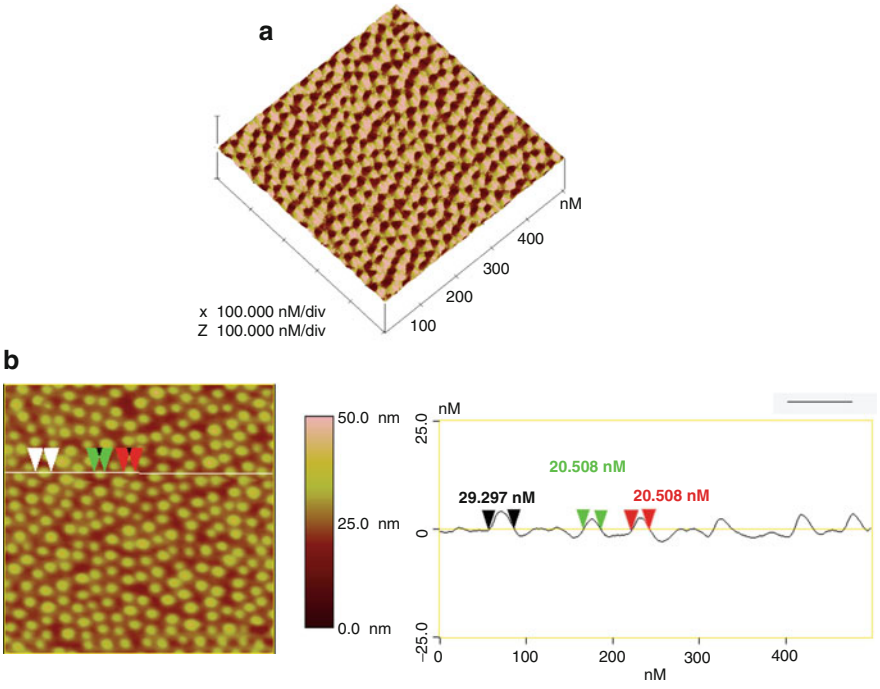

Fig. 11.16 (**a**) AFM image (1 μm × 1 μm) and (**b**) the cross-sectional analysis of a monomicellar film cast from GILMS onto a P-doped Si wafer (see [57])

in dry toluene (unloaded micellar solution: ULMS) was mixed with 0.5 equivalent of $HAuCl_4 \cdot 3H_2O$ per pyridine unit. This transparent yellow solution was diluted with a fivefold volume of toluene and reduced with HA, PTB, or TES. The reductants were dissolved in THF and used in a 30-fold excess with respect to the Au^{3+}.

Figure 11.16 present an AFM image of PS-*b*-P2VP micelles assembled on a silicon surface. The image confirms that a monomicellar layer was formed on the surface of the support, and some of the micelles appear to be arranged in a quasi-hexagonal pattern. The height profile was determined along the horizontal line crossing several micelles, seen in panel b. Cross-sectional analysis indicated a micelle diameter of 20–30 nm.

The reduction of Au^{3+} and the formation of NPs can be conveniently monitored by UV–Vis spectroscopy. The spectra continuously recorded during the reaction are presented in Fig. 11.17a–c. The originally yellow GILMS at once turned dark red on the addition of HA, indicating that nucleation commenced immediately. This is clearly visible in the spectrum series in Fig. 11.17a. The absorption maximum characteristic of the surface plasmon resonance of Au NPs appeared at 552 nm, and its intensity increased continuously. Figure 11.17d illustrates the changes in absorbance read at λ_{max}. The initially rapid reaction decelerated continuously, but hardly

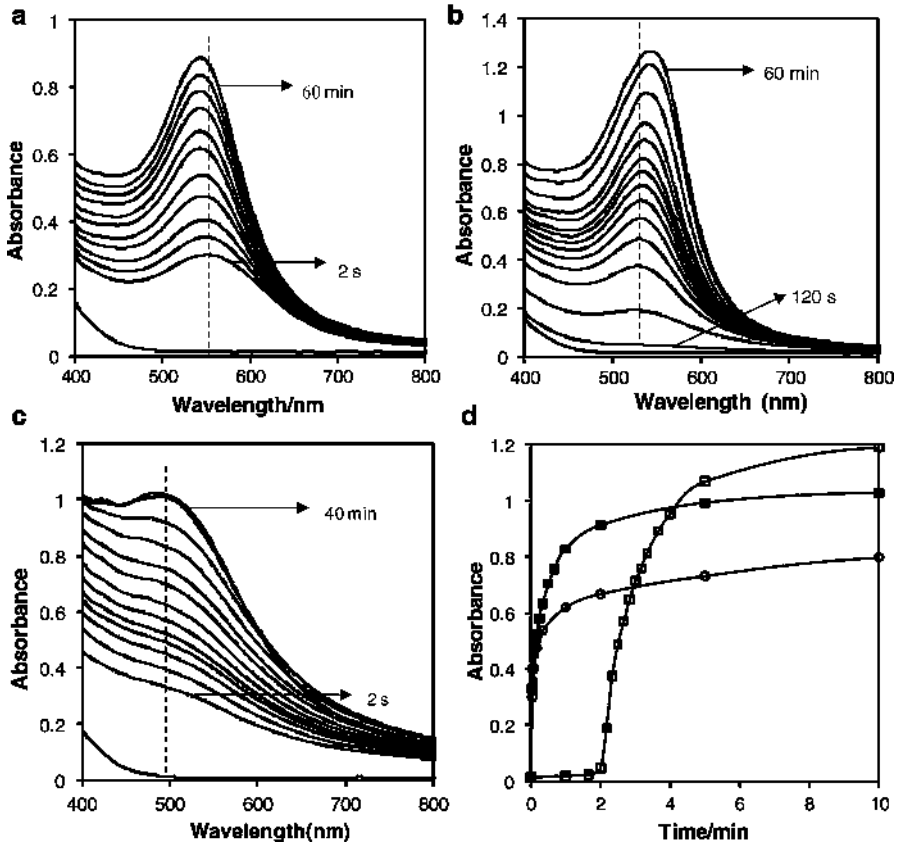

Fig. 11.17 The evolution of UV–Vis absorption spectra of Au NPs during reduction by (**a**) HA, (**b**) TES, (**c**) PTB, and (**d**) and the evolution of the absorption at λ_{max} determined from spectra under reduction process by (*circle*) HA, (*square*) TES, and (*filled square*) PTB (see [57])

changed after 60 s. Reduction with TES exhibited different kinetics. The absorption peak characteristic of the NPs (at 530 nm) appeared only ~1 min after the addition of the reducing agent. The optical density first increased slowly, then at 120 s started to rise sharply, and finally slowed down continuously until the reaction stopped. The sigmoid curve is shown in Fig. 11.17d. The spectra recorded during the reaction driven by PTB are shown in Fig. 11.17c. The resulting sol was brownish red. The characteristic absorption peak of the Au NPs was at 488 nm, pointing to a smaller NP size than after reduction with HA (this was supported by TEM measurements).

The size of the Au NPs formed was determined on the basis of TEM images [57]. Samples were withdrawn from the sols under preparation after 0.5 and 60 min following the addition of the reducing agent. Most often, there was one NP per micelle, but empty micelles also appeared in the images. Reduction with HA

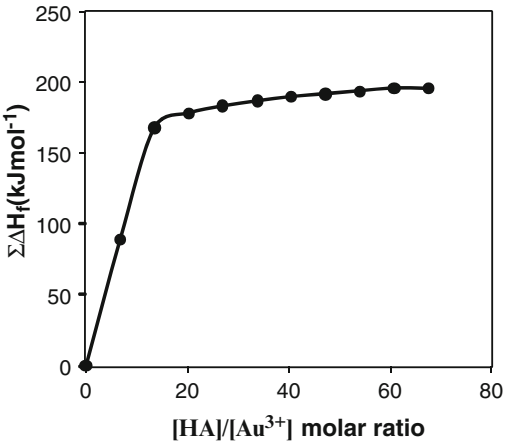

Fig. 11.18 The molar enthalpy of Au NPs formation as a function of molar ratio of HA and gold ions (see [57])

yielded Au NPs with an average diameter of 8 nm. In the case TES, the number of NPs had increased several fold during 60 min. This accords with UV–Vis results, which revealed that reduction with TES accelerates after an induction period. The average NP size increased from 2.2 nm to only 2.6 nm in 1 h. The original micellar structure underwent a significant rearrangement under reduction with PTB. The original micelles have been replaced by large droplets, and NPs are floating free in the reaction medium, or located on the interfaces of the droplets. The structure of the sol is altered in time; many smaller droplets/micelles are to be seen. This was confirmed by the DLS measurements. The majority of the NPs were situated within the smaller droplets/micelles, or are attached to the edges of the larger droplets/vesicles. The smallest NPs were formed on reduction with PTB: the average size changed from 1.1 to 1.7 nm in 1 h.

The microcalorimetric measurements clearly demonstrated that chemical reactions take place in the course of reduction with TES and PTB that cannot be distinguished from the formation of the Au NPs by reference measurements. It is possible to calculate the enthalpies of formation of Au NPs in the case of reduction with HA. Thus, the change in enthalpy of particle formation can be calculated by means of the expression: $\Delta H_f = \Delta H_{tot} - \Delta H_{mix}$, where ΔH_{tot} is the total enthalpy change measured in the reduction process and ΔH_{mix} is the enthalpy of mixing measured in the reference experiment. When the data are normalized to the amount of Au^{3+} present in the solution, the molar enthalpy of the reduction of Au^{3+} is obtained. Plots of the molar enthalpy plotted against the molar ratio of HA and Au^{3+} are shown in Fig. 11.18. The heat of formation of Au NPs in the case of reduction with HA is $\Delta H_f = -195$ kJ mol^{-1}.

NPs formation was investigated in block copolymer micelles using various reducing agents. It was found that the strength of the reducing agent determined both the size and the rate of formation of the Au NPs. The reduction of Au^{3+} was rapid with HA and PTB. TES proved to be a mild reducing agent for the synthesis of Au NPs. TEM and DLS measurements demonstrated that the original micellar

structure rearranged during the reduction with PTB. ITC measurements revealed that other chemical reactions besides Au NPs formation also occurred in the course of the reduction process.

11.3 Metal NPs Formation in Layered Silicate

11.3.1 Kinetics of Particle Formation by Heterogeneous Nucleation in Mg-Silicate Suspensions

The kinetics of NPs formation was also studied on solid surface. For studies on heterogeneous nucleation, polymer molecules were replaced with a Mg-silicate variety that forms an optically transparent suspension (hectorite, Optigel SH) as stabilizer [52].

In part of the experiments, the concentration of Pd^{2+} ions was kept constant ($c^0_{Pd^{2+}} = 0.075$ mmol/dm^3 and hectorite concentration was varied in the range of 0.5–0.001 g/100 cm^3). When $PdCl_2$ solution was added to the hectorite suspension, the pH measured was 5.8. Hectorite slows down reduction (Figs. 11.19a and 11.20) most probably because structure formation by the lamellae obstructs free flow of the reducing agent by increasing viscosity. We provided experimental proof that increasing the concentration of the suspension results in an increase in viscosity (results not shown). Thus, reduction may have become diffusion-inhibited due to the presence of hectorite lamellae. In addition to increased viscosity, another factor greatly contributing to deceleration is the fact that the majority of Pd^{2+} species are adsorbed on the surface. Adsorption of Pd^{2+} ions on hectorite was tested in a separate experiment. All the ions were bound to the surface in the concentration range studied, which means that nucleation takes place on the surface. The reaction rate increases with decreasing hectorite concentration, the apparent rate constants

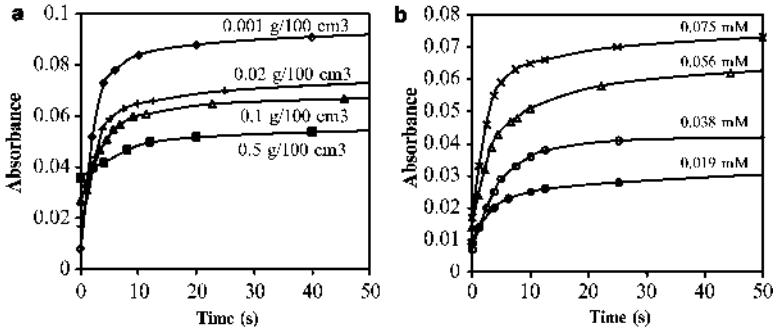

Fig. 11.19 Absorbance ($\lambda = 600$ nm) versus time curves of Pd NPs stabilized by hectorite (**a**) at constant Pd^{2+} ion and varying hectorite concentrations and (**b**) at constant hectorite and varying Pd^{2+} ion concentrations (see [52])

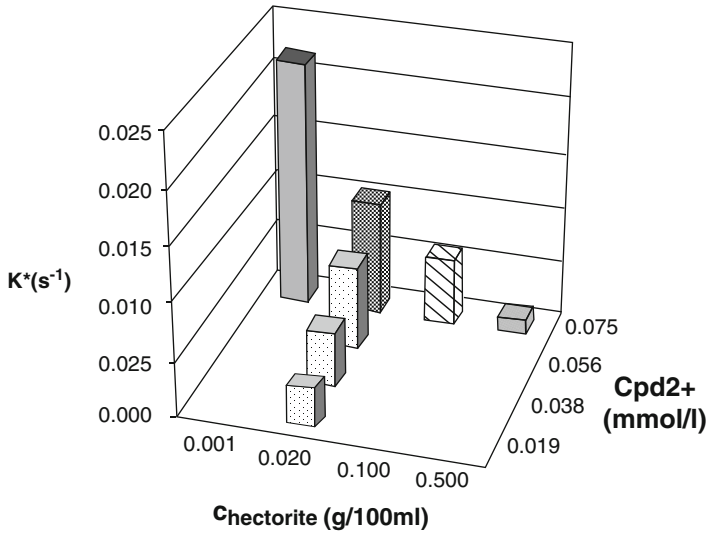

Fig. 11.20 Rate constants at different hectorite and precursor concentration (see [52])

Table 11.3 Composition of dispersions, kinetic parameters, and particle diameters

Hectorite concentration (g/100 cm^3)	$c^0_{Pd^{2+}}$ (mmol/dm^3)	Pd content (wt%)	k^* (s^{-1})	$\tau_{1/2}$ (s)
0.5	0.075	0.16	0.0013	533
0.1	0.075	0.79	0.0059	117
0.02	0.075	3.84	0.0102	68
0.02	0.056	2.89	0.0075	92
0.02	0.038	1.98	0.0048	144
0.02	0.019	1.00	0.0028	247
0.001	0.075	44.40	0.022	32

determined are listed in Table 11.3, and the A versus t functions are summarized in Fig. 11.19a. The apparent rate constant (k^*) is considerably increased (0.0013 s^{-1} → 0.022 s^{-1}) due to the 500-fold dilution.

We studied the rate-determining role of precursor ions in a hectorite suspension with constant concentration of 0.02 g/100 cm^3 (Fig. 11.19b). The concentration of the $PdCl_2$ solution was varied between 0.019 and 0.075 mmol/dm^3. The initial slope of the A versus t functions decreased with decreasing concentration, indicating deceleration of reduction. Half-life increases considerably (67.95 s^{-1} → 247.5 s^{-1}) (see Table 11.3, Fig. 11.20).

We attempted to determine, by TEM, the size of the particles formed in the course of the experiments. Due to the shielding effect of hectorite, only the image of the sample with the lowest hectorite concentration could be evaluated. The image of the hectorite/palladium composite displayed partially aggregated particles.

11.3.2 Preparation and Structural Studies on NPs/Clay Mineral Composites

NPs/support composites were prepared by heterogeneous nucleation on the surface or within the interlamellar space of layer silicate adsorbents; in this case, the layer silicate itself acts as stabilizer (i.e., as an inorganic stabilizer and, at the same time, as support matrix) for NPs. In view of the excellent stabilizing effect of polymers, we tried to make use of the joint stabilizing effect of the polymer/layer silicate complex in the syntheses. We assumed that combination of the two methods might result in the formation of outstandingly stable precious metal/polymer/layer silicate composites. In the case of heterogeneous nucleation, the interactions to be characterized are those between polymer and support, between polymer and precursor, and between polymer, support, and precursor. Adsorption of precursor ions on the silicate lamellae of the support (kaolinite, montmorillonite) has an influence on particle size. However, the effect of the polymer adsorbed on the surface of the support also has to be considered, as these may be adsorbed not only in the interlamellar space (montmorillonite) but also on the edges, in accordance with the electrostatic interactions operating between polymer and silicate. Thus, anionic, cationic, and neutral polymers may play different roles on layer silicates with negative surface charge.

11.3.2.1 Synthesis of Rh NPs on the Surface of Montmorillonite and Kaolinite Lamellae

Rhodium nanoparticles were prepared on the lamellae of montmorillonite and kaolinite by heterogeneous nucleation. Rhodium chloride solution was added to the aqueous dispersion of clay mineral and reduced with sodium borohydride.

Collective effect of solid support and macromolecules on the stabilization of generated NPs was also investigated. In these experiments, macromolecules were adsorbed on the support previous to reduction process. Nonionic PVP was added to the dispersion at Rh/PVP monomer ratios of 1:1, 1:5, and 1:20. Cationic PDDACl [poly(diallyldimethylammonium chloride)] of three and PSSN of two different molecular masses were used only at Rh/polymer monomer ratio 1:1 [58]. The particle size was determined by TEM. The structure of composites was studied by X-ray diffraction and small-angle X-ray scattering.

Interlamellar incorporation of NPs was confirmed by X-ray diffraction. By the evidence of XRD pictures, basal spacing in air-dry montmorillonite is $d_L = 1.48$ nm, due to the presence of adsorption water between the lamellae. With PVP as stabilizing agent, another new peak appears at about $d_L = 2.5$ nm as the monomer/Rh ratio is increased; at a ratio of 20:1, the original reflection of montmorillonite disappears and the structure is completely altered (Fig. 11.21). At high PVP content (21.5 wt%), as well as in the presence of the anionic PSSN, part of the NPs was not adsorbed on the surface of the support. Part of the large amount of PVP added could

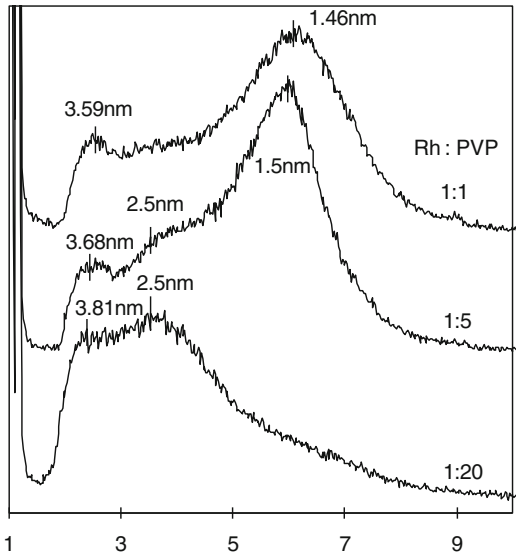

Fig. 11.21 XRD patterns of PVP-protected Rh/montmorillonite at different polymer content showing Rh NPs intercalated in the interlamellar space (see [58])

not bind to the support or intercalate; thus, this excess polymer stabilized the newly formed NPs in the bulk phase. In the case of PSSN, Rh NPs are practically not bound to the surface of the montmorillonite, due to repulsion by negative charges. No intercalation is observed on the X-ray diffractograms of these samples, and the size of Rh NPs is not affected by the presence of the support. In PVP/montmorillonite/rhodium composites, the particle size increases with increasing metal content. It may be a consequence of polymer/support interactions. A fraction of the polymer chains is adsorbed on the surface before the addition of Rh^{3+} ions; therefore, the polymer molecules remaining in the bulk phase can stabilize the NPs—which will attach to the surface of the support as soon as they are formed—only at a low Rh/monomer ratio. This is why a reaction medium containing montmorillonite and a relatively low amount of strongly adsorbing polymer (PVP, PDDA) will yield NPs of higher average size than would homogeneous nucleation. In this case, heterogeneous nucleation is no longer the case.

Rh NPs were also grown on kaolinite, using similar techniques. The adsorption nanoreactor preparation technique is successfully applicable also on kaolinite. A large specific surface area is essential for NPs growth and can be created by delamination of kaolinite lamellae. There are several compounds suitable for this purpose mentioned in the special literature; of these, we chose dimethyl sulfoxide (DMSO). Since the lamellar packages of kaolinite are split to elementary lamellae by intercalation of DMSO, the interlamellar space is rendered suitable for the growth of metal NPs [58].

X-ray diffraction measurements revealed that basal spacing increased from 0.72 to 1.12 nm during the intercalation process (Fig. 11.22). The reflection of delaminated kaolinite disappears in aqueous medium, and the lamellae are partially rearranged to their original position, an interlamellar distance of 0.72 nm.

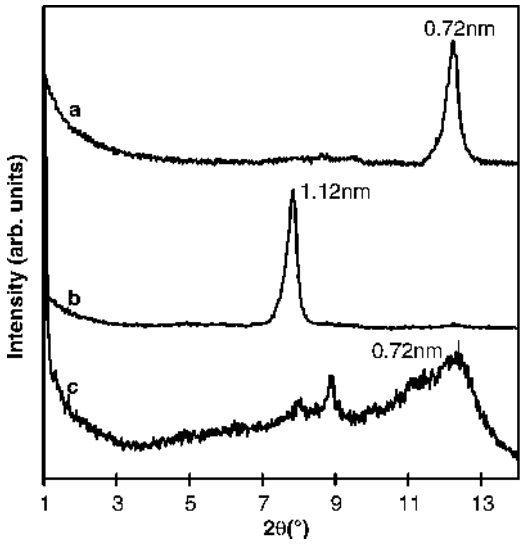

Fig. 11.22 XRD patterns of kaolinite (**a**), DMSO-treated kaolinite (**b**), and DMSO-treated kaolinite after washing by ethanol and water (**c**) (see [58])

We studied polymer incorporation between the disaggregated kaolinite lamellae. Since the specific surface area and the ion exchange capacity of kaolinite are low (14 m^2/g and 6–8 meq/g, respectively), this may only mean the incorporation of a small percentage of the molecular chains. Polymers are adsorbed not only on the external surfaces of the support but also on the internal surfaces lining the interlamellar space, pushing part of the lamellae apart to a distance of ~3.7 nm. In Rh/polymer/kaolinite composites, a new peak appears at $d_L \sim 2.7$ nm (Fig. 11.23). In the case of the cationic PDDA, molecular mass was varied. The effect of increasing chain length on structure was similar to that of increasing PVP concentration. PSSN, an anionic polymer, is not capable of binding to the negatively charged surface of kaolinite.

The particle size analysis (TEM) shows that smaller Rh NPs are presented on kaolinite lamellae than on montmorillonite. Depending on the stabilization method employed and the concentration of the precursor Rh^{3+} ions, average particle size falls in the range of 1–3 nm on montmorillonite and 1–2 nm on kaolinite (Figs. 11.24 and 11.25).

These results indicate that NPs can be stabilized with the lamellae of clay minerals. This simple colloidal method is suitable for preparation of supported metal NPs. The particles size is controllable easily by precursor concentration. However, the size of extremely small NPs—prepared with hard reducing agent—is not changed significantly by the polymer added.

Changes in the structural properties of clay minerals and the presence of NPs or polymer chains on the support may also be detected by SAXS experiments [58]. Measurements were started with support samples without NPs and polymers determined. SAXS parameters calculated from the $\log I = f(\log h)$ representations and $I \times h^3 = f(h^3)$ (so-called Porod representations) are given in Table 11.4. The log

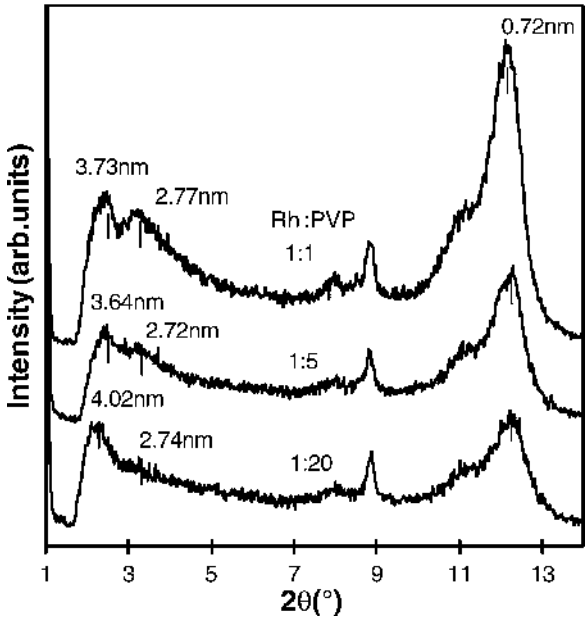

Fig. 11.23 XRD patterns of PVP-protected Rh/kaolinite at different polymer content (see [58])

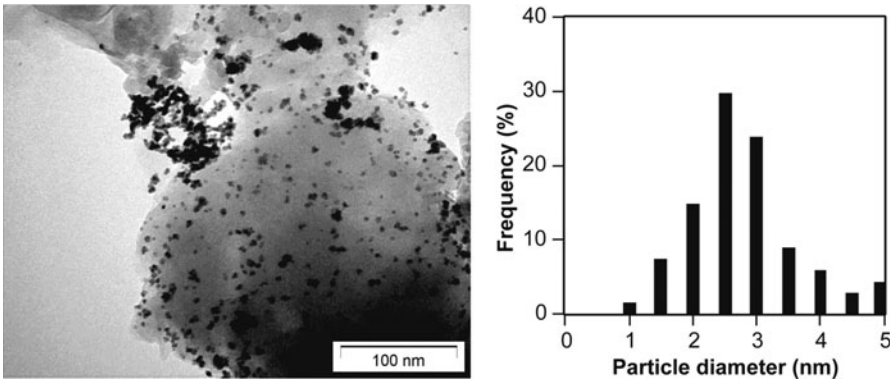

Fig. 11.24 TEM image and particle-size distribution of PVP-protected Rh/montmorillonite (2 wt% Rh) (see [58])

(I)–log(h) scattering functions of montmorillonite and kaolinite demonstrates well the difference between the two types of clay mineral (Fig. 11.26). The scattering intensity (I) and the slope of the curve are smaller for montmorillonite than for kaolinite. The surface fractal dimensions (D_s) calculated from the slope of the curve are the following: D_s (kaolinite) = 2.42 and D_s (montmorillonite) = 2.91. In the case of a smooth surface, the value of the surface fractal dimension is $D_s = 2.0$.

Table 11.4 SAXS parameters of clay minerals and intercalated samples

SAXS parameters	Montmorillonite	PVPM	RhM (0.5 wt %)	RhM (1.0 wt %)	Kaolinite	PVPK	RhK (0.5 wt %)	RhK (1.0 wt %)
D_s	2.91	3.08	3.07	3.09	2.42	2.46	2.55	2.52
K_p (Cps/nm^3)	222.3	296.4	478.9	422.5	58.6	66.9	178.7	230.3
M_1 (Cps/nm^2)	3,600.2	3,176.5	3,707.9	3,296.9	1,388.8	1,552.1	2,318.1	1,941.7
K_p/M_1	0.0617	0.0933	0.1292	0.1282	0.0422	0.0431	0.0771	0.1186
S/V (nm^2/nm^3)	0.050	0.089	0.129	0.125	0.036	0.042	0.047	0.116
S_p (m^2/g)	73.4	93.3	102.5	118.1	40.9	49.4	75.6	108.8
l_c (nm)	21.1	18.5	21.8	22.0	45.9	44.9	40.2	38.6

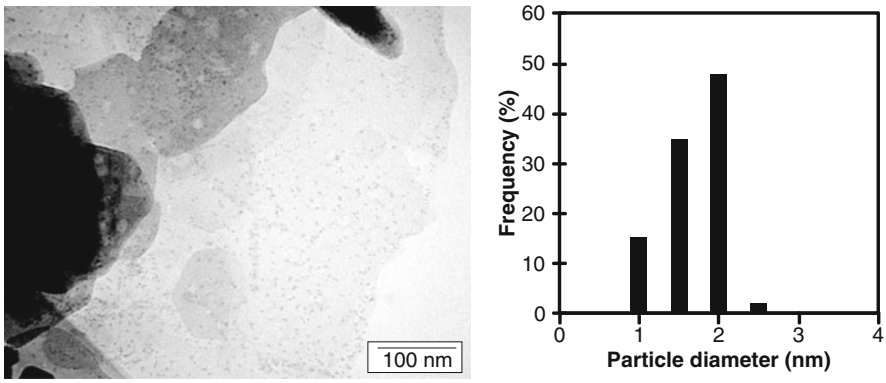

Fig. 11.25 TEM image and particle-size distribution of Rh/kaolinite (0.5 wt% Rh) (see [58])

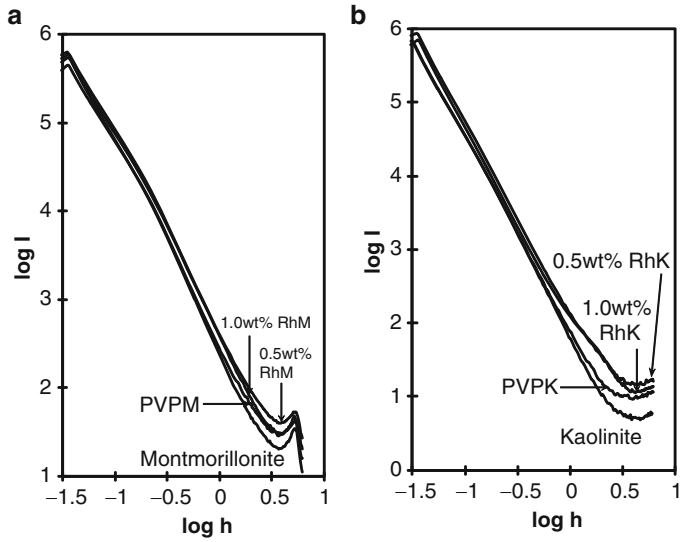

Fig. 11.26 Log–Log plot of SAXS curves of Rh/montmorillonite (**a**) and Rh/kaolinite samples (**b**) (see [58])

Thus, in our case, the surface of kaolinite is not smooth, but will be uneven and the surface of montmorillonite is much rougher. These values are further enhanced by introduction of PVP and Rh NPs. The intensity of X-ray scattering is enhanced by the higher electron density of metal NPs located on the surface; therefore, intensity is seen to increase with increasing metal content (Fig. 11.26). Differences between the samples are also confirmed by the Porod representation (Fig. 11.27). The intersections yield the values of the tail-end constants K_p determinated by linear extrapolation for each sample. The value of K_p, proportionate to the magnitude of the interfaces of the individual phases, tends to increase with increasing the quantity of Rh NPs in samples.

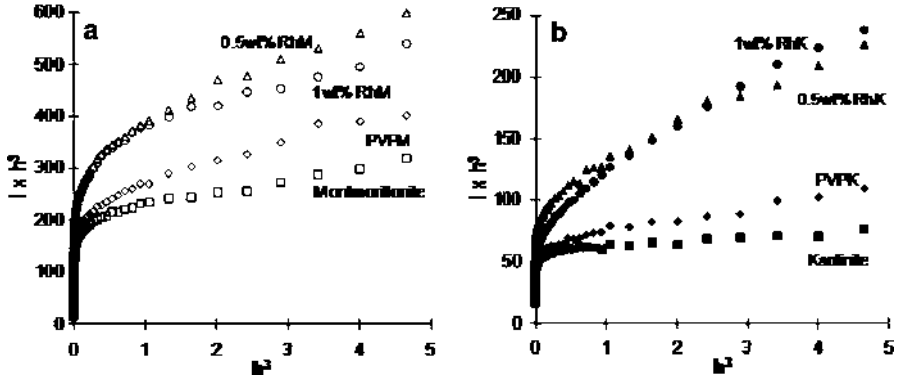

Fig. 11.27 The Porod plot of the SAXS curves of Rh/montmorillonite (**a**) and Rh/kaolinite samples (**b**) [58]

When Rh NPs are intercalated into the kaolinite lamellae, the K_p is increased significantly. Its value is $K_p = 58.6$ Cps/ nm^3 for kaolinite, and it increases to 178.7 and 230.3 Cps/ nm^3 in the sample containing 0.5 and 1.0 wt% rhodium. In the case of Rh/montmorillonite samples, it may be also observed increasing of the Porod constant. The specific surface area (S_p) calculated from the K_p/M_1 is larger for montmorillonite ($S_p = 73.4$ m^2/g) (it has rough surface), and its value increases if we incorporate polymer ($S_p = 93.3$ m^2/g) or metal NPs ($S_p = 102.5$ m^2/g) in the interlamellar space of the clays. At identical metal content, scattering intensity is increased more in the case of montmorillonite. The value of the correlation length l_c, calculated from K_p, does not change significantly in montmorillonite samples and hardly changes in kaolinite, showing the effects of disaggregation in these samples (Table 11.4). SAXS experiments are also suitable for the detection of polymer chains and Rh NPs on the surface of supports. Changes in structural parameters characterize the internal structural changes resulting from the intercalation of Rh NPs.

11.3.2.2 Synthesis of Palladium NPs on Montmorillonite and Kaolinite Lamellae

Palladium nanoparticles have been generated in the interlamellar space of montmorillonite and kaolinite by different methods in aqueous media. The in situ preparation method was based on the preferential sorption of precursor ions in the ethanol-rich interlamellar space of montmorillonite in ethanol—water binary liquid mixture and the subsequent reduction of Pd^{2+} ions at 65°C [49, 59]. Reduction was also performed with $NaBH_4$ replacing ethanol. Palladium particle size was controlled via the metal content. Theoretical and experimentally determined (ICP) Pd contents, the structural parameters of the composites, and particle sizes are listed in Table 11.5.

Additional effect of polymer molecules on particle size was also investigated. Compositions of the metal/polymer/montmorillonite composites are presented in

Table 11.5 Structural parameters of Pd/montmorillonite samples

Sample code	Reductant	Pd content (wt%)	PVP content (wt%)	d_{XRD} (nm)	d_{TEM} (nm)	d_L (nm)
Na montmorillonite	–	–	–	–	–	1.44
PVPM	–	–	12.4	–	–	1.58
PdM1	Ethanol	0.5 (0.50)[a]	–	10.7	2.2	4.15;1.49
PdM2	Ethanol	1.0 (1.00)[a]	–	18	4.7	3.74; 1.49
PdM3	Ethanol	2.5 (2.53)[a]	–	22	6.3	3.71; 1.48
PdM4	$NaBH_4$	1	–	–	4.1	3.95; 1.57
PdM5	$NaBH_4$	2	–	–	5.8	1.54
PVPPdM1	Ethanol	2.0 (1.95)[a]	2.1	20.2	5.9	5.68;1.45
PVPPdM2	Ethanol	2.0 (1.93)[a]	4.1	16.2	3.8	3.24; 1.46
PVPPdM3	Ethanol	2.0 (1.68)[a]	12.4	11.5	2.3	1.54
PVPPdM4	$NaBH_4$	1	3.8	–	2.8	3.82;1.52

[a]Pd content determined by ICP

Table 11.5. Palladium contents in the samples determined by ICP decrease with increasing polymer concentration. In these cases, stabilized metal NPs of brownish-black color were visually observed to be retained in the supernatant after centrifugation.

X-ray diffractograms also yield information on polymer adsorption and on the incorporation of NPs formed in the course of reduction. A new reflection appearing at larger angles (d_L = 3.24–5.68 nm) seems to confirm the interlamellar presence of NPs. Size distribution functions constructed from the data of TEM images suggest that the composites also contain larger NPs (5–10 nm). These NPs probably grew on the external surfaces (Fig. 11.28a). Particle size is seen to increase with metal content. The addition of stabilizing polymer led to the formation of smaller NPs; increasing the amount of polymer added resulted in a further decrease in size. Reduction by $NaBH_4$ led to the formation of smaller NPs than did reduction by ethanol ($d_{ave.}$ = 4.1 and 5.8 nm, respectively). Polymer addition further decreased particle size also in the case of reduction by $NaBH_4$ ($d_{ave.}$ = 2.8 and 4.1 nm in the presence and absence PVP, respectively). It was established that the size of Pd NPs on montmorillonite can be successfully decreased by adding polymer to the support in the course of synthesis, prior to reduction of palladium ions.

The samples were analyzed in the angle range of 2Θ = 38–42° for the presence of metallic palladium. When using CuKα radiation, the (111) reflection characteristic of palladium appears at 40.15° (see Fig. 11.29). Due to the decrease in particle size, the lattice constant is altered, as a consequence of which the location of the reflection is also shifted. Particle sizes calculated from the broadening of the half width of the reflection by the Scherrer equation (10–22 nm) exceed those determined by electron microscopy. The reason for this is that XRD analyzes the entire sample that may contain large crystallites, but fails to observe smaller, amorphous NPs.

Pd NPs were prepared on kaolinite at different metal content and at different metal/polymer monomer ratios. The adsorbed Pd^{2+} ions were reduced by hydrazine and $NaBH_4$. Reductant was applied in a fourfold excess. The metal contents of the products were 0.95 and 1.9 wt%. The compositions and structural parameters of the samples are shown in Table 11.5. A new reflection appears in the diffractograms at small 2θ angles ($d_L \sim 3.6$ nm) in the case of PVP/kaolinite composites. Formation of Pd clusters in PVP/kaolinite system caused a shift of reflection from d_L = 3.6 to 4.4 nm (Fig. 11.30).

Kaolinite samples containing palladium were prepared without PVP stabilization. The Pd/kaolinite samples prepared in the aqueous system yielded comparatively large palladium clusters of polydisperse size distribution covering densely the lamellae. The particle size and polydispersity increased by increasing palladium content. The incorporation of the NPs increases basal spacing according to the XRD patterns. In the case of composites containing larger NPs, the (001) reflection of kaolinite is shifted to smaller angles on the diffractograms (Table 11.6).

The size distribution of NPs formed can be determined on the basis of TEM images (Fig. 11.31). TEM image of sample PVPPdK1 displays spherical NPs measuring 2–6 nm, situated separately on the lamellae, with no sign of aggregation (Fig. 11.31a). When PVP content is increased (Fig. 11.31b), strings of metal NPs are seen to cling to the edges of the lamellae of the support, whereas particle diameter is not modified significantly. This allows one to conclude that the part

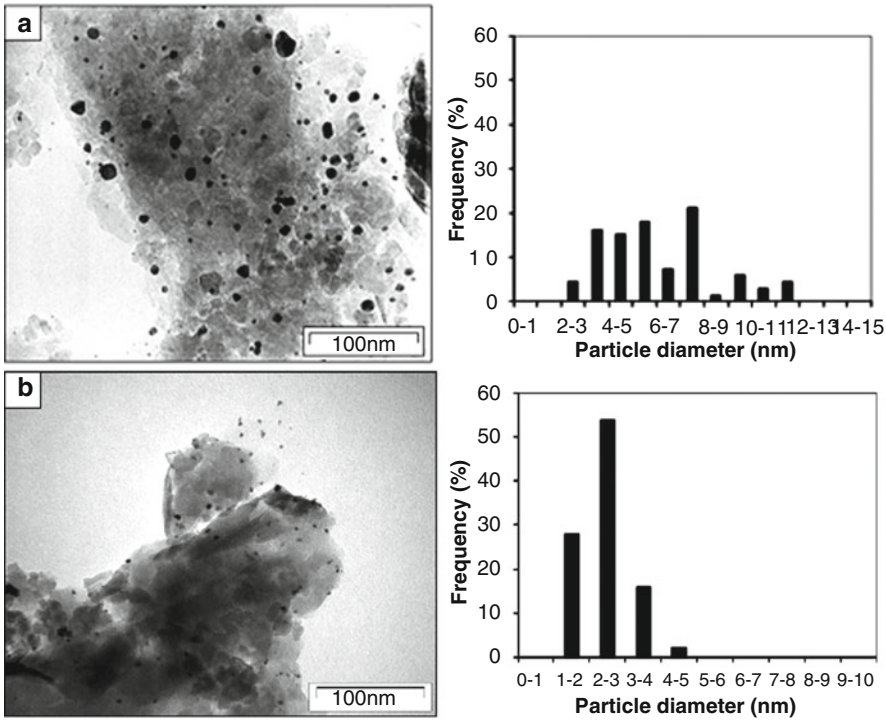

Fig. 11.28 TEM micrograph and size distribution of Pd/montmorillonites (**a**) PVPPdM1, $d_{ave.} = 5.9$ nm, and (**b**) PVPPdM4, $d_{ave.} = 2.8$ nm (see [49])

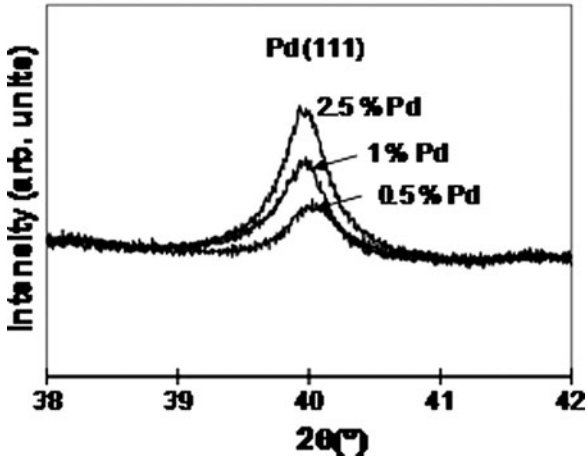

Fig. 11.29 Pd(111) reflection of PVP/Pd/montmorillonite samples with different Pd content (see [49])

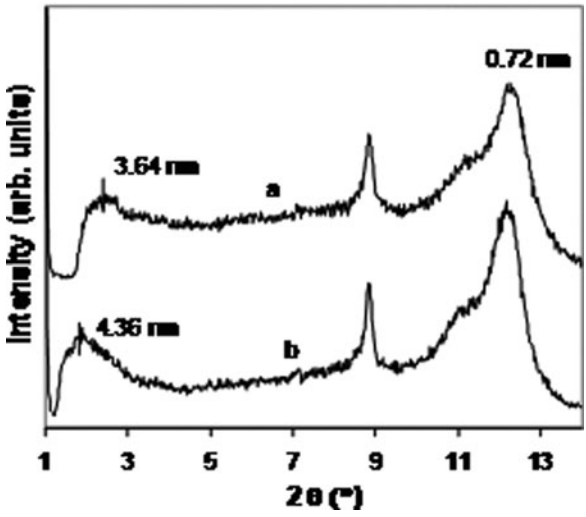

Fig. 11.30 XRD patterns of (**a**) PVPK and (**b**) PVPPdK3 samples

Table 11.6 Structural parameters of Pd/kaolinite samples

Sample code	Reductant	Pd content (wt%)	PVP content (wt%)	d_{TEM} (nm)	d_L(nm)
PdK1	Hydrazine	0.95	–	7.2	3.64
PdK2	Hydrazine	1.9	–	14.3	4.13
PVPPdK1	Hydrazine	0.95	3.8	2.8	5.33
PVPPdK2	Hydrazine	1.9	3.8	5.8	–
PVPPdK3	Hydrazine	0.95	28.0	2.6	4.36
PdK3	$NaBH_4$	0.95	–	6.0	5.95
PdK4	$NaBH_4$	1.9	–	8.1	6.87

of polymer chains, which could not get adsorbed on kaolinite, remained in the bulk phase and stabilized the NPs forming in the course of reduction. These "large" units could only attach to the external surface of the lamellae. When palladium content is increased at constant polymer content, larger NPs are formed (0.95 wt% → 2.8 nm; 1.9 wt% → 5.8 nm). When palladium content is raised to 2 wt% without polymer stabilization and the slower reduction method (hydrazine) is applied, crystalline NPs of diversified morphology measuring as large as 20–30 nm are formed. Comparison of the syntheses of palladium and rhodium particles shows that, under identical conditions, $RhCl_3$ gives rise to smaller particles than does $PdCl_2$.

11.3.2.3 The Role of Macromolecules in Surface Fixation of Pd NPs

The role of NPs in polymer adsorption on solid support was also investigated. The adsorption isotherm of PVP and PVP-stabilized Pd NPs were determined on Na montmorillonite. The clay mineral was dispersed in polymer solutions of various concentrations, and the suspensions were stirred at room temperature for 2 days,

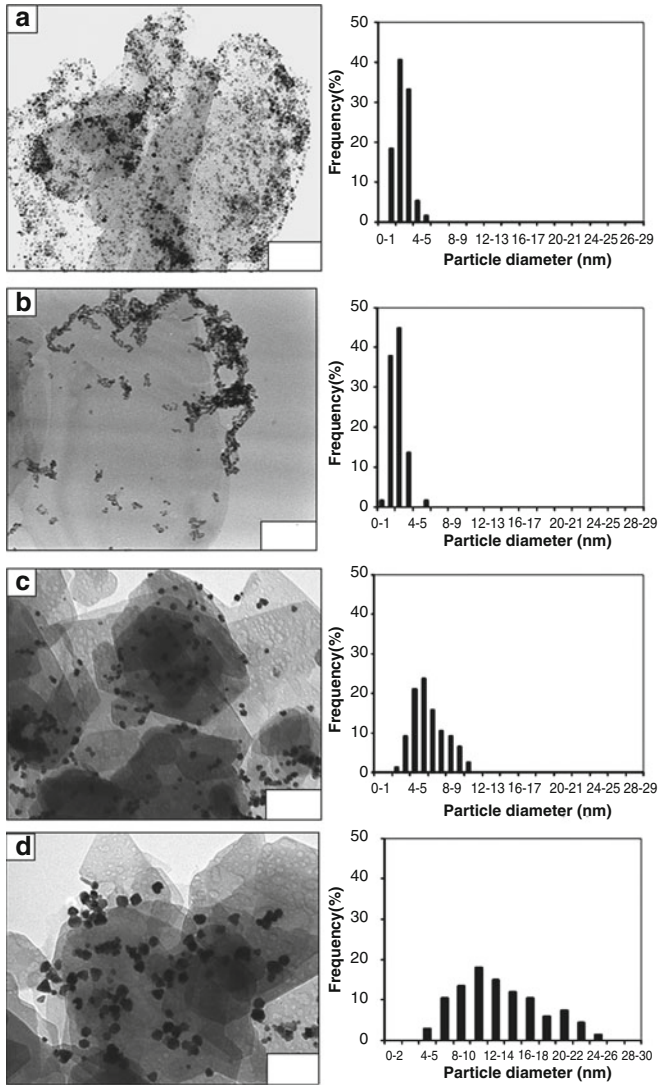

Fig. 11.31 TEM micrograph and particle-size distribution of (**a**) PVPPdK1, $d_{ave.} = 2.8$ nm; (**b**) PVPPdK3, $d_{ave.} = 2.6$ nm; (**c**) PdK1, $d_{ave.} = 7.2$ nm; and (**d**) PdK2, $d_{ave.} = 14.3$ nm (see [59])

until adsorption equilibrium was reached. The suspensions were centrifuged and the carbon content of the polymer solution (supernatant) was determined in a TC apparatus. The amount of bound polymer was calculated as the difference of the initial (c_0) and postadsorption (c_e) concentrations. Montmorillonite concentration in the suspensions was 1 g/100 cm^3 in all cases. The amount of adsorbed polymer was calculated by the relationship $n^s_{pol} = V^0(c_0 - c_e)/m$, where V^0 is the volume of the

polymer solution and m is the mass of montmorillonite. Amounts of adsorbed material were determined in the concentration range of 0.025–2.5 g/100 cm^3. As shown in Fig. 11.32a, molecular coils of PVP are easily adsorbed on montmorillonite lamellae.

We examined how the adsorption isotherms of macromolecules used as stabilizers change when polymer chains linked to NPs—rather than free polymer molecules—are bound to the surface. In these experiments, polymer solutions uniformly contained 0.02 mM Pd and the average diameter of Pd NPs was 1.5–2 nm. Larger amounts of PVP were observed to bind per unit surface (Fig. 11.32b), possibly due to reduced expansion of the polymer chains stabilizing the NPs.

Incorporation of particles into the interlamellar space was monitored by X-ray diffraction. Figure 11.33 shows that the intensity of the (001) montmorillonite reflection appearing at 14.2 nm is reduced, the peak is gradually flattened, whereas the intensity of the new peak appearing at 3.91 nm simultaneously increases, indicating intercalation of the polymer-coated Pd° particle. The ratios of the intensities of the two peaks (I_d = 1.42 nm:I_d = 3.91 nm) at Pd contents of 0.5, 1, 2, and 4 wt% are 2.3, 1.3, 0.8, and 0.3, respectively, a data series that can be considered as a measure of the structural transformation taking place.

These experiments show that Pd NPs promoted the adsorption of PVP molecules on montmorillonite. It was found that the polymer-protected palladium particles not only adhere to the external surfaces but are also capable of incorporation between the lamellae of the clay mineral.

11.3.2.4 Synthesis Ag NPs on the Surface of Disaggregated Kaolinite Lamellae

Ag NPs were synthesized on kaolinite previously delaminated with DMSO [60, 61]. The effects of photoreduction and $NaBH_4$ reduction on particle size were compared. The kaolinite was dispersed in aqueous $AgNO_3$ solution, and the adsorbed Ag^+ ions were reduced on the surface of kaolinite lamellae with $NaBH_4$ or UV light irradiation. Silver ions were added to the disaggregated kaolinite samples at ratios of 1, 2, 5, and 10 wt% Ag/kaolinite. The photoreduction was achieved as follows: dispersion was poured into a quartz beaker and irradiated with a Xe lamp for 1 h, from a distance of 10 cm under constant stirring. After reduction, the suspension was centrifuged, washed, and dried as described above (Fig. 11.34).

After reduction of adsorbed metal ions, a new Bragg reflection is observed at $2\theta = 2.05°$, defining $d_L = 4.42$ nm for the photoreduced 1 wt% Ag/kaolinite samples and $d_L = 4.28$ nm for the sample reduced by $NaBH_4$. These increased basal spacing prove that, in the course of ion exchange, Ag^+ ions are bound not only on the edges and the external surface of kaolinite but also within the interlayer space. Comparison of the X-ray diffractograms of samples with the same silver content but reduced by different methods reveals significant differences [60, 61]. The intercalation reflection of the photoreduced samples is more intensive and appears at larger $2\theta°$. The reason is that larger Ag NPs was formed during the photoreduction, than in the case of reduction by $NaBH_4$. The size distribution of the

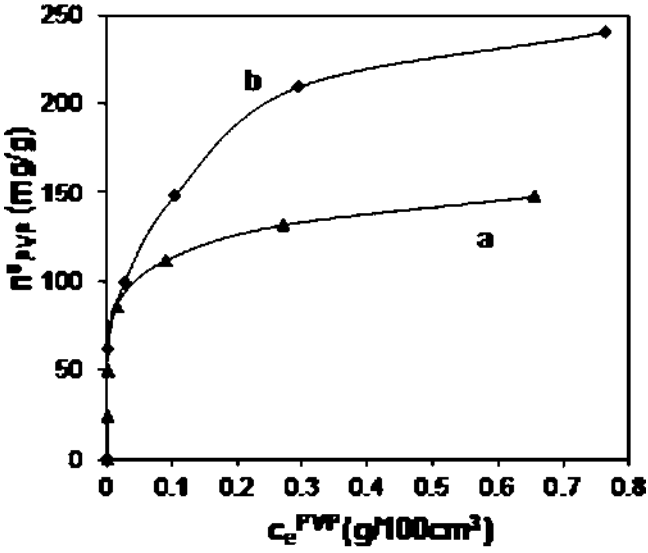

Fig. 11.32 Adsorption isotherms of (**a**) PVP (**b**) PVP-protected Pd NPs in aqueous solution on Na montmorillonite (see [59])

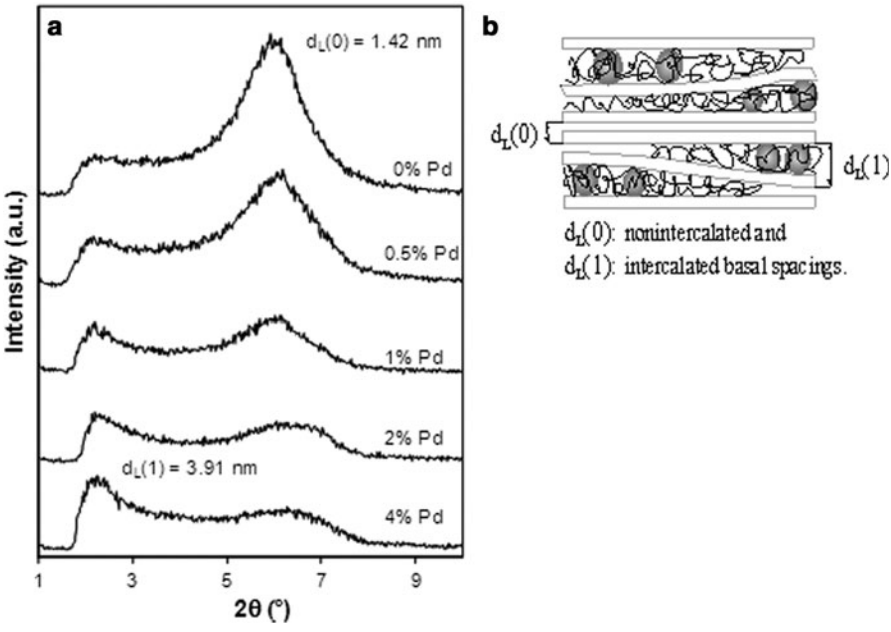

Fig. 11.33 (**a**) XRD patterns of polymer-protected Pd/montmorillonite showing Pd NPs intercalated in the interlamellar space, at different Pd contents and (**b**) schematic representation of intercalated montmorillonite (see [59])

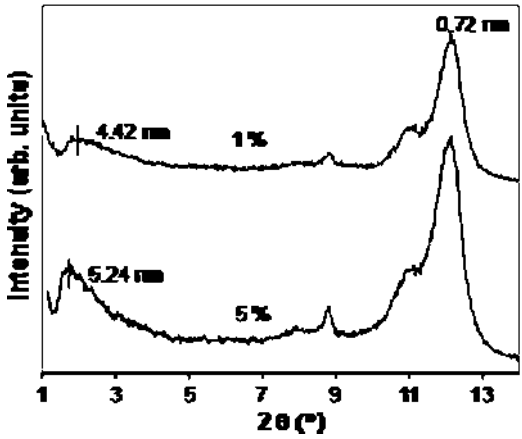

Fig. 11.34 XRD patterns of 1 and 5 wt% Ag/kaolinite prepared by photochemical reduction (see [60])

Ag NPs was determined by TEM (Fig. 11.35, Table 11.7). As the metal content is increased, the average size of the NPs prepared by all methods increased. Particle size of the sample containing 2 wt% Ag–kaolinite (photoreduction) was $d_{TEM} = 8.7$ nm; at 10 wt% Ag/kaolinite, $d_{TEM} = 14.8$ nm. As shown by electron micrographs, NPs spacing was denser in the $NaBH_4$ reduced samples because all Ag^+ ions present were rapidly reduced by $NaBH_4$ added in excess, a process favoring nucleation. In the photoreduction experiment, reduction is slower, which favors NPs growth. A similar result was obtained when the Ag (111) ($2\theta = 38.3°$) Bragg reflections of the various samples were compared (Fig. 11.36). In the case of samples reduced with $NaBH_4$, reflection intensities increased and half-widths decreased with increasing silver content because the size and crystallinity of the Ag NPs increased. The particle size as calculated by the Scherrer equation varied within $d_{Sch} = 12.7$–24.0 nm. In the photoreduced samples, however, there was no significant variation between samples with different silver contents: the average particle size calculated from half the width was $d_{Sch} = 10.1$–11.3 nm.

Comparing the two reduction methods, it was established that in the case of photoreduction, larger Ag NPs were formed.

11.3.3 Analysis of Pd, Rh, and Ag NPs by X-Ray Photoelectron Spectroscopy

X-ray photoelectron spectra (XPS) studies were aimed at the assessment of the surface oxidation state of the NPs. Figure 11.39 displays the spectra of Pd/montmorillonite (2 wt%) and Pd/kaolinite (1.9 wt%) samples, resolved to the lines of the Pd° and Pd^{4+} oxidation states. Input parameters are the binding energies of $Pd3d_{3/2}$ peaks, the difference of the binding energies of the $Pd3d_{3/2}$ and $Pd3d_{5/2}$ peaks,

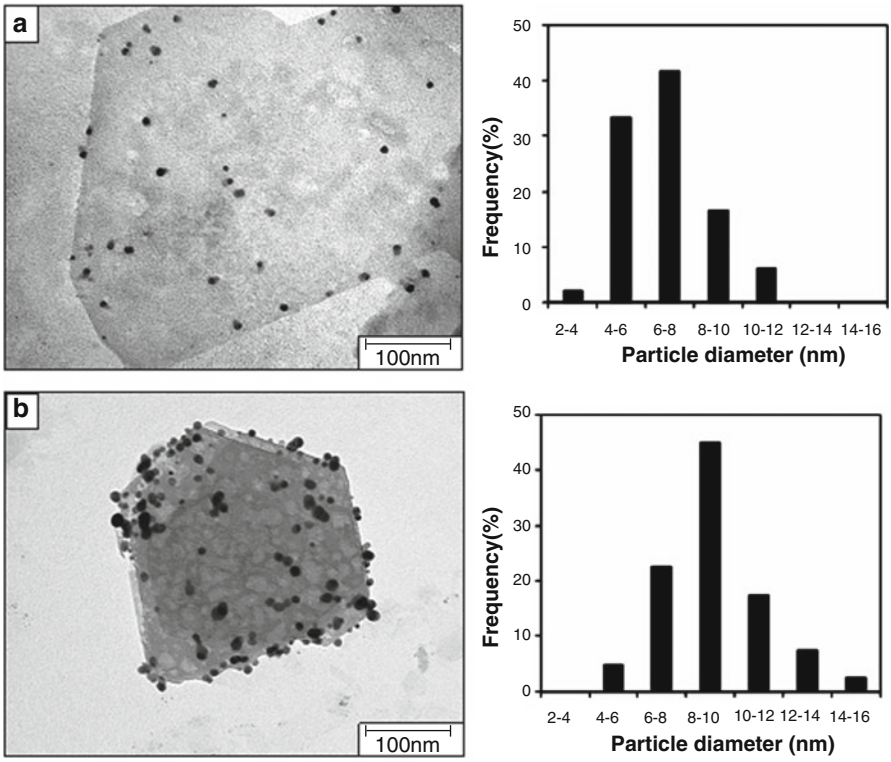

Fig. 11.35 TEM image and particle-size distribution of 2 wt% Ag/kaolinite prepared by (**a**) photochemical and (**b**) $NaBH_4$ reduction (see [60])

Table 11.7 Structural parameters of Ag/kaolinite samples

Sample code	Reductant	Ag content (wt%)	d_{XRD} (nm)	d_{TEM} (nm)	d_L (nm)
AgK1	$NaBH_4$	0.5	10.7	5.6	4.58
AgK2	$NaBH_4$	1.0	12.7	7.1	4.28
AgK3	$NaBH_4$	1.5	13	7.6	4.24
AgK4	$NaBH_4$	2.0	13.1	8.3	4.39
AgK5	$NaBH_4$	5.0	24.0	10.5	4.95
AgK6	Photoreduction	1.0	10.1	8.3	4.42
AgK7	Photoreduction	2.0	10.2	8.7	5.64
AgK7	Photoreduction	5.0	11.3	11.2	5.24
AgK7	Photoreduction	10.0	10.1	14.8	3.69

and the ratio of the intensities of the two peaks. Half-widths were identical for each peak in the different samples (Figs. 11.37).

In addition to the peaks at 335.0 and 340.6 eV corresponding to the binding energies attributable to the doublets of $3d_{3/2}$ and $Pd3d_{5/2}$ of palladium in zero oxidation state, peaks also appear at 337.7 and 342.7 eV. These peaks are

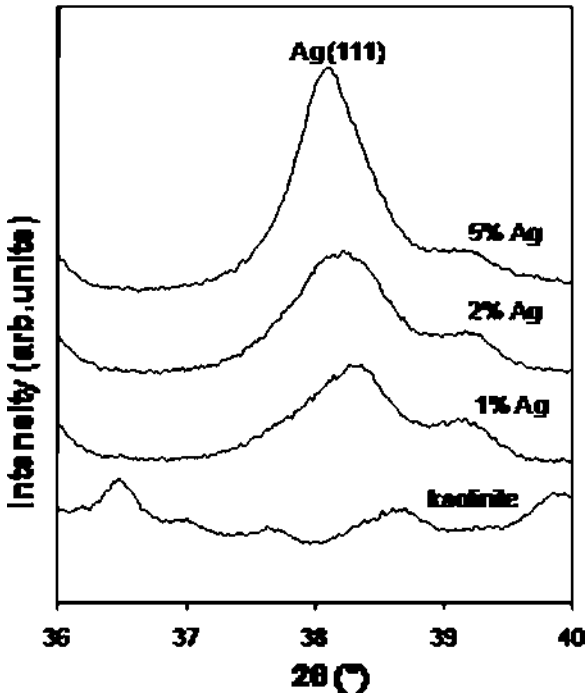

Fig. 11.36 Ag(111) reflection of $NaBH_4$-reduced Ag/kaolinite samples (see [61])

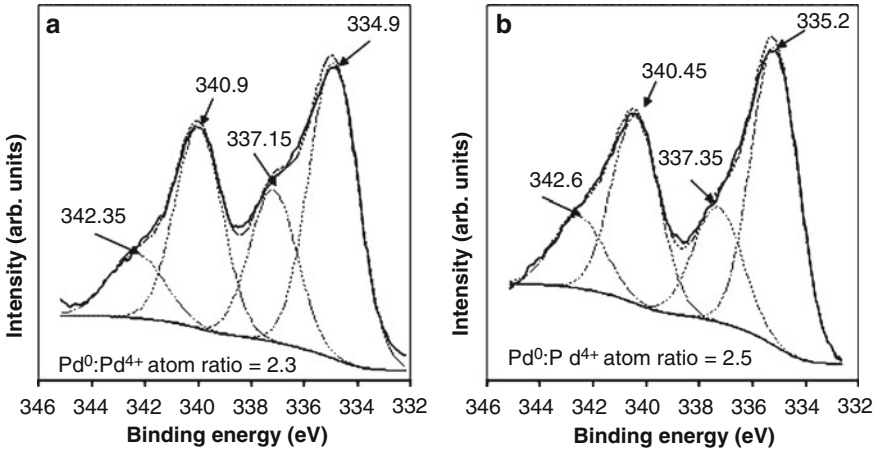

Fig. 11.37 XPS Pd3*d* spectra of (**a**) Pd/montmorillonite and (**b**) Pd/kaolinite samples (see [59])

characteristic of the Pd^{4+} oxidation state. In addition to metal atoms in zero oxidation state, all Pd-containing samples studied contain ions in the Pd^{4+} oxidation state. This means that there is no PdO on the surface, but Pd° and PdO_2 are present. These results indicate that either only part of the metal ions added to the support

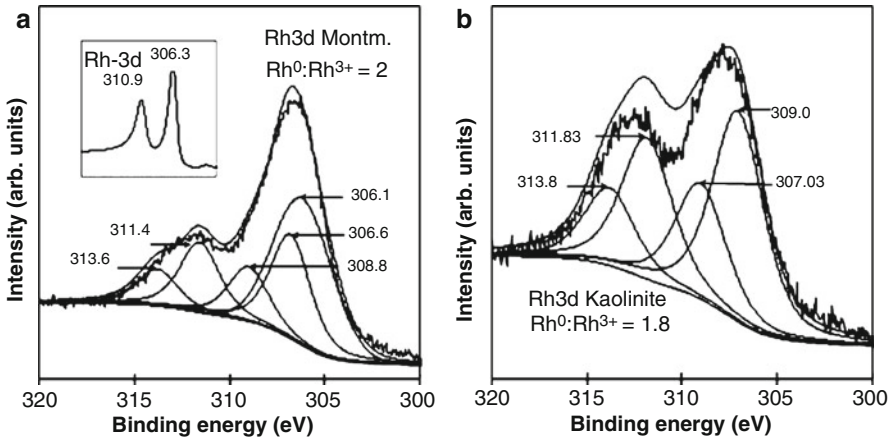

Fig. 11.38 XPS Rh3*d* spectra of (**a**) Rh/montmorillonite and (**b**) Rh/kaolinite samples (see [58])

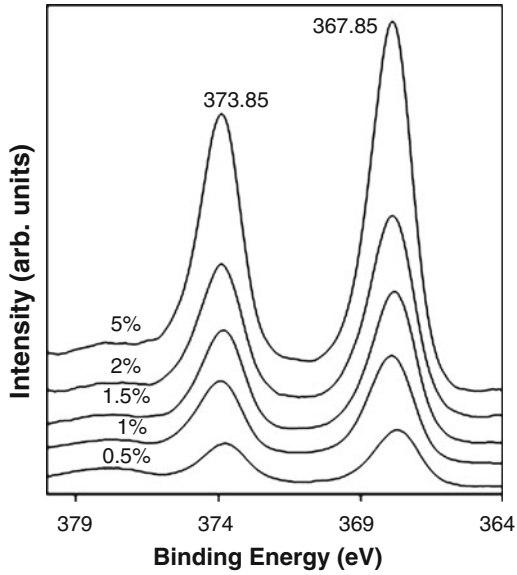

Fig. 11.39 Ag3*d* X-ray photoelectron of Ag/kaolinite samples (0.5, 1, 1.5, 2, and 5 wt% Ag contents) (see [61])

was reduced in the course of synthesis or all were reduced, but some were converted to metal oxide by reacting with oxygen on the surface. It cannot be excluded from possible reasons that the presence of forms in higher oxidation states is due to a metal-support interaction on the surface.

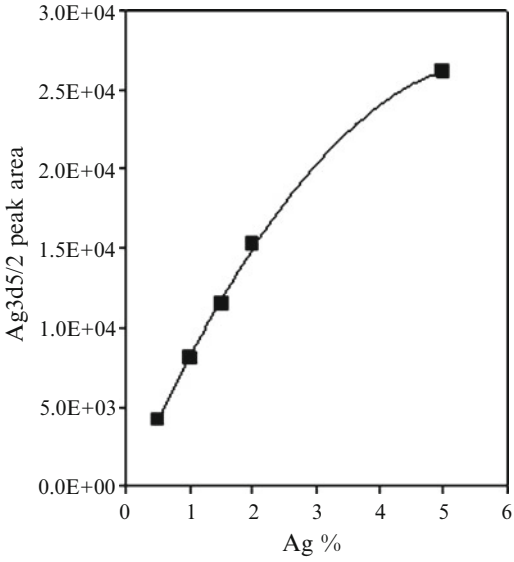

Fig. 11.40 Ag3*d* peak area of Ag/kaolinite samples as a function of Ag content (see [61])

The valence of the Rh NPs on the support surface was examined by XPS analysis. Rh3*d* XP spectra of the Rh/montmorillonite (2 wt%) and Rh/kaolinite (2 wt%) composites are displayed on Fig. 11.40. The broad peaks of Rh3*d* suggest more than one type of rhodium. Both spectra show the characteristic 3*d* doublet plus an Mg auger line in the case of Rh/montmorillonite sample (at 306.1 eV). The spectra were deconvoluted into two states: Rh° and Rh^{3+}. The input parameters were the approximate binding energies of the Rh3$d_{5/2}$ peaks, the energy difference between the Rh3$d_{3/2}$ and Rh3$d_{5/2}$ peaks (4.8 eV), and the intensity ratio of the two peaks (2:3). An additional condition was that the full widths of half maximums should be equal for all peaks (Fig. 11.38).

The binding energies of the doublet for Rh3$d_{5/2}$ and Rh3$d_{3/2}$ (306.6 and 311.4 eV) are characteristic of Rh°. Moreover, the peaks at 308.8 and 313.6 eV are observed. These peaks at higher binding energy may be accounted for oxidized state of the rhodium. Since the peak areas are proportional with the number of the given type of atoms at or near the surface, the deconvolution may help determine the Rh°/Rh^{3+} ratio. Thus, in the case of montmorillonite-supported Rh, this ratio was around 2. This value was ca. 1.8 for the kaolinite-supported sample. So—taking into account the precision of this method—we can say that the Rh°/Rh^{3+} ratio was the same in both cases. These results indicate that Rh^{3+} was reduced to Rh° and that the surface of Rh NPs was partially oxidized in air to Rh_2O_3. The reason might be that ultrafine Rh NPs are very active, which is a common feature for nanometer-sized metal particles, and the Rh^{3+}-ions were not fully reduced by sodium borohydride at the preparation of NPs with the various reduction processes. The possibility that the presence of Rh^{3+} on the surface is a consequence of the metal-support interaction cannot be excluded either.

Ag3*d* XPS of the samples with different silver contents are presented in Fig. 11.39. Binding energies of Ag3$d_{5/2}$ peaks were in the range of 367.7–367.9 eV, whereas those of Ag3$d_{3/2}$ peaks in the range of 373.75–373.9 eV. The location of the peak is characteristic of metallic silver and is independent of silver concentration. Full widths at half maximum (FWHM) ranged from 1.81 to 1 83 eV, except for sample that contains 5 wt% of Ag that displayed a value of 1.68 eV. Binding energies and values of FWHM were within the limits of experimental error.

Since peak areas are directly proportional with the number of atoms present, the areas allow estimation of the silver content of the samples. The magnitude of the Ag3*d* peak as a function of theoretical silver content is shown in Fig. 11.40. It is clearly seen that the function is linear up to 2 wt% Ag^+ content and then bends toward the *x* axis, indicating that the actual silver content is lower than the value expected on the basis of the amount of Ag^+ added. This is in accordance with the spectrophotometric results, i.e., above a certain concentration, no more Ag^+ ions can be adsorbed on the surface of kaolinite; therefore, NPs are also formed in the liquid phase.

References

1. Wilcoxon JP, Williamson RL, Baughman R (1993) Optical properties of gold colloids formed in inverse micelles. J Chem Phys 98:9933–9950
2. Parsapour F, Kelley DF, Craft S, Wilcoxon JP (1996) Electron transfer dynamics in MoS_2 nanoclusters: normal and inverted behavior. J Chem Phys 104:4978–4987
3. Pocard NL, Alsmeyer DC, McCreery RL, Neenan TX, Callstrom MR (1992) Nanoscale platinum(0) clusters in glassy carbon: synthesis, characterization, and uncommon catalytic activity. J Am Chem Soc 114:769–771
4. Steigerwald ML, Brus LE (1990) Semiconductor crystallites: a class of large molecules. Acc Chem Res 23:183–188
5. Chan YNC, Schrock RR, Cohen RE (1992) Synthesis of silver and gold nanoclusters within microphase-separated diblock copolymers. Chem Mater 4:24–27
6. Zhao M, Sun L, Crooks RM (1998) Preparation of Cu nanoclusters within dendrimer templates. J Am Chem Soc 120:4877–4878
7. Bradley JS (1994) In: Schmid G (ed) Clusters and colloids: from theory to applications. VCH, New York, pp 459–536
8. Rampino LD, Nord FF (1941) Preparation of palladium and platinum synthetic high polymer catalysts and the relationship between particle size and rate of hydrogenation. J Am Chem Soc 63:2745–2749
9. Boutonnet M, Kizling J, Stenius P, Maire G (1982) The preparation of monodisperse colloidal metal particles from microemulsions. Colloids Surf 5:209–225
10. Wang CC, Chen DH, Huang TC (2001) Synthesis of palladium nanoparticles in water-in-oil microemulsions. Colloids Surf A Physicochem Eng Asp 189:145–154
11. Nickel U, Castell A, Pöppl K, Schneider S (2000) A silver colloid produced by reduction with hydrazine as support for highly sensitive surface-enhanced Raman spectroscopy. Langmuir 16:9087–9091
12. Zhao MQ, Crooks RM (1999) Intradendrimer exchange of metal nanoparticles. Chem Mater 11(11):3379–3385
13. Nakao Y, Kaeriyama K (1986) Preparation of noble-metal sols in the presence of surfactants and their properties. J Colloid Interface Sci 110:82–87

14. Pillai ZS, Kamat PV (2004) What factors control the size and shape of silver nanoparticles in the citrate ion reduction method? J Phys Chem B 108:945–951
15. Heard SM, Grieser F, Barraclough CG, Sanders JV (1982) The characterization of Ag sols by electron-microscopy, optical-absorption, and electrophoresis. J Colloid Interface Sci 93:545–555
16. Hoogsteen W, Fokkink LGJ (1995) Polymer-stabilized Pd sols: kinetics of sol formation and stabilization mechanism. J Colloid Interface Sci 175:12–26
17. Hirai H, Nakao Y, Toshima N (1979) Preparation of colloid transition-metals in polymers by reduction with alcohols of ethers. J Macromol Sci Chem A 13:727–750
18. Teranishi T, Miyake M (1998) Size control of palladium nanoparticles and their crystal structures. Chem Mater 10:594–600
19. Henglein A (1999) Radiolytic preparation of ultrafine colloidal gold particles in aqueous solution: optical spectrum, controlled growth, and some chemical reactions. Langmuir 15:6738–6744
20. Jana NR, Gearheart L, Murphy CJ (2001) Evidence for seed-mediated nucleation in the chemical reduction of gold salts to gold nanoparticles. Chem Mater 13:2313–2322
21. Privman V, Goia DV, Park J, Matijević E (1999) Mechanism of formation of monodispersed colloids by aggregation of nanosize precursors. J Colloid Interface Sci 213:36–45
22. Ji XH, Song XN, Li J, Bai Y, Yang W, Peng X (2007) Size control of gold nanocrystals in citrate reduction: the third role of citrate. J Am Chem Soc 129:13939–13948
23. Watzky MA, Finke RG (1997) Transition metal nanocluster formation kinetic and mechanistic studies. A new mechanism when hydrogen is the reductant: slow, continuous nucleation and fast autocatalytic surface growth. Chem Mater 9:3083–3095
24. Leisner T, Rosche C, Wolf S, Granzer F, Woste L (1996) The catalytic role of small coinage-metal clusters in photography. Surf Rev Lett 3(1):1105–1108
25. Tauschtreml R, Henglein A, Lilie J (1978) Reactivity of silver atoms in aqueous solution, a pulse radiolysis study. Ber Bunsenges Phys Chem 82(12):1335–1343
26. Cai M, Chen J, Zhou J (2004) Reduction and morphology of silver nanoparticles via liquid-liquid method. Appl Surf Sci 226:422–426
27. Ayyappan S, Gopalan RS, Subbana GN, Rao CNR (1997) Nanoparticles of Ag, Au, Pd, and Cu produced by alcohol reduction of the salts. J Mater Res Soc 12(2):398–401
28. Busser GW, Ommen JG, Lercher JA (1999) Preparation and characterization of polymer-stabilized rhodium sols. I. Factors affecting particle size. J Phys Chem B 103(10):1651–1659
29. Huang HH, Ni XP, Loy GL, Chew CH, Tan KL, Loh FC, Deng JF, Xu GQ (1996) Photochemical formation of silver nanoparticles in poly(N-vinylpyrrolidone). Langmuir 12:909–912
30. Esumi K, Itakura T, Torigoe K (1994) Preparation of organo palladium sols from palladium complexes in various alcohols. Colloids Surf A 82:111–113
31. Mie G (1908) Beitrage zur Optik Truber Medien, Speziell Kolloidaler Metallosungen. Ann Phys 25:377–445
32. Seregina MV, Bronstein LM, Platonova OA, Chernyshov DM, Valetsky PM, Hartmann J, Wenz E, Antonietti M (1997) Preparation of noble-metal colloids in block copolymer micelles and their catalytic properties in hydrogenation. Chem Mater 9:923–931
33. Antonietti M, Wenz E, Bronstein L, Seregina M (1995) Synthesis and characterization of noble metal colloids in block copolymer micelles. Adv Mater 7:1000–1005
34. Spatz JP, Sheiko S, Möller M (1996) Ion-stabilized block copolymer micelles: film formation and intermicellar interaction. Macromolecules 29:3220–3226
35. Saptz JP, Mössmer S, Hartmann C, Möller M, Herzog T, Krieger M, Boyen HG, Ziemann P, Kabius B (2000) Ordered deposition of inorganic clusters from micellar block copolymer films. Langmuir 16:407–415
36. Yoon NM, Yang HS, Hwang YS (1987) Reducing characteristics of potassium triethylborohydride. Bull Korean Chem Soc 8:285–291

37. Mössmer S, Spatz JP, Möller M, Aberle T, Schmidt J, Burchard W (2000) Solution behavior of poly(styrene)-block-poly(2-vinylpyridine) micelles containing gold nanoparticles. Macromolecules 33:4791–4798
38. D'Aprano A, Donato ID, Pinio F, Liveri VT (1990) Complex formation in aerosol OT reversed micelles between sodium counterion and Kryptofix 221D macrobicyclic ligand. J Solution Chem 19:589–595
39. Arcoleo V, Cavallaro G, Manna GL, Liveri VT (1995) Calorimetric investigation on the formation of palladium nanoparticles in water/AOT/n-heptane microemulsions. Thermochim Acta 254:111–119
40. Aliotta F, Arcoleo V, Buccoleri S, Manna GL, Liveri VT (1995) Calorimetric investigation on the formation of gold nanoparticles in water/AOT/n-heptane microemulsions. Thermochim Acta 265:15–23
41. Patakfalvi R, Dékány I (2005) Nucleation and growing of silver nanoparticles under control of titration microcalorimetric experiment. J Therm Anal Calorim 79:587–594
42. Bonnemann H, Brijoux W, Brinkmann R, Tilling AS, Schilling T, Tesche B, Seevogel K, Franke R, Hormes J, Kohl G, Pollmann J, Rothe J, Vogel W (1998) Selective oxidation of glucose on bismuth-promoted Pd-Pt/C catalysts prepared from NOct(4)Cl-stabilized Pd-Pt colloids. Inorg Chim Acta 270(1–2):95–110
43. Király Z, Veisz B, Mastalir Á, Rázga Z, Dékány I (1999) Preparation of an organophilic palladium montmorillonite catalyst in a micellar system. Chem Commun 19:1925–1926
44. Reetz MT, Helbig W (1994) Size-selective synthesis of nanostructured transition metal clusters. J Am Chem Soc 116(16):7401–7402
45. Reetz MT, Quaiser SA, Breinbauer R, Tesche B (1995) A new method for the preparation of nanostructured metal clusters. Angew Chem Int Ed Engl 34:2240–2241
46. Wang Q, Liu H, Wang H (1997) Immobilization of polymer-stabilized noble metal colloids and their catalytic properties for hydrogenation of olefins. J Colloids Interface Sci 190:380–386
47. Wang Y, Liu H, Huang Y (1996) Immobilization of polymer-protected metal colloid catalysts by the formation of polymer hydrogen bond complexes. Polym Adv Techol 7:634–638
48. Dékány I, Turi L, Szűcs A, Király Z (1998) Preparation of semiconductor and transition metal nanoparticles on colloidal solid supports. Colloids Surf A 141:405–417
49. Papp S, Szűcs A, Dékány I (2001) Preparation of Pd nanoparticles stabilized by polymers and layered silicate. Appl Clay Sci 19:155–172
50. Király Z, Dékány I, Mastalir Á, Bartók M (1996) In situ generation of palladium nanoparticles in smectite clays. J Catal 161:401–408
51. Szűcs A, Király Z, Berger F, Dékány I (1998) Preparation and hydrogen sorption of Pd nanoparticles on Al_2O_3 pillared clays. Colloids Surf A Physicochem Eng Asp 139:109–118
52. Papp S, Dékány I (2006) Nucleation and growth of palladium nanoparticles stabilized by polymers and layer silicates. Colloid Polym Sci 284:1049–1056
53. Patakfalvi R, Virányi Z, Dékány I (2004) Kinetics of silver nanoparticle growth in aqueous polymer solutions. Colloid Polym Sci 283(3):299–305
54. Patakfalvi R, Papp S, Dékány I (2007) The kinetics of homogeneous nucleation of silver nanoparticles stabilized by polymers. J Nanoparticle Res 9:353–364
55. Esumi K, Hosoya T, Yamahira A, Torigoe K (2000) Formation of gold and silver nanoparticles in aqueous solution of sugar-persubstituted poly(amidoamine) dendrimers. J Colloid Interface Sci 226:346–352
56. Dobos D (1979) Electrochemical tables. Műszaki könyvkiadó, Budapest
57. Papp S, Kőrösi L, Gool B, Dederichs T, Mela P, Möller M, Dékány I (2010) Formation of gold nanoparticles in diblock copolymer micelles with various reducing agents: kinetic and thermodynamic studies. J Therm Anal Calorim 101:865–872
58. Papp S, Szél J, Oszkó A, Dékány I (2004) Synthesis of polymer-stabilized nanosized rhodium particles in the interlayer space of layered silicates. Chem Mater 16:1674–1685

59. Papp S, Patakfalvi R, Dékány I (2008) Metal nanoparticle formation on layer silicate lamellae. Colloid Polym Sci 286:3–14
60. Patakfalvi R, Dékány I (2004) Synthesis and intercalation of silver nanoparticles in kaolinite/DMSO complexes. Appl Clay Sci 25(3–4):149–159
61. Patakfalvi R, Oszkó A, Dékány I (2003) Synthesis and characterization of silver nanoparticle/kaolinite composites. Colloids Surf A Physicochem Eng Asp 220(1–3):45–54

Chapter 12
Synthesis, Structure, and Photocatalytic Activity of Titanium Dioxide and Some of Its Surface-Modified Derivatives

László Kőrösi, Szilvia Papp, and Imre Dékány

Abstract Titania-based heterogeneous photocatalysis has been extensively studied at both solid–liquid and solid–gas interfaces. Numerous efforts have been directed to improving the photocatalytic activity of TiO_2 in both the UV and the visible wavelength ranges. To enhance the photoactivity, a number of techniques for the doping of TiO_2 with various elements have been developed. This chapter presents a brief discussion of three promising materials: phosphate-, nitrogen-, and silver-modified TiO_2. Phosphate- and silver-modified TiO_2 exhibited very high photocatalytic activity under UV irradiation, while the nitrogen-doped TiO_2 had visible light activity. The modified TiO_2 derivates were prepared by simple chemical methods and studied by various surface and structural investigation techniques. The effects of the dopant concentration on the structure and photocatalytic activity are discussed.

12.1 Introduction

The accumulation in surface waters and in the atmosphere of environmentally harmful compounds that are not readily biodegradable has prompted the development of efficient water and air purification technologies. Heterogeneous photocatalysis is a well-known environmentally friendly process for the degradation or

L. Kőrösi • S. Papp
Supramolecular and Nanostructured Materials Research Group of the Hungarian Academy of Sciences, University of Szeged, Aradi vértanúk tere 1, H-6720 Szeged, Hungary

I. Dékány (✉)
Supramolecular and Nanostructured Materials Research Group of the Hungarian Academy of Sciences, University of Szeged, Aradi vértanúk tere 1, H-6720 Szeged, Hungary

Department of Physical Chemistry and Materials Science, University of Szeged, Aradi vértanúk tere 1, H-6720 Szeged, Hungary
e-mail: i.dekany@chem.u-szeged.hu

L. Guczi and A. Erdőhelyi (eds.), *Catalysis for Alternative Energy Generation*,
DOI 10.1007/978-1-4614-0344-9_12,

transformation of volatile organic compounds (VOCs). As regards practical applicability, the ideal photocatalyst would be chemically stable, easy to prepare and use, cheap to produce, safe for humans and the environment, and an efficiently catalyst. Among various metal oxides (TiO_2, ZnO, WO_3, SnO_2, etc.), TiO_2 meets nearly all of these requirements. Both TiO_2 polymorphs, anatase and rutile, are extensively used as photocatalysts. In most reactions, anatase exhibits higher photocatalytic activity [1, 2] probably due to its slightly higher Fermi level and its higher surface density of OH groups [3, 4]. Attempts have been made to improve the photoactivity of TiO_2 in both the visible and the UV ranges. Doping and the surface modification of TiO_2 with this aim, using a variety of elements, has become an intensively studied research area. The application of nonmetals for this purpose is relatively recent but has already yielded many noteworthy results.

TiO_2 can utilize only a small region of the solar spectrum due to its wide bandgap energy. Consequently, improvement of the response to visible light (i.e.,photosensitization) is one of the most important aspects of heterogeneous photocatalysis. Doping of TiO_2 with various metals or metal ions (Pt, Ag, Au, Cr, Fe, Cu, etc.) has been widely used as a technique to extend light absorption to the visible region [5–10]. The surface modification or doping of TiO_2 is usually carried out by methods such as impregnation, photodeposition, or a sol–gel technique. The effect of the doping agent on the photodegradation efficiency is not evident. The positive effect of metal deposits has been explained by improved interfacial charge-transfer processes [11]. However, some metals on the TiO_2 surface have no effect, or the doping results in a detrimental effect on the photocatalytic degradation of the organic compound [12, 13]. This miscellaneous behavior may frequently be explained by the difference in nature of the studied VOCs. TiO_2–clay mineral nanocomposites, as efficient photocatalysts, can be prepared either doped or nondoped TiO_2 and layer silicates [14–17]. The large specific surface area of the applied layer silicate favors the adsorption of organic compounds [18, 19]. The combination of adsorption and heterogeneous photocatalysis may be an efficient and economical means of accumulating, removing, and oxidizing organic contaminants, and its application is in accordance with the growing environmental demands [14, 20, 21].

Doping with nonmetal anions is preferred to metal ion doping, because anions tend to form fewer recombination centers on the surface of TiO_2. Several studies have been devoted to anionic modifications of TiO_2, and halide ions have received special attention. Minero and coworkers investigated the effects of fluoride ions on the photocatalytic degradation of phenol in aqueous TiO_2 suspension [22, 23]. They found that the rate of degradation of phenol increased as a function of the fluoride concentration. Luo et al. [24] studied the efficiency of Br^- and Cl^- co-doped TiO_2 in water splitting and found higher photocatalytic activity than with commercial Degussa P25 TiO_2. Sulfated TiO_2 also exhibits enhanced photoactivity for several substrates, such as hexane, methanol, benzene, and trichloroethylene [25–27]. The phosphate modification of TiO_2 has been the subject of a considerably smaller number of studies, and the results proved highly diverse from a photocatalytic aspect probably in consequence of differences in preparation techniques and in phosphate contents. Colón et al. [28] used different oxoacids (HNO_3, H_2SO_4, and H_3PO_4) to modify TiO_2. They reported that the photoactivity decreased strongly

after H_3PO_4 treatment. The poor photocatalytic behavior is determined by the appearance of pyrophosphate-like species on the surface. In contrast, Yu et al. [29] found that the photocatalytic activity of phosphate-modified TiO_2 was higher. The effect was explained by the increased bandgap energy, the large surface area, and the existence of Ti ions in tetrahedral coordination. Visible light-driven photocatalysis can be achieved by applying nitrogen-doped TiO_2 (N–TiO_2) [30–32]. The N-doping of TiO_2 was found to result in a significant bandgap narrowing. Nakamura et al. reported that the increased visible light absorption of N–TiO_2 is due to an N-induced mid-gap level, which was generated slightly above the O 2*p* valence band [33]. Ihara et al. [34] concluded that oxygen-deficient sites generated on the grain boundaries in the N–TiO_2 polycrystalline structure are also important for the visible light activity. N–TiO_2 photocatalysts can be prepared by either physical (e.g., magnetron sputtering [35]) or chemical (e.g., sol–gel [36]) methods. Chemical methods make use of organic N-sources such as amines [37] or urea [38], while others use inorganic sources such as NH_3 [39, 40].

Photocatalytic oxidation of organic pollutants in the gas phase is a subject of considerable interest. Alkanes, alcohols, aldehydes, ketones, aromatics, and halogenated hydrocarbons have been efficiently degraded at solid–gas interfaces [41]. The photooxidation of ethanol is well known from the literature [42, 43]. Nimlos et al. [44] proposed the reaction pathway ethanol → acetaldehyde → acetic acid → formaldehyde → formic acid → CO_2, in which acetaldehyde is the main gas-phase intermediate. The first complete kinetic model for the photocatalyzed oxidation of ethanol and acetaldehyde was published by Sauer and Ollis [45].

In this chapter, we briefly discuss the structural and photocatalytic properties of various TiO_2 derivatives, such as (1) phosphate-, (2) nitrogen-, and (3) silver-modified TiO_2. These derivatives were prepared by using different chemical surface treatment methods. The procedures used for the structural characterization of the samples included X-ray powder diffraction and nitrogen adsorption measurements. To determine the optical properties and bandgap energies of the modified TiO_2 samples, diffuse reflectance UV–Vis spectroscopy measurements were made. The surface features and compositions were studied by diffuse reflectance infrared and X-ray photoelectron spectroscopy. The photocatalytic activities of pure and modified TiO_2 samples were compared at both solid–liquid and solid–gas interfaces. We examined the processes of photodegradation of phenol and thiodiglycol (TDG) in the liquid phase and of ethanol in the gas phase. We report here on the effects of surface-bound species on the rates of photooxidation of these organic compounds.

12.2 Experimental Details

12.2.1 Materials and Methods

Phosphate-modified TiO_2 samples with varying phosphate contents were prepared by a sol–gel method [46]. Titanium(IV) isopropoxide was hydrolyzed with water, and the amorphous $TiO_2 \cdot nH_2O$ obtained was treated with H_3PO_4 solution, at P/Ti

molar ratios of 0.01, 0.05, 0.10, 0.2, and 0.3. These molar ratios are included in the designation of the samples (e.g., P–TiO_2/0.10). The dried powders were calcined at various temperatures in the range 100–900°C.

N-doped TiO_2 samples were prepared by a simple precipitation method [47]. Titanium isopropoxide was added dropwise to urea solution under vigorous stirring at N/Ti molar ratios of 1, 3, and 5. The precipitates obtained were filtered off and dried at 30°C. The dried powders were calcined at 400°C for 4 h in air. These samples are denoted N–TiO_2/1.0, N–TiO_2/3.0, and N–TiO_2/5.0, respectively.

H_2SO_4-treated N-doped TiO_2 samples (denoted N–TiO_2-*sulf*) were prepared by an impregnation method. The N–TiO_2 samples were dispersed in 0.5 M H_2SO_4 solutions, and the acidic dispersions were stirred for 1 h and then filtered. The solid fractions were dried at 30°C.

Silver-modified TiO_2 samples were prepared from a Degussa P25 TiO_2 dispersion and $AgNO_3$ by a photodeposition method [11]. The TiO_2 aqueous dispersions containing the desired amount of $AgNO_3$ were irradiated by a UV-light source (Xe-lamp, 300 W) for 1 h. The dispersions obtained were centrifuged and dried at 60°C. The calculated Ag contents of the samples were 0.1, 0.5, and 1.0 w/w%. These samples are denoted Ag–TiO_2/0.1 wt%, Ag–TiO_2/0.5 wt%, and Ag–TiO_2/1.0 wt%, respectively.

The Ti and P contents of the samples were determined by all-argon sequential (Jobin-Yvon 24, France) inductively coupled plasma-atomic emission spectrometry (ICP-AES). The intensities of the (P I) and (Ti II) spectral lines were measured at 213.62 and 337.28 nm, respectively.

X-ray diffraction (XRD) patterns were collected on a Philips PW 1,830 powder diffractometer, using CuK_α radiation ($\lambda = 0.1542$ nm).

Porosity and surface area were studied on a Gemini 2375 (Micromeritics) instrument by recording N_2-sorption isotherms at −196°C. Before the adsorption measurements, the samples were evacuated (10^{-5} torr) at 120°C overnight. Specific surface areas were calculated by using the Brunauer–Emmett–Teller equation.

Transmission electron microscopy (TEM) images were obtained with a Philips CM-10 electron microscope at an accelerating voltage of 100 kV. Scanning electron microscopy (SEM) was performed with a Hitachi S-4700 FE-SEM instrument.

Diffuse reflectance UV–Vis spectra were recorded on CHEM 2000 UV–Vis (Ocean Optics Inc.) spectrophotometer equipped with an integrated sphere.

XP spectra were taken with a SPECS instrument equipped with a PHOIBOS 150 MCD 9 hemispherical electron energy analyzer operated in the FAT mode.

Diffuse reflectance infrared Fourier transform spectroscopy (DRIFTS) measurements were made with a Bio-Rad Digilab Division FTS-65A/896 spectrometer, with 256 scans per sample, at a resolution of 4 cm^{-1}.

Photocatalytic test reactions in the gas phase were performed at 25 ± 0.1°C in a cylindrical photoreactor (Fig. 12.1a, b) with a volume of ~700 ml. The scheme of the experimental setup can be seen in Fig. 12.2. The photoreactor consisted of two concentrically positioned tubes. The inner tube was made from quartz and the outer one from Pyrex glass. A 15-W low-pressure mercury lamp (GCL307T5L/CELL LightTech, Hungary) with a characteristic emission wavelength of 254 nm was

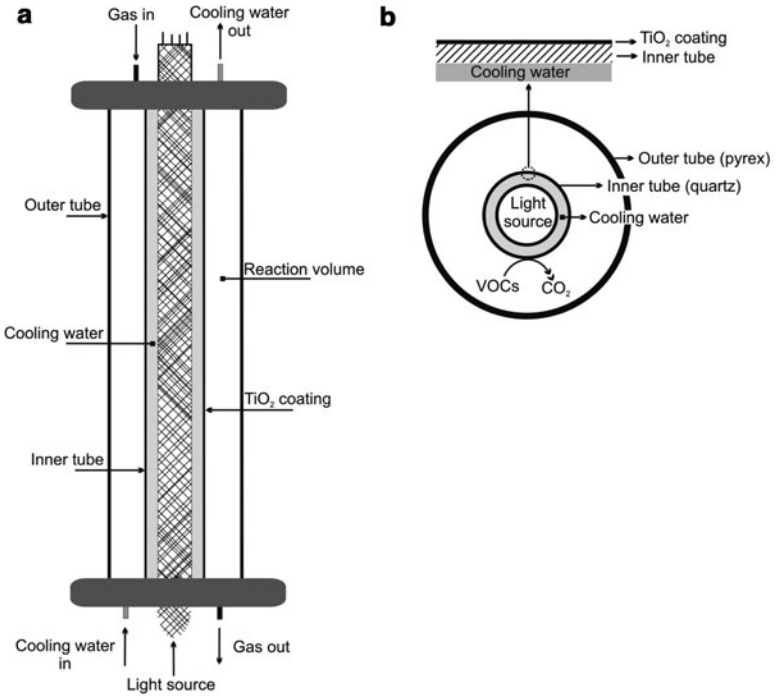

Fig. 12.1 Schematic drawing of (**a**) the cylindrical KL700 photoreactor [46] and (**b**) its cross-sectional view [11]

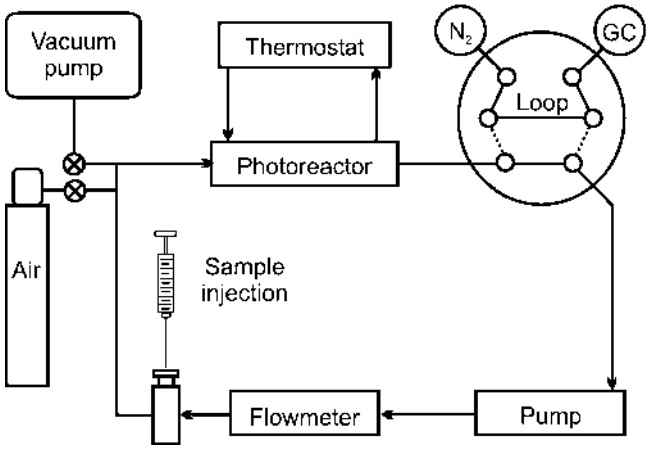

Fig. 12.2 Schematic outline of the experimental setup [46]

placed at the center, as shown in Fig. 12.1b. The TiO_2 samples were sprayed onto the outer side of the inner quartz tube using 30% (w/v) aqueous dispersion. The surface area of the TiO_2 film was 175.8 cm^2. Sampling from the gas phase was performed at selected time intervals, and the composition was analyzed in a gas chromatograph (Shimadzu GC-14B) equipped with a thermal conductivity (TCD) and a flame ionization detector (FID).

Photocatalytic experiments at the solid–liquid interface were carried out in a 400-ml batch reactor thermostated at 25°C. For sample irradiation, a 150-W immersion-type high-pressure mercury lamp (Heraeus TQ 150) was used, surrounded by a glass filter in order to filter out the high-energy photons ($\lambda < 310$ nm). The concentration of phenol was determined by HPLC, with a UV–Vis detector at 210 nm. Phenol and its intermediates were separated on a C-18 column [LiChrospher 100 RP-18 (5 μm)], using a mixture of acetonitrile:water (20:80) as eluent at a flow rate of 1 ml min^{-1}.

12.3 Results and Discussion

12.3.1 Phosphate-Modified TiO_2

12.3.1.1 Composition and Structure of Phosphate-Modified TiO_2

Phosphate-modified titanium dioxide (P–TiO_2) can be prepared by the treatment of $TiO_2 \cdot nH_2O$ with H_3PO_4. The sol–gel synthesis method applied was divided into two main steps: (1) In the course of the reaction of titanium(IV) isopropoxide and water, amorphous $TiO_2 \cdot nH_2O$ was formed by hydrolysis of the precursor and subsequent condensation of the product. (2) $TiO_2 \cdot nH_2O$ reacted with H_3PO_4, and phosphate species were chemisorbed on the surface of the oxide nanoparticles. The DRIFT spectra of TiO_2 and P–TiO_2 samples are compared in Fig. 12.3. After the treatment of TiO_2 with H_3PO_4, a new absorption peak appeared in the range 980–1,200 cm^{-1}. This broad band is associated with the characteristic stretching vibrations of phosphate groups, and its intensity was proportional to phosphate content. The peak at 1,630 cm^{-1} can be assigned to the bending mode of water. The broad band at ~3,400 cm^{-1} is assigned to the O–H stretching mode. The intensities of these bands also increased with the phosphate content. The DRIFT spectra revealed that, in the course of H_3PO_4 treatment of the TiO_2 suspension, phosphate species are bonded to the surface of the TiO_2 in amounts proportional to the H_3PO_4 concentration applied [48]. The protonated surface hydroxyl groups ($–OH_2^+$) of TiO_2 can react with HPO_4^{2-} [49]. Connor and McQuillan [50] studied the adsorption of orthophosphate on the surface of TiO_2 from aqueous solution by in situ internal reflectance spectroscopy and reported the strong binding of the bidentate form of phosphate to the surface.

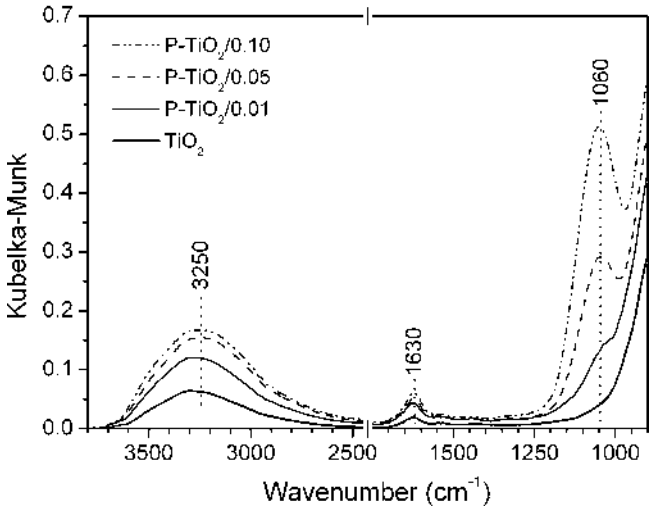

Fig. 12.3 DRIFT spectra of pure TiO_2 and different P–TiO_2 samples [52]

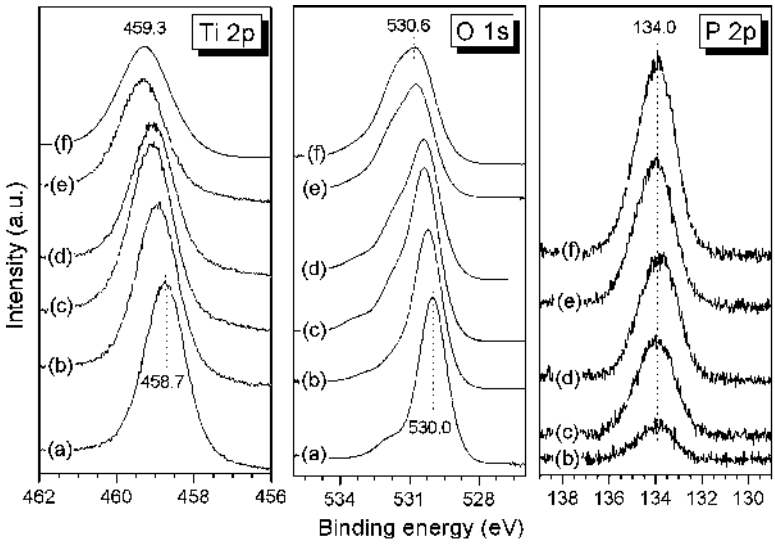

Fig. 12.4 High-resolution XP spectra of the Ti 2*p*, O 1*s*, and P 2*p* regions on (a) Degussa P25, (b) P–TiO_2/0.01, (c) P–TiO_2/0.05, (d) P–TiO_2/0.10, (e) P–TiO_2/0.20, and (f) P–TiO_2/0.3 [46]

High-resolution XP spectra were taken from the Ti 2*p*, O 1*s*, P 2*p*, and C 1*s* regions. The carbon was present as surface adventitious carbon and served as a binding energy reference. The spectra obtained are shown in Fig. 12.4. The bottom Ti $2p_{3/2}$ and O 1*s* spectra are those of Degussa P25. It can be seen from the figure that the Ti $2p_{3/2}$ spectra are symmetric in each case. The Ti $2p_{3/2}$ peak for Degussa

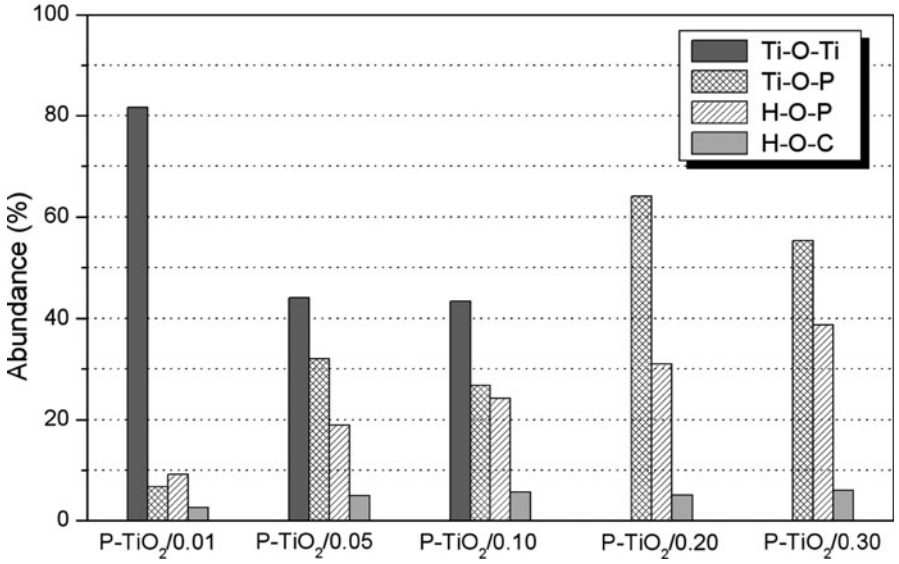

Fig. 12.5 Relative content of O in various P–TiO_2 samples in different chemical environments: (Ti−O−Ti), (Ti−O−P), (H−O−P), and (H−O−C) [46]

P25 is at 458.7 eV and corresponds to the value generally reported in the literature for Ti^{4+} in TiO_2. As the P concentration was increased, the peak position of the Ti $2p_{3/2}$ spectral envelope shifted slightly from 458.9 to 459.3 eV, and at the same time, the full width at half maximum (FWHM) increased from 1.29 to 1.51 eV at the highest P content. These results can be explained by the formation of Ti–O–P bonds upon the addition of phosphate to the system. The O 1*s* spectra showed obvious asymmetry for each phosphated sample studied. In Degussa P25, the O 1*s* binding energy was measured to be 530.0 eV, characteristic of lattice oxygen in TiO_2. The small shoulder on the high binding energy side of the peak is caused by the surface and near-surface OH groups of TiO_2. In response to phosphate addition, the maximum of the envelope shifted from 530.2 to 530.6 eV with increase of the P content. The nature and the extent of this positive shift were quite similar to those observed in the Ti $2p_{3/2}$ spectra, and these features were more pronounced at the two highest atomic ratios P:Ti. The individual components were determined by deconvoluting the spectra. A reasonably good fit was achieved by decomposing the envelope into four synthetic peaks with the constraint that FWHM should be the same for them. The result of the decomposition is displayed in Fig. 12.5. It was assumed that the four components increasing in energy can be assigned to oxygen participating in Ti−O−Ti, Ti−O−P, H−O−P, and H−O−C bonds. The formation of H−O−C may be attributed to different types of carbon–oxygen bonds related to the adventitious carbon content of the sample. Its concentration of ~5% was practically independent of the sample composition. The area of the peak at ~530 eV decreased with increasing ratio P:Ti and attained a value of zero for the two most

Table 12.1 Chemical compositions of P–TiO_2 samples calcined at 700°C [46]

Sample ID	P (at%)	Ti (at%)	O (at%)	$(P:Ti)_{XPS}$[a] atomic ratio	$(P:Ti)_{ICP}$[b] atomic ratio
P–TiO_2/0.01	1.9	29.0	69.2	0.065	0.012
P–TiO_2/0.05	4.2	24.0	71.8	0.176	0.055
P–TiO_2/0.10	6.3	22.8	71.0	0.275	0.106
P–TiO_2/0.20	8.2	22.0	69.8	0.373	0.205
P–TiO_2/0.30	10.2	19.0	70.7	0.537	0.308

[a]Determined by XPS measurements
[b]Determined by ICP-AES measurements

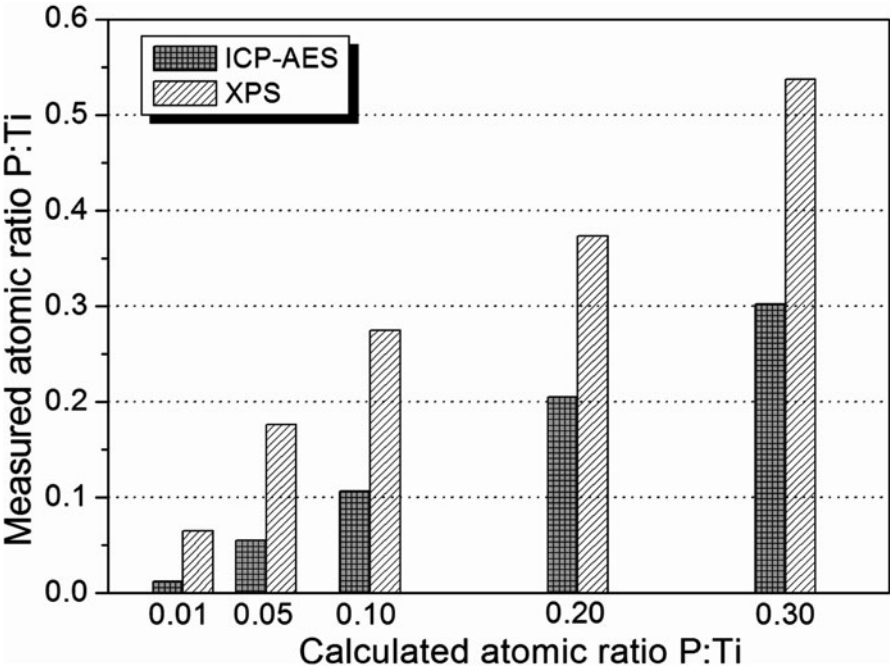

Fig. 12.6 Atomic ratio P:Ti (based on XPS and ICP-AES) of P–TiO_2 as a function of the calculated atomic ratio P:Ti. The samples were calcined at 700°C [46]

P-rich samples. At the same time, the intensities of the peaks associated with the Ti−O−P and H−O−P bonds increased from ~7 to 60% and from 9 to 39%, respectively. The detected P 2*p* did not exhibit asymmetry, and the peak position was practically independent of the P concentration. The P 2*p* binding energy, 134.0 eV (±0.1), is characteristic of P in the phosphate ion. We did not detect a peak at ~128 eV, which rules out the existence of Ti−P on the sample surface.

The atomic ratios P:Ti were determined by XPS from the peak areas, taking into account the sensitivity factors for the atomic orbitals, and also by ICP-AES. The results are listed in Table 12.1 and are plotted in Fig. 12.6. It is immediately clear from both the table and the figure that higher values for the atomic ratio P:Ti

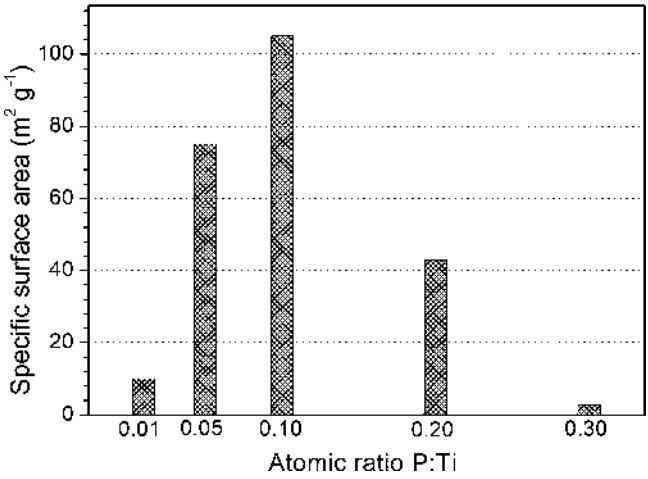

Fig. 12.7 Effect of phosphate modification on the specific surface area of TiO_2 [46]

were observed with the surface-sensitive XPS than with ICP-AES, which detects signals from the bulk phase as well. This means that the P was accumulated on the surface of the TiO_2 particles [46].

Angle-resolved XP spectra were taken from the sample P–TiO_2/0.05. The takeoff angle of the photoelectrons with respect to the surface normal was varied by tilting the sample holder around the horizontal axis of the manipulator. No change was observed either in the position or in the shape of the P 2*p* spectra. This result again suggests that the P-rich near-surface layer is thicker than the escape depth of P 2*p* electrons from the sample. XP measurements support the idea that added phosphate is incorporated into the TiO_2, forming titanium phosphate species in the surface and near-surface regions. The thickness of this layer is possibly more than the escape depth of P 2*p* photoelectrons [46].

The N_2-sorption isotherms of the samples clearly demonstrated that the porosity of the P–TiO_2 samples also depends on their phosphate content. At atomic ratios of P:Ti = 0.01–0.10, a hysteresis loop indicative of a mesoporous structure was seen. The most characteristic pore diameters determined by BJH evaluation were 3.3, 4.9, and 3.1 nm for P–TiO_2/0.05, P–TiO_2/0.10, and P–TiO_2/0.20, respectively. The specific surface area as a function of the phosphate content passed through a maximum (Fig. 12.7); it increased with increasing P content up to P:Ti = 0.10 (105 m^2 g^{-1}) and decreased at higher P contents. The specific surface area of P–TiO_2/0.30 was as low as 2.7 m^2 g^{-1}.

Since the anatase content has a significant effect on the photocatalytic activity of TiO_2, we examined the effect of phosphate modification on the crystallization of amorphous TiO_2. The XRD patterns of P–TiO_2 samples with various phosphate contents calcined at 700°C are shown in Fig. 12.8. The measurements clearly demonstrated that the intensity and the FWHM of the (101) anatase peak decreased with increasing phosphate content. The former indicates a decrease in anatase

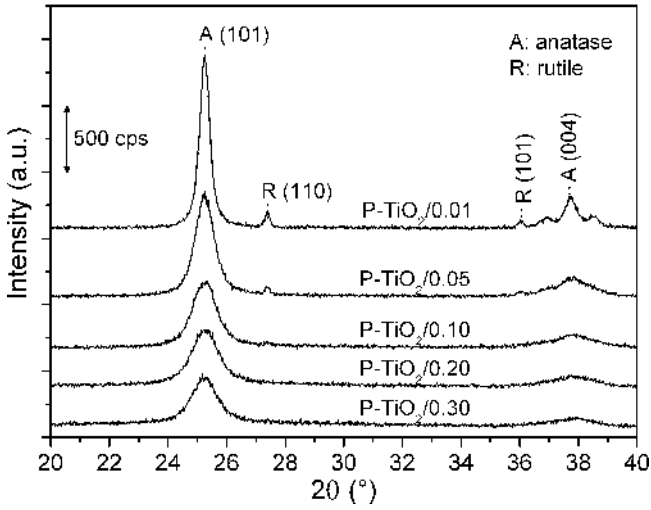

Fig. 12.8 XRD patterns of different P–TiO_2 samples calcined at 700°C [46]

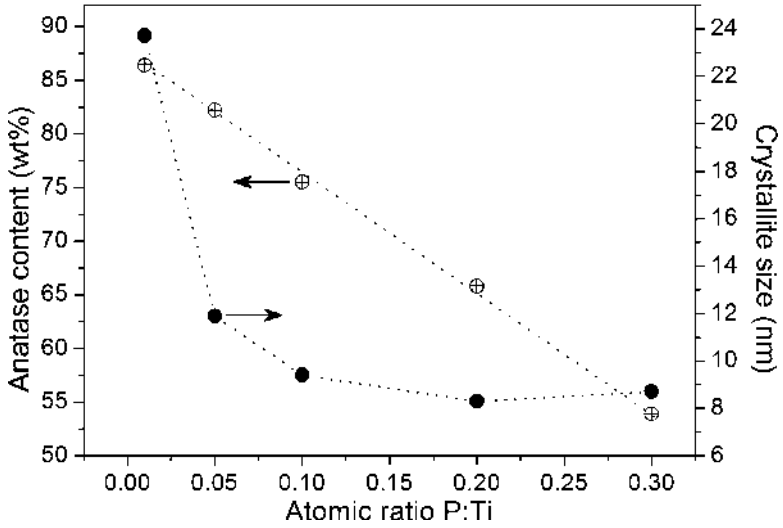

Fig. 12.9 Anatase content and its crystallite size in P–TiO_2 samples (based on XRD measurements) [46]

content, and the latter a reduction in crystallite size. The rutile content of P–TiO_2/0.01 was only 4 w/w%, whereas at atomic ratios P:Ti $>$ 0.10 rutile formation was not observed at all. The average crystallite diameter was determined from the FWHM of the (101) peak by using the Scherrer equation. Changes in anatase content and average crystallite diameters as a function of atomic ratio P:Ti are presented in Fig. 12.9. As the phosphate content was increased, the anatase content

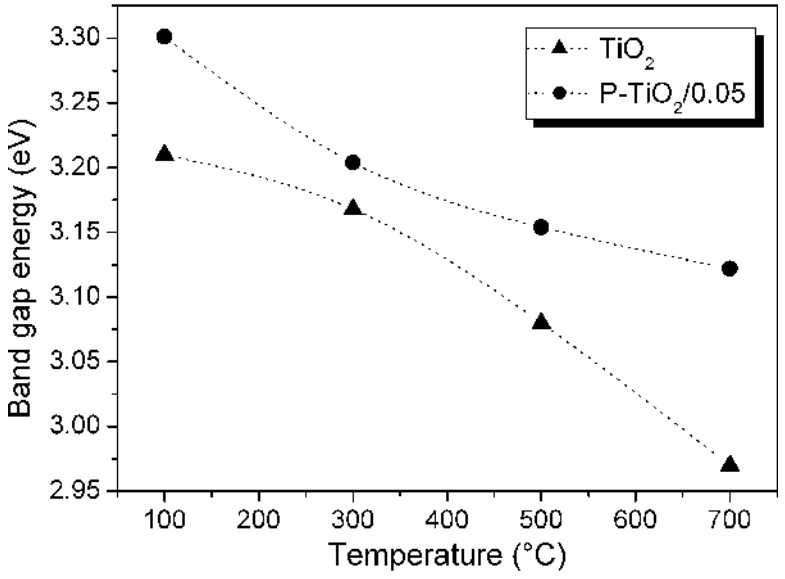

Fig. 12.10 Bandgap energy of TiO_2 and P–TiO_2/0.05 as a function of calcination temperature [52]

decreased from 86 to 54 w/w% in a nearly linear fashion. Consequently, the presence of phosphate inhibits the crystallization of TiO_2; thus, 10–46 w/w% of the samples (depending on phosphate content) comprises a mixture of amorphous TiO_2 and amorphous titanium phosphate. Figure 12.9 also demonstrates that the growth of anatase crystallites was inhibited in the P–TiO_2 samples. The average crystallite size of anatase at an atomic ratio P:Ti = 0.01 was 24 nm, whereas at higher phosphate contents the size was only 8–12 nm. When samples with relatively high phosphate contents (P:Ti > 0.05) were calcined at 900°C, crystalline titanium phosphate was identified (JCPDS: 38-1468). Our X-ray studies indicated that, in the course of calcination, the presence of titanium phosphate species significantly affected both the formation of the anatase and rutile phases and the crystallite size.

Bandgap energies (E_g) determined from the absorption edge are presented in Fig. 12.10. It can be seen that E_g for P–TiO_2 exceeded that for pure TiO_2 at each calcination temperature. The higher bandgap energy of P–TiO_2 is partly accounted for by the change in the structure of the TiO_2 surface (chemisorbed phosphate) and partly by the smaller anatase crystallite size [51]. The bandgap energy decreased with increasing calcination temperature for both the pure TiO_2 and P–TiO_2; however, this was less significant in the case of the P–TiO_2 samples. The red shift observed in the course of calcination may be due in part to increasing anatase crystallite size and in part to the anatase–rutile phase transformation (between 500 and 700°C) [52].

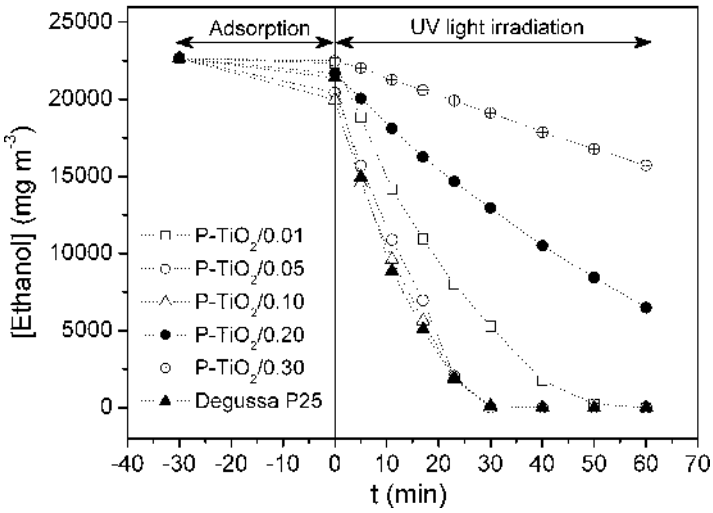

Fig. 12.11 Photodegradation of ethanol on Degussa P25 TiO_2 and various P–TiO_2 samples under dry initial conditions [46]

12.3.1.2 Photocatalytic Activity of Phosphate-Modified TiO_2

The photocatalytic activities of P–TiO_2 samples were tested in the photooxidation of ethanol at the solid–gas interface. The reactions were carried out both in the absence and in the presence of water vapor. The reference photocatalyst was the well-known Degussa P25 TiO_2. Photooxidation experiments were also performed without catalyst, resulting in a negligible decrease in ethanol concentration (below 2%) during the 1-h irradiation applied. When the experiment was carried out in the absence of TiO_2 films, there was no detectable formation of carbon dioxide. After the addition of ethanol or ethanol/water, the system was left to stand for 30 min for equilibrium to set in. This time period (negative range) is separated from the irradiation period by a vertical line in the kinetic curves of ethanol degradation.

Comparison of the kinetic curves of ethanol degradation under dry (Fig. 12.11) and humid initial conditions ($RH_i = 74\%$) (Fig. 12.12) reveals significant differences. The rate of ethanol degradation depends both on the phosphate content of TiO_2 on the one hand and on RH_i. Under both dry and humid initial conditions, the dependence of the reaction rate on the phosphate content of the samples displayed a maximum; the highest photoactivity was detected at atomic ratios P: Ti = 0.05 and 0.10 (regarded as optimal phosphate content). In the case of P–TiO_2 samples, the rate of ethanol photooxidation was higher in the presence than in the absence of water vapor. In contrast, on Degussa P25 TiO_2, the initial rate of ethanol photooxidation was lower in the presence of water, although the entire quantity of ethanol was transformed in 30 min under both sets of reaction conditions [46].

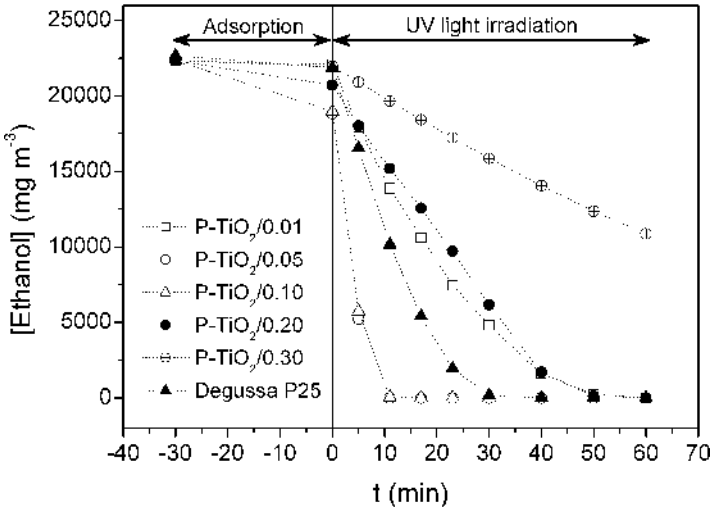

Fig. 12.12 Photodegradation of ethanol on Degussa P25 TiO_2 and various P–TiO_2 samples at 74% initial relative humidity [46]

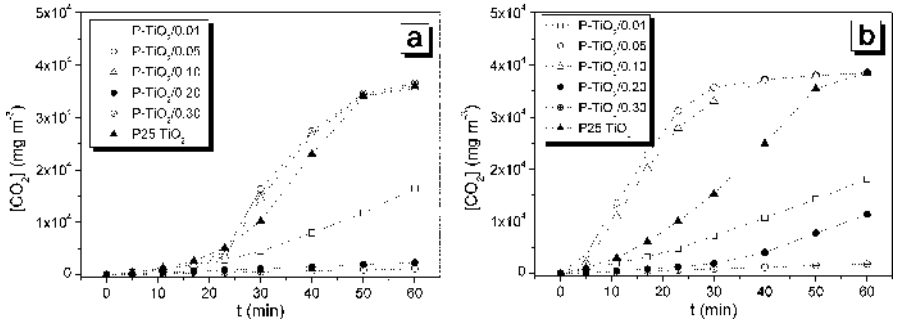

Fig. 12.13 Formation of CO_2 on bare (Degussa P25) and P–TiO_2 samples as a function of irradiation time at an initial relative humidity of (**a**) 0% and (**b**) 74% [46]

The kinetic curves of carbon dioxide formation (Fig. 12.13a, b) support the notion that the rate of total mineralization is strongly dependent on the phosphate content of the samples and on RH_i. The curves clearly show that carbon dioxide formation was very slow for the samples with higher phosphate contents (P–TiO_2/0.20 and P–TiO_2/0.30) under dry initial conditions. Slow carbon dioxide formation was observed even under humid conditions on P–TiO_2/0.20, although the entire quantity of ethanol was transformed. As a consequence of this partial oxidation, the intermediates (mainly acetaldehyde) were accumulated in the course of irradiation.

The effect of RH_i was studied by using P–TiO_2/0.05 sample. Figures 12.14 and 12.15 illustrate how the reaction rates increased when the amount of water was gradually increased at the onset of the reaction. It should be stressed, however, that

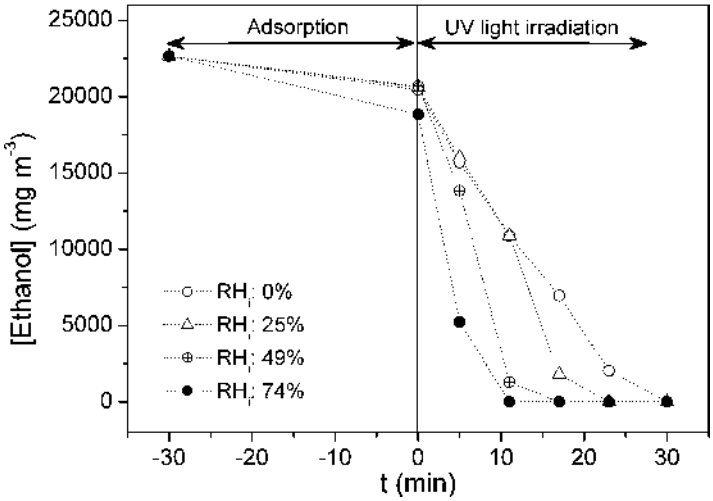

Fig. 12.14 Kinetic curves of ethanol degradation on P–TiO_2/0.05 at different initial relative humidities (0–74%) [46]

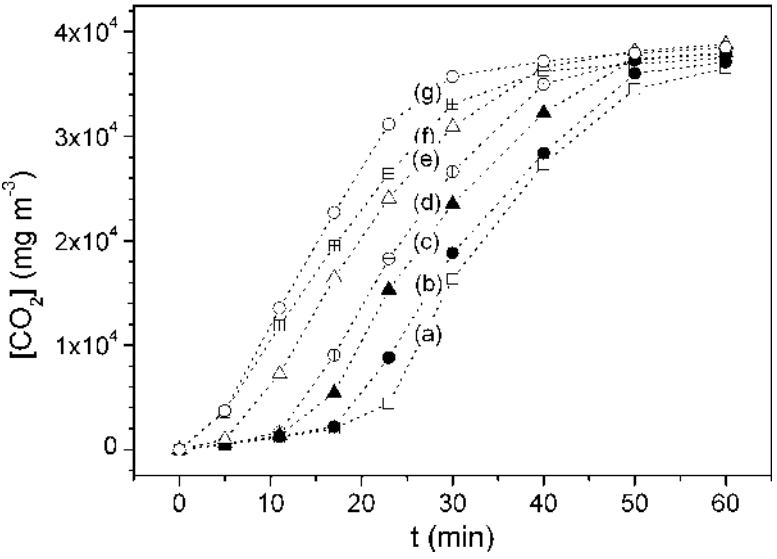

Fig. 12.15 Kinetic curves of CO_2 formation on P–TiO_2/0.05 at different initial relative humidities: (a) 0%, (b) 12%, (c) 25%, (d) 37%, (e) 49%, (f) 62%, and (g) 74% [46]

the RH_i given refers only to the initial conditions, since the total photooxidation of ethanol is accompanied by the formation of water. The water formed increases the rate of ethanol photodegradation, as indicated by the breakpoints in the kinetic curves presented in Fig. 12.14. Breakpoints tended to appear at increasingly earlier

Table 12.2 Specific surface areas ($a_{BET}{}^{s}$) and *crystalline phase compositions* of various P–TiO_2 samples calcined at 700°C [46]

Sample ID	$a^{s}_{BET}{}^{a}$ ($m^2\ g^{-1}$)	Anatase/rutile (wt%)
Degussa P25	51	87/13
P–TiO_2/0.01	10	86/4
P–TiO_2/0.05	75	82/2
P–TiO_2/0.10	105	75/–
P–TiO_2/0.20	43	66/–
P–TiO_2/0.30	3	54/–

[a]Calculated by using the Brunauer–Emmett–Teller equation

Table 12.3 Comparison of adsorption and photocatalytic properties of P25 TiO_2 and various P–TiO_2 samples [46]

Sample ID	RH_i (%)	$m_{EtOH}{}^{s}$ ($mg\ g^{-1}$)	$k_{(EtOH)}$ ($mg\ m^{-3}s^{-1}$)	$k_{(CO2)}$ ($mg\ m^{-3}s^{-1}$)	$w_{(CO2)}$ ($mg\ m^{-2}$)
Degussa P25	0	18	21.5	1.7	410
	74	11	17.8	3.6	612
P–TiO_2/0.01	0	4	11.8	1.3	181
	74	7	7.6	2.6	288
P–TiO_2/0.05	0	28	15.9	1.6	655
	74	49	51.1	12.4	1,433
P–TiO_2/0.10	0	34	17.9	1.3	585
	74	48	44.1	7.0	1,325
P–TiO_2/0.20	0	13	5.4	0.8	46
	74	26	9.0	0.8	77
P–TiO_2/0.30	0	3	1.5	–	23
	74	10	3.5	0.4	35

RH_i: initial relative humidity
$m_{EtOH}{}^{s}$: the amount of ethanol adsorbed on 1 g of catalyst
$k_{(EtOH)}$ and $k_{(CO2)}$: initial rate of ethanol photodegradation and CO_2 formation, respectively
$w_{(CO2)}$: amount of CO_2 formed on UV-irradiated surface unit after 30 min

times with increasing RH_i, i.e., at about 17, 11, and 5 min at $RH_i = 0$, 25, and 49%, respectively. After these initial periods, the reaction was accelerated due to the formation of additional water. This was confirmed by the kinetic curves of carbon dioxide formation, whose low-rate induction period became increasingly shorter as the RH_i was gradually increased (Fig. 12.15).

The structural parameters of the P–TiO_2 samples, the amounts of ethanol adsorbed prior to the lamp being switched on, initial rates of ethanol consumption (k_{EtOH}) and of carbon dioxide formation (k_{CO2}) are listed in Tables 12.2 and 12.3. The amounts of ethanol adsorbed were proportional to the BET surface area of the P–TiO_2 samples. Since the BET surface of P–TiO_2 displayed a maximum as a function of the ratio P:Ti, it was the samples with medium phosphate contents (P–TiO_2/0.05 and P–TiO_2/0.10) that adsorbed the largest amounts of ethanol under both dry and humid conditions. Furthermore, the P–TiO_2 samples adsorbed more ethanol in the presence than in the absence of water vapor. Conversely, the amount of ethanol adsorbed on Degussa P25 TiO_2 was less in the presence of water vapor than under dry conditions, due to the role of water as a competitor for surface sites [53].

Table 12.4 Effects of initial relative humidity (RH_i) on ethanol adsorption and photocatalytic activity of P–TiO_2/0.05 [46]

RH (%)	$m_{EtOH}{}^s$ mg g^{-1}	$k_{(EtOH)}$ mg $m^{-3}s^{-1}$	$k_{(CO2)}$ mg $m^{-3}s^{-1}$	$w_{(CO2)}$ mg m^{-2}
0	28	15.9	1.6	655
12	28	16.0	1.6	754
25	28	15.9	1.9	944
37	28	16.1	2.2	1,067
49	30	22.8	3.3	1,240
62	35	45.4	11.9	1,327
74	49	51.1	12.4	1,433

$m_{EtOH}{}^s$: the amount of ethanol adsorbed on 1 g of catalyst
$k_{(EtOH)}$ and $k_{(CO2)}$: initial rate of ethanol photodegradation and CO_2 formation, respectively
$w_{(CO2)}$: amount of CO_2 formed on UV-irradiated surface unit after 30 min

The initial rates of photooxidation of ethanol and of the formation of carbon dioxide as functions of phosphate content exhibited maxima. The highest initial rates (k) were observed for P–TiO_2/0.05 and P–TiO_2/0.10. The rate of photooxidation on P–TiO_2 was increased by adsorbed water; the presence of water also promoted ethanol adsorption on the surface of the photocatalyst. The data in Tables 12.2 and 12.3 demonstrate that the phosphate content regulates not only the specific surface area of the samples and the amount of ethanol adsorbed but also the anatase content responsible for the photoactivity. Since samples with high phosphate contents contained lower percentages of the anatase phase, the reaction rate decreased. The effect of the anatase content is well illustrated by the comparison of the photocatalytic activities of P–TiO_2/0.01 and P–TiO_2/0.20. The specific surface area of P–TiO_2/0.20 is about four times larger than that of P–TiO_2/0.01, yet the reaction proceeded faster on P–TiO_2/0.01, whose surface area is smaller, but whose anatase content is higher by 20%. The last column in Tables 12.3 and 12.4 reports the amounts of carbon dioxide produced per surface unit of TiO_2 samples irradiated for 30 min (w). Although, under dry initial conditions, the highest initial reaction rates were measured on Degussa P25 TiO_2, the value of w was highest on P–TiO_2/0.05. The reason for this is that water is produced in the course of photooxidation, which increases the adsorption of ethanol on the P–TiO_2 catalyst surface, thereby increasing the rate of photooxidation.

The amount of ethanol ($m_{EtOH}{}^s$) adsorbed on P–TiO_2/0.05 and its photoactivity at different relative air humidities are to be seen in Table 12.4. The initial rate of ethanol photooxidation (k_{EtOH}) was proportional to the amount of ethanol adsorbed. Both the amount of adsorbed ethanol and the rate of its photooxidation increased at $RH_i > \sim 50\%$. Thus, the increase in reaction rate observed at higher RH_i (>50%) may be caused by the larger amount of ethanol adsorbed. The initial rate of carbon dioxide formation ($k_{(CO2)}$) also increased significantly at $RH_i > \sim 50\%$. The initial rate of CO_2 formation at $RH_i = 74\%$ was about eight times higher than that measured under dry conditions.

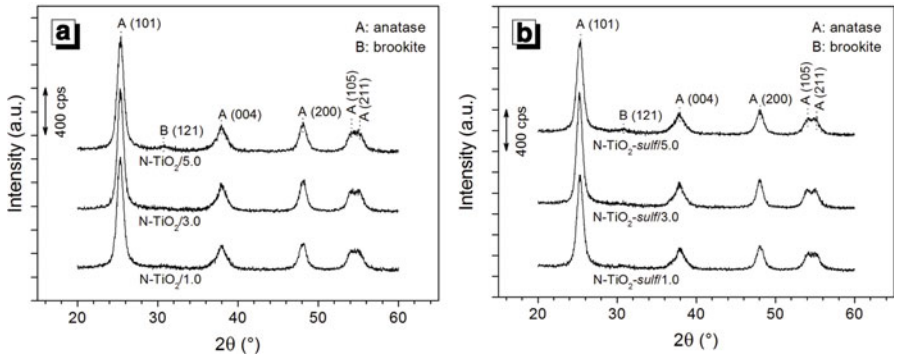

Fig. 12.16 XRD patterns of various (**a**) N–TiO_2 and (**b**) N–TiO_2-*sulf* samples [47]

In summary, it can be concluded that phosphate modification significantly affects both the structural and photocatalytic properties of titanium dioxide. The surface-bound phosphate affects the formation of photoactive anatase and helps to preserve the high specific surface area of the samples. On the other hand, the phosphate modification of the TiO_2 surface may promote the photooxidation of ethanol by enhancing charge separation. The rate of photooxidation of ethanol is highest on P–TiO_2 catalysts with highest specific surface area and anatase content. These criteria are satisfied in the composition range P:Ti = 0.05–0.10. Moreover, $RH_i > 50\%$ significantly increased the amount of ethanol adsorbed on P–TiO_2 catalysts. In the presence of water vapor, both the conversion of acetaldehyde, the main intermediate of the reaction, and the rate of complete mineralization increased significantly.

12.3.2 N-Doped TiO_2

12.3.2.1 Structure and Surface Composition of N-Doped TiO_2

X-ray diffractograms of calcined N–TiO_2 samples are presented in Fig. 12.16a. Each diffraction peak indexed (denoted by *A*) corresponds to the anatase phase, and rutile could not be detected. The peak with very low intensity at 30.8° corresponds to the (121) reflection of the brookite phase (denoted by *B*). Brookite was identified (JCPDS No. 29-1360) only for the nondoped and the N–TiO_2/5.0 sample. In spite of the high N contents of the N–TiO_2 samples, no compounds Ti_xN_y could be detected. Comparison of the XRD patterns of N–TiO_2 and N–TiO_2-*sulf* (Fig. 12.16a, b) revealed that the crystalline phase and the crystallite size did not change significantly in response to sulfuric acid treatment. The average crystallite size was calculated from the anatase (101) reflection by using the Scherrer equation.

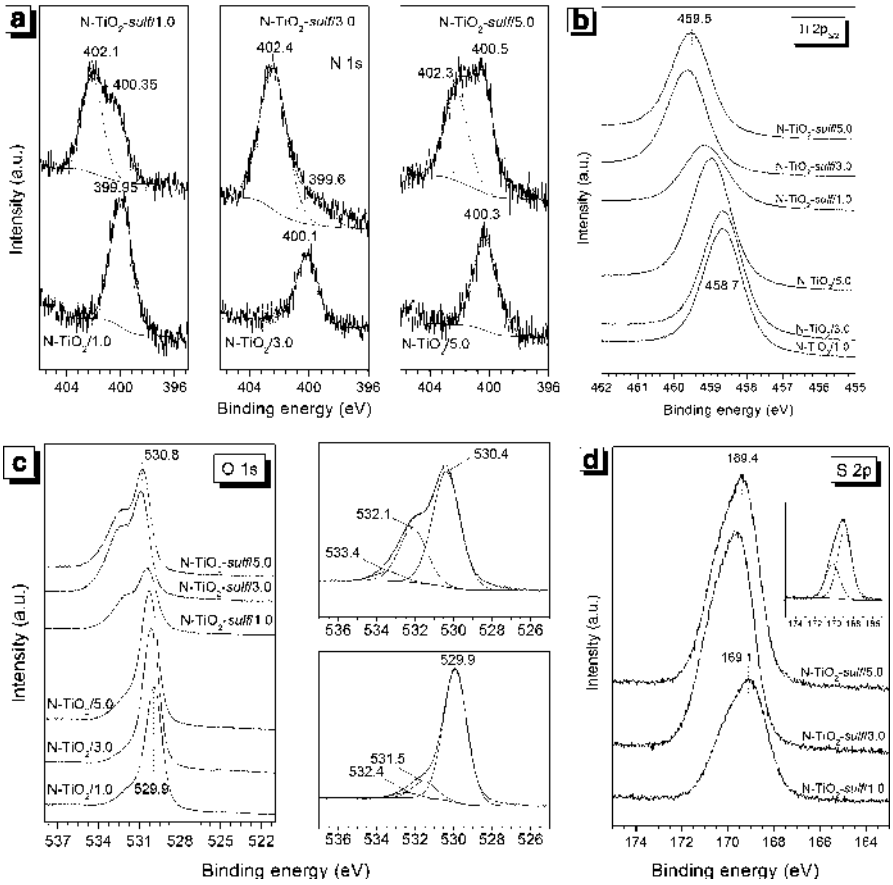

Fig. 12.17 High-resolution XP spectra of (**a**) N 1*s*, (**b**) Ti $2p_{3/2}$, (**c**) O 1*s*, and (**d**) S 2*p* regions on N–TiO_2 and N–TiO_2-*sulf* [47]

The average crystallite size of the N–TiO_2 samples (9.7 nm) is slightly lower than that of the N–TiO_2-*sulf* samples (11 nm). The lowest crystallite size, 8.5 nm, was observed for nondoped TiO_2 [47].

The high-resolution XP spectra contained only one peak, with maximum at ~400 eV, for all three untreated samples. According to literature data, this signal can be attributed to the N–N bond of adsorbed γ-N_2. The recorded spectra and their deconvolutions are presented in Fig. 12.17a. The N 1*s* binding energy changed only slightly with the composition: It was 399.95, 400.1, and 400.3 eV for the N–TiO_2/1.0, N–TiO_2/3.0, and N–TiO_2/5.0, respectively. Sulfuric acid treatment of the samples led to the appearance of another component on the higher binding energy side of the N 1*s* spectrum envelope. The binding energy of this component was 402.1–402.4 eV for all compositions. Since the error in the energy measurement was at least ± 0.1 eV, these values are virtually identical. The origin of this feature

is still debated in the literature. Asahi et al. [54] concluded that it is due to N_2 weakly physisorbed on the surface. Fang and coworkers [55] modified this idea somewhat, postulating that both the 400 and 402 eV peaks are due to γ-N_2 molecularly chemisorbed on the surface. On the other hand, Qiu [56] stated that the peaks arising from γ-N_2 appear at 400 and 405 eV. Another explanation was given by Sathish et al. [57], who ascribed the feature between 401 and 402 eV to some kind of oxidized nitrogen, possibly NO or NO_2. Most authors agree that the appearance of N 1*s* features (including those with binding energy below 400 eV) depends strongly on the nature of the starting materials and the methods by which the N-doped TiO_2 was produced.

Ti 2*p*, O 1*s*, and S 2*p* high-resolution spectra were also investigated. The Ti $2p_{3/2}$ binding energy was 458.7 eV, which corresponds to Ti^{4+}. After treatment with H_2SO_4, the Ti $2p_{3/2}$ binding energy was shifted upward since adsorbed sulfate species form bidentate bridged structures and these could strongly abstract electrons from the neighboring Ti^{4+} [58]. Figure 12.17b presents the Ti $2p_{3/2}$ spectra of the two series (i.e., N–TiO_2 and N–TiO_2-*sulf*); a strong shift from 458.7 to 459.6 eV (i.e., Ti 2*p*3/2) can be observed upon acid treatment, indicating a strong interaction between SO_4^{2-} and Ti^{4+}. The O 1*s* spectra could be deconvoluted into several components (Fig. 12.17c). The most intense peak, located at ~530 eV, corresponds to the lattice oxygen in TiO_2. A slight increase in this binding energy was observed after H_2SO_4 treatment. Two further components could be identified in the O 1*s* spectra. The more intense peak with binding energy 531–532 eV can be attributed to O−H and Ti−O−N bonds, while that at 532.5–533.5 eV may be due to different C−O bonds originating from adventitious carbon. The S $2p_{3/2}$ peak maximum was located at 168.9–169.4 eV, and that of S $2p_{1/2}$ at 170 eV (Fig. 12.17d), corresponding to the binding energy generally reported for SO_4^{2-}.

With increasing ratio N:Ti, the color of the N-doped samples changed from pale-yellow to vivid-yellow. The diffuse reflectance UV–Vis spectra of nondoped and N-doped TiO_2 samples are compared in Fig. 12.18. It can be seen that the light absorption edge of nondoped TiO_2 is at ~410 nm, while the N-doped TiO_2 samples have a broad absorption band in the wavelength range 400–500 nm. Consequently, N–TiO_2 samples can absorb a higher fraction of photons from the visible region.

12.3.2.2 Photocatalytic Properties of N-Doped TiO_2

The photocatalytic activity of N–TiO_2 samples in the degradation of phenol was studied by using a UV ($p = 150$ W, $\lambda = 240$–580 nm) and a visible ($p = 15$ W, $\lambda = 400$–630 nm) light source [47]. The degradation curves are shown in Fig. 12.19. It can be seen that the rate of photodegradation was highest on nontreated N–TiO_2 samples. The phenol conversion in the aqueous suspension increased with increasing N-content of N–TiO_2 (Fig. 12.20). Since H_2SO_4 treatment decreased the specific surface area of the samples, lower reaction rates were observed on each N–TiO_2-*sulf*. The reaction rate was also lower on the acid-treated nondoped TiO_2 (TiO_2-*sulf*) than on the nontreated one. In spite of the decreased

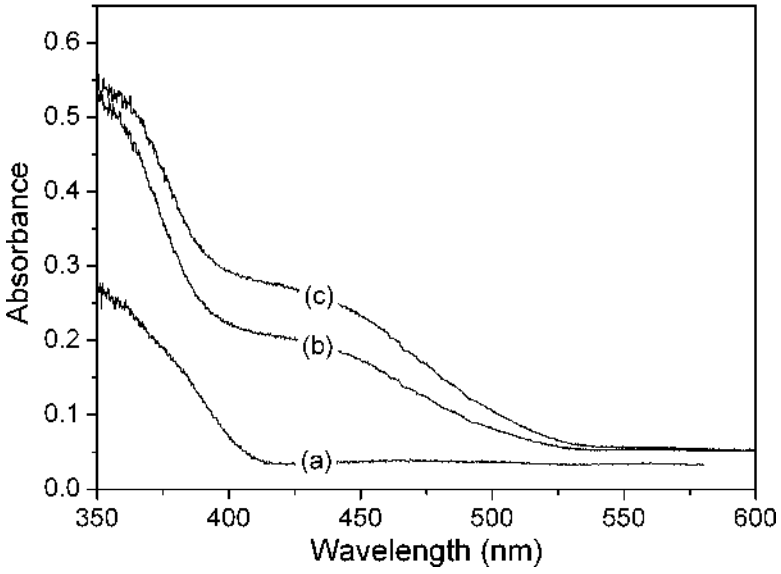

Fig. 12.18 Diffuse reflectance UV–Vis spectra of (a) nondoped TiO_2, (b) N–TiO_2/1.0, and (c) N–TiO_2/5.0 [47]

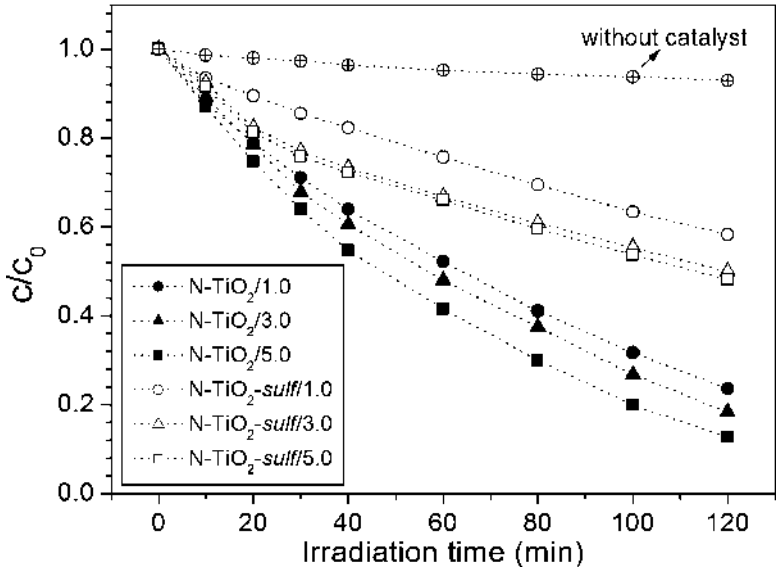

Fig. 12.19 Phenol degradation curves under UV-rich illumination using different N-doped TiO_2 catalysts [47]

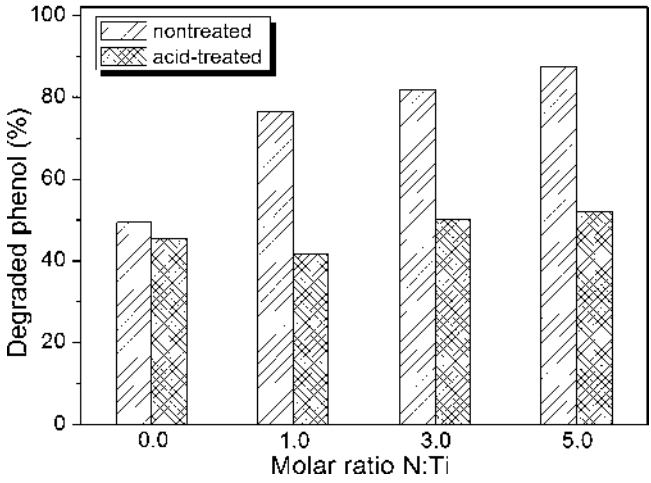

Fig. 12.20 Degraded phenol content after irradiation for 2 h with a UV-rich lamp. The molar ratio N:Ti was calculated from the amounts of the precursors [47]

surface area and changing pore characteristics, the acid-treated catalysts exhibited considerable photocatalytic activity. Taking into account the specific surface areas of the catalysts, the specific amounts of phenol degraded can be calculated (Table 12.5). These normalized data indicated that the amount of phenol degraded was highest on the use of N–TiO_2-*sulf* catalysts. The adsorbed SO_4^{2-} species can increase the surface acidity due to the formation of Brönsted acid centers. From the results of the surface acidity measurements, it was found that nontreated N–TiO_2 samples had a surface acidity of ~0.05–0.06 mmol g^{-1}, while acid-treated ones demonstrated at least one order of magnitude higher surface acidity (i.e., 0.5–0.9 mmol g^{-1}). Colón and coworkers [59] also found that the specific activity of sulfated TiO_2 was significantly higher than those of similarly prepared nonsulfated TiO_2 or pure Degussa P25.

12.3.3 Ag-Modified TiO_2

12.3.3.1 Surface Composition and Optical Properties of Ag-Modified TiO_2

Figure 12.21 shows the Ti 2*p*, O 1*s*, and Ag 3*d* regions of the high-resolution XP spectra of pure and Ag-modified TiO_2. After Ag modification of TiO_2, the binding energy of the Ti 2*p* doublet (Ti $2p_{3/2}$, $2p_{1/2}$) was unchanged; its shape was symmetrical both before and after the photodeposition of Ag, indicating a single chemical state in a chemical environment of the Ti–O–Ti type. The position of the Ti $2p_{3/2}$ components at 458.7 eV corresponded to Ti^{4+}. The O 1*s* spectra were asymmetric; they exhibited a low-intensity shoulder on the high binding energy

Table 12.5 Photocatalytic efficiency data on phenol degradation using various N–TiO_2 and N–TiO_2-*sulf* samples [47]

Sample ID	Residual phenol content[a] (%)		Specific amount of phenol degraded[b] (μmol m^{-2})	
	UV (p = 150 W, λ = 240–580 nm)	Vis (p = 15 W, λ = 400–630 nm)	UV (p = 150 W, λ = 240–580 nm)	Vis (p = 15 W, λ = 400–630 nm)
N–TiO_2/1.0	23.6	83.3	3.19	0.75
N–TiO_2/3.0	18.3	85.1	3.42	0.67
N–TiO_2/5.0	12.6	76.1	3.29	1.01
N–TiO_2-*sulf*/1.0	58.3	82.9	2.95	1.29
N–TiO_2-*sulf*/3.0	49.9	81.6	4.73	1.72
N–TiO_2-*sulf*/5.0	48.1	74.3	3.77	1.86
TiO_2	50.6	85.7	1.87	0.53
TiO_2-*sulf*	54.5	88.5	2.05	0.55
Without catalyst	92.9	96.3	–	–

[a]Nonspecified data after an irradiation time of 2 h
[b]Amount of phenol degraded per specific surface area of catalysts after an irradiation time of 2 h

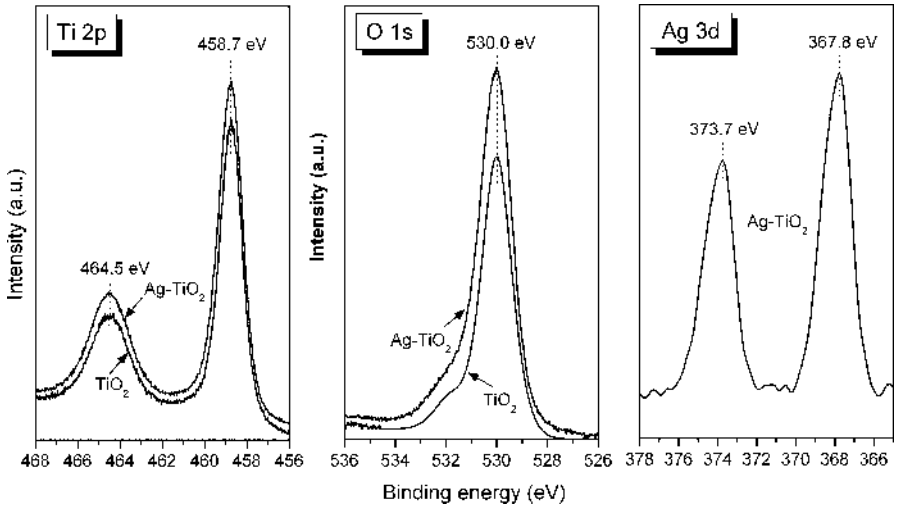

Fig. 12.21 High-resolution XP spectra of the Ti 2*p*, O 1*s*, and Ag 3*d* regions on P25 TiO_2 and Ag–TiO_2/1.0 wt% [11]

side. The positions of the higher-energy but lower-intensity oxygen components obtained by deconvoluting the spectra were at 532.2 eV and 531.6 eV, whereas the maximum of the main component was at 530.0 eV. The peak at 532.2 eV is assignable to C−O bonds and that at 531.6 eV can be attributed to OH groups on the surface of TiO_2. The presence of bonds of the C=O or C−O−C type is probably due to the adventitious carbon. The spectrum of the Ag 3*d* region of the

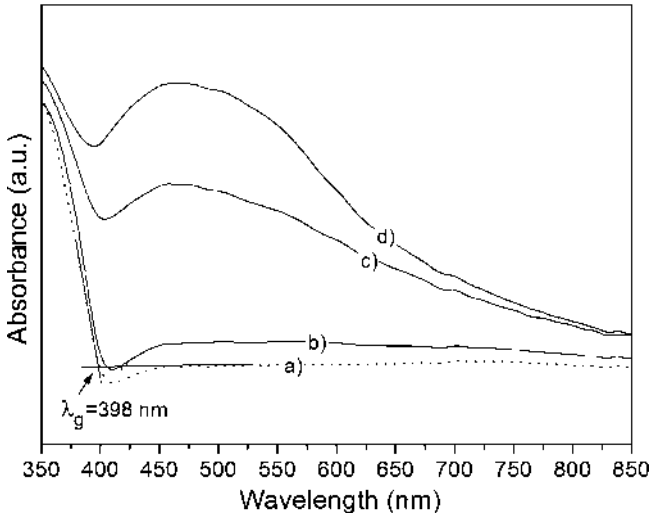

Fig. 12.22 Diffuse reflectance UV–Vis spectra of (*a*) unmodified P25 TiO_2 (*b*) Ag–TiO_2/0.1 wt%, (*c*) Ag–TiO_2/0.5 wt%, and (*d*) Ag–TiO_2/1.0 wt% [11]

Ag-modified sample was also symmetrical; the $3d_{5/2}$ component was situated at 367.8 eV, indicating the presence of silver oxides. The Ag content of the Ag–TiO_2/1.0 wt% sample determined by XPS was 0.238 at.%, a value reasonably close to the calculated Ag content (0.249 at.%). The silver oxide was presumably formed on the TiO_2 surface in the course of the oxidation of photoreduced Ag. Our XRD measurements indicated, the presumed silver oxide on the surface of TiO_2 was amorphous, which may be explained by the fact that, in the course of synthesis, the samples were dried at 60°C rather than calcined.

The diffuse reflectance UV–Vis spectra of pure and Ag–TiO_2 samples are compared in Fig. 12.22. It can be seen that the Ag–TiO_2 samples furnished a broad absorption band in the visible range, with maximum of 455 nm. The position of the absorption edge characteristic of pure TiO_2 was 400 ± 3 nm, independently of the Ag content of the samples.

12.3.3.2 Photocatalytic Activity of Ag–TiO_2 at the Solid–Gas Interface

The photocatalytic activity of TiO_2 samples with or without Ag loading in the photodegradation of ethanol was tested at the solid–gas interface, under dry initial conditions [11]. The ethanol concentration is depicted as a function of adsorption time (the negative range of the diagram) and irradiation time (the positive range of the diagram) in Fig. 12.23. The amounts of ethanol adsorbed by pure and Ag-modified TiO_2 samples in 30 min are compared in Table 12.6. The amount of ethanol adsorbed increased only slightly with increasing Ag content of the samples, whereas the rate of photooxidation was significantly increased, starting at Ag contents of 0.5 and 1.0 wt%. The rate of ethanol conversion on Ag–TiO_2/1.0 wt%

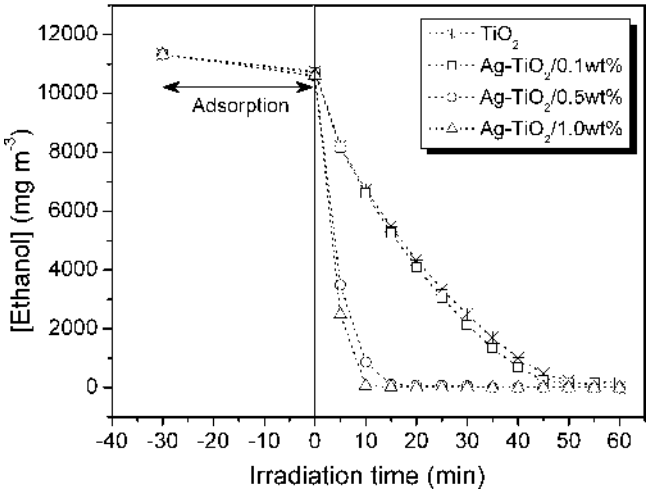

Fig. 12.23 Photodegradation of ethanol on P25 TiO_2 and Ag–TiO_2 under dry initial conditions [11]

Table 12.6 Amount of ethanol adsorbed and photocatalytic efficiency of bare P25 TiO_2 and Ag-modified TiO_2 [11]

Sample ID	Adsorbed ethanol (mg g^{-1})	Conversion of ethanol after 5 min (%)	Total mineralization after 60 min (%)
Degussa P25 TiO_2	18	24	38
Ag–TiO_2/ 0.1 wt%	20	24	57
Ag–TiO_2/ 0.5 wt%	24	67	77
Ag–TiO_2/ 1.0 wt%	26	77	94

was three times as high as on bare Degussa P25 TiO_2. The kinetic curves clearly demonstrate that the entire amount of ethanol was degraded within 15 min on the Ag–TiO_2/0.5 wt% and Ag–TiO_2/1.0 wt% samples, whereas 100% ethanol conversion was observed on the bare TiO_2 and Ag–TiO_2/0.10 wt% only after 50 min.

The changes in acetaldehyde concentration with time are presented in Fig. 12.24. These kinetic curves have maxima, which shifted toward shorter reaction times with increasing Ag content. In other words, both the formation and the subsequent conversion of acetaldehyde were considerably faster on samples with increasing Ag contents than on bare TiO_2. In the initial phase of photooxidation, a major proportion (60–90%) of the ethanol was converted to acetaldehyde, indicating that total mineralization was not significant at this stage. Additional intermediates such as formaldehyde, acetic acid, and formic acid were also observed. Water, carbon dioxide, and methane too were identified as final products of the photoreaction. Kinetic curves of methane formation are presented in Fig. 12.25. For the Ag–TiO_2

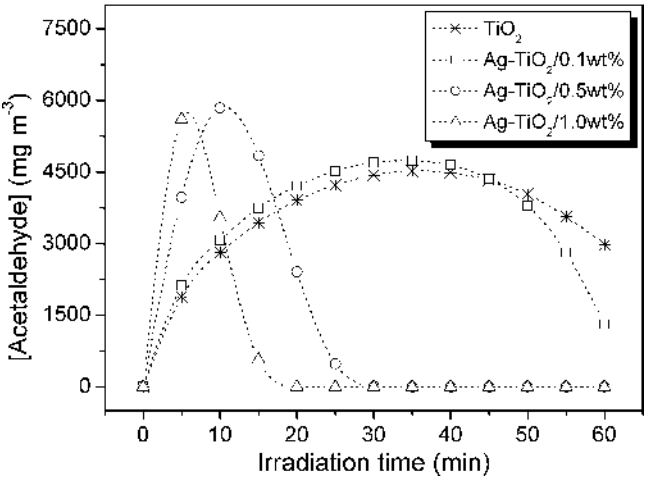

Fig. 12.24 Changes in acetaldehyde concentration as a function of irradiation time, using P25 TiO_2 and Ag–TiO_2 [11]

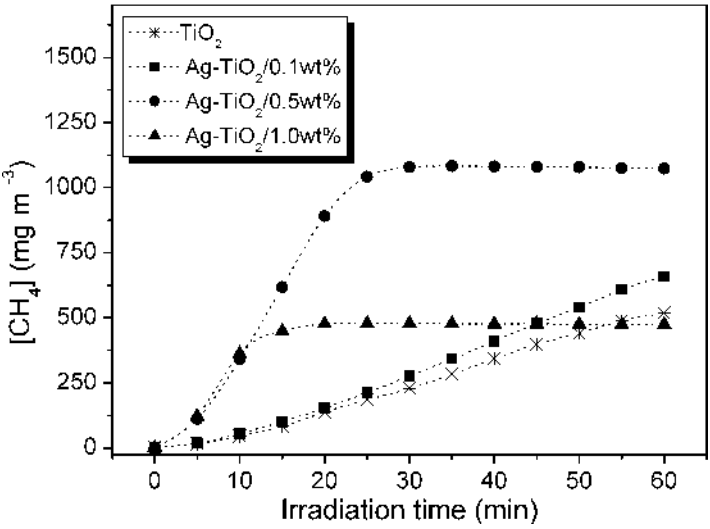

Fig. 12.25 Formation of CH_4 as a function of irradiation time, using P25 TiO_2 and Ag–TiO_2 [11]

samples with higher photoactivity (0.5 and 1.0 wt% Ag loading), these curves were of the saturation type: After 20–25 min, the concentration of methane did not change. This time corresponds to the duration of the total conversion of acetaldehyde, after which no significant additional methane formation occurred. For samples with lower activities, such as pure TiO_2 and Ag–TiO_2/0.1 wt%, where acetaldehyde was present throughout the entire reaction time, methane formation was continuous. The kinetic curves of CO_2 formation on Ag–TiO_2/0.5 wt% and

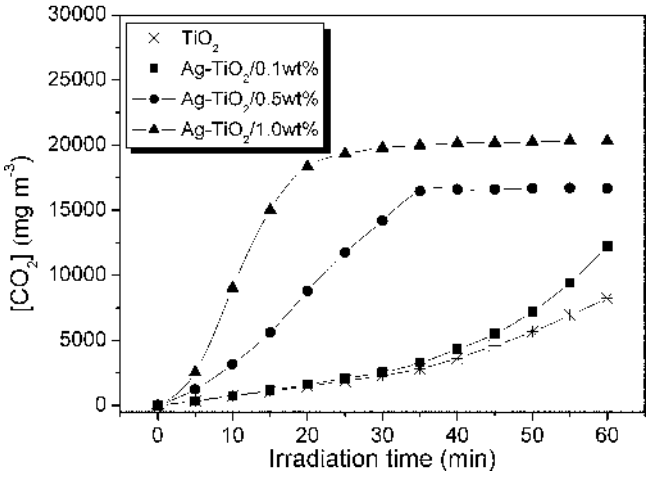

Fig. 12.26 Formation of CO_2 as a function of irradiation time, using P25 TiO_2 and Ag–TiO_2 [11]

Ag–TiO_2/1.0 wt% were also of the saturation type (Fig. 12.26). The total mineralization of ethanol on Ag–TiO_2/1.0 wt% after 60 min was 94%, whereas on bare TiO_2, it was only 38% (Table 12.6).

Photooxidation experiments on the solid–gas interface revealed that Ag modification of TiO_2 significantly increased the rates of photooxidation of both ethanol and the intermediates formed in the course of the reaction. The samples with 0.5 and 1 wt % Ag content displayed a significant improvement as compared with bare TiO_2.

12.3.3.3 Photocatalytic Activity of Ag–TiO_2 at the Solid–Liquid Interface

The photooxidation of TDG in aqueous suspensions containing 0.1 w/v% catalysts was studied at 25°C. The concentrations of TDG and of the intermediates formed were monitored by UV–Vis spectroscopy. Figure 12.27a shows spectra recorded at various time points of the photooxidation of TDG on unmodified Degussa P25 TiO_2. In the course of photooxidation, the maximum in the absorption spectrum ($\lambda = 204$ nm) shifted toward shorter wavelengths. At an irradiation time of 30 min, a new absorption band appeared in the range 225–300 nm, which also indicates the formation of various intermediates. The intensity of this band decreased after 30 min, i.e., the concentration of the intermediates as a function of the irradiation time exhibited a maximum. When bare P25 TiO_2 was used, the absorbance of the organic compounds (at the wavelength of maximum absorption) decreased by only 14% after 60 min (Table 12.7). The Ag–TiO_2/0.5 wt% displayed significantly larger decreases in absorbance (Fig. 12.27b) revealing the enhanced catalytic activity. The samples with 0.5 and 1 w/w% Ag contents proved to be most active at the solid–liquid interface, just as at the solid–gas interface. A decrease in absorbance

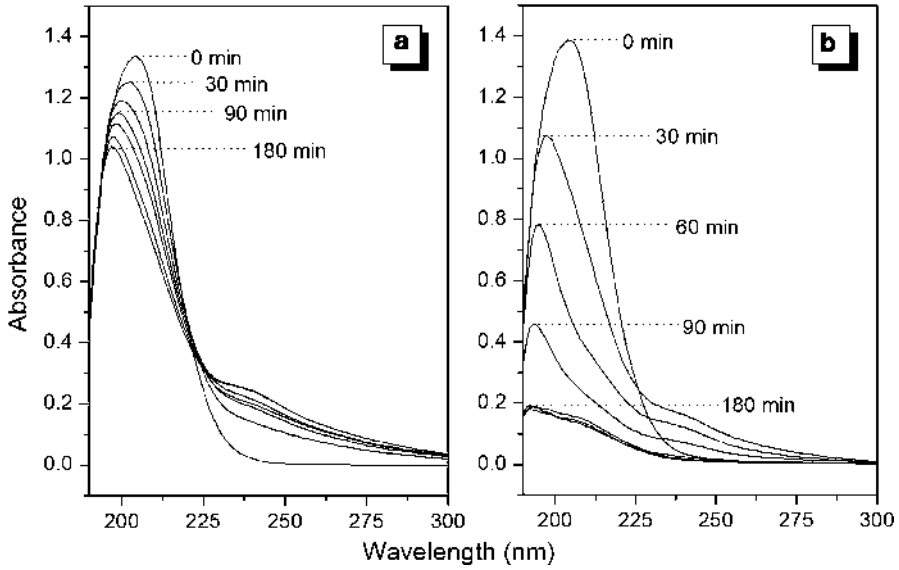

Fig. 12.27 Photodegradation of TDG, using (**a**) bare P25 TiO_2 and (**b**) Ag–TiO_2/0.5 wt% [11]

Table 12.7 Photocatalytic efficiency of bare P25 TiO_2 and Ag–TiO_2 samples for TDG decomposition [11]

Sample ID	$[1 - (A^{60\ min}/A^{0\ min})]$
Degussa P25 TiO_2	0.14
Ag–TiO_2/0.1 wt%	0.45
Ag–TiO_2/0.5 wt%	0.64
Ag–TiO_2/1.0 wt%	0.62

$A^{0\ min}$: absorbance at 204 nm and $t = 0$ reaction time
$A^{60\ min}$: absorbance at maximal wavelength in the UV range on Fig. 12.27 after 60 min

in excess of 60% was recorded after 60 min on using these samples. The results of the photocatalytic experiments are summarized in Table 12.7.

To summarize, it was established that the Ag modification of TiO_2 significantly increased the rate of photooxidation of both ethanol and TDG; at the same time, however, there was no detectable difference between the specific surface areas of the bare and Ag-modified TiO_2. We therefore assume that the improved photoactivity observed is due to charge-transfer processes favorably affected by silver oxide. Silver oxide on the surface of TiO_2 may inhibit the recombination of photogenerated charge carriers (electrons and holes). The probability of the reaction of the charge carriers (whose lifetime is thereby increased) with the adsorbed species is therefore enhanced [11].

The results presented indicate that the application of various chemical surface treatments of TiO_2 and exploitation of the advantages of sol–gel chemistry allow the simple and cost-effective preparation of highly efficient photocatalysts.

References

1. Linsebigler AL, Lu G, Yates JT Jr (1995) Photocatalysis on TiO_2 surfaces: principles, mechanisms, and selected results. Chem Rev 95:735–758
2. Tanaka K, Capule MFV, Hisanga T (1991) Effect of crystallinity of TiO_2 on its photocatalytic action. Chem Phys Lett 187:73–76
3. Bickley RI, Gonzales-Carreno T, Lees JL, Palmisano L, Tilley RJD (1991) A structural investigation of titanium dioxide photocatalysts. J Solid State Chem 92:178–190
4. Gerischer H, Heller A (1992) Photocatalytic oxidation of organic molecules at TiO_2 particles by sunlight in aerated water. J Electrochem Soc 139:113–118
5. Hufschmidt D, Bahnemann D, Testa JJ, Emilio CA, Litter MI (2002) Enhancement of the photocatalytic activity of various TiO_2 materials by platinisation. J Photochem Photobiol A Chem 148:223–231
6. Coleman HM, Chiang K, Amal R (2005) Effects of Ag and Pt on photocatalytic degradation of endocrine disrupting chemicals in water. Chem Eng J 113:65–72
7. Gao YM, Lee W, Trehan R, Kershav R, Dwight K, Wold A (1991) Improvement of photocatalytic activity of titanium (IV) oxide by dispersion of Au on TiO_2. Mater Res Bull 26:1247–1254
8. Herrmann JM, Disdier J, Pichat P (1984) Effect of chromium doping on the electrical and catalytic properties of powder titania under UV and visible illumination. Chem Phys Lett 108:618–622
9. Arana J, Dona-Rodríguez JM, González-Díaz O, Tello Rendón E, Herrera Melián JA, Colón G, Navio JA, Pérez Pena J (2004) Gas-phase ethanol photocatalytic degradation study with TiO_2 doped with Fe, Pd and Cu. J Mol Catal A Chem 215:153–160
10. Di Paola A, Marci G, Palmisano L, Schiavello M, Uosaki K, Ikeda S, Ohtani B (2002) Preparation of polycrystalline TiO_2 photocatalysts impregnated with various transition metal ions: characterization and photocatalytic activity for the degradation of 4-nitrophenol. J Phys Chem B 106:637–645
11. Kőrösi L, Papp S, Ménesi J, Illés E, Zöllmer V, Richardt A, Dékány I (2008) Photocatalytic activity of silver-modified titanium dioxide at solid–liquid and solid–gas interfaces. Colloid Surf A: Physicochem Eng Aspects 319:136–142
12. Siemon U, Bahnemann D, Testa JJ, Rodriguez D, Litter MI, Bruno N (2002) Heterogeneous photocatalytic reactions comparing TiO_2 and Pt/TiO_2. J Photochem Photobiol A Chem 148:247–255
13. Mills A, Le Hunte S (1997) An overview of semiconductor photocatalysis. J Photochem Photobiol A Chem 108:1–35
14. Mogyorósi K, Dékány I, Fendler JH (2003) Preparation and characterization of clay mineral intercalated titanium dioxide nanoparticles. Langmuir 19:2938–2946
15. Ilisz I, Dombi A, Mogyorósi K, Farkas A, Dékány I (2002) Removal of 2-chlorophenol from water by adsorption combined with TiO_2 photocatalysis. J Appl Catal B Environ 39:247–256
16. Ménesi J, Kékesi R, Kőrösi L, Zöllmer V, Richardt A, Dékány I (2008) The effect of transition metal doping on the photooxidation process of titania-clay composites. Int J Photoenergy p 9 Article ID 846304. doi:10.1155/2008/846304
17. Ménesi J, Kőrösi L, Bazsó É, Zöllmer V, Richardt A, Dékány I (2008) Photocatalytic oxidation of organic pollutants on titania–clay composites. Chemosphere 70:538–542

18. Kun R, Mogyorósi K, Dékány I (2006) Synthesis and structural and photocatalytic properties of TiO_2/montmorillonite nanocomposites. Appl Clay Sci 32:99–110
19. Kun R, Szekeres M, Dékány I (2006) Photooxidation of dichloroacetic acid controlled by pH-stat technique using TiO_2/layer silicate nanocomposites. Appl Catal B Environ 68:49–58
20. Mogyorósi K, Farkas A, Dékány I, Ilisz I, Dombi A (2002) TiO_2-based photocatalytic degradation of 2-chlorophenol adsorbed on hydrophobic clay. Environ Sci Technol 36:3618–3624
21. Ilisz I, Dombi A, Mogyorósi K, Dékány I (2003) Photocatalytic water treatment with different TiO_2 nanoparticles and hydrophilic/hydrophobic layer silicate adsorbents. Colloid Surf A Physicochem Eng Aspects 230:89–97
22. Minero C, Mariella G, Mauriono V, Pelizzetti E (2000) Photocatalytic transformation of organic compounds in the presence of inorganic anions. 1. Hydroxyl-mediated and direct electron-transfer reactions of phenol on a titanium dioxide−fluoride system. Langmuir 16:2632–2641
23. Minero C, Mariella G, Mauriono V, Vione D, Pelizzetti E (2000) Photocatalytic transformation of organic compounds in the presence of inorganic ions. 2. Competitive reactions of phenol and alcohols on a titanium dioxide−fluoride system. Langmuir 16:8964–8972
24. Luo H, Takata T, Lee Y, Zhao J, Domen K, Yan Y (2004) Photocatalytic activity enhancing for titanium dioxide by co-doping with bromine and chlorine. Chem Mater 16:846–849
25. Deng X, Yue Y, Gao Z (2002) Gas-phase photo-oxidation of organic compounds over nanosized TiO_2 photocatalysts by various preparations. Appl Catal B Environ 39:135–147
26. Muggli DS, Ding L (2001) Photocatalytic performance of sulfated TiO_2 and Degussa P-25 TiO_2 during oxidation of organics. Appl Catal B Environ 32:181–194
27. Gómez R, López T, Ortiz-Islas E, Navarrete J, Sánchez E, Tzompantzi F (2003) Effect of sulfation on the photoactivity of TiO_2 sol–gel derived catalysts. J Mol Catal A Chem 193:217–226
28. Colón G, Sánchez-Espana JM, Hidalgo MC, Navío JA (2006) Effect of TiO_2 acidic pre-treatment on the photocatalytic properties for phenol degradation. J Photochem Photobiol A Chem 179:20–27
29. Yu JC, Zhang L, Zheng Z, Zhao J (2003) Synthesis and characterization of phosphated mesoporous titanium dioxide with high photocatalytic activity. Chem Mater 15:2280–2286
30. Tachikawa T, Takai Y, Tojo S, Fujitsuka M, Irie H, Hashimoto K, Majima T (2006) Visible light-induced degradation of ethylene glycol on nitrogen-doped TiO_2 powders. J Phys Chem B 110:13158–13165
31. Sathish M, Viswanathan B, Viswanath RP, Gopinath CS (2005) Synthesis, characterization, electronic structure, and photocatalytic activity of nitrogen-doped TiO_2 nanocatalyst. Chem Mater 17:6349–6353
32. Belver C, Bellod R, Stewart SJ, Requejo FG, Fernandez-Garcia M (2006) Nitrogen-containing TiO_2 photocatalysts: part 2. Photocatalytic behavior under sunlight excitation. Appl Catal B Environ 65:309–314
33. Nakamura R, Tanaka T, Nakato Y (2004) Mechanism for visible light responses in anodic photocurrents at N-doped TiO_2 film electrodes. J Phys Chem B 108:10617–10620
34. Ihara T, Miyoshi M, Iriyama Y, Matsumoto O, Sugihara S (2003) Visible-light-active titanium oxide photocatalyst realized by an oxygen-deficient structure and by nitrogen doping. Appl Catal B Environ 42:403–409
35. Asahi R, Morikawa T, Ohwaki T, Aoki K, Taga Y (2001) Visible-light photocatalysis in nitrogen-doped titanium oxides. Science 293:269–271
36. Valentin CD, Pacchioni G, Selloni A, Livraghi S, Giamello E (2005) Characterization of paramagnetic species in N-doped TiO_2 powders by EPR spectroscopy and DFT calculations. J Phys Chem B 109:11414–11419
37. Belver C, Bellod R, Fuerte A, Fernandez-Garcia M (2006) Nitrogen-containing TiO_2 photocatalysts: part 1. Synthesis and solid characterization. Appl Catal B Environ 65:301–308
38. Kobayakawa K, Murakami Y, Sato Y (2005) Visible-light active N-doped TiO_2 prepared by heating of titanium hydroxide and urea. J Photochem Photobiol A Chem 170:177–179

39. Yin S, Ihara K, Aita Y, Komatsu M, Sato T (2006) Visible-light induced photocatalytic activity of $TiO_{2-x}A_y$ (A = N, S) prepared by precipitation route. J Photochem Photobiol A Chem 179:105–114
40. Kosowska B, Mozia S, Morawski AW, Grzmil B, Janus M, Kalucki K (2005) The preparation of TiO_2–nitrogen doped by calcination of $TiO_2 \cdot xH_2O$ under ammonia atmosphere for visible light photocatalysis. Sol Energy Mater Sol Cells 88:269–280
41. Carp O, Huisman CL, Reller A (2004) Photoinduced reactivity of titanium dioxide. Prog Solid State Chem 32:33–177
42. Muggli DS, Lowery KH, Falconer JL (1998) Identification of adsorbed species during steady-state photocatalytic oxidation of ethanol on TiO_2. J Catal 180:111–122
43. Vorontsov AV, Dubovitskaya VP (2004) Selectivity of photocatalytic oxidation of gaseous ethanol over pure and modified TiO_2. J Catal 221:102–109
44. Nimlos MR, Wolfrum EJ, Brewer ML, Fennell JA, Bintner G (1996) Gas-phase heterogeneous photocatalytic oxidation of ethanol: pathways and kinetic modeling. Environ Sci Technol 30:3102–3110
45. Sauer ML, Ollis DF (1996) Photocatalyzed oxidation of ethanol and acetaldehyde in humidified air. J Catal 158:570–582
46. Kőrösi L, Oszkó A, Galbács G, Richardt A, Zöllmer V, Dékány I (2007) Structural properties and photocatalytic behaviour of phosphate-modified nanocrystalline titania films. Appl Catal B Environ 129:175–183
47. Kun R, Tarján S, Oszkó A, Seemann T, Zöllmer V, Busse M, Dékány I (2009) Preparation and characterization of mesoporous N-doped and sulfuric acid treated anatase TiO_2 catalysts and their photocatalytic activity under UV and Vis illumination. J Solid State Chem 182:3076–3084
48. Kőrösi L, Dékány I (2006) Preparation and investigation of structural and photocatalytic properties of phosphate modified titanium dioxide. Colloid Surf A Physicochem Eng Aspects 280:146–154
49. Alfaya AAS, Gushikem Y, de Castro SC (1998) Highly dispersed phosphate supported in a binary silica−titania matrix: preparation and characterization. Chem Mater 10:909–913
50. Connor PA, McQuillan AJ (1999) Phosphate adsorption onto TiO_2 from aqueous solutions: an in situ internal reflection infrared spectroscopic study. Langmuir 15:2916–2921
51. Beydoun D, Amal R, Low G, McEvoy S (1999) Role of nanoparticles in photocatalysis. J Nanoparticle Res 1:439–458
52. Kőrösi L, Papp S, Bertóti I, Dékány I (2007) Surface and bulk composition, structure, and photocatalytic activity of phosphate-modified TiO_2. Chem Mater 19:4811–4819
53. Piera E, Ayllon JA, Domenech X, Peral J (2002) TiO_2 deactivation during gas-phase photocatalytic oxidation of ethanol. Catal Today 76:259–270
54. Asahi R, Morikawa T (2007) Nitrogen complex species and its chemical nature in TiO_2 for visible-light sensitized photocatalysis. Chem Phys 339:57–63
55. Fang X, Zhang Z, Chen Q, Ji H, Gao X (2007) Dependence of nitrogen doping on TiO_2 precursor annealed under NH_3 flow. J Solid State Chem 180:1325–1332
56. Qiu X, Burda C (2007) Chemically synthesized nitrogen-doped metal oxide nanoparticles. Chem Phys 339:1–10
57. Sathish M, Viswanathan B, Viswanath RP (2007) Characterization and photocatalytic activity of N-doped TiO_2 prepared by thermal decomposition of Ti–melamine complex. Appl Catal B 74:307–312
58. Wang X, Yu JC, Liu P, Wang X, Su W, Fu X (2006) J Photochem Photobiol A Chem 179:339–347
59. Colón G, Hidalgo MC, Munuera G, Ferino I, Cutrufello MG, Navío JA (2006) Probing of photocatalytic surface sites on SO42−/TiO2 solid acids by in situ FT-IR spectroscopy and pyridine adsorption. Structural and surface approach to the enhanced photocatalytic activity of sulfated TiO_2 photocatalyst. Appl Catal B 63:45–59

Chapter 13
Photocatalysis: Toward Solar Fuels and Chemicals

Guido Mul

13.1 Introduction

13.1.1 Solar Fuels

The world is facing a tremendous energy challenge. Since reserves of oil and other fossil fuels are diminishing at an increasing pace, and considering the tremendous environmental impact of the use of these, alternative processes have to be developed, both to provide society with sustainable energy and transportation fuels, as well as with renewable-based chemical products [1]. Focus is currently on biomass-derived fuels and products. However, from the viewpoint of converting solar energy into chemical energy, growth of biomass is in fact inefficient. Only ~12% of solar radiation is suitable for conversion by the most effective biological systems, whereas at least 40% of the energy is used by plants for other (respiration) processes [2]. All in all, the efficiency is at best around 1% in locations such as typical for Northern Europe. While for the short- to mid-term use of biofuels and bio-derived chemicals can compensate for the reducing availability of fossil feedstock, artificial solar conversion systems have much greater potential. Significant advances have been made in photovoltaic technologies for the conversion of solar energy into electrical energy. However, production and demand need to be balanced both in time and across different locations, which requires the scalable conversion of solar energy into fuel as a transportable storage medium [1]. The platform reactions for solar energy storage and fuel production are (13.1) and (13.2):

$$2H_2O \rightarrow 2H_2 + O_2, \tag{13.1}$$

G. Mul (✉)
Photocatalytic Synthesis group, Impact Institute, Faculty of Science and Technology, University of Twente, P.O. Box 217, Enschede 7500 AE, The Netherlands
e-mail: g.mul@tudelft.nl

L. Guczi and A. Erdőhelyi (eds.), *Catalysis for Alternative Energy Generation*,
DOI 10.1007/978-1-4614-0344-9_13,

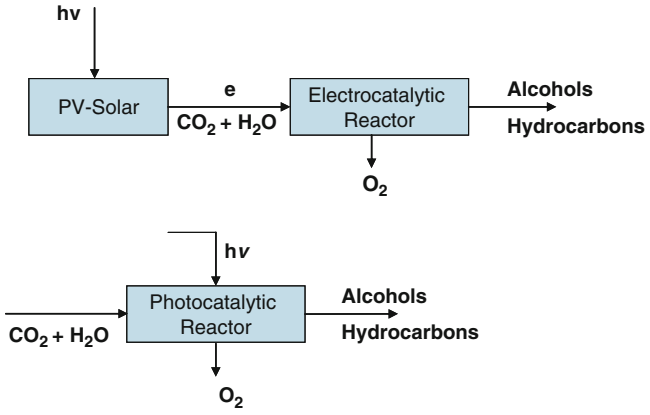

Fig. 13.1 Process options for artificial photosynthesis. (*Top*) Photovoltaic conversion of light into electricity, followed by electrocatalytic fuel generation. (*Bottom*) Photocatalytic process, which requires only one reactor and allows for gas-phase process operation

$$2CO_2 + 4H_2O \rightarrow 2CH_3OH + 3O_2. \tag{13.2}$$

Process options for artificial solar to fuel (S2F) systems to achieve either reaction (13.1) or (13.2), can roughly be divided into two. One option is to use the previously mentioned advanced photovoltaic solar panels, converting solar energy into electricity with efficiencies as high as 20%, while the generated electricity can be used in a second step to convert water (preferably together with CO_2) into thermodynamically uphill products electrocatalytically [3–6]. Electrolyzers for hydrogen production [reaction (13.1)] currently have a reasonable efficiency in the order of 70–80%, the major efficiency loss being the large overpotential required for oxygen evolution (effectively this leads to generation of heat) [2]. Unfortunately for electrocatalytic conversion of CO_2, the efficiency is much lower and amounts to at best 1% [7]. This is partly related to the relatively low concentration of CO_2 in water and the kinetically preferred reduction of $2H^+$ to H_2. In other words, many studies of electrocatalytic CO_2 reduction show that in fact a highly diluted stream of hydrocarbons in H_2 is obtained [7]. Furthermore, electrodes are prone to deactivation [8]. A more simple process would be to directly convert solar photons into chemical products by so-called photocatalysis, which not only requires just one process step but also allows reactor operation in the gas phase, which is advantageous with respect to mass transfer limitations (diffusion constants are typically much more favorable in the gas phase). The second option appears thus more attractive, and development of highly efficient photocatalytic S2F catalysts is the first objective addressed in the present chapter (Fig. 13.1).

Besides S2F conversion, additionally photocatalysis can contribute to process intensification, in particular by increasing reaction selectivity, thus improving energy efficiency in achieving chemical conversion [9].

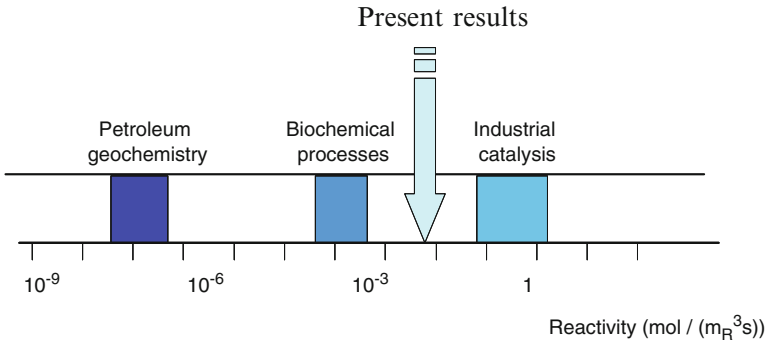

Fig. 13.2 Overview of the rates of various relevant processes. Present results achieved for photocatalysis are indicated by the *arrow*, which are clearly outside the regime of industrial catalysis [13]

13.1.2 Light-Enabled Process Intensification

Various processes operated in the chemical industry, and in particular selective oxidation of hydrocarbons, suffer from low energy efficiency as a consequence of unselective conversion. This results in the necessity of energy-intensive separation steps, to obtain purified products. Intensification of such processes is highly desired. Light has already been identified in a recent review by Stankiewicz and Moulijn [9] as an attractive alternative energy source for process intensification. Light has proven its value in (non-catalytic) processes in particular in combination with microreactor platforms [10–12]. Whether or not a great future will be lying ahead for light in catalytic chemical production will be dependent on the activity of future generations of catalysts and efficacy of exposure of these to light. A major challenge is to improve on the low rates that are presently achieved in photocatalytic conversion. For S2F conversion, the area that is needed for collection of solar energy should be minimized. For chemical transformations, the following evaluation is illustrative to demonstrate the need for efficiency improvement. Generally for catalytic processes to be economically feasible, a reactivity of 1 mol/m^3 reactor/s is required [13]. This means that roughly a 100–1,000-fold improvement in performance of photocatalysis processes is required (Fig. 13.2). The endeavors reported in the literature to improve understanding and performance of heterogeneous photocatalysis cover a wide range of disciplines including (1) bandgap engineering and defect chemistry, (2) material science to synthesize (nano)structured materials, (3) (ultra)fast spectroscopies to study the lifetime of photo-excited states, (4) studies of surface composition and catalytic events, and finally, (5) photoreactor design. In the second part of this chapter focusing on the synthesis of chemicals by employing light energy, attempts in achieving optimization of process conditions, and use of structured reactors allowing efficient exposure of the catalyst to light, will be addressed.

13.2 Theory

13.2.1 What Is Photocatalysis?

It is important to realize what photocatalysis actually is. Principally light can be used without any catalyst to activate chemical bonds if of high enough energy, which is the field of photochemistry. The latter is also referred to as photolysis. Photocatalysis is the use of a photon-excited catalyst to accelerate a *thermal* reaction, in which the catalyst should not undergo a permanent transition but be restored in the initial configuration. In photocatalysis, the wavelength of the light should be of high enough energy to excite the catalyst but of low enough energy to prevent direct photoactivation of the reactant. This might lead to undesired chemistry/selectivity, as will be illustrated later for the case of selective oxidation of cyclohexane to cyclohexanone [14].

When a photocatalyst absorbs UV/Vis light energy, a transition in the electronic state occurs, yielding the photo-excited state. For molecular catalysts, the light absorption process involves electron excitation from the highest occupied molecular orbital (HOMO) to the lowest unoccupied molecular orbital (LUMO) of a chromophore (light-absorbing entity). For isolated Ti sites, e.g., in a mesoporous material, this can be described by the process: Ti^{4+}–$O^{2-} \rightarrow Ti^{3+}$–$O^{-}$ [15]. After light absorption by molecular catalysts, the energy of the excited state may be lost in various ways, often predominantly by thermal degradation (i.e., heat is produced), or by photon emission (radiative decay by fluorescence) (immediate conversion of absorbed light into reemitted energy) or phosphorescence (light energy is stored in a reservoir from which it slowly leaks) [16]. Besides molecular catalysts, quite often, crystalline materials are applied in photocatalysis, the most abundantly investigated being TiO_2 [17]. Then, one speaks of a valence band (occupied with electrons in the ground state) and conduction band (contains electrons in the excited state). The energy difference between the highest energy level of the valence band and lowest level of the conduction band is referred to as the "bandgap." The nature of the active sites thus created by excitation of the crystalline catalysts is typically described by the terminology "holes," which are capable of oxidizing a substrate by accepting an electron, and "electrons," which are able to reduce a (second) substrate. One can thus state that two active sites are created upon absorption of one photon.

The usual illustration that is shown in textbooks to describe heterogeneous photocatalysis is presented in Fig. 13.3. Besides by the above-described redox reactions, relaxation of the excited state occurs by volume recombination or surface recombination, the energy being dissipated in the form of heat or luminescence, similar to that discussed for molecular catalysts. In fact, these processes are much more likely than the employment of the excited state in redox reactions, explaining the typically observed low rates ($mol_{product}.g_{cat}{}^{-1}.s^{-1}$) in photocatalysis (see, e.g., in [18, 19]).

Determination and manipulation of the quantity and lifetime of surface-excited states (i.e., the catalytically active sites) is important for improving photocatalytic processes. The analysis of these features of the applied materials is in the domain of

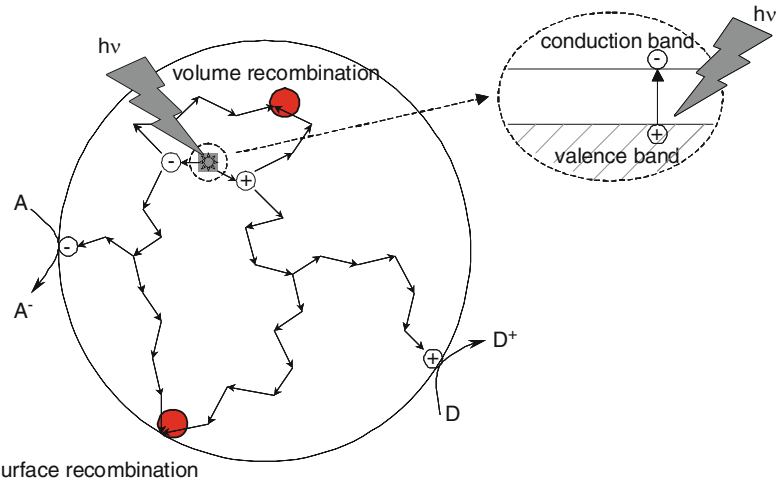

Fig. 13.3 Representation of the processes occurring upon light absorption by a crystalline semiconductor particle. An excited state is created which principally can lead to the formation of two active surface sites, one capable of reduction and the other of oxidation of surface-adsorbed substrates. Volume or surface recombination (indicated by the *red circles*) decreases the efficiency of the photocatalytic process

spectroscopists and physicists, and the theory behind these methodologies will not be extensively discussed here. Various theoretical aspects of semiconductor behavior are well described by Cox [20]. In the following, the latest approaches and achievements in photocatalyst development are reviewed.

13.3 Solar to Fuel Conversion

13.3.1 Design of Crystalline Catalysts

Solar hydrogen production has been discussed extensively in textbooks [1], including descriptions of irradiated semiconductor–liquid interfaces. Studies on the latter option are related to heterogeneous photocatalysis and mostly inspired by the data reported by Fujishima and Honda in 1972 [21]. They demonstrated that hydrogen and oxygen evolution from water splitting induced by UV light was possible in an electrochemical cell, using a TiO_2 photoanode and a Pt counter electrode. The advantage of this configuration is that H_2 and O_2 are produced in separate compartments, eliminating the possibility of the back reaction of $2H_2 + O_2 \rightarrow 2H_2O$. Many examples in the literature exist, showing that the electrochemical cell is principally not necessary. Light-harvesting units based on the principle of colloidal suspensions of platinized TiO_2 in one simple reactor are described. Furthermore, it was demonstrated that using platinized TiO_2, gas-phase conversion of H_2O was possible [22].

The function of a noble metal promoter (e.g., Pt) on TiO_2 is twofold: it enhances the lifetime of the photo-excited state (i.e., alters physical properties), and it catalyzes the formation of H_2. The disadvantage of noble metal promoters is that these are also able to catalyze the back reaction of $2H_2 + O_2 \rightarrow 2H_2O$. This reaction can be prevented by poisoning the Pt sites with, e.g., CO, which has indeed been found to inhibit the undesired back reaction. Also Na poisoning induced by conducting the photocatalytic water decomposition in a Na_2CO_3 solution has been demonstrated to positively affect the overall efficiency of the system in the stoichiometric photodecomposition of water. Finally, the back reaction can be prevented by creation of a protective oxide layer on the surface of the noble metal particles. This has been achieved for Rh-promoted photocatalysts by deposition of a Cr_2O_3 layer [23]. This layer allows the hydrogen produced at the Rh surface to escape but prevents the diffusion of oxygen to the metal surface necessary for the reaction of H_2 and O_2.

13.3.2 Adding an Efficient Water Oxidation Catalyst

Oxygen generation by TiO_2 surfaces, as well as of other photoactive materials, is not very effective. While thermodynamically feasible, apparently the surfaces are not very suited to effectively enable the four-electron reaction transfer that is required to decompose water. In other words, the kinetics should be improved. Grätzel and coworkers have pioneered the use of RuO_2 as oxidation catalyst in Pt/TiO_2 formulations [24, 25]. While this oxide is effective, recently research groups have made significant progress in developing water oxidation catalysts based on cheaper and more abundant elements. In particular, $CoPO_x$ was found very effective as anode in water electrolyzers [3–6], whereas nanostructured Co_3O_4 or MnO_x in silica scaffolds have recently been identified as efficient water oxidation catalysts [26–28]. It is important to note that the water oxidation activity of these oxides appears to be able to match the solar flux to the catalyst [27].

13.3.3 The Quest for Visible-Light-Sensitive Systems

Development of improved visible-light-activated systems is necessary to enhance the solar to chemical production rate (solar light contains roughly a tenfold higher content of visible light, as compared to UV light). For example, "N" and "C" doping have been investigated extensively to shift the bandgap energy of TiO_2 toward the visible [17]. Also addition of ions into the lattice (e.g., Rh^{3+} into TiO_2 [29] or Cr^{n+} in TiO_2 [30]) has been demonstrated to be effective. The majority of research has focused on modification of TiO_2-based systems. This is related to the beneficial properties of this catalyst that determine the applicability, which are chemical stability (the catalyst should not change state or dissolve in the process), the price,

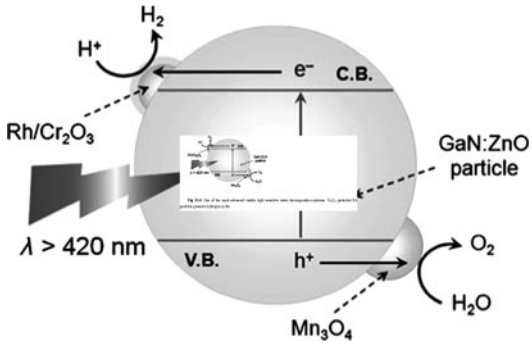

Fig. 13.4 One of the most advanced visible-light-sensitive water decomposition systems. Cr_2O_3-protected Rh particles generate hydrogen in the absence of the back reaction of $2H_2 + O_2 \rightarrow 2H_2O$, whereas Mn_3O_4 mediates the oxidation of water, using holes generated in the GaN:ZnO particles upon exposure to visible light. Copied from [33]

and the low toxicity. Significant efforts on achieving visible light sensitivity with other catalysts than TiO_2 have been reported by, e.g., Grätzel and coworkers, focusing on CdS particles, which do not necessarily have catalytically active surfaces but principally allow water splitting thermodynamically. Activity was established again by addition of promoter particles; Pt for hydrogen evolution and RuO_2 for oxygen evolution [31, 32]. Also recently, significant progress has been made. In particular, the group of Domen and coworkers has focused on the development of (oxy)nitrides, of which the most successful is a mixed GaN–ZnO system Ga(Zn)ON [33].

Principally this research group has used an advanced Grätzel approach to make these catalytically active, using Cr_2O_3-protected Rh as hydrogen evolving catalyst [23, 34], and Mn_3O_4 as water oxidation catalyst. In summary, significant improvements after the early reports of Honda and Grätzel are the development of visible-light-sensitive systems, replacing Pt for Cr_2O_3-protected Rh (preventing the H_2 and O_2 back reaction), and use of Mn_3O_4 as a cheap and effective water oxidation catalyst.

An interesting alternative design route to create a visible-light-sensitive water decomposition system is based on the so-called Z-scheme. This Z-scheme system is based on the combination of two metal oxides with visible light absorbance, as shown in Fig. 13.4, and was in particular investigated by Kudo and coworkers [35]. The system includes a visible-light-active O_2-photocatalyst catalyzing O_2 evolution, but the energy level of the photo-excited electrons is not high enough to induce H_2 formation. The second catalyst is also excited by visible light, leading to hydrogen generation, but now the hole is not of sufficient energy to oxidize water. However, the energy levels of the conduction band electrons of the O_2-photocatalyst and valence band holes of the H_2-photocatalyst are such that recombination is feasible through the mediation of a Fe^{2+}/Fe^{3+} couple. Further improvement of these systems is still necessary, in particular concerning the efficiency of electron transfer reactions.

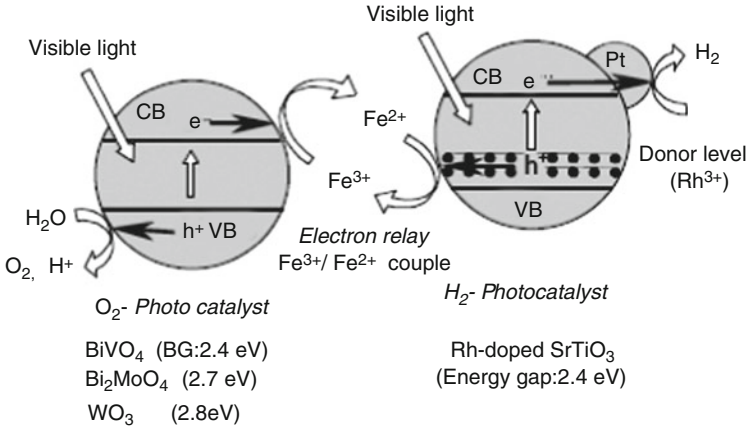

Fig. 13.5 Representation of a Z-scheme process, mediated by the Fe^{2+}/Fe^{3+} couple. Over oxides such as $BiVO_4$, Bi_2MoO_4, and WO_3 O_2 evolution is thermodynamically feasible, while Rh^{3+}-doped, Pt-promoted $SrTiO_3$ is very effective in visible-light-induced H_2 evolution. Copied from [35]

It should be noted that Kudo and coworkers have recently reported electron transfer without using the electron relay couple, explained by self-assembling contact between photoactive catalyst particles [29].

13.3.4 Supported Chromophores

Rather than focusing on crystalline materials as indicated above, the option also exists to synthesize chromophores in well accessible inert support materials. Just as in thermocatalysis, the photocatalysis community has embraced the advent of well-structured mesoporous materials, such as ETS-10, MCM-41, SBA-15, etc., giving the opportunity to structure photocatalytically active sites and to enhance performance. These systems have been investigated in the gas-phase conversion of CO_2 and H_2O (g). Using supported TiO_2-based systems, CH_4 and CH_3OH (in a reported ratio of 4:1) were the main products formed in significantly larger quantities than achieved with crystalline TiO_2. Large differences in performance were observed for various silica scaffolds, SBA-15 yielding the highest activity [36–39].

Isolation of visible-light-sensitive chromophores in silica scaffolds has also been attempted, in particular by the group of Frei [40]. The most advanced system of this group consists of a Zr-oxo, bridged to a Cu(I) center (see Fig. 13.5). The bimetallic Zr(IV)–O–Cu(I) site undergoes metal-to-metal charge-transfer (MMCT) absorption upon exposure to radiation from the UV region to about 500 nm. It was demonstrated that this center is capable of reducing CO_2 and H_2O to CO and OH radicals [40].

Also other bimetallic systems have been explored, including a Ti(IV)–O–Cr(III) → Ti(III)OCr(IV) MMCT catalyst. The Ti(IV)–O–Cr(III) entity was also

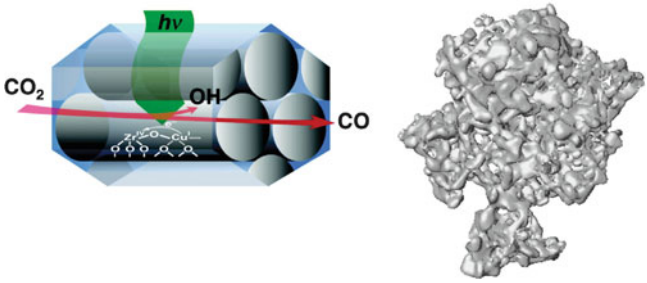

Fig. 13.6 Representation of a bimetallic chromophore in a silica matrix [42]. The bimetallic chromophore is visible light sensitive. *Right*: Model of the spongelike structure of TUD-1

coupled to IrO_x nanoparticles in the scaffold, which catalyzes water oxidation. It was indeed demonstrated that a binuclear charge-transfer chromophore coupled to a water oxidation catalyst is capable of visible-light-induced oxidation of water [41] (Fig. 13.6).

The application of the MCM-41 scaffold has its advantages in synthesizing the molecular structures but does not seem to be most accessible. Other silica scaffolds have recently been described and used, of which TUD-1 and KIT-6 are examples. The former promoted by Ti-, Cr-, or V-sites was demonstrated to be effective in photon-induced selective alkane and alkene conversions [43–45], whereas the latter has been successfully applied in water oxidation after functionalization with cobalt oxide clusters [26]. Various research groups focus on further optimization of the structure of the scaffold for relevant photon-induced reactions.

13.3.5 Mechanism of Photoactivation of H_2O Over Crystalline Catalysts

In most studies on photocatalysis, the photo-excited active sites have not been chemically identified. Since the lifetime of these species is extremely short, advanced spectroscopies have to be used to identify the nature of the (primary) catalytic sites formed by light absorption. For TiO_2, the most investigated photocatalytic material in photon-induced reactions, the chemical nature of the surface-excited sites has been suggested to include surface hydroxyl radicals (generated by reaction with the "hole"), in combination with a Ti^{3+} site, which transfers an electron to surface-adsorbed oxygen in oxidation processes, forming superoxide anions, O_2^-. Both the surface hydroxyl radical and superoxide anion are capable of oxidizing hydrocarbon substrates.

The photochemical steps in the conversion of H_2O over photo-excited catalyst sites are not exactly known. Again, only for TiO_2 surfaces, detailed proposals for the reaction pathway have been provided [46, 47]. An early proposal involves the

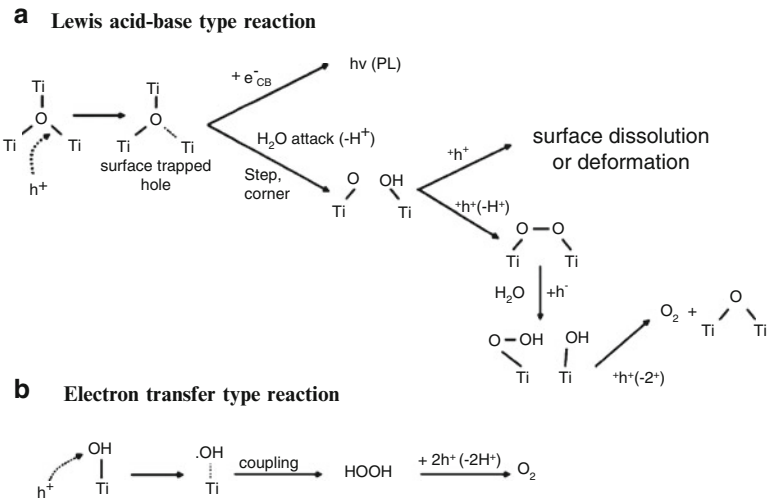

Fig. 13.7 Proposed schemes for the mechanism of water oxidation over TiO_2 surfaces (copied from [49]). (**a**) Lewis acid–base-type reaction and (**b**) electron-transfer-type reaction

following steps. Upon photoexcitation, a surface Ti^{4+}–OH group is converted to a Ti^{3+}–$OH^{\bullet}$ radical (similar to proposed for hydrocarbon oxidation reactions), followed by recombination with surface-adsorbed water according to:

$$4Ti^{3+} - OH^{\bullet} + 2(HOH)_{ads} \rightarrow 4Ti^{4+} - OH^{-} + 4OH^{\bullet} + 2H_2, \tag{13.3}$$

$$4OH^{\bullet} \rightarrow 2H_2O_2 \rightarrow 2H_2O + O_2. \tag{13.4}$$

Recombination of the transient OH radicals to H_2O_2 and finally decomposition to oxygen and H_2O complete the catalytic cycle [48]. The present level of understanding is best summarized by Nakamura et al. [49], who have proposed the following schemes.

Scheme B represents a simplified form of the previously discussed route [48]. Evidence is provided in [49] for rutile surfaces, a particular TiO_2 crystal form, that the oxygen photo-evolution reaction is not initiated by the electron-transfer-type oxidation but initiated by a nucleophilic attack of a H_2O molecule (Lewis base) to a surface-trapped hole (Lewis acid), accompanied by bond breaking (initial steps route (A) in Fig. 13.7). The final step in oxygen evolution is proposed to be the recombination of surface peroxide (Ti–OOH) and a hydroxyl group, yielding O_2 and a bridged Ti–O–Ti group. ESR spectroscopy has been instrumental in determining the involvement of OH-radicals in photo-induced reactions over TiO_2, whereas recent photoluminescence studies advocate the formation of the surface-trapped holes in Ti–O–Ti sites as the primary step in photooxidation reactions (route B). DFT calculations have more recently been reported [46], supporting several steps of the above indicated mechanisms.

With ESR spectroscopy, it is principally not possible to analyze the origin of the OH radicals (TiO_2 surfaces contain usually various OH groups of different reactivity), whereas also photoluminescence studies do not provide direct information on surface molecular composition. Future studies should be focused on refining the pathway of photocatalytic water splitting over less well-defined and anatase TiO_2 surfaces. Application of advances in IR spectroscopic technology appears particularly suitable and interesting. Indeed, infrared measurements using internal reflection elements have been successfully performed [50]. These studies revealed significant irreversible changes in the surface composition of TiO_2 on the minute to hour timescale, but the reversible, i.e., catalytic steps involved in the reaction on the millisecond to second timescale, were not analyzed in detail. Furthermore, the studies were performed on only a few TiO_2 systems (often rutile surfaces), without systematically investigating the role of TiO_2 morphology (crystallinity, phase composition, particle size) on the surface chemistry involved. The role of metal promotion [51], such as nano-sized Pt or Au particles, significantly enhancing the performance of TiO_2, on the surface chemical steps is also still largely unknown, whereas methodologies for deposition of these metal promoters might significantly alter the surface OH-population [52, 53]. Time-resolved IR spectroscopy on all timescales relevant for the reaction (from $<$100 fs up to seconds) [44, 54] to unravel the mechanism of photocatalytic oxygen production on TiO_2 appears feasible, where the use of isotopically labeled D_2O, or $H_2{}^{18}O$, inducing specific shifts in infrared frequencies facilitating spectral interpretation, can be instrumental. The future will show if these studies confirm or disprove the current level of understanding.

13.3.6 Crystalline Catalysts: CO_2 Reduction

Mechanistic studies focused on photo-induced CO_2 activation over crystalline catalysts are rare. Rasko et al. [55, 56] observed bent CO_2^- species on pre-reduced TiO_2 upon illumination at 190 K. CO was detected only on a pre-reduced Rh/TiO_2 catalyst. Recently, the surface chemistry of crystalline $Cu(I)/TiO_2$ was further investigated, employing a combination of DRIFT spectroscopy and isotopically labeled $^{13}CO_2$ [57]. Cu-promoted TiO_2 was reported to be highly efficient in CO_2 reduction reactions [57, 58]. The strong adsorption of CO on Cu(I) sites was used to identify the origin of this product, indicating that carbon residues are very important in determining the initial reactivity of photocatalysts active in CO_2 reduction. Moreover, a rich surface carbonate chemistry was observed for $Cu(I)/TiO_2$, with an interconversion of CO_2-induced carbonate, formed in the dark, to CO-induced carbonate formed upon illumination. The implications of this study for studies in the literature using photoactive materials synthesized with carbon-containing precursors is that H_2O-induced photocatalytic carbon gasification should be carefully considered and compared with the evaluation of CO_2 photoreduction [57]. Studies using the aforementioned time-resolved IR spectroscopic techniques are highly recommended to further elucidate the role of surface states in the adsorption

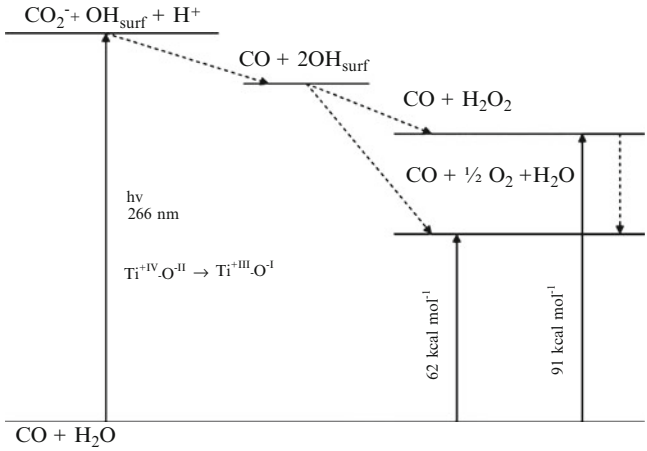

Fig. 13.8 Scheme for CO_2 reduction in the presence of H_2O over isolated Ti sites in the MCM-41 framework. The conversion is induced by a 266-nm laser pulse (after Frei and coworkers) [15]

of CO_2 and subsequent conversion. Attenuated total reflection spectroscopy appears useful for liquid-phase processes [59], whereas transmission or diffuse reflectance experiments are suitable for analysis of reactions in the gas phase [57].

13.3.7 Supported Chromophores: CO_2 Reduction

Despite numerous studies on photoreduction of CO_2 over TiO_2-based catalysts, relatively little is known about the surface chemistry and the mechanism of the reaction leading to CH_4 or other hydrocarbons. Anpo et al. proposed a mechanism for isolated excited (Ti^{+III}–O^{-I}) sites in silica scaffolds, based on EPR data [60], over which simultaneous reduction of CO_2 and decomposition of H_2O is proposed to lead to CO and C radicals, and H and OH radicals, respectively. Subsequently, these photo-induced C, H, and OH radicals recombine to final products, such as CH_4 and CH_3OH.

In a recent advanced IR study on Ti supported on MCM-41, CO could be demonstrated as being the primary product of the reaction. An energetic scheme was proposed as indicated in Fig. 13.8 [15].

Excitation of the Ti–O ligand to metal charge-transfer transition of Ti centers leads to transient Ti^{+III} and a hole on a framework oxygen (O^{-I}). Electron transfer from Ti^{+III} to CO_2 yields CO_2^-, and transfer of the hole to water generates a surface OH radical and H^+. CO_2^- and H^+ recombine to CO and a second OH radical. The OH radicals either combine to yield H_2O_2 or directly dismutate to give O_2 and H_2O. Figure 13.8 indicates the free energies associated with the formation of the stable products. The only speculative energy is that of the surface OH radicals.

To evaluate the reactivity, it is extremely important to use pure mesoporous materials, free from carbonaceous residues, which is often not easy to achieve. In view of the long lifetime of OH radicals in a room temperature molecular sieve due to random walk (hundreds of microseconds), it is likely that, even at a very low concentration, OH radicals react with these carbonaceous residues, at least partly contributing to the product distribution of CO_2 reduction. Similar to the statements made for crystalline catalysts, careful evaluation of the literature data is recommended. In terms of turnover rates, the currently known catalysts are extremely inefficient for CO_2 reduction, and the rates are far from those necessary to make the dream of artificial photosynthesis a reality. It is desired to achieve further understanding on the chemical pathways involved, and in particular on the nature of the active sites, to allow the rational design of improved catalysts.

13.4 Process Intensification

Various research groups have focused on the development of catalysts for selective oxidation of hydrocarbons. Generally interesting results have been obtained. Roughly selective photocatalytic oxidation studies can be divided into gas-phase processes and liquid-phase processes, and both will be addressed, using oxidation of propane and cyclohexane, respectively, as examples.

13.4.1 Propane Oxidation

As stated, a strategy to influence the photocatalytic performance of TiO_2 is to support TiO_2 on inert SiO_2-based materials. One creates isolated molecular Ti sites in tetrahedral coordination, usually by impregnating mesoporous materials (such as MCM-41 and SBA-15) with TiO_2 precursors [61]. In these procedures, besides isolated sites, clustered Ti sites are often produced if the loading is increased above 1–2 wt%. The relative contribution of these clustered sites and/or nanoparticles to the overall photoactivity of TiO_2 supported on SiO_2-based materials is typically not considered. Studies involving TUD-1 were thus focused on this aspect. By varying the crystallization time, two samples were obtained with well-defined different nanoparticle sizes, respectively, 3 and 7 nm. The obtained photocatalytic results show that the larger the particles are, the higher the activity to products, while the selectivity to partially oxidized products seems to be larger, the smaller the particles are [45]. The selectivity determined as being formed inside the pores, and as analyzed by *operando* IR spectroscopy, amounts to approximately 40% toward acetone, with other products constituting species of higher oxidation degree (carboxylates, carbonates), which eventually decompose to form CO_2.

Besides Ti-based catalysts, also catalysts based on Cr [62] and V as chromophores have been used in selective alkane oxidation [63, 64]. In particular, for Cr-systems,

the effect of wavelength on performance has been evaluated in selective oxidation of propane to acetone [62]. To this end, an amorphous, mesoporous silica matrix loaded with 10 at.% chromium/silicon was synthesized, characterized, and tested for performance. Spectroscopy, microscopy, and X-ray diffraction show that chromium is present in this catalyst as both isolated Cr(VI)-sites and crystalline Cr(III) oxide. The photochemical reaction rate depends strongly on excitation wavelength in the range of 300–700 nm, with a well-resolved maximum at 460 nm. At this wavelength, adsorbed acetone is produced with approximately 60% selectivity over carboxylates. Only very minor variations in selectivity were observed over the same range of wavelengths. By comparison of absorbance, luminescence, and reaction-excitation spectra, the photoactivated catalytic site was identified as an excited state of isolated Cr(VI) oxide in tetrahedral coordination. Therefore, a heterogeneity of chemical structure, which is correlated with heterogeneity of an unresolved absorption spectrum, can be the basis of wavelength-dependent photocatalytic activity.

Whereas progress has been made in the characterization and identification of these catalyst formulations, it is fair to state that selectivity, in particular if related to the low conversions achieved, is not sufficiently high to establish processes in practice. It should be mentioned that much higher selectivities have been achieved in modified zeolites [65–67], but collection of the product remains difficult, in view of the strong adsorption of particularly acetone in the pores of the zeolites [68]. Perhaps evaluation of process conditions (addition of water to the feed) and temperature might lead to novel avenues to bring selective photooxidation of propane closer to reality.

13.4.2 Cyclohexane Oxidation

Cyclohexane oxidation to cyclohexanone is often chosen as the model reaction to evaluate liquid-phase selective photocatalysis in a broader context since (1) the reaction is highly selective (e.g., alkenes give a range of products), (2) the reaction is easy to handle in the lab (e.g., benzene derivates are highly carcinogenic and require special precautions), (3) products are relatively easily analytically identified (in particular by ATR spectroscopy), and (4) the reaction is of industrial relevance:

$$C_6H_{12} + O_2 \rightarrow C_6H_{10}O + H_2O. \tag{13.5}$$

In Fig. 13.9, the product formation in the photon-induced oxidation of cyclohexane over TiO_2 is shown, using different reaction conditions. The product formation in the absence of catalyst, induced by absorption of deep UV radiation by cyclohexane (this occurs only below ~270 nm), is shown in Fig. 13.9a. Clearly cyclohexanol is the preferred product of photolysis, which is for practical applications less desired over cyclohexanone. The effect of the addition of a TiO_2 catalyst on product selectivity, still in the presence of deep UV radiation, is evident by comparison of Fig. 13.9a, b. Although the catalyst decreases the overall productivity

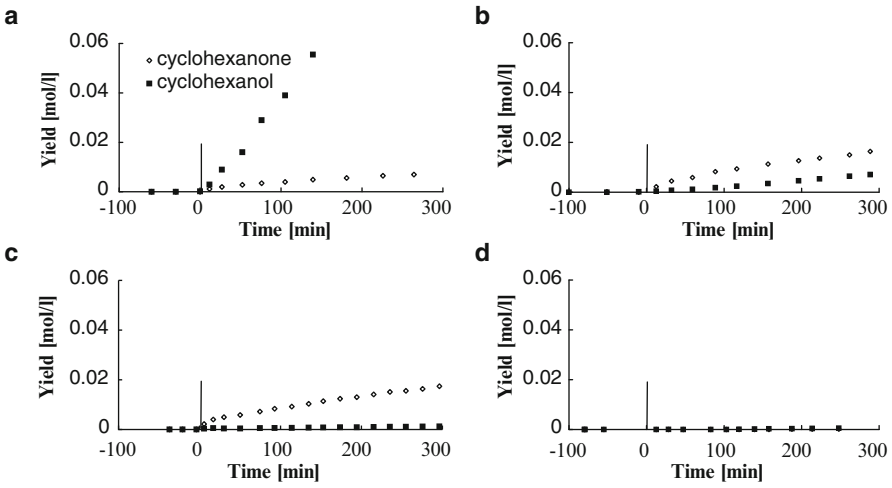

Fig. 13.9 Effect of the experimental conditions on the cyclohexanone and cyclohexanol amounts produced over Hombikat TiO_2 in photocatalytic oxidation of cyclohexane. (**a**) Quartz reactor, no catalyst (pure photolysis); (**b**) Quartz reactor, with catalyst (1 g/l of TiO_2, combination of photolysis and photocatalysis); (**c**) Pyrex reactor with catalyst (1 g/l of TiO_2, excluding photolysis); and (**d**) Pyrex reactor, no catalyst. Light was switched on at $t = 0$ min [14]

(by nonreactive light absorption), the selectivity toward cyclohexanone is largely enhanced. Figure 13.1c illustrates the selectivity if photolysis is excluded (confirmed by Fig. 13.1d), which is possible by using a pyrex reactor, filtering the UV light, and thus ensuring that only the catalyst is photoactivated (predominantly the 366-nm emission line of the Hg lamp was used). A selectivity of >90% toward cyclohexanone can thus be achieved. Principally the role of the catalyst in photocatalysis at 366 nm is similar to that in thermocatalysis: the rate is enhanced (or the catalyst allows less severe conditions, in this case, higher wavelengths), as is the selectivity to a desired product.

13.4.3 Catalyst Deactivation

A major issue that has not been very well addressed, and has frustrated practical application of photoactivated TiO_2 in selective oxidation, is catalyst deactivation. The formation of surface-bound carbonates and carboxylates by consecutive oxidation of surface-adsorbed products is likely the cause of this catalyst deactivation [59, 69]. Various strategies to stimulate desorption of the product of cyclohexane oxidation, i.e., cyclohexanone, including surface modification of TiO_2 by surface silylation [70], and optimization of the crystal structure and morphology [71, 72] have been put forward. Particle size and crystal structure have a significant

influence on photoefficiency. In particular, we observed that upon increasing the crystallite size, productivity (g^{-1} catalyst) decreases, while (1) the TOF (moles of cyclohexanone formed per minute per OH-site), (2) the rate of cyclohexanone desorption, (3) catalytic site stability, and (4) the cyclohexanol/cyclohexanone ratio increase. While catalyst performance and regenerability have been improved by these strategies, further improvement in process operation is needed, in particular when one aims for a continuous process.

Recently, humidification of the air stream was demonstrated to be a solution to the deactivation problem, in particular for a well-defined photocatalyst, such as Solaronix TiO_2. Water establishes enhanced product desorption and stimulates decomposition of deactivating surface carboxylate species, as clearly demonstrated by ATR-FTIR spectroscopy. The properties of a particular TiO_2 catalyst produced by Solaronix are much more favorable than of Hombikat UV100, in terms of a high stability in the reaction. The fact that cyclohexanone displacement by water is fast, suggests that the surface of Solaronix is quite hydrophilic. The water-induced desorption of cyclohexanone limits consecutive oxidation to deactivating species. At the same time, the previously mentioned optoelectronic properties are such, that if formed, carboxylates oxidize easily (to CO_2), regenerating active OH-sites.

The results of this study clearly demonstrate that one issue hampering practical application of photocatalysis for selective oxidation, i.e., catalyst deactivation, can be resolved. Other issues remain, including improvement of the photoefficiency of the process, i.e., the chemical conversion per unit of energy. While some advances have been reported, including particle size optimization and consequently crystal morphology, and operational conditions such as light intensity and slurry density, the photocatalytic community has not been successful in dramatically reducing the recombination rate of the holes and electrons formed upon photoactivation. Adding metal particles, such as Pt or Au, as electron acceptors have been demonstrated an option, and this certainly leaves room for further improvement.

13.4.4 Reactor Design

Currently photoreactors for liquid-phase oxidation are usually based on slurry systems, i.e., the solid phase is dispersed within the liquid in the reactor. Usually the slurry is illuminated from the top (a top illumination reactor) or by the use of an immersed light source, referred to as annular reactor. Although these designs offer ease of construction and high catalyst loading, they clearly have drawbacks, such as the difficulty of separation of catalyst particles from the reaction mixture and low light utilization efficiencies due to the scattering and shielding of light by the reaction medium and catalyst particles.

Various attempts have been made to amend the aforementioned light distribution problems by immobilizing photocatalytic systems. One approach was to employ optical fibers as a light distributing guide and support for photocatalysts. Light propagates through the fiber core, while certain amount of photons is refracted into

the coated titania layer. By this means, the optical fibers enable the remote delivery of photon energy to the reactive sites of the photocatalyst. Various groups have reported on the successful application of titania-coated optical fibers in photocatalytic purification of air and water. Still, coating of a TiO_2 catalyst layer on quartz fibers has several intrinsic drawbacks. Firstly, the adhesion strength and layer thickness of catalyst coating on the fibers strongly affect its durability and performance. As the adhesion of TiO_2 particles on quartz fibers is primarily due to electrostatic interaction, it is unlikely that the coating layer will withstand severe gas and/or liquid flow conditions in large-scale continuous operation modes. To enhance the durability of the titania coatings, fibers were often roughened before the immobilization of catalysts. However, that will inevitably result in an uneven distribution of catalyst and light along the axial direction of the fibers. Other significant problems are the short light propagating length (less than 10 cm) and the heat build-up in the bundled array, which might lead to local deactivation of the catalyst.

An alternative for coating the catalyst on the fibers is the combination of side-light emitting fibers and ceramic monoliths. The side-light fibers are evenly distributed inside a ceramic monolith structure, on the inner walls of which, e.g., a titania photocatalyst is coated. The reaction system is so constructed that flows in various hydrodynamic regimes, such as Taylor flow (alternating gas bubbles and liquid slugs) and film flow can be realized. Because no catalyst is coated on the fibers, the emitted light can reach the catalyst–reactant interface without being strongly attenuated by the solid particles. Indeed, promising results have been achieved with this concept [73], although improvements are still necessary. This includes the further evaluation of the effect of various process parameters, such as temperature, flow regime, and optimization of catalyst coating. In particular, the flow regime can stimulate enhanced mass transfer characteristics and cyclohexanone desorption, as well as the rate of regeneration, since the liquid slug of cyclohexane is well mixed and the (preferably humidified) air bubble (i.e., regenerative phase) separated from the catalyst surface only by a relatively thin cyclohexane liquid film (Fig. 13.10).

Another innovative photoreactor design is based on the microreactor concept. LED light sources are available to illuminate microreactors with well-defined wavelengths, including in the UV [7]. The distance between the light source and the catalyst is small, with the catalyst immobilized on the walls of the microchannels. Furthermore, in gas/liquid configurations, microreactors allow a well-defined control of the gas–liquid distribution. The feasibility of microreactors in photocatalysis was demonstrated in the literature. Positive effects on selectivity have been observed, both as a result of the use of monochromatic light (the advantage of LEDs vs., e.g., Hg lamps) and excellent control over the residence times of the reactants [12]. Various research groups, including our own, focus on optimization of the functionalization of the microreactors with photocatalysts, which certainly is not trivial. Only if optimized catalyst morphology is combined with optimized reactor configurations, light harvesting and chemical conversion can be achieved. Practically, fine chemical synthesis appears

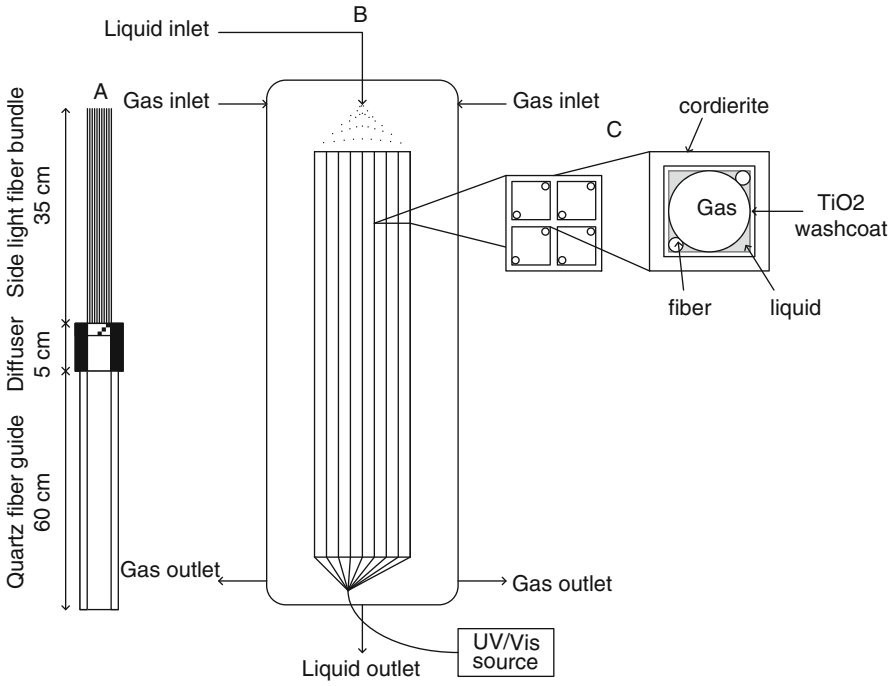

Fig. 13.10 Scheme of the internally illuminated monolith reactor setup, consisting of a ceramic monolith with square channels, on the walls of which the catalyst (TiO_2) is coated and in which two optical fibers are inserted and located in the corners of the channels. The detail shows the construction of the optical fiber bundle

more achievable through microreactor-based photocatalytic conversion then production of large-scale chemicals, although experience with the former might lead to applications in the latter area.

13.5 Concluding Remarks

More and more research groups active in the field of homo- and heterogeneous catalysis realize that light can be an attractive alternative for heat to perform a catalytic conversion. With the advent of highly efficient LED light sources and novel (micro) reactor concepts, the practical application of light-induced catalysis might become feasible. Although the field of photocatalysis has significant history, analysis of the surface composition and surface chemistry in reaction conditions with vibrational spectroscopies is rather rare, in particular in the liquid phase, and much insight is still to gain. The field would certainly benefit from an integrated approach, rather than individual studies of bandgap engineers, material scientists, spectroscopists, catalysis groups, and recently theoreticians. This will propel the science of the field and might

open up rules to rationally design novel catalyst formulations. Photocatalysis no doubt has a bright future in contributing to the various energy challenges of the chemical industry in particular, and society in general.

Acknowledgments I would like to thank Prof. J.A. Moulijn, MD, for fruitful discussions and allowing me to explore the field of photocatalysis. Contributions from PhD students Dr. P. Du, Dr. M.S. Hamdy, Dr. J.T. Carneiro, Dr. A.R. Almeida, and Dr. C-C Yang were indispensable for construction of this text. Finally, I would like to thank STW for funding my photocatalysis research in the framework of the VIDI program (DPC.7065).

References

1. Rajeshwar K, McConnel R, Licht S (2008) Solar hydrogen generation-toward a renewable energy future. New York, NY, Springer Science and Business Media
2. MacKay DJC (2009) Sustainable energy: without the hot air. UIT, Cambridge
3. Lewis NS, Nocera DG (2006) Powering the planet: chemical challenges in solar energy utilization. Proc Natl Acad Sci USA 103(43):15729–15735. doi:10.1073/pnas.0603395103
4. Lutterman DA, Surendranath Y, Nocera DG (2009) A self-healing oxygen-evolving catalyst. J Am Chem Soc 131(11):3838–3839. doi:10.1021/ja900023k
5. Surendranath Y, Kanan MW, Nocera DG (2010) Mechanistic studies of the oxygen evolution reaction by a cobalt-phosphate catalyst at neutral pH. J Am Chem Soc 132(46):16501–16509. doi:10.1021/ja106102b
6. Young ER, Nocera DG, Bulovic V (2010) Direct formation of a water oxidation catalyst from thin-film cobalt. Energy Environ Sci 3(11):1726–1728. doi:10.1039/c0ee00177e
7. Shibata H, Moulijn JA, Mul G (2008) Enabling electrocatalytic Fischer-Tropsch synthesis from carbon dioxide over copper-based electrodes. Catal Lett 123(3–4):186–192. doi:10.1007/s10562-008-9488-3
8. Hori Y, Konishi H, Futamura T, Murata A, Koga O, Sakurai H, Oguma K (2005) "Deactivation of copper electrode" in electrochemical reduction of CO_2. Electrochim Acta 50 (27):5354–5369. doi:10.1016/j.electacta.2005.03.015
9. Stankiewicz A, Moulijn JA (2002) Process intensification. Ind Eng Chem Res 41 (8):1920–1924. doi:10.1021/ie011025p
10. Lu H, Schmidt MA, Jensen KF (2001) Photochemical reactions and on-line UV detection in microfabricated reactors. Lab Chip 1(1):22–28. doi:10.1039/b104037p
11. Maeda H, Mukae H, Mizuno K (2005) Enhanced efficiency and regioselectivity of intramolecular (2 pi+2 pi) photocycloaddition of 1-cyanonaphthalene derivative using microreactors. Chem Lett 34(1):66–67. doi:10.1246/cl.2005.66
12. Van Gerven T, Mul G, Moulijn J, Stankiewicz A (2007) A review of intensification of photocatalytic processes. Chem Eng Process 46(9):781–789. doi:10.1016/j.cep. 2007.05.012
13. Moulijn JA, Makkee M, van Diepen A (2001) Chemical process technology. John Wiley & Sons Ltd, West Sussex
14. Du P, Moulijn JA, Mul G (2006) Selective photo(catalytic)-oxidation of cyclohexane: effect of wavelength and TiO_2 structure on product yields. J Catal 238(2):342–352. doi:10.1016/j.jcat.2005.12.011
15. Lin WY, Han HX, Frei H (2004) CO_2 splitting by H_2O to CO and O_2 under UV light in TiMCM-41 silicate sieve. J Phys Chem B 108(47):18269–18273. doi:10.1021/jp040345u
16. Atkins PW (1986) Physical chemistry. Oxford University Press, Oxford
17. Carp O, Huisman CL, Reller A (2004) Photoinduced reactivity of titanium dioxide. Prog Solid State Chem 32(1–2):33–177. doi:10.1016/j.progsolidstchem.2004.08.001

18. Bahnemann DW, Hilgendorff M, Memming R (1997) Charge carrier dynamics at TiO_2 particles: reactivity of free and trapped holes. J Phys Chem B 101(21):4265–4275
19. Hoffmann MR, Martin ST, Choi WY, Bahnemann DW (1995) Environmental applications of semiconductor photocatalysis. Chem Rev 95(1):69–96
20. Cox PA (1987) The electronic structure and chemistry of solids. Oxford University Press, Oxford
21. Fujishima A, Honda K (1972) Electrochemical photolysis of water at a semiconductor electrode. Nature 238(5358):37–38
22. Kawai T, Sakata T (1980) Photocatalytic decompsoition of gaseous water over TiO_2 and TiO_2-RuO_2 surfaces. Chem Phys Lett 72(1):87–89
23. Maeda K, Lu DL, Teramura K, Domen K (2010) Simultaneous photodeposition of rhodium-chromium nanoparticles on a semiconductor powder: structural characterization and application to photocatalytic overall water splitting. Energy Environ Sci 3(4):471–478. doi:10.1039/b915064a
24. Borgarello E, Kiwi J, Pelizzetti E, Visca M, Gratzel M (1981) Photochemical cleavage of water by photocatalysis. Nature 289(5794):158–160
25. Kalyanasundaram K, Borgarello E, Gratzel M (1981) Visible light induced water cleavage in CdS dispersions loaded with Pt and RuO_2, hole scavenging by RuO_2. Helv Chim Acta 64 (1):362–366
26. Jiao F, Frei H (2009) Nanostructured cobalt oxide clusters in mesoporous silica as efficient oxygen-evolving catalysts. Angew Chem Int Ed 48(10):1841–1844. doi:10.1002/anie.200805534
27. Jiao F, Frei H (2010) Nanostructured cobalt and manganese oxide clusters as efficient water oxidation catalysts. Energy Environ Sci 3(8):1018–1027. doi:10.1039/c002074e
28. Jiao F, Frei H (2010) Nanostructured manganese oxide clusters supported on mesoporous silica as efficient oxygen-evolving catalysts. Chem Commun 46(17):2920–2922. doi:10.1039/b921820c
29. Sasaki Y, Nemoto H, Saito K, Kudo A (2009) Solar water splitting using powdered photocatalysts driven by Z-schematic interparticle electron transfer without an electron mediator. J Phys Chem C 113(40):17536–17542. doi:10.1021/jp907128k
30. Borgarello E, Kiwi J, Gratzel M, Pelizzetti E, Visca M (1982) Visible light induced water cleavage in colloidal solutions of chromium-doped titatium dioxide particles. J Am Chem Soc 104(11):2996–3002
31. Kiwi J, Borgarello E, Pelizzetti E, Visca M, Gratzel M (1980) Cyclic water cleavage by visible light—drastic improvement of yield of H_2 and O_2 with bifunctional redox catalysts. Angew Chem Int Ed 19(8):646–648
32. Borgarello E, Kiwi J, Pelizzetti E, Visca M, Gratzel M (1981) Sustained water cleavage by visible light. J Am Chem Soc 103(21):6324–6329
33. Maeda K, Xiong AK, Yoshinaga T, Ikeda T, Sakamoto N, Hisatomi T, Takashima M, Lu DL, Kanehara M, Setoyama T, Teranishi T, Domen K (2010) Photocatalytic overall water splitting promoted by two different cocatalysts for hydrogen and oxygen evolution under visible light. Angew Chem Int Ed 49(24):4096–4099. doi:10.1002/anie.201001259
34. Sakamoto N, Ohtsuka H, Ikeda T, Maeda K, Lu DL, Kanehara M, Teramura K, Teranishi T, Domen K (2009) Highly dispersed noble-metal/chromia (core/shell) nanoparticles as efficient hydrogen evolution promoters for photocatalytic overall water splitting under visible light. Nanoscale 1(1):106–109. doi:10.1039/b9nr00186g
35. Kudo A, Miseki Y (2009) Heterogeneous photocatalyst materials for water splitting. Chem Soc Rev 38(1):253–278. doi:10.1039/b800489g
36. Anpo M, Yamashita H, Ikeue K, Fujii Y, Zhang SG, Ichihashi Y, Park DR, Suzuki Y, Koyano K, Tatsumi T (1998) Photocatalytic reduction of CO_2 with H_2O on Ti-MCM-41 and Ti-MCM-48 mesoporous zeolite catalysts. Catal Today 44(1–4):327–332
37. Zhang SG, Fujii Y, Yamashita K, Koyano K, Tatsumi T, Anpo M (1997) Photocatalytic reduction of CO_2 with H_2O on Ti-MCM-41 and Ti-MCM-48 mesoporous zeolites at 328 K. Chem Lett 44(7):659–660

38. Anpo M, Yamashita H, Ichihashi Y, Fujii Y, Honda M (1997) Photocatalytic reduction of CO_2 with H_2O on titanium oxides anchored within micropores of zeolites: effects of the structure of the active sites and the addition of Pt. J Phys Chem B 101(14):2632–2636
39. Yamashita H, Fujii Y, Ichihashi Y, Zhang SG, Ikeue K, Park DR, Koyano K, Tatsumi T, Anpo M (1998) Selective formation of CH_3OH in the photocatalytic reduction of CO_2 with H_2O on titanium oxides highly dispersed within zeolites and mesoporous molecular sieves. Catal Today 45(1–4):221–227
40. Lin WY, Frei H (2002) Photochemical and FT-IR probing of the active site of hydrogen peroxide in Ti silicalite sieve. J Am Chem Soc 124(31):9292–9298. doi:10.1021/ja012477w
41. Han HX, Frei H (2008) In situ spectroscopy of water oxidation at Ir oxide nanocluster driven by visible TiOCr charge-transfer chromophore in mesoporous silica. J Phys Chem C 112 (41):16156–16159. doi:10.1021/jp803994d
42. Lin WY, Frei H (2005) Photochemical CO_2 splitting by metal-to-metal charge-transfer excitation in mesoporous ZrCu(I)-MCM-41 silicate sieve. J Am Chem Soc 127 (6):1610–1611. doi:10.1021/ja040162l
43. Hamdy MS, Berg O, Jansen JC, Maschmeyer T, Arafat A, Moulijn JA, Mul G (2006) Chromium-incorporated TUD-1 as a new visible light-sensitive photo-catalyst for selective oxidation of propane. Catal Today 117(1–3):337–342. doi:10.1016/j.cattod.2006.05.058
44. Mul G, Wasylenko W, Hamdy MS, Frei H (2008) Cyclohexene photo-oxidation over vanadia catalyst analyzed by time resolved ATR-FT-IR spectroscopy. Phys Chem Chem Phys 10 (21):3131–3137. doi:10.1039/b800314a
45. Hamdy MS, Berg O, Jansen JC, Maschmeyer T, Moulijn JA, Mul G (2006) TiO_2 nanoparticles in mesoporous TUD-1: synthesis, characterization and photocatalytic performance in propane oxidation. Chem Eur J 12(2):620–628. doi:10.1002/chem.200500649
46. Hussain A, Gracia J, Nieuwenhuys B, Niemantsverdriet JW (2010) Chemistry of O- and H-containing species on the (001) surface of anatase TiO_2: a DFT study. Chem Phys Chem 11(11):2375–2382. doi:10.1002/cphc.201000185
47. Yu JG, Qi LF, Jaroniec M (2010) Hydrogen production by photocatalytic water splitting over Pt/TiO_2 nanosheets with exposed (001) facets. J Phys Chem C 114(30):13118–13125. doi:10.1021/jp104488b
48. Vandamme H, Hall WK (1979) Photoassisted decomposition of water at the gas-solid interface on TiO_2. J Am Chem Soc 101(15):4373–4374
49. Nakamura R, Okamura T, Ohashi N, Imanishi A, Nakato Y (2005) Molecular mechanisms of photoinduced oxygen evolution, PL emission, and surface roughening at atomically smooth (110) and (100) n-TiO_2 (rutile) surfaces in aqueous acidic solutions. J Am Chem Soc 127 (37):12975–12983. doi:10.1021/ja053252e
50. Nakamura R, Nakato Y (2004) Primary intermediates of oxygen photoevolution reaction on TiO_2 (rutile) particles, revealed by in situ FTIR absorption and photoluminescence measurements. J Am Chem Soc 126(4):1290–1298. doi:10.1021/ja0388764
51. Kato H, Kudo A (2002) Visible-light-response and photocatalytic activities of TiO_2 and $SrTiO_3$ photocatalysts codoped with antimony and chromium. J Phys Chem B 106 (19):5029–5034. doi:10.1021/jp0255482
52. Carneiro JT, Savenije TJ, Mul G (2009) Experimental evidence for electron localization on Au upon photo-activation of Au/anatase catalysts. Phys Chem Chem Phys 11(15):2708–2714. doi:10.1039/b820425j
53. Carneiro JT, Yang CC, Moma JA, Moulijn JA, Mul G (2009) How gold deposition affects anatase performance in the photo-catalytic oxidation of cyclohexane. Catal Lett 129 (1–2):12–19. doi:10.1007/s10562-008-9801-1
54. Shaw DJ, Panman MR, Woutersen S (2009) Evidence for cooperative vibrational relaxation of the NH-, OH-, and OD-stretching modes in hydrogen-bonded liquids using infrared pump-probe spectroscopy. Phys Rev Lett 103(22). doi:22740110.1103/PhysRevLett.103.227401
55. Rasko J, Solymosi F (1994) Infrared spectroscopic study of the photoinduced activation of CO_2 on TiO_2 and Rh/TiO_2 catalysts. J Phys Chem 98(29):7147–7152

56. Rasko J, Solymosi F (1997) Reactions of adsorbed CH_3 species with CO_2 on Rh/SiO_2 catalyst. Catal Lett 46(3–4):153–157
57. Yang CC, Yu YH, van der Linden B, Wu JCS, Mul G (2010) Artificial photosynthesis over crystalline TiO_2-based catalysts: fact or fiction? J Am Chem Soc 132(24):8398–8406. doi:10.1021/ja101318k
58. Nguyen TV, Wu JCS (2008) Photoreduction of CO_2 in an optical-fiber photoreactor: effects of metals addition and catalyst carrier. Appl Catal A Gen 335(1):112–120. doi:10.1016/j.apcata.2007.11.022
59. Almeida AR, Moulijn JA, Mul G (2008) In situ ATR-FTIR study on the selective photo-oxidation of cyclohexane over anatase TiO_2. J Phys Chem C 112(5):1552–1561. doi:10.1021/jp077143t
60. Anpo M, Yamashita H, Ichihashi Y, Ehara S (1995) Photocatalytic reduction of CO_2 with H_2O on various titanium-oxide catalysts. J Electroanal Chem 396(1–2):21–26
61. Telalovic S, Ramanathan A, Mul G, Hanefeld U (2010) TUD-1: synthesis and application of a versatile catalyst, carrier, material. J Mater Chem 20(4):642–658. doi:10.1039/b904193a
62. Berg O, Hamdy MS, Maschmeyer T, Moulijn JA, Bonn M, Mul G (2008) On the wavelength-dependent performance of Cr-doped silica in selective photo-oxidation. J Phys Chem C 112 (14):5471–5475. doi:10.1021/jp075562k
63. Amano F, Yamaguchi T, Tanaka T (2006) J Phys Chem B 110:281–288
64. Takenaka S, Tanaka T, Funabiki T, Yoshida S (1997) J Chem Soc Faraday Trans 93:4151–4158
65. Sun H, Blatter F, Frei H (1997) Oxidation of propane to acetone and of ethane to acetaldehyde by O_2 in zeolites with complete selectivity. Catal Lett 44(3–4):247–253
66. Blatter F, Sun H, Vasenkov S, Frei H (1998) Photocatalyzed oxidation in zeolite cages. Catal Today 41(4):297–309
67. Frei H (2006) Selective hydrocarbon oxidation in zeolites. Science 313(5785):309–310. doi:10.1126/science.1128981
68. Xu J, Mojet BL, van Ommen JG, Lefferts L (2005) Formation of M2+(O2)(C3H8) species in alkaline-earth-exchanged Y zeolite during propane selective oxidation. J Phys Chem B 109 (39):18361–18368. doi:10.1021/jp052941+
69. Renckens TJA, Almeida AR, Damen MR, Kreutzer MT, Mul G (2010) Product desorption limitations in selective photocatalytic oxidation. Catal Today 155(3–4):302–310. doi:10.1016/j.cattod.2009.12.002
70. Almeida AR, Carneiro JT, Moulijn JA, Mul G (2010) Improved performance of TiO_2 in the selective photo-catalytic oxidation of cyclohexane by increasing the rate of desorption through surface silylation. J Catal 273(2):116–124. doi:10.1016/j.jcat.2010.05.006
71. Carneiro JT, Almeida AR, Moulijn JA, Mul G (2010) Cyclohexane selective photocatalytic oxidation by anatase TiO_2: influence of particle size and crystallinity. Phys Chem Chem Phys 12(11):2744–2750. doi:10.1039/b919886e
72. Hernandez-Alonso MD, Almeida AR, Moulijn JA, Mul G (2009) Identification of the role of surface acidity in the deactivation of TiO_2 in the selective photo-oxidation of cyclohexane. Catal Today 143(3–4):326–333. doi:10.1016/j.cattod.2008.09.025
73. Du P, Cameiro JT, Moulijn JA, Mul G (2008) A novel photocatalytic monolith reactor for multiphase heterogeneous photocatalysis. Appl Catal A Gen 334(1–2):119–128. doi:10.1016/j.apcata.2007.09.045

Chapter 14
Concluding Remarks and Future Perspectives

András Tompos

Abstract Amongst the renewable energies the solar energy is supposed to become the dominating one in the remote future. Process intensification is necessary in order to exploit unevenly distributed solar and other renewable energy sources. This article aims to highlight the role of heterogeneous catalysts in the novel catalytic processes designed for alternative energy generation. It is essential to develop catalysts and technologies for storing and transporting energy produced from various renewable sources. Storage in batteries or in chemical forms, for example in hydrogen, is under investigations. Due to robustness of the present infrastructure built for the exploitation of fossil resources, a part of the studies is devoted to develop catalytic processes for production of liquid fuels of biomass origin or using CO_2 as carbon source. New catalysts are complex multicomponent systems with hierarchically organized 3D-nanostructures. Characterization and modeling of such systems requires the development of in situ characterization tools.

Energy generation from renewable energy sources has obtained increasing attention in the last few decades with the aim to provide a sustainable alternative to conventional fossil energy sources, depletion of which is anticipated in the not too far future. Additionally, CO_2 emission leading to increased greenhouse effect as well as emission of NO_x and different particulates upon usage of fossil energy sources in internal combustion engines and power stations pushes the changes toward the more intensive contribution of renewable sources in the future energy scenario. Emission control and the security of energy supply are two of the key areas for societal challenges.

The origin of renewable energy sources is eventually the Sun. Direct utilization can be achieved by solar collectors and photovoltaic devices while solar energy is

A. Tompos (✉)
Research Center for Natural Sciences, Hungarian Academy of Sciences,
1525 Budapest, POB 17, Hungary
e-mail: tompos.andras@ttk.mta.hu

L. Guczi and A. Erdőhelyi (eds.), *Catalysis for Alternative Energy Generation*,
DOI 10.1007/978-1-4614-0344-9_14,

converted by the "nature" to biomass, wind power, and hydroelectric power. Additionally, geothermal energy and energy from oceans can also be exploited. Primary renewable energy sources provided by the nature have to be converted into fuels, electricity, mechanical energy, and heat for the end users. As anticipated in this book, in the remote future, solar energy will be the dominating renewable source.

Although changes are unavoidable, the robustness and spaciousness of the present energy-related infrastructure (pipelines, engines, power plants) make the fossil fuel-based economy quite static and fossil fuels will remain the main energy sources in the next two to three decades. The changes toward new technologies are anticipated first in the development of new catalysts for processing of the so far neglected fossil sources such as heavy and low-quality crude oil, coal, or natural gas with significant sulfur content, and potentially methane hydrate. In the second step, still insisting on the present infrastructure, development of technologies and materials for conversion of biomass into liquid fuels compatible with diesel fuels has a high probability. Other renewable sources can be exploited to produce mainly electricity. However, for vehicular applications, because the energy density in batteries is too low, usage of liquid fuels or some other chemical form of energy storage seems to be necessary. Biomass alone cannot suffice the increasing energy demand of the society. Besides biomass, in the future other renewable energy sources have to be exploited to produce either (1) liquid fuels compatible with diesel, or (2) other liquid fuels such as methanol, ethanol, etc., or (3) hydrogen. If any of these energy storage routes will be realized, then the renewable production of hydrogen will have key importance. Hydrogen is used extensively for production of hydrocarbons from biomass and for the production of alcohols (from CO or CO_2) as well. It has to be mentioned, however, that in most of the above hydrogenation reactions, stoichiometric amount of water is produced, which (1) consumes hydrogen in a significant amount and (2) acts as an inhibitor on the catalyst during methanol synthesis. Eventually, in a long term, establishment of the infrastructure for "hydrogen economy" seems to be reasonable. In 2009, nine car manufacturing companies, Daimler, Ford, GM, Opel, Honda, Hyundai, KIA, Renault, Nissan, and Toyota signed already a declaration about significant increase in the production of hydrogen-based fuel cell cars from 2015.

In various chapters of this book it has been demonstrated that in different energy conversion steps catalysis can be considered as the key factor to meet sustainability. Processes such as hydrogenation in biomass conversion technologies, aqueous-phase reforming (APR), steam reforming, and electricity generation in polymer electrolyte membrane (PEM) fuel cells generally need noble metal-based catalysts, which have limited availability. Therefore, one of the main goals in these fields is to discover noble metal-free systems. The development of new catalysts required for energy conversion technologies needs new approaches, new concepts, and efficient tools. Application of high-throughput experimental techniques, in situ characterization tools, and study of model catalysts by means of novel surface analytical techniques are required. The new catalysts are most probably multicomponent systems. The primary goal is to identify and differentiate between possible ligand and ensemble effects in multicomponent systems. Additionally, there is a special

attention in nanoscience and nanotechnology pointed toward the fabrication of materials with uniform complex structures. The novel catalysts are not only multicomponent but they are prepared in the form of well-aligned nanorods, nanowires, and nanotubes toward a special direction, core–shell nanostructures as well as hierarchically organized structures are designed, which can significantly influence the final catalytic properties. The core technology to be developed is the preparation of novel nanomaterials with controllable sizes, shapes, and/or structures. In the novel nanostructured materials, not only the cross effects between the constituents have to be considered. There are also (1) quantum size effect due to smaller crystallite size ("true size effect") and (2) effects on the charge and mass transport. The challenge is to develop tailored 3D nanoarchitectures not only for zeolites and mesoporous materials but also for transition metal oxides.

In order to understand reaction mechanism and elementary steps occurring on the surface of novel nanosystems as well as to discover surface species participating in surface processes, novel in situ characterization tools have to be applied. Application and study of model catalysts by means of surface analytical techniques has become increasingly important. Significant progresses have been achieved in closing the "pressure gap" between surface science approaches and real catalysis. Accordingly, model catalysts can be investigated not only under ultrahigh vacuum (UHV) conditions but also under real conditions. Single-crystal surfaces or well-defined nanoclusters on surfaces are studied under clean and well-controlled conditions by means of in situ transmission electron microscopy (TEM) [1], UV and X-ray photoelectron spectroscopy (UPS and XPS) [2, 3], low-energy ion scattering (LEIS) [3, 4], polarization-modulation infrared reflection absorption spectroscopy (PM-IRAS) [3, 5], low-energy electron diffraction (LEED) [6], sum frequency generation (SFG) vibrational spectroscopy [7, 8], etc.

14.1 Energy Storage

The energy production based on renewable sources is quite unbalanced and the abundance of renewable sources is highly dependent on the local options. According to the local and temporary possibilities there are irregularly changing periods with higher and smaller energy production. In contrast to power plants based on fossil energy resources, renewable sources are not only unevenly distributed but also delocalized. Therefore, storage and dissemination/transportation of energy has crucial importance and has to be accomplished in the most efficient way, which has high diversity depending on the local possibilities. Electricity can be stored in Li-ion batteries/super capacitors and by conversion into appropriate energy carrier materials. The favorable energy carrier material can be produced from various renewable sources and carries chemical energy in high density. They have to be easily stored, transported, and efficiently converted to other forms of energy. Hydrogen is considered as a potential environment benign energy carrier of the future. A major challenge in a future "hydrogen economy"

is the development of a safe, compact, robust, and efficient means of hydrogen storage for mobile and other applications. Besides hydrogen, biodiesel and other biomass-originated liquid fuels, as concentrated and easy transportable form of energy, are supposed to have crucial importance in the close future.

Promising nanosized materials for hydrogen storage are the metal and chemical hydrides. Not only the storage capacity has to be increased but also desorption/absorption kinetics has to be improved and desorption/absorption temperature has to be tuned. Amongst the novel hydrogen storage materials, $LiBH_4$ and MgH_2 nanoparticles embedded in a nanoporous carbon aerogel scaffold have to be mentioned [9]. In this system the hydrogen desorption kinetics is significantly improved compared to bulk conditions, and the nanoconfined system has a high degree of reversibility and stability and also improved thermodynamic properties. The reversible hydrogen storage capacity of 3.9% for the nanocomposite system was found. This new scheme of nanoconfined chemistry may have a wide range of interesting applications in the future, for example, within the merging area of chemical storage of renewable energy.

Graphite and activated carbon are still the mostly used materials for lithium-ion batteries and supercapacitors, respectively. Nanostructured carbons in combination with nanostructured metal (oxides) open new perspectives for the development of advanced carbon-based electrodes for high-performance lithium-ion batteries and supercapacitors. This allows the following options [10–13]:

1. New materials with insufficient own conductivity can be introduced for both electrodes (e.g., nanocomposite electrodes, hierarchical structures).
2. Contact surface area between the electrode and the electrolyte can be increased and the electrolyte can be protected against decomposition by catalytic reactions with the electrodes.
3. The transport path length for both electrons and ions can be decreased by using carbon as structuring agent while maintaining its conductive function (e.g., highly functionalized carbon structures). A shorter transport pathway enables a high charge–discharge rate and, thus, a high power. However, the very high surface area and, consequently, the large solid-electrolyte interface enhance the irreversible capacity [10].

14.2 Conversion of Biomass: Production of Liquid Fuels

The processing of biomass-derived feedstocks is different from the processing of fossil energy sources. Biomass-derived feedstocks have low thermal stability and a high degree of functionality (typically being hydrophilic in nature), thus requiring unique reaction conditions, such as aqueous-phase processing. Additionally, unlike the fossil energy resources the biomass appears disseminated on a large area in a great diversity of composition. Therefore, the technologies of the petrochemical industry cannot be directly adapted to the conversion of biomass. Development of

new catalysts and catalytic technologies are required which can be installed near the place of biomass production, have a smaller processing capacity, and still economic. Process intensification is a strategic and interdisciplinary approach employing different tools (such as microreactor technology and modularization) to improve efficiency of energy conversion processes [14].

The conversion of biomass to different biofuels can potentially be economic depending on the actual price of the crude oil. Nevertheless, different resources for subsidies seem to be inevitable. Besides the direct effect of using biomass on the energy security and emission control, it could have an advantageous impact on the rural development as well.

First-generation biodiesels are produced from plant oils (soybeans or vegetable oils) or from used cooking oil by means of transesterification [15–18]. Oxygenated hydrocarbons are prepared from starch (corn). First, sugars are produced by means of hydrolysis of starch, which are then fermented. Sugars can be submitted to dehydration, which leads to hydrocarbons as well.

Intensive usage of catalytic processes is required to obtain second-generation biofuels. The raw materials are available mainly as lignocelluloses (herbaceous, woody, municipal solid waste), which are more abundant than raw materials used for the production of first-generation biofuels. However, lignocelluloses are difficult to be converted to sugars because of the high crystallinity of the cellulose, low surface area of the material, protection of cellulose by lignin, the heterogeneous character of biomass particles, and cellulose sheathing by hemicelluloses [19]. In order to obtain sugar monomers the following pretreatment methods are used: uncatalyzed steam explosion, treatment in liquid hot water or pH-controlled hot water, flow through liquid hot water or dilute acid, flow through acid, treatment with lime, and treatment with ammonia [19].

Aqueous-phase processing of sugar monomers can lead to a versatile spectrum of products. Production of hydrogen for biorefining processes is accomplished by APR [20, 21]. The biorefinery can also produce light alkanes ranging from C_1 to C_6 by aqueous-phase dehydration/hydrogenation (APD/H) [21, 22]. The light alkanes can be used as synthetic natural gas, liquefied petroleum gas, and light naptha stream. Aqueous-phase processing can also produce longer alkanes ranging from C_7 to C_{15} by combining the dehydration/hydrogenation reactions with an aldol condensation step prior to the APD/H step [21, 23]. These longer alkanes can be used as premium, sulfur-free diesel fuel components.

Besides aqueous-phase processes, gasification of biomass can lead to syngas ($CO + H_2$) [24]. However, the gasification process requires volatilization of water that decreases the overall energy efficiency [25]. Syngas can be used to produce alkanes by Fischer–Tropsch synthesis (FTS), methane by methanation, and methanol by methanol synthesis [26]. Methanol is a liquid under normal conditions, allowing it to be stored, transported, and dispensed easily, much like gasoline and diesel fuel used currently. It can also be readily transformed by dehydration into dimethyl ether, a diesel fuel substitute with a cetane number of 55. It has to be mentioned that Nobel prize winner George A. Olah published a book recently dedicated to the “Methanol Economy” emphasizing the production of methanol

(or dimethyl ether) by chemical recycling of CO_2 [27]. In short term, CO_2 source for methanol synthesis will be the CO_2 accumulated by means of carbon capture and sequestration (CCS) technologies, while later low concentration of atmospheric CO_2 itself could be captured and recycled via methanol.

As the processes in biomass conversion mainly laid on the usage of noble metal catalysts, it is crucial to find alternative noble metal-free systems.

14.3 Hydrogen Production by Means of Reforming

Ethanol, methanol, or biogas methane can generally be used as source of hydrogen production by means of steam reforming or in the case of methane also by means of dry reforming. Ethanol is also used directly in internal combustion engines by mixing it with the fuel. The drawback of the latter approach is that (1) water-free ethanol should be used and (2) undesired by-products are formed in the engine.

It is more reasonable to produce hydrogen from alcohols and use it in fuel cells for the production of electricity. Hydrogen has a great potential for efficient utilization of unevenly distributed renewable energy. However, process intensification in small-scale hydrogen production has to be achieved. Appropriate technologies (modularization, microreactors) and novel catalysts should be developed to get a promising future for on-site, on-demand (or maybe onboard) hydrogen production from alcohols.

In case of onboard reforming the reformer is directly connected to the fuel cell. Efficiency of this approach is still under debate. One of the major drawbacks of an onboard system is the difficulty to get rapid start-up and transient operation. For that reason, reforming can be accomplished in monolithic reactors and plate heat exchangers as well as in microreactors [28], although even in these cases it is not feasible to achieve start-up times of less than several minutes, which is unacceptable for most portable applications. Eventually, onboard reforming, purification, and subsequent electrooxidation of the reformate in a fuel cell is not more efficient than a hybrid electric vehicle technology assisted internal combustion engine.

In order to accomplish efficient onboard reforming, a fuel cell–heat engine hybrid system has been proposed, which consists of a membrane reformer, a fuel cell, and a reciprocating internal combustion engine [29]. Steam reforming of a hydrocarbon requires additional heat input, which can be recovered from the waste heat of an internal combustion engine. On the other hand, the retentate of the membrane reformer can be used in the internal combustion engine to further increase the system efficiency. Methanol is proposed as the fuel for the membrane reformer because the temperature level required is low enough to recover waste heat of reciprocating internal combustion engines for steam reforming of methanol [29]. The hybrid system proposed is more flexible than a fuel cell with an onboard reformer, because additional fuel can be directly combusted in the internal combustion engine at cold start or rapid load increase. Because fuel cell efficiency decreases with load and internal combustion engine efficiency increases with load,

the overall system efficiency is less load dependent compared to the efficiencies of each of these technologies [29].

Cobalt talc nanolayers dispersed in silica aerogel constitute a novel nanocomposite material with excellent properties for the generation of hydrogen by the steam reforming of ethanol. It displayed high catalytic activity at low temperature (312–322°C) and at repeated fast start-up after oxidation during shut-down under air [30].

Core–shell nanostructured RhNi@CeO_2 catalyst has been prepared for the oxidative steam reforming of ethanol. Complete conversion of ethanol was achieved at only 300°C with 60% H_2 and less than 0.5% CO in the product stream [31].

Epitaxially grown Pd particles embedded in layers of amorphous ZnO and mechanically stabilized by SiO_2 have been proved to be structurally and thermally stable in a broad temperature range (473–873 K). The strong particle stabilization effect (SPSE) is important for catalytic processes, such as methanol steam reforming and methanol synthesis on Pd/ZnO catalysts [32]. Using a series of in situ surface analytical techniques such as XPS, LEIS, and PM-IRAS, it has been established that surface ensembles of PdZn exhibit a "Zn-up/Pd-down" corrugation. Bifunctional active sites both for reversible water activation as ZnOH and for reaction of methanol (via formaldehyde + ZnOH) toward CO_2 have been identified [3].

14.4 Polymer Electrolyte Membrane Fuel Cell: Electrocatalysts

Fuel cells are more efficient energy converters than the internal combustion engines or turbines. The hydrogen-fueled PEMFCs attract the highest interest especially from the car manufacturing companies. Biomass-derived liquid chemicals (ethanol, in particular, but also other chemicals such as ethylene glycol) as well as methanol can be used as fuels too. In this book, there are many examples related to the development of electrocatalysts with reduced Pt content and different ways have been discussed how we can move away from the Pt catalysts by developing Pt-free electrocatalysts with appropriate stability. The focus in the design of fuel-cell electrocatalysts will be laid on the reduction of Pt content and development of Pt-free electrocatalysts in the near future as well. Pt content can be reduced simply by increasing the electrochemically active surface via the reduction in the Pt particle size. However, dispersion of Pt particles cannot be increased limitlessly, as the particles that are very small lead to an increased resistance to electron transfer and increased adsorption strength of OH_{ads} blocking the active sites [33]. In order to increase the specific activity, different Pt nanostructured materials, such as polyhedral structures, nanowires, and branched structures, have also been designed [34].

Similar to Li-ion batteries, nanostructured carbon materials, especially carbon nanotubes (CNTs), as support of active metals can significantly enhance the electrocatalytic activity. The better electrocatalytic performance can be attributed

to (1) improved electron and mass transport on the boundaries of Pt and CNT, (2) higher conductivity of CNTs, and (3) modified electron structure of Pt facilitating hydrogen adsorption [35]. Nanostructured conductive transition metal oxides as supports are also under development [36].

14.5 Photocatalysts

As it is emphasized in various chapters of this book for the long term, solar energy will most likely take the leading position in the renewable energy production. Innovative but yet immature areas are the photocatalytic water splitting for hydrogen production and application of photoelectrocatalytic (PEC) devices for production of carbohydrates and long-chain alcohols from CO_2 [37–39]. PEC reactor is different from the conventional photoelectrochemical approach. In the latter case, processes at the anode and cathode take place under liquid phase. In contrast to this in PEC device, on the photocatalytic anode gaseous water is split using solar light to produce O_2, protons, and electrons. On the electrocatalytic cathode,, based on novel nanostructured carbon-based electrodes, CO_2 in the gas phase is converted using the protons and electrons coming from the photocatalytic side and passing through a Nafion membrane and a wire, respectively. Under anaerobic conditions this cell produces hydrogen, while in the presence of CO_2, formation of acetone, alcohols, and hydrocarbons is possible depending on the cathode electrocatalysts used and the temperature applied. Long-chain hydrocarbons and alcohols up to C_9–C_{10} are formed, with preferential formation of isopropanol using CNT-based cathode electrodes [37]. However, the productivity is very low and therefore further long-term R&D is necessary for commercialization of PEC devices.

A definite problem related to PEC solar cells is the need for a specific nanostructured photoanode material. The use of an array of 1D-aligned nanostructures (nanorods, nanotubes, etc.) improves light harvesting and limits charge recombination at the grain boundaries with respect to an assembly of nanoparticles. At the same time, a high geometrical surface area is maintained, which improves the photoresponse [40, 41]. As the photocatalytic anode in PEC devices, nanostructured TiO_2 has been proposed. The appropriate preparation method is the anodic oxidation of titanium thin foils to form ordered arrays of vertically aligned titania nanotubes [41, 42].

14.6 Conclusions

In conclusion, it can be said that in the remote future the solar energy will be dominating and the energy production from renewable resources will probably be delocalized, which lead to the necessity of dispersed, small-scale on-site energy production. Economic and efficient energy production in small scale obviously

generates a need for the development of novel catalysts, new reactor designs, such as microreactors and new catalytic technologies. The locally produced forms of energy should be easily and efficiently converted into each other. The connection of local energy production sites into "smart grids" would result in a robust, flexible energy supply system. Hydrogen seems to be the most appropriate energy carrier, which can be converted into electric power in fuel cells. Nevertheless, efficient hydrogen storage is still a challenge. Development of Li-ion batteries and supercapacitors with higher energy density is also in progress.

The production of liquid fuels for vehicular application has to be accomplished from renewable sources. Currently, in commercial scale only biodiesel can be prepared from biomass. Catalytic processes using CO_2 as carbon source in the production of liquid fuels are under development. It has to be mentioned that conversion of CO_2 not only to liquid fuels but also to chemicals, especially after the complete depletion of fossil resources, will have high importance as well.

It has been evidenced that catalysis has a crucial role in alternative energy production. Development of novel nanostructures and complex compositions is quite challenging; however, by means of appropriate catalysts environmental benign and economic production of energy can be attained.

References

1. Hansen TW, Wagner JB, Hansen PL, Dahl S, Topsoe H, Jacobsen CJH (2001) Atomic-resolution in situ transmission electron microscopy of a promoter of a heterogeneous catalyst. Science 294:1508–1510
2. Somorjai GA, Li YM (2011) Impact of surface chemistry. Proc Natl Acad Sci USA 108:917–924
3. Rameshan C, Weilach C, Stadlmayr W, Penner S, Lorenz H, Hävecker M, Blume R, Rocha T, Teschner D, Knop-Gericke A, Schlögl R, Zemlyanov D, Memmel N, Rupprechter G, Klötzer B (2010) Steam reforming of methanol on PdZn near-surface alloys on Pd(111) and Pd foil studied by in-situ XPS, LEIS and PM-IRAS. J Catal 276:101–113
4. Gon AWD, Cortenraad R, Jansen WPA, Reijme MA, Brongersma HH (2000) In situ surface analysis by low energy ion scattering. Nucl Instrum Methods Phys Res Sect B Beam Interact Mater At 161:56–64
5. Rupprechter G (2007) Sum frequency generation and polarization-modulation infrared reflection absorption spectroscopy of functioning model catalysts from ultrahigh vacuum to ambient pressure. Adv Catal 51:133–263
6. Bluhm H, Havecker M, Knop-Gericke A, Kleimenov E, Schlogl R, Teschner D, Bukhtiyarov VI, Ogletree DF, Salmeron M (2004) Methanol oxidation on a copper catalyst investigated using in situ X-ray photoelectron spectroscopy. J Phys Chem B 108:14340–14347
7. Paszti Z, Hakkel O, Keszthelyi T, Berko A, Balazs N, Bako I, Guczi L (2010) Interaction of carbon monoxide with Au(111) modified by ion bombardment: a surface spectroscopy study under elevated pressure. Langmuir 26:16312–16324
8. Somorjai GA, Li YM (2010) Major successes of theory-and-experiment-combined studies in surface chemistry and heterogeneous catalysis. Top Catal 53:311–325
9. Nielsen TK, Besenberg U, Gosalawit R, Dornheim M, Cerenius Y, Besenbacher F, Jensen TR (2010) A reversible nanoconfined chemical reaction. ACS Nano 4:3903–3908

10. Su DS, Schlögl R (2010) Nanostructured carbon and carbon nanocomposites for electrochemical energy storage applications. ChemSusChem 3:136–168
11. Wilson AM, Dahn JR (1885) Lithium insertion in carbons containing nanodispersed silicon. J Electrochem Soc 142:326–332
12. Hu YS, Demir-Cakan R, Titirici MM, Müller JO, Schlögl R, Antonietti M, Maier J (2008) Superior storage performance of a Si@SiOx/C nanocomposite as anode material for lithium-ion batteries. Angew Chem Int Ed 47:1645–1649
13. Wang Y, Cao GZ (2008) Developments in nanostructured cathode materials for high-performance lithium-ion batteries. Adv Mater 20:2251–2269
14. Centi G, Perathoner S (2008) Catalysis, a driver for sustainability and societal challenges. Catal Today 138:69–76
15. Pesaresi L, Brown DR, Lee AF, Montero JM, Williams H, Wilson K (2009) Cs-doped $H_4SiW_{12}O_{40}$ catalysts for biodiesel applications. Appl Catal A Gen 360:50–58
16. MacLeod CS, Harvey AP, Lee AF, Wilson K (2008) Evaluation of the activity and stability of alkali-doped metal oxide catalysts for application to an intensified method of biodiesel production. Chem Eng J 135:63–70
17. Issariyakul T, Kulkarni MG, Meher LC, Dalai AK, Bakhshi NN (2008) Biodiesel production from mixtures of canola oil and used cooking oil. Chem Eng J 140:77–85
18. Jacobson K, Gopinath R, Meher LC, Dalai AK (2008) Solid acid catalyzed biodiesel production from waste cooking oil. Appl Catal B Environ 85:86–91
19. Mosier N, Wyman C, Dale B, Elander R, Lee YY, Holtzapple M, Ladisch M (2005) Features of promising technologies for pretreatment of lignocellulosic biomass. Bioresour Technol 96:673–686
20. Cortright RD, Davda RR, Dumesic JA (2002) Hydrogen from catalytic reforming of biomass-derived hydrocarbons in liquid water. Nature 418:964–967
21. Huber GW, Dumesic JA (2006) An overview of aqueous-phase catalytic processes for production of hydrogen and alkanes in a biorefinery. Catal Today 111:119–132
22. Huber GW, Cortright RD, Dumesic JA (2004) Renewable alkanes by aqueous-phase reforming of biomass-derived oxygenates. Angew Chem Int Ed 43:1549–1551
23. Huber GW, Chheda JN, Barrett CJ, Dumesic JA (2005) Production of liquid alkanes by aqueous-phase processing of biomass-derived carbohydrates. Science 308:1446–1450
24. Valliyappan T, Bakhshi NN, Dalai AK (2008) Pyrolysis of glycerol for the production of hydrogen or syn gas. Bioresour Technol 99:4476–4483
25. Wilhelm DJ, Simbeck DR, Karp AD, Dickenson RL (2001) Syngas production for gas-to-liquids applications: technologies, issues and outlook. Fuel Process Tech 71:139–148
26. Zwart RWR, Boerrigter H (2005) High efficiency co-production of synthetic natural gas (SNG) and Fischer-Tropsch (FT) transportation fuels from biomass. Energy Fuel 19:591–597
27. Olah GA, Goeppert A, Prakash GKS (2006) Beyond oil and gas: the methanol economy. Wiley-VCH, Weinheim
28. Ehrfeld W, Hessel V, Löwe H (2000) Microreactors-new technology for modern chemistry. Wiley-VCH, Weinheim, pp 1–283
29. Suslu OS, Becerik I (2009) On-board fuel processing for a fuel cell-heat engine hybrid system. Energy Fuel 23:1858–1873
30. Domınguez M, Taboada E, Idriss H, Molinsc E, Llorca J (2010) Fast and efficient hydrogen generation catalyzed by cobalt talc nanolayers dispersed in silica aerogel. J Mater Chem 20:4875–4883
31. Neltner B, Peddie B, Xu A, Doenlen W, Durand K, Yun DS, Speakman S, Peterson A, Belcher A (2010) Production of hydrogen using nanocrystalline protein-templated catalysts on M13 phage. ACS Nano 4:3227–3235
32. Penner S, Jenewein B, Gabasch H, Klötzer B, Wang D, Knop-Gericke A, Schlögl R, Hayek K (2006) Growth and structural stability of well-ordered PdZn alloy nanoparticles. J Catal 241:14–19

33. Gasteiger HA, Kocha SS, Sompalli B, Wagner FT (2005) Activity benchmarks and requirements for Pt, Pt-alloy, and non-Pt oxygen reduction catalysts for PEMFCs. Appl Catal B Environ 56:9–35
34. Chen JY, Lim B, Lee EP, Xia YN (2009) Shape-controlled synthesis of platinum nanocrystals for catalytic and electrocatalytic applications. Nano Today 4:81–95
35. Antolini E (2009) Carbon supports for low-temperature fuel cell catalysts. Appl Catal B Environ 88:1–24
36. Shao YY, Liu J, Wang Y, Lin YH (2009) Novel catalyst support materials for PEM fuel cells: current status and future prospects. J Mater Chem 19:46–59
37. Centi G, Perathoner S, Rak Z (2003) Gas-phase electrocatalytic conversion of CO_2 to fuels over gas diffusion membranes containing Pt or Pd nanoclusters. Stud Surf Sci Catal 145:283–286
38. Centi G, Perathoner S, Rak Z (2003) Reduction of greenhouse gas emissions by catalytic processes. Appl Catal B Environ 41:143–155
39. Centi G, Perathoner S (2010) Problems and perspectives in nanostructured carbon-based electrodes for clean and sustainable energy. Catal Today 150:151–162
40. Centi G, Perathoner S (2009) Nano-architecture and reactivity of titania catalytic materials. Bidimensional nanostructured films. In: Spivey JJ, Dooley KM (eds) Catalysis, vol 21. Royal Society of Chemistry, Cambridge, pp 82–130
41. Mor GK, Varghese OK, Paulose M, Shankar K, Grimes CA (2006) A review on highly ordered TiO_2 nanotube-arrays: fabrication, material properties and solar energy applications. Sol Energy Mater Sol Cells 90:2011–2075
42. Ampelli C, Passalacqua R, Perathoner S, Centi G, Su DS, Weinberg G (2008) Synthesis of TiO_2 thin films: relationship between preparation conditions and nanostructure. Top Catal 50:133–144

Index

L. Guczi and A. Erdőhelyi (eds.), *Catalysis for Alternative Energy Generation*,
DOI 10.1007/978-1-4614-0344-9,